Proceedings of the Second International Symposium on

DYNAMICS OF FLUIDS IN FRACTURED ROCK

Foreword

Table of Contents

February 10–12, 2004

Edited by

Boris Faybishenko and Paul A. Witherspoon

Earth Sciences Division
Ernest Orlando Lawrence Berkeley National Laboratory
University of California
Berkeley, California 94720
U.S.A

Ernest Orlando Lawrence Berkeley National Laboratory is administered for the U.S. Department of Energy by the University of California under Contract No. DE-AC03-76SF00098

Foreword

This publication contains 90 extended abstracts* of papers from 13 countries presented at the Second International Symposium on Dynamics of Fluids in Fractured Rock, held at Lawrence Berkeley National Laboratory (Berkeley Lab) February 10–12, 2004.

The challenge of adequately characterizing fluid flow and chemical transport in fractured media is a formidable one for geoscientists and engineers. Understanding fluid dynamics and transport through fractured rock is crucial for the exploitation of petroleum and geothermal reservoirs, the safe environmental management of groundwater, and the isolation of radioactive waste in underground repositories. The Second International Symposium on Dynamics of Fluids in Fractured Rock provides an occasion for review, and a forum for discussion, of the most recent theoretical and experimental investigations and modeling studies.

The First International Symposium on Dynamics of Fluids in Fractured Rocks: Concepts and Recent Advances was held at Berkeley Lab on February 10–12, 1999. (Copies of the 1999 Symposium Proceedings can be obtained from Boris Faybishenko at bfayb@lbl.gov.) The monograph *Dynamics of Fluids in Fractured Rock*, containing 26 selected papers from the First Symposium, was published by the American Geophysical Union (AGU) in the Geophysical Monograph Series, Vol. 122, 2000.

The topics of this Second Symposium are more diverse than those of the First, and are a result of the scientific and practical developments and progress achieved over the past five years. The papers of the Second Symposium are related to fluid flow and chemical transport in fractured rock, in both the unsaturated and saturated zones, including

- Recent advances in modeling, uncertainty analysis, and scaling
- Methods of field and laboratory experiments
- Investigations of coupled processes and geothermal resources, reactive chemical transport, and microbiological processes
- Nuclear waste disposal
- Oil and gas reservoirs in fractured rock
- Magma flow
- Optimization of fractured rock investigations and data analysis

We would like to emphasize that the Second Symposium includes a number of papers on geochemistry and chemical transport. Several papers are devoted to detailed investigations using small-scale imaging of flow in fractures, exploiting cutting-edge technology that is essential for better understanding of the physics of flow and transport in fractures. Other papers discuss the

* Some abstracts within this collection were prepared using U.S. government funding. As such, the government retains a nonexclusive, royalty-free, worldwide license to use those articles for internal government purposes. Questions regarding individual abstracts should be directed to the respective author(s).

application of geophysics on a field scale. In addition, some papers report on the intensive experimental field and laboratory studies that have led to the improvement of conceptual models and the development of new mathematical models for flow and transport in fractured rock. It should also be mentioned that many of these papers, directly or indirectly, demonstrate the need for researchers to use the wealth of experience gained from investigations of heterogeneous soils, in particular preferential flow phenomena observed at many sites in structured and heterogeneous soils.

We expect that the *Proceedings of the Second Symposium* (and accompanying CD with color figures) will provide valuable information for different aspects of fractured-rock investigations and will be used by governmental agencies, universities, research organizations, and private companies in solving a variety of fundamental problems in the earth sciences.

We appreciate the support for the Second Symposium provided by Berkeley Lab. We thank Daniel Hawkes, Julie McCullough, Kryshna Avina, and Donald Nadora of Berkeley Lab for production of these *Proceedings*, and Maria Atkinson for design of the cover and creation and updating of the Symposium website. We also thank Ed Casey of Confex, Inc., for the technical support of the Symposium website, and Kathleen Brower and Patricia Butler of Berkeley Lab for their organizational support.

Symposium Organizing Committee

Sally Benson, Bo Bodvarsson,
Donald DePaolo, Boris Faybishenko,
Iraj Javandel, Marcelo Lippmann,
Tadeush Patzek, and Paul A. Witherspoon

Berkeley, California
February 2004

Table of Contents

Session 1:
KEYNOTE PRESENTATION

Development of Underground Research Laboratories for Radioactive Waste Isolation

Paul A. Witherspoon, Earth Sciences Division
Lawrence Berkeley National Laboratory

The following report is a review of the development of underground research laboratories that are being used to characterize the parameters of rock systems in which repositories may be constructed for the isolation of radioactive wastes.

The Stripa project in Sweden involved the development of the first underground research laboratory (URL) in which large-scale underground investigations were carried out in a fractured granitic rock to develop the technology needed to characterize such a system and determine its suitability for the purposes of radioactive waste isolation. The project started July 1, 1977, when the Energy Research and Development Administration (ERDA) (successor to AEC and now part of DOE) executed a bilateral agreement with the Swedish Nuclear Fuel Supply Company (SKBF) to carry out a program of investigations at Stripa, an old iron-ore mine in central Sweden. The Lawrence Berkeley National Laboratory (LBNL) was designated as the lead participant for the United States. LBNL and SKBF set up a program of investigations in the granitic rock mass, at a depth of 320 m, involving hydrogeology, geochemistry and isotope hydrology, electric heater tests, and a large-scale permeability test. The results of this pioneering effort in a URL in granite attracted considerable interest, and in November 1979, representatives of Canada, Finland, Sweden, Switzerland, and the United States met in Stockholm to discuss an expansion of this effort. This led to the development of the International Stripa Project that continued a program of research activities at Stripa until 1992.

In 1980, the Nuclear Research Establishment (SCK/CEN) in Belgium started the development of their HADES project at Mol, in northeastern Belgium. This was the first URL to investigate the possibilities of using clay, the socalled “Boom clay” (Oligocene), as the host rock for a waste repository. Exploratory drilling revealed that the Boom clay satisfied expectations; this plastic material has good sorption capacities, a very low permeability, and low but sufficient heat capacity. It is sufficiently thick and homogeneous, and it is chemically and mineralogically stable. In 1980, a vertical shaft for the URL was constructed down to a depth of 245 m using a freezing procedure to stabilze the sediments; it turned out this procedure was not needed. Validation exercises for the modeling of different processes were launched and extensive performance assessment exercises were carried out. The methodology was elaborated with involvement and consensus of a large number of scientists from different countries, active in the various fields of this multidisciplinary activity. By the end of 1999, a second shaft was constructed to provide for a gallery to extend beyond the HADES URL for the PRACLAY project. Two types of investigations were envisioned. One was concerned with effects of decompression and the feasibility of digging an array of disposal galleries for a repository. That effort was successfully completed in 2002. The other investigation was to set up a pilot gallery with electrical heaters to investigate the effects of thermal loads, but in reviewing results to date, SCK/CEN has concluded that a large scale project, as initially planned, will not be possible in the near future. Therefore, the PRACLAY experiment is now being redefined.

The URL near Pinawa, in the Province of Manitoba, has been the Canadian site for geotechnical and hydrogeological investigations for 23 years. The URL is situated in a granite batholith towards the western edge of the Precambrian Canadian Shield. Between 1978 and 1996, Atomic Energy of Canada (AECL) took a lead role in developing the disposal technology. Since 1997, Ontario Power Generation, the principle producer of nuclear fuel waste in Canada has assumed the responsibility under its Deep Geologic Repository Technology Program. Starting in 1982, AECL constructed the URL at Pinawa to provide a representative geological setting for conducting research and development activities in support of the Canadian Nuclear Fuel Waste Management Program. This involved the construction of a shaft to the 240 m level for a program of investigations, and later to the 420 m level for an expansion of this program. The objective was to conduct activities to support both site evaluation and underground experimentation. The site evaluation program was to involve characterization of the rock mass, groundwater flow systems and groundwater chemistry of the geologic environment, and the underground program was to involve studies of the geologic barrier and the engineering components of the repository sealing system. The results from over twenty years of investigations at the Pinawa URL have done much to achieve these objectives.

In 1980, Nagra (National Cooperative for the Disposal of Radioactive Waste) started some exploratory drilling operations in the Bernese Alps in southern Switzerland in what became known as the Grimsel Test Site (GTS). They used the main access tunnel for an existing hydroelectric station at a point, about 450 m below the surface, where they found favorable rock (granite/granodiorite) conditions for a URL. The GTS was constructed in 1983/84 and extended in 1996 and 1998 to accommodate a growing program of investigations. In 1990, a special controlled zone (IAEA type B/C) was set up to allow *in situ* use of radionuclides. Field work at Grimsel has been ongoing since 1983, with the aim of answering geological, hydrogeological, geophysical, geochemical and engineering questions. The projects have been allocated to different technical areas that are important in the process of realizing a deep geological repository. These projects were organized in phases, and at present, the current program of investigations is in Phase V for the period 1997-2004. The various projects that Nagra has carried out over the years at Grimsel have generated considerable interest among other countries, who are working on problems of radioactive waste isolation. As a result, in developing the research program for Phase V, Nagra was able to organize an international collaboration with 19 partner organizations from 10 countries participating.

Nagra has also become very interested in exploring the possibilities of using clay formations for disposal purposes. They have had an ongoing research program in their Mont Terri URL since 1996, with the aim of investigating the geological, hydrogeological, geochemical and geomechanical properties of the Opalinus Clay. The URL is located in northwestern Switzerland in an offset of the Mont Terri motorway tunnel that passes through the clay bed at a depth of about 300 m. A layout of niches and tunnels that were excavated from a security tunnel, adjacent to the motorway, provide access to the clay bed. The Mont Terri project was setup at the very beginning as a collective effort. The project is steered and financed by eleven project partners and consists of a series of experiments organized into one-year phases. The partners can propose new experiments for each phase and decide in which experiments they wish to participate. The steering and financing of the individual experiments are then the responsibility of the participating partners. Experimental investigations in the Opalinus Clay have faced some unusual problems. Since this clay layer has a high clay content (55% non-swelling, 10% swelling) and a

very high proportion of fine rock pores, it reacts on contact with water by swelling and breaking into fine fragments at the contact surface with water. Drilling and investigation technologies developed for hard rock such as granite cannot be used directly in the Opalinus Clay. If water is used as a drilling fluid or in hydraulic packer tests, then boreholes in this clay often become unstable. They show convergence due to swelling of the clay and often collapse completely. One of the first objectives in the research program at Mont Terri has been to test and develop suitable drilling and measurement techniques for characterizing this particular clay formation.

For almost 30 years, the Swedish Nuclear Fuel and Waste Management Co. (SKB) has been considering what the repository will look like and what materials and technology will be used in its design and construction. To prepare for the siting and construction of a deep repository, SKB has built a URL on the island of Äspö outside Oskarshamn. The laboratory is designed to meet R&D requirements and consists of a 3,600 m long tunnel going down in a spiral to a depth of 450 m. The principle alternative involves encapsulating the spent fuel in copper canisters and embedding each canister vertically in bentonite clay at a depth of about 500m. The reference canister consists of a 50 mm thick copper cylinder with welded-on top and bottom. A copper canister is nearly five meters long and weighs between 25 and 27 tons when it is filled with spent fuel. In other words, it is not easy to handle, especially not in the confined spaces that exist in the five-meter emplacement tunnels that SKB envisions. To be able to insert a canister in a deposition hole, SKB has developed a prototype of a remote-controlled and radiation-shielded deposition machine, which is currently being used in emplacing and retrieving canisters at Äspö. SKB is also testing the technology for backfilling and plugging tunnels. In 1999, SKB backfilled and plugged a 30 m long test area in a drill-and-blast tunnel in Äspö, and during the next few years, the sealing capacity of the backfill and plug will be monitored. Since the proposed repository has been designed in such a way that it is possible to retrieve deposited canisters, SKB must develop and test a method for retrieval. A full-sized canister is to be placed in a deposition hole at Äspö and surrounded with bentonite; the main goal for this test is to develop the procedure for freeing the canister from water-saturated bentonite. SKB is also planning to test and demonstrate a full-scale repository at Äspö with state-of-the-art technology over a period of 10 to 15 years. This will be done in a prototype that has been constructed in accordance with what they call the KBS-3 design. All conditions in this prototype, with respect to geometry, materials and rock conditions, are identical to a real repository. However, to provide the thermal field, electric heaters will be used in place of spent fuel. The purpose of the prototype repository is to simulate the integrated function of the repository components and to provide a full-scale reference for comparison with models and assumptions.

The Yucca Mountain project in the US State of Nevada differs significantly from the other projects discussed above because of its location in a desert setting, in an alternating system of welded and nonwelded tuffs, with an arid climate and a water table that is 600 m or more below the surface. As a result, the site for a potential radioactive waste repository that is being investigated will be in the unsaturated zone (UZ) about 300 m below the surface. The evaluation of the Yucca Mountain site has evolved from intensive surface-based investigations in the early 1980s to the current focus on testing in underground drifts. A wide range of activities including drilling/excavations, testing, and modeling has been carried out in an effort to characterize the rock mass and its behavior under repository conditions. The emphasis has been on the critical factors that control fluid movement through an unsaturated and fractured system of tuff layers and how this behavior may be altered by the application of heat.

The US Department of Energy selected Yucca Mountain for detailed study and initiated site investigations in the early 1980s. A Site Characterization Plan (SCP) was completed in 1988 for systematic surface-based investigations, underground testing, laboratory studies, and modeling activities. The activities may be grouped into four distinct periods: (1) the early 1980s, (2) the period from 1986 to 1991, (3) the early 1990s, and (4) the current period (mid 1990s to the present). During the first period, the drilling of boreholes from the land surface was the main focus. Most of the early deep boreholes were drilled away from the potential repository block along nearby washes and were used to define the stratigraphy, locate the water table, collect cores, and test *in situ* borehole monitoring techniques. The results lead to a conceptual model for the Yucca Mountain site involving flow and transport through alternating welded and nonwelded tuff layers, intersected by major faults. The second period, from 1986 to 1991, was devoted to the development of characterization plans, including the formulation of quality assurance programs. Near-surface monitoring and intensive laboratory measurements of flow and transport parameters were carried out. Since the tuff layers are gently tilted to the east, the design of the original shaft access for the Exploration Studies Facility (ESF) in the SCP was revised to allow a ramp access, using nearly horizontal ramps, from the base of the eastern slope. During this period, discrete and continuum models for fractured media were explored. The heat transfer and thermal-hydrological (TH) modeling methodologies were also established. The third period, in the early 1990s, launched the specific design, preparation, and excavation of the ESF for underground access to the tuff units. Borehole drilling was resumed over the block for UZ investigations and along the North Ramp of the ESF for design and geotechnical evaluations. Collections of samples for hydrological and geochemical characterization (especially for ^{36}Cl and calcite studies) were intensified, and networks of boreholes were instrumented for pneumatic and moisture monitoring. During this period, the integration of site data into models was initiated, and the basic probabilistic approach for total system performance assessment (TSPA) was improved.

During the current period, the mid 1990s to the present, excavation of the main loop of the ESF and the Cross Drift was completed, alcoves and niches (short 10 m drifts) were excavated, and boreholes were drilled for enhanced characterization of the repository block. A Tunnel Boring Machine (TBM) was used from 1994 to 1997, to construct the 8-m-diameter ESF approximately 8 km in length. A smaller TBM was used in 1997 and 1998 to construct a 5-m-diameter Cross Drift that is 2.7 km in length. The alcoves and niches, in various parts of the ESF, have been used in a comprehensive program of underground testing. The main focus of the testing activities has been on the UZ processes that control seepage into drifts, heat transfer around drifts, and transport through the UZ. Underground studies have evolved through stages as they develop new emphases and different approaches. The effect of climate is another critical factor. Modern data have been collected in and around the Yucca Mountain site since 1998, and climate studies have also used long-term records of analog sites to project future climates. Nearly 95% of the 170 mm/year precipitation over the site is either run-off or is lost to evaporation. Considerable effort has been expended to determine the current percolation flux that is estimated to range from 1 to 10 mm/year.

In the middle 1990s, methodologies developed and deployed in surface-based testing were applied to most of the alcoves. Four alcoves along the North Ramp of the ESF and two along the Ghost Dance fault were predominantly used as drill bays for horizontal and slanted boreholes to collect cores, measure air permeability, and sample gases. Recognizing the need to address the

water issue directly, a different set of tests has evolved that use water and aqueous phase tracers to directly evaluate flow and transport processes. In addition to niches, Alcove 8, and systematic testing in the Cross Drift, Alcoves 1, 4, and 6 were utilized for liquid tests at different scales for seepage, fracture-matrix interaction, and matrix diffusion processes. Water has also been mobilized, by heating and vaporization, in evaluating the thermal-hydrological-chemical-mechanical coupled processes in fractured tuff in the single heater and drift scale thermal tests at Alcove 5.

The evolution of the geological, hydrological, transport, and thermal tests indicates that a vast amount of knowledge has been gained about the UZ processes at Yucca Mountain. The focus shifted from intensive surface-based investigations in the early 1980s to underground testing in the late 1990s.The current focus of the testing program is to capture the essence of a progression for tests to improve process understanding, remove conservative estimates, and enhance realistic representation of UZ processes at Yucca Mountain.

Session 2:
FIELD AND LABORATORY EXPERIMENTS

Active Flow Path Evaluation in the Unsaturated Zone at Yucca Mountain

J.S.Y. Wang

Earth Sciences Division
Lawrence Berkeley National Laboratory

With limited water input associated with arid climate and a thick unsaturated zone with a deep water table, the quantification of active flow paths through fractured rocks is technically challenging at Yucca Mountain. An active flow path refers to a feature with liquid water moving along it. The flow path can be located along a fracture or a fault, through fracture network, located in porous matrix, or through a combination of heterogeneous media. Both naturally occurring features and artificially induced flow paths from water injection were observed and tested for the active flow path evaluation in underground drifts at Yucca Mountain. Figure 1 illustrates an ambient flow path observed as a continuous dark feature and flow paths stained by injection of colored dyes. These images are valuable for the development of a basic understanding and for the design of subsequent tests for the evaluation and quantification of active flow paths. For example the first and only documented wet feature at the repository level in Figure 1a had a width of approximately 0.3 m (1 ft.). This width was used as a basis for setting the injection interval isolated by packers so that the induced flow paths are similar in width to the naturally occurring feature.

No continuous flowing feature has been observed along the underground drifts excavated in the late 1990s at Yucca Mountain. Ventilation-induced drying of naturally occurring active flow paths is one of the first explanations for the absence of visual evidence. This interpretation is supplemented by the capillary barrier mechanism unique to the unsaturated zone, with unsaturated matrix and fractures holding the water to the formations. If the capillary force is strong enough to overcome gravity, no flow into the drift (referred to as *seepage*), can occur. The quantification of the seepage processes, in particular the confirmation of the existence of seepage threshold flux below which no seepage can occur, was carried out by a series of seepage testing from 1997 to 2003 in five niches. The field-determined thresholds and seepage evolution data have been used to calibrate and validate fracture continuum based seepage models.

In addition to the seepage tests in niches with release of water nominally within a meter above the niche ceiling, liquid release tests have been conducted at other larger test beds. Two test beds have slots excavated below the liquid releases points to quantify mass balances. The release points are over one meter above the slots at these two test beds. A series of short-term tests have been conducted along fractures in a fractured welded tuff unit (at Alcove 6), and along a fault in a porous non-welded tuff unit (at Alcove 4). These tests quantify the interaction of flow paths with unsaturated matrix. Two large-scale long-term tests have also been conducted, with infiltration sources on the ground surface (30 m above Alcove 1) and in controlled plots (at the Alcove 8 approximately 20 m above Niche 3). These large-scale tests focus on the transport of tracers and demonstrate the importance of matrix diffusion along flow paths, in addition to seepage into the alcove or niche below.

To synthesize the findings of the hydrological field-testing results, this evaluation starts with the analyses of the variability of wetting front velocities of the first pulses after liquid releases at different sites under different testing conditions. The velocity variability is compared with the much higher variability of measured permeability, representing the spatial heterogeneity quantified by air-injection testing. Subsequent pulses have generally faster velocities and result in higher seepage. The time-dependent effects of matrix imbibition and diffusion on active flow and transport contribute to interpretation of these wetting-history-dependent results. The implication of these findings are then utilized for further understanding of seepage processes and to address fundamental hydrological issues of extrapolation of drift-scale findings to site-scale assessment, especially for the lower lithophysal tuff unit where 80% of emplacement drifts are located. Figures 1a and 1b (for a dyed flow path) illustrate the results of observations at the first niche in the middle nonlithophysal tuff unit, which is fractured with no lithophysal cavities. The flow paths are essentially vertical, indicating dominance by gravity. Figures 1c–d illustrate that the capillarity is very strong in the lower lithophysal tuff unit, overcoming the gravity to result in a nearly uniform dye pattern (Figure 1c) and with the capacity to move water and dye into the floor of a cavity (Figure 1d).

While the seepage, fracture-matrix interaction, and infiltration/matrix diffusion processes are tested at niches, alcoves, and between drifts, the effects of spatial heterogeneity and natural variability of active flow paths are not as easily quantified. Here, we analyze the available systematic testing results and complementary feature-based approaches, and summarize the current understanding of the active flow paths. With only one naturally occurring flow path (of the magnitude illustrated in Figure 1a) observed, it is a challenge, with large uncertainty, to estimate the spacing between active flow paths. The active flow path spacing is one of the important factors in determining the focusing, channeling, and redistributing of limited infiltration through the unsaturated zone into emplacement drifts. If the focusing is strong enough, the seepage threshold can be overcome, and the water can drip into the emplacement drifts, affecting the corrosion potential of engineered barrier structures located in the drift. On the other hand, if the spacing is large, only a small fraction of emplacement drifts will be intersected by the active flow paths, and the rest of the drifts will be essential dry. We evaluate active flow path spacing and flow focusing based on Figure 1a and other available information and observations of smaller wet features.

Clearly, the design of engineered structure and material emplacement can be further optimized with the active flow path evaluations. The overall advantages of using unsaturated zone attributes for waste emplacement and isolation are emphasized in this summary of active flow path evaluation in the unsaturated zone at Yucca Mountain.

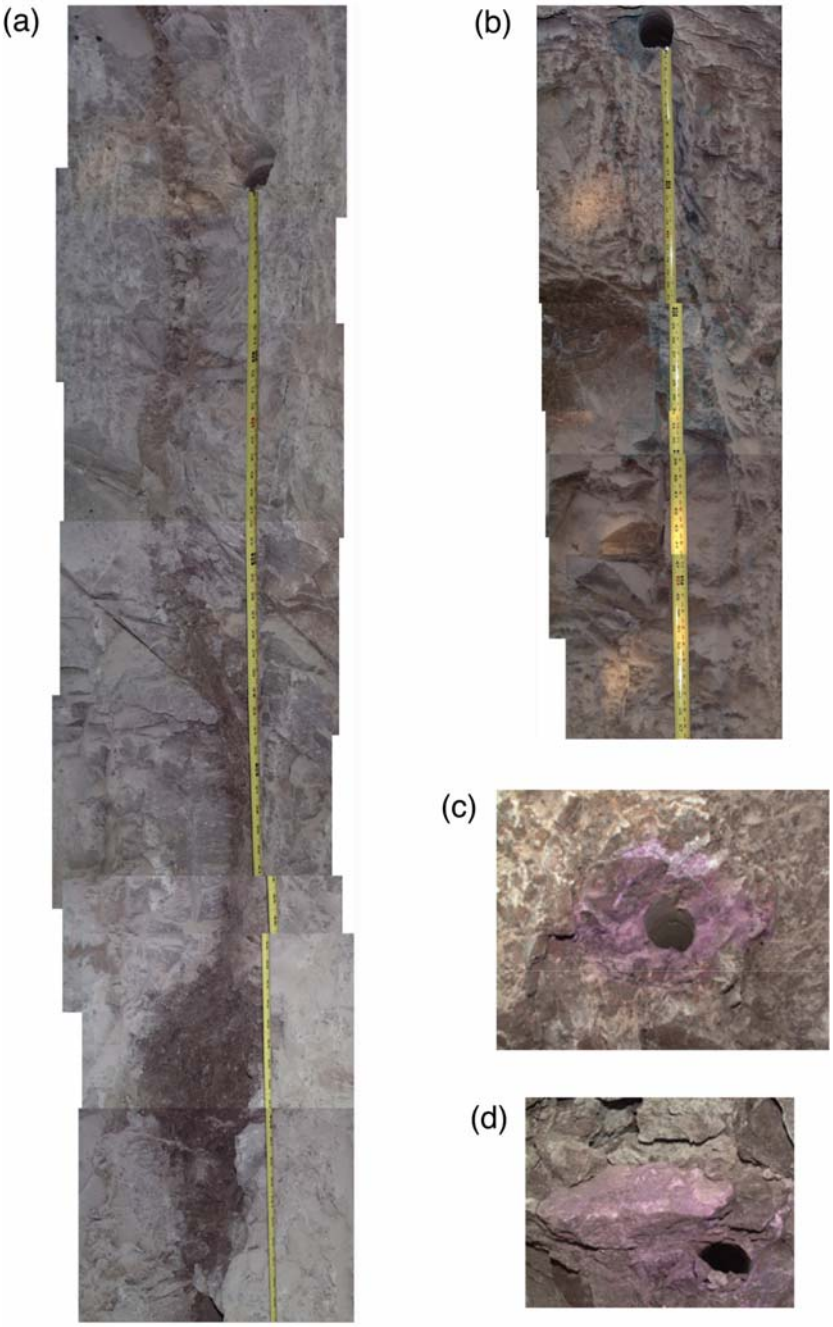

Figure 1. Photographic Illustrations of Flow Paths Observed During Niche Excavations: (a) Ambient Flow Path at Niche 1, (b) Blue-Dyed Flow Path at Niche 1, (c) Pink-Dyed Flow Path at Niche 5, (d) Pink Stain on the Floor of a Lithophysal Cavity at Niche 5. Niche 1 is the first niche located 3,566 m from the North Portal of the Exploratory Studies Facility, in the middle nonlithophysal zone of theTopopah Spring welded tuff unit (TSw). Niche 5 is the fifth niche located 1,620 m from the Cross Drift entrance in the lower lithophysal zone of the TSw.

Grimsel Test Site: 20 Years of Research in Fractured Crystalline Rocks—Experience Gained and Future Needs

S. Vomvoris, W. Kickmaier, I. McKinley
Nagra, Hardstrasse 73, CH-5430 Wettingen, Switzerland

A Brief History

The Grimsel Test Site (GTS) is located within the granitic rocks of the Alps at an altitude of approximately 1,730 meters above sea level (masl). The main tunnel system, with a diameter of 3.5 m, was excavated with a full face tunnel boring machine between May and November 1983. The remaining works, e.g., caverns and branches of the main access tunnel, were excavated by means of blasting, and the facility was finished in May 1984. The formal inauguration of GTS was on June 20, 1984.

At that time Nagra was participating in the Stripa project and was in close contact with the AECL in Canada, which was constructing the URL in Manitoba. Considering the studies undertaken or planned in those two laboratories, Nagra set forth the following objectives for GTS [1]:

- Checking the applicability of foreign research results to geological conditions in Switzerland
- Carrying out specific experiments which are necessary in the context of Nagra disposal concepts
- Acquisition of know-how in planning, implementation and interpretation of underground tests in different experimental areas
- Acquisition of practical experience in development, testing and use of experimental apparatus and measurement methods

A series of experiments in the following areas were to be carried out: excavation tests, rock stress measurements, geophysics, hydrogeology, solute migration, neo-tectonics, heat-induced processes, and laboratory experiments. The experiments were conducted by Nagra or bilaterally with BGR or GSF (later GRS) both under the auspices of the German Ministry of Research and Technology, and SKB. In 1988, as part of the USDOE/Nagra cooperative agreement, a series of additional experiments were introduced in Grimsel, focusing on geophysical techniques and development of interdisciplinary methodologies for the hydrologic and geologic characterization of fractured rocks. Also in 1988, JNC joined the migration experiment, which a few years later resulted in the first performance of *in situ* tests with radionuclides. The international cooperation was further strengthened in the mid-1990s and was significantly expanded with Grimsel Phase V (1997-2002), which was implemented in co-operation with 19 partners from 10 different countries and the European Community (Table 1).

2003—What Have We Achieved?

Twenty years later, more than 30 different projects have been performed in GTS; they are summarized in [2] and numerous publications—see also www.grimsel.com. The objectives for the GTS were successfully accomplished. One can list reasons for this conclusion:

- Tools and techniques were transferred to Switzerland,
- They were further developed, tailored to Nagra's needs and, where necessary, complemented by novel approaches,
- Local teams with wide expertise were developed,
- Cooperation with national and international partners was strengthened and solidified,
- Results from GTS were applied directly to Nagra's site characterization activities (e.g., geophysics, multi-packer borehole testing, fluid logging, borehole sealing) and performance assessment (e.g., development of geologic data-sets for performance assessment, development of models and parameters for radionuclide migration in fractured rock, site-scale groundwater flow modeling),
- GTS has played a crucial role in interacting with the general and scientific public, and it is still a frequently visited site.

Table 1. GTS Phase V experimental programs and partners.

GTS Phase V Project	**Partners ***
High pH-Plume in Fractured Rocks (HPF)	NAGRA, JNC, SKB, US-DOE, SNL, ANDRA
Colloid and Radionuclide Retardation (CRR)	NAGRA, BMWi [1)] FZK/INE, ENRESA, JNC, US-DOE, SNL, ANDRA
Gas Migration in Shear Zones (GAM)	NAGRA, ENRESA, US-DOE, SNL, ANDRA
Full-scale Engineered Barrier Experiment (FEBEX) FEBEX I ('95-'99); FEBEX II ('99-'03)	ENRESA, EC with 25 European partner organizations, NAGRA, BBW
Gas Migration Test in the EBS and Geosphere (GMT)	RWMC, NAGRA, Obayashi
Effective Parameters (EFP)	BMWi, BGR, GRS, NAGRA
Conclusion of the Tunnel Near Field (CTN)	NAGRA, BMWi, GRS, BGR, ERL/ITRI

* NAGRA: National Cooperative for the Disposal of Radioactive Waste, Switzerland / SKB: Swedish Nuclear Fuel and Waste Management, Sweden / US-DOE: US Department of Energy, USA / SNL: Sandia National Laboratories, USA / ANDRA: Agence national pour la gestion des déchets radioactifs, France / BMWi: Bundesministerium für Wirtschaft und Technologie, Germany / FZK/INE: Forschungszentrum Karlsruhe, Institut für Nukleare Entsorgungstechnik, Germany / ENRESA: Empresa Nacional de Residuos Radioactivos, Spain / GRS: Gesellschaft für Anlagen- und Reaktorsicherheit, Germany / BGR: Bundesanstalt für Geowissenschaften und Rohstoffe, Germany / RWMC: Radioactive Waste Management Center, Japan / ERL/ITRI: Energy and Resources Laboratories Industrial Technology Research Institute, Taiwan / JNC: Japan Nuclear Cycle Development Institute, Japan / EC: European Community / BBW: Swiss Federal office for Education and Science

[1)] changed due to BMWA: Bundesministerium für Wirtschaft und Arbeit, Germany

A few of the lessons (technical and non-technical) of more general interest may be highlighted:

Solute transport in fractured rocks is more complex than represented in early modes. Early models based on parallel plate or single tube concepts involved oversimplification of key processes. Through the work at GTS [3,4], we have: (i) made significant progress in the understanding of the undisturbed system; (ii) developed technology for micro-scale flow system characterization (for example, the resin immobilization technique) and (iii) obtained better models to relate laboratory studies to observations in the field. The ways forward are (a) to perform studies of the disturbed system which considers the impact of the repository itself (e.g., effect of high pH plume, colloids etc)—some of which have been initiated as part of Phase V; and (b) to conduct experiments under more realistic conditions, representing the flow systems, which would require very long term experiments (see next section).

Repository implementation (construction, remote handling, monitoring, sealing) can be substantially optimized. Through the work at GTS: (i) full or large scale demonstration projects have highlighted potential areas of improvement and had an effect on Nagra's designs (for example, combination of bentonite blocks and pellets as a buffer); (ii) monitoring technologies have been developed and tested; and (iii) important QA aspects have been identified. As can be seen in the last section however, there are many areas here where further work will be very beneficial.

Characterization and evaluation of a site is an interdisciplinary activity. It is rather the norm to structure organizations by department and, for particular projects, to try to involve the most suitably trained specialists. When it comes to characterizing and evaluating a natural site, however, there is not a single discipline that can provide all the relevant input. This inter-disciplinary nature is exemplified by the Migration Experiment [3], where the tools that Nagra uses for modeling radionuclide migration in fractures have been developed, tested and improved. The successful prediction of the last series of radionuclide migration, was due to the careful and interactive build up first of the concepts for radionuclide migration and then of the resulting numerical models. Disciplines partaking in this effort involved geology, mineralogy, hydrogeology, hydrochemistry, mathematical and chemical modeling, and laboratory experimentation to mention a few. Nagra learned from this experience and applied this experience to the crystalline program in Northern Switzerland and the evaluation of the Valanginian marls in Central Switzerland. This resulted in an improved interface between site characterization and performance assessment, the so-called "geo-dataset," which is the set of concepts, parameter values and ranges, resulting from the site characterization, tailored to the input required by performance assessment (and engineering design). This need is now recognized in other programs and the geo-dataset approach or "site investigation data flow" is adopted or further developed in several national projects.

Demonstration aspects are as important as technical ones. The benefit of communication with the public is not normally featured on the highest priority list of a scientific program (and it was not one of the original objectives of establishing GTS). 1:1 scale experiments were thus mainly driven by scientific and engineering objectives. Experience at GTS has, however, shown that issues related to waste disposal can be very effectively communicated to a broad spectrum of the public in such a facility [5]. One of the most challenging aspects is how to communicate at the appropriate abstraction level for each group, without reducing the scientific quality. Many different forms have been tried in Grimsel (brochures, leaflets, posters, videos etc) but, in the

end, nothing can substitute for the physical images and personal experience that site visitors carry away. This is now increasingly acknowledged as a key role—public acceptance being seen to be critical to repository site selection.

Knowledge and experience needs to be transferred to the next generation. The existing projects have formed a good basis for training (e.g., M.S. or Ph.D. projects). Nevertheless, a systematic effort to transfer the knowledge to the next generation, which will construct, operate and regulate future repositories, is currently lacking. Such experience cannot be transferred by lectures and books alone, but hands-on work is also required (learning by doing). A challenging program of R&D issues associated with links to Demonstration and Validation projects could form a good basis for this.

2003—Future Needs

With respect to fundamental research on the characterization of fractured rocks and understanding of the processes relevant to radioactive waste disposal, most of the work that could easily be done in GTS has been already performed. More complex, interdisciplinary experiments have also been successfully performed. Are there any needs then, for future work and operation in Grimsel? This question was posed by Nagra, internally, and it was also discussed with GTS partners in various workshops in 2002 and 2003. Many different areas of interest were identified, reflecting the progress achieved and current state on different disposal programs. Needs for a particular experiment can be dictated by, for example, science (understanding/characterization), performance assessment, engineering, licensing or implementation. There is an obvious shift for many programs towards licensing or implementation, which would pose different objectives from those noted 20 years ago.

Considering the input received and Nagra's own needs, in 2003 Nagra launched GTS Phase VI with planning horizons, set not by artificial constraints, but by the planning time-scales for implementation of repositories [6]. Phase VI objectives have also evolved from those set in 1983, including the following:

- Develop further and maintain know-how for key engineering issues like: handling, emplacement, monitoring and retrieval of high-level waste,
- Apply state-of-the-art science to validate key models over long periods (all waste types) by longer-term radionuclide retardation projects,
- Raise confidence and acceptance in key concepts prior to the repository licensing/construction by full-scale engineering projects,
- Act as a focus for scientific collaboration in the waste management community by providing access to a facility with flexible, open boundary conditions,
- Provide a center for training future generations of "nuclear waste"-experts (considering the needs of implementers, regulators and research organizations),
- Provide an infrastructure for technical PR.

Three areas will be highlighted here namely: (1) large-scale demonstration of concepts, (2) longer time scales, and (3) training. Experiments to be performed or under consideration for GTS Phase VI will be further discussed in the presentation.

As mentioned in the previous section, current demonstration tests have pointed out areas where improvements are needed. The ways forward are to: (1) perform more realistic (e.g., remote handling) full-scale tests considering concept optimization, practicability, etc, and (2) explicitly address socio-political requirements, such as recovery from operational perturbations, monitoring and retrieval. There are special issues for fractured rock, but many concerns are generic (rock-independent), and it will be beneficial to address them in a well-characterized and controlled environment such as Grimsel.

Confidence building can be obtained through the performance of long time-scale experiments. For this purpose, experiments had to be performed under accelerated conditions. For example, the hydraulic gradients imposed and the flow fields generated can be orders of magnitudes higher than those expected to occur in a natural system. The reasons for this were mainly operational and the boundary conditions set by short-term requirements of national programs. Consequently, on many occasions, the results of the experiments have to be interpreted conservatively; for example, beneficial effects of kinetics would be ignored. It will thus add to the confidence in the results used in performance assessment and remove some of the over-conservatism invoked if more realistic experiments are performed over longer time scales.

Training in waste disposal has been identified by many national and international organizations as one of the key areas to focus effort. This is not surprising, since the generation that led the development of many of the waste disposal programs in the mid- to late-70s is being lost to retirement, while, at the same time, emerging programs are confronted with many of the same issues. Grimsel provides an excellent opportunity to have hands-on training and practical experience, not only with fractured-rock specific issues, but also with the most general non-rock specific issues of engineered barrier characteristics and experiment planning and performance. Through its close links to the recently established International Training Centre (www.itc-school.org), Grimsel is actively contributing in this area and the first training course was held in the fall of 2003.

References

1 Nagra, “Grimsel Test Site—Overview and Test Programs,” Nagra Technical Report NTB 85-46, August 1985.

2 Nagra Bulletin Series: Special Edition Grimsel (1988); No. 27—Grimsel Test Site (1996); No. 34,Rock Laboratories (2003).

3 Smith P. A., W.R. Alexander, W. Heer, T. Fierz, P.M. Meier, B. Baeyens, M.H. Bradbury, M. Mazurek, I.G. McKinley, “Grimsel Test Site Investigation Phase IV (1994 - 1996) -- The Nagra-JNC in situ study of safety relevant radionuclide retardation in fractured crystalline rock; I: Radionuclide Migration Experiment—Overview 1990-996,” Nagra Technical Report NTB 00-09, December 2001.

4 Alexander W. R., K. Ota and B. Frieg, “Grimsel Test Site Investigation Phase IV (1994 - 1996) – The Nagra-JNC in situ study of safety relevant radionuclide retardation in fractured crystalline rock; II. The RRP project methodology development, field and laboratory tests,” Nagra Technical Report NTB 00-06, July 2003.

5 McCombie C., W. Kickmaier, “Underground Research Laboratories: Their Roles in Demonstrating Repository Concepts and Communicating with the Public,” in Proceedings of 7th International Eurowaste Symposium, Cagliari/Sardinia 2-9 October, 1999.

6 Vomvoris, S., W. Kickmaier, I. McKinley, “Grimsel Test Site - The next decades,” in Scientific Basis for Nuclear Waste Management XXVI (Mat. Res. Soc. Proc. 757, Warrendale. PA, 2003) in press.

A Fractured-Chalk Field Laboratory for Flow and Transport Studies on the 10- to 100-m Scale

*Daniel Kurtzman[1 *], Ronit Nativ[1] and Eilon M. Adar[2]*
[1]The Seagram Center for Soil and Water Sciences, Faculty of Agricultural, Food and Environmental Quality Sciences, the Hebrew University of Jerusalem, P.O. Box 12, Rehovot 76100, Israel
[2]The J. Blaustein Institute for Desert Research—Water Resources Center and Department of Environmental Geological Sciences, Ben-Gurion University of the Negev, Sede Boker Campus 84990, Israel
[*]Corresponding author, kurtzman@agri.huji.ac.il

Israel's national site for hazardous waste disposal and a nearby major chemical industrial complex are underlain by a fractured chalk aquitard, containing brackish groundwater. Over the past decade, substantial efforts have been made to properly monitor contaminant migration (Nativ et al., 1999) and study flow and transport in this formation. Dahan (1993) proved that solutes migrate through the fractures intersecting the unsaturated zone in this aquitard. Characterization of flow and transport processes within a single fracture in the unsaturated chalk was the research focus in this area during the 1990s. Weisbrod et al. (1999) showed that intermittent wetting (by rainwater and wastewater) changes the roughness of the fracture walls and the fracture conductivity. Dahan et al. (1999) showed that only a small part of the fracture plane conducts most of the water flowing through it and intersections between fractures form the most permeable zones. Asaf (2000) estimated the hydraulic conductivity of discrete intervals in the saturated chalk using packer tests in coreholes. He compared these values with the visible appearance of the respective tested fracture sets and concluded that the hydraulic conductivity of the fractures cannot be deduced from their appearance in cores or corehole walls. Up-scaling the research objectives to flow and transport in a fracture network in a multi-borehole site was the motivation for this research.

A suitable site for an intermediate-scale study was located east of the confluence of the Naim and Hovav washes (Figure 1). Two nearby, perpendicularly oriented, natural outcrops enabled 1D and 2D fracture surveys. Four inclined 25- to 40-m deep open boreholes served for the various hydraulic tests (RH11, Rh11a, RH11b and RH11c boreholes, the first two of which were cored). An additional three, shorter boreholes served mainly as head controls in the flow models' boundary nodes. Four piezometers placed in a trench, excavated at the intersection of the washes, enabled monitoring the head in a substantial portion of the site boundary.

Assuming that flow and transport occur mainly in fractures, the research plan for this field laboratory included the following steps:

1. Geometric surveys of fractures, from which the distributions of the fractures' orientations and lengths can be derived, and a 3D density (fracture area per rock volume) and spatial distribution model can be approximated. These products allow the construction of stochastic discreet fracture networks (DFNs) (Dershowitz et al., 1998).
2. Slug tests in packed-off intervals in the boreholes to verify the distribution of fractures' transmissivity and the general anisotropy in the hydraulic conductivity.
3. Multi-well pumping tests where one borehole is pumped and heads are monitored in all the boreholes and piezometers.

4. Analysis of flow dimensions (Barker, 1988) and classical interpretation of the pumping tests.
5. Calibration of a simple deterministic DFN flow model to the transient head field in one of the pumping tests, and validation of this model using the other tests.
6. As in (5), but with a stochastic DFN, incorporating the full results of (1) and (2).
7. A forced-gradient, multi-borehole tracer test to determine transport velocities and dispersion.
8. Modeling the tracer test using analytical methods.
9. Calibrating a transport model and validating the flow models listed under (5) and (6).

Partial results of the fracture surveys are presented in Table 1. A total of 284 sub-vertical fracture traces, from scan lines performed on outcrops and cores, were divided into two sets. The dominant set has a mean fracture pole (trend, plunge) of (328°, 2°), i.e. an average strike of 58°, while the secondary set strikes at 331°. Log-normal and exponential distributions can be fitted to the fractures' radii. The inverse problem of inferring the radius distribution and the 3D density from 2D outcrop trace maps was solved by a forward simulation approach. In this procedure, 3D simulated fracture realizations were cut by trace planes, with geometries similar to those of the outcrops, to form simulated trace maps which were then compared to the field trace maps. Semivariograms of the aerial density of fractures helped define the spatial distribution model. The FracMan system (Dershowitz et al., 1998) was used as a major tool in the analysis of the fracture-geometry data.

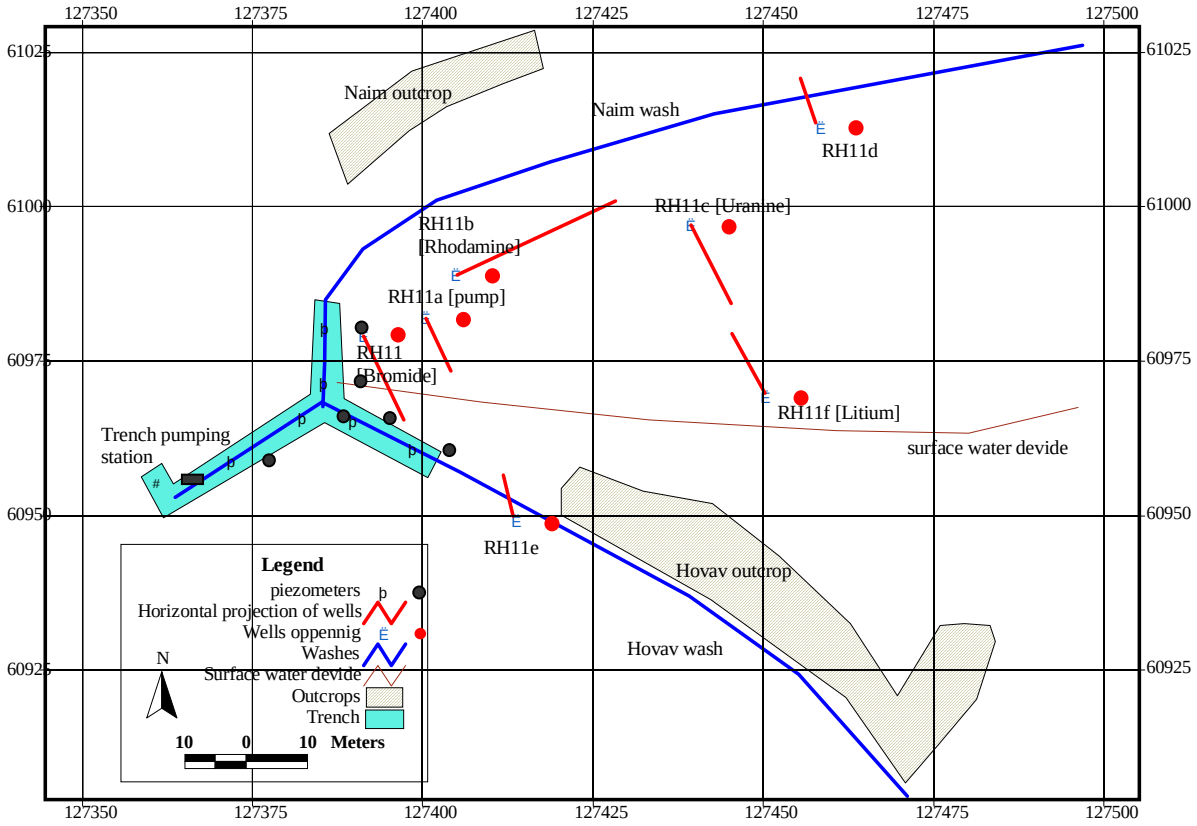

Figure 1. The Field Laboratory Site.

Table 1. Fracture sets: geometrical and hydraulic properties.

Set—Mean Pole (Trend, Plunge)	Fisher Dispersion Coefficient	Mean Fracture Radius (m) (Exponential Distribution)	3D Density (m^2/m^3)	Spatial Distribution Pattern	Fracture Transmissivity Distribution (m^2/s) [Mean, Std.] of log10 (Transmissivity)
(328, 2)	20	1.9	1.0	Uniform	[-6.8, 1.2]
(61, 7)	10	1.1	0.4	Shear zones	[-7.2, 0.7]

Transmissivity distribution of the fractures from the dominant set were derived from 25 slug tests in packed-off intervals in the RH11 and RH11c boreholes and the 1D density from the RH11 core (Figure 1). The secondary set's transmissivity distribution was derived from 10 slug tests in packed-off intervals in the RH11b borehole and the 1D density from the Naim outcrop. Hydraulic conductivity in the packed-off intervals varied by more than three orders of magnitude.

Analysis of the multi-borehole pumping tests revealed that the hydraulic response at the observation boreholes fits a 2D-flow regime (Theis response). The four pumping tests provided 12 pairs, each consisting of a pumping and observation well, while each well was involved in six pairs. Table 2 shows the average hydraulic conductivity derived from the six multi-well pumping tests for each well, as well as the hydraulic conductivity calculated from its own recovery. Our block hydraulic conductivity estimate for this area is 0.6 m/day parallel to the dominant fracture set and 0.2 m/day parallel to the secondary set. The anisotropy ratio of 3 correlates well with the 3D fracture density ratio between the dominant and secondary fracture sets (2.5) (Table 1).

The model presented in Figure 2 consists of 13 deterministic fractures (Step 5). The term "deterministic" is used because these fractures intersect the boreholes in conductive intervals (Step 2). A constant head boundary was set to the west, as the trench head did not change during the test. The southern boundary was set as a no-flow boundary, while the head at the eastern and northern boundaries varied in time and space, respectively. Heads were governed by the diffusion equation with a leakage term for flow between fractures. Figure 3 shows the actual and model-calibrated head responses to pumping in the RH11a borehole. The accuracy of this model with respect to fitting the head changes was 77% on average for all four wells and at all times. Validating this calibrated model with the other three pumping tests resulted in average predicted head changes of 62%, 62% and 48%. Stochastic models have not yet been successfully calibrated.

During the tracer test, four tracers were injected into four different wells (in brackets in Figure 1) after the RH11a borehole was pumped for a day to form steady-state forced-gradient conditions. Tracers were injected into large intervals by slowly pulling out a hose filled with the tracer solution. Large intervals were used to ensure breakthrough, if any hydraulic connection existed between the wells. Injection wells were mixed and sampled to ensure a constant tracer concentration throughout the large intervals. Eight days after the injection, 80%, 20% and 15%

of the tracer masses from the RH11c, RH11f and RH11b boreholes, respectively, were recovered at the RH11a borehole. First arrival/maximum concentrations were 28 min/13 h, 40 min/12 h and 2.6 h/20 h from the RH11c, RH11b and RH11f boreholes, respectively.

Table 2. Hydraulic conductivities from unpacked pumping tests (m/day).

Testing Method	RH11	RH11a	RH11c	RH11b
Multi-well Drawdown	0.5	0.6	0.7	0.4
Single-well Recovery	0.2	0.3	0.5	0.1

Bromide from the RH11 borehole never arrived at the pumping well because the forced gradient was not strong enough to divert the natural flow direction there. Another tracer test performed between the RH11 and RH11a boreholes, down the natural gradient, proved a hydraulic connection between these wells (Adar et al., 2001). Interpretation of the tracer test results is now in progress. Figure 4 shows the experimental breakthrough curve of uranine (from the RH11c borehole) and two fitted single-channel models. The green curve is the SFDM model (Maloszewski and Zuber, 1993), which accounts for longitudinal dispersion and molecular diffusion into the matrix. This model cannot simultaneously predict the fast appearance and the long tail. Javandel et al. (1984) present a solution for the advection-dispersion equation with an exponential decreasing source, it only accounts for longitudinal dispersion. The red curve in Figure 4 has a large dispersion coefficient of 0.17 m^2/s, which accounts for the relatively fast rise in concentration, but also a concentration drop that is too slow. Therefore, a multi-channel model is probably needed to properly model this experimental breakthrough curve.

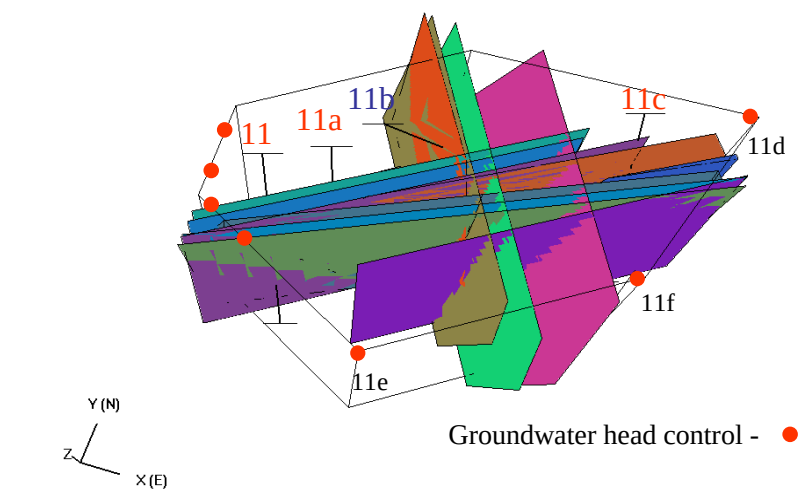

Figure 2. The thirteen subvertical fractures flow model that were calibrated
pumping test in the RH11a borehole

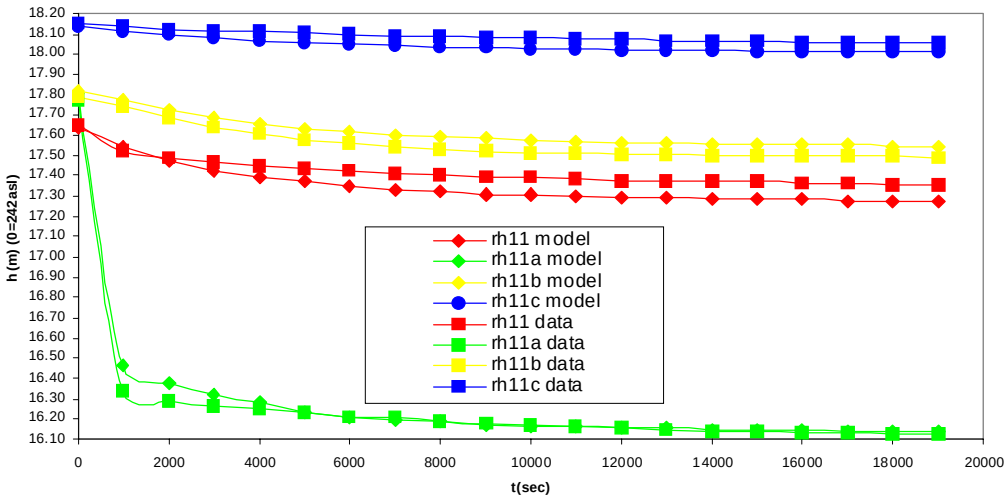

Figure 3. A comparison between actual and modeled head responses to pumping in the RH11a borehole.

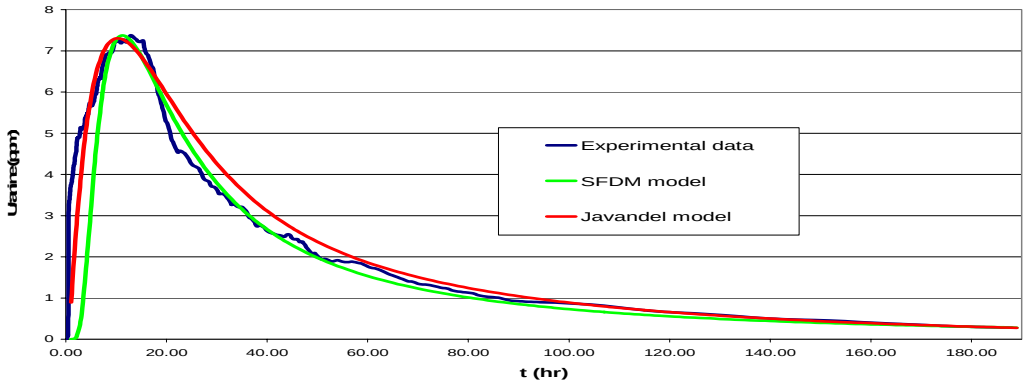

Figure 4. Experimental and single-channel analytical model breakthrough curves for uranine.

Diffusion must play an important role in the transport process because the slope of the breakthrough-curve tail on a log-log plot is -1.14, not as steep as expected from a heterogeneous advection dominated process (Becker and Shapiro, 2003).

References

Adar, E., K. Witthueser and R. Nativ, 2001. A forced gradient tracers test, in the FRACFLOW project on Contaminant Transport, Monitoring Technique and Remediation Strategies in Cross European Fractured Chalk. Third annual progress report, sec. III.4, 38-43.

Asaf, L. 2000. The hydraulic conductivity of fracture systems intersecting the Avdat group chalk, Ramat Hovav. M.Sc thesis, Hebrew University, Jerusalem (in Hebrew).

Barker, J. A. 1988. A generalized radial flow model for hydraulic tests in fractured rock. Water Resour. Res., 24, 1796-1804.

Becker, M. W. and A. M. Shapiro. 2003. Interpreting tracer breakthrough tailing from different forced-gradient tracer experiment configuration in fractured bedrock Water Resour. Res., 39(1), 1024.

Dahan, O. 1993. Water flow and solute migration through unsaturated chalk. Avdat group, Ramat Hovav. M.Sc thesis, Hebrew University, Jerusalem (in Hebrew).

Dahan, O., R. Nativ, E. Adar, B. Berkowitz and Z. Ronen, 1999. Field observation of flow in a fracture intersecting unsaturated chalk. Water Resour. Res., 35, 3315-3326.

Dershowitz, W., G. Lee, J. Geier, T. Foxford, P. LaPointe and A. Thoma, 1998. FRACMAN, Interactive Discrete Feature Data Analysis, Geometric Modeling, and Exploration Simulation. User Documentation. Golder Associates Inc., Seattle, Washington.

Javandel, I., C. Doughty and C. F. Tsang, 1984. Groundwater transport: handbook of mathematical models. American Geophysical Union. Water Resources monograph 10.

Maloszewski, P. and A. Zuber, 1993. Tracer experiments in fractured rocks: matrix diffusion and the validity of models. Water Resour. Res., 29, 2723-2735.

Nativ, R., E. Adar and A. Becker, 1999. A monitoring network for groundwater in fractured media. Ground Water, 37(1), 38-47.

Weisbrod, N., R. Nativ, E. Adar and D. Ronen, 1999. Impact of intermittent rainwater and wastewater flow on coated and uncoated fractures in chalk. Water Resour. Res., 35, 3211-3222.

Using Fracture Pore Space Geometry to Assess Degassing and Scaling Relationships in Fractured Rocks

J. E. Gale and E. Seok
Department of Earth Sciences, Memorial University of Newfoundland, Canada

Any review of laboratory- and field-measured flow and transport properties in fractured rocks will confirm the wide range in permeabilities and fluid/contaminant velocities and the high degree of anisotropy, all of which present serious challenges to predicting flux and contaminant transport in both saturated and partially saturated fractured rocks systems. Data compiled and interpreted by Clauser (1992) and by Neuman (1990), for both porous and fractured media, show that the range of hydraulic properties is greatest for small laboratory samples, with the range of values decreasing for measurements at the borehole scale and decreasing even more when interpreted for large regional aquifer systems using measured and assumed boundary conditions. Obviously, part of this scaling pattern is contributed by small-scale heterogeneities that become more significant as the size of the sample decreases. In addition, test boundary conditions and the lower measurement limits are much more precisely defined in small-scale laboratory samples and generally much more poorly defined in borehole tests, with the heterogeneities generally being averaged over significant lengths of the borehole test interval.

In low-permeability fractured rocks, it has been assumed by some investigators that flow and transport are controlled by a number of high-permeability pathways, consisting of or within discrete fractures, that are not captured by small-scale laboratory samples (Margolin, et al., 1998). However, large-scale field tests, such as the Stripa macro-permeability experiment (Witherspoon, 2000), did not show any evidence in the measured gradients that would support an interpretation that a few high permeability pathways were dominating the flux into the drift. Furthermore, single fracture borehole packer tests in the same rock mass (Gale et al., 1987), while indicating a truncated or censored distribution due to the limits on the measurement of low flow rates, did not show a bimodal fracture transmissivity distribution.

Given the need to determine how to scale-up from laboratory and borehole data sets to simulate and predict flow and transport in volumes of fractured rock that are of interest to a number of investigators, extensive numerical investigations have been conducted (Margolin et. al., 1998, among others) to determine how key parameters scale with an increase in the area of interest. However, without adequate deterministic fracture-property databases, including measured flow and transport properties, with which to calibrate and exercise the available models, it will be difficult to validate the various conceptual models of flow in fracture systems along with the appropriate scaling relationships. Databases need to be developed at different scales, and in this paper we describe a fracture-pore-space database that we are developing to determine scaling relationships at the scale of a single fracture plane.

Both single- and two-phase coupled stress-flow experiments, followed by tracer tests, have been completed on sections of fracture planes measuring 200 mm by 300 mm. At selected loads, for known flow rates and tracer velocities, the samples have been injected with a room-temperature curing resin. Once the resin cured, the fracture planes were sectioned, perpendicular to the plane, and the width (aperture) of the fracture planes were measured using a photo-microscope and

digitizer approach. Analysis of the pore-space data demonstrated that the fracture pore-space geometry, consisting of contact areas and open fracture pore space, is characterized by a bimodal distribution with a well defined spatial structure. Since the pore-space geometry was mapped along discrete sections through the fracture-plane sample, simulated annealing was used to simulated the pore-space geometry over the entire sample area (Seok, 2001). This approach was found to respect both the bimodal nature and the spatial structure of the fracture pore-space geometry.

The simulated pore space has been randomly sampled at four different scales, and the range of hydraulic properties present in these subsamples has been determined, along with the range of fracture apertures. The results of these numerical investigations have been used to evaluate the basic scaling relationships for the flow properties of the fracture planes under both single-phase and two-phase flow conditions. In addition, the results from these experimental and numerical investigations have been used to design a large laboratory scaling-up experiment on a single fracture plane in a granite sample (provided by A. Shapiro of the U.S. Geological Survey). This sample measures approximately 1 m × 1 m × 1 m. The initial set of coupled stress-flow experiments, both single- and two-phase flow, will be conducted on the full fracture plane, followed by coring of several 200 m diameter samples of the fracture plane. These samples will in turn be subjected to similar stress-flow experiments, followed by resin injection and pore-space mapping. This large-scale experiment, at the scale of a single fracture plane, will provide insight into whether high-permeability pathways dominate the hydraulic properties of single fractures. The database will help define the appropriate scaling relationships to be used in characterizing flow and transport in discrete fractures.

References

Clauser, C., 1992, Permeability of crystalline rocks. EOS Trans. AGU, Vol 73, No. 21, pp 233, 237-238.

Gale, J. E., MacLeod, R., Welhan, J., Cole, C., and L. Vail, 1987. Hydrogeological characterization of the Stripa site. SKB T.R., 87-15.

Margolin, G., Berkowitz, B. and H. Scher, 1998. Structure, flow and generalized conductivity scaling in fracture networks. Water Resources Research, Vol. 34, No. 9, pp. 2103-2121.

Neuman, S. P., 1990. Universal scaling of hydraulic conductivities and dispersivities in geologic media. Water Resources Research, Vol. 26, pp. 1749-1758.

Seok, E., 2001. Pore space characterization and implications for flow simulation in discrete fracture planes. MSc Thesis, Memorial University of Newfoundland, Canada.

Witherspoon, P.A.., 2000. The Stripa Project. International Journal of Rock Mechanics and Mining Sciences, Vol. 37. No. 1-2, pp. 385-396.

Flow Across an Unsaturated Fracture Intersection

Maria Ines Dragila[1] and Noam Weisbrod[2]
[1]Department of Crop and Soil Sciences, Oregon State University, 3017 ALS, Corvallis, OR 97331, USA
[2]Department of Environmental Hydrology & Microbiology, Institute for Water Sciences & Technologies, Blaustein Institutes for Desert Research, Ben-Gurion University of the Negev, Israel

Introduction

Fluid movement through fractured vadose zones is known to be complex, exhibiting spatial and temporal variability. It has been observed that under unsaturated conditions, not all fractures, even well-connected fractures, actively participate in transport at all times [Salve et al., 2002; Faybishenko et al., 2000] and that linear conduits formed by intersections can provide preferred paths for flow (e.g., Dahan et al., 2000). Consequently, simply knowing the geometric characteristics of a fracture or fracture system alone may be insufficient in predicting when a fracture will participate. A better understanding is needed of small-scale behavior of fluid as it reaches a discrete fracture intersection in order to develop more accurate rules for active-fracture selection. These "rules" are essential if we are to improve the reliability of modeling flow through fracture networks in the vadose zone.

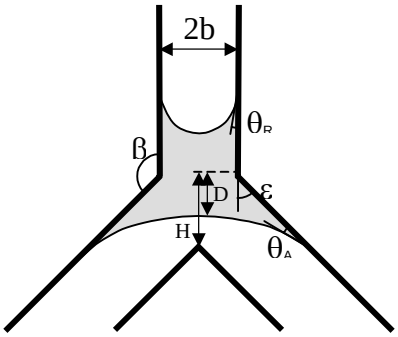

Figure 1. Schematic of inverted "Y" intersection showing droplet (gray) invading intersection

Because of the small number of experiments in fracture intersections under unsaturated conditions, and the characteristic complexity of fluid dynamics already observed in unsaturated fractures, this work was initiated with an experimental investigation of the simplest possible system. A 0.5 x 70 x 70 cm glass sheet was cut to form an inverted "Y" intersection with an aperture of 0.17 ± 0.2 cm (Figure 1). The non-porous nature of glass makes these results more applicable to flow in hard rock where sorption is negligible. The 0.5 cm width of the fracture plane coincides with the equilibrium width of droplets (Or and Gehezzei, personal communication) eliminating in-plane meandering of the flow, thus reducing the behavior to a near one-dimensional problem. Behavior of free-surface film flow and capillary droplet modes were studied at the intersection for flow rates (0.6–6.0 mL/min) that were sufficiently small enough to prevent saturation of the fracture.

Theory

The no-slip boundary condition, required to be held at the liquid-glass interface, forces a circulatory motion within droplets moving along the fracture [Frohn and Roth, 2000]; in the reference frame of the droplet, liquid moves upward along the contact with the walls and downward in the middle. How this complexity affects behavior at an intersection is not yet fully understood. The theoretical approach presented here provides a first order analysis for predicting the characteristics of fluid motion at intersections.

Enlargement of the aperture at the intersection presents a capillary barrier to incoming droplets. It is hypothesized that the response of the droplets to this barrier depends on the angle of inclination of the branches (β in Figure 1). Upon arrival at an intersection, the contact line slows down or stops, while the liquid inside the droplet continues to move, flattening the meniscus. At square intersections ($\beta = 90^o$), the weight of the droplet deforms the meniscus (for wetting fluids) into a convex shape, resulting in upward force on the droplet. The droplet forms a neck and drips when the weight of the liquid exceeds the capillary force [Frohn and Roth, 2000, Or and Ghezzehei, 2000]. Shorter droplets are trapped above the intersection. At intersections with obtuse corner angles ($\beta > 90^o$) forming an inverted Y-shaped intersection (Figure 1), the wetting line continues its progression along the contiguous fracture walls. Widening of the cavity enlarges the radius of curvature of the advancing meniscus, thus reducing the downward capillary force and decelerating the droplet. The droplet stops advancing when the gravitational body force (droplet length) equals the capillary force generated by the advancing and receding menisci [Equation (1)] (Dragila and Weisbrod, 2003a).

$$L\rho g \sin\alpha = \sigma\left(\frac{1}{R_R} - \frac{1}{R_{Ai}}\right) \qquad (1)$$

where R_R and R_{Ai} are the radii of curvature of the receding and invading menisci, respectively. At any point, the invasion distance (D) is related to R_{Ai} by the following geometric relationship (Figure 1):

$$D = R_{Ai}\left[\left(1 + \frac{\cos^2\left(\beta - \theta_A\right)}{\sin^2\beta} - \frac{\cos\left(\beta - \theta_A\right)\sin\theta_A}{\sin\beta}\right)^{1/2} - 1\right] = R_{Ai}\mathrm{F}\left(\beta, \theta_A\right) \qquad (2)$$

where θ_A is the advancing contact angle. Equation (2) applies to wetting fluids and for $\beta > 90^o$. The maximum invasion distance (D_{max}) will occur for droplets that satisfy Equation (1). The depth of invasion will therefore depend on the acuteness of the intersection corner, the value of the advancing contact angle, and the droplet length. Equations (1) and (2) are a first order approximation and do not take into account inertial effects of meniscus deformation and the reduction in droplet length as the intersection aperture widens.

If D_{max} is greater than the distance to the apex (H in Figure 1), then the droplet will touch the apex, saturate the intersection and move into the branches by capillarity. If D_{max} is less than H, the droplet will sustain a concave meniscus and liquid will flow as a film along the contiguous fracture walls (i.e., upper wall of the fracture branches). The distance to the apex (H) is given

geometrically by:

$$H = b\left(\frac{2}{\sin\beta} + \frac{1}{\tan\beta}\right) \quad (3)$$

For this experiment, Equations (1)–(3) predict that droplets longer than 0.7 cm will saturate the intersection. Shorter droplets will result in transition to film flow (assuming: b = 0.08 cm, α = 90º, β = 135º, H = 0.15 cm (from Equation (3)), and θ_R = 0º, giving $R_R = b$).

Material and Methods

A series of laboratory experiments were conducted in which distilled water was delivered by a syringe pump to the top of a vertical fracture (35 cm in length), which terminated at an intersection of two symmetrical fractures (β = 135º in Figure 1). Aperture of all fractures was 0.17 ± 0.02 cm. Blue dye tracer was used to aid visualization. Pre-testing of the system determined that flow rates were required to be below ~12 mL/min to generate droplet mode. Flow rates used were 0.6, 1.5, 3.0 and 6.0 mL/min in order to focus on droplet and film flow. Between experiments, the fracture was dried with absorbent tissues (apparatus was not disassembled). Liquid draining from the bottom of the fracture branches was collected into beakers. All experiments were conducted at a temperature of 20–22 ^{o}C and a relative humidity of 20–40%. Ambient atmospheric pressure was not controlled. Flow behavior at the imbibition point, the main fracture, and intersection was captured by a digital still camera and digital video camera simultaneously. Video data was used to calculate droplet length and speed.

Results

Prior to arrival at the intersection, behavior in the main fracture was highly variable, resulting in a wide range of droplet size and speed at the intersection entrance. Although a detailed description of this behavior is beyond the scope of this text, it is worth mentioning that the arrival velocity of droplets at the intersection was substantially suppressed relative to that predicted by plug flow theory. There was strong indication that the velocity suppression may be caused by inertial changes in the contact angle of the advancing meniscus (Dragila and Weisbrod, 2003b). In general, droplets exhibited characteristics as reported in the literature (Su et al., 1999), where a pear-shaped droplet locally saturates the aperture and moves down gradient, maintaining its connection to the water delivery pipette by a capillary thread or rivulet (Figure 2a–c). The imbibing fluid continues to feed the droplet until the rivulet snaps, and a new droplet begins to form. The term “film” describes flow that occurs only along a fracture wall at a time (Figure 2d–e).

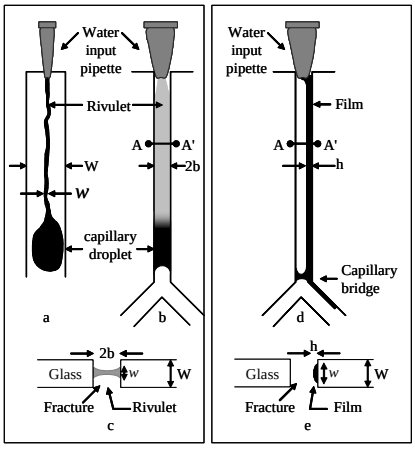

Figure 2. (a) Droplet and rivulet in plane of fracture wall. (b) View of droplet (black) and rivulet (gray) in plane of aperture. (c) Cross section of very thin rivulet spanning the aperture. (d) Water bridge spanning aperture, and free-surface film flow in plane of aperture wetting only one wall. (e) Cross section of film flow.

Four categories of transport phenomena were observed at the intersection: (1) formation of a water bridge above the intersection; (2) fluid films that crossed the aperture using the water bridge; (3) droplets that transformed to film flow at the intersection and continued as films into the branches; and (4) droplets that saturated the intersection and continued as droplets into the branches. Each of these is discussed in more detail below. In addition, there was a family of associated behavior observed (such as rivulets) that stayed connected to both droplet halves after the droplets entered the fracture branches, water bridges trapped in the branches that excluded further water entry, and changes in the surface waviness of the film as it crossed the intersection. Discussion of these is beyond the scope of this abstract.

The water bridge (Figure 3) was formed either by droplets that were too small to overcome the capillary barrier, by a portion of water left behind during droplet passage through the intersection, or for film flow during the initial release of fluid into an unprimed (dry) glass fracture. The water bridge played a crucial role in transport of film flow, which allowed the film to switch walls and flow along the upper wall of either or both fracture branches (Figure 3).

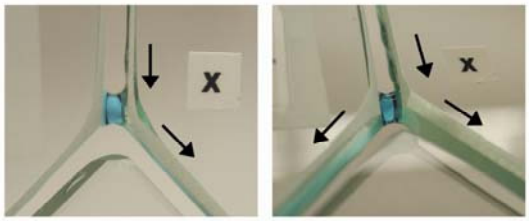

Figure 3. Film flowing down right wall of vertical fracture is redistributed via water bridge. Left: film continues along contiguous wall. Right: film is redistributed along upper wall of both fracture branches.

Capillary droplets exhibited one of three transport modes upon entering the intersection—mode selection strongly dependent on initial droplet length, irrespective of delivery flow rate. (1) Droplets shorter than ~0.5 cm stopped at the capillary barrier, formed a concave meniscus and drained into the upper wall of both fracture branches as a film (Figure 4a and Figure 5); (2)

Droplets between ~0.5 and ~1.5 cm in length started to drain as a film, but eventually saturated the aperture and continued as capillary droplets into both branches (Figure 4b); and (3) Droplets longer than ~1.5 cm saturated the intersection and continued down one or both branches in capillary droplet mode (Figure 4c). In general, higher flow rates produced a greater proportion of saturation events. At higher flow rates the rivulet stayed attached for a longer period of time, resulting in larger overall droplets at the intersection. At all flow rates, larger droplets also formed by the coalescing of two of three droplets prior to arrival at the intersection.

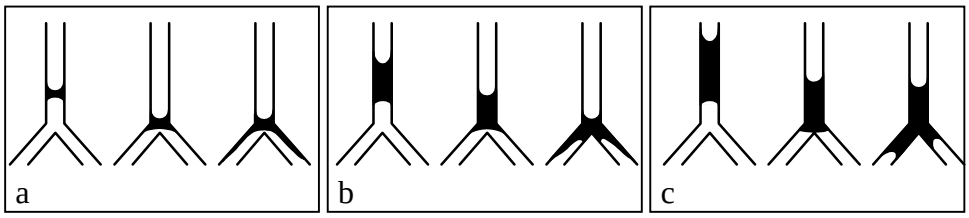

Figure 4. Three types of transport across intersection: (a) Droplet mode to film flow. (b) Droplet mode initiate transition to film flow, but eventually saturating the intersection. (c) Droplet mode saturating the intersection and entering fracture branches as droplets.

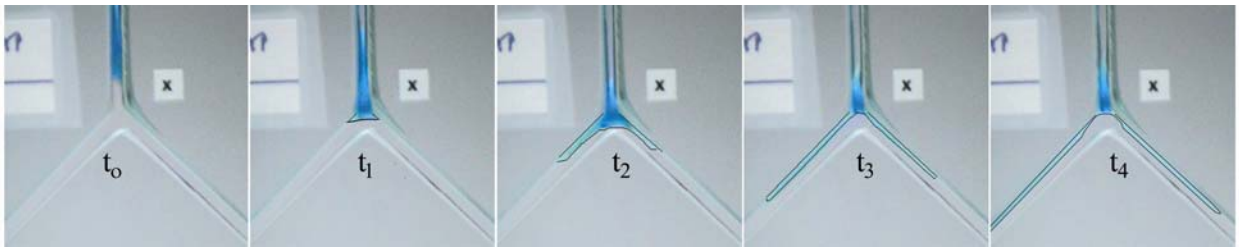

Figure 5. Transition between droplet and film flow modes at intersection. Time difference between frames is 1/30 sec.

Discussion

Theoretical analysis predicting both modes (saturation invasion and transition to film flow) is supported by experimental results. Some droplets that caused saturation invasion were shorter (~ 0.3 cm) than the minimum length predicted (~ 7 cm) (Figure 6), which may be accounted for by Equations (1) and (2) ignored inertial effects that could cause stretching and rebounding of the meniscus. The intersection will saturate if the stretch is sufficient to cause the droplet to touch the apex of the intersection prior to rebounding.

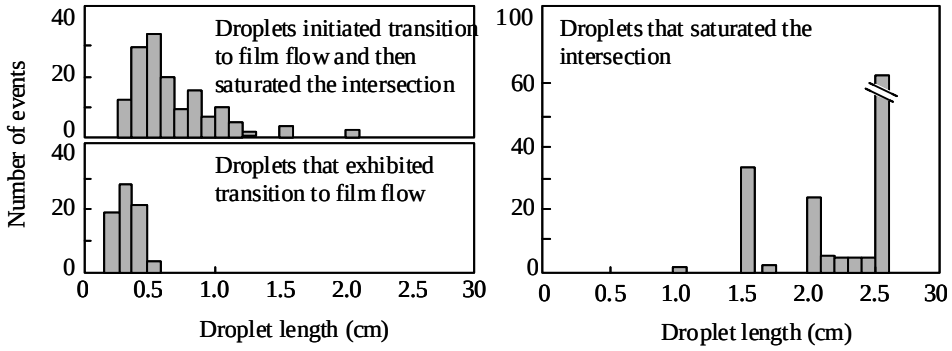

Figure 6. Graphs show initial droplet length grouped by intersection dynamic exhibited.

Conclusion

This work presents an initial investigation of wetting-fluid behavior at an unsaturated intersection and confirms that two fluid modes are possible. Invasion dynamics also may depend on fracture and fluid properties, such as the liquid surface tension, relationship of the advancing contact angle to the intersection angle, and the effect of fracture texture and sorption on the creation of liquid bridges and the sustainability of rivulets. In nature, further complexity is expected to be generated by aperture variability causing channeling and meandering within the fracture plane.

References

Dahan, O., R. Nativ, E. M. Adar, B. Berkowitz, and N. Weisbrod. 2000. On fracture structure and preferential flow in unsaturated chalk. Ground water 38:444-451.

Dragila, M. I., and N. Weisbrod. 2003a. Fluid motion through an unsaturated fracture junction. Water resources research in review.

Dragila, M. I., and N. Weisbrod. 2003b. Parameters affecting fluid transport in large aperture fractures. Advances in Water Resources in press.

Faybishenko, B., C. Doughty, M. Steiger, J. C. S. Long T. R. Wood, J. S. Jacobsen, J. Lore, and P. T. Zawislanski,. 2000. Conceptual model of the geometry and physics of water flow in a fractured basalt vadose zone. Water resources research 36:3499-3520.

Frohn, A., and N. Roth. 2000. Dynamics of Droplets. Springer, Berlin.

Or, D., and T. A. Ghezzehei. 2000. Dripping into subterranean cavities from unsaturated fractures under evaporative conditions. Water resources research 36:381-393.

Salve, R., J. S. Y. Wang, and C. Doughty. 2002. Liquid-release tests in unsaturated fractured welded tuffs: I. Field investigations. Journal of hydrology 256:60-79.

Su, G. W., J. T. Geller, K. Pruess, and F. Wen. 1999. Experimental studies of water seepage and intermittent flow in unsaturated, rough-walled fractures. Water resources research 35:1019-1037.

Effects of Pore Volume Variability on Transport Phenomena

Ivan Lunati[1,†], Wolfgang Kinzelbach[1] and Ivan Sørensen[2]
[1] Institute for Hydromechanics and Water Resources Management, ETH Zürich,
HIL G34.2, ETH Hönggerberg, CH-8093 Zurich, Switzerland
E-mail: lunati@ihw.baug.ethz.ch
[2] Department of Hydromechanics and Water Resources, Technical University of Denmark

The description of solute transport in a porous medium requires an accurate description of the pore velocity, which is the relevant velocity for transport phenomena. For this reason, information about the transmissivity field is not sufficient to model the solute behavior correctly and an adequate description of pore-volume variability is essential. We demonstrate that in hydraulically equivalent media characterized by exactly the same transmissivity field, the displacement of a solute can show striking differences if the media have different pore-volume spatial distributions. In particular, we demonstrate that correlation between pore volume and transmissivity yields a much smoother and more homogeneous distribution of the solute concentration (Lunati 2003; Lunati et al. 2003).

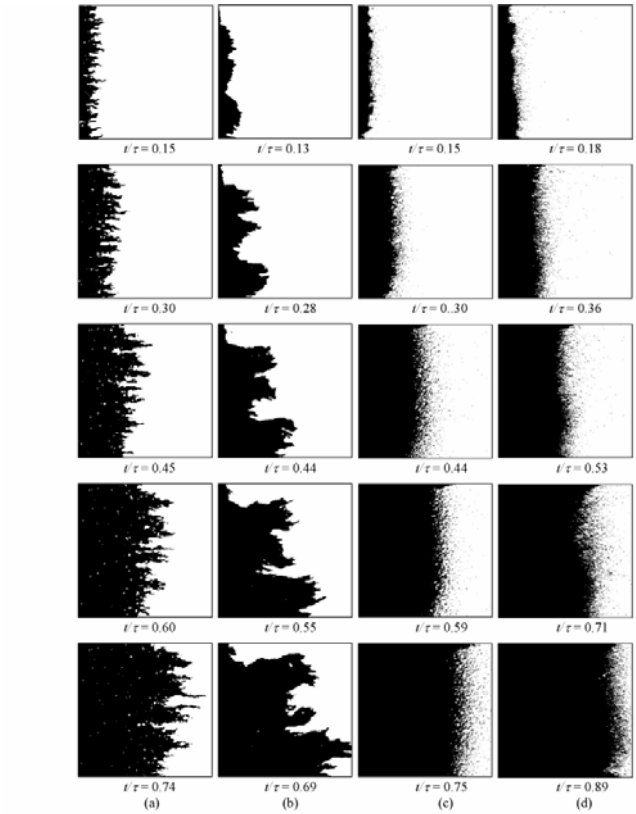

Figure 1. Tracer distributions at five different time steps. From left to right: (a) empty exponential, (b) empty fractal, (c) glass-beads filled exponential, and (d) glass-beads filled fractal models.

[†] Presently: Institute of Fluid Dynamics, ETH Zurich, ETH Zentrum, Sonneggstrasse 3, CH-8092, Zurich, Switzerland

Several laboratory experiments are performed in two artificial fractures. The fractures are made of two Plexiglas plates into which a space-dependent aperture distribution was milled (Su and Kinzelbach, 1999). One fracture has an exponential covariance function of the aperture field with a finite correlation length, whereas the other fracture has a power-law covariance function of the aperture field, which produces a self-similar process with an infinite integral scale. A solution is injected into the fractures and the solute transport is observed using visualization by a light transmission technique. The experiments are first performed in the empty fractures and then repeated after filling the fractures, with glass powder, which plays the role of a homogeneous fault-gouge material (Sørensen, 1999). In both fractures, the solute behavior is much smoother and more regular after the fractures are filled (Figure 1). Differences are due to the different pore-volume variability in the empty and in the filled models. When the models are filled with glass powder, the correlation between pore volume and transmissivity is perfect and the pore velocity becomes more regular: it does not depend on the transmissivity directly, but only indirectly through the hydraulic gradient, which is a much smoother function.

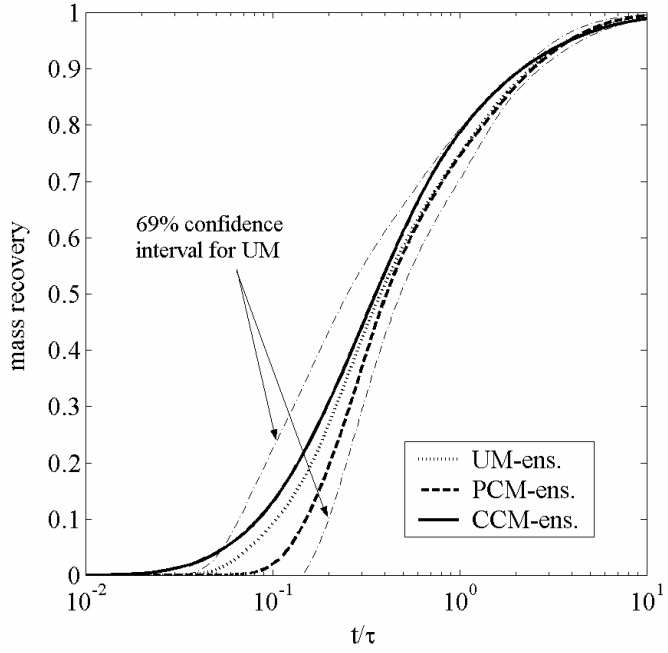

Figure 2. Solute recovery curves at the extraction borehole averaged over 20 realizations as a function of the dimensionless time: UM, parallel-plate fracture with homogeneous fault-gouge; PCM rough-walled empty fracture; CCM, rough-walled fracture with heterogeneous fault-gouge. Mean transmissivity 2 10^{-10} m^2/s, log-transmissivity variance σ_{lnT}=7.4, correlation scale approximately 0.07 times the dipole size.

The effects of the pore-volume variability are also investigated by numerical simulations of tracer tests in a dipole flow field. Three different conceptual models are used: an empty fracture, a rough-walled fracture filled with a homogeneous material, and a parallel-plate fracture with a heterogeneous fault gouge. All three models are hydraulically equivalent, yet they have different pore-volume distributions. Even if piezometric heads and specific flow rates (Darcy velocities) are exactly the same at any point of the domain, the transport process differs dramatically, showing the importance of describing the pore-volume variability (Lunati, 2003; Lunati et al., 2003). The limiting cases are identified in the parallel-plate fracture and in the rough-walled

fracture filled with homogeneous fault gouge. The empty fracture yields an intermediate situation between these two benchmarks. The numerical simulations confirm the smoothing property of the correlation between pore volume and transmissivity: the parallel-plate fracture, in which pore-volume and transmissivity are uncorrelated, exhibits channeling effects and a more irregular concentration distribution than the rough-walled filled fracture, in which the correlation between pore-volume and transmissivity is perfect.

Despite these tremendous differences, the possibility of discriminating *in situ* among the conceptual models is affected by scarcity of information. During field measurement campaigns, only information at the boreholes is available, typically solute breakthrough curves. Studying the solute breakthrough curves and recovery curves at the extraction wells for our numerical case studies, we show that discrimination is impossible in most realistic cases, because the variability from realization to realization dominates the effect due to assuming different conceptual models. This is illustrated in Figure 2, which plots the ensemble-average of the recovery curves computed over 20 realizations of the transmissivity field with the same statistical properties. A tracer test in a dipole flow field is simulated in each realization using all three different conceptual models. The ensemble-averaged recovery curves of the three conceptual models lie within the 69% confidence interval of the parallel-plate model, showing that the three models are statistically undistinguishable. Discrimination becomes possible only under very favorable conditions i.e. the integral scale of the transmissivity field has to be known and small compared to the dipole size. If the latter conditions are satisfied, the effects of local variability on the recovery curve are limited because of averaging along the streamlines and the variability from realization to realization diminishes. Discrimination between the rough-walled fracture filled with a homogeneous material and the other two models is possible (e.g., on the basis of the different peak arrival time to mean arrival time ratios), whereas the parallel-plate fracture with a heterogeneous fault gouge and the empty fracture still shows identifiability problems. The latter may be solved by inspection of aperture and pressure testing.

References

Lunati, I., *Conceptual Models of Single and Multiphase Transport in a Fracture*, Eidgenössische Technische Hochschule Zürich, Ph.D. Thesis no. 15082, 2003 http://e-collection.ethbib.ethz.ch/cgi-bin/show.pl?type=diss&nr=15082

Lunati, I., W. Kinzelbach, and I. Sørensen, Effects of pore volume-transmissivity correlation on transport phenomena, *J. Contam. Hydrol.*, 67(1-4), 195-217, 2003

Sørensen, I., *Solute Transport and Immiscible Displacement in Single Fractures*, Master Thesis C938719, Technical University of Denmark, 1999

Su, H., and W. Kinzelbach, Application of 2-D random generators to the study of solute transport in fractured porous medium, *Water 99: Handbook and Proceedings*, 627-630, Queensland, Australia, 1999

Linear Flow Injection Technique for the Determination of Permeability and Specific Storage of a Rock Specimen: Flow Control versus Pressure Control

Insun Song[1], Jörg Renne[1], Stephen Elphick[2], and Ian Main[2]
[1]Institute for Experimental Geophysics, Ruhr-University Bochum, D-44780, Bochum, Germany
[2]School of Geoscience, University of Edinburgh, Edinburgh EH9 3JW, Scotland, UK

Permeability of a rock specimen can be determined from the linear relationship between fluid flux and pressure gradient along the specimen in a steady state of pressure which could be established by linear flow injection. Before the steady state is reached, an initial transient stage of pressure exists, and lasts for a long period of time in low-permeability experiments. Instead of waiting for the steady state, Brace et al. (1968) suggested a method to obtain the hydraulic properties from the transient character which is dependent on both permeability and specific storage. The pulse transient technique does not require the measurement of flow rate, which was at that time technically much more difficult than measuring pressure in low-permeability tests. The calculation of the two unknowns relies on a tedious graphical method or a history matching routine of comparing experimental data with theoretical curves (Hsieh et al., 1981; Zeynaly-Andabily and Rahman, 1995).

However, fluid flux is a valuable parameter in hydraulic characterization. Also, today's fluid pumps enable fluid injection with precise control of either flow or pressure. Moreover, we could control the duration of the transient stage by changing the test system compliance. We introduce the conceptual design and application of linear flow injection techniques for simultaneously deriving fluid permeability and specific storage of a rock sample from records of the flow rate and pressure variation in steady state of fluid pressure along the specimen. The experimental arrangement is composed of a cylindrical rock specimen placed between two reservoirs, one of which is connected to a flow pump that injects fluid into the cored rock specimen (Figure 1). In our experiments, linear flow injection was carried out by two different methods: flow control and pressure control. Using the Laplace transform method, we solved the governing diffusion equation with two different boundary conditions for fluid injection: flow control and pressure control at a constant rate. The analytic solutions are composed of two parts: an asymptotic linear function of time t at a given position, and a transient part which decays to zero as time increases. Based on our solutions, we suggest a straightforward method to calculate the two hydraulic characters from some linear equation parameters of the pressure records of the two reservoirs and fluid pumping rate.

Flow Control

For the large time, t, the asymptotic solution for the upstream and downstream pressures, $p_u(t)$ and $p_d(t)$, are expressed as a linear function of time as follows:

$$p_u(t) = \frac{Qt}{S_s AL + S_u + S_d} + \frac{\mu QL}{kA}\left(\frac{1}{3} + \frac{S_d}{S_s AL} + \frac{{S_d}^2}{{S_s}^2 A^2 L^2}\right)\left(1 + \frac{S_u + S_d}{S_s AL}\right)^{-2} \quad (1)$$

$$p_d(t) = \frac{Qt}{S_s AL + S_u + S_d} - \frac{\mu QL}{kA}\left(\frac{1}{6} + \frac{S_u + S_d}{2S_s AL} + \frac{S_u S_d}{{S_s}^2 A^2 L^2}\right)\left(1 + \frac{S_u + S_d}{S_s AL}\right)^{-2} \quad (2)$$

where S_s, k, L, and A are the specific storage, permeability, the length, and the cross-sectional area of a cored sample; S_u and S_d are the storage capacities of the upstream and downstream reservoirs; Q and μ are the flow rate generated by an intensifier and the dynamic viscosity of the fluid, respectively. According to these two linear equations, the specific storage and the permeability of the rock sample are given by the slope of the differential pressure between the two reservoirs, if S_u and S_d are determined independently:

$$S_s = \frac{Q - (S_u + S_d)dp/dt}{AL \cdot dp/dt} \quad (3)$$

$$k = \frac{\mu QL}{\Delta PA}\left(\frac{1}{2} + \frac{S_d}{S_s AL}\right)\left(1 + \frac{S_u + S_d}{S_s AL}\right)^{-1} \quad (4)$$

where ΔP is the differential pressure between the upstream and downstream reservoirs, and dp/dt is the slope of the linear pressurization record in both reservoirs. If the downstream pressure is not recorded, the permeability can be calculated from the zero intercept of the linear upstream fluid pressure variation. However, the differential pressure is more reliable than the intercept, because the former is a direct measure, whilst the latter is an extrapolation. Details are given in the paper by Song et al. (2003).

Pressure Control

The asymptotic solution for the pressure along the specimen as a function of position x and time t when the fluid injection is controlled by the linear pressurization and is given by:

$$p(x,t) = \left(t + (x^2 - L^2)\frac{\mu S_s}{2k} + (x - L)\frac{\mu S_d}{kA}\right)\frac{dp}{dt} \quad (5)$$

and from Darcy's law, the one-dimensional flow at the upstream boundary ($x = L$) is given by:

$$q_x(L,t) = \frac{k}{\mu}\frac{\partial p(L,t)}{\partial x}A \quad (6)$$

where $q_x(L,t)$ is a flow rate along the specimen at $x = L$ and expressed as $Q - S_u \frac{dp(L,t)}{dt}$, and $\frac{\partial p(L,t)}{\partial x} = \frac{\mu}{k}\left(S_s L + \frac{S_d}{A}\right)\frac{dp}{dt}$ from equation (5). Using these relationships, we can express the specific storage and permeability by:

$$S_s = \frac{Q - (S_u + S_d)dp/dt}{AL \cdot dp/dt} \tag{7}$$

$$k = \mu L\left(\frac{Q - (S_u - S_d)dp/dt}{2A\Delta P}\right) \tag{8}$$

Equation (7) is identical to equation (3). Equation (8) is exactly the same as Equation (4) if equation (3) is substituted for S_s in equation (4). Consequently, there is no difference in the asymptotic solutions between the two different boundary conditions, flow control and pressure control, in terms of the slope and the differential pressure. The calculation of the hydraulic properties is quite straightforward as no tedious history curve matching is required.

Test Results

Our proposed methods have been applied to the measurement of permeability and the specific storage of cored rock specimens. We report here two selected test results in two well-known rock types: Westerly granite for the flow control method and Fontainebleau sandstone for the pressure control method. Westerly granite has 0.5% of crack-porosity, whilst Fontainebleau sandstone has 10% porosity composed mostly of spherical shaped pores and tube-shaped network. During the tests, the confining pressure was kept constant at 35 MPa for Westerly granite and 320 MPa for Fontainebleau sandstone. A typical example of the time-based record of fluid pressure variation at the upstream and downstream reservoirs rising from different pore pressures by constant-rate flow injection is given in Figure 2. From each test record, we determined the slope (*dp/dt*) using a linear regression method and the differential pressure (ΔP) of the linear segments of pressure curves following the initial transient stages. We calculated the specific storage S_s and the permeability k of each specimen using Equations (6) and (7), respectively. The test conditions, system compliance, equation parameters, and hydraulic properties are listed in Tables 1 and 2, for Westerly granite and Fontainebleau sandstone, respectively. Also the specific storage and permeability as a function of effective confining pressure are shown in Figures 3 and 4, respectively, for both rock types. The hydraulic parameters are severely effective-stress dependent in Westerly granite, but much less dependent in Fontainebleau sandstone. We cannot compare directly these distinct behaviors because of the huge difference in the effective stress range. Even so, we believe that this discrepancy is related to the difference in the shape of pores between the two rock types.

Table 1. Hydraulic test condition and result in Westerly granite (P_{eff}^*: the effective confining stress).

P_{eff}^*	Q	S_u	S_d	dp/dt	ΔP	S_s	k
MPa	m^3/sec	m^3/Pa	m^3/Pa	Pa/sec	Pa	Pa^{-1}	m^2
21.39	1.05×10^{-10}	6.48×10^{-14}	1.03×10^{-15}	1590	1774300	4.22×10^{-12}	3.94×10^{-20}
17.50	1.05×10^{-10}	6.35×10^{-14}	1.03×10^{-15}	1613	1557300	1.48×10^{-11}	5.43×10^{-20}
14.00	1.05×10^{-10}	6.20×10^{-14}	1.03×10^{-15}	1620	1399300	4.37×10^{-11}	8.74×10^{-20}
10.33	1.05×10^{-10}	6.10×10^{-14}	1.03×10^{-15}	1560	1209600	1.30×10^{-10}	1.86×10^{-19}
7.24	1.05×10^{-10}	6.08×10^{-14}	1.03×10^{-15}	1493	1128100	2.09×10^{-10}	2.75×10^{-19}

Table 2. Hydraulic test condition and result in Fontainebleau sandstone.

P_{eff}^{*}	dp/dt	S_u	S_d	Q	ΔP	S_s	k
MPa	Pa/sec	m^3/Pa	m^3/Pa	m^3/sec	Pa	Pa^{-1}	m^2
280	5.0×10^{-6}	2.10×10^{-14}	2.28×10^{-14}	2.76×10^{-7}	148000	2.33×10^{-9}	8.17×10^{-14}
280	1.0×10^{-7}	2.10×10^{-14}	2.28×10^{-14}	5.26×10^{-7}	303000	2.27×10^{-9}	7.62×10^{-14}
240	5.0×10^{-6}	2.13×10^{-14}	2.31×10^{-14}	2.47×10^{-7}	147000	2.21×10^{-9}	7.38×10^{-14}
240	1.0×10^{-7}	2.13×10^{-14}	2.31×10^{-14}	4.89×10^{-7}	269000	2.20×10^{-9}	7.99×10^{-14}
200	5.0×10^{-6}	2.17×10^{-14}	2.35×10^{-14}	2.20×10^{-7}	118000	2.11×10^{-9}	8.22×10^{-14}
200	1.0×10^{-7}	2.17×10^{-14}	2.35×10^{-14}	4.42×10^{-7}	244000	2.11×10^{-9}	7.99×10^{-14}
140	5.0×10^{-6}	2.25×10^{-14}	2.42×10^{-14}	2.00×10^{-7}	110000	2.05×10^{-9}	8.04×10^{-14}
140	1.0×10^{-7}	2.25×10^{-14}	2.42×10^{-14}	4.02×10^{-7}	235000	2.05×10^{-9}	7.56×10^{-14}

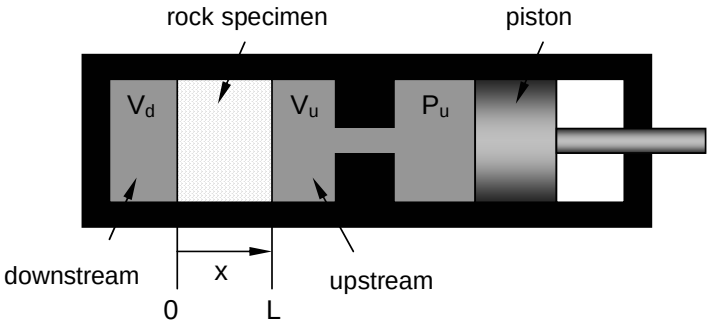

Figure 1. Schematic diagram of the test system.

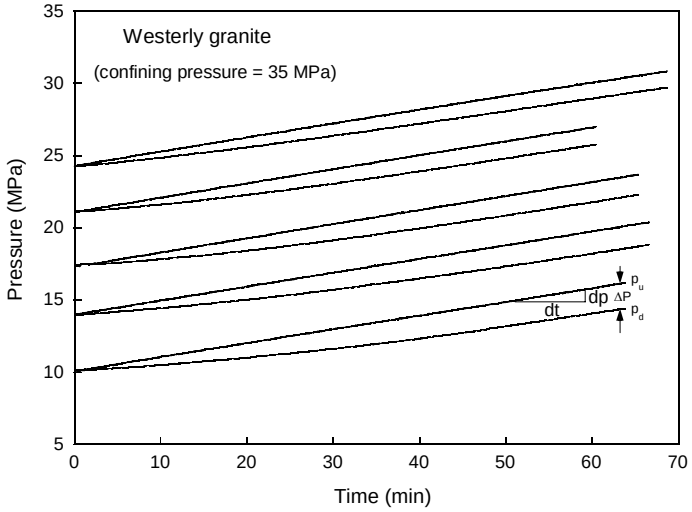

Figure 2. An example of test record for Westerly granite. Fluid injection with a constant flow rate was conducted at several different levels of pore pressure. Injection was continued until a linear segment of pressure increase at both reservoirs was clearly shown after the transient stage. Note that the differential pressure ΔP decreases with increasing pore pressure.

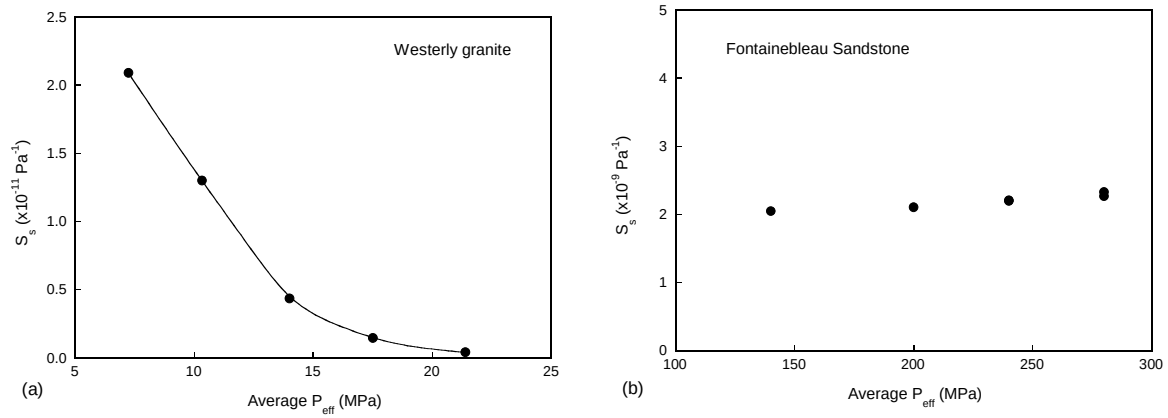

Figure 3. Variation of specific storage as a function of average effective confining pressure for (a) Westerly granite and (b) Fontainebleau sandstone. Confining pressure was constant at 35 MPa and 320 MPa for Westerly granite and Fontainebleau sandstone, respectively.

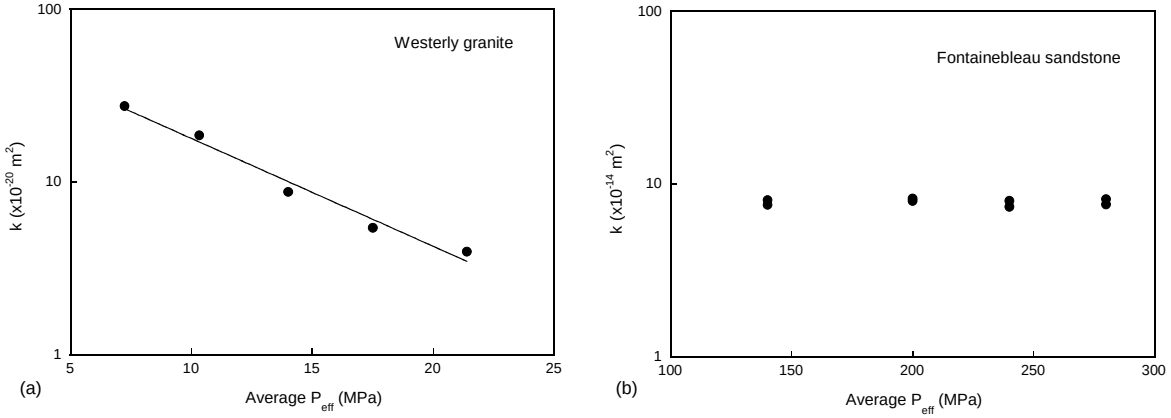

Figure 4. Variation of permeability as a function of average effective confining pressure for (a) Westerly granite and (b) Fontainebleau sandstone. Confining pressure was constant at 35 MPa and 320 MPa for Westerly granite and Fontainebleau sandstone, respectively.

References

Brace, W.F., J.B. Walsh, and W.T. Frangos, Permeability of granite under high pressure, *J. Geophys. Res.*, *73*, 2225-2236, 1968.

Hsieh, P.A., J.V. Tracy, C.E. Neuzil, J.D. Bredehoeft, and S.E. Silliman, A transient laboratory method for determining the hydraulic properties of tight rocks-I. Theory, *Int. J. Rock Mech. Min. Sci. & Geomech. Abstr.*, *18*, 245-252, 1981.

Song, I., S.C. Elphick, I.G. Main, B.T. Ngwenya, N.W. Odling, and N.F. Smyth, One-Dimensional Fluid Diffusion Induced by Constant-Rate Flow Injection; Theoretical Analysis and Application to the Determination of Fluid Permeability and Specific Storage of a Cored Rock Sample, *J. Geophys. Res.*, 2003 (accepted).

Zeynaly-Andabily, E.M. and S.S. Rahman, Measurement of permeability of tight rocks, *Meas. Sci. Technol.*, *6*, 1519-1527, 1995.

Acknowledgments

This research project was funded by the specific programme on EESD “Energy, Environment and Sustainable Development” (Project reference number EU: EVR1-2000-40005), and also by the German Science Foundation (SFB526 “Rheology of the Earth”).

Imaging Permeability Structure in Fractured Rocks: Inverse Theory and Experiment

[1]Tokuo Yamamoto, [2]Junichi Sakakibara, and [3]Tatsuo Katayama
[1]Geoacoustics Lab., RSMAS; University of Miami, Miami, FL. USA; [2]JFE Civil Co., Taito-ku, Tokyo, Japan; [3]Kanden Kogyo, Inc., Kitaku, Osaka, Japan

Summary

Imaging the permeability within the earth has been an important unsolved problem of acoustics and seismic. Usually the measured attenuations by acoustic and seismic methods are too large to use them for inversions of permeability based on the poro-elastic theories. The apparent attenuations by volume scattering due to the acoustic velocity fluctuations are found to be the major parts (30 to 90 %) of the measured attenuations at an acoustic wave frequency of 4 kHz. When these scattering attenuations are removed from the measured attenuation, the experimentally measured intrinsic attenuations become comparable to the attenuations predicted by the poro-elastic theory of Biot, enabling the permeability image inverted from the measured intrinsic attenuations and the acoustic velocities. The permeability image of the fracture zone inverted by the inverse theory agrees excellently with the measured permeability of fracture zone 300 md by injection tests.

Introduction

Can permeability be measured by acoustic and seismic methods? This question has been asked since M. Biot (1956) published the poro-elastic theory of acoustic wave propagation through fluid-saturated porous earth materials. Experimental data from the fields and in the laboratories at all frequencies showed that the measured attenuations are much higher than the attenuation predicted by the Biot theory (Pride et al., 2003). In this paper, the case of fractured hard shale having acoustic velocity of the order of 5.5 km/s is reported. The apparent attenuations from volume scattering are calculated using the scattering theory by Yamamoto (1996) using velocity and density fluctuations measured by a crosswell tomography experiment at a frequency of 4 kHz. The Biot theory and an empirical elasticity-porosity relation were combined to make a permeability-porosity inversion theory. The inverted permeability image is campared with the injection test results conducted at the fracture zone.

Permeability Inverse Theory

The theory of volume scattering is given in Yamamoto (1996). The scattering attenuation Q^{-1}_{s}, the total attenuation Q^{-1}_{total}, and the absorption due to the viscosity μ of pore fluid, Q^{-1}_{abs} are related by, $Q^{-1}_{abs} = Q^{-1}_{total} - Q^{-1}_{s}$. The elastic moduli of a fractured rock are affected by porosity ϕ. For carbonate rocks, Yamamoto (2003) found the following relationship between the elastic moduli of the rock frame and the porosity, $K = K_r(1-\phi)^n$, where K is the bulk modulus of the frame, K_r is the bulk modulus of solid, and n is the power law constant (n = 3.8). A constant Poison's ratio of the rock solid and the frame of the rock is found to be: $\nu = 0.286$. It has been assumed that these relationships also hold for the fractured hard shale that is treated in this paper. The values of the bulk modulus, shear modulus, and plane wave modulus of the solid of the rock

are found to be: K_r = 4.85*e*10 (Pa), G_r = 2.42 (Pa), and M_r = 8.06 (Pa). The porosity of the fractured rocks is inverted iteratively from the measured acoustic wave velocity V_P through: $\phi = 1-(M/M_r)^{1/n}$, and $M = \{\rho_r(1-\phi)+\rho_f\phi\}V_P{}^2$, where ρ_r is the density of the solid, and ρ_f is the density of the pore-fluid. We now know all the elastic moduli of the skeletal frame and the solid of rocks as well as the porosity of the rocks for a given measured P-wave velocity at a given frequency. Only the permeability k and the added mass coefficient C_a of the skeletal frame are unknown. The added mass coefficient of the fused glass beads measured by Polona and Johnson (1984) is 0.35, which was used for the added mass coefficient of the skeletal frame of the fractured rocks in this study. The permeability k is obtained by finding the roots of the implicit quadratic equation in k formed by equating the theoretical intrinsic attenuation $Q^{-1}{}_{theory}(k)$ and the experimentally measured absorption $Q^{-1}{}_{abs}$, $Q^{-1}{}_{theory}(k)$ - $Q^{-1}{}_{abs}$ = 0. The implicit expression $Q^{-1}{}_{theory}(k)$ is given by the Biot theory.

Experiment

The crosswell tomography experiments were conducted at the basement for a multi-purpose dam located in Gifu Prefecture of Japan. The main component of the rocks is the green shale but the rocks have sporadic thin potion of limestone randomly included in the green shale. Two open holes of 60 mm in diameter were drilled down to 70 m below the basement surface with a fracture zone between wells that are separated by a horizontal distance of 40 m. A 45 mm diameter x 400 mm long cylindrical piezoelectric source with a 180 dB broadband output at center frequency of 4 kHz was used to emit a 4095 cycle PRBS signals. The receiver array consists of 16-channel hydrophones (Bentoth model AQ-10) having an inter-element separation of 1 m. Figure 1 shows example source gather data of the arrival wave fields after correlation. The first arrival travel time and amplitude inversion method by Bregman et al. (1989 a and b) was used for the velocity and attenuation inversions.

Results

Acoustic velocity tomogram. The acoustic velocity tomogram inverted from the first arrival time data of the PRBS arrival wave fields is shown in Figure 2. Relatively low velocity area below the high velocity area indicates the possible existence of fracture zones within in Figure 2.

Total attenuation, scattered attenuation, and absorption. The total measured attenuation (Figure 3a), the calculated scattered attenuation (Figure 3b), and the absorption (the total attenuation minas the scattered attenuation) (Figure 3c) for the fractured hard rock are shown to demonstrate the effect of scattering on the acoustic wave attenuation. After removing the scattering attenuation (Figure 3b) from the total attenuation (Figure 3a), the fractured zone is clearly revealed in the absorption image in Figure 3c.

Permeability images. The permeability image inverted from the velocity image (Figure 2) and the absorption image (Figure 3c) using the Biot (1956a) theory is shown in Figure 4. The fracture zone with permeability of roughly 300 md is clearly imaged. The injection tests performed at the fracture zone also measured the permeability of roughly 300 md providing a perfect agreement.

Conclusions

The long lasted mystery of the large discrepancy between the observed attenuation and the much smaller intrinsic attenuation predicted by the Biot (1956) theory has been resolved: the cause of the large discrepancy was found to be the apparent attenuation due to the scattering of the incident acoustic waves by velocity fluctuations. The removal of the apparent scattering attenuation from the measured total attenuation clearly revealed the intrinsic attenuation image of the fracture zone where the attenuation is actually from the acoustic energy dissipation due to the viscosity of pore-fluid undergoing the Darcy flow.

Acknowledgments

The theoretical portion of this research was sponsored by a grant from the Office of Naval Research Code 321OA. The experiment was conducted through a contract from the Kansai Power and Light Corporation.

References

Biot, M. A., 1956, Theory of propagation of elastic waves in fluid-saturated porous solid. Low-frequency range: J. Acoust.. Soc. Am. 28, 168-178.

Bregman, N. D., Bailey, R. C., and Chapman, C. H., 1989a, Crosshole seismic tomography: Geophysics, 54, 200-215.

Bregman, N. D., Chapman, C. H., and Bailey, R. C., 1989b, Travel time and amplitude analysis in seismic tomography: J. Geoph. Res., 94(6), 7577-7587.

Pride, S. R, Harris, J. M., Johnson, D. L., Mateeva, A., Nihei, K. T., Nowack, R. L., Rector, J. W., Spetzler, H., Wu, R., Yamamoto, T., Berryman, J. G., and Fehler, M., Permeability dependence of seismic amplitudes The Leading Edge: 2003, June Issue.

Polona, T. J., and Johnson D. L., 1984, Acoustic properties of porous systems: I. Phenomenological description, in *Physics and Chemistry of Porous Media*, Johnson, D. L. and Sen, P. N. (edited), American Institute of Physics, 89 – 104.

Yamamoto, T., 1996, Acoustic scattering in the ocean from velocity and density fluctuations in the sediments, J. Acoust. Soc. Am., 99, 866-879.

Yamamoto, T., 2003, Imaging permeability structure within the highly permeable carbonate earth: Inverse theory and experiment, Geophysics: 2003, July-August Issue.

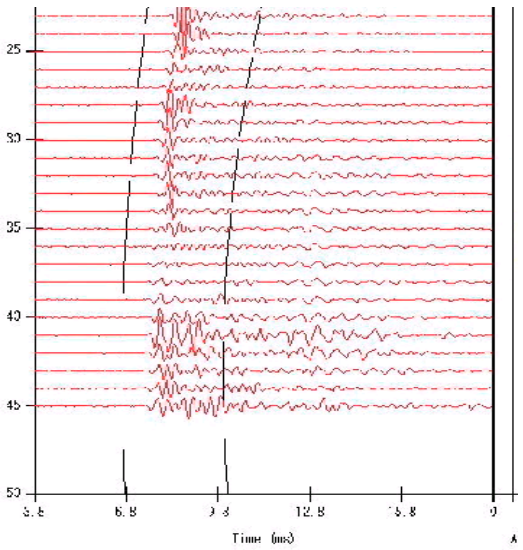

Figure 1. Example source gather data.

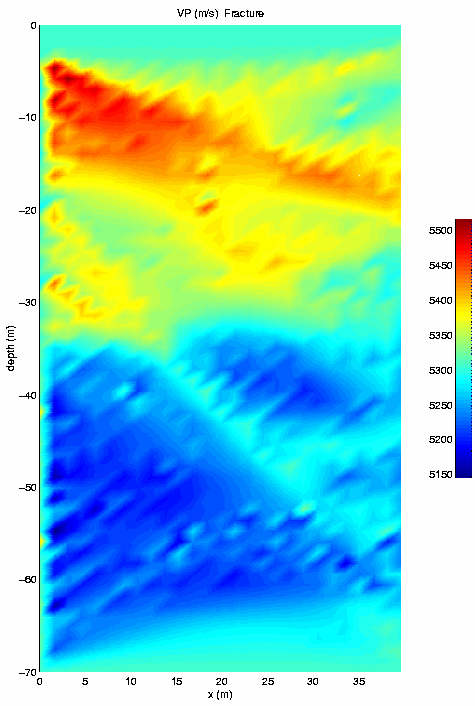

Figure 2. Velocity tomogram.

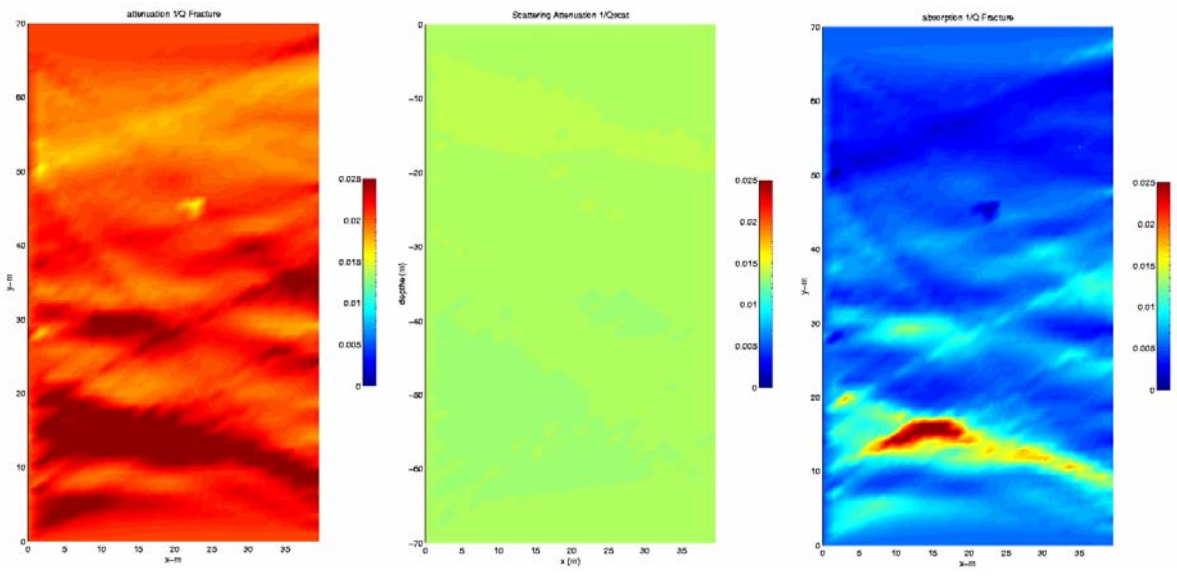

(a) (b) (c)

Figure 3. (a) Total attenuation, (b) scattering attenuation, and (c) absorption.

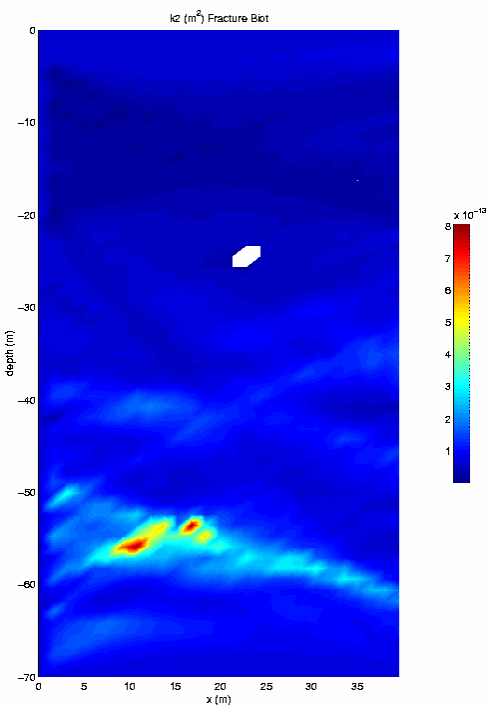

Figure 4. Permeability Image.

Session 3:
GEOCHEMISTRY, COUPLED AND MICROBIAL PROCESSES, AND GEOTHERMAL RESOURCES

Progress toward Understanding Coupled Thermal, Hydrological, and Chemical Processes in Unsaturated Fractured Rock at Yucca Mountain

Eric Sonnenthal[1] and Nicolas Spycher
Earth Sciences Division, Lawrence Berkeley National Laboratory
1 Cyclotron Rd, MS90-1116, Berkeley, CA 94720
elsonnenthal@lbl.gov

Introduction

The emplacement of nuclear waste into the proposed repository at Yucca Mountain is expected to result in a period of several hundred to over a thousand years in which the rock that surrounds emplacement drifts (i.e., the near-field) has been heated to above-boiling temperatures. Predictions of the thermal response at a larger scale indicate that much of the unsaturated zone (UZ) both above and below the repository would also experience significantly elevated temperatures. A considerable amount of research has therefore focused on the effects of long-term heating on the thermal, hydrological, mechanical, and chemical evolution of the UZ over time periods on the order of 100,000 years.

The performance of the proposed nuclear waste repository at Yucca Mountain has been linked to three main issues that have a direct relation to coupled thermal, hydrological, and chemical (THC) processes. First, there is the effect of mineral precipitation in fractures above the emplacement drifts, potentially leading to the formation of a low permeability "cap" and resulting in changes to drift seepage. The second major issue is the chemistry of water that could potentially seep into drifts and the composition of the gas in the drifts, which together have a strong influence on corrosion processes that may take place at the surface of the waste package. Finally, at a larger spatial scale, the effects of elevated temperatures on the mineralogical and hydrological characteristics of the vitric and zeolitic units, primarily below the repository, could have a significant impact on the transport of radionuclides and their retardation via ion exchange, sorption, and matrix diffusion. The thermal load of the proposed repository will also markedly control the importance and extent of these processes (Spycher et al., 2003a).

In this paper, we address only thermal-hydrological-chemical (THC) processes, yet it should be recognized that mechanical effects (e.g., fracture closure or slip) could modify the permeability evolution of the system (Rutqvist and Tsang, 2003). Such mechanical changes, however important, are unlikely to significantly alter the important chemical processes. The investigations into THC processes have included laboratory experiments, large-scale *in situ* heater tests, geochemical/isotopic sampling and analyses, natural analogues, geochemical modeling, and reaction-transport modeling. Progress in the development of conceptual and predictive models for THC processes to address these issues, results of the analyses, and their validation through comparison to thermal test measurements are summarized in this contribution.

Conceptual Models for THC Processes and Their Validation

The chemical evolution of waters, gases, and minerals in the UZ is intimately coupled to thermal-hydrological processes that involve liquid and vapor flow, heat transport, boiling and condensation, drainage through fractures, and fracture-matrix interaction. The conceptual model for THC processes must consider aqueous and gaseous species transport and water-gas-rock reactions, leading to changes in mineral assemblages and abundances. The distribution of condensate water in the fracture system, as well as the spatial and temporal evolution of the boiling zone, determines where mineral dissolution and precipitation can take place and where there can be direct interaction (via diffusion) between matrix pore waters and fracture waters. Finally, changes in hydrological properties (i.e., porosity, permeability, and capillary pressure) must be linked to mineral dissolution and precipitation.

TH processes in the fractured welded tuffs at Yucca Mountain have been examined theoretically and experimentally since the early 1980s (Pruess et al., 1984; 1990; Buscheck and Nitao, 1993; Tsang and Birkholzer, 1999; Kneafsey and Pruess, 1998). To summarize the important TH processes, heat conduction from the drift wall into the rock matrix results in vaporization and boiling, with vapor migration out of matrix blocks into fractures. The vapor moves away from the drift through the permeable fracture network by buoyancy and by the increased vapor pressure caused by heating and boiling. In cooler regions, the vapor condenses on fracture walls, where the condensate water then drains through the fracture network either down toward the heat source, or into the rock underlying the heat source. Imbibition of water from fractures into the rock matrix leads to increases in the liquid saturation. A dryout zone may develop closest to the heat source, separated from the condensation zone by a nearly isothermal zone maintained at about the boiling temperature. Where characterized by a continuous process of boiling, vapor transport, condensation, and migration of water back to the heat source (either by capillary forces or gravity drainage), this nearly isothermal zone has been termed a heat pipe (Pruess et al., 1990). Recently, validation of the TH models and the associated uncertainties, based on comparson to measurements from the Drift Scale Test, have been presented by Mukhopadhyay and Tsang (2003).

Extensive experimental and geochemical modeling studies of water-rock reactions had been performed for several years prior to the thermal tests (e.g., Knauss et al., 1986; Murphy and Pabalan, 1994; Glassley and Boyd, 1994). Preliminary reactive transport modeling as well as analyses of possible mineral alteration paths were also presented by Lichtner and Seth (1996), Sonnenthal et al. (1997), and Hardin (1998). The development of conceptual models of coupled THC processes were extended greatly for predictions of the Drift Scale Test (Sonnenthal et al., 1998; Xu et al., 2001) along with continued model and code development and validation performed using chemical measurements of gas and water samples (Sonnenthal et al., 2001a).

Results of these studies have demonstrated that the TH processes of boiling, vapor transport, condensation, and drainage lead to strong differences in aqueous species concentrations in fractures relative to the rock matrix, as well as to different effective reaction rates. These strong differences necessitate the use of multiple continuum models (e.g., dual-permeability) to capture chemical as well as pressure gradients. The effects of TH processes on water chemistry further depend on the behavior of the dissolved species with respect to mineral-water reactions.

Conservative species (i.e., those that are unreactive and nonvolatile), such as chloride (Cl^-), become concentrated in waters undergoing vaporization or boiling, but are essentially absent from the vapor condensing in the fractures. Therefore, the concentration of conservative species in the draining condensate waters is determined by mixing with fracture pore waters and diffusive mixing with matrix pore waters. In addition to these processes, concentrations of aqueous species such as calcium (Ca^{+2}) are also affected by mineral dissolution or precipitation (e.g., calcite), but as well by reactions involving other Ca-bearing minerals such as zeolites, clays, and plagioclase feldspar. Even though the variation in aqueous species in space and time has been generally captured by models of the Drift Scale Test, the variation in pore-water compositions over the repository footprint will lead to a greater range in the chemistry of potential seepage waters (Spycher et al., 2003b).

Another important aspect of the system is the exsolution of CO_2 from the liquid phase as temperature increases. The exsolution of CO_2 in the boiling zone results in a local increase in pH, and a decrease in pH in the condensation zone into which the vapor enriched in CO_2 is transported and condensed. The extent to which the pH is shifted depends also on the rates of mineral-water reactions. Because the diffusivities of gaseous species are several orders of magnitude greater than those of aqueous species, and because the advective transport of gases can be more rapid than that of liquids, the region where CO_2 degassing affects water and gas chemistry can be much larger than the region affected by the transport of aqueous species. This effect has been predicted in the long-term mountain-scale THC simulations, as well as documented in the Drift Scale Test measurements (Conrad and Sonnenthal, 2001).

The distribution of precipitating mineral phases is strongly related to differences in solubility as a function of temperature. Precipitation of amorphous silica is likely to be confined to a narrow zone where evaporative concentration from boiling exceeds its solubility. In contrast, calcite may precipitate in fractures over a broad zone of elevated temperature, because of its lower solubility at higher temperatures. Although there has been documented evidence of mineral precipitation in fractures in the boiling zones of the thermal tests, detailed analyses have not been performed to map out the spatial distribution sufficiently, or to investigate mineral zonation within the rock matrix adjacent to a fracture, in a similar manner to that observed as a function of distance along a transport path (e.g., Steefel and Lichtner, 1998).

Evidence for complete sealing of fractures by mineral precipitation has been documented in laboratory experiments, yet extrapolation of these results over the time scales of repository heating, and considering the range of expected percolation fluxes, suggests that complete sealing is not likely to take place (Dobson et al., 2003). Natural heterogeneity in fracture aperture also plays a role in the modification of hydrological properties, as water-rock reactions have been shown to be favored in the smaller aperture fractures where greater capillary suction leads to higher liquid saturations (Sonnenthal et al., 2001b). Therefore, mineral precipitation in unsaturated heterogeneous fractured rock is likely to result in an increase in focused flow because of preferential filling of smaller aperture fractures.

Conclusions and Remaining Uncertainties

The overall conclusions and uncertainties regarding THC effects on the UZ at Yucca Mountain—reached through combined experimental, theoretical, and numerical modeling studies—are as follows:

(1) The development of a continuous mineralized cap above the proposed repository is unlikely, yet some flow focusing may result in local increases in the percolation flux. The main uncertainties that remain are related to effects of local differences in the fracture aperture, the effect of lithophysal cavities on vapor and water flow, the extent of three-dimensional flow focusing, and also in future climate changes leading to increased percolation fluxes.

(2) The major element chemistry of potential seepage water is different from that originally predicted based on saturated zone water samples, but has a fairly narrow range in composition (about one order of magnitude for many components) that is fairly well-bounded by measurements and modeling. The outstanding uncertainties are primarily related to the unknown spatial distribution of percolating water compositions and to the limited number of samples from proposed repository host rocks. In addition, the chemistry of minor elements and some species important to corrosion (e.g., nitrate) are less well known.

(3) Some mineralogical alteration of the vitric and zeolitic tuffs is likely, yet will be limited owing to the relatively short time over which temperatures are elevated, and because the maximum temperature will generally remain below about 80°C in these units. Quantitative prediction of the alteration of vitric and zeolitic tuffs is limited by the greater uncertainties in the thermodynamic and kinetic data for reactions involving volcanic glass and zeolites.

References

Buscheck, T.A. and J.J. Nitao, 1993. Repository-heat-driven hydrothermal flow at Yucca Mountain, Part I: Modeling and analysis. Nuclear Technology, 104, (3), 418-448.

Conrad, M.E. and E.L Sonnenthal, 2001. Isotopic constraints on the thermochemical evolution of the Drift-Scale Heater Test at Yucca Mountain. Eleventh Annual V.M. Goldschmidt Conference. Lunar and Planetary Institute Contribution, 3722.

Dobson, P.F., T.J. Kneafsey, E.L. Sonnenthal, N.F. Spycher, and J.A. Apps, 2003. Experimental and numerical simulation of dissolution and precipitation: Implications for fracture sealing at Yucca Mountain, Nevada. Journal of Contaminant Hydrology. 62-63: 459-476.

Glassley, W.E. and S. Boyd, 1994. Preliminary estimate of the rates and magnitudes of changes of coupled hydrological-geochemical properties. Yucca Mountain Project Milestone MOL79. Lawrence Livermore National Laboratory.

Hardin, E.L., 1998. Near-field/altered zone models. Milestone Report SP3100M4, Lawrence Livermore National Laboratory.

Knauss, K.G., J.M. Delany, W.J. Beiringer, and D.W. Peifer, 1986. Hydrothermal interaction of Topapah Spring Tuff with J-13 water as a function of temperature. Proceedings of the Materials Research Society Symposium, 44, 539-546.

Kneafsey, T.J. and Pruess, K. 1998. Laboratory experiments on heat-driven two-phase flows in

natural and artificial rock fractures. Water Resources Research, 34, (12), 3349-3367.
Lichtner, P.C. and M.S. Seth, 1996. Multiphase-multicomponent nonisothermal reactive transport in partially saturated porous media. International Conference on Deep Geologic Disposal of Radioactive Waste, Canadian Nuclear Society.
Mukhopadhyay, S., and Y.W. Tsang, 2003. Uncertainties in coupled thermal-hydrological processes associated with the drift scale test at Yucca Mountain, Nevada. Journal of Contaminant Hydrology, 62–63, 595–612.
Murphy, W.M. and R.T. Pabalan, 1994. Geochemical investigations related to the Yucca Mountain environment and potential nuclear waste repository. NUREG/CR-6288. Washington, DC: Nuclear Regulatory Commission.
Pruess, K., Y.W. Tsang, and J.S.Y. Wang, 1984. Numerical studies of fluid and heat flow near high-level nuclear waste packages emplaced in partially saturated fractured tuff. LBL-18552. Berkeley, California: Lawrence Berkeley Laboratory.
Pruess, K., J.S.Y. Wang, and Y.W. Tsang, 1990. On thermohydrologic conditions near high-level nuclear wastes emplaced in partially saturated fractured tuff, 1. Simulation studies with explicit consideration of fracture effects. Water Resources Research, 26 (6), 1235-1248.
Rutqvist, J. and C-F. Tsang, 2003. Analysis of thermal-hydrologic-mechanical behavior near an emplacement drift at Yucca Mountain. Journal of Contaminant Hydrology, 62-63: 637-652.
Sonnenthal, E., J. Birkholzer, C. Doughty, T. Xu, J. Hinds, and G. Bodvarsson, 1997, Post-emplacement site-scale thermohydrology with consideration of drift-scale processes. Level 4 Milestone SPLE2M4. Lawrence Berkeley Laboratory.
Sonnenthal, E., N. Spycher, J. Apps, and A. Simmons, 1998. Thermo-hydro-chemical predictive analysis for the Drift-Scale Heater Test. Level 4 Milestone SPY289M4, v1.1. Lawrence Berkeley National Laboratory.
Sonnenthal, E.L., N.F. Spycher, J.A. Apps, and M.E. Conrad, 2001a. A conceptual model for reaction-transport processes in unsaturated fractured rocks at Yucca Mountain: Model validation using the Drift Scale Heater Test. Eleventh Annual V.M. Goldschmidt Conference. Lunar and Planetary Institute Contribution, 3814.
Sonnenthal, E., N. Spycher, and C. Haukwa, 2001b. Effects of water-rock interaction on unsaturated flow in heterogeneous fractured rock. EOS, Trans. AGU, F518.
Spycher, N, E. Sonnenthal, and J. Apps, 2003a. Prediction of fluid flow and reactive transport around potential nuclear waste emplacement tunnels at Yucca Mountain, Nevada. Journal of Contaminant Hydrology, 62-63: 653-673.
Spycher, N., E.L Sonnenthal, P.F. Dobson, T.J. Kneafsey, and S. Salah, 2003b. Drift-Scale coupled processes (DST and THC seepage) models, REV02. LBID-2478, Lawrence Berkeley National Laboratory, California.
Steefel, C.I. and P.C. Lichtner, 1998. Multicomponent reactive transport in discrete fractures: I. Controls on reaction front geometry. Journal of Hydrology, 209, 186-199.
Tsang, Y.W. and J.T. Birkholzer, 1999. Predictions and observations of the thermal-hydrological conditions in the Single Heater Test. Journal of Contaminant Hydrology, 38, (1-3), 385-425.
Xu, T., E. Sonnenthal, N. Spycher, K. Pruess, G. Brimhall, and J.A. Apps, 2001. Modeling multiphase fluid flow and reactive geochemical transport in variably saturated fractured rocks: 2. Applications to supergene copper enrichment and hydrothermal flows. American Journal of Science, 301:34-59.

Plumbing the Depths: Magma Dynamics and Localization Phenomena in Viscous Systems

Marc Spiegelman
Dept. Of Earth & Env. Sciences; Dept of Applied Physics & Applied Mathematics, Columbia University

Understanding fluid flow in fractured rock is one of the most challenging problems in coupled fluid/solid mechanics. For this reason, I work on the somewhat *easier* problem of reactive fluid-flow in viscously deformable, permeable media. Nevertheless, the magma migration problem has some features that may be useful for understanding fluid flow in brittle media within a more tractable theoretical framework that also allows exploration of large scale coupled melt/solid dynamics in the Earth's mantle. This abstract and presentation review results and progress on this problem.

The initial formulation of the magma migration problem is due to McKenzie (1984) and others (i.e., Scott and Stevenson, 1984, 1986; Fowler, 1985) who derived a system of conservation equations describing the behavior of two interpenetrating continua: a low viscosity fluid in a creeping, permeable solid. The important feature of this formulation is a consistent coupling of fluid pressure and permeability with solid stresses and deformation. In the limit of infinite solid viscosity, these equations reduce to the standard formulation for fluid flow in rigid porous media. However, the addition of a viscous rheology and solid deformation allows a host of new behavior ranging from melt-driven solid convection to non-linear porosity waves. The physics of the equations for mass and momentum conservation are described in detail in Spiegelman (1993a,b), suggesting that magma migration is inherently time-dependent. These equations have also been applied to model Earth science problems such as the behavior and chemical consequences of melt-transport beneath mid-ocean ridges (e.g., Spiegelman, 1996). While these results suggest that the flow of the solid can have observable consequences on melt chemistry, these initial calculations assumed that melt flow was essentially distributed. This assumption, however, is at odds with field and chemical observations that suggest that magma migration in the mantle is localized into some form of "channel" network (e.g., Kelemen et. al, 1997).

More recently, the formulation has been extended to investigate several mechanisms for flow localization. The first mechanism is channelization by reactive fluid flow in a solubility gradient (Aharonov et. al., 1995). This problem was motivated by observations of "replacive dunites" seen in ophiolites which have been interpreted to be relic melt channels where one of the principal phases (orthopyroxene) has been dissolved out of the matrix (e.g., Kelemen et. al, 1995). Full numerical solutions (Spiegelman et. al, 2001) in a static medium show that this mechanism can produce strong channeling in sufficiently reactive systems. The compactibility of the solid matrix actually enhances this instability by allowing the regions between channels to compact to near impermeability. This compaction is driven by lower fluid pressures within the channels that extract melt from the inter-channel regions. The spontaneous development of a two-porosity system has significant effects on the trace element signature of melts in these systems and can lead to extreme chemical variability even from a chemically homogeneous source (Spiegelman and Kelemen, 2003). We are currently exploring the full stability of reactive flow in adiabatically melting systems.

In addition to chemical mechanisms for localization, we have also been exploring purely mechanical processes that may have some bearing on crack-forming systems. Again, this work has been motivated by observations, this time of laboratory experiments which demonstrate spontaneous generation of melt rich bands in multi-phase mixtures undergoing simple shear (Holtzmann et al., 2003). These experiments provide, for the first time, the ability to validate the general framework. So far the results are encouraging. A linear stability analysis (Spiegelman, 2003) shows that low-angle melt-rich shear bands are admitted by the equations and form by an interaction of shear with a melt weakening solid shear-viscosity. Weaker regions preferentially dilate under shear reducing the pressure within the weak region which draws in further melt in a runaway affect. The linear analysis has no preferred wave-length of instability, however, initial non-linear calculations suggest that a screening effect or surface energy effects could provide a short wavelength cut-off as is observed in the experiments.

In general, we suspect that a combination of chemical and mechanical mechanisms are responsible for the observed localization in magmatic systems. To date, we have only explored purely viscous problems, however, it is likely that elastic or visco-elastic mechanisms may also contribute. The basic formulation should be extendible to elastic and brittle systems and should eventually be made consistent with current work for fractured media.

References

Aharonov E, Whitehead Ja, Kelemen Pb, et al. [1995] Channeling instability of upwelling melt in the mantle. J GEOPHYS RES-SOL EA 100 (B10): 20433-20450 □

Fowler, Ac. [1985]. A mathematical model of magma transport in the asthenosphere. Geophys. Astrophys. Fluid Dyn. 33:63-96.

Holtzman Bk, Groebner Nj, Zimmerman Me, et al. [2003]. Stress-driven melt segregation in partially molten rocks. Geochem Geophy Geosy 4: Art. No. 8607

Kelemen, Pb, Shimizu, N and Salters, Vmj. [1995]. Extraction of mid-ocean-ridge basalt from the upwelling mantle by focused flow of melt in dunite channels. Nature, 375:6534, 747-753.

Kelemen, Pb, G. Hirth , N. Shimizu, M. Spiegelman and Hb Dick. [1997]. A review of melt migration processes in the adiabatically upwelling mantle beneath oceanic spreading ridges. Philos. Trans. R. Soc. London, Ser. A, 355:1723, 283-318.

McKenzie, D. [1984]. The generation and compaction of partially molten rocks. J. Petrology 25 (3): 713-765

Scott Dr, Stevenson Dj [1984]. Magma Solitons, GRL 11 (11): 1161-1164

Scott Dr, Stevenson Dj [1986]. Magma ascent by porous flow. J Geophys Res-Solid 91 (B9): 9283-9296

Spiegelman, M. [1993]. Flow in deformable porous media. part 1. Simple analysis. J. Fluid Mech., 247:17 38

Spiegelman, M. [1993]. Flow in deformable porous media. part 2. Numerical analysis The relationship between shock waves and solitary waves. J. Fluid Mech., 247:39 63.

Spiegelman, M. [1996]. Geochemical consequences of melt transport in 2-D: The sensitivity of trace elements to mantle dynamics. Earth Planet. Sci. Lett., 139:115 132

Spiegelman, M., P. B. Kelemen, and E. Aharonov [2001]. Causes and consequences of flow organization during melt transport: The reaction infiltration instability in compactible media. J. Geophys. Res., 106(B2):2061 2077.
Spiegelman, M. and P. B. Kelemen [2003]. Extreme chemical variability as a consequence of channelized melt transport. Geochem. Geophys. Geosyst., 4(8). Article 1055.
Spiegelman, M. [2003]. Linear analysis of melt band formation by simple shear. Geochem. Geophys. Geosyst. 4: 9, Article 8615,

The Potential for Widespread Groundwater Contamination by the Gasoline Lead Scavengers Ethylene Dibromide and 1,2-Dichloroethane

Ronald W. Falta
School of the Environment, Departments of Environmental Engineering and Geological Sciences, Clemson University, Clemson, SC 29634-0919
(864) 656-0125, faltar@clemson.edu

Abstract

Ethylene dibromide (EDB) and 1,2 dichloroethane (1,2-DCA) are highly toxic organic chemicals added to all leaded gasoline in the U.S. since the mid-1920s. These chemicals are relatively soluble in water, they are mobile in the subsurface, and they appear to be resistant to biodegradation. Past investigations and remediation efforts at sites contaminated by leaded gasoline have rarely addressed the potential for EDB or 1,2-DCA contamination. There is a substantial likelihood that undetected EDB and 1,2-DCA groundwater plumes above drinking water standards may exist at tens of thousands of sites where leaded gasoline has leaked or spilled.

Introduction

Groundwater contamination by gasoline and other hydrocarbon fuels is common throughout the industrialized world. In the US, there have been 385,000 documented releases of gasoline from leaking underground storage tanks (Johnson et al., 2000). The principal contaminants of concern from these releases have been the relatively soluble aromatic hydrocarbons benzene, toluene, ethylbenzene, and xylenes, known collectively as BTEX. These BTEX compounds make up a significant fraction of gasoline, typically about 15% or more. Benzene is by far the most hazardous of the BTEX compounds, with an EPA MCL of 5 μg/L.

Extensive efforts were undertaken in the late 1980s and 1990s to characterize and remediate sites contaminated by BTEX. This work led to the observation that dissolved BTEX compounds may biodegrade both aerobically and anaerobically in natural groundwater systems (see, for example, a review by Bedient et al., 1999). Analyses of BTEX plumes at hundreds of sites in California and Texas by Rice et al. (1995) and Mace et al. (1997) showed that the benzene plumes were limited in most groundwater systems, with average plume lengths from underground storage tank sites on the order of 100 m or less. These studies did not attempt to analyze possible plumes of EDB or 1,2-DCA from gasoline spills. The limited plume length of dissolved BTEX compounds in groundwater is much different than field experience with chlorinated organics, which tend to form much longer plumes due to their resistance to biodegradation.

With very few exceptions, little attention has been paid to the groundwater contamination threat posed by leaded gasoline additives. The compounds EDB and 1,2-DCA were added to leaded gasoline in significant quantities from the mid 1920s until the phase-down of lead in gasoline concluded in the late 1980s. EDB has an aqueous solubility of 4,300 mg/L (Montgomery, 1997),

and 1,2-DCA has an aqueous solubility of 8,700 mg/L (Bedient et al., 1999). Both EDB and 1,2-DCA were present in gasoline at sufficient concentrations to produce equilibrium groundwater concentrations of thousands of μg/L. Moreover, there is strong field evidence that these compounds are mobile, and persistent in groundwater. Some chemical properties of EDB, 1,2-DCA, and benzene are listed in Table 1.

These compounds are both suspected carcinogens, and EDB has an extremely low EPA drinking water MCL of 0.05 μg/L (the MCL for 1,2-DCA is 5 μg/L). The EPA has calculated drinking water concentrations that correspond to specific cancer risk levels. These levels are defined as the concentration of a known or probable carcinogen in drinking water that leads to a 10-4, 10-5, or 10-6 probability for excess risk of cancer due to a lifetime exposure. Table 2 lists the drinking water concentrations for these cancer risk levels for benzene (EPA, 2003), 1,2-DCA (EPA, 1991), and EDB (EPA, 1997). According to the EPA, the excess cancer risk associated with drinking water containing benzene at the MCL of 5 μg/L is about 10-6, the risk for 1,2-DCA at the MCL of 5 μg/L is about 10-5, and the risk for EDB at the MCL of 0.05 μg/L is about 10-4. Put another way, drinking water containing EDB at a concentration of 0.04 μg/L poses the same cancer risk (10-4) as water containing benzene at 100 to 1000 μg/L. Similarly, to achieve a 10-6 cancer risk, EDB drinking water concentrations would need to be reduced to 0.0004 μg/L or 0.4 parts per trillion, a level that is probably not detectable with current analytical techniques. Reviews of EDB toxicology may be found in Alexeeff et al. (1990) and Cal/EPA (2002).

The extent and magnitude of groundwater contamination by EDB and 1,2-DCA due to leaks and spills of leaded gasoline is not currently known. There have been roughly 135,000 documented underground storage tank releases prior to 1979 (Johnson et al., 2000). These early documented releases (and many undocumented releases) would have involved leaded gasoline containing EDB and 1,2-DCA.

Leaded Gasoline Additives

The problem of gasoline engine knocking greatly restricted the development of more powerful and efficient engines in the period immediately following World War I. This led to an extensive search for gasoline additives that could act as engine knock suppressors. In 1921, Midgley and Boyd (1922) discovered that tetraethyllead was a particularly effective antiknock agent, requiring only a few grams per gallon of gasoline to suppress knock in their test engines. Later experiments, however, revealed that the use of tetraethyllead by itself caused severe engine fouling in the form of solid deposits on engine valves and spark plugs. This resulted in a second search for additives that could act as lead scavengers to remove the lead from the engine. It was soon discovered that organic compounds of bromine, or of bromine and chlorine, could perform this function (Boyd, 1950).

Since the first commercial sale of leaded gasoline in 1923, leaded gasoline has contained brominated organic compounds, with various amounts of chlorinated compounds (Jacobs, 1980; Thomas et al., 1997). Since the early 1940's, leaded automotive gasoline has contained EDB and 1,2-DCA in proportion to the amount of tetraalkyllead, with molar ratio of Pb:Cl:Br of 1:2:1 (Jacobs, 1980; Thomas et al., 1997). Aviation gasoline does not contain 1,2-DCA, and uses a

Pb:Br molar ratio of 1:2, or twice the amount of the standard automotive "motor mix" (Jacobs, 1980; Thomas et al., 1997).

Because the proportion of lead scavengers to lead has been nearly constant during this period, the average EDB and 1,2-DCA concentrations closely track the lead concentration, at a proportion of about 45% and 48% of the lead concentration, respectively. The average EDB and 1,2-DCA concentrations in US automotive gasoline were likely between about 0.250 g/L and 0.320 g/L prior to the lead phase-down in 1974.

Dissolution in Groundwater

Gasoline is a complex mixture, composed of hundreds of hydrocarbons. Of these compounds, the low-molecular-weight aromatic hydrocarbons benzene, toluene, ethylbenzene, and xylenes are the most soluble, and have proven to be hazardous to human health. The composition of gasoline is variable depending on the date, refinery, grade, season, and location. Table 3 gives representative values for the average concentrations of BTEX (API 2002) and EDB and 1,2-DCA in leaded gasoline.

The partitioning of a gasoline component between the gasoline phase and the aqueous phase is described by a partition coefficient as the ratio of the equilibrium gasoline phase concentration (C_o^i) to the equilibrium aqueous phase concentration (C_w^i).

$$K_p^i = \frac{C_o^i}{C_w^i}$$

Gasoline-water partition coefficients for BTEX components in gasoline were measured by Cline et al. (1991) and are listed in Table 3. Pignatello and Cohen (1990) report a partition coefficient value of 152 for EDB in leaded gasoline.

Calculated aqueous concentrations of BTEX, EDB, and 1,2-DCA in equilibrium with leaded gasoline are shown in Table 3. These are the maximum dissolved chemical concentrations that could be expected in groundwater near a leaded gasoline spill. As can be seen from the table, all of these compounds can dissolve from leaded gasoline into groundwater at concentrations of thousands of μg/L. Comparing these dissolved concentrations to the EPA drinking water MCLs, it is clear that EDB and 1,2-DCA from leaded gasoline could pose a substantial contamination threat to groundwater supplies. Significantly, the ratio of EDB equilibrium aqueous concentration to its MCL is approximately 5 times greater than the benzene ratio and nearly 30,000 times greater than the xylenes ratio. Similarly, the ratio of 1,2-DCA equilibrium aqueous concentration to MCL is about 15 times greater than the toluene ratio, and more than 500 times greater than the xylenes ratio.

If the EPA lifetime excess cancer risk from Table 2 is used as a basis for estimating the contamination potential of these chemicals, the cancer risk from 1,2-DCA would be comparable to benzene. Using the same calculation, the cancer risk from EDB would be hundreds of times higher than that posed by benzene.

References

Alexeeff, G.V., W.W. Kilgore, and M.Y. Li, 1990, Ethylene dibromide: toxicology and risk assessment, Reviews of Environmental Contamination and Toxicology, Vol. 112, p. 49-122.

API, 2002, Evaluating Hydrocarbon Removal from Source Zones and its Effect on Dissolved Plume Longevity and Magnitude, American Petroleum Institute Publication Number 4715.

Bedient, P.B., H.S. Rifai, and C.J. Newell, 1999, Ground Water Contamination Transport and Remediation, 2nd Ed., Prentice Hall PTR, Upper Saddle River, NJ.

Boyd, T.A., 1950, Pathfinding in fuels and engines, SAE Quarterly Transactions, Vol., 4, No. 2, p. 182-195.

Cal/EPA, 2002, Draft Public Health Goal for Ethylene Dibromide (1,2-Dibromoethane) in Drinking Water, Office of Environmental Health Hazard Assessment, California Environmental Protection Agency, 33p.

Cline, P.V., J.J. Delfino, and P.S.C. Rao, 1991, Partitioning of aromatic constituents into water from gasoline and other complex solvent mixtures, Environmental Science and Technology, Vol., 25, Not. 5, p. 914-920.

EPA, 1991, Integrated Risk Information System, 1,2-Dichloroethane, http://cfpub.epa.gov/iris/quickview.cfm?substance_nmbr=0149

EPA, 1997, Integrated Risk Information System, 1,2-Dibromoethane, http://cfpub.epa.gov/iris/subst/0361.htm.

EPA, 2003, Integrated Risk Information System, Benzene, http://cfpub.epa.gov/iris/quickview.cfm?substance_nmbr=0276.

Jacobs, E.S., 1980, Use and air quality impact of ethylene dichloride and ethylene dibromide scavengers in leaded gasoline, Banbury Reports, 5:239-255.

Johnson, R., J. Pankow, D. Bender, C. Price, and J. Zogorski, 2000, MTBE: to what extent will past releases contaminate community water supply wells?, Environmental Science and Technology, Vol. 34, No. 9, p. 210a-217a.

Mace, R.E., R.S. Fisher, D.M. Welch, and S.P. Parra, Extent, Mass, and Duration of Hydrocarbon Plumes from Leaking Petroleum Storage Tank Sites in Texas, Bureau of Economic Geology, University of Texas at Austin, Austin, TX, 1997.

Midgley, T., and T. A. Boyd, 1922, The chemical control of gaseous detonation with particular reference to the internal combustion engine, The Journal of Industrial and Engineering Chemistry, Vol. 14, No. 10, p. 894-898.

Montgomery, J.H., 1997, Agrochemicals Desk Reference, 2nd Edition, CRC Lewis Publishers, Boca Raton, FL.

Pignatello, J.J., and S.Z. Cohen, 1990, Environmental chemistry of ethylene dibromide in soil and ground water, Reviews of Environmental Contamination and Toxicology, Vol. 112, p. 2-47.

Rice, D.W., R.D. Grose, J.C. Michaelsen, B.P. Dooher, D.H. MacQueen, S.J. Cullen, W.E. Kastenberg, L.G. Everett, M.A. Marino, California Leaking Underground Fuel Tank (LUFT) Historical Case Analysis, Lawrence Livermore National Laboratory, UCRL-AR-122207, 1995

Thomas, V.M., J.A. Bedford, and R.J. Cicerone, 1997, Bromine emissions from leaded gasoline, Geophysical Research Letters, Vol. 24, No. 11, p. 1371-1374.

Table 1. Chemical properties of EDB, 1,2-DCA, and benzene.

Property	**Ethylene Dibromide**[a]	**1,2-Dichloroethane**[b]	**Benzene**[b]
Molecular Weight, g/mol	187.86	98.96	78.11
Aqueous Solubility, mg/L	4,321	8,520	1,750
Vapor Pressure, kPa	1.47	8.10	8.00
Octanol-Water Partition Coeff., K_{ow}	58	30	130
Henry's Constant (dimensionless)	0.029	0.050	0.220

[a]Montgomery, 1997; [b]Bedient et al., 1999.

Table 2. Drinking water concentrations (µg/L) at specified cancer risk levels for a lifetime exposure.

Chemical	**10^{-4} (1 in 10,000)**	**10^{-5} (1 in 100,000)**	**10^{-6} (1 in 1,000,000)**
Benzene[a]	100-1,000 µg/L	10-100 µg/L	1-10 µg/L (MCL = 5 µg/L)
1,2-Dichloroethane[b]	40 µg/L	4 ugµg/L (MCL = 5 µg/L)	0.4 µg/L
Ethylene Dibromide[c]	0.04 µg/L (MCL = 0.05 µg/L)	0.004 µg/L	0.0004 µg/L

[a]EPA (2003); [b]EPA (1991); [c]EPA (1997).

Table 3. Approximate Composition of BTEX and lead scavengers in leaded gasoline.

Compound	**Concen. in Gasoline, g/L**	**Gasoline-Water partition coefficient**	**Equil. Aqueous Concen., µg/L**	**USEPA MCL in drinking water, µg/L**	**Ratio of Eq. Aq. Conc. to the MCL**
Benzene	13.0 g/L	350[c]	37,100	5	7,420
Toluene	57.7 g/L	1250[c]	46,200	1,000	46
Ethylbenzene	13.3 g/L	4500[c]	3,000	700	4.3
Xylenes	54.2 g/L	4150[c,d]	13,100	10,000	1.3
Ethylene dibromide	0.290[b] g/L	152[e]	1,900	0.05	38,000
1,2-dichloroethane	0.310[b] g/L	84[f]	3,700	5	740

[a]API, 2002; [b]Average values from 1950 through 1974; [c]Cline et al., 1991; [d]Average of o, m, p-xylene; [e]Pignatello and Cohen, 1990; [f]Estimated using Raoult's Law.

Diffusion between a Fracture and the Surrounding Matrix: The Difference between Vertical and Horizontal Fractures

Amir Polak,[1,2,3] Abrahm S. Grader,[2] Rony Wallach[3] and Ronit Nativ[3]
[1]Department of Civil and Environmental Engineering, Technion, Israel Institute of Technology, Haifa 32000, Israel. amirp@tx.technion.ac.il
[2]Energy Institute and Department of Energy and Geo-Environmental Engineering Pennsylvania State University, University Park, PA 16802, USA
[3]The Seagram Center for Soil and Water Sciences, Faculty of Agricultural, Food and Environmental Quality Sciences, The Hebrew University of Jerusalem, P.O. Box 12, Rehovot 76100, Israel

Introduction

Subsurface solute diffusion from fractures into the rock matrix has long been recognized as one of the major controls on contaminant attenuation and remediation in fractured rocks. As such, laboratory and field diffusion testing has become a necessary component in the overall design and evaluation processes associated with waste-disposal practice in fractured terrain (e.g., Neretnieks, 1980; Maloszewski and Zuber, 1993; Jardine et al., 1999). However, there are relatively few studies reporting laboratory or field measurements of the diffusion process (Birgersson and Neretnieks, 1990; Mazurek et al., 1996; Wan et al., 1996; Tidwell et al., 2000). This is because direct measurements of the concentration distributions inside a rock matrix are destructive and the results represent the concentration distribution at the time of the measurements rather than with time. Concentration changes inside a rock due to matrix diffusion from fractures are typically estimated by solving the diffusion equation, following a measurement of breakthrough curves at the fracture outlet.

This study focuses on tracking and modeling the diffusion of a tracer (NaI) from a vertical and horizontal fractures into and within a chalk matrix using computed tomography (CT). The CT system is a non-destructive imaging technique that employs x-rays and mathematical reconstruction algorithms to nondestructively view a cross-sectional slice of an object. A more detailed description on the use and limitations of x-ray CT in geosciences can be found in Stock (1999), Ketcham and Carlson (2001), and Wildenschild et al. (2002).

Materials And Methods

The two chalk samples used in the experimental study were retrieved from coreholes located in the northern Negev desert, Israel. A detailed description of the study area can be found in Nativ et al. (1999). The cores were fractured using a Brazilian-like test, creating a longitudinal plane fracture in each of them, which was effected by compressing the cylindrical sample between two opposite plates, thereby inducing tensile stress at its center. The artificially fractured confined cores were placed in a medical scanner, and a tracer solution was injected into the fracture. The concentration distribution over time within the matrix was monitored using consecutive CT scans. The experimental system used in both experiments included a multi-phase fluid-flow system, a core-holder assembly that controls confining pressure, and an x-ray CT-imaging system. A schematic of the system is shown in Figure 1.

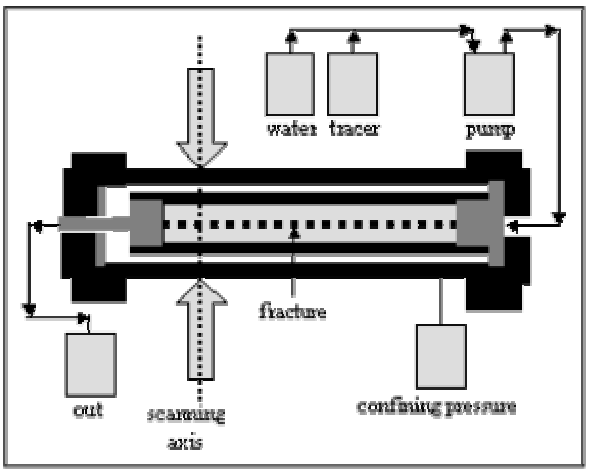

Figure 1 Schematic description of the experimental setup.

Two CT systems were used to monitor the solute concentrations during the experiments. In the horizontal fracture experiment, a second-generation medical-based X-ray CT scanner (Deltascan 100) was used to produce two-dimensional slices with a thickness of 8 mm and an in-plane pixel resolution of about 0.4 mm at an energy level of 120 kV at 25 mA (Polak et al., 2003b). In the vertical fracture experiment, a fourth-generation medical-based X-ray CT scanner (Universal System HD 250) was used to produce two-dimensional slices with a thickness of 4 mm and an in-plane pixel resolution of about 0.25 mm at an energy level of 130 kV at 105 mA (Polak et al., 2003a).

In both experiments, prior to closing the two halves of the core sample, small pieces of crushed chalk were placed at a few points along the fracture to keep it open, as the sample was later subjected to a confining pressure of 0.35 MPa. The confining pressure was applied to keep the core sample in place during the experiment and to minimize fluid bypass along its outer edges. After closing the two halves of the core, the core sample was placed in a Viton® rubber sleeve that separated it from the confining fluid. The sleeve containing the core sample was placed inside the coreholder; the latter was sealed using the end plugs and placed inside the CT system. Water was then pumped into the space between the rubber sleeve and the aluminum-tube walls to create the confining pressure (0.35 MPa). Following the core packing, the first scan was carried out (dry calibration) to determine whether the fracture was completely open throughout its length. After the first scan, the core was put under vacuum for 24 h. Following vacuum generation, distilled water was injected into the core, while closing the vacuum pump, and saturation of the core began.

During this process, a number of scans were taken until the core was completely saturated. The difference between the dry and wet scans (first and last scans, respectively) at each pixel was used to determine the porosity distribution within the sample. Following core saturation, a tracer solution (5% by weight of NaI) was injected into the fracture at a constant concentration and rate of 2.5 cm^3min^{-1}. This injection process lasted for 7 and 6 days (for the horizontal and vertical experiments, respectively), during which time the core was scanned nine and eight times (horizontal and vertical experiments, respectively).

Results and Discussion

The tracer's lateral distribution in the matrix during the eight scan sequences of the vertical fracture experiment is shown in Figure 2. Both sides of the fracture resemble each other, resulting in a similar temporal diffusion pattern as evidenced by the identical colored bands in the eight scanning sequences. The red color represents high concentrations [hot colors] and the blue color represents low concentrations [cold colors].

The tracer distribution away from the fracture in the horizontal experiment between the upper and lower core parts is qualitatively shown at different sequences (times) in Figure 3. The different tracer-penetration distances imaged in the matrix above and below the horizontal fracture are indicative of a greater tracer mass penetrating into the lower part. The tracer solution penetrated into the lower core part faster than into the upper one. Consequently, the tracer's front reached the core's bottom at the lower part and started accumulating there while still migrating upward in the upper core's part (Scan Sequences 3 and 4, taken 24 and 36 hours, respectively, after tracer injection; Figures 3, Sequences 3 and 4). Tracer accumulation was observed at the edge of the upper core 63 hours after tracer injection (Figure 3, Sequence 6). Tracer invasion across the entire matrix in the examined cross section was observed 134 hours after the beginning of its injection (Figure 3, Sequence 9). Again, such differences in tracer-penetration distance into the fracture's surrounding matrix were not observed in the vertical experiment (Figure 2).

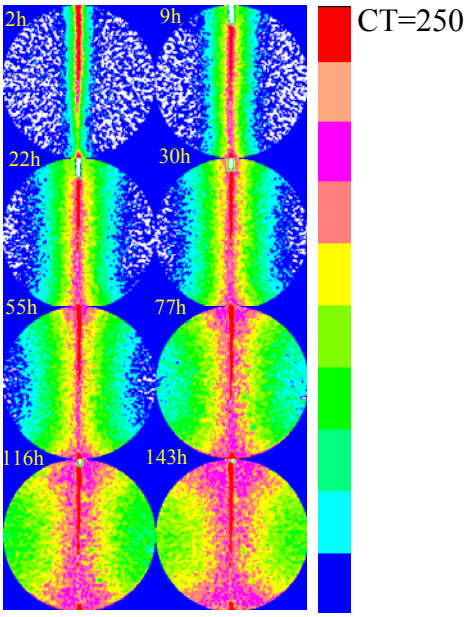

Figure 2. Tracer distribution during the diffusion phase in the scanned core. The CT numbers refer to the attenuation coefficient.

The enhanced tracer transport in the lower part of the matrix could be attributed to the density gradient along the vertical axis, resulting from the initial setup of a denser tracer solution (1.038 g cm^{-3}) in the fracture with respect to the distilled water in the surrounding saturated matrix.

While diffusion controlled the tracer transport in the matrix of the upper core part, both advection and diffusion controlled its transport in the lower one. It is suggested that this advection was caused by a Rayleigh-Darcy instability (Phillips, 1991) that takes place when the density difference between an upper dense fluid and a lower, less dense fluid is sufficiently large. This instability occurs when the random perturbations at the interface formed initially between the two fluids (in our case at the fracture-matrix interface) are not suppressed or smoothed out. It is assumed that their amplification and growth induced the enhanced transport in the lower core part, compared to the slower, diffusion-related transport taking place in the upper part. This assumption was tested against a separate calculation of migration time related to regular advection and diffusion. Tracer migration from the horizontal fracture to the upper and lower parts of the core was solved using a mathematical model (Polak et al., 2003b) that was used successfully in the vertical fracture experiment, indicating, in that experiment, that diffusion indeed controlled tracer invasion.

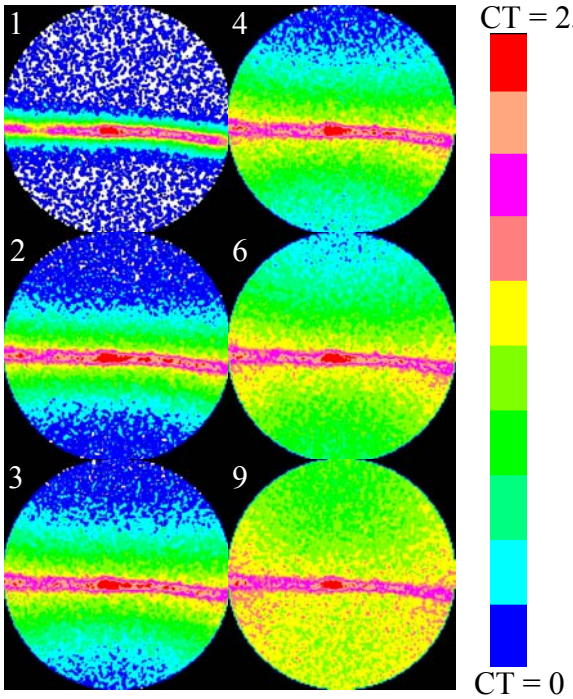

Figure 3: Net tracer distribution in the matrix during six of the nine scans. Numbers refer to the different time sequences.

This model postulates a transition layer at the matrix/fracture interface where the diffusion coefficient is significantly higher than that of the bulk matrix but lower than that in the fracture. Higher porosity, mini-fissures and small fractures characterize this transition layer. The transient behavior of the tracer concentration is described by Equation (1) and by the boundary and initial conditions [Equation (2)].

$$\frac{\partial c}{\partial t} = D \frac{\partial^2 c}{\partial x^2} \qquad (1)$$

$$-\frac{\theta D}{b}\frac{\partial c(0,t)}{\partial x} = k[c_0 - c(0,t)] \qquad \frac{\partial c(L+\delta,t)}{\partial x} = 0 \qquad c(x,0) = 0 \tag{2}$$

where: D [L^2 T^{-1}] is the uniform effective diffusion coefficient for the bulk matrix, c(x,t) is the concentration within the matrix, b[L] is half of the fracture's aperture, L [L] is the distance between the transition layer/matrix interface and the core edge, δ [L] is the thickness of the transition layer, which is *a priori* unknown, k [T^{-1}] is the mass-transfer coefficient per unit fracture width, c_0 is the concentration of the tracer within the fracture which, owing to the experimental time scale and flow velocity, is equal to the tracer concentration at the fracture's inlet. The assumption underlying the left part of Equation (2) is that the concentration varies linearly between its value at the fracture and that at the interface between the transition layer and the bulk matrix. This model was solved for the vertical fracture experiment (Polak et al., 2003a) yielding the concentration distribution within the matrix in the Laplace domain as follows:

$$\overline{C}(\eta,s) = -\frac{[e^{-\sqrt{s}(\eta-1)} + e^{\sqrt{s}(\eta-1)}]}{s[-\varepsilon\sqrt{s}e^{\sqrt{s}} + \varepsilon\sqrt{s}e^{-\sqrt{s}} - e^{\sqrt{s}} - e^{-\sqrt{s}}]} \tag{3}$$

$$\text{where } \varepsilon = \frac{\theta D}{b L k}$$

C(x,t) can be obtained by applying the inverse Laplace transform to Equation (Equation 3). Since a general analytical inverse Laplace transform does not exist, a numerical inversion was applied using the Stehfest algorithm. Comparison of the model to the case of diffusion from a horizontal fracture allows evaluations of the various processes involved. For the case of a horizontal fracture, three of the nine time sequences (3, 6, and 9, measured 24, 63 and 134 h following the beginning of the experiment, respectively) were considered. Once the best model fit for each time sequence was evaluated, the diffusion coefficient and the mass-transfer coefficient (free parameters) were recorded.

The concentration profiles of time sequences 3 and 6 were successfully simulated when fixed diffusion coefficients of 7 and 9.5 cm^2s^{-1} were used for the upper and lower halves of the sample, respectively. The larger fitted value of the diffusion coefficient for the lower half of the sample can be attributed to the enhanced transport owing to the density-induced instability. Furthermore, the higher fitted values of the mass-transfer coefficient, k, in the lower part, for time sequences 3 and 6, indicate enhanced transport through the lower transition layer. Because the mass-transfer coefficient in the film-type model [Equation (2)] is positively correlated to the diffusion coefficient, the higher fitted k values for the lower transition layer can be related to the enhanced tracer diffusion in the lower part of the core. The fitted values of the diffusion coefficients for the last time sequence (9), 11 and 14 cm^2s^{-1} for the upper and lower halves of the sample, respectively, are higher than those obtained for the earlier time sequences 3 and 6. The inability of the one-dimensional model [Equation (1)] to properly describe the radial symmetry around the core's edge probably accounts for these high values. Note that the tracer's concentration profiles at early times are less affected by the sample's radial shape. Consequently, it is suggested that the one-dimensional model is more suitable for simulating tracer propagation in the core matrix at early and intermediate time scales, before the significant radial convergence takes place.

Our observations suggest that tracer propagation by advection-diffusion in the matrix below the fracture is characterized by both higher rates and concentrations relative to its propagation by diffusion to the matrix above the fracture. The experimental results suggest that a prediction of contaminant migration in a rock intersected by both vertical and horizontal (e.g., along bedding planes) fractures is difficult because of density effects that result in different solute-penetration rates.

References

Birgersson, L., and I. Neretnieks, Diffusion in the matrix of granite rock: field test in the Stripa mine. Water Resour. Res. 26:2833-2842, 1990.

Jardine, P.M., W.E. Sanford, J.P. Gwo, O.C. Reedy, D.S. Hicks, J.S. Riggs, and W.B. Bailey, Quantifying diffusive mass transfer in fractured shale bedrock. Water Resour. Res. 35:2015-2030, 1999.

Ketcham, R.A., and W.D. Carlson, Acquisition, optimization and interpretation of X-ray computed tomographic imagery: applications to the geosciences. Comp. Geosc. 27:381-400, 2001.

Maloszewski, P., and A. Zuber, Tracer experiments in fractured rocks: matrix diffusion and the validity of models. Water Resour. Res. 29:2723-2735, 1993.

Mazurek, M., W.R. Alexander, and A.B. MacKenzie, Contaminant retardation in fractured shales: matrix diffusion and redox front entrapment. J. Contam. Hydrol. 21:71-84, 1996.

Nativ, R., E. Adar, and A. Becker, A monitoring network for groundwater in fractured media. Ground Water 37:38-47, 1999.

Neretnieks, I., Diffusion in the rock matrix: an important factor in radionuclide retardation? J. Geophys. Res. 85(B8):4379-4397, 1980.

Phillips, O.M., Flow and Reactions in Permeable Rocks, Cambridge University Press, Cambridge, 1991.

Polak, A., A.S. Grader, R. Wallach, and R. Nativ, Chemical diffusion between a fracture and the surrounding matrix: measurement by computed tomography and modeling. Water Resour. Res. 39(4), 1106, doi:10.1029/2001WR000813, 2003a.

Polak, A., A.S. Grader, R. Wallach, and R. Nativ, Tracer diffusion from a horizontal fracture into the surrounding matrix: measurement by computed tomography. J. Contam. Hydrol. 67:95-112, 2003b.

Stock, S.R., X-ray microtomography of materials. Int. Mater. Rev. 44(4):141-164, 1999.

Tidwell, V.C., L.C. Meigs, T. Christian-Frear, and C.M. Boney, Effects of spatially heterogeneous porosity on matrix diffusion as investigated by X-ray absorption imaging. J. Contam. Hydrol. 42:285-302, 2000.

Wan, J., T.K. Tokunaga, C.F. Tsang, and G.S. Bodvarsson, Improved glass micromodel methods for studies of flow and transport in fractured porous media. Water Resour. Res. 32:1955-1964, 1996.

Wildenschild, D., J.W. Hopmans, C.M.P. Vaz, M.L. Rivers, D. Rikard, and B.S.B. Christensen, Using X-ray computed tomography in hydrology: systems, resolutions, and limitatations. J. Hydrol. 267:285-297, 2002.

Numerical Simulations of Fluid Leakage from a Geologic Disposal Reservoir for CO_2

Karsten Pruess
Earth Sciences Division, Lawrence Berkeley National Laboratory, Berkeley, CA 94720

Introduction

Among the different concepts currently being studied for reducing atmospheric emissions of greenhouse gases, primarily carbon dioxide (CO_2), one of the more promising ones involves disposal into deep geologic formations. Containment of CO_2 in geologic structures is not expected to be perfect. CO_2 may leak along pre-existing faults or fracture zones, and an assessment of the feasibility of geologic disposal requires an understanding of the manner in which CO_2 may escape and ultimately be discharged at the land surface. The behavior of CO_2 depends on the hydrogeologic properties of the pathways along which it migrates, on the thermodynamic regime encountered (temperature and pressure conditions), and on the thermophysical properties of CO_2 and resident aqueous fluids.

In a previous study the pathway for CO_2 escape from the storage reservoir was modeled as a circular vertical channel of 3 m radius, embedded in a porous medium of lower permeability, and extending from 1000 m depth straight up to the ground surface (Pruess, 2003). In the present paper we consider migration along a 2-D planar feature that is intended to represent a generic fault or fracture zone (Figure 1). Our main interest is in the thermodynamic regime and the coupled fluid flow and heat transfer effects during migration of CO_2.

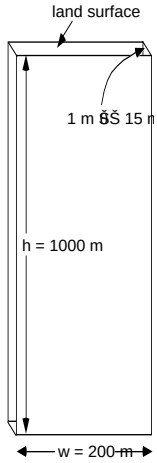

Figure 1. Simple model of a fracture zone used for modeling CO_2 escape from a geologic disposal reservoir. A rectangular high-permeability zone of 200 m width is assumed to extend from a CO_2 reservoir at 1000 m depth all the way to the land surface. CO_2 migration was studied for different thicknesses of this zone in the range from 1 to 15 m.

Thermodynamic Issues

The thermodynamic issues relevant to upflow of CO_2 from a deep storage reservoir are illustrated in Figure 2a. The saturation pressure of CO_2 as a function of temperature is shown along with two hydrostatic pressure profiles, calculated for a typical geothermal gradient of 30˚C per km, for two average land surface temperatures of 5˚C and 15˚C, respectively. Both profiles pass in the vicinity of the critical point of CO_2 (T_{crit} = 31.04 ˚C, P_{crit} = 73.82 bar), and the one for 5 ˚C surface temperature intersects the CO_2 saturation line. In the latter case a bubble of CO_2 that is migrating upward would undergo a phase transition from liquid to gas at a pressure of approximately 63 bars, corresponding to a depth of approximately 630 m. Leakage of CO_2 from a deeper brine formation may induce some overpressure, which would shift the pressure profiles towards higher values. Phase change from liquid to gas is to be expected if CO2 escapes upward at rates large enough so that not all of the leaking CO_2 dissolves in the aqueous phase. Boiling of liquid CO_2 may have large effects on leakage rates, because CO_2 density is much lower for the gaseous than for the liquid state (Figure 2b). At subsurface (T,P) conditions, CO_2 is always less dense than aqueous phase and thus is subject to upward buoyancy force. A transition to gaseous conditions would greatly enhance the buoyancy forces and accelerate fluid leakage, as well as causing a rapid increase in fluid pressures at shallower horizons. This in turn could open pre-existing faults and fractures, enhancing their permeability and further increasing leakage rates.

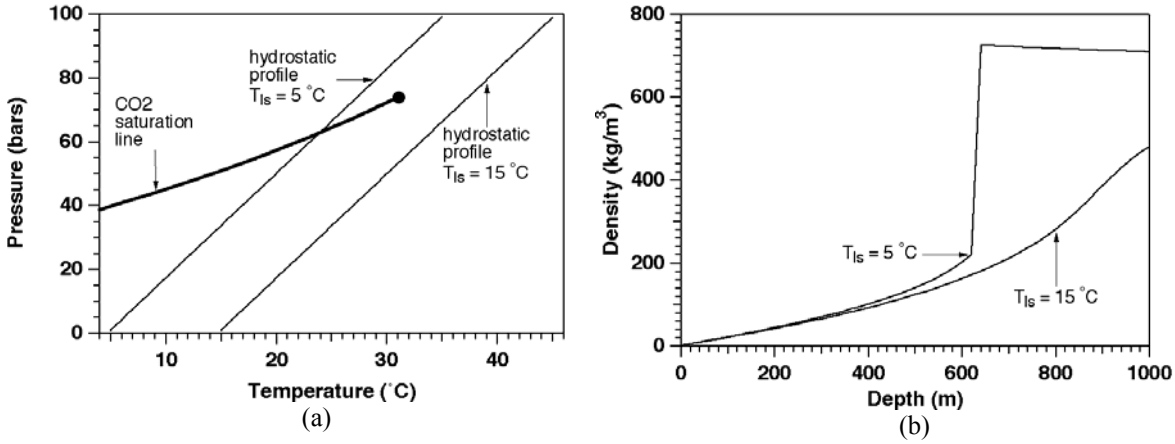

(a) (b)

Figure 2. (a) CO_2 saturation line and hydrostatic pressure-temperature profiles for typical continental crust; (b) density of CO_2 vs. depth for the two hydrostatic profiles shown in Figure 2a.

The specific enthalpy of CO_2 increases upon decompression, even if no phase change occurs, so that CO_2 migrating upward towards lower pressures would tend to undergo cooling as it expands. Inside a porous medium, the temperature decline is buffered by heat transfer from the solids. Heat transfer between rocks and fluids occurs locally on the pore scale, and also over larger distances by means of heat conduction from the low-permeability country rock towards the CO_2 pathway. Additional thermal effects occur when advancing CO_2 partially dissolves in aqueous fluids, giving rise to a small temperature increase from heat-of-dissolution effects.

Approach

The fracture zone considered in this paper is shown in Figure 1, and is modeled as a porous medium sandwiched between impermeable walls. Permeability is assumed as 10^{-13} m^2, and porosity is taken as 0.35. Initial conditions are prepared by allowing a water-saturated system to run to steady state corresponding to land surface conditions of T_{ls} = 15˚C, P_{ls} = 1.013 × 10^5 Pa, and a geothermal gradient of 30˚C/km (see Figure 2a). Boundary conditions at 1000 m depth are a temperature of 45˚C, and a hydrostatic pressure of 98.84 × 10^5 84 × 10^5 Pa. Leakage is initiated by applying CO_2 at a slight overpressure of 99.76 × 10^5 76 × 10^5 Pa over a width of 6 m at the bottom left hand side of the fracture zone. Boundary conditions at the top are maintained unchanged throughout the simulation. Lateral boundaries are "no flow." The walls bounding the fracture zone are assumed impervious to fluids, but are participating in conductive heat exchange with the fluids in the fracture.

All simulations were performed with our the general-purpose code TOUGH2 (Pruess et al., 1999), using a newly developed fluid property module that treats all seven possible phase combinations in the three-phase system system—aqueous, liquid CO_2, gaseous CO_2 (Pruess, 2003). Thermophysical properties of CO_2 are represented, within experimental accuracy, by the correlations of Altunin (Altunin, 1975; Pruess and García, 2002). Conductive heat exchange with the impermeable wall rocks is modeled with the semi-analytical method of Vinsome and Westerveld (1980). This obviates the need to explicitly include the wall rocks into the definition domain of the numerical model, reducing the dimensionality of the flow problem to 2-D. Salinity effects were neglected. As will be seen below, there is a tendency for thermodynamic conditions to be drawn towards the critical point during the system evolution, and to remain very close to the CO_2 saturation line for extended periods of time, in some cases undergoing frequent changes between all gas or all liquid conditions. These features make the calculation quite challenging, requiring special techniques to avoid time steps being reduced to impractical levels.

Results

The CO_2 entering the column partially dissolves in the aqueous phase, but most of it forms a separate supercritical phase. Cross sections of CO_2 plumes for the case of a 15 m thick fracture zone are shown in Figure 3 at two different times. A three-phase zone forms which initially is thin and of limited areal extent. With time this zone becomes thicker, broader, and migrates towards shallower elevations. Fluid mobility is reduced from interference between the three phases. This tends to divert upflowing CO_2 sideways, broadening the three-phase zone. Continuing heat loss resulting from boiling also causes this zone to become thicker with time and to migrate towards shallower elevations. Temperatures attain a local minimum at the top of the three-phase zone, where boiling rates are largest, and over time decrease to low values, approaching the freezing point of water (Figure 4). Our simulator currently has no provisions to treat solid ice, but there is little doubt that for the conditions investigated in this simulation, water ice and hydrate phases would form at later time. Discharge of CO_2 at the land surface begins after approximately 6 years, first by exsolution of dissolved CO2 from water that is flowing out at the top, and followed within a few months by a free CO_2-rich gas phase reaching the top

boundary of the fracture zone. Figure 4 also shows that at early time there is a temperature increase of approximately 2-3˚C, which is due to heat-of-dissolution effects.

It is instructive to plot thermodynamic conditions in a temperature-pressure diagram. Figure 5 shows such a diagram for the leftmost column of grid blocks above the CO_2 injection region at different times. Initial conditions are represented by the line labeled "hydrostatic profile." After 6.07 yr the CO_2 injection has caused temperatures to decline in the high (T,P)-region, at the bottom of the fracture zone. The underlying mechanism is cooling from expansion of CO_2. At the lowest pressures (shallow elevations) temperatures have increased due to heat-of-dissolution effects. After a three-phase zone has formed, thermodynamic conditions track the CO_2 saturation line (15.65 and 30.69 yr in Figure 5).

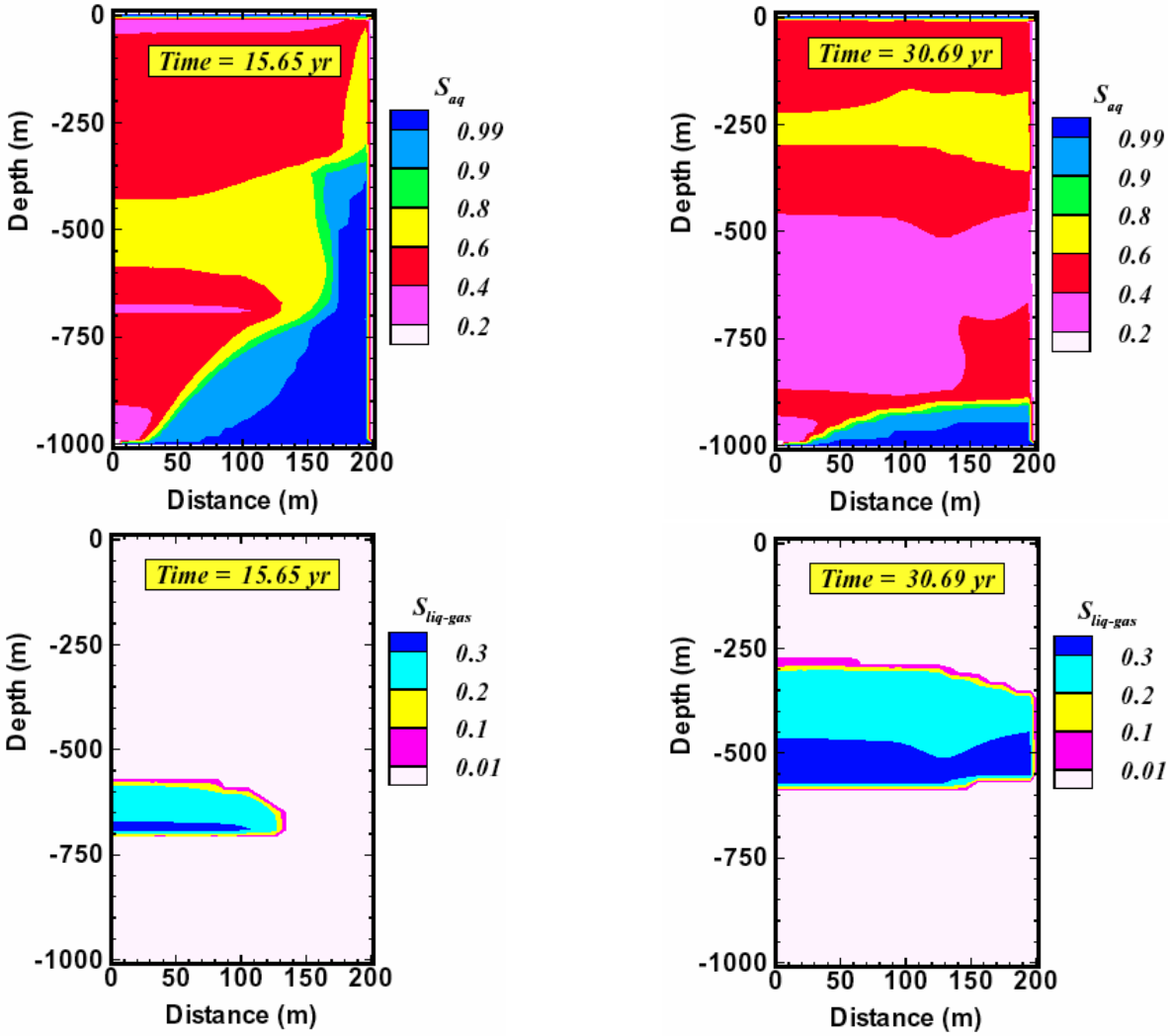

Figure 3. Snapshots of system evolution at two different times, showing CO_2 plumes (top) and extent of three-phase zone (bottom). The parameter Sliq-gas is defined as $\sqrt{S_{liq} \cdot S_{gas}}$, which is non-zero only for three-phase conditions.

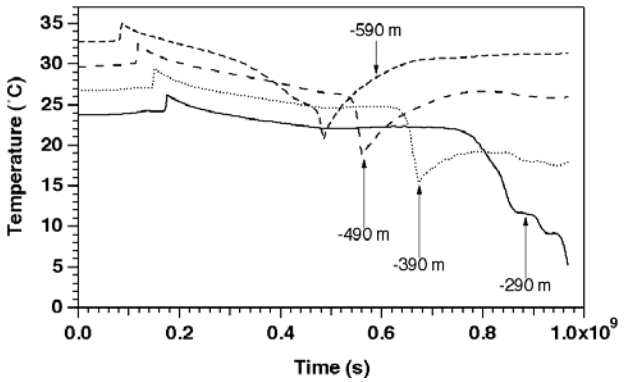

Figure 4. Temperatures at four different elevations in the leftmost column of grid blocks for a fault zone of 15 m thickness.

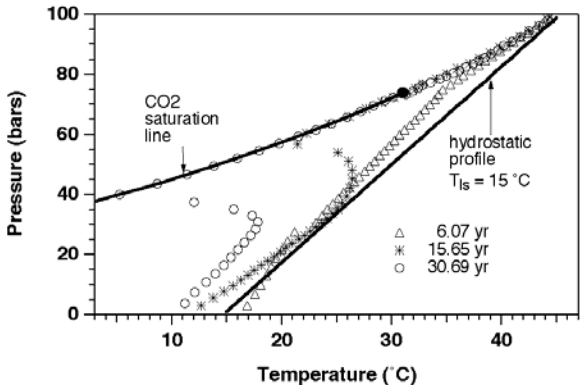

Figure 5. Pressure-temperature profiles in the leftmost column of grid blocks for a fault zone of 15 m thickness at different times.

Concluding Remarks

CO_2 migration behavior depends on the relative rates of fluid flow and heat transfer. Simulation results presented above and additional results not shown here demonstrate the following.

- Upward migration of CO_2 along a fracture zone is strongly affected by heat transfer effects. Limited cooling occurs from expansion, while much stronger cooling takes place when liquid CO_2 boils into gas.
- CO2 migration to elevations shallower than about 750 m may generate a three-phase aqueous, liquid CO_2, gaseous CO_2 fluid system, even if the initial hydrostatic-geothermal profile does not intersect the CO_2 saturation line.
- There is a strong tendency for thermodynamic conditions to be drawn towards the critical point of CO_2 (T_{crit} = 31.04˚C, P_{crit} = 73.82 bar), and to remain close to the CO_2 saturation line. This gives rise to severely non-linear behavior and makes numerical simulations of leakage processes very challenging.
- The tendency towards development of three-phase zones increases with increasing thickness of the fracture zone (increasing rate of CO_2 discharge). When CO_2 migrates through thin fracture zones, three-phase zones may not form at all or may form and dissolve in a transient manner.

- Fluid mobility is reduced in three-phase zones, due to interference between the phases. This impedes upflow, diverting CO_2 sideways and making these zones areally more extensive.
- Continued heat loss in boiling causes temperatures to decline over time, so that three-phase zones tend to grow in thickness and advance towards shallower elevations. Depending on the fracture zone thickness and permeability (CO_2 discharge rate), temperatures may reach the freezing point of water, and water ice and hydrate phases may form.
- The interplay between multiphase flow effects, phase change, and heat transfer may give rise to non-monotonic flow and temperature behavior.

Acknowledgments

Thanks are due to Pat Dobson and Chris Doughty for a careful review and suggestions for improvements. This work was supported by the Director, Office of Science, Office of Basic Energy Science of the U.S. Department of Energy under Contract No. DE-AC03-76SF00098.

References

Altunin, V.V. Thermophysical Properties of Carbon Dioxide, Publishing House of Standards, 551 pp., Moscow, 1975 (in Russian).

Pruess, K. Numerical Simulation of CO2 Leakage from a Geologic Disposal Reservoir, Including Transitions from Super- to Sub-Critical Conditions, and Boiling of Liquid CO2, submitted to SPE Journal, Berkeley, CA 94720, June 2003. (LBNL-52423)

Pruess, K. and J. García. Multiphase Flow Dynamics During CO2 Injection into Saline Aquifers, Environmental Geology, Vol. 42, pp. 282 - 295, 2002.

Pruess, K., C. Oldenburg and G. Moridis. TOUGH2 User's Guide, Version 2.0, Lawrence Berkeley National Laboratory Report LBNL-43134, Berkeley, CA, November 1999.

Vinsome, P.K.W. and J. Westerveld. A Simple Method for Predicting Cap and Base Rock Heat Losses in Thermal Reservoir Simulators, J. Canadian Pet. Tech., 19 (3), 87–90, July-September 1980.

Development of an Interfacial Tracer Test for DNAPL Entrapped in Discrete Fractured Rock

Beth Sekerak and Sarah Dickson
Civil Engineering at McMaster University, Ontario, Canada

Abstract

Denser-than-water, non-aqueous phase liquids (DNAPLs) are contaminants that pose a serious threat to groundwater quality, because of their high toxicity and ease of mobility once released into the groundwater system. In order to effectively assess the risk to human and ecological health, and to select an appropriate remediation strategy, the DNAPL source zone must be accurately characterized. The area of the DNAPL-water interface is one feature commonly used to characterize the DNAPL source zone; it is significant as it measures the surface area available for DNAPL mass transfer into the groundwater causing contamination. Additionally, many remediation strategies depend on the inter-phase mass transfer. At present, interfacial tracer tests have been successful for determining the DNAPL-water interfacial area in unconsolidated porous media, yet no study has applied this technique to fractured rock systems. As such, the purpose of this study is to develop an interfacial tracer technique for determining the DNAPL-water interfacial area in fractured rock environments. This work develops the interfacial tracer test at the lab scale; further work is required to evaluate the tracer test methodology for field applications.

Introduction

Denser-than-water, non-aqueous phase liquids (DNAPLs) pose a serious threat to groundwater quality when present in the subsurface, due to their unique chemical properties. Because the drinking water standards for these contaminants can be as many as five orders of magnitude lower than their aqueous-phase solubilities, relatively small amounts of DNAPL have the ability to contaminate large volumes of groundwater. In addition, DNAPLs have relatively high densities and low viscosities, which permit them to sink into the groundwater system and migrate over sizable distances. As a result, DNAPLs are considered a long-term threat to groundwater quality.

Once released into the subsurface, DNAPLs migrate into the fractured rock formations threatening the integrity of the surrounding groundwater. In order to assess the risk to human and ecological health, select an effective remediation technique, or develop a suitable monitoring strategy, the DNAPL source zone in the fractured rock system must be accurately characterized. Because of the complex distribution of the DNAPL source zone, traditional point measurement techniques (e.g., core sampling, cone penetrometer testing, and geophysical logging) used in unconsolidated porous media provide limited estimations of the true DNAPL source zone (Willson et al., 2000) particularly in heterogeneous environments such as fractured rock.

It has been suggested that tracer techniques may be both more reliable and cost-effective than traditional point-measurement techniques in unconsolidated porous media environments (Annable, 1998). Advantages offered by this technique include the fact that it is non-invasive, it

does not require a description of the solid geometry, and it samples a larger volume of the contaminated aquifer. Together, these properties make the tracer test ideal for characterizing DNAPL source zones in fractured rock at the field scale. Although this method has shown promise for accurate DNAPL source zone characterization in unconsolidated porous media, its use has yet to be investigated in fractured rock environments. As such, the purpose of this paper is to develop an interfacial tracer test methodology for determining the DNAPL-water interfacial area in fractured rock systems. This work was conducted at the lab-scale using a single discrete fracture, with the intention of field scale application in the future.

Methodology

Two transparent casts of unique discrete fractures (one limestone and the other granite) were used in a two-phase flow visualization experiment, where the water was dyed red and the DNAPL remained transparent. Digital photos were taken of the two fluids in the casts; the interfacial area was calculated using visualization software (XCAP) and compared to the interfacial area obtained experimentally using an interfacial tracer test adapted from those used in unconsolidated porous media studies. The visualization experiments provided a means of both calibrating and verifying the tracer test methodology.

(1) Transparent Casts of Rock Fractures

Rock samples containing a plane of weakness (e.g., styolite) were collected in the field and fractured in the lab using a uniaxial compression machine. Transparent casts of two unique fractures (limestone and granite) were made using a method developed by Dickson (2001) as illustrated in Figure 1. Silicone negative moulds of the fracture were constructed using liquid rubber (RTV-4018, Silchem). Then the transparent positive of the fracture was cast using an epoxy (Stycast 1264, Emerson Cuming).

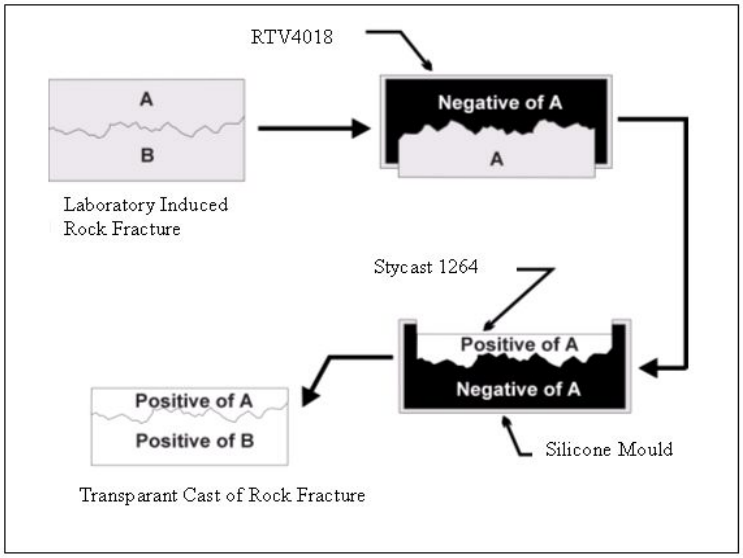

Figure 1. Schematic of the casting process.

(2) Fracture Characterization

The synthetic rock fractures were characterized using both hydraulic and tracer tests. The hydraulic aperture, e_h, of the fracture is defined as the equivalent aperture that satisfies the bulk cubic law (Tsang, 1992).

Tracer tests using Rhodamine Dye as the tracer were performed on each synthetic fracture to determine the mass balance and the frictional loss apertures. The mass balance aperture is a measure of the aperture required to balance a known volume of fluid over the aerial extent of the tracer transport. Whereas the frictional loss aperture is based on the mean residence time of the tracer's transport velocity across the fracture plane, assuming that the specific discharge for flow through parallel plates applies to rough-walled fractures (Tsang, 1992).

(3) DNAPL Entrapment

The experimental procedure involved trapping a known mass of DNAPL (HFE7100) in the fracture plane under a fixed capillary pressure, and observing the resulting DNAPL flow and distribution. The fracture plane was initially saturated with water; then a volume of HFE7100 was discharged at the fracture inlet at a certain flow rate. The capillary pressure induced by the set flow rate caused HFE7100 to move along the fracture plane in a path that preferred larger apertures, i.e. those corresponding to a lower capillary pressure. Once the HFE7100 was emplaced, water was flushed through the fracture plane in an attempt to flush out the HFE7100. Yet a portion of the HFE7100 became entrapped in the fracture due to the small aperture regions that induce a large capillary pressure (larger than the set capillary pressure corresponding to the HFE7100 flow rate). The entrapped HFE7100 results from the capillary forces exceeding the combination of gravitational and viscous forces. The volume and geometric distribution of HFE7100 entrapped in the system is controlled by the geometry of the pore network, the fluid-fluid properties (interfacial tension, and viscosity density of the fluids), fluid-solid properties (wettability), and external forces on the fluids (pressure gradients and gravity).

(4) Estimating Interfacial Area from Photos

After flushing with water, the interfacial area between the two fluids was calculated using the visualization software, XCAP. Digital photos of the fluid-fluid phases together in the transparent cast were taken, where the water was dyed red (the dark phase in Figure 2) and the HFE7100 remained transparent (the light phase in Figure 2).

The digital images were then imported into the XCAP software used for interactive image analysis. XCAP calculates the interfacial area of the fluid-fluid interface by setting the threshold pixel values, which partitions the image into a foreground (blobs of interest) and the background, according to light intensity.

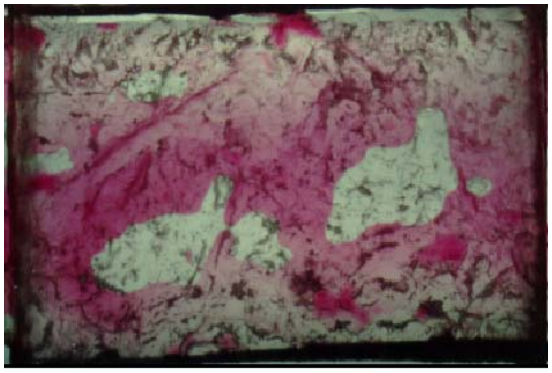

Figure 2: A plan-view digital picture taken of the two immiscible fluids (DNAPL as the light phase and water as the dark phase) in a synthetic fracture.

(5) Interfacial Tracer Test (IFT)

The interfacial tracer technique estimates the DNAPL-water interfacial area. It has been successful in several unconsolidated porous media studies (e.g., Annable et al., 1998; Saripalli et al, 1997; Kim et al., 1999); however no work has been reported to date regarding the application of these techniques in fractured rock.

The interfacial tracer technique involves injecting a pulse of non-reactive and reactive tracers into the fracture system. Simultaneously, the time for the reactive tracer to pass through the system is delayed due to the interfacial tracer's ability to adsorb at the interface of the two immiscible fluids, without partitioning into the bulk phase of either fluid. This effect is measured by a 'retardation factor', defined from the advection-dispersion theory of reactive solute transport through porous media, assuming that the interfacial tracer adsorbs at the fluid-fluid interface only [Equation (1)]

$$R_{ift} = \frac{\mu_{ift}}{\mu_{nr}} = 1 + \frac{a_{nw} K_i}{\theta w} \tag{1}$$

where μ is the area above the breakthrough curve measured for a continuous tracer input, and the subscripts ift and nr refer to the interfacial and non-reactive tracer respectively. The μ value is calculated using (Saripalli et al., 1998):

$$\mu = \int_0^\infty (1 - C^*) dt \tag{2}$$

Here $C^*(t)$ [-] = $C(t)$ [M · L^{-3}] / Co [M · L^{-3}] is the normalized concentration of tracer, Co [M · L^{-3}] is the influent tracer concentration, Θw [-] is the volumetric water content, and K_i is the interfacial adsorption distribution coefficient. The K_i [-] value is calculated as the ratio of interfacial tracer concentration in the sorbed phase, Go [M · L^{-3}], to initial concentration, Co [M · L^{-3}]. For non-linear isotherms, K_i values must be estimated at each input concentration using the Gibbs Adsorption Equation. For a tracer step-input concentration, Co, K_i is calculated as follows (Kim et al., 1999; Saripalli et al., 1998):

$$Ki = \frac{Go}{Co} = -\frac{1}{2RT}\left(\frac{\partial \gamma}{\partial C}\right)_{Co,T} \quad (3)$$

where R [M · L^2 · T^{-2} · mol · temp] is the ideal gas constant, γ [M · T^{-2}] is the interfacial tension, C [mol · L^{-3}] is the bulk tracer concentration, T [temp] is the temperature, and it is assumed that the aqueous solution is dilute (Rosen, 1978).

The K_i value was obtained from DNAPL-water interfacial tension measurement data (γ vs C) using a drop volume tensiometer (Lauda, TVT1). The data were plotted in order to obtain the slope ($\partial \gamma / \partial C$) at a constant temperature for a given initial tracer concentration.

In these experiments, HFE7100 was used as the DNAPL, sodium dodecyl benzene sulfonate (SDBS) was used as the reactive tracer, and sodium bromide (NaBr) was used as the non-reactive tracer. After DNAPL entrapment, the two tracers were injected at the inlet of the fracture plane. Samples were then taken over time at the outlet and analyzed using the gas chromatograph (Varian CP-3800). The normalized breakthrough curves of the reactive and non-reactive tracers were plotted and analyzed to obtain the retardation factor (R_{ift}) from which the interfacial area of the fluid-fluid interface was obtained using Equation 1. This value for interfacial area was compared to that obtained through the visualization experiment.

Initial results indicate that this method is suitable for measuring interfacial area in fractures, however several factors must be considered in environments as heterogeneous as fractured rock, including errors introduced by the hydrodynamic accessibility of the interfacial tracer to the DNAPL-water interface, and non-equilibrium mass transfer rates (Rao et al., 2000). DNAPL pools are subject to significant mass transfer limitations, which results in a tailing effect in the observed tracer breakthrough curve (Willson et al., 2000). As such the breakthrough curve tailing effect should be monitored for a prolonged period of time (Willson et al., 2000; Rao et al., 2000).

Significance of Work

As long as there are waste impoundments in the subsurface that are underlain by fractured rock, there is a risk of DNAPL leakage causing groundwater contamination. In order to develop effective monitoring and remedial strategies and to determine the risk to human and ecological health, it is necessary to accurately characterize the DNAPL source zone present in fractured rock environments. The purpose of the work outlined in this paper is to define a method for characterizing the interfacial area of the DNAPL-water interface at the lab scale for eventual applications in the field. By accurately estimating the DNAPL-water interfacial area in the field, the surface for which DNAPL mass transfer processes occur can be quantified thereby enabling an estimate of the level of groundwater contamination and the development of improved remedial strategies.

References

Annable, M.D., Jawitz, J.W., Rao, P.S.C., Dai, D.P., Kim, H., and A.L. Wood. 1998. Field Evaluation of Interfacial and Partitioning Tracers for Characterization of Effective NAPL-

Water Contact Areas. Groundwater. V36 (3), pp 495-502.
Jin, Minquan, Delshad, Mojdeh, Dwarakanath, Varadarajan, McKinney, Daene C., Pope, Gary A., Sepehrnoori, Kamy, and Charles E. Tilburg. 1995. Partitioning tracer test for detection, estimation, and remediation performance assessment of subsurface nonaqueous phase liquids. Water Resources Research. V31(5) pp 1201-1211.
Kueper, B.H. and D.B. McWhorter. 1991. The behaviour of dense, non-aqueous phase liquids in fractured clay and rock. Ground Water. V29(5), pp 716-728.
Kim, H., Rao, P. Suresh C. and M.D. Annable. 1999. Consistency of the interfacial tracer technique: experimental evaluation. Journal of Contaminant Hydrology. V 40, pp 79-94.
Rao, P.S.C., M.D. Annable, and H. Kim, 2000. NAPL source zone characterization and remediation technology performance assessment: recent developments and applications of tracer techniques. Journal of Contaminant Hydrology. V45, pp 63-78.
Rosen, Milton J. 1978. Surfactants and Interfacial Phenomena. John Wiley and Sons: Toronto, ON.
Saripalli, K. Prasad, Annable, M. D., and P.S.C. Rao. 1997. Estimation of Nonaueous Phase Liquid-Water Interfacial Areas in Porous Media following Mobilization by Chemical Flooding. Environmental Science Technology. V31, pp 3384-3388.
Saripalli, K.Prasad, Rao, P.S.C., and M.D. Annable. 1998. Determination of specific NAPL-water interfacial areas of residual NAPLs in porous media using the interfacial tracers technique. Journal of Contaminant Hydrology. V30, pp 375-391.
Tsang, Y.W. 1992. Usage of “equivalent apertures” for rock fractures as derived from hydraulic and tracer tests. Water Resources Research. V28(5), pp 1451-1455.
Willson, C.S., Pau, J.A. Pedit, and C.T. Miller, 2000. Mass transfer rate limitation effects on partitioning tracer tests. Journal of Contaminant Hydrology. V45, pp 79-97.

Competition Among Flow, Dissolution, and Precipitation in Fractured Carbonate Rocks

Olga Singurindy and Brian Berkowitz
Department of Environmental Sciences and Energy Research
Weizmann Institute of Science
Rehovot 76100 Israel
olga.singurindy@weizmann.ac.il ; brian.berkowitz@weizmann.ac.il

The importance of fractures in the transport of contaminants in groundwater systems is well-known. While the hydraulic conductivity of fractures is usually orders of magnitude larger than that of the host rock matrix, dissolution and precipitation processes can significantly modify the physical and chemical properties of fractured porous media. Indeed, the coupling among transport, precipitation, and dissolution within fractures and rock matrices is important for controlling groundwater quality. Understanding these processes, and their interaction with both anthropogenic and natural pollutants, is fundamental to management and protection of water resources, as well as to the analysis of geological formations.

In spite of the importance of these problems, few analyses exist, and the available literature provides only partial understanding of hydraulic conductivity evolution by coupled flow, precipitation and dissolution in fractured rocks. A model simulation describing dissolution and precipitation of minerals during water-rock interaction in fractured granite is given by Sausse et al. (2001). The permeability calculation of this model is based on description only of the fracture network, with the microcrack (fracture) and matrix permeabilities being neglected. Another study of coupled precipitation and dissolution processes in fractured rocks is based on a multicomponent reactive transport model in fractured dolostone (Ayora et al., 1998). This 1D model accounts dedolomitization during diffusion from a fracture towards the rock matrix and during advective flow along a fracture. Together, these processes were seen to cause changes in fracture/matrix volume and porosity.

The main aim of this current experimental study is to investigate the evolution of hydraulic conductivity structure caused by flow, dissolution of calcium carbonate, and precipitation of gypsum—and the competition among them—in fractured carbonate rocks. Specifically, effects of fracture orientation, fracture wall roughness, fluid flow rate, and coupled dissolution/precipitation reaction mechanisms on overall hydraulic conductivity and porosity are determined in laboratory flow cells. These detailed measurements enable understanding of the interplay between fracture and porous medium flows.

Calcareous sandstone (97.5% $CaCO_3$, 2.5% SiO_2) was identified for laboratory study from the Rosh-Hanikra coast of northern Israel. Sulfuric/hydrochloric acid mixtures acted as the reacting fluid within the rock samples. The simultaneous effect of calcium carbonate dissolution by sulfuric and hydrochloric acids, along with gypsum precipitation, is given according to the following reactions (Krauskopf, 1967):

$$CaCO_3 + 2H^+ = Ca^{2+} + CO2 + H_2O$$

$$CaCO_3 + 2H^+ + SO_4^{2-} + H_2O = CaSO_4 \times 2H_2O + CO2$$

The series of experiments using flow experiments considered mixtures of 0.1M HCl + 0.1M H_2SO_4 and 0.1M HCl + 0.3M H_2SO_4 at flow rates of 1, 5 and 9 cm^3/min.

Two types of flow experiments were carried out. One series of experiments focused on three-dimensional (3D), linear corefloods, while the second series examined reactive flow in (quasi-2D) rock fractures. Porous cylindrical cores of approximately 5 cm diameter and 9 cm length were used in the coreflood experiments. Cores with artificial "fracture" cuts were used, with configurations as shown in Figures 1a, 1b, and 1c, in order to study the interplay between fracture flow and the host porous rock. Similar experiments were also carried out on undisturbed (unfractured) cores. In the quasi-2D experiments, rock "slices" (1 cm thick, 2 cm width, 14 cm length) contained either a smooth cut "fracture" or an artificially-induced "natural" (rough) fracture, as shown in Figures 1d and 1e. Both series of experiments permitted study of the evolution in the overall hydraulic conductivity and total porosity when flow, dissolution and precipitation occur simultaneously.

Measurements of pressure differences across the core sample were taken at specific time intervals during the experiments, using differential pressure transducers. The overall hydraulic conductivity (K) of each sample, as a function of time, was then estimated according to Darcy's law. In addition, the effluent mixture was collected from the outlet at the same time intervals. The effluent was analyzed for concentrations of Ca^{2+} (using atomic adsorption spectroscopy) and SO_4^{2-} (using high pressure liquid chromatography) in order to calculate porosity changes. After each experiment the rock sample was retrieved and sectioned in order to study the pore space geometry and micromorphology changes, using SEM.

In the present work the competition among flow, dissolution and precipitation, leading to temporal oscillations in the hydraulic conductivity and porosity, were observed in flow experiments. The interplay between precipitation and dissolution is highly dependent on the injection rate of the reacting fluid, in agreement with results obtained by Singurindy and Berkowitz (2003) for "homogeneous" porous media. The orientation of the fracture in the coreflood systems was found to strongly influence the general behavior of the hydraulic conductivity and the porosity in the flow system. For example, the results presented in Figure 2 demonstrate that the through-flow fracture led to a dissolution-dominated system, with hydraulic conductivity and porosity increasing over time. In contrast, under the same experimental conditions, the system clogged (i.e., it was subject to precipitation dominance) when it contained an isolated fracture. A similar experiment on an undisturbed core also become clogged, but at a slower rate. Visual examination of the isolated fracture core after the experiment showed that the fracture was totally filled with precipitated gypsum. In all cases, a strong similarity in the temporal behavior between the overall hydraulic conductivity (Figure 2a) and the overall estimated porosity (Figure 2b) was found. According to these results, it can be concluded that calcium carbonate dissolution and gypsum precipitation control oscillations in the hydraulic conductivity.

Results of the quasi-2D fracture flow experiments show that the natural fracture (Figure 1e) clogged faster than the artificial one (Figure 1d), under the same experimental conditions. On the other hand, when experimental conditions led to dissolution dominance, the artificial fracture tended to dissolve faster than the natural one. In at least one case, experimental conditions were

such that dissolution was dominant in the artificial fracture, while precipitation was dominant in the natural fracture.

References

Ayora, C., C. Taberner, M.W. Saaltink, and J. Carrera, The genesis of dedolomites: a discussion based on reactive transport modeling, Journal of Hydrology, 209, 346-365, 1998.

Krauskopf, K.B., Introduction to Geochemistry, International Series in the Earth and Planetary Sciences, McGraw-Hill Book Company, 1967.

Sausse, J., E. Jacquot, B. Fritz, J. Leroy, and M. Lespinasse, Evolution of crack permeability during fluid-rock interaction. Example of the Brezouard granite (Vosges, France), Tectonophysics, 336, 199-214, 2001.

Singurindy, O. and B. Berkowitz, Evolution of hydraulic conductivity by precipitation and dissolution in carbonate rock, Water Resources Research, 39(1), 1016, doi:10.1029/2001WR001055, 2003.

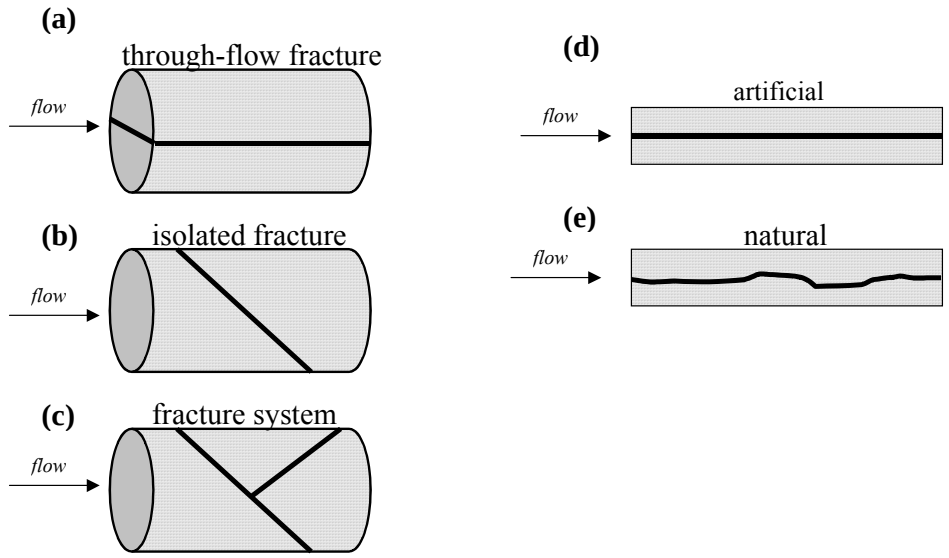

Figure 1. Types of fracture-porous medium systems used in the experiments. Linear (3D) coreflood experiments (a, b, c) and quasi-2D single fracture flow experiments (d, e).

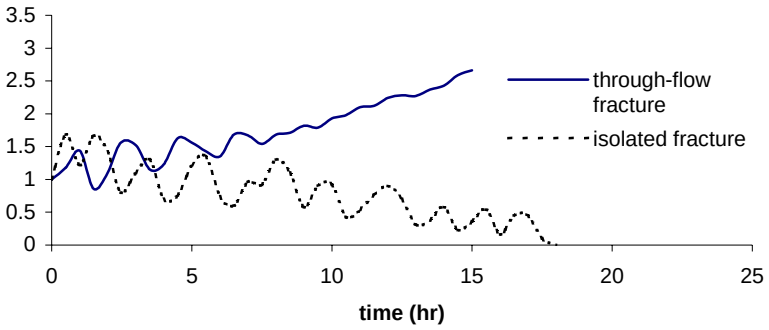

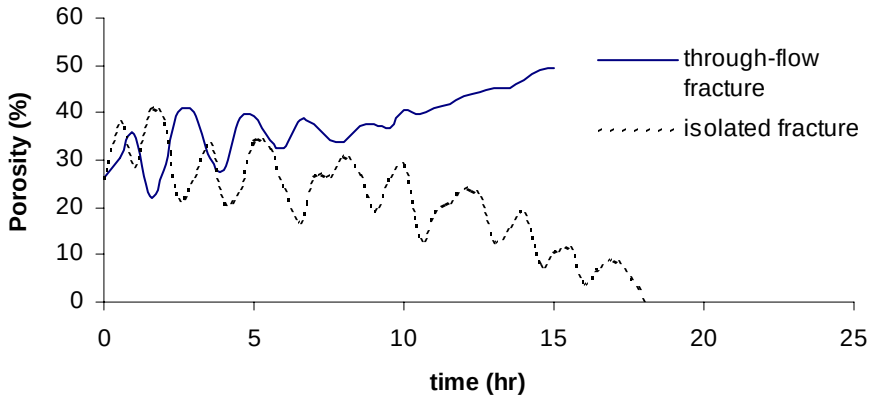

Figure 2. Evolution of overall core (a) hydraulic conductivity and (b) total porosity, Q = 5 cm^3/min, 0.1M HCl/ 0.1M H_2SO_4.

Dry-Steam Wellhead Discharges from Liquid-Dominated Geothermal Reservoirs: A Result of Coupled Nonequilibrium Multiphase Fluid and Heat Flow through Fractured Rock

John W. Pritchett
Science Applications International Corporation

In many geothermal fields around the world, it is observed that (1) the vertical distribution of fluid pressure in the undisturbed reservoir is approximately liquid-hydrostatic (7–9 kPa per meter of depth), but that (2) when a well is drilled into the reservoir and fluid is withdrawn, the enthalpy (or steam fraction) of the stable fluid discharge is often anomalously high – frequently the well discharges steam alone. As will be seen, this apparent paradox cannot be explained unless the reservoir is highly *heterogeneous* on a local scale, with a sharp permeability contrast between the relatively impermeable matrix rock and the "fracture zones" that penetrate it and provide channels for fluid flow. Also, anomalous wellhead discharge enthalpies will not be observed unless *two-phase flow* of a water/steam mixture is taking place deep within the reservoir itself. Finally, it is noteworthy that this so-called "excess enthalpy effect" is inherently *transient* in character and discharge enthalpies will eventually decline, although many years may pass before the deterioration in system performance becomes noticeable.

To illustrate, first consider a liquid-dominated (but two-phase) geothermal reservoir treated as a conventional porous medium. It will be useful to define:

P = pressure,
T = temperature,
$\rho_w(\rho_s)$ = mass density of water (steam) phase,
$E_w(E_s)$ = specific enthalpy of water (steam) phase,
$\nu_w(\nu_s)$ = kinematic viscosity of water (steam) phase,
$R_w(R_s)$ = relative permeability to water (steam) phase,
k = absolute permeability,
κ = thermal conductivity, and
g = acceleration of gravity.

For horizontal flow of a mixture of water and steam in a porous medium (towards a production well, for example), Darcy's Law provides the mass flux:

$$\text{Horizontal mass flux} = -k\left(\frac{R_w}{\nu_w}+\frac{R_s}{\nu_s}\right)\frac{\partial P}{\partial x} \tag{1}$$

and the corresponding horizontal heat flux will be given by:

$$\text{Horizontal heat flux} = -k\left(\frac{R_w}{\nu_w}E_w+\frac{R_s}{\nu_s}E_s\right)\frac{\partial P}{\partial x}-\kappa\frac{\partial T}{\partial x} \tag{2}$$

where the first term represents convection and the second accounts for heat conduction. It is

useful to define the "flowing enthalpy" E_f as the ratio of heat flux to mass flux:

$$E_f = \text{heat flux / mass flux} = E_w + Q_f (E_s - E_w) + \delta E \tag{3}$$

where Q_f represents the "flowing steam quality" (steam mass flux/total fluid mass flux):

$$Q_f = \frac{R_s \nu_w}{R_s \nu_w + R_w \nu_s} \tag{4}$$

and where the quantity "δE" represents the effects of heat conduction, and is sometimes called the "excess enthalpy":

$$\delta E = \frac{\kappa}{k} \frac{\partial T}{\partial P} \frac{\nu_w \nu_s}{R_s \nu_w + R_w \nu_s} \tag{5}$$

Using steam-table fluid properties for $T = 270°C$ ($P = 5505$ kPa) and adapting $R_w = R_s = 0.5$ and $\kappa = 3$ W/m-°C as "typical," we may estimate the magnitude of δE as

$$\delta E \approx \frac{7400}{k} \quad \text{kJ/kg} \tag{6}$$

where k is expressed in microdarcies (μd); 1 μd = 10^{-18} m^2. The average permeability in a geothermal reservoir will usually be at least 10^4 μd (10^{-14} m^2) and may be considerably higher; geothermal production wells will be unable to sustain discharge otherwise. Consequently, the "excess enthalpy" δE for flow in a porous-medium geothermal reservoir will usually be 1 kJ/kg or less, and may be ignored for practical purposes.

Next, consider a region of stable vertical two-phase flow in an undisturbed geothermal reservoir. The classical "heat pipe" description of such a system entails upward flow of steam and downward flow of liquid water in equal amounts, and provides an efficient mechanism for upward heat transfer. For a porous medium, Darcy's Law again provides the flow rates of water and steam:

$$\text{Downward water mass flux} = k \frac{R_w}{\nu_w} \left(\Gamma_w - \Gamma \right) \tag{7}$$

$$\text{Upward steam mass flux} = k \frac{R_s}{\nu_s} \left(\Gamma - \Gamma_s \right) \tag{8}$$

where Γ is the actual vertical pressure gradient $\partial P / \partial z$ prevailing in the reservoir (z is depth, positive downward) and where

$$\Gamma_w = \rho_w g$$
$$\Gamma_s = \rho_s g$$

Setting (7) equal to (8) and solving for the pressure gradient shows that the actual stable gradient (Γ) will lie between the liquid (Γ_w) and steam (Γ_s) hydrostatic gradients, with the exact value depending on the flowing steam quality Q_f (see Eqn. 4 above):

$$\Gamma = \Gamma_w - Q_f \left(\Gamma_w - \Gamma_s \right) \tag{9}$$

Combining Equations (3) and (9) to eliminate Q_f provides an expression for the flowing enthalpy (the discharge enthalpy from nearby production wells) in terms of the value of the stable vertical reservoir pressure gradient:

$$E_f = E_w + (E_s - E_w) \frac{\Gamma_w - \Gamma}{\Gamma_w - \Gamma_s} + \delta E \tag{10}$$

and, as noted above, the excess enthalpy δE is negligible for porous-medium geothermal reservoirs. Consequently, if the actual stable pressure gradient is near liquid-hydrostatic ($\Gamma \approx \Gamma_w$), the flowing enthalpy E_f likewise cannot be too different from the liquid-phase enthalpy E_w. The only way that the flowing enthalpy can approach that of dry steam ($E_f \approx E_s$) is if the reservoir pressure gradient is very small ($\Gamma \approx \Gamma_s$). This latter situation prevails in "vapor-dominated" geothermal fields such as The Geysers and Lardarello.

Pruess and Narasimhan (1982) were the first to provide the explanation for the apparent paradox (dry-steam production from liquid-hydrostatic systems), and devised a numerical technique known as "MINC" to treat the problem. The explanation arises from the fact that most geothermal reservoirs exhibit a remarkable degree of intermediate-scale heterogeneity, with regions of nearly impermeable "matrix rock" penetrated by an interconnected network of "fracture zones" of very high permeability. Most of the transmissivity of the system is provided by the "fracture zone" network, but most of the fluid mass (and most of the heat energy) lies in the impermeable "matrix regions."

Consider the behavior of a single fragment of unfractured low-permeability matrix rock surrounded on all sides by the permeable fracture network. When wells begin to discharge, the fluid pressure within the fracture network will be reduced and, if the starting conditions are at or near the boiling point, liquid water will flash to steam within the fractures. As the fluid boils and the pressure declines, the temperature within the fractures will also decline, following the saturation curve for water/steam mixtures. As a result, at the periphery of the matrix fragment (which can be regarded as a "porous medium"), both pressure and temperature decrease abruptly. This causes the onset of outward flow of both fluid mass and heat near the periphery, from the matrix region into the fracture zone. As time goes on, the region of disturbed pressure and temperature penetrates deeper and deeper into the fragment. Since the starting conditions are at or near the boiling point, this will be accompanied by phase change, with a boiling front moving into the fragment from the outer surface.

As noted previously, high average permeability ($k > 10^4$ μd or so) is a necessary prerequisite to the economic production of geothermal fluids, which means that the "excess enthalpy" δE will be negligible if the reservoir is a "porous medium" [Equation. (6)]. However, in a fractured reservoir, this prerequisite applies only to the volumetric average of the permeabilities of the

"fracture zone" and of the "matrix region." In the "fracture zone," permeability will usually exceed one darcy ($k >> 10^6$ μd), whereas in the "matrix region" permeability can be very small. Laboratory tests on core samples of volcanic rocks from geothermal fields have found intergranular permeabilities in the microdarcy and sub-microdarcy range. Accordingly, although δE will be negligible in a "porous medium" reservoir and in the "fracture zone" of a fractured reservoir, it will not always be negligible in the "matrix region." Under "typical" geothermal conditions (270°C) the latent heat of vaporization of liquid water ($E_s - E_w$) is about 1600 kJ/kg. Thus, if $\delta E \geq 1600$ kJ/kg, "excess enthalpy" will suffice to boil water completely to steam. If this occurs, steam will be the only fluid phase to enter the "fracture zone" from the "matrix region," and the production wells will discharge dry steam. This will only be the case for low values of the matrix region permeability of course, that is, for

$$k \leq \frac{\kappa \nu_w \nu_s}{\left(R_s \nu_w + R_w \nu_s\right)\left(E_s - E_w\right)} \frac{\partial T}{\partial P} \approx 5 \times 10^{-18} \mathrm{m}^2 = 5\ \mu\mathrm{d} \tag{11}$$

To examine this question further, numerical calculations were performed on a 1-D spherical representative element of matrix material (a spherical "fragment"), surrounded by the "fracture zone." To minimize numerical discretization errors, high resolution was employed in both space (300 equal-volume concentric "shells") and time (> 18,000 steps). In the matrix region, porosity is 0.04, formation grain density is 2730 kg/m^3, and grain heat capacity is 830 J/kg-°C. Relative permeabilities are of the "straight-line" type. Thermal conductivity is 3 W/m-°C. Initially, pressure and temperature are uniform, and pressure is equal to the saturation pressure (5505 kPa) for the initial temperature (270°C), but no steam is present. Starting at $t = 0$, the pressure in the fracture zone is reduced to 4694 kPa (saturation temperature = 260°C) and maintained at that value thereafter. Boiling begins immediately in the matrix region adjacent to the fracture surface, and propagates inward. Calculations were carried forward until a stable state (with matrix region pressure = fracture zone pressure everywhere) was reached. Computations were performed for various values of the matrix region permeability. Results are:

Matrix Permeability (μd)	Apparent Heat Capacity (J/kg-°C)	Apparent Conductivity (W/m-°C)	Fluid Mass Fraction Withdrawn
∞	1833	∞	0.763
100	1789	39.42	0.728
30	1717	14.83	0.670
10	1541	6.86	0.530
3	1236	4.61	0.287
1	1030	3.61	0.122
0.3	928	3.21	0.041
0.1	895	3.07	0.015
0.03	883	3.03	0.005
0.01	879	3.01	0.002
0	876	3.00	0

Here, *"apparent heat capacity"* is defined as the total thermal energy transferred from the matrix region to the fracture zone divided by the total initial mass of the matrix region, per degree of temperature change (total is 10°C). *"Apparent conductivity"* is a measure of the heat transfer

rate, and is the thermal conductivity value that would be required to transfer the energy at the calculated average rate by heat conduction alone. *"Fluid mass fraction withdrawn"* is the fraction of the total fluid mass initially in place in the matrix region that flows into the fracture zone.

So long as the matrix region permeability is less than one microdarcy or so, these calculations indicate that very little of the fluid stored in the pores will flow into the fracture zone and up the production wells. Furthermore, heat transfer to the fracture zone will be completely dominated by conduction, and will occur in amounts and at rates that are nearly independent of permeability. Therefore, if matrix permeability is sufficiently low, it is possible to ignore it altogether, neglect the mass transfer from matrix to fractures, and treat heat transfer as arising from unsteady heat conduction only. If this approximation is permissible, the result is a massive simplification of the computational problem when modeling the process numerically in practical reservoir simulation calculations. Since the problem of following matrix-region conditions has been reduced to unsteady heat conduction (a linear process), calculations can be performed at comparable computing cost to the equivalent porous-medium problem (e.g., Pritchett, 1997), thereby reducing the computational burden by between one and two orders of magnitude relative to a full "MINC" treatment.

Finally, it is important to note that the "excess enthalpy" effect is inherently transient in character. This fact has important implications for long-term resource management planning. High wellhead discharge steam fractions will eventually decline, as heat conduction gradually brings about a state of temperature equilibrium between the matrix region and the surrounding fractures carrying fluid to the wells. For thermal properties representative of geothermal reservoir rocks, 50% of the excess heat available initially within the matrix region will be gone after a time t_H, given by:

$$t_H \text{ (days)} \approx 0.07 \times \lambda^2 \tag{12}$$

where λ is the *"average fracture separation,"* in meters—the average distance between the interconnected fractures that make up the large-scale fracture network through which fluids circulate in the reservoir. Note that if λ is small (1–10 m), "excess enthalpy" production will last only a few hours or days, and is likely to be overlooked amidst other transient effects associated with the startup of a new geothermal well. But for the deterioration rate to be unimportant economically (t_H values of a century or more), the average fracture separation required is quite large ($\lambda > 0.7$ km). Under many practical circumstances, intermediate values for λ are likely to result in substantial decline in steam output over the practical economic lifetime of a geothermal project.

References

Pritchett, J. W. (1997), "Efficient numerical simulation of nonequilibrium mass and heat transfer in fractured geothermal reservoirs," Proc. 22nd Workshop on Geothermal Reservoir Engineering, Stanford Univ., pp. 287–293.

Pruess, K. and T. N. Narasimhan (1982), "On fluid reserves and the production of superheated steam from fractured, vapor-dominated geothermal reservoirs," J. Geophys. Res. v. 87 no. B11, pp. 9329-9339.

Fluid Flow Patterns Calculated From from Patterns of Subsurface Temperature and Hydrogeologic Modeling: Example of the Yuzawa-Ogachi Geothermal Area, Akita, Japan

Shiro Tamanyu
Geological Survey of Japan, AIST
AIST Tsukuba Central 7th building, 1-1-1 Higashi, Tsukuba, Ibaraki, 305-8567 Japan

Abstract

Subsurface temperature and fluid flow vectors have been calculated in a broad sense on the basis of borehole temperature logging data for the Yuzawa-Ogachi area, Akita, Japan. The fluid flow vectors are described by numerical simulation based on geometrical parameters, permeability distributions inferred from geological modeling, topographic features and subsurface temperature. The fluid flow in the Cenozoic formations except cap rock is mainly controlled by hydrothermal convections driven by the topographic gradient, subsurface permeability contrast and subsurface temperature gradient. On the contrary, conductive heat transfer is dominant in the Tertiary cap rock and pre-Tertiary basement. The fluid flows from top of the mountain to the Uenotai field and fluid circulations in the lower Tertiary formations at the Uenotai, Kijiyama and Oyasu fields are well reconstructed.

Introduction

The Uenotai geothermal field is located in the Yuzawa-Ogachi area, and the Uenotai geothermal power plant was constructed and started operation as a 27.5 MW electric power generation facility in 1994. The plant is operated by Tohoku Electric Power Co., Inc. and steam is supplied by Akita Geothermal Energy Company.

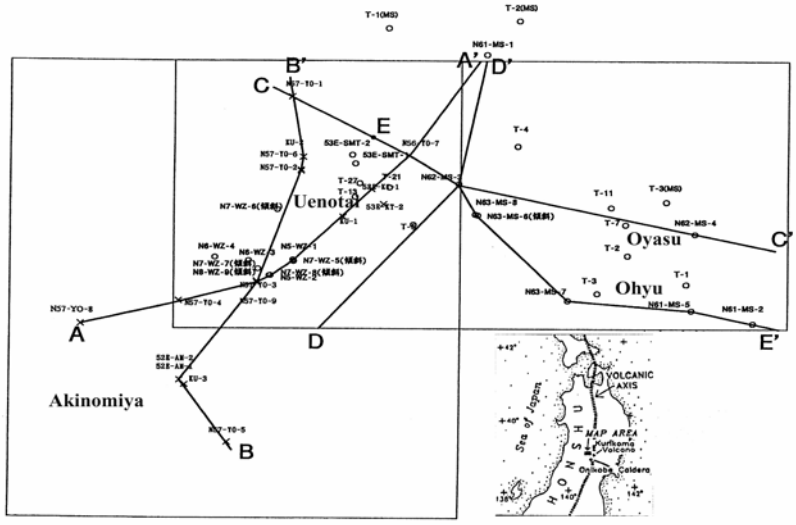

Figure 1. Maps showing the locations of boreholes and cross-sections.

The geothermal fluid flow has been investigated on a regional scale in the Yuzawa-Ogachi geothermal area by the fluid flow simulation along 5 cross sections using temperature profiles of 48 boreholes (Figure 1). Fluid flow paths were inferred from subsurface temperature contour maps at -500 m relative to sea level (NEDO, 1985, 1990). The fluid migration concept was proposed from the viewpoint of general geology and geothermal fluid chemistry (e.g., Robertson-Tait, et al., 1990; Inoue, et al., 2000). Fracture systems related to fluid flow were analyzed by fracture and hydrothermal vein analysis on the surface, and a fluid migration model was proposed (Tamanyu and Mizugaki, 1993).

In and around the Uenotai geothermal field, 56 wells, including slim holes and production boreholes, have been drilled. Using data from these wells, detailed geothermal reservoir performance has been studied. The fracture system related to the geothermal reservoir in the Uenotai area seems to be very complicated (Naka and Okada, 1992), so direct analysis of drill core samples has been done to make clear the relationship between the fluid flow in the reservoir and fracture characteristics (Tamanyu, et al., 1998).

Fluid Flow Patterns in the Yuzawa-Ogachi Area

A numerical simulation code for coupled heat and two-phase fluid flow was developed for 3D simulation of fluid flow in porous media by Nikko Exploration & Development Co., Ltd. (Yamaishi, et al., 1987). The spatio-temporal changes of fluid pressure, mass flux, flow rate and temperature can be calculated. This simulator was adopted for the convenient calculation of fluid flow vectors along specific cross sections by means of subsurface temperature and permeability distributions in the Yuzawa-Ogachi area.

The data files of horizontal and vertical plane gridding are made from positions of cross-sections, boundary condition and topographic data files. The horizontal plane is discretized by 250 m-wide cells with additional 4 km extensions at both ends, and the vertical plane by 100 m–thick cells interval from surface to -2,000 m asl and larger intervals step by step with depth until -5,000 m.

Table 1. List of geologic codes allocated for meshes along cross-sections in the Yuzawa-Ogachi area.

Geologic Codes	Hydro-geologic criteria	Permeability (m^2)	Porosity
1	permeable formations	1.0×10^{-15}	0.15
2	pre-Tertiary basement (< 374 C)	1.0×10^{-17}	0.03
3	pre-Tertiary basement (> 374 C)	1.0×10^{-19}	0.03
4	less permeable formations (cap rock)	1.0×10^{-17}	0.15

The values of permeability and porosity are allocated to all meshes based on hydro-geologic criteria: permeable formations, less permeable formations (cap rocks) and pre-Tertiary basement (subdivided by water critical temperature, 374 deg C) (Figure2 upper diagram). The permeability is fixed as 10^{-15} m^2 for permeable formations, 10^{-17} m^2 for poor permeable formations (so-called cap rock), 10^{-17} m^2 for pre-Tertiary formation lower than 374 deg C, and 10^{-19} m^2 for pre-Tertiary formation higher than 374 deg C respectively, with reference to the conventional reservoir simulation. In this study, the Quaternary volcanics and lower Tertiary (Doroyu Formation) are regarded as permeable formation, and upper Tertiary (Sanzugawa and Minase Formations) as poor permeable formations.

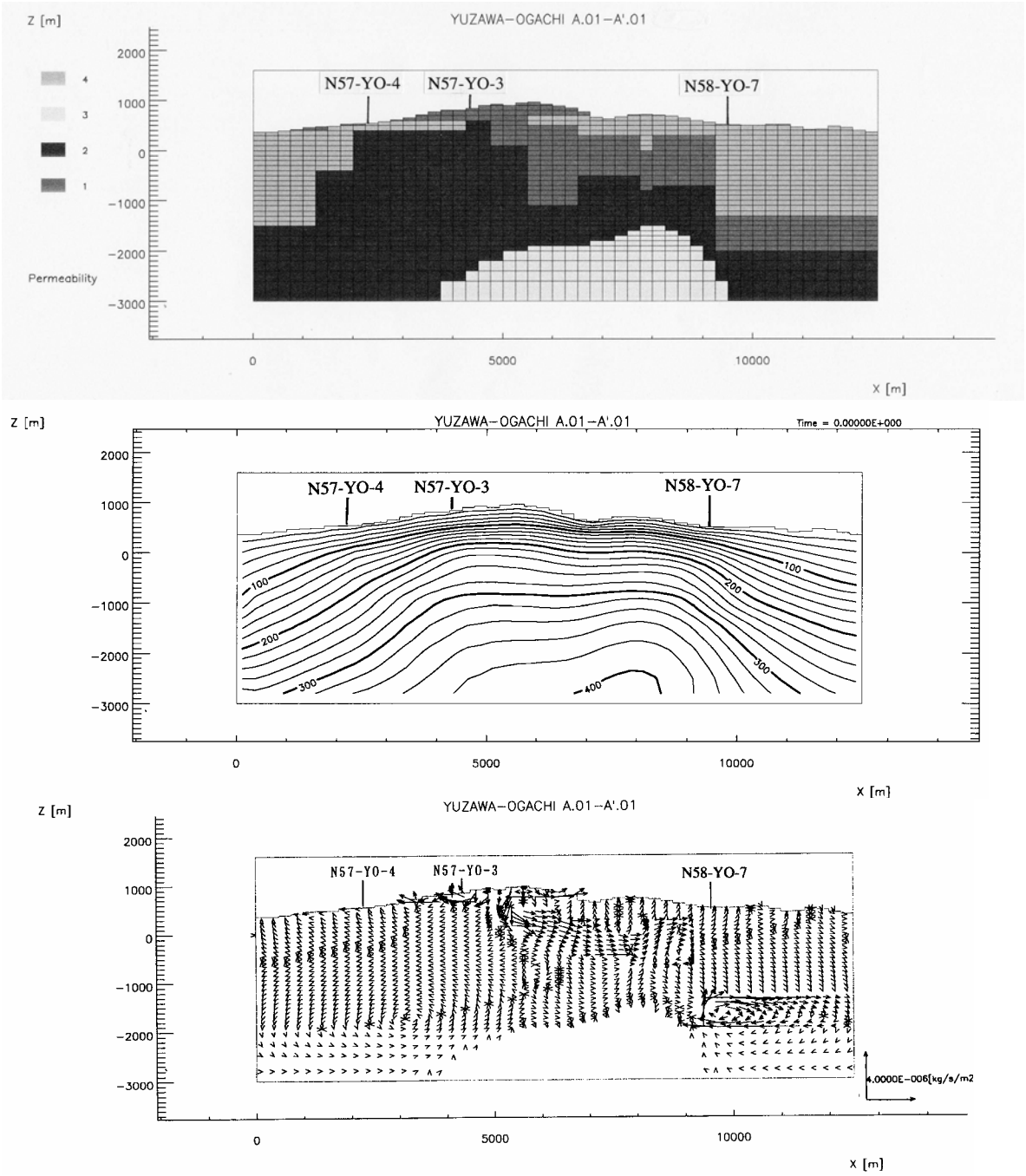

Figure 2. Cross-sections from southwest to northeast (A-A' line) through Uenotai field.

permeable formations (so-called cap rock), 10^{-17} m^2 for pre-Tertiary formation lower than 374 deg C, and 10^{-19} m^2 for pre-Tertiary formation higher than 374 deg C respectively, with reference to the conventional reservoir simulation. In this study, the Quaternary volcanics and lower Tertiary (Doroyu Formation) are regarded as permeable formation, and upper Tertiary (Sanzugawa and Minase Formations) as poor permeable formations.

Subsurface temperature distribution was calculated by the relaxation method, and it is adopted for the fluid flow simulation as fixed temperature data (Figure 2 middle diagram). This assumption poses no problem in the case of slow fluid flow that satisfies the heat equilibrium between host rock and fluid. The initial pressure is assumed as hydrostatic pressure. The temperature of surface is fixed as 10 deg C. The boundaries of both sides and bottom are impermeable and insulated against mass and heat transfer. However, the 4 km extensions on each side are set to avoid artificial edge effects in the simulation results.

For the fluid flow simulation, the subsurface temperature distribution is calculated first using 32 borehole logging data, and then fluid flow vectors are calculated along 5 cross sections. Only A-A' line is shown in Figure 2 lower diagram. This is the cross section from southwest to northeast, and intersects the Uenotai field. The distribution map of fluid flow vectors along A-A' line suggests that heat transfer in the Quaternary and Tertiary formations is mainly driven by the topographic gradient and controlled by permeability contrast, and whereas heat transfer in the pre-Tertiary basement is driven by heat conduction. The fluid circulation in lower Tertiary formations should be regarded as potential geothermal resources.

Conclusion

The conceptual fluid flow model is proposed for the Yuzawa-Ogachi area based on 2-D flow simulation models along 5 cross sections using the distribution maps of subsurface temperature and permeability distributions (Figure 3). Subsurface temperature are calculated based on the relaxation method using borehole temperature logging data, and subsurface permeability and porosity are assumed by correlation between geologic units and the values of permeability and porosity. The vector maps of subsurface fluid flow constructed using a flow simulation model, indicates that fluid flow in Quaternary volcanics is mainly controlled by topography, and the subsurface fluid flows in lower Tertiary formations by permeability distribution and subsurface temperature distribution. The production reservoirs at the Uenotai power station have been generally reconstructed in this study. A more detailed distribution map of permeability, in particular fractures permeability along Doroyu and other faults should be obtained as input data for a more precise fluid flow simulation controlled by topography, and the subsurface fluid flows in lower Tertiary formations by permeability distribution and subsurface temperature distribution. The production reservoirs at the Uenotai power station have been generally reconstructed in this study. A more detailed distribution map of permeability, in particular fractures permeability along Doroyu and other faults should be obtained as input data for a more precise fluid flow simulation.

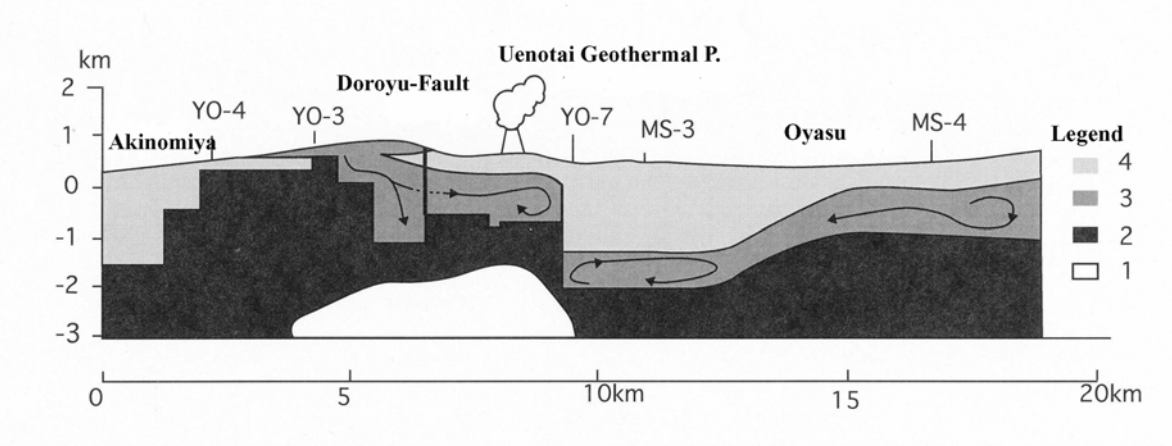

Figure 3. Conceptual model for fluid flows in the Yuzawa-Ogachi fields.

References

Inoue, T., Suzuki, M., Yamada, K., Fujita, M., Huzikawa, S., Fujiwara, S., Matsumoto, I. and Kitao, K. 2000. Geological structure and subsurface temperature distribution in the Wasabizawa area, Akita prefecture, Japan. Proceedings World Geothermal Congress 2000, 2093-2097.

Naka, T. and Okada, H.(1992) Exploration and development of Uenotai geothermal field, Akita prefecture, northeastern Japan. J. Jpn. Mining Geology, 42, 223-240, in Japanese.

New Energy Development Organization (NEDO) (1985) Final report on Survey to identify and promote geothermal development at Yuzawa-Ogachi field, No.7, 814P, in Japanese.

New Energy Development Organization (NEDO) (1990) Final report on Survey to identify and promote geothermal development at Minase field, No.20, 1281P, in Japanese.

Robertson-Tait, A., Klein, C.W., McNitt, J.R., Naka, T., Takeuchi, R., Iwata, S., Saeki, Y. and Inoue, T.(1990) Heat source and fluid migration concepts at the Uenotai geothermal field, Akita prefecture, Japan. Trans. Geother. Resourc. Counc. 14(II), 1325-1331.

Tamanyu, S., Fujiwara, S., Ishikawa, J. & Jingu, H. 1998. Fracture system related to geothermal reservoir based on core samples of slim holes -Example from the Uenotai geothermal field, Northern Honshu, Japan-. Geothermics, 27, 143-166.

Tamanyu, S. and Mizugaki, K.(1993) The fracture system related with geothermal fluid flows - Examples in the Yuzawa-Ogachi geothermal field, Akita, Japan-. J. Jpn. Geotherm. Res.Soc. 15, 253-274, in Japanese.

Yamaishi, T., Kamata, J. Nomura, K., 1987. Numerical simulation of heat and two-phase fluid flow in fractured geothermal reservoir. Extended abstract for 77th annual meeting of The Society of Exploration Geophysicists of Japan, 260-265, in Japanese.

Microbial Processes in Fractured Rock Environments

Nancy E. Kinner and T. Taylor Eighmy
Bedrock Bioremediation Center,
University of New Hampshire, Durham, NH

Overview

Until recently, there was almost no information available on the microbial communities that inhabit fractured rock. Moreover, there was some doubt as to whether microbes existed there at all. Starting in the late 1990s and continuing to today, the microbial communities in only a few rock environments have been studied, with particular emphasis on the prokaryotes present. A range of bedrock environments has been examined: a deep tunnel through granitic bedrock in Sweden (potential nuclear waste disposal site); a basalt formation in Idaho, USA, contaminated by radionuclide and sewage sludge wastes; a gold mine in South African in the Carbon Leader formation; and a chlorinated solvent-contaminated site in a New Hampshire, USA. Information from these sites and others will form the basis for this overview of currently known microbial processes in fractured rock environments.

Microbial processes occur on a very small scale. Hence, use of the term "fractured rock" is too general when trying to understand how microbes are interacting with their immediate environment. In some cases, fractured rock can be structurally weathered. This rock is usually broken up and groundwater flows through it much more like flow through porous media than through the discrete fractures in competent rock. The latter has much fewer fractures per unit volume with much more complex groundwater flowpaths. However, hydraulics in these formations are not easily characterized or modeled.

Most of the microbial research has centered on competent rock. Microbial colonization and metabolism are mostly taken place in open microfractures in the bedrock, which are connected with larger fractures. Fracture surfaces confer numerous advantages to bacteria and can influence metabolic processes. In bench-scale fractured bedrock column studies (Lehman et al., 2001a), microbial communities were compositionally different from those in the water flowing through fractures. Fracture surfaces were enriched in gram-positive bacteria and α-Proteobacteria and depleted in β-Proteobacteria. Lehman et al. (2001b) suggest that microbial communities will be partially controlled by the surrounding geological media.

There is a growing body of literature on microbe-mineral interactions. Adherent or endolithic bacteria can cause mineral weathering (Fisk et al., 1998). They are involved in the deposition of minerals in extracellular regions, frequently within the extracellular polymeric substance (EPS) region, on cell surfaces, and on cell appendages. Some recent examples of calcite, dolomite, and ferroan dolomite deposition have been provided (Brassant et al., 2002; Horath et al., 2002; Rogers and Bennett, 2001). Lower et al. (2001) report nanoscale interactions involved in "recognition" of goethite by *Shewanella*.

There is also a growing body of evidence that microbes seek out surfaces to adhere to that may be of nutritional benefit. In Fe-limited growth media, *Pseudomonas* sp. will preferentially attach to the Fe(III)-bearing minerals goethite (α-FeOOH) and hematite (Fe_3O_4) and use the Fe

nutritionally (Forsythe et al., 1998). Dissimilatory iron reducing bacteria will also preferentially attach to α-FeOOH (Lower et al., 2001).

Kalinowski et al. (2000a; 2000b) and Lierman et al. (2000b) have recently determined that an *Arthrobacter* species will produce a Fe-siderophore, when attached to the mineral horneblend and extract the Fe from the mineral with these chelators. Biofilms (or perhaps biopatches) can produce a measurable changes in pH across the biofilm, which helps to enhance mineral dissolution and may be related to growth rate, production of low molecular weight organic acids, physical properties of the synthesized EPS, or production of the siderophore (Lierman et al., 2000a). In carbon-rich anoxic groundwater, where P is scarce, microbes will colonize hornblende surfaces that have apatite [$Ca_5(PO4)_3OH$] inclusions and solubilize the P for nutritional use (Rogers et al., 1998).

At the petroleum-contaminated aquifer site in Bemidji, Minnesota, *in situ* distribution of attached bacteria is related to the nutritional content of the host minerals (Rogers et al., 1998 and 1999; Bennett et al., 1999). Research by Bennett et al. (1996; 2000; 2001), Hiebert and Bennett (1992) and Rogers et al. (2001) has also shown that colonized mineral surfaces weather faster than uncolonized surfaces. Adherent microorganisms can dissolve growth-limiting nutrients from a variety of silicate minerals, which, in turn, can enhance growth and biodegradation of the contaminants at the site (Rogers et al., 1999 and 2001). Preference is shown for silicates containing P and Fe, rather than for silicates containing Al, Pb, and Ni (Rogers et al., 1998 and 1999).

Fracture Systems and Microfracture Network

Within competent rock, there are often two sizes of fractures that microbes can inhabit: open fractures that have a bigger aperture (mm to cm scale) with a relatively large volume of groundwater flowing through them; and microfractures with much smaller apertures (μm to mm scale), which are often partially sealed by minerals or clays, and a very small groundwater velocity. Depending on the formation, microfractures may comprise a significant portion of the total fracture porosity in the rock. In open fractures with high groundwater velocities, there are fewer mass transfer constraints. In microfractures with dominated diffusion processes, mass transfer may be highly constrained. Hence, the environmental conditions in microfractures may be dominated by small-scale (on the order of μm) interaction between the pore water and the microfracture surfaces, which is not reflected in the groundwater sampled from the borehole.

The characterization of microbial processes in the fractures is further complicated by the geochemistry of the rock. The microbes appear to be associated with different minerals (i.e., on the surface of or embedded in them) as well as in crevices on the host rock surface. Because most competent bedrock is very heterogeneous (e.g., many mineral inclusions), especially on the scale of μm to cm, the rock may have a potentially large number of microhabitats. This may explain the microbial diversity identified by molecular techniques over small (cml (centimeter to meter) distances within a given bedrock formation (Eighmy et al., 2004). Hence, broad generalizations about microbial processes in competent fractured rock must be subcategorized by fracture or microfracture type.

Important Questions about Microbial Processes in Competent Rock

A number of important questions need to be posed to further the understanding of microbial processes and activity in fracture systems or microfractures:

- How does large-scale metabolic activity and dominant terminal electron acceptor processes in the open fractures translate to the microscale within microfractures? Might heterogeneity at the microscale afford another level of zonation? Do locally absorbed natural organic matter (NOM) or Fe and S associated with host rock and microfracture surface minerals affect the microbial activity or dominant terminal electron acceptor/donor processes?
- What is the importance of microbial activity in microfractures compared to that in open fractures when characterizing a bedrock environment?
- How predominant are the microfracture population components compared to open fracture components given diffusion limited processes, but perhaps significant specific surface area contributions afforded by the microfractures?
- Are metabolic rates (or potential) greater for surface-associated populations or free-swimming (planktonic) populations? Does this change as a function of a fracture size and contamination?
- What roles do surfaces and thigmotrophy play in determining microbial population distribution community structure and metabolic activity?
- Are metabolic rates (or potential) greater for surface-associated populations or groundwater (planktonic) populations?
- How much syntrophy is involved in the complex and diverse prokaryotic populations on the fracture surfaces?
- How does large-scale metabolic activity (aerobic, iron, nitrate, sulfate-reducing, methanogenic, or carbonate-reducing activity) translate to the microscale within fractures?
- How should microbial processes in the open microfractures be modeled?

Some of these questions are partially addresses in the synthesis provided below.

Determination of Predominant Microbial Processes in Competent Rock

Several approaches have been used to determine the large scale metabolic activity predominant in organically-contaminated aquifers. For example, important biogeochemical parameters (e.g., dissolved oxygen, nitrate, sulfate, iron, methane) can be monitored and used in various natural attenuation models. Chapelle et al. (1995; 2003) have developed and implemented a strategy to use hydrogen [$H_2(g)$] measurements to quantify various redox couples (Fe^{3+}/Fe^{2+}, NO_3^-/NO_2^-, SO_4^{2-}/S^{2-}) and the presence or absence of metabolic end products to deduce the dominant terminal electron acceptor processes in the formation or plume. Both of these approaches also measure the progeny of the contaminants needed for the estimation of predominant metabolic process. This approach has worked for a number of field investigations (Chapelle et al., 2003; McGuire et al., 2000; USEPA, 1997 and 2002). However, it has not been applied systematically in competent bedrock, nor in microfracture networks.

Another approach, not necessarily mutually exclusive, is the use of molecular methods (e.g., PCR/DGGE, FISH, PLFA) to identify the existing populations of microbes and to deterine whether they have DNA with the genetic code needed to produce a specific material for transcription to RNA and expressed as protein enzymes of metabolic significance. Using molecular quantification methods to determine specific groups of microbes (e.g., sulfate-reducing bacteria, methylotrophs, methanogens), which inhabit a fracture, can indicate the types of predominate biogeochemical processes. Furthermore, molecular methods that focus on transcribed RNA can indicate if the enzymes with a specific potential are being produced by the microbes and can serve as an indication of what metabolic reactions are occurring *in situ*.

Most of the microbial research currently available on competent rock focuses on the prokaryotes (Eubacteria and Archaea). A wide variety of prokaryotes have been reported in the fractured rock literature, including autotrophs and heterotrophs, Eubacteria and Archaea (Onstott et al., 1998 and 2003; Colwell et al., 1997; Krumholz et al., 1997; Baker et al., 2003; Haverman et al., 1999; Pedersen et al., 1990, 1996, and 1997; Takai et al., 2001; Pedersen, 2001; Ekendahl et al., 1994). Quality control of the data has played an important part in many of the studies (Fredrickson and Phelps, 1997; Colwell et al., 1992; Smith et al., 2000; McKinley and Colwell, 1996; Pedersen et al., 1997; Onstott et al., 2003; Griffiths et al., 2002) with particular concern centering on the possibility that contamination of the bedrock cores and groundwater occurs during drilling and sample collection. Using a variety of tracers (e.g., microspheres, bromide, Rhodamine WT and ice nucleating active bacteria), it has been shown that while contamination occurs to some extent, the diversity observed *in situ* is not solely the result of inoculation of the bedrock with microbes from above or the drilling fluid.

Little is known about the availability of the necessary electron donors/acceptors in the fractures. This may also be a key to understanding microbial processes in competent bedrock. The groundwater collected, even during discrete interval sampling in a borehole, is an aggregate of what is happening in the hydraulically predominant fractures, which are probably open fractures, and may not be at all representative of microfracture conditions. Recent attempts have been made to relate groundwater chemistry, microbial community structure, and geochemical modeling (Eighmy et al., 2004), but this work is only the beginning of what needs to be done to understand the biogeochemical interactions between the prokaryotic community and the groundwater and rock surface geochemistry.

There are data that suggest that the microbial communities in saturated fractured rock are metabolically active. Studies by Pedersen et al. (1990, 1992a and 1992b; Ekendahl et al., 1994) and microcosms (e.g., Yager et al., 1997; Fredrickson et al., 1997) have shown that organic carbon can be actively degraded by microbial communities from the groundwater or rock. Unfortunately, there is little uniformity in the microcosm methods used (e.g., groundwater alone, freshly crushed rock, weathered surfaces). Indeed, the extent of the interaction between the groundwater (planktonic) and rock surface-associated microbial communities and “fresh” and chemically weathered mineral surfaces is unknown. Hence, the representativeness of the biodegradation rates derived from these microcosms with respect to conditions existing *in situ* is unresolved.

Microbial Abundance in Competent Bedrock

Overall, the abundance of microbes is relatively low in the rock environment where microbial investigations have been conducted (10^3-10^5 cells/mol groundwater; 10^2-10^3 cells/cm^2 fracture surface; 10^2-10^3 cells/g rock) (Pedersen et al., 1997; Onstott et al., 2003; Tisa et al, 2002) as compared to porous media. These low abundances are expected because the mass of electron donors available in most rock environments is minimal. Most of the natural organic matter (NOM), which might serve directly as an electron donor or undergo fermentation to produce hydrogen as an electron donor, is used in the overburden and never transported to the underlying rock. The exception to this may occur in those environments where competent bedrock is near the surface and the groundwater flow is strongly linked hydraulically over relatively short time scales (days to months) with overlying NOM sources (e.g., wetlands). Often, the pollutants that migrate into competent bedrock are aliphatic chlorinated solvents and their progeny (e.g., PCE, TCE, DCE, VC) because these are denser than water and thus tend to sink even after they encounter saturated conditions. The chlorinated solvents, primarily electron acceptors, generally cannot serve as electron donors unless they have few chlorines (e.g., VC) and there is a strong electron acceptor present (e.g., oxygen). The latter condition is rare because oxygen often does not exist in competent rock environments because of mass transfer limitations.

Surface-Associated versus Planktonic Microbial Communities

Research in porous media has shown that the prokaryotic communities inhabiting the groundwater and media surfaces are different (e.g., Harvey et al., 1984). This phenomenon has also been found in competent rock (Lehman et al., 2001). In pristine porous media, metabolic activity is mostly associated with the microbes on the media surfaces. In polluted porous media, this relationship is changed and the groundwater community becomes more important in microbial processes (Murphy et al., 1997) because there are fewer mass transfer limitations affecting the availability of electron donors/acceptors and nutrients. The distribution of metabolic activity between the microbes on the media surfaces and in groundwater in competent rock is unknown, but it is documented that under pristine conditions or those with low levels of pollutants (μg/L range), NOM and contaminants are associated with the fracture surfaces (Eighmy et al., 2004). In polluted environments, the hydrophobic contaminants can be sorbed into the rock matrix. The extent to which *in situ* microbes degrade the sorbed contaminants in the matrix is unknown. Concern has been expressed at sites where *in situ* remediation occurs (i.e., materials to enhance biological, physical or chemical degradation are injected into the subsurface) that reappearance of the contaminant may occur after the bulk groundwater appears clean and active remediation has ceased. In porous media, this rebound effect has been attributed to release of contaminants from less porous lenses of the aquifer materials (e.g., silts and clays). It is hypothesized that this pattern may occur in fractured rock if the microfractures harbor contamination that is not biodegraded and subsequently diffuses into the actively flowing groundwater in the open fractures.

Role of Protists

A recent study (Kinner et al., 2002) has shown that protists can inhabit competent rock environments. While their abundances are low (10^2-10^3/L), there appears to be a potential

predator-prey relationship between the prokaryotes and eukaryotes. Furthermore, a perturbation of the bedrock microenvironment with dissolved organic carbon can result in an increase in protistan abundances (Kinner et al., 2002), classically associated with protistan stimulation of prokaryotic biodegradation (Hunt et al., 1977; Kuikman et al., 1990). Again, more research is necessary to understand this dynamic and its impact on microbial processes.

Microbial Transport in Fractures

Studies by Harvey (1997) and Becker et al. (2003) using microbial tracers have shown that colloid-sized particles can move very rapidly through the major fracture pathways, most likely through the open fractures with high hydraulic conductivities. The transport of non-surface-associated microbes in microfractures is unknown, but likely to be very small, if they diffuse into these pathways at all. Fredrickson et al. (1997) found that core samples dominated by pore throats <0.2 μm generally did not support microbial activity in shale and sandstone because this width is believed to be the lower limit for microbial transport into fractures. Similarly, Colwell et al. (1997) found that cores with pore throat widths <1 μm, porosities <5%, and permeabilities <0.001 mD did not contain significant biomass or metabolic activity.

Models of Microbial Processes in Competent Bedrock

Modeling the fate and transport of contaminants in competent rock is generally very difficult because of the complexity of the hydraulics and number of reactions that can affect chemical species present. Generally, few such models have been attempted and most of those have focused on abiotic processes. Yager (2002) incorporated microbial activity into his model of a dolomite site contaminated with chlorinated solvents using biodegradation rates obtained from groundwater microcosms.

Conclusion

While the body of knowledge available on microbial processes in competent bedrock environments has expanded greatly in the past several years, there still have been few sites studied and many questions remain unanswered. Research on microbial processes in fractured rock is vital and must be increased because of using groundwater for water supply, selecting optimal methods of bioremediation of polluted groundwater; and considering fractured rock as a long-term repository for high level radioactive wastes (e.g., in Sweden and Yucca Mountain, NV).

References

Bennett, P.C., F.K. Hiebert, and W.J. Choi. 1996. Microbial colonization and weathering of silicates in a petroleum-contaminated groundwater. Chemical Geology 132: 45-53.

Bennett, P.C., J.R. Rogers, F.K. Heibert, and W.J. Choi. 1999. Mineralogy and mineral weathering: fundamental components of subsurface microbial ecology. U.S. Geological Survey Toxic Substances Hydrology Program. Proceedings Of the Technical Meeting,

Charleston, S.C., March 8-12, 1999, Water-Resources Investigations Report 99-4018c, 169-176.
Bennett, P.C., F.K. Hiebert, and J.R. Rogers. 2000. Microbial control of mineral-groundwater equilibria: macroscale to microscale. Hydrogeology Journal 8: 47-62.
Bennett, P. C., J.R. Rogers, and W.J. Choi. 2001. Silicates, silicate weathering, and microbial ecology. Geomicrobiology Journal 18:3-19.
Baker, B.J. et al. 2003. Environmental Microbiology 5: 267-277.
Becker, M.W. et al. 2003. Groundwater 41: 682-689.
Brassant, O., M. Aragno, and E.P. Verrecchia. 2002. Calcium carbonate crystal morphology and mineralogy, why are bacteria in control? Abstract 225, p.61, Book of Abstracts, 2002 International Subsurface Microbiology Conference, Copenhagen, Denmark, September 9-15, 2002.
Chapelle, F.H.et al. 1995. Water Resources Research 31: 359-371.
Chapelle, F.H. et al. 2003. Water-Resources Investigations Report 03-4057, U.S Geological Survey, Denver, Colorado.
Colwell, F.S. et al. 1992. J. Microbiological Methods 15: 279-292.
Colwell, F.S. et al. 1997. FEMS Microbiology Reviews 20: 425-435.
Fisk, M.R., S.J. Giovanoni, and I.H. Thorseth. 1998. Alteration of oceanic volcanic glass: textural evidence of microbial activity. Science 281: 978-980.
Hiebert, F.K., and Bennett, P.C. 1992. Microbial control of silicate weathering in organic-rich ground water. Science 258:278-281.
Horath, T., W. Von Sigler, T. Neu, and R. Bachofen. 2002. Endolithic microbial populations in dolomite rock. Abstract 207, p.53, Book of Abstracts, 2002 International Subsurface Microbiology Conference, Copenhagen, Denmark, September 9-15, 2002.
Kalinowski, B. E., L.J. Liermann, S.L. Brantley, A. Barnes, and C.G. Pantano. 2000a. X-ray photoelectron evidence for bacteria-enhanced dissolution of hornblende. Geochimica et Cosmochimica Acta 64:1331-1343.
Kalinowski, B. E., L.J. Liermann, S. Givens, and S.L. Brantley. 2000b. Rates of bacteria-promoted solubilization of Fe from minerals: a review of problems and approaches. Chemical Geology 169: 357-370.
Lehman, R. M., F.S. Colwell, and G. A. Bala. 2001a. Attached and unattached microbial communities in a simulated basalt aquifer under fracture- and porous-flow conditions. Applied Environmental Microbiology 67: 2799-2809.
Lehman, R. M., F.F. Roberto, D. Earley, D.F. Bruhun, S.E. Brink, S.P. O.Connell, M.E. Delwiche, and F.S. Colwell. 2001. Applied Environmental Microbiology 67: 2095-2106.
Eighmy, T.T. et al. 2004. Draft BBC Final Report to U.S. EPA. University of New Hampshire.
Ekendahl, S. et al. 1994. Microbiology 140: 1575-1583.
Fredrickson, J.K. and T.J. Phelps. 1997. In Manual of Environmental Microbiology. Hurst, C.J. (ed.) ASM Press. Washington, D.C.
Griffiths, E.C. et al. 2002. International Symposium Subsurface Microbiology. Copenhagen, Denmark.
Harvey, R.W. 1997. FEMS Microbiology Reviews 20: 461-472.
Harvey, R.W. et al. 1984. Applied Environmental Microbiology 48: 1197-1202.
Haverman, S.A. et al. 1999. Geomicrobiology J. 6: 277-294.
Hunt, H.W. et al. 1977. Microbial Ecology 3: 259-278.
Kinner, N.E. et al. 2002. International Symposium Subsurface Microbiology. Copenhagen,

Denmark.
Krumholz, L.R. et al. 1997. Nature 386: 64-66.
Kuikman, P.J. et al. 1990. Soil Biology Biochemistry 22: 1063-1073.
Lehman, R.M. et al. 2001. Applied Environmental Microbiology 67: 2799-2809.
Liermann, L. J., A.S. Barnes, B.E. Kalinowski, X. Zhou, and S.L. Brantley. 2000a. Microenvironments of pH in biofilms grown on dissolving silicate surfaces. Chemical Geology 171: 1-16.
Liermann, L. J., B. E. Kalinowski, S.L. Brantley, and J. G. Ferry. 2000b. Role of bacterial siderophores in dissolution of hornblende. Geochimica et Cosmochimica Acta 64: 587-602.
Lower, S.K., M.F. Hochella, and T.J. Beveridge. 2001. Bacterial recognition of mineral surfaces: nanoscale interactions between Shewanella and α-FeOOH. Science 292: 1360-1363McGuire, J.T. et al. 2000. Chemical Geology 169: 471–485.
McKinley, J.P. and F.S. Colwell. 1996. J. Microbiological Methods 26: 1-9.
Murphy, E.M. et al. 1997. Water Resources Research 33: 1087-1103.
Onstott et el. 1998. In Enigmatic Microorganisms and Life in Extreme Environment. Seckback, J. (ed). Kluwer Academic Pub. Dordrecht, Netherlands.
Onstott, T.C. et al. 2003. Environmental Microbiology 5: 1168–1191.
Pedersen, K. 2001. In Subsurface Microbiology and Biogeochemistry. Fredrickson, J.K. and M. Fletcher (eds.) Wiley-Liss. New York.
Pedersen, K. et al. 1992a. Microbial Ecology 22: 1-14.
Pedersen, K. et al. 1996. FEMS Microbiology Ecology 19: 249-262.
Pedersen, K. et al. 1997. J. Microbiological Methods 30: 179-192.
Pedersen, K. and S.E. Kendahl. 1990. Microbial Ecology 20: 37-52.
Pedersen, K. and S.E. Kendahl. 1992b. J. General Microbiology 138: 369-376.
Smith, D.C. et al. 2000. Geomicrobiology J. 17: 207-219.
Takai, K. et al. 2001. Applied Environmental Microbiology 67: 5750–5760.
Tisa, L.T. et al. 2002. International Symposium Subsurface Microbiology. Copenhagen, Denmark.
Rogers, J.R. and P.C. Bennett. 2001. Ferroan dolomite mineralization by iron-reducing bacteria. EOS Transaction AGU 82(47), Fall Meeting Supplement, Abstract B12C-0141.
Rogers, J. R., P.C. Bennett, and W.J. Choi. 1998. Feldspars as a source of nutrients for microorganisms. American Mineralogist 83: 1532-1540.
Rogers, J. R., P.C. Bennett, and F.K. Heibert. 1999. Patterns of microbial colonization on silicates. U.S. Geological Survey Toxic Substances Hydrology Program--- Proceedings Of the Technical Meeting, Charleston, S.C., March 8-12, 1999, Water-Resources Investigations Report 99-4018c, 237-242.
Rogers, J.R., P.C. Bennett, and W.J. Choi. 2001. Enhance weathering of silicates by subsurface microorganisms: a strategy to release limiting inorganic nutrients? Water-Rock Interaction- Proceedings of then Tenth International Symposium on Water-Rock Interaction, Villasimus, Italy, 10-15 July, 2001, A.A. Balkema, the Netherlands.
USEPA. 1997. U.S. EPA Report EPA/540/R-97/504, Washington, D.C.
USEPA. 2002. U.S. EPA Report EPA/600/R-02/002, Washington, D.C.
Yager, R.M. 2002. U.S.G.S. Water Resources Investigations Report 00-4275.
Yager, R.M. et al. 1997. Environmental Science Technology 31:3138-3147.

The Impact of Microbial Activity on Fractured Chalk Transmissivity

Shai Arnon[1,2], Eilon Adar[1,2], Zeev Ronen[1], Alexander Yakirevich[1] and Ronit Nativ[3]
[1]Dept. Environmental Hydrology and Microbiology, Institute for Water Sciences and Technologies
J. Blaustein Institute for Desert Research,Ben-Gurion University of the Negev, Sede-Boker, Israel
[2]Dept. Geological and Environmental Sciences, Ben-Gurion University of the Negev, Israel
[3 1] Dept. Soil and Water Sciences, The Hebrew University of Jerusalem, Israel

A reduction in the saturated hydraulic conductivity (K_s) of geological materials has been reported in many laboratory experiments and field studies. In porous media, utilization of substrate and a consequent biomass accumulation were reported to account for a K_s reduction of three to four orders of magnitude (Vandevivere and Baveye, 1992). A special case of the interaction between microbial and hydrological processes and the consequent clogging occurs when contaminants reach the subsurface. In some cases, the clogging might limit the use of *in situ* bioremediation by limiting the nutrient supply. In other cases, deliberate clogging of an aquifer is used to control groundwater movement for its containment or bio-treatment (Ross et al., 2003). Whereas the biological clogging of porous media has been reported for several decades (e.g., Avnimelech and Nevo, 1964), only a few studies on fracture bio-clogging have been published, all during recent years (Ross et al., 2001; Hill and Sleep, 2002).

This paper focuses on the mechanisms involved in hydraulic changes due to microbial activity in natural fractures within chalk cores using (1) transmissivity measurements before and during biofilm growth; (2) measurements of chemical constituents indicating biodegradation activity along the fracture; and (3) bacteria counts on the fracture surfaces together with direct images of biofilm formation, via scanning electron microscopy (SEM). The impact of microbial activity on the hydraulic properties of fractured chalk was tested in horizontal cores, drilled along a vertical fracture. The cores were saturated under vacuum using degassed artificial groundwater (AGW). Ion concentrations of the AGW were: 3,700 mg/L Cl^-, 1,030 mg/L SO_4^{2-}, 245 mg/L HCO_3^-, 340 mg/L Ca^{2+}, 200 mg/L Mg^{2+}, 2100 mg/L Na^+ and 22 mg/L K^+. These concentrations are similar to those found in uncontaminated groundwater east of the study site (Nativ and Adar, 1997). Each fractured core was fixed inside a PVC casing using epoxy cement (Duralite®). Teflon inlet and outlet chambers were attached to both sides of the flow boundaries of the fracture, while the other two boundaries were sealed.

A schematic illustration of the experimental apparatus appears in Figure 1. Four stainless steel injection ports (1 mm i.d.) were inserted through the inlet chamber into the fracture plane, 2 cm from the inlet boundary. The injection ports were used to inject the substrate during the biodegradation experiments directly into the fracture (Pump #3), while AGW (Pump #1) was supplied through the inlet chamber. The AGW flux was kept at twice the substrate injection flux to prevent substrate backflow toward the inlet chamber. Pump #2 circulated continuously the AGW to ensure the inlet chamber is well-mixed. A pair of sampling ports (Teflon tubes, 1 mm i.d.) were located approximately every 10 cm from the inlet toward the outlet of the core. The experiments were conducted with the fractures in a vertical position, to mimic the *in situ* fracture orientations in the related study site (Nativ and Adar, 1997).

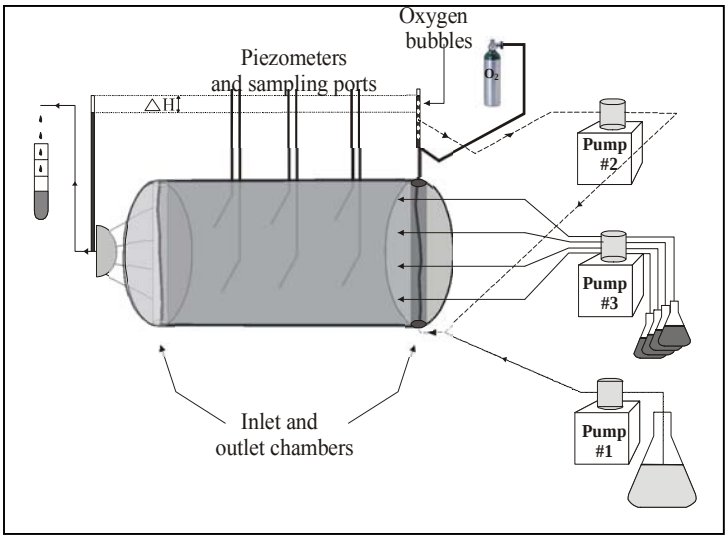

Figure 1. Schematic configuration of the experimental setup.

Hydraulic tests were conducted to determine the transmissivity of the fractures in the three cores. Following the initial hydraulic characterization of the fractures, a nutrient solution containing 2, 4, 6-tribromophenol (TBP) as a representative contaminant was continuously injected into the fracture. TBP concentrations together with Br^- (indicative of TBP degradation) and oxygen concentrations were monitored routinely at the inlet and outlet of the "flow through system" and along the fracture length through the preinstalled piezometers. The various fractures were operated over 100 to 630 days under different conditions including variations in flow rates, TBP, and oxygen concentrations. *Phase 1* of the experiments (days 0-400) was characterized by TBP inlet concentrations of <50 mg/L, low oxygen concentrations (<4 mg/L) and relatively slow flow rates (1.3-7.8 mL/hr). *Phase 2* involved only Cores #2 and #3 and lasted for an additional ~200 days. It was characterized by TBP concentrations of ~100 mg/L, over-saturated oxygen concentrations (~20 mg/L) and relatively high flow rates (8-40 mL/hr). At the end of the experiments, one core was cut open and bacteria on the fracture surface were counted. Several samples were also taken for scanning electron microscopy (SEM) analysis.

The changes in the normalized transmissivity over time, along with the removal rate of TBP (log scale), are illustrated in Figure 2. The initial transmissivity of the fracture, T_0, and the initial equivalent hydraulic apertures are listed in Table 1.

Table 1. Transmissivity, hydraulic conductivity and aperture calculations from laboratory experiments in fractured chalk cores.

	Transmissivity (m^2/day)	Equivalent hydraulic aperture-$2b_h$ (μm) [a]	Hydraulic conductivity (m/day) [a]
Core # 2	8.632	495	18489
Core # 3	0.695	207	3233
Core # 4	5.156	403	12377

[a]Derived from the cubic law

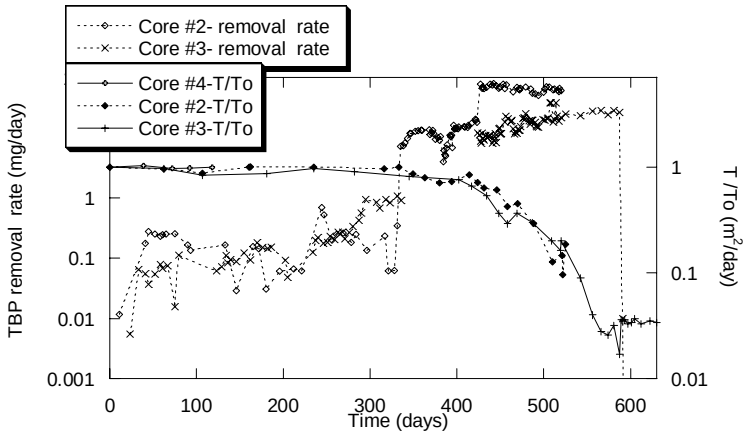

Figure 2. TBP removal rate and the related changes in normalized transmissivity.

The change in transmissivity between Phase 1 of the experiments (Days 0-330) and Phase 2 (after Day 330) was remarkable. During the first phase of the experiments, the relative transmissivity of the three cores fluctuated slightly and reached as low as 18% less than the initial value (Core #3). The relative transmissivity fluctuation of a control sample could be followed in Core #4, which was run without substrate addition, thus screening the effect of intensive microbial activity processes on the transmissivity (T/T0 = ±2.5%). During Phase 2 of the experiments, the transmissivity decreased by ~90% (T/T0 = 0.1) in Core #2 and ~97% in Core #3 after 590 days. The equivalent hydraulic apertures were reduced by 240 μm and 160 μm in Cores #2 and #3, respectively. The transmissivity decrease (on a log scale) follows a non-linear pattern with slight recoveries. In Core #3, the transmissivity was slightly increased after Day 590 and then remained relatively constant until the end of the experiment (Day 630). The abrupt recovery occurred immediately after the substrate was removed from the inlet solutions and a biocide (Sharomix-mci, 30 mg/L) was added. The biocide was added to prevent further TBP degradation due to microbial activity that might result in TBP release to the fracture by back diffusion. The other experimental conditions (i.e., flow rate, oxygen supply, injection procedure,) remained the same. This confirms that microbial activity accounted for the transmissivity reduction, which is directly related to TBP removal rate. During Phase 1, the removal rate was in the order of ≤1 mg (TBP)/day, and no noteworthy reduction was observed (Days 0-330). When the removal rate was increased to ~10 mg (TBP)/day, the transmissivity started to decline in both cores. In addition, when the removal rates were on the order of several tens of mg (TBP)/day, the transmissivity reduction was eminent. This pattern of transmissivity reduction was similar for both cores, although their initial transmissivity values differed by one order of magnitude (Figure 2). Nevertheless, to achieve a similar reduction in the relative transmissivity, less substrate was needed in the case of Core #3 due to its lower initial transmissivity. The total degraded TBP mass in Cores #2 and #3 was 7500 and 3600 mg, respectively.

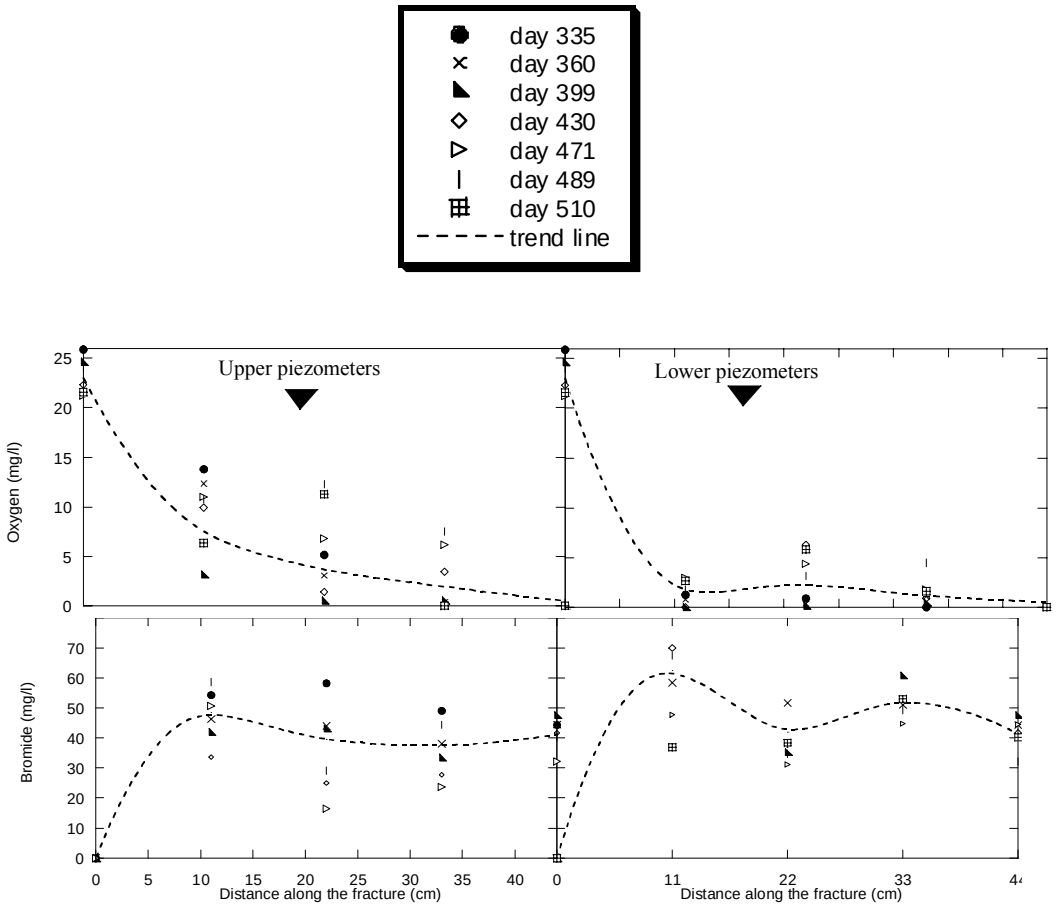

Figure 3. Spatial and temporal distribution of oxygen and Br^- (core #2).

Br^- and oxygen concentrations were used to estimate the biodegradation activity along the fracture. The general trends of concentration along the fracture-intersecting Core #2 are displayed in Figure 3 by the dashed lines. The lines are shown for guidance only, and the fact that each data point is independent should be stressed. The results are presented in two sets that differentiate between the upper and the lower array of piezometers, where the terms "upper" and "lower" refer to the fracture in the vertical position. The oxygen along the fracture was rapidly depleted within the first 10 cm. On average, about 68% of the initial oxygen was depleted in the upper (11 cm) piezometer and as much as 94% in the lower one. In some cases, an increase from the first piezometer value to the second one (on the same array) indicates that these piezometers do not share the same flow channel (e.g., Day 430). For such cases, the general trend of concentration decline along the fracture, as depicted by the trend lines, is misleading. The pattern of Br^- release mirrors that of the oxygen (Figure 3). Most of the Br^- was formed in the initial part of the fracture, whereas during the rest of the fracture the concentrations remained relatively constant. These concentration profiles suggest that the majority of microbial activity takes place close to the inlet. On the other hand, the "scatteredness" of the data suggests that biodegradation is a dynamic process, which, despite maintaining relatively constant conditions, did not reach a steady state over a prolonged duration (over 100 days).

The spatial distribution of the total viable bacteria on the opened fracture surface, as determined

by a drop plate method on R2A medium, was measured in a 2 × 2 cm grid. The integrated biomass on both surfaces along the fracture is displayed in Figure 4. The highest concentrations of bacteria were observed close to the substrate injection ports (~3 cm from the inlet). Following this zone, the numbers dropped from ~1.1 × 10^8 to ~2 × 10^7 CFU/cm^2 along a distance of 18 cm from the inlet. A second increase in bacteria numbers appeared toward the second half of the fracture (35 cm). The existence of large biomass close to the inlet chamber was confirmed by SEM photomicrographs (Figure 5). The photomicrograph Figure 5a serves as a control for the chalk fracture surface that was not exposed to AGW and TBP solution, displaying fragmented fossils (see arrows).

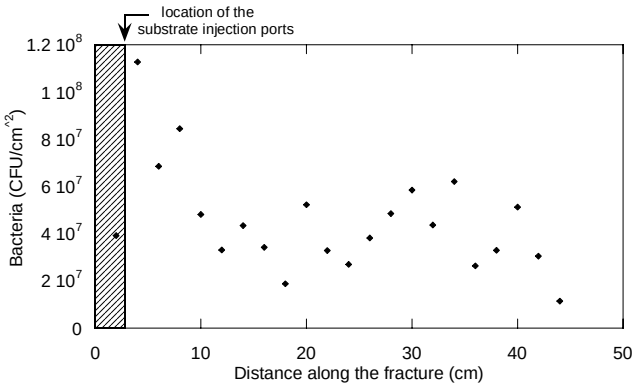

Figure 4. The spatial distribution of the attached viable bacteria along the fracture (Core #2).

The samples taken 5 cm from the inlet chamber were heavily colonized with respect to those taken farther from the fracture inlet. However, even within the samples taken close to the inlet, the distribution was very irregular, ranging from surfaces with no bacteria to heavily populated regions (5a and b). In some cases the bacteria formed 3-D structures interconnected with a dense mesh of extracellular polymeric substances (EPS) (Figure 5b). In Figure 5c, clear mushroom-like biofilm structures can be seen without EPS. In a number of cases, the procedure of fixation with glutaraldehyde has been shown to destroy or shrink the EPS (Vandevivere and Baveye, 1992); it is believed that EPS might be even more pronounced, and its absence in some photomicrographs.

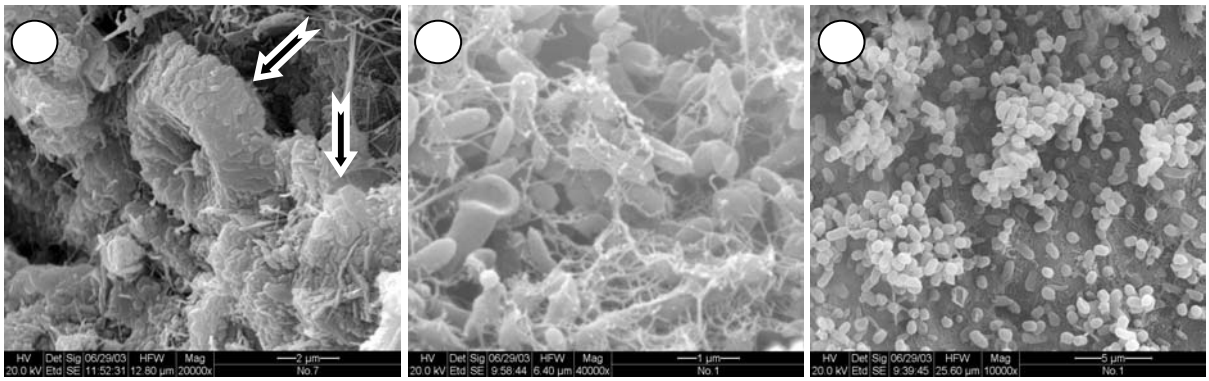

Figure 5. Scanning electron micrographs taken on samples from the fracture surface of core #2 at the end of the experiments. (a) Photomicrograph of a characteristic chalk sample (no bacteria). (b) and (c) Photomicrographs taken 5 cm from the inlet at the upper side of the fracture. The bars correspond to 2 μm, 5 μm and 1 μm for photomicrographs (a), (b), and (c), respectively.

In conclusion, microbial activity in the fracture was inferred by TBP removal and the consequent Br^- release. The outcome of this activity, biomass growth and accumulation, was shown to cause a significant change in the fracture transmissivity. During the experiments, the fracture transmissivity was reduced by as much as 97% ($T/T_0 = 0.03$) without any indication regarding leveling of the clogging rate (Figure 2). The transmissivity reduction was clearly related to the rate of TBP removal (Figure 2). Biological clogging of saturated subsurface environments can have many causes, such as physical clogging, EPS excretion, gas production, mineral precipitation and fluid density and viscosity changes. Evidence of intense microbial activity (Figure 3) and biomass accumulation with EPS excretion close to the inlet (Figures 4 and 5) suggests that physical clogging is responsible for the transmissivity reduction. Gas bubbles were excluded as a cause for transmissivity reduction, since they were not visible during the experiments. No change in the transmissivity in the control samples (Core #4 during *Phase 1* and Core #3, Days 590-620, during *Phase 2*) implies that mineral precipitation/dissolution was not taking place within the fracture. Finally, fluid density and viscosity changes could contribute to the transmissivity reduction, but in a much smaller amount than the physical clogging.

References

Avnimelech, Y. and Nevo, Z., 1964. Biological clogging of sands. Soil Sci. 98, 222-226.

Hill, D.D. and Sleep, B.E., 2002. Effects of biofilm growth on flow and transport through a glass parallel plate fracture. J. Contam. Hydrol. 56(3-4), 227-246.

Nativ, R. and Adar, E., 1997. Assessment of groundwater contamination in the Ramat-Hovav industrial complex. Report submitted to the Ramat-Hovav industrial council (in Hebrew).

Ross, N., Bickerton, G., Lesage, S., Deschenes, L., Samson, R. and Novakowski, K., 2003. Biobarriers in fractured bedrock: from laboratory concept to field demonstration, Second European Bioremediation conference, Chania, Crete, Greece, pp. 21-24.

Ross, N., Villemur, R., Deschenes, L. and Samson, R., 2001. Clogging of a limestone fracture by stimulating groundwater microbes. Water. Res. 35(8), 2029-2037.

Vandevivere, P. and Baveye, P., 1992. Saturated hydraulic conductivity reduction caused by aerobic bacteria in sand columns. Soil Sci. Soc. Am. J. 56(1), 1-13.

Session 4:
FIELD AND LABORATORY EXPERIMENTS

Evolution of Fracture Permeability

Stephen R. Brown, New England Research, Inc.
Ronald L. Bruhn, University of Utah
Harlan W. Stockman, Sandia National Laboratories
Katherine A. Ebel, New England Research, Inc.

Pore fluid flow and fluid composition within fractured rocks is a subject of primary importance to fields including hazardous waste isolation and remediation, oil and gas production, geothermal energy extraction, and formation of vein fillings and ore deposits. For these reasons, considerable effort has been placed on characterization and modeling flow in fractures and fracture systems. We are investigating the complex active chemical interaction between pore fluid and fractures that causes the fluid composition, permeability and topography of these systems to change over time.

We are constructing physical models and analyzing several configurations of flow and transport of chemically active fluids through single fractures and through fracture intersections. Our experimental model consists of $CaSO_4$ (Kerr Suprastone Green dental plaster) samples pressed against an inert textured reference surface (either textured glass or an epoxy cast of a rough surface). Experiments with either fixed-displacement or constant normal stress boundary conditions between the two contacting surfaces can be performed. Pore fluids ranging from unsaturated to supersaturated which are at a variety of flow rates are introduced to one end of the sample in order to actively alter the topography of the plaster surface. The topography of the textured surface induces heterogeneous flow along the plaster specimens.

The flow system is gravity-fed with a constant pressure head. Permeability changes are monitored either by collecting fluid on an electronic laboratory balance or by recording the differential pressure drop along a fixed-length capillary tube. We monitor the electrical conductivity of the outlet fluid as a proxy for calcium saturation, which is calibrated by selective sampling. We are able to photograph the state of the sample and flow system through the transparent reference surface. Using a laser profiler, we can quantify the changing surface topography over time as it relates to the measured sample permeability and calcium saturation of the pore fluid.

These methods allow us to create and analyze many features seen in natural fractures, including high-flow dissolution channels, plateaus, and caverns formed from precipitate. In addition, the laser scan of the sample surface can be used to produce a map of aperture across the sample. Using this information, we have applied numerical modeling via finite difference and lattice Boltzmann methods to calculate fluid flow direction and magnitude within the fracture.

We have found that when experimental parameters (initial surface topography, flow rate history, and total experiment time) are duplicated, the topography developed on the plaster sample is reproducible. Some of the initial contacts between the reference surface and the plaster develop into plateaus, which do not easily dissolve. These plateaus are at the nucleus of stagnant flow regions, which become more prominent as the experiment proceeds, leaving ever-deepening high flow channels between them. Thus the flow channel networks, as observed visually and through

numerical simulations, evolve from a homogeneous system to one more (self) organized and complex. The permeability initially drops as the experiment begins and the surfaces settle into place, then gradually rises with several further smaller decreases as some plateaus are destroyed.

In a parallel study at the University of Utah, we are investigating veins and drill core from the Awibenkok Geothermal Field (see Figure 1). Digital photography and image analysis data will be used as a guide for our physical modeling experimental design and data analysis.

We selected core intervals for direct inspection based on vein mineral type and geometry. Geometrical properties of interest included single veins, vein intersections, and veins containing alteration halos or selvages. Several fault-controlled veins were identified and also selected for sampling in addition to the more commonly occurring extensional veins. Digital images of the veins were collected using a flatbed scanner. Also, a digital camera under ultraviolet light was used to record details of vein geometry revealed by fluorescence of calcium carbonate minerals. Thin sections of some specimens were prepared. Rubber casts were also made of several vein walls to prepare samples for measuring wall roughness. We developed a procedure to partially automate measurements of vein thickness, area and roughness directly from the digital images.

We found that multi-phase mineralization due to chemical dissolution and re-precipitation as well as mechanical fracturing was a common feature in many of the veins and that it had a significant role for interpreting vein tortuosity and history of permeability. We used our micro- and macro-scale observations to construct four hypothetical permeability models. In each model, permeability changes, and in most cases fluctuates, differently over time as the tortuosity and aperture of veins are affected by the precipitation, dissolution, and re-precipitation of minerals, and also by mechanical fracturing. In each case we see a first-phase mineral dissolution stage where permeability gradually declines as the vein is blocked by inward growing minerals. Hereafter, permeability may briefly increase with the onset of internal fracturing within the vein or by a phase of mineral dissolution opening up new pathways for fluid flow. Eventually we infer that permeability will decline again as second stage minerals are deposited in the fluid flow pathways.

Our current experimental results are not readily comparable to these vein systems because the fluid interaction within veins is dominated by precipitation rather than dissolution. This results in a significantly different permeability history. We hope to emulate the natural veins in further experiments involving precipitation on the plaster samples.

In summary, the nature of fluid/rock chemical interaction within the fracture system is fundamental to determining the growth or loss of permeability. Flow channels are a common feature that strongly impact the developing permeability of a fracture network. In flow channels, the fluids and the solutes they contain (which can interact chemically with the wall rock) are in contact with smaller areas of the fracture surfaces and for less time than in uniform flow. We suggest that surface roughness and the consequent channeling of pore fluid direct chemical precipitation or dissolution of the matrix and are responsible for the accompanying fracture system permeability change. The integration of these mechanisms is the focus of our effort to understand the evolution of fracture geometry and permeability.

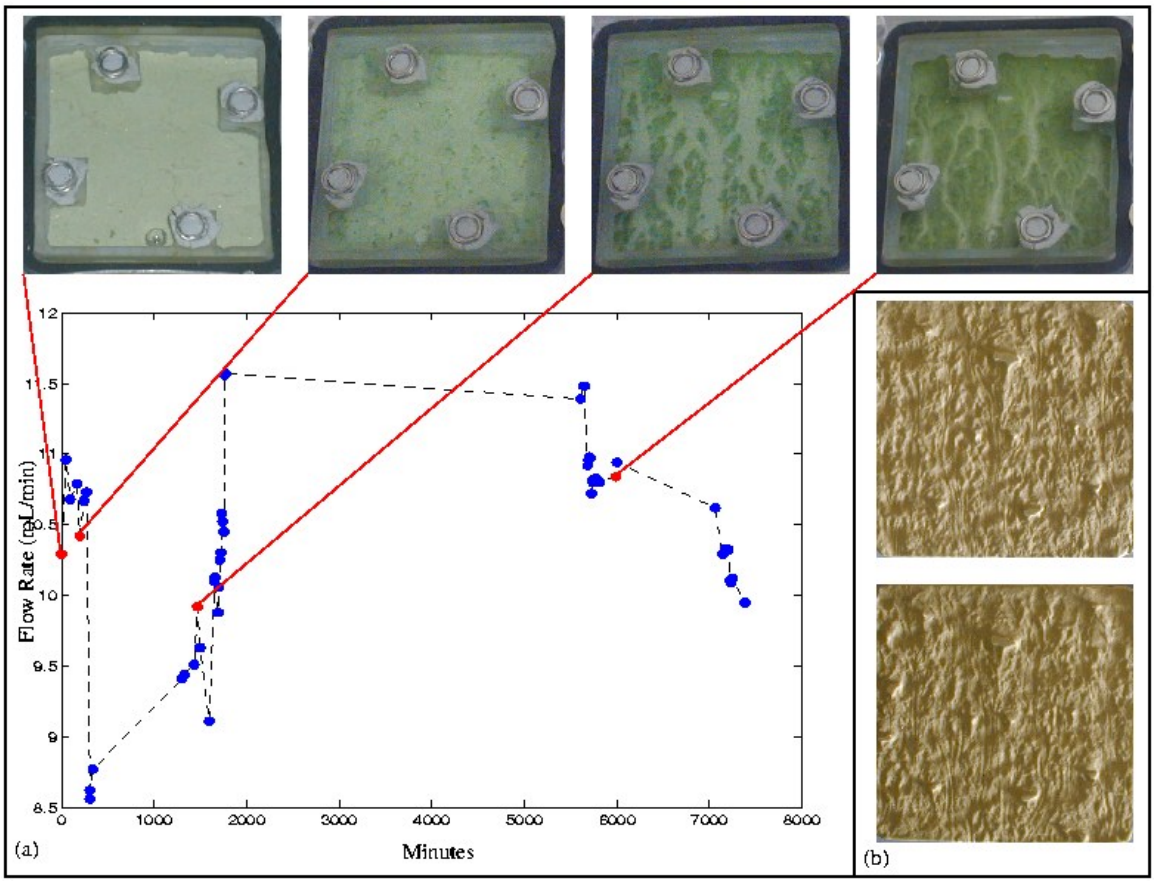

Figure 1: Results of a dissolution-dominated experiment. (a) Graph tracking the flow rate (permeability) of a sample over the course of an experiment. The photographs corresponding with points on the graph catalog the evolution of the high-flow channels (light colored regions) and stagnant zones around the topographic plateaus (dark colored regions). (b) Two plaster samples resulting at the termination of runs using the same experimental parameters. The plaster samples were initially smooth and flat. Note prominent dissolution features including plateaus and channels, as well as the overall reproducibility of the experiments.

Synchrotron-based Microtomography of Geologic Samples for Modeling Fluid Transport in Real Pore Space

Frieder Enzmann[1], Michael Kersten[1] & Marco Stampanoni[2]
[1]Geoscience Institute,University of Mainz, Becherweg 21, D-55099 Mainz, Germany
[2]SLS-PSI, Villingen, Switzerland

The goal of this paper is to present data illustrating that the X-ray tomographic microscopy (XTM at beamline MS-Tomo, SLS) is highly suitable to provide data for *ab initio* fluid simulations in real pore space at an appropriate voxel resolution.

Background

The pore space of geologic materials not only controls the hydrodynamic behavior of the porous material, but is also the site of many relevant chemical reactions involving element portioning between fluid and solid matrix. Even so, most (reactive) advective-dispersive transport models consider the pore space as a black box and try to fit its retarding behavior by gross parameters. However, *ab initio* simulations of fluid transport in real pore space can provide an insight into the complexity of hydrodynamic behavior on a micro-scale (Ferreol and Rothman 1995, Martys & Chen 1996).

Materials and Methods

The porous geologic samples used in this study were different specimens of typical sandstone from southwest Germany ("Pfälzer Buntsandstein"). Micro-borehole samples with diameters around 1.5 mm and different lengths (up to 15 mm) were prepared, both with and without epoxy resin filling. The porosity of the well-known sandstones has a wide range of 1–25% as a result of different geologic formation conditions.

Microtomography parameters set at MS-Tomo were 13.5 keV, rotation around the x-axis at (1,000 steps each) 3.5 s for Sample S1a and 2.2 s for Sample S1b. Sample S1b was generated in stack blocks with a thickness of 200 μm along the entire lengths of the sample. Sinograms were generated on the fly in a Linux-Cluster, together with back reconstruction into slices from the charge-coupled-device dump data.

Results

Figure 1 shows a reconstructed slice through sample S1a. The resolution of this example is 500 × 500 pixels of 1.7 μm. The CT-numbers are scaled in an 8-bit range (0–255 possible values). Figure 2 shows the impression for a stacked slices sequence.

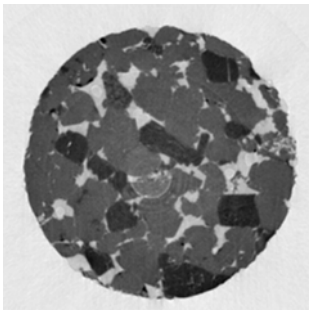

Figure 1. Reconstructed 2D slice through Sample S1a.

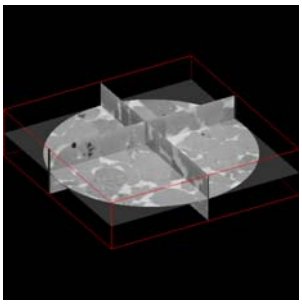

Figure 2. Sketch of a 3D sequence of slice planes of Sample S1a.

To identify the pore space ("Boolsches model"), the CT-numbers representing the pore voxels must be selected. In Figure 3, all CT numbers are displayed in a frequency scale. For each component in the voxel system (quartz, feldspar, resin, and air), a gaussian distribution of the CT numbers can be identified, and all CT numbers greater than 82 have been allocated to "pore" voxels.

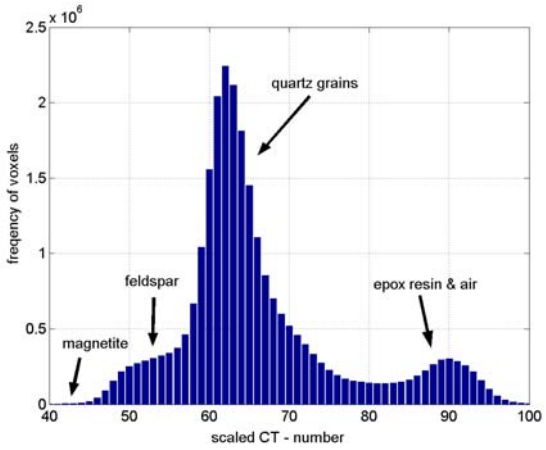

Figure 3. Distribution of scaled CT numbers for S1a.

With the pore identification process accomplished, the total pore space can now be displayed as isosurfaces (Figure 4). For *ab initio* simulations of a migration experiment, only the connected (open) pore structure between two potential boundaries is of interest. Given a digital image or tomogram of a porous material, one can easily access the connectivity of any phase using the so-called "burning algorithm" (Stauffer, 1975). This algorithm enables identification of all cluster members of connected voxels with equal or quasi-equal CT numbers in a tomogram.

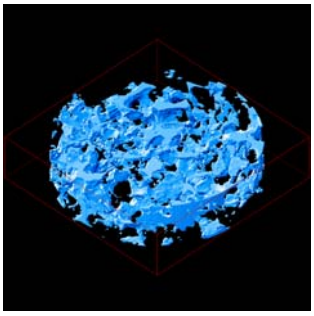

Figure 4. Reconstructed 3d total pore structure S1a.

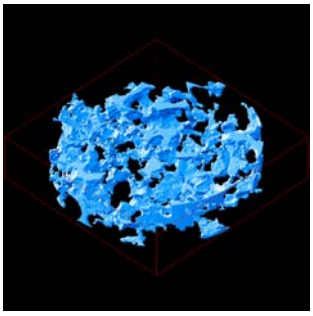

Figure 5. Reconstructed clustered pore structure S1a.

Figure 5 shows the clustered pore structure, and Figure 6 the open pore structure as potential fluid transport pathways from bottom to top in sample S1a.

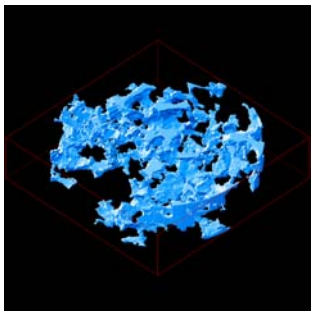

Figure 6. Constructed potential percolated pore structure, S1a.

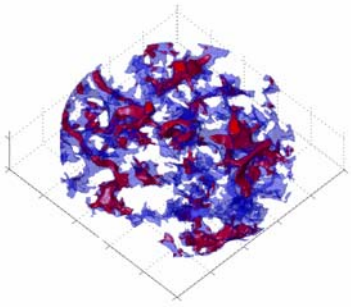

Figure 7. Isosurfaces simulating fluid velocity in percolated pore space, S1a.

For modeling the fluid flow, the lattice Boltzmann equation (LBE) method has been used, because it relies favorably on the real pore-space structure as a boundary condition input (Ferreol and Rothman, 1995). Our code "PoreFlow" uses a D3Q19 geometry (3-D cell spanned by 19 lattice vectors; Qian et al., 1992). The given formalism and special conditions (e.g., low numerical Mach and Knudson numbers) lead to a velocity field as a solution of the Navier-Stokes equation at a given kinematic viscosity (Marthys and Chen, 1996; Nourgaliev et al., 2003). A preliminary test run was performed with a stationary inflow boundary condition. The result is an inhomogeneous flow field in the connected pore structure, with variations of velocity values and directions leading to a dispersed transport of conservative tracer particles. The isosurfaces of a defined fluid velocity are shown in Figure 7. Note that this structure needs nearly 2,000,000 active nodes for the LBM simulations, which are currently the limit for our parallelized computer code on a 4-processor PC. Figures 8 and 9 show structures with nearly 25,000,000 active nodes for fluid calculations. An enhanced code is to be developed to process these data.

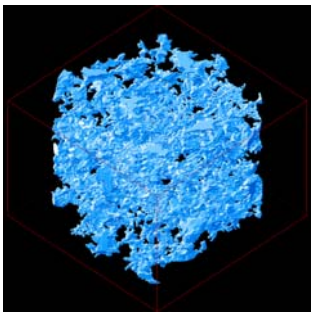

Figure 8. Constructed clustered pore space of Sample S1b.

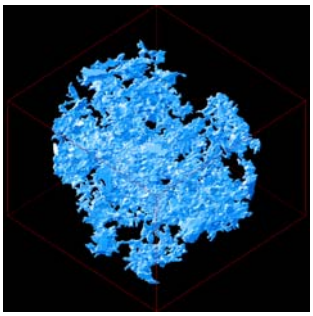

Figure 9. Constructed potential percolated pore structure of Sample S1b.

This elaborated open pore-structure data can be used for direct validation of the average hydro-dynamical parameters. Porosity, both absolute and specific surface, can be calculated directly from the structure. The permeability can be calculated using a relationship between porosity and specific surface (Carman, 1937). The only gross parameter that can be estimated by other techniques for porous materials is the pore size distribution, such as derived by mercury-porosimetry. Table 1 documents the data from Sample S1a, and Table 2 from Sample S1b. Note that this is the same sandstone with (a) and without (b) epoxy resin.

The parameters represent the typical range for sandstones. However, using the tomography data, we were able to show the heterogeneity of these parameters at a microscale; and, moreover, even some anisotropic dispersion effects along textural inhomogeneities. Figure 10 (for example) shows local enhanced porosity along the slice planes in the z-direction.

Table 1. Geometric characterization of sample S1a.

500×500×125 a 1.7 µm Voxels	**Total**	**Cluster**	**Percolate**
Porosity	11.80	11.49	10.06
Surface [m²]	4.003E-6	3.715E-6	3.208E-6
Specific Surface [m²/g]	1.455E-2	1.346E-2	1.143E-2
Permeability [mD]	360.0	386.2	347.7

Table 2. Geometric characterization of sample S1b.

700×700×500	Total	Cluster	Percolate
Porosity	9.27	7.95	6.08
Surface [m²]	3.074E-5	2.151E-5	1.555E-5
Specific Surface [m²/g]	1.361E-2	9.375E-3	6.634E-3
Permeability [mD]	188.3	233.2	187.4

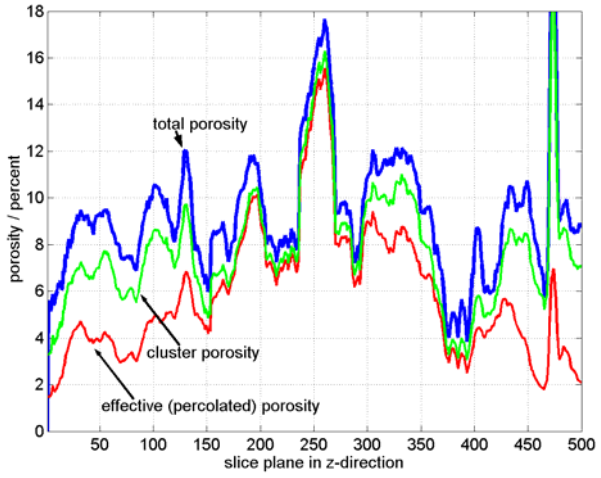

Figure 10. Distribution of local porosity through slice planes percolated from bottom to top of Sample S1b.

Future Requirements

The resolution of the samples S1a and S1b of 1.7 µm per voxel has never been reported for a geologic sample from XTM. However, it is still not yet sufficient, as demonstrated by Figure 11. The deviations between the open pore-size distribution derived from XTM (red curve) and from that derived by mercury porosimetry (blue curve) results mainly from the sample size for the latter method (ca. 1 cm³), which shows both open pore sizes down to 0.7 µm, and a secondary maximum pore sizenear 100 µm. For the XTM data to cover the full porosity field, we need to enhance both the resolution (down to the sub-µm size) and the sample volume (by appropriate stacking). However, the main limit is not the XTM technique but rather the computer capacity, which ultimately necessitates use of a linux cluster for both data reduction and modeling. We hope soon to have access to a 64-processor linux cluster.

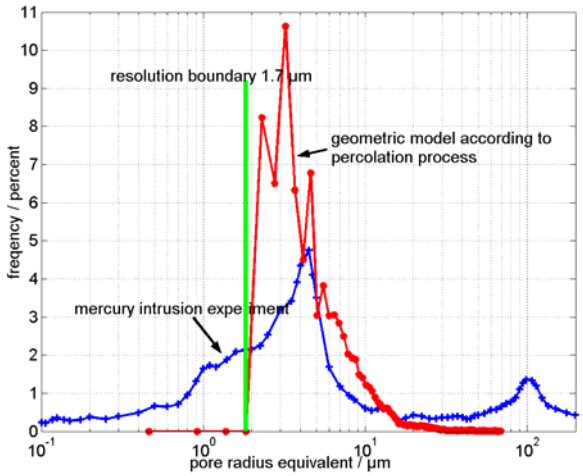

Figure 11. Comparison for pore-size distribution derived from mercury porosimetry data and from a percolation simulation run.

References

Ferreol B. and Rothman D.H. (1995): Lattice-Boltzmann simulations of flow through Fontainebleau sandstone. Trans. Porous Media 20, 3-20.

Carman P.C. (1937): Fluid flow through granular beds. Trans. Inst. Chem. Eng. 15, 150-166.

Martys N.S. and Chen H. (1996): Simulation of multicomponent fluids in complex three-dimensional geometries by the lattice Boltzmann method, Phys. Rev. E, 53,743-750.

Nourgaliev R.R., Dinh T.N., Theofanous T.G. and Joseph D. (2003): The lattice Boltzmann equation method: theoretical interpretation, numerics and implications. Int. J. Multiphase Flow 29, 117-169.

Qian Y.H., D'Humières D. and Lallemand P. (1992): Lattice BGK models for Navier-Stokes equation. Europhys. Lett. 17, 479-484.

Stauffer D. and Aharony A. (1992): Introduction to Percolation Theory, Taylor & Francis, London.Verberg R. and Ladd A.J.C. (2002): Simulations of erosion in rough fractures. Phys. Rev. E, 65:056311.

RIMAPS and Variogram Characterization of Water Flow Paths on a Fracture Surface

Néstor O. Fuentes[1] and Boris Faybishenko[2]
[1]Comisión Nacional de Energía Atómica. CAC- UA Materiales; Av. Del Libertador 8250, 1429–Buenos Aires.Argentina; Email: fuentes@cnea.gov.ar
[2]Lawrence Berkeley National Laboratory. Earth Sciences Division; 1 Cyclotron Road, MS 90-1116 - Berkeley, CA 94720. USA; Email: bfayb@lbl.gov

Introduction

An understanding of the flow geometry within a fracture is one of the key elements needed for the prediction of flow and transport in fractured rock, including fracture-matrix interaction, fracture permeability, trapping or removal of contaminants from fractures and the matrix, dripping frequency, flow instabilities, and chaos[1,2]. The chief limitation in studying dripping phenomena at the field scale is that the geometry and physics of flow along fracture surfaces cannot be identified or quantified using direct measurements. One of the approaches to studying flow processes in a fracture is to use laboratory experiments using fracture blocks or fracture models to simulate various water dripping rates and droplet sizes to better understand flow in unsaturated fractures. Laboratory experiments [3-7] have shown intermittent water flow and the pervasiveness of highly localized and extremely nonuniform intrafracture flow paths. Moreover, water channels undergo cycles of draining and filling, with small connecting threads snapping and reforming as time progresses. This sporadic behavior is sustained even under constant boundary conditions such as constant pressure or constant flowrate.[5-7]

Although deterministic models of flow (based on Richards' equation and Darcy's law) with stochastically distributed hydraulic properties can be used to describe the volume- and time-averaged characteristics of liquid flow,[8,9] these models are unable to reproduce the temporal behavior of intermittent and localized preferential flow.

Method

One of the approaches to understanding three-dimensional physical processes taking place on a fracture surface is the interpretation of irregular-shaped surface images obtained using photographic cameras, CCD cameras, and microscopes (optical and electronic). In this paper, we describe the interpretation of images characterizing the geometry of flow paths using a new RIMAPS (Rotated Image with Maximum Average Power Spectrum) technique.[10-12] RIMAPS is based on the digital acquisition and a 2-D Fourier transform (FT) analysis of information from rotating images (RI) of a rough surface. This technique has been developed to characterize the irregular topography of a rough surface from the videotaped images of flow in a fracture model. We also present the results from a verification of the RIMAS technique, comparing the predicted areal extent and directions of water channels, detected on the fracture model surface, with those determined from a water-injection experiment in a fracture model (rough glass plates) conducted at Berkeley Lab.[13]

The RIMAPS technique can be used to characterize the fracture surface topography, which is one of the main factors affecting intermittent water flow channeling along a fracture surface.

Results

Figure 1 shows two videotaped images of the water distribution at the fracture surface taken during the water injection experiment, which are superimposed onto the regions (thick line) predicted from the aperture distribution map using the RIMAS analysis. These images indicate that water flows through the fracture model in discrete channels, and flow paths undergo cycles of snapping and reforming. The photographs presented in the figure clearly demonstrate that the overall area involved in flow along the fracture surface is located within the red line area identified using the RIMAPS technique. It can further be seen from Figure 1 that the preferential flow fingers within the predicted flow region approximately coincide with the main directions of flow channels. Figure 1 shows that the directions of flow paths remained essentially the same with time.

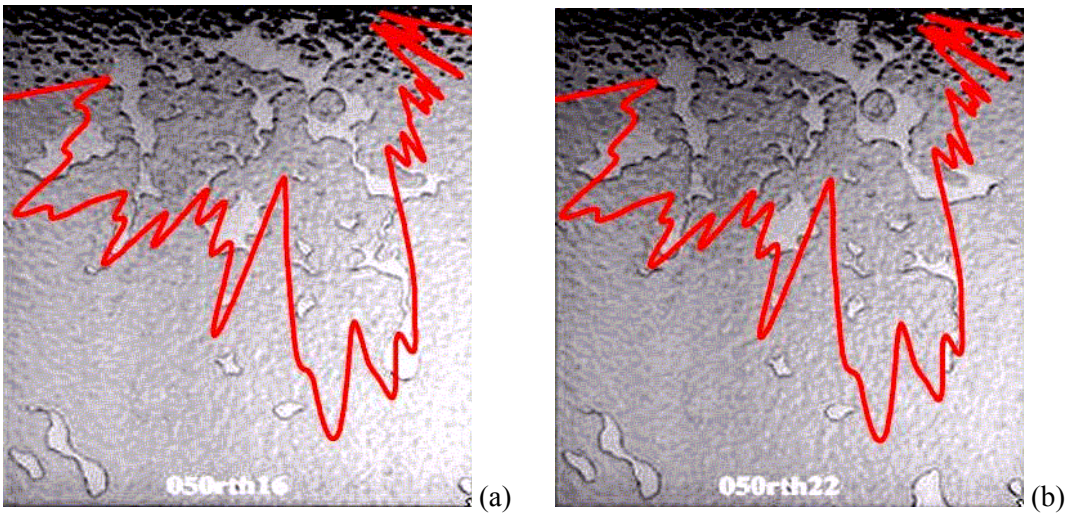

Figure 1. Evolution of regions of flow (red line) determined from the fracture image superimposed onto the photographs of flow distribution for two moments of time at the fracture surface from the laboratory experiment.

To obtain the different characteristic lengths that represent the fracture surface, the variogram method is used to characterize the fracture surface topography from the dry fracture aperture distribution and the distribution of water at the wetted surface videotaped during flow experiments. The analysis includes a log-log representation of the aperture distribution and the size of the wetted area versus the size of the sampled area. In the cases of the digitized images of the Berkeley Lab experiment, the mathematical variance (σ^2), which is related to the root-mean-square deviation of the size of the sampled area, is plotted against .the size of sampled area from the image analyzed. The results of the variogram analysis of images of the dry fracture surface aperture and the wetted surfaces (shown in Figure 1) are illustrated in Figure 2. The examination of Figure 2 shows that the variograms of a dry fracture aperture distribution and wet surfaces in the flow experiment are essentially identical.

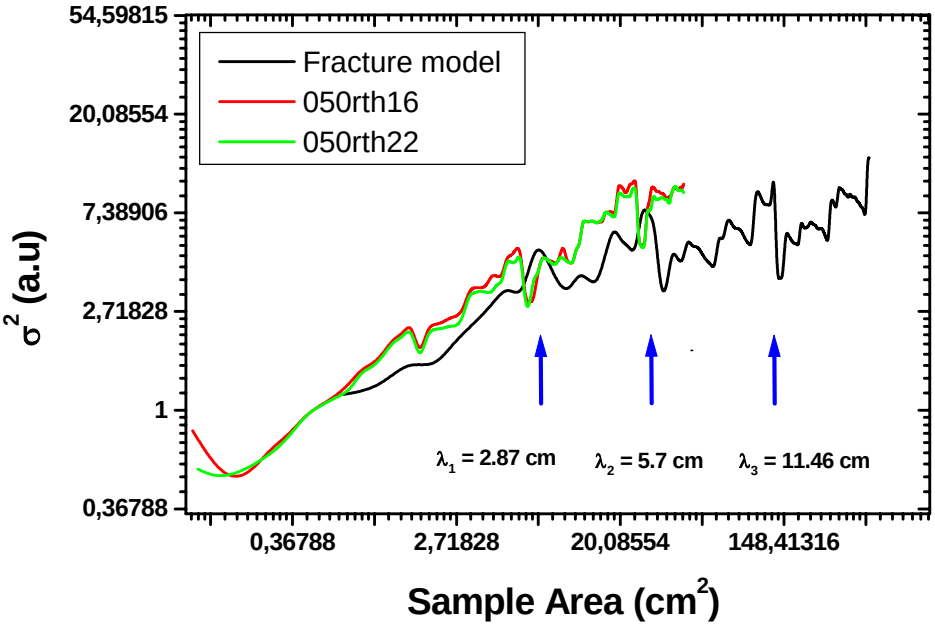

Figure 2. Variogram results indicating the existence of characteristic lengths for a dry fracture model surface and wetted surfaces (experiments 050rth16 and 050rth22, performed with the flow rate of 0.5 mL/hr) developed during fluid dripping evolution.

Results in Figure 2 indicate that the variogram method yields detailed information on length scale dependence of surface topography, which is not available from a classical roughness analysis. From the variogram of the fracture surface, we identified three main length scales characterizing the variable aperture fracture. These scales are related to each other as follows: $\lambda_3 = 2\lambda_2$, $\lambda_2 = 2\lambda_1$. The variogram analysis of digitized images of water dripping on the fracture surface also indicates the three scale lengths, which are described in terms of the water path length (λ_w) and are related to the topography scale according to the equation $\lambda_{w1}=\lambda_1/2$. These results are most likely related to the size of intermittent paths of dripping water.

Conclusions

The RIMAPS technique can be used to analyze digitized images of rough surfaces. It also provides the principal topographic characteristics of a fracture surface, which are extremely difficult, if not impossible, to obtain from a visual examination of surface images. Variogram results indicate the existence of three characteristic lengths, which are identical for a dry fracture surface aperture and wetted surfaces from the flow experiments developed during fluid dripping evolution.

Acknowledgments

This work is part of the project within the framework of the Agreement for Scientific and Technical Cooperation between the National Atomic Energy Commission of Argentina (CNEA) and the U.S. Department of Energy (DOE). In addition, we appreciate the review of the abstract and comments provided by Jil Geller of Lawrence Berkeley National Laboratory.

References

1. Podgorney, R., Wood, T.R, Faybishenko, B., and Stoops, T., "Spatial and temporal instabilities in water flow through variably saturated fractured basalt on a one-meter scale," in *Dynamics of Fluids in Fractured Rock*, edited by B. Faybishenko, P. A. Witherspoon and S. M. Benson, AGU Geophysical Monograph 122 (2000).
2. Faybishenko, B., Witherspoon, P. A., Doughty, C., Geller, J. T., Wood, T., and Podgorney, R., "Multi-scale investigations of liquid flow in a fractured basalt vadose zone," in *Flow and Transport in Fractured Rocks* , American Geophysical Union Monograph, T. J. Nicholson and D. D. Evans, eds. (2001).
3. Or, D. and Ghezzehei, T. A., "Dripping into subterranean cavities from unsaturated fractures under evaporative conditions," *Water Resour. Res*., Vol. 36, No. 2, pp. 381-393 (2000).
4. Nicholl, M. J., Wheatcraft, S. W., and Tyler, S. W., "Is Old Faithful a strange attractor?" *Journal of Geophysical Research*, Vol. 99, No. B3, pp. 4495-4503 (1994).
5. Persoff, P. and Pruess, K., "Two-phase flow visualization and relative permeability measurement in natural rough-walled rock fractures." *Water Resour. Res*., Vol. 31, No. 5, 1173-1186 (1995).
6. Su, G., Geller, J. T., Pruess, K. and Wen, F., "Experimental studies of water seepage and intermittent flow in unsaturated, rough-walled fractures." *Water Resour. Res.,* Vol. 35, No. 4, 1019-1037 (1999).
7. Geller, J. T., Holman, H-Y., Su, G., Conrad, M. S., Pruess, K., and Hunter-Cevera, J. C., "Flow dynamics and potential for biodegradation of organic contaminants in fractured rock vadose zone," *J. of Contam. Hydrol*., Vol. 43, No. 1, 63-90 (2000).
8. Pruess, K. and Tsang, Y. W., "On two-phase relative permeability and capillary pressure of rough-walled rock fractures," *Water Resour. Res.,* Vol. 26, No. 9, 1915-1926 (1990).
9. Pruess, K., "On water seepage and fast preferential flow in heterogeneous, unsaturated rock fractures," *J. of Contam. Hydrol*., Vol. 30, 333-362 (1998).
10. Fuentes, N. O., Favret, E. A., and Castillo Guerra, R. A., "RIMAPS technique: the fingerprint detection of surface damage," *Unique, Unusual and New Techniques in Microscopy*, Honorable Mention Award, (IMS/ASM). Indianapolis, Indiana. USA. (2001).
11. Fuentes, N. O., and Favret, E. A., "A New Surface Characterization Technique: RIMAPS (Rotated Image with Maximum Average Power Spectrum)," *Journal of Microscopy*. 206: 72-83 (2002).
12. Fuentes, N. O., and Favret, E. A., "Surface Characterization of Materials using the RIMAPS Technique," *Microscopy and Analysis*, 56: 5-7 (2002).
13. Geller, J. T., Borglin, S. E., and Faybishenko, B. A., "Experiments and evaluation of chaotic behavior of dripping water in fracture models." LBNL- 48394, Department of Energy under Contract no. DE-AC03-76SF00098 (2001).

Fracture Analysis of a VMS-Related Hydrothermal Cracking Horizon, Upper Bell River Complex, Matagami, Quebec: Application of Permeability Tensor Theory

S. E. Ioannou[1] and E. T. C. Spooner
Department of Geology, University of Toronto, 22 Russell Street,
Toronto, Ontario, Canada M5S 3B1; [1]Email: ioannou@geology.utoronto.ca

It has long been recognized that subvolcanic intrusions play a key role in the formation of volcanogenic massive sulfide (VMS) deposits. Not only do such intrusions provide the heat source necessary to drive large-scale hydrothermal convection, but it has also been suggested that they may contribute directly to a system's metal budget (e.g., de Ronde, 1995). Moreover, a temperature dependence on permeability has been recognized in the direct vicinity of magma chambers that can be envisioned as a hydrothermal cracking horizon (HCH) or zone.

First described by Lister (1974), and later analyzed and modeled in more detail by Cathles (1983, 1993), the HCH forms in rocks that are cooled during thermal contraction in a thermal boundary layer adjacent to the hot parts (>1,200^{o}C) of an intrusion. The HCH acts as a primary zone of enhanced permeability which allows significant volumes of convecting fluid to flow around the intrusion, acquiring heat (>350^{o}C) and dissolved components, including metals, before subsequently discharging through seafloor 'black smoker' vents.

Field observations support thermal cracking in and around well preserved intermediate and mafic intrusions (e.g., Manning and Bird, 1986; Shiffries and Skinner, 1987), in ophiolite settings (e.g., Nehlig and Juteau, 1988; Nehlig, 1994; van Everdingen, 1995; Gillis and Roberts, 1999), and in deep exposures of *in situ* oceanic crust (e.g., Gillis, 1995; Manning et al., 1996). However, despite documentation of thermal cracking in numerous geologic environments, little has been done to quantify the physical properties associated with this process. The following study investigates permeability limits that can be expected in an HCH. The values obtained are based on permeability tensor calculations made from field measurements collected in the Matagami VMS camp of Quebec (Sharp, 1965), a district that preserves clear evidence of hydrothermal cracking within its exposed subvolcanic intrusion, the Bell River Complex (BRC).

The BRC is a tholeiitic layered gabbroic/anorthositic body ($^{U\text{-}Pb}$2724.6 +2.5/-1.9 Ma) Mortensen, 1993) which acted as the heat 'engine' responsible for driving Archean VMS-related hydrothermal circulation in the area. Abundant fractures and veins crosscutting the western lobe of the BRC represent a spectrum of temperatures from 250^{o}C to 700^{o}C. The 250-400^{o}C assemblage quartz-epidote±sericite±chlorite±plagioclase is the most widespread and occurs as parallel, orthogonal, sinusoidal, and random vein sets (Figure 1). Vein densities average between 15 and 25 veins per m^2, locally reaching as high as 40-60+ veins per m^2. These veins, averaging 1-3 mm thick, are thought to represent thermal cracking and hydrothermal-fluid invasion during VMS deposit formation in the camp.

Figure 1. HCH quartz-epidote veining in the town of Matagami.

Detailed field measurements of quartz-epidote vein geometries from 83 sites (1,325 veins) together with permeability tensor theory have produced a first-order approximation of the maximum model permeability structure of the HCH. Representative district-wide values indicate maximum model bulk permeabilities of 10^{-10} to 10^{-8} m^2 for the HCH (Table 1). Furthermore, a high-flow zone located within the central parts of the HCH is characterized by a maximum model permeability of 10^{-7} m^2. On a localized scale (< 1 m^2), the high flow zone reaches maximum model permeability values as high as 10^{-6} to 10^{-5} m^2.

Table 1. Quartz-epidote vein two-dimensional permeability tensor results.[1]

Area	k_1 Log Magnitude (m^2)	k_1 Trend (^{o})	k_2 Log Magnitude (m^2)	k_2 Trend (^{o})
Matagami Town	-10.1 ± 2.4	004.2 ± 30.3	-7.5 ± 1.3	094.2 ± 30.3
(n = 71)	(-18.0:-8.0)	(000.1:178.4)	(-10.0:-5.0)	(028.3-150.0)
Cold Spring Rapids	-9.2 ± 0.8	106.4 ± 31.3	-8.4 ± 2.1	016.4 ± 31.3
(n = 5)	(-10.0:-8.0)	(079.7:152.2)	(-10.0:-5.0)	(001.1:173.6)
De Isles Rapids	-9.8 ± 0.5	101.4 ± 19.8	-9.0 ± 0.0	011.4 ± 19.8
(n = 4)	(-10.0:-9.0)	(087.2:130.2)	(-9.0:-9.0)	(008.8:179.6)

[1] Top number expresses the mean (± corresponds to 1σ); bracketed numbers express the range; n = the number of measurements.

The tensor calculation, described in detail by Oda (1985), is based on Darcy's law and considers a cubic flow region homogeneously cut by disc-shaped cracks of diameter *r* and aperture *t*. The orientation of each crack is defined by two parallel but of-opposite-direction unit vectors ***n*** that are normal to the major plane of the crack. The uncracked BRC is considered impermeable,

restricting fluid flow to the cracks. The resultant permeability tensor $k_{ij}^{(c)}$ for the crack system is defined as:

$$k_{ij}^{(c)} = \lambda(P_{kk}\delta_{ij} - P_{ij}) \quad (1)$$

where λ is a dimensionless constant = 1/12, δ_{ij} is the Kronecker delta and:

$$P_{ij} = \frac{\pi\rho}{4}\int_0^{t_{max}}\int_0^{r_{max}}\int_0^{\Omega} r^2 t^3 n_i n_j E(\boldsymbol{n},r,t)\,d\Omega\,dr\,dt \quad (2)$$

where ρ is the volume density of cracks, $E(\boldsymbol{n},r,t)$ is a probability density function to describe the directional distribution of crack surfaces, $d\Omega$ is the entire solid angle encompassing the crack orientations and:

$$P_{kk} = P_{11} + P_{22} + P_{33} \quad (3)$$

P_{ij}, defined by Oda (1985) as the crack tensor, is a symmetric second-rank tensor related exclusively to the crack geometry (length, aperture, orientation).

Tensor theory applied to field measurements is a proven method for modeling permeability accurately. For example, Oda et al. (1987) have compared numerically derived tensor data from measured active fractures/joints with field measurements obtained through large-scale hydraulic conductivity (Wilson et al., 1983) and packer injection (Gale and Rouleau, 1985) tests in granite from the Stripa Mine, Sweden (Witherspoon, 2000) and have found that the three different approaches yield the same (order of magnitude) results. The permeability magnitudes calculated for Matagami are in good agreement with *in situ* based measurements for fractured rocks (Brace, 1980) and field measurement based calculations done for other VMS-related fractured systems (Nehlig and Juteau, 1988; van Everdingen, 1995; 10^{-12} to 10^{-6} m^2). Hence, they appear to be reasonable maximum model permeabilities.

Mapping has shown that the HCH is confined to a ~350 m thick interval located within a strongly layered gabbro-anorthosite horizon of the Layered Zone, upper BRC. The base of this interval is 1,000 m below the top of the BRC (Figure 2). Furthermore, in and around the town of Matagami, the dominant orientation of quartz-epidote veins parallels the orientation of the layering (110 ± 15°). This parallelism is further reflected in the orientation of the calculated quartz-epidote vein two-dimensional permeability tensors [k_2 = 094.2 ± 30.3°; (1σ; n = 71); Figure 3). The parallelism suggests that heterogeneities associated with the layer contacts provided planes of low tensile strength along which the hydrothermal cracks preferentially developed. Such an interpretation further explains why the HCH appears to be restricted to the strongly layered zone; there are many more low tensile strength planes.

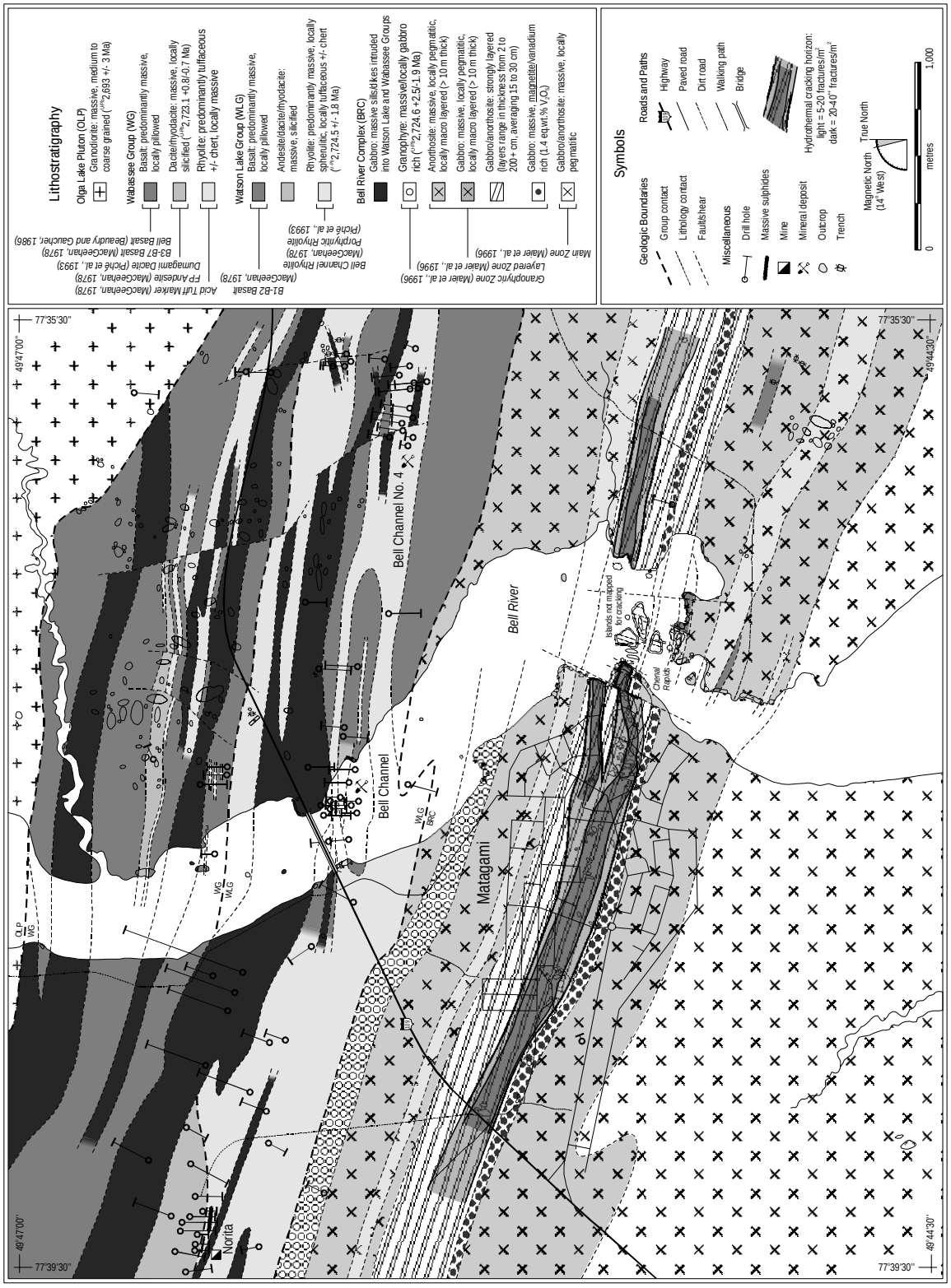

Figure 2. Geology, including the location of the HCH, in and around the town of Matagami, Quebec. Note that stratigraphy dips subvertically and youngs to the north.

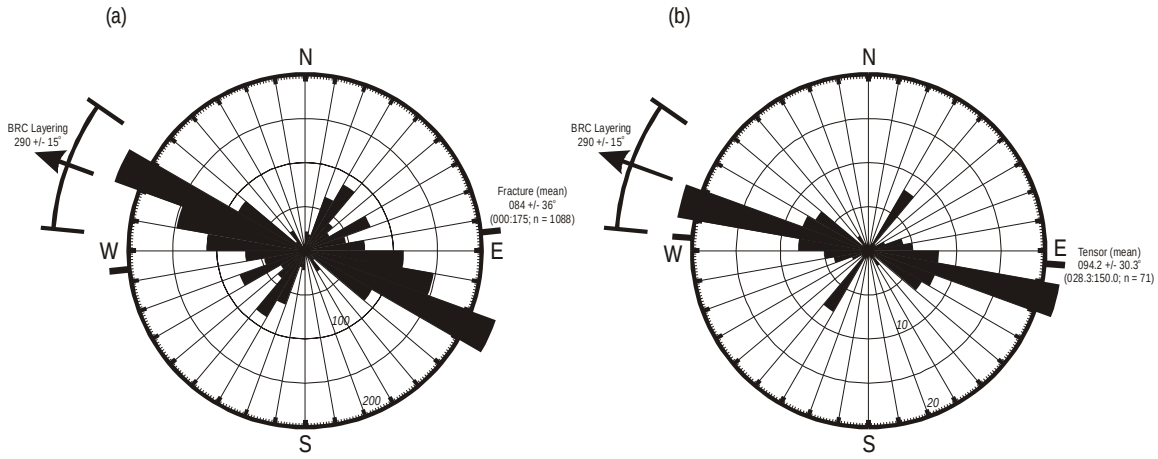

Figure 3. Two-dimensional fracture orientation (a) and permeability tensor orientation (b) rose diagrams for the town of Matagami.

Zones of quartz-epidote veining approximately orthogonal to layering are also present. The orthogonal veins are usually less continuous and commonly truncated (but not crosscut) by layer-parallel veins. The orthogonal subset of veins is interpreted to represent short pathways that allowed fluids to travel between adjacent layer-parallel veins. However, locally, longer layering orthogonal quartz-epidote veins may represent initial conduits that allowed fluids to travel into overlying stratigraphy and through to the original seafloor.

Acknowledgments

We would like to thank Grant Arnold and Noranda Inc. for their logistical support during the acquisition of field data from the Matagami camp. Dominic Bruscia's help during the collection of field measurements during summer, 2000 is greatly appreciated. Funding for this research was provided by NSERC (File 661-069-97 and a PGS-B scholarship), CAMIRO (Project 96E01), and the Ontario Government Graduate Scholarship (OGS and OGSST) program.

References

Cathles, L.M., 1993, A capless 350°C flow zone model to explain megaplumes, salinity variations, and high temperature veins in ridge axis hydrothermal systems: Economic Geology, v. 88, p. 1977-1988.

Oda, M., 1985, Permeability tensor for discontinuous rock masses: Géotechnique, v. 35, p. 483-495.

Sharpe, J.I., 1968, Geology and sulfide deposits of the Matagami area, Abitibi-East County: Quebec Department of Natural Resources, Geological Report 137, 122 p.

van Everdingen, D.A., 1995, Fracture characteristics of the sheeted dike complex, TroodoOphiolite, Cyprus; implications for permeability of oceanic crust: Journal of Geophysical Research, v. 100, p. 19,957-19,972.

Measuring and Analyzing Transient Changes in Fracture Aperture during Hydraulic Well Tests: Preliminary Results

L.C. Murdoch[1], T. Schweisinger[1], E. Svenson[1], L.Germanovich[2]*
[1]Department of Geological Sciences, Clemson University;
[2]Geosystems Engineering, Georgia Institute of Technology
**Email: lmurdoch@clemson.edu*

Fractures either dilate or contract in response to head changes during hydraulic well tests. Dropping the hydraulic head will increase effective stress, compressing asperities on fracture surfaces and causing apertures to diminish. Increasing hydraulic heads during an injection test, or during the recovery following pumping, will relieve the effective stress on asperities and dilate fracture apertures. Significant increases in head during injection into a well may cause the fracture walls to separate completely and no longer be supported by asperities. Continued injection may elevate the stress intensity enough to cause propagation and the creation of new fracture surface by hydraulic fracturing. Termination of injection will cause the fracture to close once again and rest on asperities (Rutqvist, 1995; NRC, 1996).

The qualitative behavior of fractures during a well test outlined above is widely recognized, but published field data describing transient changes in aperture is limited (e.g., Gale, 1975; Thompson and Kozak, 1991; Martin et al., 1990; Hesler et al., 1990). We are measuring the changes in aperture in an effort to increase the information obtained from hydraulic well tests. The measurements are made with a borehole extensometer that can be temporarily anchored to the walls of an open borehole. Current investigations have focused on isolated, flat-lying fractures, so axial displacements are assumed to equal changes in aperture. Field data are interpreted using a model that couples fluid flow and deformation of a flat-lying, circular fracture.

Equipment

The borehole extensometer was designed to be a robust tool that can be used routinely during short-term tests, but that will also remain stable during longer term tests. Related devices are described by Thompson and Kozak (1991), Hesler and others (1990), and Martin and others (1990). Remotely actuated, mechanical anchors that remain passively locked in place without requiring power were developed to promote long-term stability. The anchors can be deactivated to recover, or move the device. An LVDT is used to measure axial displacement between pairs of anchors, and those measurements are recorded along with pressure and temperature during a well test. The linear variable differential transducer (LVDT) can resolve displacements of approximately 0.1 micron, but accuracy appears to be several times greater than the resolution, on the order of 0.3 to 0.5 μm using the current device. Spacing between the anchors is currently 1.1 m.

Limiting sensitivity of the device to changes in temperature has been an important aspect of ensuring accuracy during transient tests. Rods connecting the anchors are made of invar, a material with an exceptionally low coefficient of thermal expansion. The LVDT itself exhibits small displacements during temperature changes, and this effect was considered in the design.

The device is configured so the thermal expansion of the LVDT is equal in magnitude and opposite in sign to the thermal expansion of the invar connector rods and anchors. The effective thermal expansion of the device is calculated to be less than 0.2 μm per ^{o}C.

Field Tests

Preliminary tests have made use of boreholes cutting fractures in biotite gneiss in western South Carolina. The wells are cased through saprolite to depths of approximately 21 m, and they are open to total depths of 60 m to 120 m. Fractures were identified on the walls of boreholes using a video camera, and those results were supplemented with caliper logs and data from slug tests using overlapping straddle packers. The packer tests indicate that three intervals a few meters thick, at depths of 26 m, 35 m, and 50 m, are several orders of magnitude more transmissive than elsewhere in the borehole. The video survey and correlation among neighboring wells indicates the presence of three, roughly flat-lying fractures or fracture zones at those depths. The borehole extensometer was deployed across intervals where significant fractures are evident, and across intervals that appear to be free of fractures. Constant-rate pumping tests followed by recovery were conducted and displacements, which are assumed to correspond to changes in aperture, were monitored along with changes in pressure and temperature. The initial suite of tests was conducted by pumping from open boreholes while measuring displacements at selected depths.

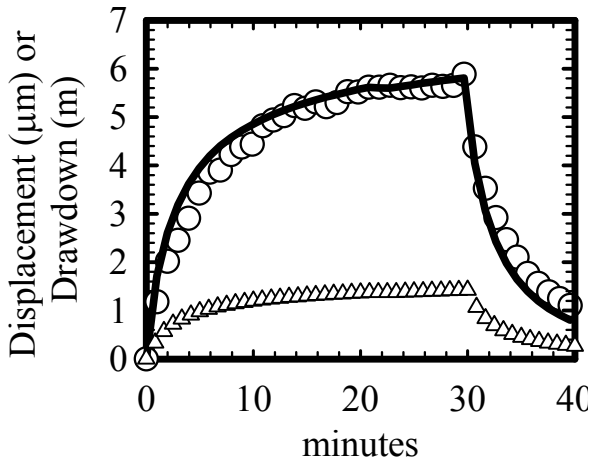

Figure 1. Observed displacement (circle) and drawdown (triangle) during constant rate pumping test. Heavy line is the displacement predicted using parameters determined by IFFCO.

The results show that displacements accompany changes in hydraulic head during and following pumping tests. Displacements of up to 10 microns were observed accompanying drawdowns of up to several meters, and in general the displacement as a function of time resembles drawdown (Figure 1). The ratio of displacement to drawdown is assumed to be equivalent to an effective normal compliance of the fracture (inverse of normal stiffness). The current results show that the normal compliance ranges from 5 μm/(m of drawdown) to less than 0.5 μm/m. Similar compliance values were measured in the field by Martin and others (1990).

Normal compliance can be used to estimate an effective uniaxial specific storage, suggesting that

this approach could measure storativity using data from a single well. Dividing the compliance by the spacing between the anchors and converting to pressure gives the specific storage (assuming the displacement causes an equivalent change in fluid storage volume per unit area). The current results give values for specific storage ranging from 0.5×10^{-4} $MPa^{-1}$to 5×10^{-4} MPa^{-1}. These results are consistent with Schwartz and Zhang (2003), who give a range of 3×10^{-4} MPa^{-1} to 7×10^{-4} MPa^{-1} for the specific storage of fractured rock, and they claim that the specific storage of intact rock is less than 3×10^{-4} MPa^{-1}. It is possible to use the borehole extensometer to determine specific storage as a function of depth. Integrating these values along the length of the bore could provide a means for estimating aquifer storativity using data from a pumping well alone.

Model

Transient changes of aperture and head during well tests are being analyzed using a model that considers fluid flow along a flat-lying, circular deformable fracture embedded in a porous material. The fracture is assumed to be initially supported by asperities, but the fracture walls can separate and the fracture can even propagate if the driving pressure becomes high enough. The model treats the fracture as a circular cavity embedded in an elastic medium and loaded by an arbitrary, axisymmetric pressure. This approach is attractive because the displacements can be determined quickly by superimposing analytical solutions. The model uses a new analytical solution to the displacements caused by a uniform pressure applied over a narrow ring for this purpose. The effect of propping by asperities is included by assuming the fracture is partly supported by an effective stress, in addition to the fluid pressure. The effective stress distribution is assumed to occur so that the aperture determined by the elastic cavity solution is equal to the aperture determined using a hyperbolic model of displacements similar to Goodman (1976) and Bandis et al. (1983). Fluid flow through the fracture and 2D partially saturated flow in the matrix are fully coupled to the displacements.

The model has been used with parameter estimation schemes with acceptable results. PEST and an implicit-filtering algorithm called IFFCO (Choi et al., 2001) have been used to calibrate the model to displacement data obtained during constant-rate pumping tests. The parameter estimation techniques are capable of fitting data as in Figure 1 using 40 to 60 model runs (Figure 1). This takes roughly an hour on a desktop computer using reasonable grids and time discretization. The results of this effort indicate that it is feasible to include transient displacement data in a parameter estimation analysis, just as transient drawdown data are used in conventional analyses of well tests.

The model also predicts that changes in fracture aperture could cause significant errors during well tests where pressure changes are relatively large. Changes in head of tens of meters could result in changes in fracture aperture of tens of microns or more, for example. This could markedly change the apparent transmissivity of a fracture and cause significant errors where tests are intended to determine transmissivity under ambient conditions. Including measurements of aperture change during a well test provides a mechanism for avoiding this potential problem.

Conclusions

Axial displacements of a borehole are roughly proportional to drawdown during transient wells tests and appear to be due to changes in fracture aperture. Observations in a borehole in biotite

gneiss give normal compliance values that vary from 0.5 μm/(m of drawdown) to 5 μm/m. Larger values of compliance occur where flat-lying fractures cut the well and smaller values are in relatively unfractured intervals. Compliance values can be used to estimate specific storage, and specific storages obtained using this approach are typical of fractured rock. A theoretical analysis of a deformable fracture has been developed to simulate the well tests and predict aperture changes. The analyses can be inverted to predict in situ hydromechanical properties of fractures.

Both the theoretical and field results suggest that the aperture, and therefore the transmissivity, of a fractured aquifer will change with pressure. Well tests that make use of large changes in pressure (to induce flow in tight rocks, for example) may significantly change the transmissivity of the fractures they are seeking to measure. Measuring changes in aperture is one approach to addressing this potential problem.

Acknowledgments

We appreciate the support from NSF grant EAR0001146.

References

Bandis, S.C., A.C. Lumsden, and N.R. Barton. 1983. Fundamentals of rock joint deformation. Int. J. Rock Mech. Min. Sci. and Geomech. Abstr. v. 20, no. 6. p 249-268.

Choi, T.D., O.J. Eslinger, P.A. Gilmore., C.T. Kelley, H.A. Patrick. 2001. User's Guide to IFFCO. http://www4.ncsu.edu/~ctk/iffco.html.

Gale, J.E. 1975. A Numerical, Field and Laboratory Study of Flow in Rocks with Deformable Fractures. Ph.D. thesis, University of California, Berkeley, 255 p.

Goodman, R.E. 1976. Method of Geological Engineering in Discontinuous Rock. West Publishing. New York. 472 p.

Hesler, G.J., Z. Zheng, and L.R. Meyer. 1990. In-situ fracture stiffness determination. Rock mechanics contributions and challenges. Hustrulid and Johnson, eds. Balkema, Rotterdam. 405- 411.

Martin, C.D., C.C. Davison, and E.T. Kozak. 1990. Characterizing normal stiffness and hydraulic conductivity of a major shear zone in granite. Rock Joints. Barton and Stephansson, eds. Balkema, Rotterdam, 549-556.

Raghaven, R., J.D. Scorer, and F.G. Miller. 1972. An investigation by numerical methods of the effects of pressure-dependent rock and fluid properties on well flow tests. Soc Pet. Eng. Jour. 12: 267-275.

National Research Council. 1996. Rock Fractures and Fluid Flow. National Academy Press, 551 p.

Rutqvist, J. 1995. Coupled Stress-flow Properties of Rock Joints from Hydraulic Field Testing. Ph.D. Thesis. Swedish Royal Institute of Technology.

Schwartz, F.W. and H. Zhang. 2003. Fundamentals of Ground Water. John Wiley, New York. 583 p.

Thompson, P.M. and E.T. Kozak. 1991. In situ measurement of coupled hydraulic pressure/fracture dilation in stiff crystalline rock. Field Measurements in Geotechnics, Balkema, Rotterdam, 23-31.

Laboratory and Numerical Evaluation of Borehole Methods for Subsurface Horizontal Flow Characterization

William H. Pedler (RAS Integrated Subsurface Evaluation, 311 Rock Avenue, Golden, CO 80401 PedlerRAS@aol.com)
Richard Jepsen (Sandia National Laboratory, rajepse@sandia.gov)
Wayne Mandell (U.S. Army Environmental Center, wayne.mandell@us.army.mil)

Introduction

This study is the third phase of a multi-year evaluation and comparison of horizontal flow measurements in the fractured and karst setting. The first phase involved a comparison of four different techniques in two karst settings with the results summarized by Wilson, et al., 1999. The conclusions of this report were that the particle tracking type measurements (fixed focal point colloidal borescope and acoustic Doppler flow meter) had a wide range of results, were not comparable with each other, not repeatable and varied considerably over short vertical distances. The hydrophysical logging (HPL) method continued to display its superior capability in identifying horizontal flow intervals and had comparable velocity results with the KV heat dilution device. Based on these results, and the discovery of the Scanning Colloidal borescope developed at Lawrence Livermore National Laboratory, Phase II of this study was a focused field application of the HPL and SCBFM at Camp Crowder in Missouri. Unlike the fixed focal point colloidal borescope deployed during phase one, the SCBFM can scan through a 500mm interval. This was the first application of the SCBFM in the fractured karst environment and proved very enlightening. By using HPL to locate the horizontal flow areas and then deploying the SCBFM, it was discovered that the horizontal flowing intervals were very thin (4-5cm) and of high velocity and consistent direction. Another important discovery was the identification of swirling intervals above and below the identified fast pathway. These swirling cells were highly variable in direction and velocity, and sometimes consistently flowing at 180 degrees from the identified fast pathway. These discoveries put the Phase I data into context for the first time. The importance of resolving the flow over an interval, as opposed to a fixed point, becomes paramount to accurately evaluating horizontal flow in a borehole in the fractured regime.

After the success of Phase II, when the combined approach of HPL and the SCBFM was determined to accurately find and characterize horizontally flowing features, the question arose regarding how representative horizontal flow in a wellbore was to the surrounding fractured system. This is a complex issue and begs the longstanding question; "How representative is *anything* in the borehole to the system as a whole?"

As such, this phase of the study looked at a simple fracture, set in a known and controllable horizontal flowing environment, to simulate flow behavior in both a numerical and laboratory setting. In addition, the effect of the scanning borescope itself on the flow field was numerically modeled for several flow conditions and simple fracture geometries.

Laboratory Simulator Experimental Setup

Laboratory Simulator: Based on the work of Drost (1967) and others, a laboratory scale horizontal flow chamber was constructed. The objective of this chamber was to create a stable

horizontal flowing condition in a porous medium. The dimensions of the simulator were 3 ft wide by 4 ft deep by 7 ft long. Two six inch reservoirs were located at each end such that the overall length was 8 feet, and such that water could be circulated in both directions through the chamber at a known flow rate with an associated observable horizontal gradient.

Once the flow simulator was constructed and filled with sand, the actual permeability of the flow simulator was calculated to be 2.1E-9 m^2. The sand was a well-rounded, well-sorted coarse sand (8/16 type) with a bulk porosity of 34.5 %. The permeability for this sand type is reported to be between 1.0E-9 and 1.0E-10 m^2 (Bear et al., 1968). The actual hydraulic conductivity was determined s 2.06E-2 m/s.

Well Simulation: To simulate a simple horizontal fracture regime, two slots were cut in a 4-inch acrylic tube that was installed in the center of the flow chamber. These slots were 1.5 millimeter wide and diametrically opposed to each other with a 90 degree cut out on each side. The openings were oriented perpendicular to the long axis (flowing direction) of the simulator. This was designed to simulate a simple horizontal fracture with a partial (50%) opening.

Four re-circulating rates were employed during horizontal flowing simulations and corresponded to similar flow rates used for the numerical modeling. The scanning colloidal borescope and the advanced hydrophysical tool were deployed during these pumping rates.

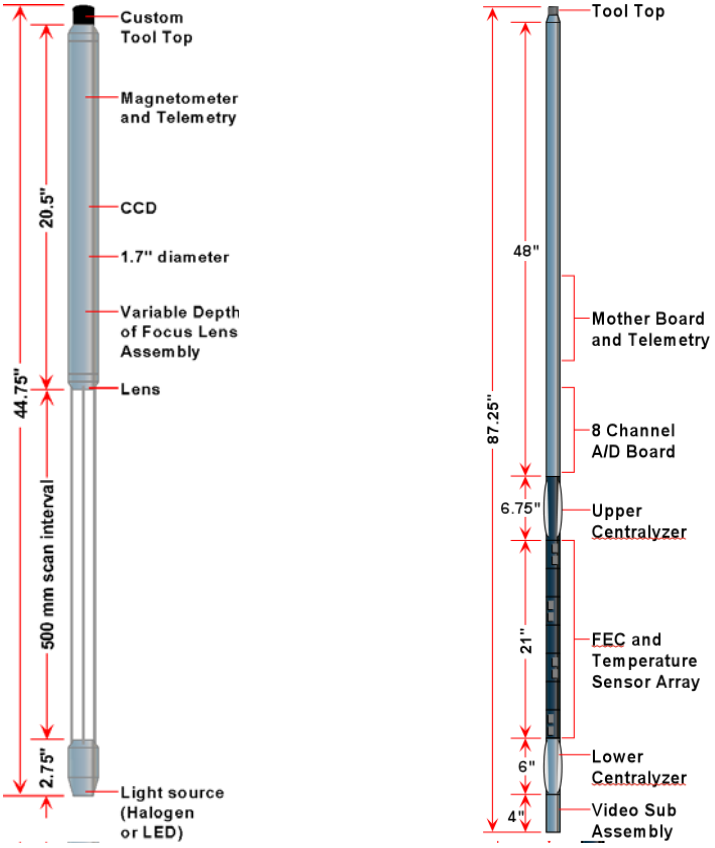

Figure 1. Schematic of RAS multi-sensor HPL tool with optional video subassembly (right) and Scanning Colloidal Borescope Flow Meter (left).

Hydrophysical Logging: RAS's proprietary advanced hydrophysical logging method (NxHpL™) (Pedler and Urish, 1988, Pedler et al. 1990, 1992, 1993, Tsang, et al, 1990 and Anderson, et al., 1993) is based on replacing the fluid column in a wellbore with deionized water and then profiling the induced changes in the electrical properties of the emplaced fluid column. The electrical properties are profiled as a function of time with a proprietary, high-resolution fluid electrical conductivity (FEC) and temperature tool. RAS's multi-sensor tool employs up to eight FEC and temperature sensors in a variety of configurations. For the project in the horizontal flow simulator, RAS employed a four-sensor array, with the sensors vertically spaced six inches apart and rotated horizontally at ninety degrees.

Scanning Colloidal Borescope Flow Meter (SCBFM): Figure 1 is used to evaluate horizontal groundwater flow direction and velocity. The SCBFM employs a CCD, magnetometer, light source and a remotely controlled, variable focal point lens mechanism to track colloidal sized particles (1-5 μm).

Naturally occurring colloids move advectively with the native groundwater system. By recording the output of the CCD and using advanced particle-tracking computer software, the compass direction and advective velocity of horizontal groundwater flow in a well can be evaluated. The scanning feature allows a 500mm interval to be evaluated, as opposed to a single fixed point. This scanning feature allows for a three dimensional evaluation such that swirling, non-representative flow cells can be identified and more importantly, "fast pathways" can be detected and characterized. The SCBFM was originally conceived and developed by Lawrence Livermore National Laboratory (LLNL).

Results of SCBFM and Hydrophysical Logging

The SCBFM was deployed during 0, 0.4, 1.0, and 2.5 gpm flow tests. The SCBFM was also applied during the 4.0 gpm flow test, but the in-hole velocity, estimated at over 5000μm/sec, exceeded the capability of SCBFM's present software. This is a software limitation and not an inherent limitation.

Hydrophysical logging was conducted at flow rates similar to those for the SCBFM and under similar, and previously described, procedures.

A summary of the average flow velocity measured by the SCBFM and NxHpL™ results is presented below in Table 1.

Table 1. Summary of Hydrophysical Logging and SCBFM Results.

	Hydrophysical Logging				SCBFM
	Integral Analysis		Dilution Analysis		Velocity at borehole center (μm/sec)
Pumping Rate (gpm)	Flowrate (gpm)[1]	Inlet Fracture Velocity (μm/sec)	Flow velocity (ft/day)[2]	Inlet Fracture Velocity (μm/sec)[3]	
0.4	0.003	1,590	2.66	9.50	55
1.0					110
1.3	0.005	2,647	6.04	21.6	
2.5	0.008	4,235	7.47	26.7	1600
4.0	0.010	5,294	13.04	46.6	

[1]Flowrate based on integral method of analysis.
[2]Flow velocity based on dilution analysis.
[3]Calculated on 3.57 μm/sec = 1 ft/day.

Numerical Simulator—Computer Modeling

Modeling studies were performed for all geometries and flow conditions used in the laboratory flow simulator experiments. The numerical models were generated using Adaptive Research's Stormflow computational fluid dynamic software to simulate flow fields subject to specified initial and boundary conditions.

Numerical computations were done for three basic purposes: (1) to determine appropriate design for flow simulator dimensions; (2) to determine the inlet velocity at the fracture into the open well from the porous media; (3) to determine the flow conditions inside the well with the borescope; and (4) to evaluate the effect the SCBFM had on the horizontal flow.

Prior to construction, the RAS flow simulator was modeled to investigate the effects of the well and the sidewalls on the flow field. This was done using a porous media in the flow simulator with a permeability of 2.1E-9 m^2.

The results demonstrate that the effects on the flow field due to the well obstruction and sidewalls are very local. The effects of the well obstruction are not seen beyond 15 cm of the well. Thus, the flow simulator has sufficient dimensions for the tests to be performed. In addition, a smaller model geometry and grid size can be used to determine the inlet velocity into the fractured well from the flow conditions in the flow simulator.

The model results for the Inlet Velocity for Fractured Well showed that the well does not affect the flow field beyond 15 cm from the well boundary. Therefore, the geometry was reduced to this size and the grid cells were significantly reduced for the computations involving the velocity of the inlet fracture in the well. The grid used in the well interior has 16 cells in the x-direction in order to gain a fine resolution near the inlet. Since the fracture is 1.5 mm in the y-direction, only three cells were used in the fracture region.

Results from the numerical model showed that flow was symmetric about the center of the well in the z-direction. Therefore, only four cells were monitored and recorded for the inlet velocity. Since the fractured well provides a preferential pathway with respect to the porous media, flow accelerates towards the fracture in the porous media near the well. Table 2 shows the results for

flow conditions in the porous media away from the effects of the fractured well and the increased velocity at the inlet for the range of flow rates used in the flow simulator. In addition, Table 2 presents the effect of the preferential pathway through the fracture and the increased velocity at the inlet compared to that found far away from the fracture at the center of the wellbore.

Table 2. Flow through the porous media outside of the effects of the well and fracture inlet velocities for various pump rates.

Pump Rate (gpm)	Darcy Velocity (μm/s) (porous media)		Linear Advective Velocity[1] (μm/sec) (porous media)		Average Fracture Inlet Velocity (μm/sec) for cells 10,19,8 / 10,10,9 / 11,10,8 / 11,10,9
	model	drawdown	model	drawdown	
0.4	3.1E+1	2.95E+0	8.99E+01	8.55E+0	2.1E+3
1.0	7.7E+1		2.23E+02		4.7E+3
1.3	1.15E+2	5.89E+0	3.33E+02	1.71E+1	7.0E+3
2.6	1.9E+2	1.06E+1	5.51E+02	3.07E+1	1.0E+4
4.0	3.1E+2	2.52E+2	8.99E+02	7.30E+2	1.65E+4

Scanning Colloidal Borescope Flow Meter (SCBFM) in Fractured Well

The inlet velocities calculated above (Table 2) are the input for the inlet conditions of the model used for the interior of the well. This includes the Scanning Colloidal Borescope placed in the well such that the center of the viewing range of the borescope is located at the fracture horizon.

This model was run five times for each inlet condition calculated above. An example of these results are shown in Figure 2 . The results show that for the lowest flow rate (0.4 gpm), the inlet velocity dissipates quickly in the open hole and there is little effect of the velocity from the fracture inlet on the flow in the well. In the center of the well, where the SCBFM measures velocity and direction, the velocity is approximately 100 μm/s in the x-direction. This is more than two orders of magnitude slower than the velocity at the fracture inlet. However, at the highest flow rate (4.0 gpm), the effects of the fracture inlet pass well through the center of the well and the velocity in the center is approximately 5000 μm/s. This is only three times slower than the fracture inlet velocity. For the given conditions, the fracture inlet appears to have the greatest impact on the center of the well at pump rates at or above 1.5 gpm in the flow simulator. Slower flow rates and associated inlet velocities dissipate in the open hole and their effects at the center of the hole are minimal.

In addition, the model shows that the scanning borescope itself is not interfering with the flow field. This can be seen in Figure 2 for the 3-¼ inch diameter light source. Figure 2 shows that the flow from the fracture inlet dissipates into vertical circulation cells without reaching the housing for the borescope sensor (top) and light source (bottom). The tops of the circulation cells where the flow reverses direction across the center of the well are approximately 15 cm

[1] Linear Advective Velocity = *Sd/porosity.*

above and below the centerline. This would suggest that when the SCBFM is deployed in a real borehole in a fractured environment, the depth of the tool should be adjusted such that the flow interval of interest is kept 150 mm from the top and bottom of the scanned interval.

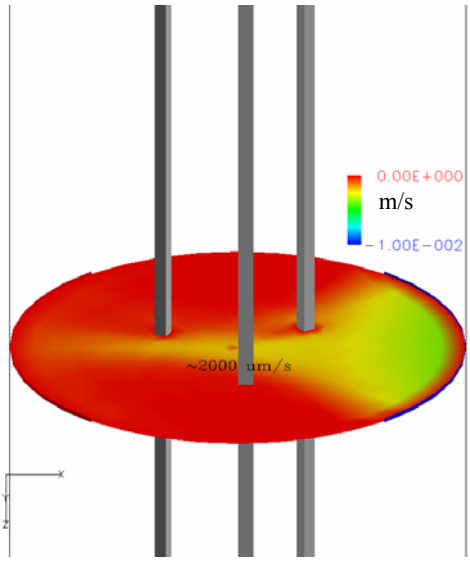

Figure 2. Example of velocity distribution across simple horizontal fracture at 1.5 gpm pumping rate. The color scale is for velocity in the x-direction in m/s. The fracture inlet is on the right and flow is from right to left. Support rods (3) for the SCBFM are shown through the center. The camera is above and light source is below the fracture horizon.

Other Fracture Configurations

Two additional modeling tests were performed to investigate the width of the fracture. The fracture height of 1.5 mm was kept the same and the width was changed to 10 degrees and 180 degrees from the previous tests of 90 degrees. These configurations could be representative of a parallel plate model equivalent fracture (180 degrees) and a channel-type equivalent fracture (10 degrees). Results are shown in Figure 3 for an inlet velocity of 2E-3 m/s. Results show that the velocity at the center is similar for the 180 and 90-degree case. However, for the 10-degree case, the effects of the inlet are very local to the location of the fracture. A significant inlet velocity would have to be used to generate a velocity at the well center for the 10-degree fracture width.

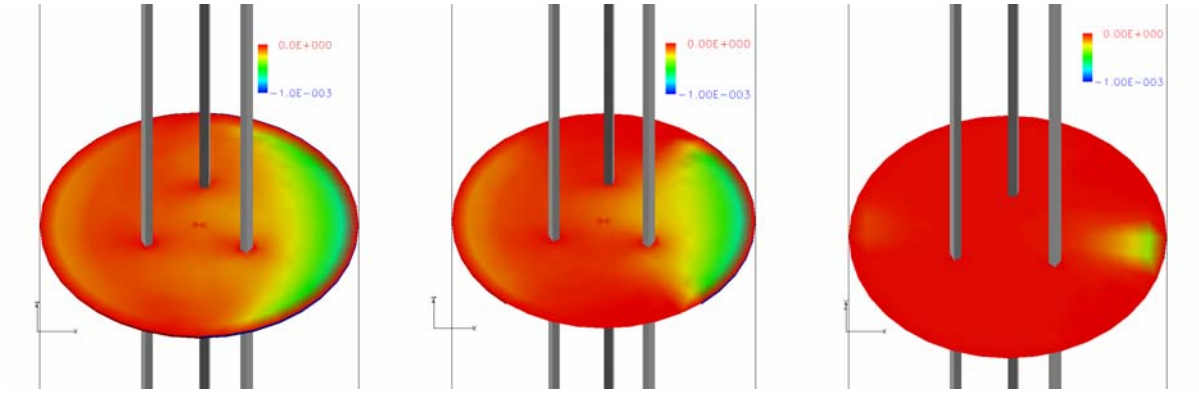

Figure 3. Model results for 180, 90, and 10-degree fracture widths. Color scale is for velocity (m/s) in the x-direction. *Note the color scale is different from that shown in Figure 2.*

Comparisons of Model and Experimental Results

Both the hydrophysics and SCBFM measurements allow for comparisons to modeling results. The hydrophysics comparison is primarily for the results regarding the fracture velocity and the SCBFM comparison is for the velocity at the center of the well.

Fracture Inlet Velocity

The hydrophysical measurements allow for an estimate of the total flow rate through the well. Since the flow in and out of the well was confined to the 1.5 mm inlet and outlet fractures, a velocity at the fracture could be calculated (Section 3.2). The model calculated an inlet velocity from the method described in Section 4.2. A comparison of the experimental and modeling results is shown in Table 3.

Table 3. Comparison of model and experimental results for inlet fracture velocity.

Flow Rate Across Simulator (gpm)	Hydrophysics Measurement from Integral Analysis (μm/s)	Model Result (μm/s)
0.4	1590	2100
1.3	2647	6100
2.5	4235	10000
4.0	5294	16500

The model results match closely at the low flow rate but are higher by a factor of 2 to 3 for the larger flow rates.

Velocity at the Center of the Well

The SCBFM directly measures the velocity of the colloidal particles at the center of the well. The model specifically calculates the conditions in the interior of the well based on a given inlet fracture velocity. Table 4 compares the results for the model near the center of the well with that measured by the Scanning Colloidal Borescope.

Table 4. Comparison of model and experimental results for velocity at the center of the well.

Flow Rate Across Simulator (gpm)	Borescope Measurement (μm/s)	Model Result (μm/s)
0	2	0
0.4	55	~100
1.0	110	~1000
1.5	-	~2000
2.5	1600	~3000
4.0	-	~5000

Again, the model results give larger values by about a factor of two. This is similar to the results for the fracture velocity.

The experiments also indicated that the flow through the center of the well was a very narrow jet. Visual observation of the colloids from the SCBFM demonstrated that the particles traveled faster on one side of the viewing area compared to the other side. This observation is consistent with the model results shown in Figure 2 in which a narrow jet through the center is clearly visible at the higher flow rates.

In addition, the scanning option on the SCBFM was used to investigate the flow field above and below the fracture at the higher flow rates (>2 gpm). Visual observation noted virtually no flow immediately (>1 cm) above and below the fracture horizon. At distances approximately 10 to 15 cm above and below the fracture horizon, flow of a lesser magnitude was observed in the opposite direction compared to that at the fracture. This indicated the outer limit of a circulation cell within the well caused by the relatively high flow velocity entering the well at the fracture inlet. Data collected by the SCBFM showed a circulation cell where the extent of the circulation was 15 cm above and below the fracture horizon.

Conclusions

The results of this work show that: (1) the flow simulator is an excellent method for testing the Scanning Colloidal Borescope Flow Meter (SCBFM) and hydrophysical tools under known, controlled conditions; (2) the measurements made by the two experimental tools are in good agreement at all flow rates tested; and (3) the model is capable of predicting flow conditions in the simulator and interior of the well. The properties and flow rates used in the simulator provide a wide range of conditions in the well that are similar to those observed in field tests. The model predicted qualitatively similar results with regard to the observed flow characteristics in the well. This was noted by the prediction of the jet through the center of the well and the circulation cells above and below the fracture horizon. However, the model over-predicted both the fracture inlet velocity and velocity across the center of the well by about a factor of two. Nonetheless, it is very encouraging that the model is consistently higher by the same factor. It appears that the origin of the difference between the model and the measurements is the calculation of the inlet fracture velocity. A modification of the model used to calculate the inlet velocity could be done to: (1) create a higher grid resolution near the fracture; or (2) create a geometry such that the grid cell center is at the edge of the well rather than using the cell immediately inside and outside the well. If the inlet velocity as predicted by the model were reduced by a factor of two, the

subsequent calculation of the center velocity in the well would likewise be reduced by the same multiple.

The preliminary conclusions of this work suggest the following: (1) horizontal flow in the fractured medium which is representative of the near field flow conditions can be established in a wellbore; (2) that this horizontal flow can be accurately measured and numerically predicted; (3) that the establishment of directionally quantifiable horizontal flow is dependent on four parameters: borehole diameter, structure, permeability and the hydraulic gradient of the flowing feature; and (4) by measuring three of these four parameters, the fourth parameter can be numerically derived through computer simulations.

In summary, the results for the design, construction, and testing of the flow simulator along with the creation of the numerical models were very successful. Future work could focus on making small improvements with regard to the model grid and geometry for the calculation of the inlet velocity. Once this is accomplished and tested, further investigations of various fracture configurations in the flow simulator could be done. The model could be used to guide decisions on fracture configurations that would provide the most useful information. This would lead to a much-improved understanding of the benefits and limitations of the tools used to measure properties in the borehole and relating them to the subsurface media.

Acknowledgments

RAS acknowledges Paul Daley, Albert Lamarre, and Dorothy Bishop of Lawrence Livermore National Laboratory for developing and contributing the scanning colloidal borescope for this study.

The authors would like to thank Randy Buhalts for his assistance in setting up and assisting during the laboratory simulator experiments and Jesse Roberts and Scott James for their assistance with the modeling.

The US Army Environmental Center funded this project. US Army Corps of Engineers Branch Chief Jim Daniels is cited for his vision and efforts to bring new and effective environmental technologies for characterization and remediation of defense related sites.

References

Bear, J., D. Zaslavsky, and S. Irmay, 1968. *Physical Principals of Water Percolation and Seepage*, UNESCO, Paris, 465 pp.

Anderson, W.P., Evans, D.G., and Pedler, W.H., "Inferring Horizontal Flow in Fractures Using Borehole Fluid Electrical Conductivity Logs," EOS, Transactions of the American Geophysical Union Fall Meeting Vol. 74, No. 43, pg. 305, Dec. 1993.

Pedler, W.H., and Urish, D.W., "Detection and Characterization of Hydraulically Conductive Fractures in a Borehole: The Emplacement Method," EOS, Transactions of the American Geophysical Union Fall Meeting Vol. 69, No. 44, pg. 1186, Dec. 1988.

Pedler, W.H., Barvenik, M.J., Tsang, C.F., Hale, F.V., "Determination of Bedrock Hydraulic Conductivity and Hydrochemistry Using a Wellbore Fluid Logging Method," Proceedings of the Fourth National Water Well Association's Outdoor Action Conference, Las Vegas, NV,

May 14-17, 1990; reprint LBL-30713, Lawrence Berkeley Laboratory, University of California, Berkeley, CA.

Pedler, W.H., Head, C.L. and Williams, L.L., "Hydrophysical Logging: A New Wellbore Technology for Hydrogeologic and Contaminant Characterization of Aquifers," Proceedings of Sixth National Outdoor Action Conference, National Groundwater Association, May 11-13, 1992.

Pedler, W.H., "Evaluation of Interval Specific Flow and Pore Water Hydrochemistry in a High Yield Alluvial Production Well by the Hydrophysical Fluid Logging Method" EOS, Transactions of the American Geophysical Union Fall Meeting Vol. 74, No. 43, pg. 304, Dec. 1993.

Tsang, C.F., F.V. Hale, and P. Hufschmied, "Determination of Fracture Inflow Parameters with a Borehole Fluid Conductivity Logging Method," Water Resources Research, vol. 26, no.4, pp. 561-578, April 1990 and LBL 24752, Lawrence Berkeley Laboratory, University of California, Berkeley, CA, and NDC-1, NAGRA, Baden, Switzerland, September 1989.

Wood, W.K., Ferry R.F., and Landgraf, R.K., Direct Ground Water Flow Direction and Velocity Measurements Using the Variable-Focus (Scanning) Colloidal Borescope at Sandia National Laboratory, 1997, Lawrence Livermore National Laboratory Report, UCRL-AR-126781.

Wilson, J.T., Mandell, W.A., Paillet, F.L., Bayless, E.R., Hanson, R.T., Kearl, P.M., Kerfoot, W.B., Newhouse, M.W., and Pedler, W.H., An Evaluation of Borehole Flowmeters Used to Measure Horizontal Ground-Water Flow in Limestones of Indiana, Kentucky, and Tennessee,1999, Water-Resources Investigations Report 01-4139

Preferential Flow in Welded and Non-Welded Tuffs: Observations from Field Experiments

Rohit Salve
MS 14-116, Lawrence Berkeley National Laboratory, Berkeley, CA97720
E-mail: R_Salve@lbl.gov
Phone: 510-486-6416

Introduction

The U.S. Department of Energy (DOE) is currently assessing Yucca Mountain, located 160 km north of Las Vegas, Nevada, as a potential site for disposing spent nuclear fuel and high-level radioactive waste. The development of a permanent storage facility for the geological disposal of high-level nuclear waste at this location is contingent on a clear understanding of flow and transport in the unsaturated fractured rock environment. In the proposed repository design, the waste is to be stored in packages that will be placed in nearly horizontal cylindrical drifts.

A key factor for evaluation regarding repository performance is the likelihood of precipitation entering the mountain to percolate a vertical distance of ~300 m through unsaturated rock, into drifts containing the waste. The amount of water that flows into drifts is thought to control the corrosion rates of waste packages, as well as the mobilization and transport of radionuclides. Subsequently, much effort has been directed towards estimating seepage from the near-drift environment into underground openings from both field experiments (Trautz and Wang, 2002) and numerical modeling exercises (e.g., Birkholzer et al., 1999).

In addition to the investigations of seepage into drifts, some effort has been directed towards understanding flow and transport through the unsaturated rock (e.g., Salve and Oldenburg, 2001; Salve et al., 2002; Salve et al., 2004). The broad objective of these *in situ* liquid-release experiments was to characterize wetting-front movement, flow-field evolution, and drainage as tracer-laced water was released into welded and nonwelded tuffs. The results from these experiments have provided insights into the relative dominance of faults and fractures over the surrounding matrix in transmitting water and dissolved tracers in welded and nonwelded tuffs, along vertical flow paths ranging between ~1 m and ~20 m in length.

This paper summarizes the spatial and temporal dynamics associated with flow in welded and nonwelded tuffs that were observed during a series of experiments conducted at the Exploratory Studies Facility at Yucca Mountain. Also included are techniques developed to conduct the *in situ* field experiments and a discussion on the important implications of these observations.

Methods

The *in situ* experiments involved the release of water along isolated sections of tuffs that included a fault, fracture/s or nonfractured matrix (Table 1). During and after the release of water, changes in moisture content in the formation and the resulting seepage were continuously monitored and continuously recorded by an automated data acquisition system.

Water was released either into a borehole or along the floor of an excavated cavity. The infiltration zone in boreholes was defined by a 0.3 m section, isolated by inflated packers, from which water entered the surrounding formation under constant-head or constant-rate conditions. The release of water along a 5.15 m length of fault located along the floor of an excavated cavity was facilitated by the construction of a small trench. Water was also released over a 3 × 4 m plot.

At each location, constant-head tests were first conducted to determine the maximum rates at which the zone could take in water. For a subsequent set of tests, water was released into the formation at predetermined rates. Both the constant-head method and the constant-rate method of injection were incorporated in the fluid-release apparatus.

During the field tests, relative changes in saturation and water potential were measured continuously along boreholes located below the infiltration zone. Changes in resistance were measured with electrical resistivity probes (ERPs) (Salve et al., 2000). Water-potential measurements were made with psychrometers. The core of the borehole monitoring system was a Measurement and Control System (MCS), [*Model CR7, Campbell Scientific Inc., Logan, Utah*]. To permit the monitoring of a large number of sensors during field investigations, up to seven multiplexers [*Model A416, Campbell Scientific Inc., Logan, Utah*], each with a capacity to house 48 sensors, were attached to this unit.

The lower boundary of each test bed was defined by an excavated cavity, the ceiling of which was blanketed with an array of trays. Seepage rates were continuously monitored with a water collection system that included collection bottles, pressure transducers, and a recording system. When water began to seep, it was diverted from the collection trays to a bottle, the bottom of which was connected to a pressure transducer. A computer system continuously recorded the transducer outputs.

Observation

Our experiments show that when water was introduced along a fault and fractures located in *welded tuff*, the features served as the primary vertical flow path. However, whereas seepage was observed at discrete points along an extended section of fault/fracture, the limited area occupied by each seepage point suggests that these flow paths are small relative to the surface area of the fault/fracture. In the adjacent fractured matrix, water moved laterally and vertically. When water was introduced over a relatively large surface encompassing a large number of fractures, distinct flow paths ~1–2 m wide developed along the formation below.

When water was introduced along a fault located in *nonwelded tuff*, much of the water was initially imbibed by the surrounding matrix. Although the fault began to dry immediately after an infiltration event, the matrix remained wet for long periods (extending to months). While episodic infiltration events were dampened by an initially dry matrix, the fault (embedded in nonwelded tuff) conveyed a pulse of water over larger distances after the matrix was wetted. However, this effect may have been offset (as suggested) by the observation that over a longer period (days to weeks) of wetting, the fault permeability appeared to decrease relative to the initially dry fault.

Observations of flow velocities, flow path volumes, and recovered seepage from these experiments are summarized in Table 2.

Discussion

When water flows in unsaturated fractured rock, preferential flow is inevitable given the contrast in hydraulic conductivities of the fractures and porous matrix. When present, high-permeability conduits act as preferential flow paths if there is a continual supply of water. Not surprisingly, in various field and laboratory studies conducted for the development of conceptual models for flow and transport in unsaturated rocks, preferential flow, identified as either fracture, funneled, or unstable/finger flow, has emerged as a dominant process.

While these experiments have provided some insights into flow in welded and nonwelded tuffs, they have also demonstrated the complexity of flow in this unsaturated environment. This is evident in the spatial and temporal variability of infiltration and seepage rates, and the wetting patterns of the fractured formation, even when there was long-term steady supply of water. This persistent, unstable behavior has been demonstrated before in laboratory experiments (e.g., Glass et al., 2002) and field experiments (e.g., Dahan et al., 1999; Faybishenko et al., 2000; Podgorney et al, 2000) in unsaturated fractured rock environments, and brings into question the validity of large-scale volume averaging concepts currently used to model flow and transport in this environment. Clearly, the modeling approaches adapted for representing larger scale geologic features (i.e., effective continuum, double porosity, dual permeability and multiple interacting continua models) cannot adequately address the spatially and temporally varying flow phenomena. A more realistic approach would be to develop experiments and models that identify and address spatially varying details that impact flow through fractured rock.

Acknowledgments

This work was supported by the Director, Office of Civilian Radioactive Waste Management, U.S. Department of Energy, through Memorandum Purchase Order EA9013MC5X between Bechtel SAIC Company, LLC and the Ernest Orlando Lawrence Berkeley National Laboratory (Berkeley Lab). The support is provided to Berkeley Lab through the U.S. Department of Energy Contract No. DE-AC03-76SF00098.

References

Birkholzer, J., G. Li, C.-F. Tsang, and Y. Tsang, Modeling studies and analysis of seepage into drifts at Yucca Mountain, J. Contam. Hydrol., 38, 349-384, 1999.

Dahan, O., R. Nativ, E. Adar, and B. Berkowitz, Measurement system to determine water flux and solute transport through fractures in the unsaturated zone, Ground Water, 36, 444-449, 1998.

Faybishenko, B., C. Doughty, M. Steiger, J.C.S. Long, T.R. Wood, J.S. Jacobsen, J. Lore, and P.T. Zawislanski, Conceptual model of the geometry and physics of water flow a fractured basalt vadose zone, Water Resour. Res., 36, 3499-3520, 2000.

Glass, R. J., M. J. Nicholl,. S. E. Pringle, and T. R. Wood, Unsaturated flow through a fracture-matrix network: Dynamic preferential pathways in mesoscale laboratory experiments Water Resour. Res. 38:1281, doi:10.1029/2001WR001002, 2002.

Podgorney, R. K., T. R. Wood, B. Faybishenko, and T. M. Stoops, Spatial and temporal instabilities in water flow through variably saturated fractured basalt on a one-meter field scale, in Dynamics of Fluids in Fractured Rock, B. Faybishenko et al., eds., Geophysical Monograph Series, V. 122, American Geophysical Union, 2000.

Salve, R., J. S. Y. Wang, and T. K. Tokunaga, A probe for measuring wetting front migration in rocks, Water Resour. Res., 36, 1359–1367, 2000.

Salve, R., J. S. Y. Wang and C. Doughty, Liquid flow in unsaturated fractured welded tuffs: I. Field investigations. Journal of Hydrology, 256, 60-79, 2002.

Salve, R., and C. M. Oldenburg,Water flow in a fault in altered nonwelded tuff. Water Resources Research, 37: 3043-3056, 2001.

Salve, R., Hudson, D., Liu, H. H. and J. S Y. Wang, Development of a wet plume following liquid release along a fault. (Submitted to Water Resources Research), 2004.

Trautz, R.. C., and J. S. Y. Wang, Seepage into an underground opening constructed in unsaturated rock under evaporative conditions, Water Resour. Res., 38, 1188, 2002.

Experiment #	Unit	Feature	Upper Boundary	Infiltration Rate (m/day)	Vertical Length of Test bed (m)	Volume of Water Released (L)
1	Welded Tuff	Matrix	Constant head	0.03	1.6	1.5
2a	Welded Tuff	Fracture	Constant head	5.04-11.34	1.6	16.3
2b	Welded Tuff	Fracture	Constant head	5.04-8.19	1.6	17.3
2c	Welded Tuff	Fracture	Constant flux	4.35	1.6	18.4
2d	Welded Tuff	Fracture	Constant flux	3.34	1.6	17.5
2e	Welded Tuff	Fracture	Constant flux	2.39	1.6	18.4
2f	Welded Tuff	Fracture	Constant flux	1.83	1.6	18.2
2g	Welded Tuff	Fracture	Constant flux	0.88	1.6	9.4
2g	Welded Tuff	Fracture	Constant flux	0.31	1.6	3.4
3	Welded Tuff	Fault	Constant head	0.06-0.22	20	72,000
4	Welded Tuff	Multiple fractures	Constant head	0.04-0.33	20	22,000
5	Non-Welded Tuff	Matrix	Constant head	0.02-0.06	0.35	6.5
6a	Non-Welded Tuff	Fault	Constant head	8.71	3	42.9
6b	Non-Welded Tuff	Fault	Constant head	7.26	3	41.4
6c	Non-Welded Tuff	Fault	Constant head	5.17	3	21.3
6d	Non-Welded Tuff	Fault	Constant head	4.42	3	29.5
6e	Non-Welded Tuff	Fault	Constant head	3.79	3	22.2
6f	Non-Welded Tuff	Fault	Constant head	3.09	3	17.1
6g	Non-Welded Tuff	Fault	Constant head	3.03	3	18.9
6h	Non-Welded Tuff	Fault	Constant head	10.35	3	45.4
6i	Non-Welded Tuff	Fault	Constant head	7.19	3	55.8
6j	Non-Welded Tuff	Fault	Constant head	6.75	3	34.7

Table 1. Details of liquid release experiments in weld and non-welded tuffs

Experiment #	Wetting Front Velocity (m/day)	Flow Path Volume (L)	Recovered Seepage (%)
1	N/A	N/A	0
2a	305	0.41	71
2b	509	0.17	70
2c	509	0.14	62
2d	509	0.14	64
2e	218	0.26	80
2f	218	0.2	72
2g	22	0.9	49
2h	5	1.51	11
3	0.6	3,380	~8
4	1.5	10,617	8
5	N/A	N/A	0
6a	6	34.9	0
6b	15	12.5	0
6c	7	19.2	0
6d	13	10	0
6e	19	5	0
6f	2	~40	0
6g	4	17.3	0
6h	6	41.9	0
6i	13	16.8	0
6j	15	7.8	0

Table 2. Observations from liquid release experiments in weld and non-welded tuffs

Determination of Moisture Diffusivity for Unsaturated Fractured Rock Surfaces

Robert C. Trautz and Steve Flexser
Lawrence Berkeley National Laboratory, 1 Cyclotron Rd., 90R1116,
Berkeley, CA, USA 94720
(510) 486-7954, rctrautz@lbl.gov

Introduction

Trautz and Wang (2002) described a series of field experiments performed in an underground test facility constructed in an unsaturated, fractured volcanic tuff located at Yucca Mountain, Nevada. The primary purpose of the testing program was to determine whether water percolating down from the land surface through the unsaturated zone would be diverted around an underground tunnel because of the existence of a capillary barrier at the tunnel ceiling. Trautz and Wang (2002) showed that by releasing water in boreholes located above a 3.25 meter (m) high by 4 m wide drift, a capillary barrier is revealed, leading to lateral flow of water around the opening.

The seepage tests described by Trautz and Wang (2002) provide a unique opportunity to observe the arrival and movement of water across a suspended, unsaturated fractured rock surface. The spread of water from its initial point of arrival at the tunnel surface across the ceiling will be used in this paper to estimate the moisture diffusivity, $D(\theta)$, along the ceiling surface and adjacent rock.

Test Description and Observations

Water was released at a constant rate over a 2-day period into a 0.3 m section of borehole UL, installed 0.7 m above the tunnel (Figure 1). Fractures intersecting the test interval conducted water from the borehole to the tunnel ceiling, where it initially appeared as isolated wet spots (Points 1 and 2 on Figure 2). The capillary barrier prevented water from immediately dripping into the opening, causing the water to spread laterally across the ceiling. Its advance was recorded using time-lapse video, allowing the position of the wetting front to be mapped from the resulting images. Figure 2 shows the position of the wetting front 1, 3, 8, 18, 28, and 48 hours after arriving at the ceiling. Despite the presence of numerous visible fractures and irregularities in the ceiling surface, the wetting front spread in a surprisingly homogenous, radial symmetric pattern. The equivalent radial distance (r_f) that the wetting front has traveled from the point of first arrival (assuming a radial flow field) is calculated as $r_f = (A/\pi)^{1/2}$, where A is the area of the wetted rock contained within the boundaries of the wetting front (Figure 3).

Eventually, the rock surface became saturated near the location of the first arrival and water dripped or seeped into the tunnel. Seepage typically takes place from topographic low points on the ceiling surface in close proximity to the first-arrival location. The position of the wetting front at the time that dripping started (8 hours after the first arrival) is shown as a dashed line and individual drip locations (48 hours after first arrival at the end of the test) are shown as x's in Figure 2. The wetting front continued to spread as long as water was supplied to the ceiling from

the overlying borehole. The measured release rate into the test borehole, the seepage rate into the opening, and the supply rate are plotted in Figure 3. Note that the supply rate is defined as the difference between the release and seepage rates and, therefore, represents the amount of water feeding or supplying the advancing wetting front (assuming negligible evaporation).

Conceptual Flow Model

The observations described above can be conceptualized as two unsaturated flow processes that are commonly described in the soil physics literature. The first process, *infiltration*, occurs when water is released into the borehole located above the opening and infiltrates through vertical fractures to the tunnel ceiling. Trautz and Wang (2002) determined that the capillary strength of the fractures associated with the test was very weak, and they concluded that infiltration through the fracture system was predominately a gravity-driven (as opposed to a capillary-driven) process.

The second process, spreading, is analogous to horizontal absorption described by Philip (1969) for soils. It begins once the wetting front reaches the relatively flat, horizontal ceiling and begins to move or spread laterally. During the earliest stage of spreading, the rate that water is supplied to the ceiling may be less than that being released to the overlying borehole because of a time lag for the infiltration flux to fully reach the ceiling. At later stages, the supply rate may equal the release rate, creating a constant flux inner boundary condition as the wetting front advances. This is shown conceptually as a zone of "increasing flux" ($r < r_o$) on Figure 4.

As time progresses, the rock surface becomes saturated, and dripping begins when the supply rate at the tunnel ceiling exceeds the rate that water can be transmitted laterally through the matrix, fractures, and along surface films that develop at the tunnel-wall rock interface. It is at this point that the boundary condition changes from one of increasing or near-constant flux to one of constant water content, θ (Figures 3 and 4). The wetting front advances under constant θ conditions from this point forward. However, it should be noted that the supply rate may continue to change for a period of time after dripping begins (Figure 3) as the initially strong capillary forces diminish with time. The time required to reach constant-θ conditions is often referred to in the literature as the "time to ponding" (t_p), and the radial distance (r_o) at which this transition from constant flux to constant-θ conditions first occurs is defined herein for our radial model as the equivalent radial distance that the wetting front has traveled when dripping begins (Figure 4). This occurs at $r_f = r_o = 212$ mm (Figure 3) and corresponds to the actual wetting-front position shown by the dashed line on Figure 2. It is important to realize that r_o represents the approximate radius of the constant-θ supply surface or source.

Data Analysis

Philip (1969) and many others have published a number of solutions to the equation governing unsaturated water movement through nonswelling soils for a homogeneous, semi-infinite medium with a constant-θ condition at the fixed boundary. Exact and/or approximate solutions have been derived for infiltration and absorption from 1-D surfaces, 2-D cylinders, and 3-D spheres (Philip 1969). Philip (1968) derived the following dimensionless solution for a step increase in θ at the cylindrical supply boundary (r_o) of a horizontal 2-D radial flow domain:

$$T = \frac{2}{\pi}\left[(1+2I)\log(1+2I) - 2I\right] \quad (1)$$

where

$$T = \frac{D\,t}{r_o^2} \qquad \text{and} \qquad I = \frac{r_f - r_o}{r_o} \quad (2)$$

and D is the moisture diffusivity [m^2/seconds (s)], t is time [s], and r_o and r_f are the radial distance [m] to the water supply and wetting front boundaries, respectively, defined earlier. The solution above uses the same plug-type flow condition originally developed by Green and Ampt (1911) for vertical infiltration. It assumes that the wetting front advances as a "square wave" with a "sharp" wetting front (i.e., infinitely steep water potential gradient). The water content behind the wetting front is everywhere the same and equal to the water content imposed at the water supply boundary, θ_o, at t = 0. Therefore, D takes on a constant value $D(\theta_o)$ and drops instantaneously at the wetting front to $D(\theta_i)$ where θ_i is the ambient water content of the medium at initial condition $t \leq 0$. Green and Ampt-type solutions have been shown to predict infiltration and absorption reasonably well for early times for very dry and/or coarse media. Distinct, sharp (i.e., not diffused) wetting fronts were observed during the seepage tests, providing qualitative support for the use of (1) to analyze the r_f –derived data in Figure 3.

Conclusion

Equation (1) was used to derive the type-curve shown on Figure 5 for an arbitrary set of I and T. The radius of the water supply r_o and equivalent radial front position r_f shown on Figure 3, and the corresponding elapsed time from the start of ponding (t) for each front position, were substituted, along with an initial guess for D into (2) to produce I and estimates of $T = T_{est}$. The resulting value of I was then substituted into (1) to produce predicted values of $T = T_{pred}$. The optimum value of D was determined by repeating the process, iteratively using successive values for D that minimized the sum of residuals ($T_{pred} - T_{est}$) squared as follows:

$$\text{Minimize} \quad \sum_{n=1}^{\#\ of\ Data} \left(T_{pred,\,n} - T_{est,\,n}\right)^2 \quad (3)$$

The final fit of the data, compared to the analytical solution in Figure 5, produces a value of moisture diffusivity D equal to 3.2E-7 m^2/s. This value agrees with measured 1-D surface film diffusivities reported by Tokunaga et al. (2000) equal to 3.2E-7 and 1.7E-7 m^2/s for a glass cast of a granite fracture and roughened glass surface, respectively. This leads us to believe that the primary mechanism for wetting-front movement across the ceiling is by surface film flow. This is substantiated by the fact that preferential flow along visible fractures is not evident in the wetting patterns of Figure 2, suggesting that visible fractures do not control the wetting process (other than to serve as the water source from above). Vertical absorption from the advancing wetting front into the overlying rock matrix could also influence the process by contributing to the "sharpness" of the observed wetting front. However, behind the front, this process is expected to be relatively minor. This is because the rock matrix diffusivity drops rapidly at the wetting front, where the water-potential gradient is very steep, to a very low value behind the front, where the gradient decreases quickly because of the very low conductivity of the matrix (4.0E-11 m/s, Flint 1998). The low conductivity of the matrix causes saturated conditions to develop quickly in the matrix at the ceiling surface-rock matrix interface. The corresponding

rapid reduction in the water-potential gradient and rate of absorption into the matrix allows surface films to persist at water potentials perhaps as large as -100 kPa in our case (Figure 4 in Tokunaga and Wan, 2001).

References

Flint , L.E., Characterization of hydrogeologic units using matrix properties, Yucca Mountain, Nevada, U.S. Geol. Sur. Water Resour. Invest. Rep., 97-4243, 64 pp., 1998.

Green, W.H. and G.A. Ampt, Studies of soil physics: Part I – The flow of air and water through soils, J. Agricultural. Sci., Vol. IV, 1-24, 1911.

Philip, J.R., Theory of Infiltration, Adv. Hydrosci., 5, 215-295, 1969.

Philip, J.R., Absorption and infiltration in two- and three-dimensional systems, in Water in the Unsaturated Zone, Proceedings of the Wageningen Symposium 1966, Vol. 1, published by IASH/UNESCO, Paris, France, 503-516, 1968.

Trautz, R.C. and J.S.Y. Wang, Seepage into an underground opening constructed in unsaturated fractured rock under evaporative conditions, Water Resourc. Res., 38(10), 6-1 – 6-14, 2002.

Tokunaga, T.K., J. Wan, and S.R. Sutton, Transient film flow on rough fracture surfaces, Water Resourc. Res., 36(7), 1737 – 1746, 2000.

Tokunaga, T.K. and J. Wan, Approximate boundaries between different flow regimes in fractured rocks, Water Resourc. Res., 37(8), 2103 – 2111, 2001.

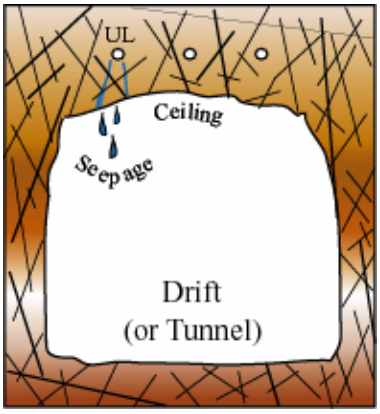

Figure 1. Test configuration.

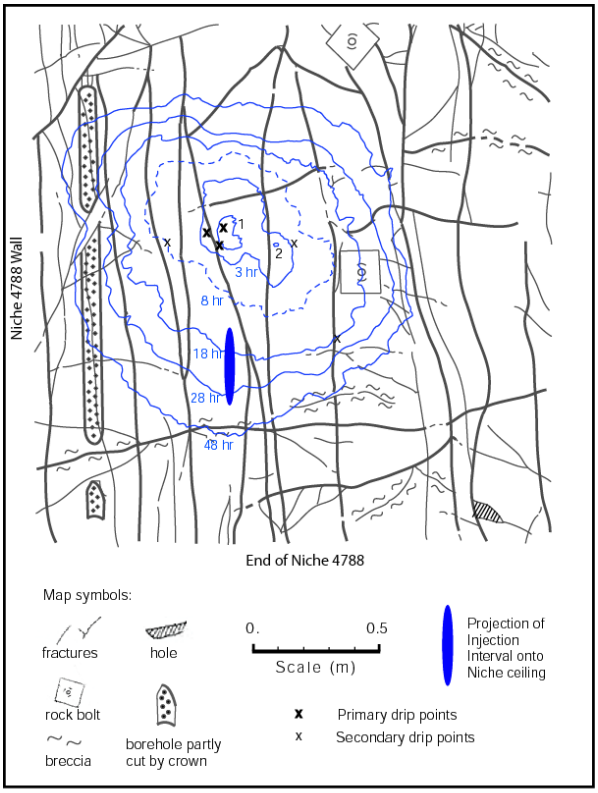

Figure 2. Spread of the wetting front across the tunnel ceiling. Front positions are shown 1,3 ,8, 18, 28 and 48 hours after the first arrival (contour labeled 1 and 2).

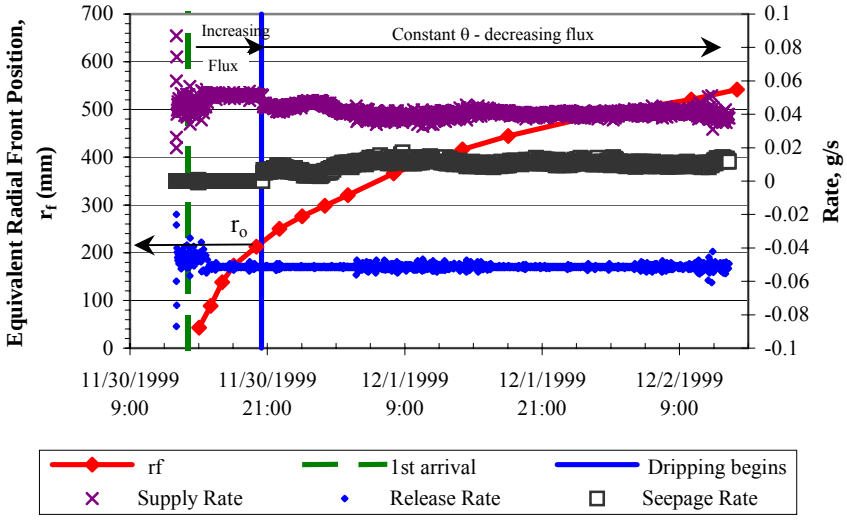

Figure 3. Wetting front radial position and release, seepage and supply rates for test.

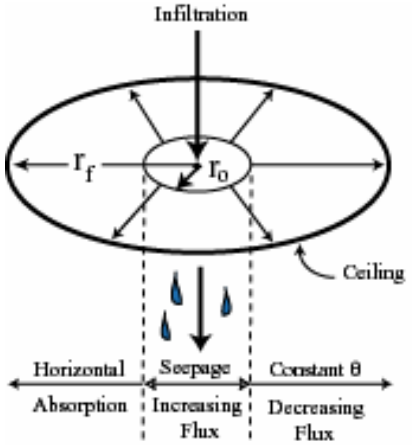

Figure 4. Conceptual flow model showing 2-D radial absorption along horizontal surface of tunnel ceiling.

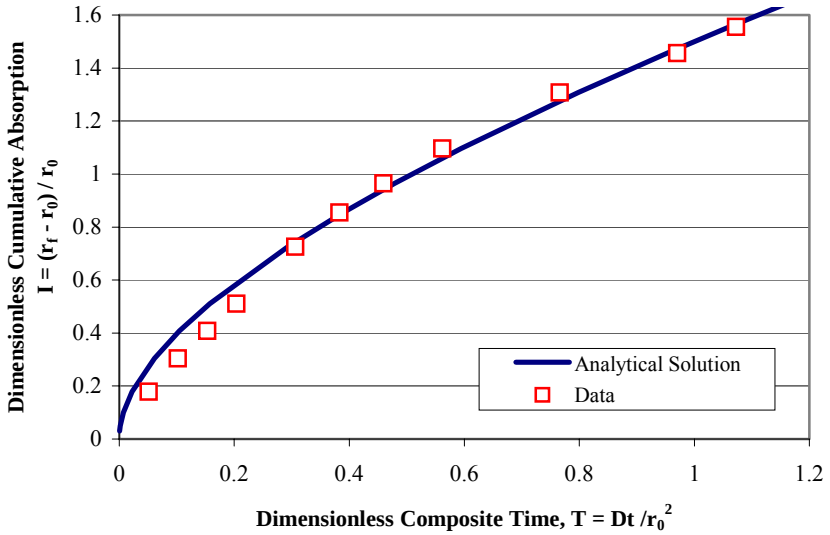

Figure 5. Best fit of data to analytical solution (Philip 1986) using moisture diffusivity D(θ) equal to 3.2E-07 m^2/s.

Session 5:
GEOCHEMISTRY, COUPLED AND MICROBIAL PROCESSES, AND GEOTHERMAL RESOURCES

Biodegradation of 2,4,6-Tribromophenol during Transport: Results from Column Experiments in Fractured Chalk

Shai Arnon[1,2], Zeev Ronen[1], Eilon Adar[1,2], Alexander Yakirevich,[1] and Ronit Nativ[3]
[1]Department of Environmental Hydrology and Microbiology,
Institute for Water Sciences and Technologies, J. Blaustein Institute for Desert Research,
Ben-Gurion University of the Negev, Sede-Boker, Israel
[2]Department of Geological and Environmental Sciences,
Ben-Gurion University of the Negev, Israel
[3]Department of Soil and Water Sciences, The Hebrew University of Jerusalem, Israel

Biodegradation of dissolved organic contaminants in the subsurface has been studied extensively over the past 20 years. However, only a limited number of studies dealt with biodegradation processes in fractured rocks. Biodegradation within low permeability fractured aquitards appears an attractive treatment scheme for contaminated groundwater, because the more conventional remediation techniques, such as pump and treat, are difficult to apply. Yager et al. (1997) provided clear evidence of in situ biodegradation of trichloroethylene (TCE) in fractured dolomite under saturated conditions. Spence et al. (2002) demonstrated, using carbon and sulfur isotope fractionation, that biodegradation of unleaded fuel occurred within a saturated fractured chalk. Other studies by Johnson et al. (2000) and Kristensen et al. (2001) have demonstrated the potential for pesticide biodegradation in a chalk aquifer by a set of batch experiments. Yet, the ability to estimate reactive contaminant migration and the possibility of using in-situ bioremediation for treating contaminated fractured aquifers, still rely on additional understanding of the dynamic behavior and the spatial distribution of microbial processes in the presence of organic contaminants in fractured rocks.

This paper focuses on the biodegradation of 2,4,6-tribromophenol (TBP), a model contaminant, during transport within fractured chalk. These include aspects of the spatial distribution of microbiological processes. In order to study the biodegradation processes in fractured chalk, horizontal cores were drilled along a vertical fracture (Dahan et al., 1998). The cores were saturated under vacuum using degassed artificial groundwater (AGW). The composition of AGW was: 3700 mg/L Cl^-, 1030 mg/L SO_4^{2-}, 245 mg/L HCO_3^-, 340 mg/L Ca^{2+}, 200 mg/L Mg^{2+}, 2100 mg/L Na^+, and 22 mg/L K^+. This composition is similar to that of the uncontaminated groundwater east of the study site in the north of the Israeli Negev desert (Nativ and Adar, 1997). Each fractured core was fixed using epoxy cement (Duralite®) inside a PVC casing. Teflon inlet and outlet chambers were attached to both sides of the flow boundaries of the fracture while the other two boundaries were sealed. A schematic illustration of the experimental apparatus appears in Figure 1. Four stainless steel injection ports (1 mm i.d.) were inserted through the inlet chamber into the fracture plane, 2 cm from the inlet boundary. The injection ports were used to inject the substrate directly into the fracture during the biodegradation experiments (Pump #3), while AGW (Pump #1) was supplied through the inlet chamber with elevated oxygen concentrations (~24 mg/L). The AGW flux was kept at twice the substrate injection flux to prevent substrate backflow toward the inlet chamber. Pump #2 continuously circulated the AGW to ensure that the inlet chamber was well-mixed. A pair of piezometers/ sampling ports were located approximately every 10 cm from the inlet toward the outlet of the core. The biodegradation experiments were conducted with the fractures in a vertical position, similar to the *in situ* fracture orientations in a related study site (Nativ and Adar, 1997).

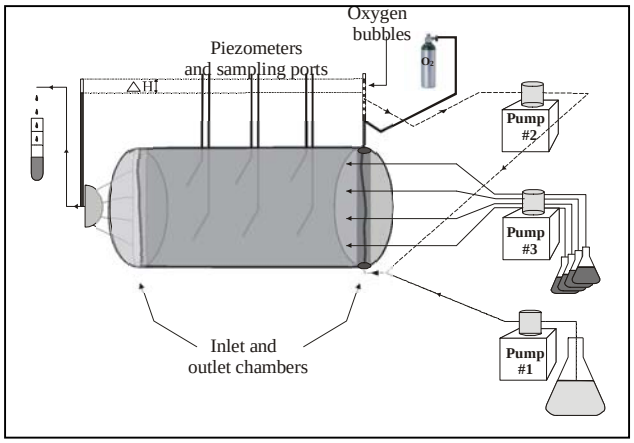

Figure 1. Schematic illustration of the experimental setup.

The various fractures were operated over 100-630 days under different experimental conditions including several flow rates, TBP concentrations and oxygen concentrations. *Phase 1* of the experiments (Days 0-400) was characterized by TBP inlet concentrations of <50 mg/L, low oxygen concentrations (<4 mg/L) and relatively slow flow rates (1.3-7.8 ml/hr), and was applied to six cores. *Phase 2* lasted for an additional ~200 days on two cores. It was characterized by TBP concentrations of ~100 mg/L, over-saturated oxygen concentrations (~20 mg/L) and relatively high flow rates (8-40 ml/hr). When the experiments ended, one core was cut open and bacteria on the surface were counted. Several samples were also taken for scanning electron microscopy (SEM) analysis.

This paper focuses on the results obtained during *Phase 2* of the experiments. A detailed description of the experimental procedures and the results of the biodegradation experiments during *Phase 1* appear in Arnon (2003). During *Phase 2*, a nutrient solution containing AGW, 25 mg/L K_2HPO_4, 3.7 mg/L NH_4CL and 300 mg/L 2, 4, 6-tribromophenol (TBP), as a representative contaminant, was continuously injected into the fracture. TBP concentrations together with bromide (Br^-), which is indicative of degradation of TBP, and oxygen concentrations were monitored routinely at the inlet and outlet of the fractures and along the fracture length through the pre-installed piezometers.

Several indications were used to identify the biodegradation of TBP. These included: (1) biodegradation of TBP by bacteria isolated from the experimental "flow through system"; (2) TBP disappearance and Br^- formation; and (3) the effect of biocide addition on the microbial activity and TBP transport in the column.

Several bacteria capable of degrading TBP were isolated from the effluent of the fractured flow through system based on morphology characteristics. Identification with Biolog® GN plates indicated that some of the TBP degrading isolates belong to the genus *Alcaligence,* similar to the TBP degrading bacterium *Achromobacter piechaudii*, strain TBPZ. Strain TBPZ was isolated from the soil overlying the fractured chalk used in this study (Ronen et al., 2000).

The second approach for estimating TBP biodegradation was through Br^- measurements. The expected Br^- concentrations were calculated based on a stochiometric release of Br^- from the attenuated TBP, where attenuated TBP is defined as the difference in TBP concentrations

between the inlet and the outlet of the core (Δ–1 mg/L TBP = Δ+0.723 mg/L Br^-). HPLC analysis revealed no metabolites, either aerobic or anaerobic (e.g. 2,6-dibromohydroquinone, 6-bromohydroxyquinol, hydroxyquinol, 2,4-dibromophenol, 4-bromophenol and phenol (Padilla et al., 2000; Ronen and Abeliovich, 2000). Other organic compounds expected to result from TBP biodegradation are considered relatively biodegradable and will therefore not be discussed.

To provide unconditional evidence that bacterial activity is responsible for at least part of the TBP disappearance within the fracture, a biocide was added to the injected solution. A short time after the biocide was introduced, the oxygen concentrations in the inlet chamber and later at the outlet started to increase, and the total number of bacteria started to decrease. Incomplete TBP recovery after 22 days suggests that, besides biodegradation, diffusion and adsorption also play a major role in TBP transport. At this stage, when no bacteria existed in that core, the transport of TBP together with non-reactive solute was characterized. The parameters derived during this stage were used to estimate, using a numerical transport code, Sinfra2d (Yakirevich et al., 2000), the transport of TBP without the effect of biodegradation.

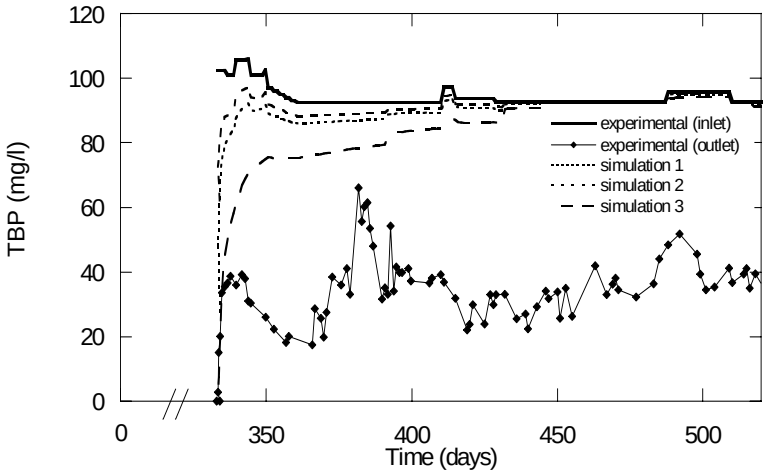

Figure 2. Biodegradation of TBP during transport in fractured chalk.

Figure 2 illustrates the results obtained by the transport model using the experimental conditions during *Phase 2*. The three simulations represent 3 combinations of parameters; among these are the extreme cases (Simulations 2 and 3) and the most feasible simulation (Simulation 1). The inlet concentration was calculated based on TBP concentrations and the flux ratio between the nutrient solution injection and the AGW injection (see Figure 1). The area between the simulation and the experimental data in Figure 2 represents a rough estimate of the amount of TBP that was biodegraded. The estimated amount of TBP biodegradation was confirmed by Br^- release measurements at the outlet (Arnon, 2003). Within the fractured core, TBP was degraded only in the fracture void. TBP that was entrapped in the matrix by diffusion was not available to the bacteria, since more than 99% of the pore sizes are less then 0.4 μm, which is much smaller then the average bacteria size (1 μm). This was verified by the finding that no bacteria were detected from several chalk samples taken about 3 mm perpendicular to the fracture surface after the experiment was terminated. In addition, the TBP distribution coefficient on the fracture coating materials was relatively low, K_f = 0.05 ml/g (Wefer-Roehl et al., 2001); therefore we assume that

the substrate within the fracture void was fully bioavailable.

Since TBP was never fully consumed within the fractures and oxygen concentrations above zero were not detected at the outlet, we suggest that oxygen was a major factor controlling the biodegradation process. This is further supported by the link between the biodegraded TBP and the consumed oxygen (Figure 3).

Measurements of TBP, Br^- and oxygen in the fracture piezometers revealed that microbial activity was not uniform within the fracture. This was depicted adequately by the spatial distribution of bacteria on the fracture surfaces (Figure 4).

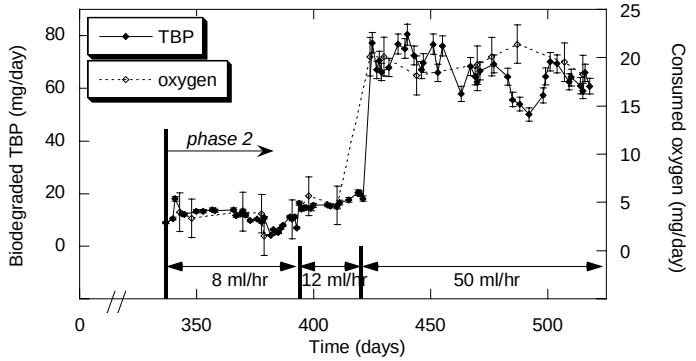

Fig. 3 Biodegraded TBP and the consequent oxygen consumption

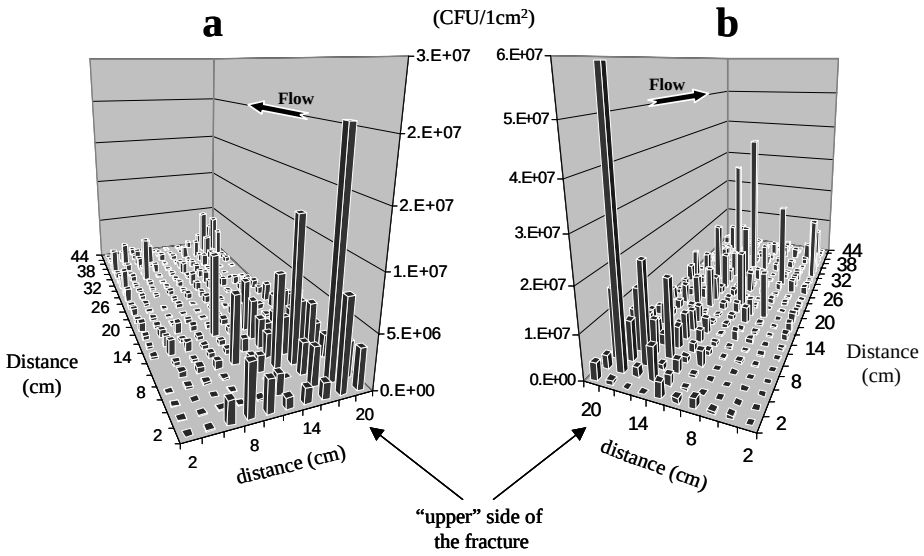

Figure 4. Spatial distribution of bacteria on the fracture surfaces.

The total viable bacteria counts, as determined by the drop plate method on R2A medium, were measured in a 2 × 2 cm grid. The highest viable counts were observed close to the inlet in the upper part of the fracture. This was also seen by SEM photomicrographs. The upper side of the fracture was previously found to have the fastest flow channels and the highest oxygen concentrations (Arnon, 2003). Despite the evidence for the spatial distribution of the

biodegradation activity, it was shown by a short pulse of a dye (brilliant blue FCF, 200 mg/L) prior to the enumeration of bacteria on the fracture surfaces, that most of the fracture void was accessible to water. This finding suggests that preferential flow paths control the nutrient supply to specific regions within the fracture void.

The experimental results have shown that the surface of the fracture provides an adequate environment for microbial activity, including biodegradation of organic pollutants, despite the limitations imposed by the chalk matrix characteristics on microbial penetration into the matrix. The biodegradation of TBP was clearly related to the amount of oxygen available to the microorganisms. Thus, as in bioremediation of porous media, supplementation of electron acceptors (oxygen) is essential to ensure microbial activity. Yet, it must be kept in mind that it is possible to use anaerobic processes as an alternative treatment. In the experimental system, biodegradation of TBP did not reach a steady state, due to several processes that affected the microorganisms. For example, continuous reduction in the fracture's transmissivity by 1-2 orders of magnitude caused by fracture clogging with biomass constrains the dynamic environment for the microorganisms. The initial spatial distribution of the hydrological characteristics (mainly flow channels) controls the substrate and nutrient supply to the microorganisms on the fracture surface. The microbial activity and the consequent clogging further control the dynamic hydrological and microbial activity within the fracture. Neither the clogging nor the biodegradation rates reached steady-state conditions, indicating the link between these processes.

References

Arnon, S., 2003. The effect of microbial activity on fluid flow and 2,4,6-tribromophenol transport in fractured chalk. Ph.D Thesis, Ben-Gurion University of the Negev, Beer-Sheva.

Dahan, O., Nativ, R., Adar, E. and Berkowitz, B., 1998. A Measurement system to determine water flux and solute transport through fractures in the unsaturated zone. Ground Water. 36, 444-449.

Johnson, A.C., White, C. and Bhardwaj, C.L., 2000. Potential for isoproturon, atrazine and mecoprop to be degraded within a chalk aquifer system. J. Contam. Hydrol. 44, 1-18.

Kristensen, G.B., Sorensen, S.R. and Aamand, J., 2001. Mineralization of 2,4-D, mecoprop, isoproturon and terbuthylazine in a chalk aquifer. Pest. Manag. Sci. 57(6), 531-536.

Nativ, R. and Adar, E., 1997. Assessment of groundwater contamination in the Ramat-Hovav industrial complex. Report submitted to the Ramat-Hovav industrial council (in Hebrew).

Padilla, L., Matus, V., Zenteno, P. and Gonzalez, B., 2000. Degradation of 2,4,6-trichlorophenol via chlorohydroxyquinol in *Ralstonia eutropha* JMP134 and JMP222. J. Basic Microbiol. 40(4), 243-249.

Ronen, Z. and Abeliovich, A., 2000. Anaerobic-aerobic process for microbial biodegradation of Tetrabromobisphenol A. Appl. Environ. Microbiol. 66, 2372-2377.

Ronen, Z., Vasiluk, L., Abeliovich, A. and Nejidat, A., 2000. Activity and survival of tribromophenol-degrading bacteria in a contaminated desert soil. Soil Biol. Biochem. 32, 1643-1650.

Spence, M.J., Thornton, S.F. and Richnow, H.H., 2002. A stable isotope investigation of MTBE/BTEX degradation in the upper chalk, International symposium on Subsurface Microbiology, Copenhagen.

Wefer-Roehl, A., Graber, E.G., Borisover, M.D., Adar, E.M., Nativ, R. and Ronen, Z., 2001. Sorption of organic contaminants in a fractured chalk formation. Chemosphere. 44, 1121-1130.

Yager, R.M., Bilotta, S.E., Mann, C.L. and Madsen, E.L., 1997. Metabolic adaptation and in situ attenuation of chlorinated ethenes by naturally occurring microorganisms in a fractured dolomite aquifer near Niagara falls, New York. Environ. Sci. Tech. 31(11), 3138-3147.

Yakirevich, A., Adar, E. and Wefer-Roehl, A., 2000. Retardation of organic contaminants in a fractured chalk formation: Modeling tracer experiments in a single natural fracture, Proceedings of the XIII International conference on Computational Methods in Water Resources, pp 299-306.

Abiotic and Biotically Mediated Rock Mineral Oxidation

Magnus Sidborn and Ivars Neretnieks
Dept. Chemical Engineering and Technology, Royal Institute of Technology
S-100 44 Stockholm, Sweden

Investigations of deep fractured rocks indicate a great variety of subterranean microorganisms gaining energy from various reactions (Ghiorse and Wilson, 1988; Pedersen, 1996; 1997). Energy derived from the reactions is used by the microbes for growth and maintenance. The size of the microbes (approximately 1 micrometer) prevents them from migrating into the micropores of the rock matrix, and hence, they are present in the larger fractures only. For survival, the microbes need an electron acceptor such as oxygen, substrates for the energy-giving reaction, and a carbon source for growth. These prerequisites are fulfilled in many subterranean systems. In the present work, the limitation of substrate availability was studied from a long-term perspective. As long as oxidizable minerals are available inside or in the vicinity of the fractures, the availability may support the growing culture and consume the intruding oxygen. However, over time, the fracture is depleted with respect to oxidizable minerals, and substrates must be transported out of the porous rock matrix to support the microbe population in the fracture. As an example, the competition between abiotic and biotically mediated oxidation of ferrous iron minerals is addressed in the present work. There are many possible parallel paths for the fate of oxygen, some of which are studied in the present work. Additionally, each parallel path may comprise two or more serial processes such as matrix diffusion and reaction, the slowest of which will be rate limiting. In Figure 1, the processes considered in the models are illustrated.

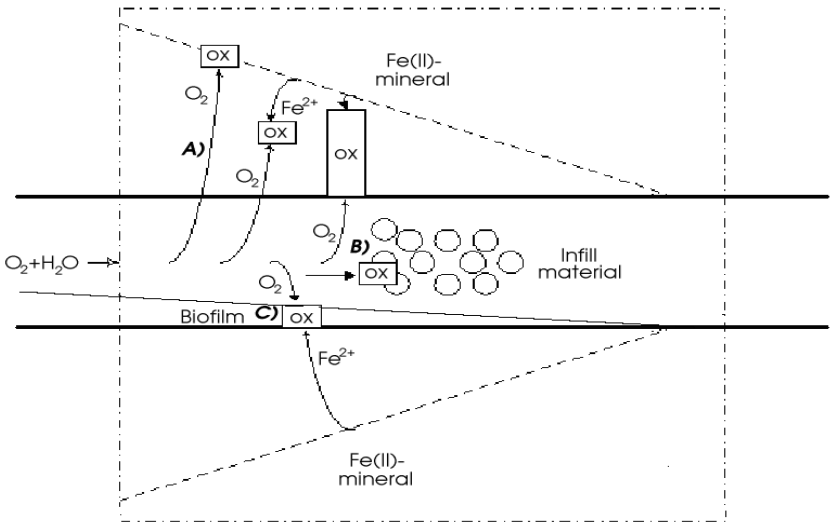

Figure 1. Oxidation processes considered in the models. Bold lines represent fracture walls: (A) abiotic oxidation of matrix minerals; (B) oxidation of fracture minerals, and (C) biotic oxidation of matrix minerals.

The processes shown in Figure 1 act either in parallel or in series. A scheme for the rates is shown in Figure 2.

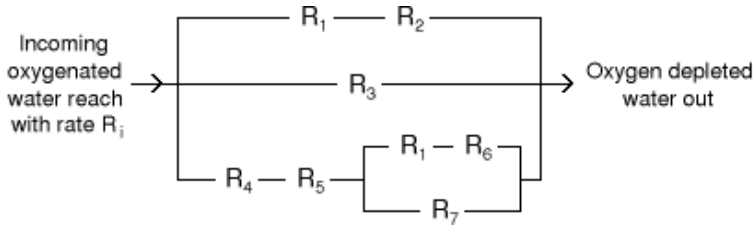

Figure 2. Scheme of parallel paths with comprised serial processes: R_1. Matrix diffusion of oxygen: R_2. Abiotic pyrite oxidation reaction; R_3. Biotic oxidation reaction of fracture surface pyrite; R_4. Non-oxidative dissolution of ferrous minerals; R_5. Matrix diffusion of ferrous ions; R_6. Abiotic ferrous iron oxidation reaction; R_7. Biotic oxidation reaction of ferrous ions.

Several models were developed making it possible to compare the different rates involved in the oxidation of fracture infill and rock matrix pyrite by oxygen. The rates for the different processes (R_1-R_7) were compared and evaluated according to the following: The processes involved in each parallel path were studied in separate models (i.e., for the first path, the abiotic reaction rate (R_2), was compared to the matrix diffusion rate of oxygen (R_1), and so on. The slowest process in the series will limit the overall rate along each parallel path, whereas the fastest parallel path will mostly affect the overall oxygen consumption. Even if it would be possible to include all of the considered processes in one model, such an approach would make interpretation of the results difficult. Consequently, the present approach was chosen to facilitate result transparency. Both simple batch models and transient transport models were used for the evaluation. The rate expressions of the processes were obtained from the literature, and data used for the calculations represent central values found in the literature or which can be deemed typical for Swedish bedrock. The results show that as long as there are oxidizable minerals available in the fracture, either as infill material or fracture wall minerals, the biotically mediated reaction rate is rate limiting for the oxidation. When the oxidizable minerals are depleted in the vicinity of the fracture, matrix diffusion limits the oxidation rate. For diffusion distances in the matrix of more than one millimeter, matrix diffusion is a slower process than all of the different reaction rates. The conclusion is therefore that from a long-term perspective, oxidation of matrix minerals is governed by transport processes in the rock matrix, whereas in the short term reaction and dissolution rates may be important.

We wish in this work primarily to explore the relative importance of the various processes expecting some to be important at early times and others to dominate at longer times after oxygen intrusion commences.

References

Ghiorse, W.C. and J.T. Wilson, Microbial ecology of the terrestrial subsurface. *Adv Appl Microbiol*, 33:107-172, 1988.

Pedersen, K., Investigations of subterranean bacteria in deep crystalline bedrock and their importance for the disposal of nuclear waste. *Can J Microbiol*, 42:382-391, 1996.

Pedersen, K., Microbial life in deep granitic rock, *FEMS Microbiol Rev*, 20:399-414, 1997.

DNAPL Invasion into a Partially Saturated Dead-end Fracture

Grace W. Su and Iraj Javandel
Earth Sciences Division, Lawrence Berkeley National Laboratory, Berkeley, CA 94720
gwsu@lbl.gov; 510-495-2338

Introduction

Fractures in the unsaturated zone act as preferential pathways for the transport of water and contaminants such as dense nonaqueous phase liquids (DNAPLs). Although DNAPLs can quickly migrate through a connected fracture network, DNAPLs will inevitably encounter dead-end fractures, where they become entrapped. The volume of DNAPL entrapped in these dead-end fractures could be large, which could have serious implications for site remediation.

This study investigates DNAPL entry into a partially saturated dead-end fracture. The theoretical criteria for DNAPL entry into a partially saturated dead-end fracture is presented, followed by laboratory experiments conducted on an analog parallel plate fracture.

Criteria for DNAPL Entry

In this study, we are considering DNAPL entry into a partially saturated dead-end fracture that is filled with water uniformly across the width of the fracture, as shown in Figure 1.

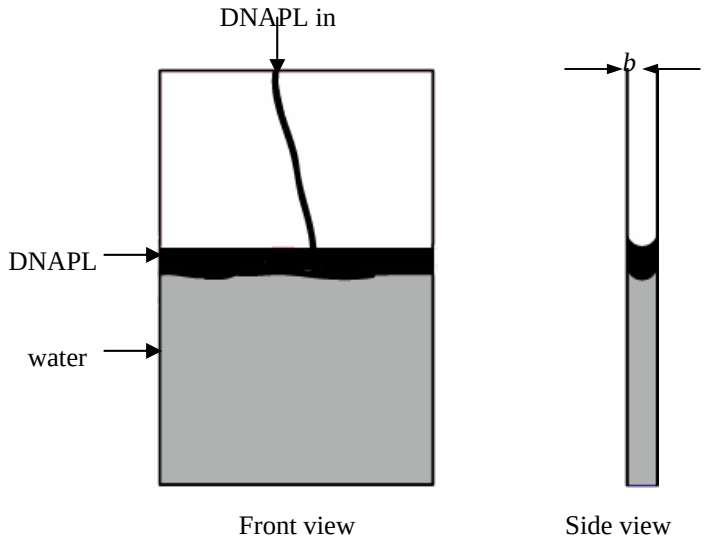

Figure 1. Schematic of a partially saturated dead-end fracture and a DNAPL pool above the water.

DNAPL entry into a partially saturated fracture, as illustrated in Figure 1, is similar to the scenario of DNAPL entry into the capillary fringe. The critical height for DNAPL entry, $h_{DNAPL,entry}$, into the capillary fringe is given by the following equation (Cohen and Mercer, 1993):

$$h_{DNAPL,entry} = \frac{2\sigma_{DNAPL/water}\cos\phi}{\rho_{DNAPL} g b} \quad (1)$$

where $\sigma_{NAPL/water}$ is the interfacial tension between the DNAPL and water, ϕ is the wetting contact angle, ρ_{DANPL} is the DNAPL density, g is the gravitational acceleration, and b is the pore size or aperture width.

Equation 1 does not, however, account for the capillary force due to the DNAPL-air interface. This force can be incorporated into the criterion for DNAPL entry by performing a force balance of the DNAPL pool overlying the water. Assuming hydrostatic equilibrium, the pressure at the top of the water, $P_{water,top}$, is

$$P_{water,top} = \rho_{DNAPL} g h_{DNAPL} - \frac{2}{b}(\sigma_{DNAPL/air}\cos\phi_1 + \sigma_{DNAPL/water}\cos\phi_2) \quad (2)$$

where h_{DANPL} is the height of the DNAPL pool above the water, $\sigma_{DNAPL/air}$ is the surface tension between the DNAPL and air, ϕ_1 is the wetting contact angle at the DNAPL/air interface, and ϕ_2 is the wetting contact angle at the DNAPL/water interface.

The DNAPL will not invade the water as long as the DNAPL/water curvature is concave up, which occurs when $P_{water,top}$ is negative. When the height of DNAPL reaches the critical pressure, where $P_{water,top}$ becomes zero, the DNAPL will invade the water. The criterion for DNAPL entry therefore becomes

$$h_{NAPL,entry} = \frac{2}{\rho_{NAPL} g b}(\sigma_{NAPL/air}\cos\phi_1 + \sigma_{NAPL/water}\cos\phi_2) \quad (3)$$

The critical heights for DNAPL entry calculated using Equations 1 and 3 will be compared to experimental observations.

Experimental Methods

Glass parallel plates with an aperture of 0.03125 cm were sealed with epoxy on the sides and bottom to create an analog dead-end fracture. The dimensions of the plates were 15.2 cm × 20.3 cm. Water was manually injected into the top of the fracture using a syringe to partially saturate the fracture. The injected water flowed to the bottom of the fracture and was injected until it filled about ¾ of the fracture volume. TCE dyed with oil red dye was injected manually into the partially saturated fracture, using a syringe. Two experiments were performed. In the first experiment, TCE was injected slowly but nearly continuously into the fracture until the TCE began to invade the water. Once the TCE began entering the water, the TCE injection was stopped. In the second experiment, TCE was slowly injected until the pool height above the water reached between 1.0 and 1.5 cm, but the TCE did not immediately enter the water. No additional TCE was injected to investigate whether or not the TCE would eventually invade the water. Observations from these experiments were recorded using a digital video camera. The TCE properties from the literature are: ρ_{TCE} = 1460 kg/m^3; $\sigma_{TCE/air}$ = 28.8 mN/m; $\sigma_{TCE/water}$ = 35 mN/m. Using these values and assuming a contact angle of zero, the critical height for TCE entry into the

water is 1.6 cm (using Equation 1) and 2.9 cm (using Equation 3).

Results and Discussion

Experiment 1

In Experiment 1, TCE was injected nearly continuously into the fracture until the TCE began to enter the water. Once the TCE entered the water, the blob of TCE would flow to the bottom of the dead-end fracture. Figure 1 contains a sequence of images showing the TCE entering the water. Note that when the TCE enters the water, the pool of TCE attached to the invading finger is also pulled into the water.

The TCE height required to enter the water was measured from captured video images of the experiment. The corresponding volume of TCE that entered the water for each of these events was also measured. There did not appear to be any correlation between these two parameters. The average height of TCE for entry into the water is 1.7 cm, which is close to the critical height predicted by Equation 1.

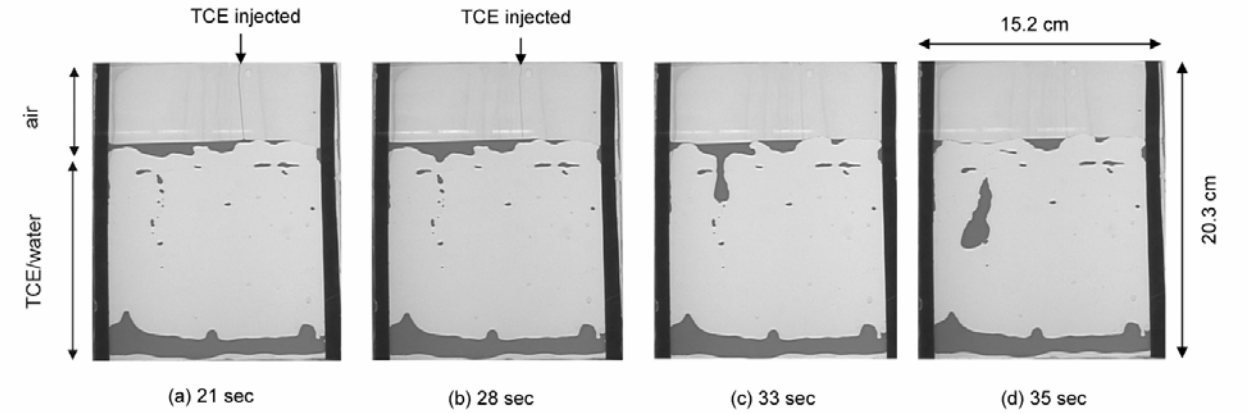

Figure 2. Sequence of images of the TCE (dark gray) entering the partially saturated dead-end fracture. TCE accumulated at the bottom of the fracture is from previous injections. Time denotes seconds after TCE was injected to form the pool observed at the top.

Experiment 2

The purpose of Experiment 2 was to examine if the TCE would eventually invade the water when the height of the TCE was less than the critical height provided by Equation (1). TCE was slowly injected until the TCE pool height above the water reached about 1 cm. After 10 minutes, the TCE pool had still not entered the water, and after 20 minutes it was evident that the pool height had decreased because the TCE had volatilized. The TCE pool was therefore immobile at a height of 1 cm. Since the TCE did not enter the water at this height, additional TCE was added to this pool until its height reached approximately 1.5 cm. The pool remained immobile for nearly 10 minutes, and then began to slowly redistribute itself, forming a finger of TCE. After reaching a height of 2.8 cm, the finger quickly entered the water, pulling the TCE pool connected to it. Another run was performed in which TCE was injected until the pool height reached 1.5 cm. The

TCE once again eventually invaded the water after slowly redistributing itself and forming a finger. This finger slowly increased in length until reaching 2.8 cm before the entire pool of TCE entered the water. The length of 2.8 cm is close to the critical height of 2.9 cm predicted by Equation (3).

The results of these two experiments indicate that DNAPL invasion into a partially saturated dead-end fracture (or the capillary fringe) can occur at two critical heights, which are given by Equations (1) and (3). The first critical height, corresponding to Equation (1), applies when there is a nearly continuous supply of DNAPL. The second critical height, corresponding to Equation (3), occurs when hydrostatic conditions are present. Experiment 2 also demonstrates that time is an important component of fluid instability in this air/DNAPL/water system. The DNAPL pool can remain immobile for a period of time before eventually redistributing itself and entering the water.

Reference

Cohen, R.M. and J.W. Mercer, DNAPL Site Evaluation, Boca Raton, Florida: C.K. Smoley, 1993.

The Fate of Industrial-Organo Bromides in a Fractured Chalk Aquifer

Shai Ezra[1], Shimon Feinstein[1], Itzhak Bilkis[2], Eilon Adar[1,3], Jiwchar Ganor
[1]Department of Geological and Environmental Sciences,
Ben Gurion University of the Negev, Beer Sheva 84105, Israel
[2]Institute of Biochemistry and Food Science,
The Hebrew University of Jerusalem, Rehovot 76100, Israel
[3]Department of Environmental Hydrology and Microbiology, Institute for Water Sciences & Technologies, Ben Gurion University of the Negev, Sede Boqer Campus, 84105, Israel

Introduction

The rapid development of the chemical industry and the enormous variety of its by-products present a complicated challenge to our ability to protect aquifers from chemical pollution. The present study is focused on two compounds of brominated neopenthile alcohol which are used as flame retardants, 3-bromo-2,2-bis(bromomethyl)propanol (TBNPA) and | 2,2-bis(bromomethyl)propan-1,3-diol (DBNPG). These compounds are known to be carcinogenic (Dunnick et al., 1997). Moreover, one of the decomposition products found in this study is the 3,3-bis(bromomethyl)oxetane (BBMO). This product is similar to the more familiar chlorinated molecule 3,3-bis(chloromethyl)oxetane (BCMO) which has been included recently in the USA environmental protection agency (EPA) list of hazardous chemicals. Since the bromine atom is a better leaving group than the chlorine atom (Schwarzenbach et al., 1993), theoretically the BBMO should be more toxic. These chemicals are mainly known as polymerizers, which are fixed to other chemicals by a nucleophilic substitution (Krespan, 1974; 1978). In the same way these chemicals can react with amino acids in proteins, connect different parts, change their structure and damage their functioning.

In low-permeability rocks, like the Eocene chalk underlying the industrial complex studied, discontinuities and fractures permit a preferential flow network where water and solutes move rapidly. This rapid flow magnifies the risk of pollution to the aquifer (Nissim, 1991; Nativ et al., 1995; Lapcevic et al., 1999; Nativ et al., 1999 Dahan, 2000;). The retardation of organic pollutants like the BNA transported through these fractures is governed mainly by diffusion, sorption-desorption and/or biological decay (Lapcevic et al., 1999). Different molecules have different sensitivities to these processes. Therefore, movement through the fracture could cause differential effects on their relative concentrations (Schwarzenbach et al., 1993; Landmeyer et al., 1998; Broholm et al., 1999).

Methods

Sampling: A groundwater monitoring network has operated in the studied aquifer since 1997. This monitoring network today includes 87 boreholes and ten surface sampling points scattered around and in the polluted aquifer. The boreholes are sampled annually for analyses of specific inorganic and organic solutes (Nativ and Adar, 1997).

Extraction and analysis: 250 ml water samples were filtered through 0.45 micron membranes and 0.5% methanol was added to the filtrate solution. The solution was passed though Envi^{TM}-18 disk by vacuum. The disk was left 15 minutes under vacuum and then was washed with 12ml of dichloromethane. The dichloromethane solution was concentrated to 1 ml. 1 μl of this extract was injected into a gas chromatograph-mass spectrometer (GC-MS) equipped with a DB-5 fused silica column (30 m, 0.25 mm i.d., 0.25 μm film).

Chemical Degradation Experiments

The chemical stability of the TBNPA and DBNPG was studied in pH ranging from 9.5 to 7, using different pH buffers (the pH measured in the groundwater is usually basic, ranging between 6.6 and 10.7) and temperature range between 25°C to 70°C. The batch experiments were analyzed for BNA concentration, bromide concentration, and pH.

Results and Discussion

The Eocene aquifer underlying the industrial complex is heavily polluted with an enormous variety of organic contaminants, many of which are yet to be identified. The TBNPA and the DBNPG are among the major semi-volatile contaminants in the study area. The wide distribution of the TBNPA and the DBNPG is probably due to their good solubility (2 and 20g/L, respectively) and resistance to the retardation process.

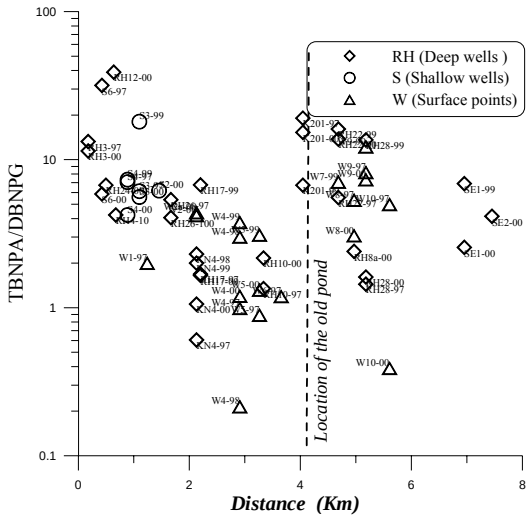

Figure 1. Variation in the TBNPA/DBNPG ratio along a flow gradient.

Spatial variations in the ratio of TBNPA to DBNPG were detected in the groundwater in the monitoring wells (Figure 1). Clearly, the ratio TBNPA/DBNPG decreases with distance from the source factory at least as far as the wastewater evaporation ponds, where the ratio goes up again and a second, less clear, decrease of the ratio with distance begins. Wastewater evaporation ponds there are known to have been leaking (Nativ and Adar, 1997). The solute composition in the monitoring boreholes is a function of: (1) initial composition of the leakage; (2) the degree of dilution and mixing; and (3) the retardation processes that occur in the fractures. Since these

contaminants have the same source, mixing in the aquifers could not cause change in ratio. Such systematic spatial change in ratio can arise from differential effects of the retardation processes on these chemicals. The retardation of organic pollutants in the fractures is governed mainly by diffusion, sorption-desorption and/or biological decay (Lapcevic et al., 1999).In low-permeability rocks such as the Eocene chalk, diffusion becomes the dominant transport mechanism between the fracture and the matrix (Grisak and Pickens, 1980; Polak et al. in press; Witthuser et al. 2000). There is negative correlation between the size or weight of a molecule and its diffusion coefficient in water (Hayduk and Laudie, 1974). The molecular weights of TBNPA and DBNPG are 324.8 and 261.9 respectively. Hence according to the Hayduk and Laudie (1974) correlation, the diffusion coefficient (D_e) of TBNPA is slightly smaller then that of DBNPG, and the ratio TBNPA/DBNPG is expected to increase as a function of diffusion, and hence diffusion appears unlikely to be the mechanism for the change in the ratio observed.

TBNPA is an order of magnitude less soluble then DBNPG therefore it is reasonable to assume that TBNPA will preferentially move into the solid phase. The differential sorption constants of these two compounds were estimated using the EPIWIN model (a code used by the EPA). This model calculates the sorption constant to soils (K_{oc}). Although soils contain much higher amounts of organic matter, we can still learn from this model about the difference in sorption constants. The K_{oc} values for TBNPA and DBNPG show an order of magnitude difference (23 vs. 1, respectively). Apparently, the anticipated effect of a greater TBNPA sorption coefficient agrees, in principle, with the observed variation in their molecular ratio.

Nevertheless, the white Eocene chalk is lean in organic matter and its K_d values determined for other organic molecules suggest very low sorption capacity (Wefer-Roehl et al., 2001). Moreover, sorption to the chalk matrix is also restricted by the relatively slow diffusion rate. However, this apparent contradiction does not preclude the possibility that effective sorption does take place within the fractures.

Figures 2 A and B show the concentration of TBNPA and DBNPG, respectively, to bromine in the water sampled from the monitoring wells. The factory producing TBNPA and DBNPG is the main source of bromide. The linear curve represents a mixing curve between fresh water and the concentrations measured in the industrial sewage. In Figure 2A all but one sample are either on or below the sewage dilution line. Assuming that the sewage composition has not changed dramatically over the years, we can infer that the main processes affecting TBNPA are dilution (distribution along the curve) and retardation (distribution below the curve). In contrast, a large number of the DBNPG concentrations are placed above the sewage dilution line (Fig. 2B). If the sewage sample is representative, these points are probably the result of DBNPG produced in the subsurface. This production could take place either via biodegradation that does not culminate in complete mineralization, or via chemical transformation. Theoretically, when comparing the TBNPA and the DBNPG structures, and the variations in their ratios TBNPA could be used as a source material for the production of DBNPG.

The steric structure and crowding of the bromine group delay enzymatic degradation and provide resistance to biological reactivity (Ashby et al., 1984). Furthermore, when we consider biodegradation of such resistant products, we should take into account that in most cases this product comes with other pollutants, which are preferentially degraded by the microorganisms. Biodegradation modeling on TBNPA and DBNPG using the EPIWIN code estimates for both,

based on their structure and functional groups, reveals relatively high resistance to biodegradation under aerobic conditions, with somewhat higher resistance of the TBNPA molecule. According to these models the TBNPA/DBNPG ratio should increase, in contrast to our field observation.

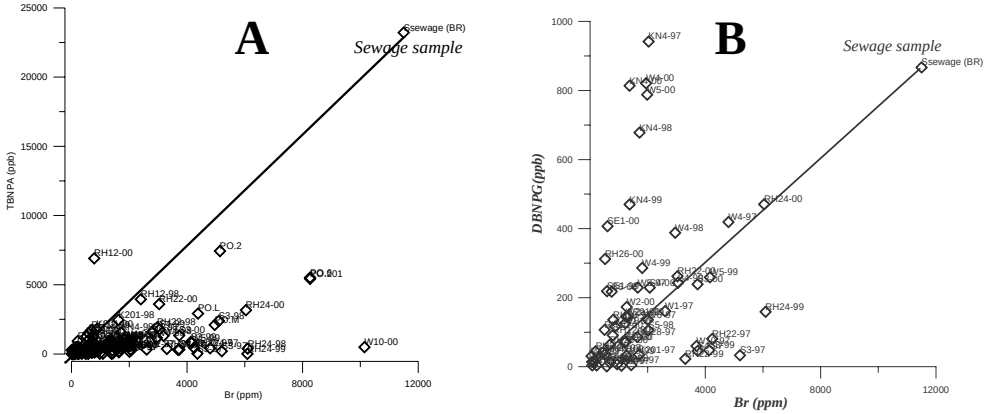

Figure 2. (A) TBNPA vs. bromide concentrations, in the groundwater and in the wastewater (sampled from the sewage line) on site, (B) DBNPG vs. bromide concentrations, in the groundwater and in the wastewater on site.

The bromine atoms are considered relatively good leaving group. It is therefore reasonable to assume that one of the bromine atoms in the TBNPA is replaced by a hydroxyl group during hydrolysis and as a result TBNPA is transformed to DBNPG (+ Br^-). Nevertheless, testing of the TBNPA stability in basic conditions reveals another degradation product. This degradation product was identified by GC-MS and NMR analysis as BBMO. The transformation rate of TBNPA depends on the OH concentration and its pseudo activation energy is 23.5 $Kcal*mol^{-1}*K^{-1}$. BBMO is present in the aquifer but is not known to occur in any of the industries draining into the disposal system. Their source was not identified until the present study. Our results indicate that this compound is product of TBNPA decomposition. Preliminary experiments show that the activation energy of the decomposition of DBNPG in the study condition (different pH) is smaller. According to these activation energies the TBNPA/DBNPG ratio should increase, in contrast to our field observation, as noted above for the biodegradation models (Figure 1).

Systematic experiments of diffusion, sorption, biodegradation and chemical degradation will provide a better understanding of the spatial pattern shown in Figure 1 and the retardation mechanisms. This will enable development of a large-scale model that integrates flow, transport, degradation and sorption of BNA's contaminants in fractured chalk formation and will: (1) help to determine remediation strategy for the polluted aquifer and (2) permit the use of the BNA compounds as tracers inherent to the system for analysis of water and contaminants in the aquifer.

References

Ashby, J., Callander, R.D. and Gilman, D., 1984: Lack of mutagenicity to S. typhimurium of neopentyl bromide and pentaerythrityl tetrachloride: relation to chemical structure. Mutation Research, 140: 71-74.

Broholm, K., Hansen, A. B., Jorgensen, P. R., Arvin, E. and Hensen, M., 1999. Transport and biodegradation of creosote compounds in a large, intact, fractured clayey yill column. Journal of Contaminant Hydrology, 39, 331-348.

Dahan, O., 2000: Water flow through fractures in unsaturated chalk. Ph.D. Thesis., The Hebrew university of Jerusalem.

Dunnick, J.K., Heath, J.E., Farnell, D.R., Prejean, J.D., Haseman, J.K. and Elwell, M.R. (1997). Carcinogenic activity of the flame retardant, 2,2-bis(bromomethyl)-1,3-propanediol in rodents, and comparison with the carcinogenicity of other NTP brominated chemicals. Toxicol Pathol, 25(6): 541-548.

Grisak, G.E. and Pickens, J.F., 1980: Solute transport through fractured media. 1. The effect of matrix diffusion. Water Resources Research, 16: 719-730.

Hayduk, W. and Laudie, H., 1974. prediction of diffusion coefficients for non electrolytes in dilute aqueous solutions. AIChE, J., 20, 611-615.

Krespan, C.G. 1974. Macroheterocycles. The oxetane function spiro to macrcrocyclic polyether rings. Journal of Organic Chemistry 31(16): 2351-2355.

Krespan, C.G. 1978. The □effect in□-Chlorofluoro ketones. Journal of Organic Chemistry 43(4): 637-640.

Landmeyer, J.E., Chapelle, F.H., Petkewich, M.D. and Bradley, P.M., 1998. Assessment of natural attenuation of aromatic hydrocarbons in groundwater near a former manufactured-gas plant, South Carolina, USA. Environmental Geology, 34(4), 279-292.

Lapcevic, P.A., Novakowski, K.S. and Sudicky, E.A., 1999: Groundwater flow and solute transport in fractured media. In: Handbook of Groundwater Engineering. CRC Press 1717-39.

Material safety data sheet MSDS. 1999 version 4, MSDS code: 8324. Bromine Compounds LTD.

Nativ, R. and Adar, E., 1997: Assessment of groundwater contamination in the Northern Negev industrial complex. Reported submitted to the Industrial Council.

Nativ, R., Adar, E.M. and Becker, A., 1999: Designing a monitoring network for contaminated ground water in fractured chalk. Ground Water 37: 38-47.

Nativ, R., Adar, E.M., Dahan, O. and Geyh, M., 1995: Water recharge and solute transport through vadose zone of fractured chalk under desert conditions. Water Resources Research, 31: 253-261.

Nissm, I., 1991. Characterization of a hydrological system in an arid zone— the (Eocene) Avdat Group chalk, central and northern Negev, Israel. M.Sc. Thesis., The Hebrew university of Jerusalem (in Hebrew).

Polak, A., Grader, A.S., Wallach, R. and Nativ, R., in press: Measurements of diffusion into chalk using computerized tomography. Water Resources Research.

Schwarzenbach, R.P., Gschwend, P.M. and Imboden, D.M., 1993: Environmental organic chemistry. John Willey & Sons, NY.

Wefer-Roehl, A., Graber, E.R., Borisover, M.D., Adar, E., Nativ, R. and Ronen, Z., 2001: Sorption of organic contaminants in a fractured chalk formation. Chemosphere, 44: 1121-1130.

Witthuser K., Hotzl, H., Reichert, B., Stichler, W. and Nativ, R., 2000: Laboratory experiments for diffusion transport processes in fractured chalk. IAHS-AISH-Publication, 262, 303-308.

Evaporation from Surface-Exposed Fractures: Potential Impact of Atmospheric Convection and Salt Accumulation

Noam Weisbrod[1], Maria Ines Dragila[2], Clay Cooper[3], Christopher Graham[2], James Cassidy[2]
[1]Department of Environmental Hydrology & Microbiology, Institute for Water Sciences & Technologies, Blaustein Institutes for Desert Research, Ben-Gurion University of the Negev, Israel
[2]Department of Crop & Soil Sciences, Oregon State Univeristy, Corvallis, OR, USA
[3]Division of Hydrologic Sciences, Desert Research Institute, Reno, NV, USA

Introduction

It is widely acknowledged that fractures in unsaturated rock can play a major role in enhancing solute transport from the land surface to underlying aquifers (Nativ et al., 1995; Faybishenko et al., 2000; Evans et al., 2001). Numerous field and laboratory observations have shown that solute transport can be much faster through fractures than porous matrix. While most efforts have been extended toward better understanding of fractures as a fast conduit for liquids, few studies have focused on the potential impact of gas (air and water vapor) flow through fractures, and even fewer have investigated the role of pore-water evaporation and the formation of salt crust on fracture surfaces.

Motivation.

This work is motivated by observations associated with a series of field experiments carried out in the fractured chalk of the Negev Desert in Israel (Dahan et al., 1999; Weisbrod et al., 2000, 2002). These experiments explored the concentration and composition of salt solutions that migrated through natural fractures following long drying events, as well as the mineralogical composition of salt crust at and near exposed fracture surfaces up to one meter below the land surface.

These results showed that (1) salt precipitated on fracture surfaces and high concentrations of salts in the pore water were observed down to a depth of one meter (Weisbrod et al., 2000); and (2) high solute concentrations (up to EC/EC_0 ~13, where EC is the electrical conductivity of the effluent and EC_0 is the electrical conductivity of the influent) were measured from effluent flushed from the upper meter of a fracture during the first two hours of a flow experiment. Solute concentration decreased to $EC/EC_0 < 2$ over time (Figure 1). Subsequent flow events carried out approximately 6 months after the first flow experiment resulted in a similar pattern (Dahan et al., 1999; Weisbrod et al., 2000; 2002; Figure 2), suggesting that salt precipitated on fracture surfaces during the subsequent 6-month dry season. In several cases in the Negev desert it was observed that fractures with large exposed apertures were apparently hydraulically sealed with precipitated salts, mainly gypsum, barite, and selectite. This observation suggests that evaporation from fractures exposed to the land surface may enhance salt precipitation until eventually the aperture becomes completely clogged.

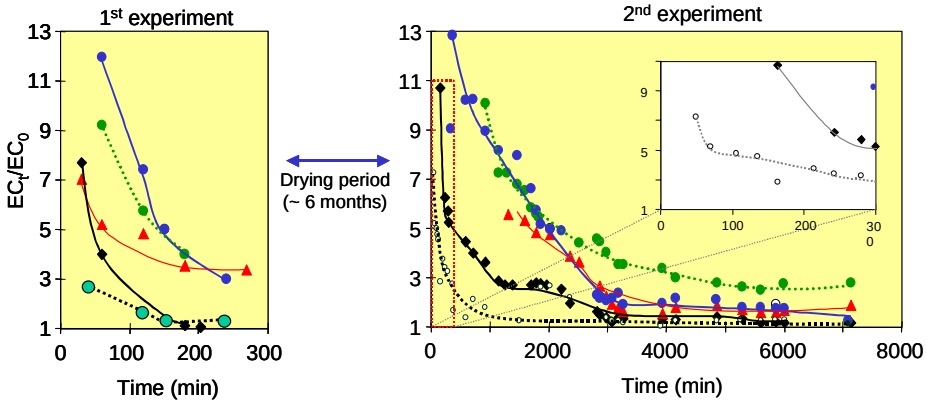

Figure 1. Relative EC (electrical conductivity) of the outflows drained through a natural fracture into a sampler during two field experiments (5 and 119 h). The inset displays a close-up of the first 300 min of the second flow experiment. Each line represents a different flow channel (after Weisbrod et al., 2000).

Conceptual Model

There are several mechanisms to which massive accumulation of salt on and near fracture surfaces can be attributed. The hypothesis we are testing is that cool nighttime temperatures, typical in high deserts, will impose an unstable temperature gradient leading to convection of the gas phase (air and water vapor) within the fracture. By venting the moist vapor to the land surface, the fracture may dry out, enhancing lateral movement of liquid water from the adjacent matrix toward the fracture surface. Evaporation of this pore water could precipitate dissolved solids on the fracture surface, resulting in the formation of a crust. During the wet season, infiltrating precipitation would dissolve the salt, resulting in a slug of salt to the underlying aquifer. This mechanism is schematized in Figure 2. This hypothesis is being tested by means of a combination of small- and large-scale laboratory experiments, modeling, and measurements within in situ fractures.

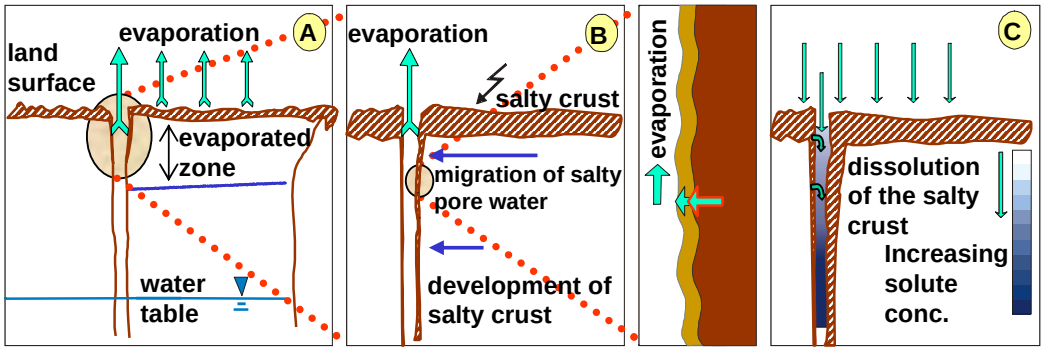

Figure 2. Schematic diagram of a model describing the cyclic sequence of minerals precipitation on and near the fracture surface during the dry season, and their subsequent flushing to the groundwater during the rainy season. Pore water evaporates from both the land surface and the surfaces of fractures (A). Evaporation triggers capillary transport of both water and soluble salts from the bulk rock matrix towards fracture surfaces, resulting in salt accumulation on the fracture walls (B). Recharge events that activate water flow through fractures result in the dissolution of the precipitated salts and the dissolved ions are transported toward the water table (C) (modified from Weisbrod et al., 2000).

Laboratory observations: Free convection of gas in a fracture has been observed in the laboratory using rock slabs with a controlled temperature gradient (Figure 3). Dry ice was placed above two slabs (30 cm x 30 cm) separated by a 5 mm gap and oriented at 5º from vertical, with the aperture sealed on three sides (open on top). Ice was placed such that thermometers placed above the fracture and within the aperture measured a temperature difference of 20ºC, which could be typical of desert conditions in which the nighttime atmospheric air is much cooler than air within the upper several meters of the ground.

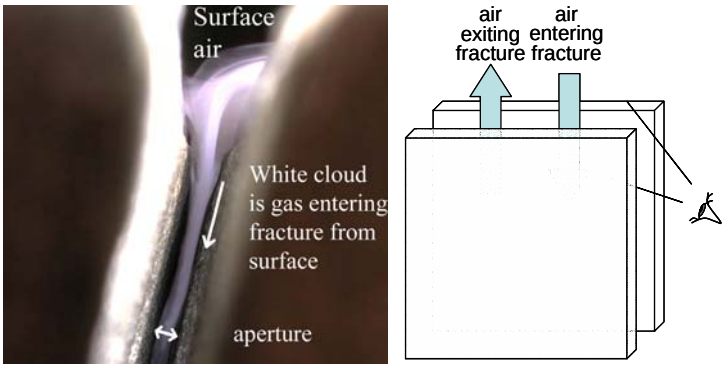

Figure 3. Photograph showing CO_2 gas and water vapor (tracer) moving downward into aperture between parallel rock slabs. Gas exits the fracture at another location that is in the plane of the fracture. Right hand sketch shows perspective taken by photograph.

This proof-of-concept experiment is being expanded to systematically investigate convection through a range of boundary and initial conditions. Experiments are being conducted in a climate-controlled chamber where cores are allowed to evaporate under diffusive (no convection) and convective (free-evaporation) conditions. Preliminary data taken for sandstone cores (evaporative area ~ 25 cm^2) show evaporation rates under convective conditions to be approximately three times higher than under diffusive conditions (Figure 4). Experiments are continuing to study (1) long-term effects of salt crust buildup on evaporation rate; (2) long-term accumulation rate of precipitate for diffusive and convective conditions; and (3) the impact of core permeability and matric potential on salt-water evaporation.

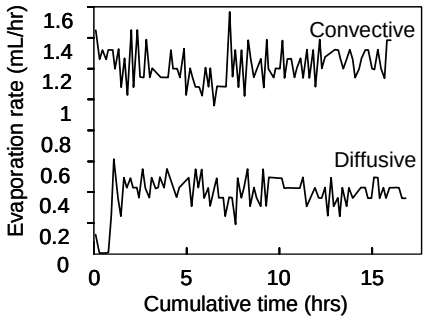

Figure 4. Evaporation rate under convective and diffusive conditions in a fractured rock core.

Theoretical Considerations

Convection theoretically occurs in fractures when the Rayleigh number (Ra), which compares buoyant and viscous forces, exceeds a critical (Rac) value. For convection of gas between smooth-walled parallel plates (where temperature-dependent volume changes of gas are considered negligible, such that there is no latent heating due to gas compressibility), Ra is defined as (Nield, 1982)

$$Ra = \frac{\beta \Delta T g k L}{\alpha \nu} \tag{1}$$

where β is the coefficient of thermal expansion, ΔT is the temperature difference between the atmosphere and the fracture air over a length scale L, g is the gravitational constant, k is the fracture permeability, α is the thermal diffusivity, and ν is the dynamic viscosity. Based upon theoretical considerations, onset would occur for $0 < Ra_c < 4\pi^2$ (Nield, 1982). The value of Ra_c is a function of the boundary conditions (Nield and Bejan, 1999).

Convection in fractures may occur due to conductive diurnal heating and cooling from the lower atmosphere. The following equation (*Hillel,* 1998) models conductive temperature changes in soil as a function of diurnal and annual time scales:

$$T(z,t) = T_{ave,y} + A_y \left[\sin\left(\omega_d t - \frac{z}{d_y} \right) e^{\frac{-z}{d_y}} \right] + A_d \left[\sin\left(\omega_d t - \frac{z}{d_d} \right) e^{\frac{-z}{d_d}} \right] \tag{2}$$

where T is temperature, A is the amplitude of the daily and yearly temperature variation, ω is the radial frequency of the temperature variability (2π frequency), t is the time, z is the depth (positive) from the land surface, d is the damping (or characteristic) depth (defined below), and the subscripts d and y refer to daily and yearly values, respectively. The damping (or characteristic) depth, $d_d = (2K/C_v\omega_d)^{0.5}$, (where K is the thermal conductivity and C_v is the volumetric heat capacity) is the depth at which the temperature amplitude is reduced by 1/e of the soil surface temperature amplitude (i.e., the e-folding depth). Values of $T_{ave,y}$ = 25ºC, A_y = 10º, A_d = 10º, ω_d and ω_y is $2\pi/24$ hrs and $2\pi/365$ days, d_d = 0.123 m, d_y = 2.35 m were used to map the diurnal temperature profile of fracture air (Figure 5).

Equation (2) represents the fracture wall temperature. If it is assumed that in the absence of convection, air temperature will equilibrate to the temperature of the fracture walls, then the model predicts a sufficient unstable gradient would be imposed and fracture venting would begin near the surface at ~4:00 PM, and progress downward reaching a maximum depth of 40 cm at ~3:00 AM. This is determined by calculating *Ra* for the destabilizing temperature gradients and not merely by the presence of such a gradient. A stable temperature gradient in the upper 10 cm would return at ~4:00 AM. Internal convection may continue until approximately 9:00 AM at depths between 10-40 cm. This shortens the distance over which diffusion is the primary venting mechanism for moist fracture air.

Convective air velocity can be calculated assuming that density is affected only by temperature—(Equation (1)). For a 5 mm aperture (cubic law assumption), ΔT = 10ºC, ρ = 1.2 kg/m^3, β = 3.67

$\times 10^{-3}$ ºC^{-1}, μ = 1.82 x 10^{-5} kg/m-s, the vertical velocity would be ~ 5 $\times 10^{-2}$ m/s.

$$w = \frac{k\rho g\beta\Delta T}{\mu} \tag{3}$$

This would be the characteristic velocity of the streamlines in a closed convection cell under steady-state conditions, Equation (3) represents a maximum value for velocity, as it does not take into account reduction in velocity due to temperature loss from thermal diffusion, effect of fracture aperture variability, or fracture surface texture. The value for velocity was used to determine a maximum theoretical moisture loss from the fracture of 2 x 10^{-4} kg/m^{2}s (water evaporated per unit area of fracture wall face) assuming water availability is not limited, and the initial relative humidity of atmospheric air entering the fracture is ~50%.

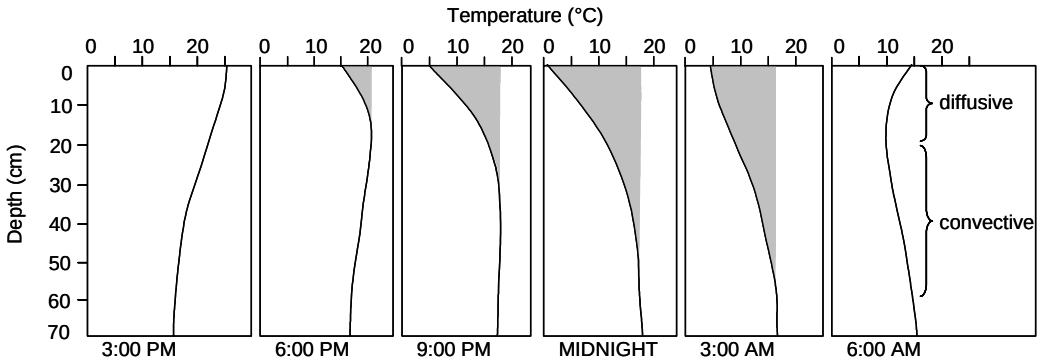

Figure 5. Soil temperature profile on a summer day for different times of the day. Shading indicates approximate depth of possible convection cell.

Modeling

The EWASG module of the TOUGH2 program (Pruess et al., 1999) is being used to build a numerical model to test the validity and sensitivity of the conceptual model for a range of climatologic, hydrologic and fracture geometry scenarios. The EWASG (**E**quations of state for **WA**ter, **S**alt and **G**as) module of TOUGH2 was developed to model three-component fluid mixtures of water, salt (NaCl) and non-condensable gas in porous media. The salt precipitation and fracture flushing cycle is modeled for both convection and diffusion dominated regions (e.g., Figure 6). Initial results suggest that the conceptual convection driven model could account for nearly a threefold increase in salt precipitation and subsequent flushing to groundwater, confirming the preliminary laboratory cores studies. Salt precipitation rate is strongly influenced by rock permeability. Work continues for comparing the salt flux from fracture flushing to what would be expected to move down the porous matrix, and thereby identify the importance of this mechanism in various climatic regimes, and its relative importance in hydrologic systems.

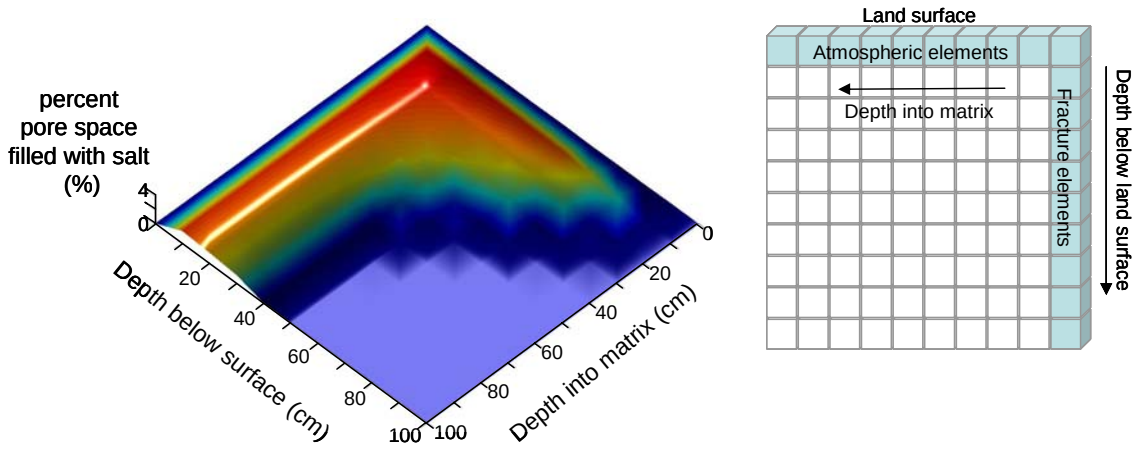

Figure 6. TOUGH simulation of cumulative salt precipitation in a rock slab after 100 days of simulation. Element size is 10 × 10 cm. Evaporation allowed along atmospheric and fracture elements. No flux condition on all remaining boundaries. Evaporation rate is high along the soil surface and within the fracture down to 80 cm, where convection dominates vapor loss. Salt precipitation is reduced dramatically below 80 cm where diffusion processes control vapor loss in the fracture. First row and first column of blocks (gray shading) are modeled as atmosphere blocks, the remainder are modeled as clay-loam soil blocks. Color is used as visualization aid for third axis (blue to red is low to high value).

Ongoing Research

In addition to furthering our research on each of the above components, fieldwork on *in-situ* fractures is in progress to study the impact of depth (distance from land surface) on salt composition and distribution along fracture surfaces and within the matrix near the fracture, and its relationship to fracture properties. This will be corroborated with large-scale laboratory studies in which atmospheric conditions are being carefully controlled to enable quantitative monitoring of evaporation from the fracture.

Acknowledgments

This research is partially funded by the NSF (#0208384). Current efforts of large-scale laboratory experiments and field-scale work are funded by the US-Israel Binational Science Foundation, BSF (contract #2002058) and the International Arid Lands Consortium, IALC.

References

Dahan, O., Z. Ronen, R. Nativ, E. M. Adar, and B. Berkowitz. 1999. Field observation of flow in a fracture intersecting unsaturated chalk. *Water Resources Research* **35**:3315-3326.

Evans, D. D., T. C. Rasmussen, and T. J. Nicholson. 2001. Flow and Transport Through Unsaturated Fractured Rock: An Overview. Pages 1-18 *in* D. D. Evans and T. J. Nicholson, editors. *Flow and Transport Through Unsaturated Fractured Rock.* American Geophysical Union, Washington, DC.

Faybishenko, B., P. A. Witherspoon, and S. M. Benson. 2000. *Dynamics of Fluids in Fractured Rock*, Geophysical Monograph Series 122. American Geophysical Union, Washington, DC.

Hillel, D. 1998. *Environmental Soil Physics*. Academic Press Publishers.

Nativ, R., E. Adar, O. Dahan, and M. Geyh. 1995. Water recharge and solute transport through the vadose zone of fractured chalk under desert conditions. *Water Resources Research* **31**:253-261.
Nield, D.A., 1982, Onset of convection in a porous layer saturated by an ideal gas, *Int. J. Heat Mass Transfer*, v. 25(10), pp. 1605-1606.
Nield, D.A., and A. Bejan. 1999, *Convection in Porous Media*, Springer-Verlag, 2nd edition, 546 pp.
Pruess, K., C. Oldenburg, and G. Moridis. 1999. TOUGH2 User's Guide, Version 2.0. Lawrence Berkeley Lab Report LBNL-43134.
Weisbrod, N., O. Dahan, and E. M. Adar. 2002. Particle transport in unsaturated fractured chalk under arid conditions. *Journal of Contaminant Hydrology* **56**:117-136.
Weisbrod, N., R. Nativ, E. M. Adar, and D. Ronen. 2000. Salt accumulation and flushing in unsaturated fractures in an arid environment. *Ground Water* **38**:452-461.
White, F. M. 1991. *Viscous Fluid Flow*, 2nd Ed. McGraw Hill.

Contaminant Discharge from Fractured Clays Contaminated with DNAPL

Ronald W. Falta
School of the Environment, Clemson University
Clemson, SC

Reynolds and Kueper (2002) provide some compelling analyses of the behavior of DNAPLs in fractured clays. Much of their paper focuses on the breakthrough time for a DNAPL spill to penetrate a fractured clay aquitard. They have also simulated the long term behavior of the contaminants in the fractured clay following the end of a DNAPL release to the fracture. Specifically, they considered a case where 5 ml of various DNAPLs were spilled into a 30 μm aperture fracture in a 3 m thick clay under a DNAPL pool capillary pressure of 4300 Pa. Given the fracture pore volume (for a unit thickness) of 90 mL, this spill amounts to an average DNAPL saturation of a bit over 5%. The clay in their simulation has a very low permeability (1×10^{-17} m^2), a high fraction of organic carbon (.01), and a moderate porosity (.3). Reynolds and Kueper found that under these conditions, the DNAPL penetrated only about half of the fracture depth before the 5ml was depleted from the source. Following the DNAPL release, they simulated the immediate flushing of the fracture with clean water under a gradient of .01. Considering the fracture permeability of 7.5×10^{-11} m^2, this corresponds to a Darcy velocity of 0.64 m/day, or a water flow rate of 19.2 ml/day. Due to the very large surface area and small volume of the fracture, the DNAPL only persists in the fracture for a few hours or days, and essentially all of it diffuses into the clay matrix, despite the clean water flush of the fracture. A significant result of their analysis is that the chemical concentration leaving the fracture remains above regulatory limits for 1,000 years or more under this scenario.

Because of the implications of the Reynolds and Kueper (2002) study on the long term behavior of DNAPL components in fractured systems, it is valuable to examine a few similar cases using different parameter values. A brief numerical study was performed using the T2VOC compositional multiphase flow simulator, developed at the Lawrence Berkeley Laboratory (Falta et al., 1995). The simulation grid is similar to that used by Reynolds and Kueper (2002), and it explicitly discretizes a single fracture and the clay, with a very fine grid spacing (~100 μm) in the clay near the fracture. The fracture aperture is either 30 or 100 μm, the clay is 3 m thick, and it has the same properties as in the Reynolds and Kueper case. The DNAPL is given the properties of TCE.

In order to focus mainly on the long term behavior of this TCE source, the DNAPL emplacement process is simplified somewhat compared to Reynolds and Kueper. Instead of simulating a 5 ml DNAPL spill, the initial condition in these simulations is a DNAPL residual saturation of 10% or 3% throughout the fracture, depending on its aperture. This corresponds to an initial TCE mass of 13.56 g for either fracture. Due to symmetry, only half of the fracture/clay is simulated, and a no-flow outer boundary at 1.45 m corresponds to an equivalent fracture spacing of 2.9 m. The simulations each consist of two parts. In part 1, the 13.56 g of TCE DNAPL is placed in the fracture with no water flow, and allowed to equilibrate for a period of 20 years. Interestingly, the DNAPL phase disappears from the fracture in a few hours in this scenario, due to aqueous phase diffusion into the clay matrix. This is somewhat faster than Reynolds and Kueper simulated, but

their DNAPL saturations in the upper part of the fracture were higher due to their DNAPL release scenario. As Reynolds and Kueper (2002) have pointed out, behavior of DNAPL in the fracture is very sensitive to the precise initial and system conditions.

Figure 1 shows the aqueous concentration of TCE in the fracture over the 20 year equilibration period for the case that uses the same parameter values as in the Reynolds and Kueper study. Once the DNAPL phase disappears, the concentration in the fracture shows a logarithmic decline down to a value of about 2270 μg/L, a reduction of a factor of 440, due to diffusion into the matrix. All of the initial TCE mass remains in the volume.

Part 2 of the simulation models clean water flushing of the fracture as in Reynolds and Kueper at a Darcy velocity of 0.64 m/day, or a flow rate of 19.2 mL/day. At 100 years, the concentration gradients in the clay have become very low, but the fracture effluent concentration remains fairly high, and only about 7% of the TCE has been removed from the system. Even at 2851 years (the end of the simulation), a substantial fraction of the TCE remains in the system, and the fracture effluent concentration is still about 240 μg/L. In other words, in nearly 3000 years of fracture flushing, the fracture concentration has only dropped by a factor of about 10, and much of that drop could be attributed to further diffusion into the clay, rather than the effects of TCE removal by flushing the fracture.

The upper curve with the solid squares in Figure 2 shows the variation of effluent fracture TCE concentration as a function of time for this simulation. As noted by Reynolds and Kueper, the removal by fracture flushing occurs in this case on a time scale measured in the thousands of years, however it should be recognized that this scenario did not consider any type of chemical or biological degradation of the TCE. To illustrate the possible importance of TCE degradation, a second simulation was run, using identical parameters, but assuming that the TCE can degrade in the aqueous phase, with a half life of 10 years. This simulation also uses a lower fraction of organic carbon in the clay compared to the previous simulation, 0.002 instead of 0.01. The same initial TCE mass is present in both cases. The fracture effluent from this case with TCE degradation is shown as the curve with solid triangles in Figure 2. While the early time behavior is similar to the simulation with no degradation, a large effect is seen beginning at about 10 years. The fracture effluent concentration drops below 1 μg/L in less than 300 years in this case.

The amount of flushing that takes place in a 30 μm fracture is relatively small due to the small area of the fracture. As the fracture aperture increases, the flow rate through the fracture increases approximately as the cube of the aperture. Thus, a 100 μm fracture would conduct 37 times more water than a 30 μm fracture under the same gradient. A pair of additional simulations were carried out using a 100 μm fracture aperture. The other system parameters were maintained at their previous values, and the total TCE mass initially in the fracture was the same as in the previous cases. Following the 20 year equilibration period, the fracture was flushed at a Darcy velocity of 7.1 m/day, or a flow rate of 710 ml/day, corresponding to a hydraulic gradient of 0.01. The simulated fracture effluent is shown in Figure 3 for a case with TCE degradation (solid triangles), and a case without TCE degradation (solid squares). Here, the larger rate of flushing leads to a more rapid depletion of the TCE mass in the clay, and the curves begin to drop after about 1 year. Although the decline in fracture concentration is more rapid in this case than it was for the 30 μm case, the time scale for achieving regulatory limits in the fracture is still on the

order of 1000 years for the case without any TCE degradation. As would be expected, including TCE degradation speeds up this process, and the fracture concentration drops below 1 μg/L at about 150 years.

Considering the potentially large timeframes for cleaning up fractured clays, it is useful to try to put the fracture discharge into some perspective. Although the fracture has a high permeability, it's cross-sectional area is very small, so its ability to transmit water is limited. Consider, for example, a 30 m by 30 m DNAPL source zone that leads to this sort of contamination of the fractured clay aquitard. If we assume a single set of 30 μm fractures with an average spacing of about 2.9 m (as in the simulation), then we would have 10 contaminated fractures in our source zone. Given the same downward hydraulic gradient (.01), the total water flow rate through the fractures would be (19.2 ml/day*m) (10 fractures)(30 m), or 5.76 liters per day. This rate would be multiplied by the appropriate effluent curve in Figure 2 to get the total TCE discharge through the fractured clay aquitard.

Now, suppose that there was an otherwise pristine aquifer below the contaminated fractured clay. This aquifer would be receiving 5.76 liters of contaminated water per day from the aquitard. By considering the regional flow though the aquifer, one can estimate the dilution factor in the source area. For example, if the aquifer was 6 m thick, with a hydraulic conductivity of 1×10^{-2} cm/s (about 10 Darcy), and if the hydraulic gradient was 4/1,000, then the total water flow through the source region would be about 6,200 liters per day. Thus the dilution factor would be about 1080, assuming some sort of mixing. With this view, the average aquifer TCE concentration would be approximately equal to the regulatory limit at early times for the no-degradation case, and it would decline below the limit in a few years.

For the 100 μm fracture case, using the same scenario, the total water flow rate through the fractures would increase by a factor of 37, up to 213 liters per day, resulting in a lower dilution factor of about 29. Using Figure 3 to compute the average aquifer TCE concentrations, it is clear that they would be well above regulatory limits at early times, and would not drop to acceptable levels until after about 50 to 150 years. Therefore, although contaminants are flushed out of the clay aquitard more rapidly by a larger fracture, contamination near such a fracture is also more likely to lead to a serious degradation of the underlying aquifer.

References

Falta, R.W., K. Pruess, S. Finsterle, and A. Battistelli, T2VOC User's Guide, *Lawrence Berkeley Laboratory Report LBL-36400,* March, 1995.

Reynolds, D.A., and B.H. Kueper, Numerical examination of the factors controlling DNAPL migration through a single fracture, *Ground Water, Vol. 40, No. 4, 368-377*, 2002.

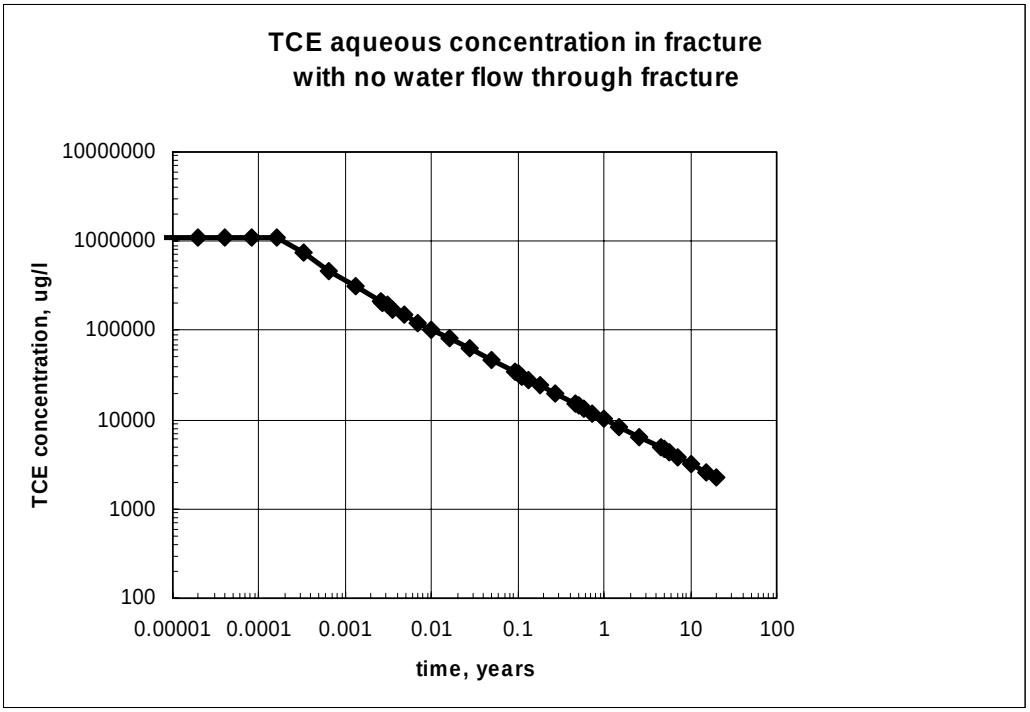

Figure 1. Simulated TCE aqueous concentration in the fracture during the 20 year equilibration period for a 30 micron fracture, with no TCE decay, and a clay foc of 0.01.

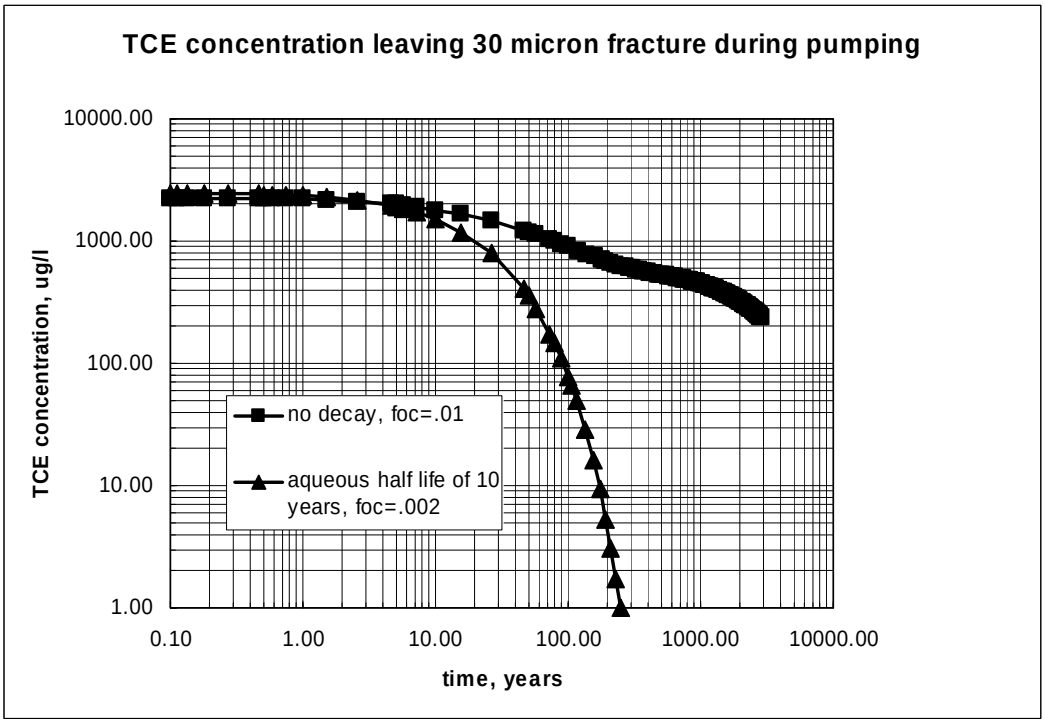

Figure 2. TCE concentration in the fracture effluent assuming a 30 micron fracture with a Darcy velocity of .64 m/day in the fracture.

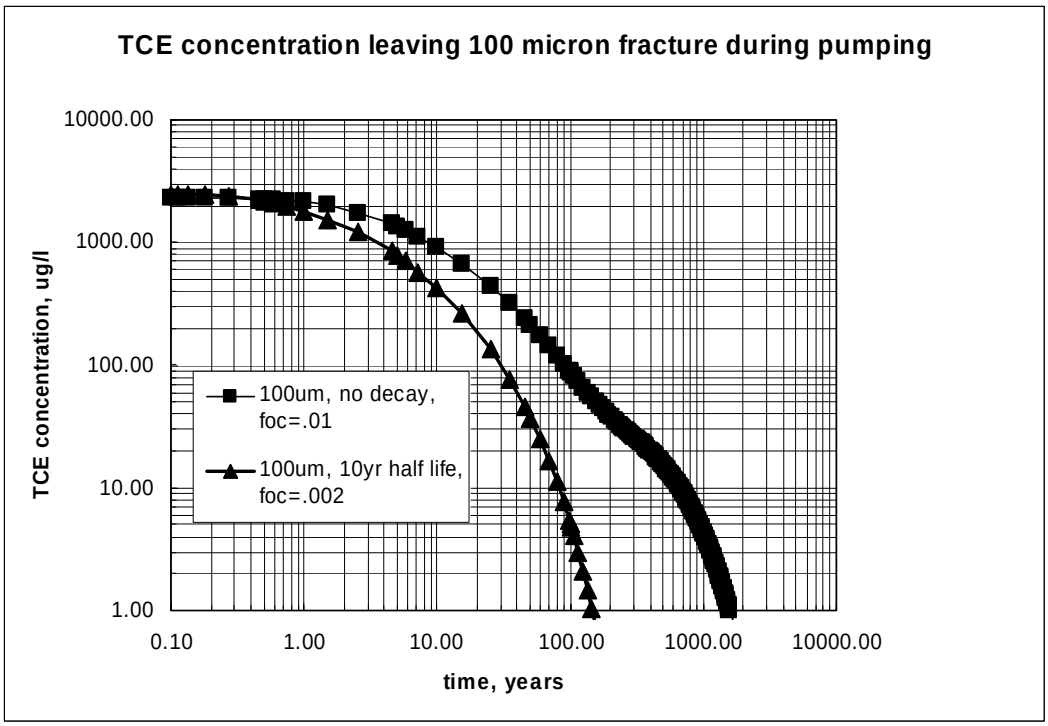

Figure 3. TCE concentration in the fracture effluent assuming a 100 micron fracture with a Darcy velocity of 7.1 m/day in the fracture.

Session 6:
RECENT ADVANCES IN MODELING, SCALING, AND UNCERTAINTY EVALUATION

Why Use Stochastic Fractal Models for Heterogeneous Log (Conductivity) and What Might Cause Such Structure?

Fred J. Molz[1], Mark Meerschaert[2] and Tom Kozubowski[3]
[1] Environmental Engineering, Science and Geology, Clemson University, 342 Computer Court, Anderson, SC 29625. [fredi@Clemson.edu]
[2] Department of Mathematics and Statistics, University of Nevada, Reno, NV 89557-0045. [mcubed@unr.edu]
[3] Department of Mathematics and Statistics, University of Nevada, Reno, NV 89557-0045. [tkozubow@unr.edu]

Where is the order in the hydraulic properties of natural heterogeneous sedimentary materials, upon which an understanding of such properties can be built? Early efforts at understanding used deterministic concepts built around assumed homogeneity within units, or else smooth, gradual variation. This was followed by the rise of stochastic theory in hydrogeology, based initially on treating heterogeneous property distributions as stationary, correlated, random processes. Here, the order was assumed to be in the statistical characterization (probability density functions [PDFs], means, variances, etc.) of the properties themselves or the logarithms of the properties. This approach has had only limited success, because property distributions based on these statistically homogeneous concepts were too regular. The next step in the search for order was to consider statistically heterogeneous concepts that conceptualize heterogeneity in terms of nonstationary stochastic processes with stationary increments, the mathematical basis for stochastic fractals. The hoped-for order then lies in the property or log(property) *increment* PDFs. Such increment PDFs usually display non-Gaussian shapes, with the Levy-stable PDF suggested initially as a candidate distribution. Recent studies show that the Laplace (double exponential) and related distributions (Weibull or "stretched exponential") are better candidates for the observed increment PDFs. There is an interesting type of central limit theorem, based on geometric sums of random variables, that applies to the Laplace PDF (Kotz et al., 2001). Thus, a geometric sum of normal random variables will converge to a Laplace random variable. This, combined with the little-appreciated fact that the Laplace distribution is infinitely divisible, leads to a new type of fractal that we are calling fractional Laplace motion (FLaM) (Meerschaert et al., 2004). The basis for these ideas will be presented, along with the intriguing observation that similar increment distributions are showing up in studies of flow and transport in turbulent fluids.

References

Kotz, S., T.J. Kozubowski and K. Podgorski, The Laplace Distribution and Generalizations: A Revisit with Applications to Communications, Economics, Engineering and Finance, Birkhauser, Boston, 2001.

Meerschaert, M.M., T.J. Kozubowski, F.J. Molz and S.Lu, Fractional Laplace Model for Hydraulic Conductivity, Geophysical Research Letters, in press, 2004.

Percolation-Continuum Modeling of Evaporative Drying: Homogeneous or Patchy Saturation?

H. F. Wang[1], T. E. Strand[1], and J. G. Berryman[2]
[1] University of Wisconsin-Madison
[2] University of California, Lawrence Livermore National Laboratory

Abstract

A pore-scale, percolation model coupled with a continuum model for water vapor diffusion (Prat 1993, 2002) has been implemented to simulate evaporative drying of a rock core. As drying proceeds for smaller grain sizes, the initial, continuous, water cluster breaks up into smaller and smaller clusters with an increasing surface-area-to-volume ratio. Drying times are a function of the number and location of boundary surfaces, but the surface-area-to-volume ratio is approximately the same for a given saturation. For small Bond number (ratio of gravitational to capillary forces), over 90% of water-filled cells are at the air-water interface for water saturation between zero and 40%. Assuming that water-filled pores at the interface behave in a drained fashion, the effective elastic modulus shows overall drained behavior over this saturation range. For larger Bond numbers, the percentage of water-filled cells at the air-water interface decreases rapidly for water saturations between zero and 40%, leading to effective elastic behavior that is representative of patchy saturation behavior.

Introduction

Evaporative drying is a two-phase, immiscible displacement process, which occurs in a variety of earth-science contexts, from the behavior of a nuclear waste repository in the unsaturated zone to laboratory studies for determining how elastic wave velocities vary with water saturation (e.g., Murphy, 1984; Knight and Nolen-Hoeksema, 1990). In common with other drainage processes that involve competition among forces of gravity, capillarity, and pressure, the pore-level detail of water distribution cannot be obtained using continuum models based on averaging over a representative elementary volume (REV). This paper presents results for evaporative drying of laboratory-sized rectangular parallelepipeds using a combined percolation (water phase) and continuum (air phase) model from Prat (1993, 2002). Several permutations of open and closed boundary surfaces are employed. In addition, the simulations are performed for different Bond numbers (ratio of gravity to capillary forces). The simulations are examined qualitatively and quantitatively for the nature of the drying front and for the distribution of water cluster size changes as drying occurs. The results are further examined for estimating elastic moduli and conceptualizing the pattern of matrix saturations in a dual-porosity medium during drying.

Drying Model

The porous medium is represented statistically on a three-dimensional lattice. The lattice periodicity is determined by the mean grain size R_g. Two different distribution functions are

used to represent the non-wetting radii R_{nw} and wetting radii R_w. The non-wetting radius is the minimum radius of curvature on the grain scale and provides the maximum local resistance to drainage, and the wetting radius is the maximum radius of curvature and provides the maximum local resistance to imbibition. The wetting radii are the pores, which are the sites of the lattice, and the non-wetting radii are the throats, which are the bonds of the lattice emanating from the sites with a coordination number Z_c representing the average number of connections between sites.

The coupled modified invasion percolation (MIP–continuum model (Prat, 1993, 2002) is implemented at each percolation step as follows:

1. Individual water clusters are identified.
2. The largest non-wetting radius at the air-water interface of each cluster is invaded. The percolation events in each water cluster are treated independently. Air invasion occurs as long as gravitational force exceeds the minimum capillary force on the interface.
3. The evaporation flux is calculated at the boundary of each cluster.
4. The diffusion model is coupled with the percolation model by invading the cluster that loses a pore volume due to evaporation. Percolation events are temporally sequenced among water clusters. Water vapor diffusion in the air phase means that there are no trapped clusters.

Drying Simulation Results

Three simulations with different boundary conditions are shown in Figure 1. Each panel represents a vertical cross section of the initially 100% water-saturated sample, where black represents a water-filled cell and white represents an air-filled cell. Each vertical column follows the drying for a particular set of open surfaces. Each horizontal row depicts the water-air distribution at a given saturation calculated as a volume average over the entire sample. For all three cases, drying can be viewed as a two-stage sequence. In the first stage, the initial, single water cluster breaks into many as the drying front moves downward. The drying front for the case of an open top is relatively flatter. The cluster size and width and roughness of the front depend on the Bond number. The secondary drying front moves inward from all open sides, progressively eliminating residual water clusters. The spatial location of residual water clusters depends significantly on the boundary conditions. The air-saturated region occupies the space between the residual water clusters and the open surfaces.

A measure of the size distribution of water clusters is the fraction of water-filled cells at the air-water interface shown as a function of water saturation for different grain sizes (Bond numbers) in Figure 2. Although the results are for the case of only the top surface being open, simulations showed that, the fraction of cells at the water-air interface for a given grain size and saturation is fairly independent of boundary conditions, even though contours of saturation distribution within the rock sample can be quite different. The drying process appears to produce similar cluster sizes at different saturations. In other words, the functional form of the fraction of water-filled cells on the interface depends primarily on water saturation and is greater for a given water saturation for decreasing Bond number, i.e., relatively greater capillarity. For the smallest Bond number, over 90% of water-filled cells are at the air-water interface for water saturation between zero and 40%. For the largest Bond number, the percentage of water-filled cells at the interface

decreases rapidly over the same water saturation range, so that most of the water resides in the interior of clusters. Thus, for a given water saturation, water tends toward larger clusters and can be characterized as "patchier" for larger Bond numbers. The core scale simulations suggest that generalizations may be possible for the distribution of water clusters as a function of saturation in the matrix during drying of a dual-porosity medium, if fractures crosscutting matrix blocks act as open boundaries.

Elastic-Wave Velocities

The frequency-dependent, elastic behavior of partially-saturated rock is important for interpreting geophysical measurements in petroleum reservoir and environmental applications. Berryman et al. (2002) examined how the phase distribution of gas and liquid influences the ratio λ / μ, where λ is Lamé's parameter and μ is shear modulus, as a function of saturation at low frequencies. All values must fit within a bounding triangle. The base is the dry or drained value when the gas and liquid are homogeneously mixed. The hypotenuse connects drained and undrained values when gas and liquid are segregated with some patches containing only gas while other patches contain only liquid. Laboratory data at higher frequencies typically plot within the triangle indicating behavior intermediate between homogeneous and patchy.

The distribution of water clusters as drying occurs is used to estimate elastic moduli based on the assumption that pores containing water on the two-phase interface will drain even at high frequency. The volume of these cells together with that of air-filled cells is assumed to behave elastically in a drained manner and all interior, water-filled cells are assumed to behave in an undrained manner. The effective elastic moduli are computed as a Voigt volume average. The results in Figure 3 are based on the values shown in Figure 2. All model results fit within the triangle defined by Berryman et al. (2002) in which the Gassmann result (homogeneous fluid mixing) forms the base and the Voigt average (patchy saturation) forms the hypotenuse. The key determinant of elastic behavior is the surface-area-to-volume ratio of water clusters. The model plots of λ/μ versus water saturation mimic experimental results (Figure 4). Massillon sandstone displays approximately drained behavior between $S_w = 0$ and $S_w = 0.4$ whereas Schuler-Cotton Valley sandstone follows the larger grain size results and approaches the patchy saturation limit.

Conclusion

The distribution of water cluster sizes during evaporative drying is primarily a function of water saturation and is relatively independent of the number of open surfaces at the boundary. Combining a percolation-based drying model and the assumption that water-filled pores at the water-air interface behave in a drained fashion yields high-frequency elastic behavior as a function of saturation that approximates the behavior of partially-saturated sandstones.

Acknowledgments

We thank Rosemary Knight for providing us/JGB with the sandstone data in digital format. This research was supported by the Geosciences Program of the Office of Basic Energy Science (through Grant DE-FG02-98ER14852 for HFW and under the auspices of the U.S. Department

of Energy Contract W-7405-ENG-48 for JGB at the University of California, Lawrence Livermore National Laboratory). TES acknowledges a dissertation year fellowship awarded him by the Department of Geology and Geophysics at the University of Wisconsin-Madison.

References

Berryman, J.G., Berge, P.A., and Bonner, B.P., "Estimating rock porosity and fluid saturation using only seismic velocities," *Geophysics,* Vol 67, No 2, March-April 2002, pp 391-404, 2002.

Knight, R., and Nolen-Hoeksema, R., "A laboratory study of the dependence of elastic wave velocities on pore scale fluid distribution," *Geophys. Res. Lett.,* Vol 17, pp 1529-1532, 1990.

Murphy,W.F.,III, "Acoustic measures of partial gas saturation in tight sandstones," *J. Geophys. Res.,* Vol 89, pp 11549-11559, 1984.

Prat, M., "Percolation model of drying under isothermal conditions in porous media," *Int. J. Multiphase Flow,* Vol 19, No 4, pp 691-704, 1993.

Prat, M., "Recent advances in pore-scale models for drying of porous media," *Chem. Eng. J.,* Vol 86, No 1-2, pp 153-164, 2002.

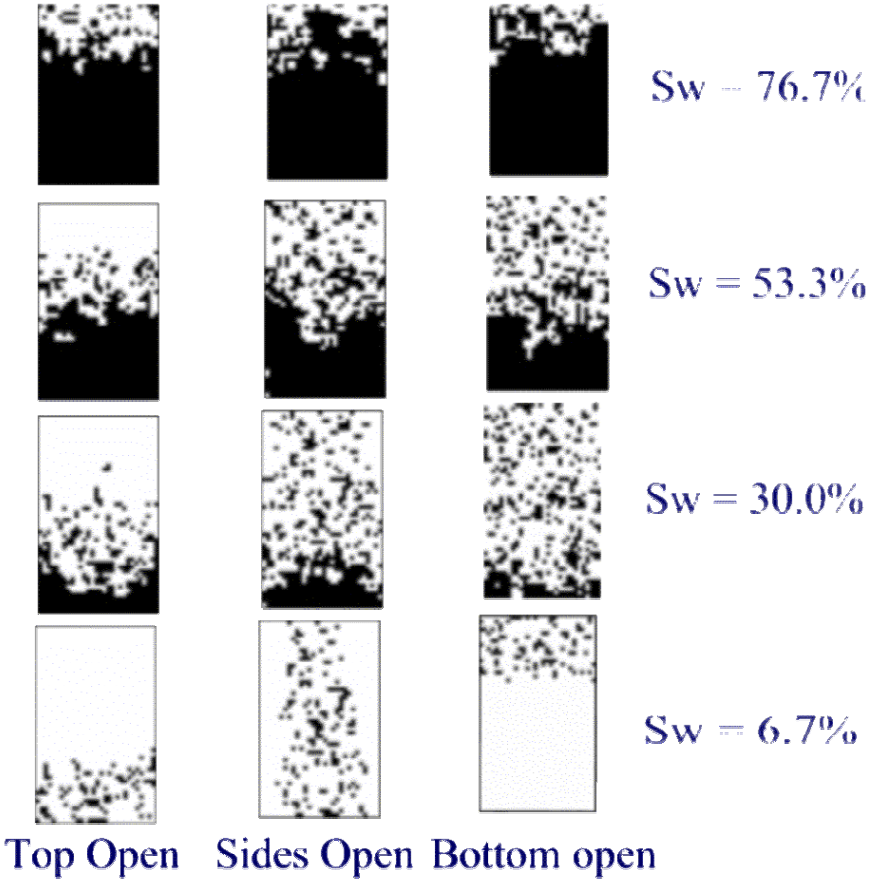

Figure 1. Drying simulations with different boundary conditions.
Drying sequence is from top to bottom in each column. System size is 1.6 × 1.6 × 2.4 cm.

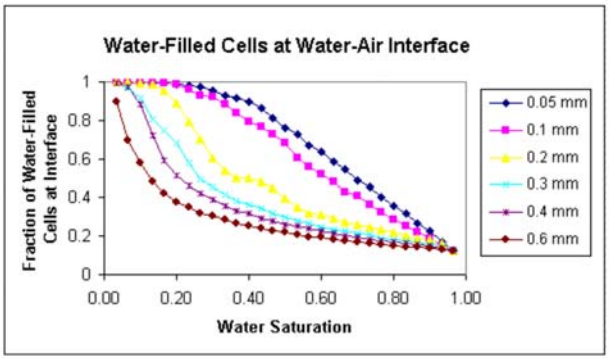

Figure 2. Variation of the fraction of water-filled cells at the air-water interface with water saturation parameterized for different grain sizes (Bond numbers).

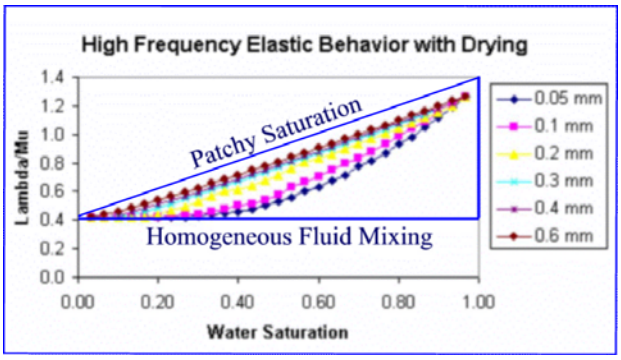

Figure 3. λ/μ versus water saturation calculated from volume average of cells assumed to behave in drained and undrained manner.

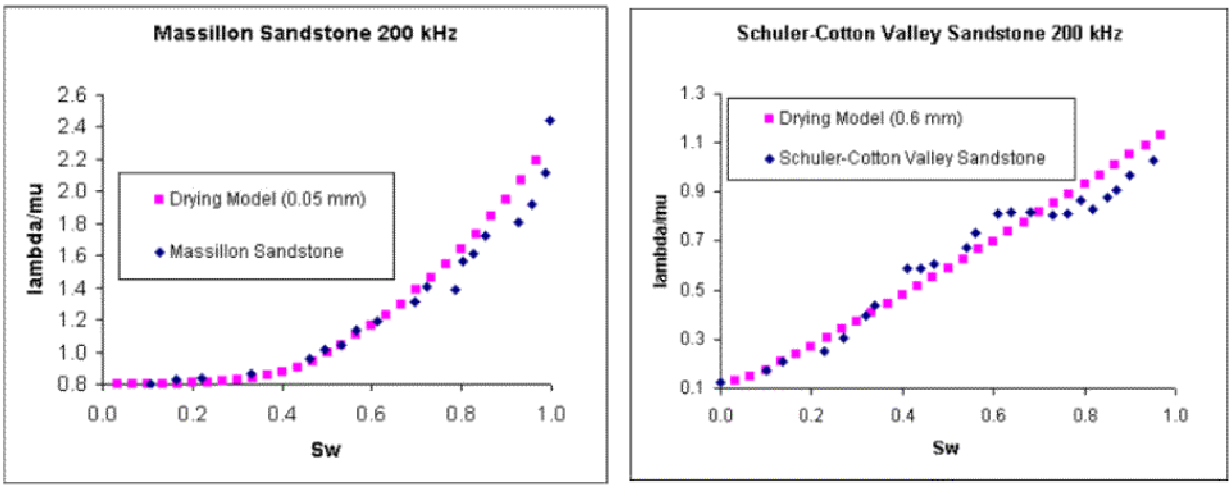

Figure 4. Massillon Sandstone and Schuler-Cotton Valley Sandstone data with superimposed model data from volume averaging of drained and undrained moduli based on drying model.

Qualification and Validity of a Smeared Fracture Modeling Approach for Transfers in Fractured Media

André Fourno[1,2], Christophe Grenier[1], Frederic Delay [3] Emmanuel Mouche[1], Hakim Benabderrahmane[2]
[1]CEA (Commissariat à l'Energie Atomique). C.E. Saclay 91191 Gif sur Yvette Cedex,. France
[2]ANDRA (Agence nationale pour la gestion des déchets radioactifs) Parc de la Croix Blanche. 1-7 rue Jean Monnet. 92298 Châtenay-Malabry, France
[3]HYDRASA Université de Poitiers 40, avenue du Recteur Pineau 86022 Poitiers, France

Overview

Modeling transfers in fractured media is a key issue in the field of nuclear waste storage. We propose here a continuous approach to representing fractured rock and simulating transfers. This approach is referred as a smeared fracture approach. We developed this approach for a mixed and hybrid finite element scheme, including estimation of associated flow and transport parameters, and implemented it in our code (CAST3M). We present here an evaluation of the approach, providing the results for various test cases, different mesh sizes, and a large range of transport regimes (depending on the importance of matrix diffusion). This is achieved by comparing the smeared-fracture-approach simulations with reference calculations obtained by explicitly meshing the fractured system. The smeared-fracture-approach, like other continuous approaches, is most appropriate for slow transfers, typical of post-closure situations (where matrix diffusion plays a major role). It has the advantage of being able to take actual block geometries into account, as well as providing accurate results at low computer costs. Here, we apply our approach to fractured media with permanent-flow and transitory Eulerian transport within the entire system.

Background and Methods

The basic idea of the smeared fracture approach is not to mesh the fracture network, but rather to take the presence of fractures into account by means of continuous heterogeneous fields (permeability, porosity, head, velocity, concentration). This approach, which is followed by a number of investigators (e.g., to Svensson [2001] and Tanaka et al. [1996]), is referred to as the smeared fracture approach. No dedicated spatial discretization effort is required for this scheme: we use a basic, regular mesh, and simulations can be done with a rough mesh saving computer time. This advantage makes this kind of approach very promising for taking into account heterogeneity of properties as well as uncertainties within a Monte Carlo framework. Furthermore, the geometry of the matrix blocks where transfers proceed by diffusion is fully accounted for contrary to classical simplified 1D approaches. Nevertheless, continuous heterogeneous field representation of a fracture medium requires a homogenization process at the scale of the mesh considered, and constant mesh size might not be appropriate to simulate contrasted regimes.

Initially, working with a regular mesh, we have to identify meshes corresponding to a fracture,

the number of X type cells N_X and Y type cells N_Y (Figure 1). Then, we provide the adapted parameter (such as transmissivity, porosity, dispersivity) values to the mesh. To establish the hydraulic media equivalent properties, we guarantee the validity of the conservation of mass flow for a single fracture.

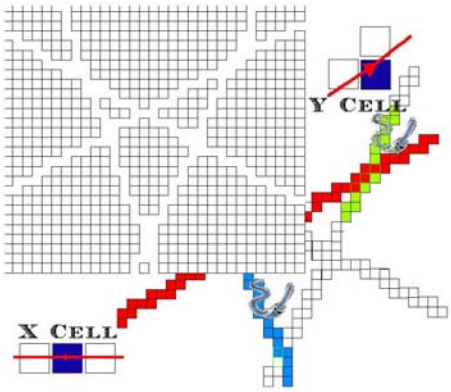

Figure 1. Smeared Fractures mesh with X and Y type cells.

- The equivalence of the flux through the reference fracture and the equivalent conductor is easy to write, based on the numerical scheme considered. For mixed and hybrid finite element modeling, conservation of the quantities is guaranteed for each mesh by the introduction of four variables (traces affected at the center of the element edges in addition to the classical variables corresponding to the elements' center). These allow for jointed estimation of the fluxes (gradients) as well as the values of the variables within the mesh (see Dabbene 1998). Thus, we can determine a relation between T_{sf} and T_{ref} :

$$*T_{sf} = \frac{(3N_X + 2N_Y).e}{3L}.T_{ref}. \quad (1)$$

where e and L are respectively the aperture and the length of the fracture (sf = smeared fracture and ref = explicit modeling). The equivalence is exact for a single fracture.

- The equivalent dispersion tensor is here derived as a scalar value based on the same considerations as for the equivalent transmissivity.

- Equivalent porosity is estimated by calculating transition times associated with a Lagrangien approach for both models (smeared fractures and reference):

$$*\varpi_{sf} = \frac{L.e}{(N_x + N_Y)\Delta x^2}.\varpi_{ref} \quad (2)$$

For a fracture network, the same procedure is applied for each conductor, and the value associated with the intersection is the maximum of all met in this mesh. The type of transfer at fracture intersections is full mixing.

The smeared fracture approach has been tested on different fracture networks (Figure 2) for permanent flow simulations and has yielded good results. Preliminary results involving Eulerian transport limited to the fractured network were promising.

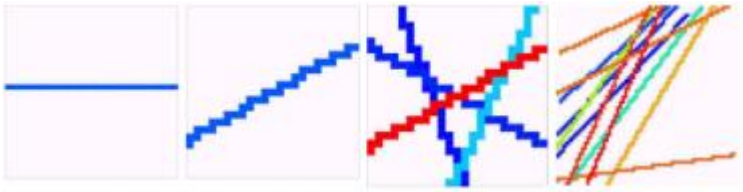

Figure 2. The set of geometries studied with increasing levels of complexity and realism.

Results

The next step involves transfers with matrix diffusion effects. This mechanism is identified as an important retention process. One of the key numerical issues is, can we model quick transfers (fracture zone) and slow transfers (matrix zone) with the same discretization. Here we present two test cases to answer this question.

1. Different Flow Regimes within a Single Fracture System

The retention effect associated with matrix zones depends upon the contact time with the plume, porosity coefficient, and the pore diffusion coefficient. For quick flow conditions (typically forced flow conditions), advection in the fracture network is dominant, and retention effects associated with matrix diffusion are limited. For slower regimes (typically postclosure conditions for nuclear waste disposal), matrix diffusion plays a major role, resulting in a globally diffusion dominant regime. In evaluating the smeared fracture approach for different flow regimes as well as discretization strategies, we consider (for sake of illustration) a simple system involving a single fracture within a porous block (tilted 30°) and three regimes (Figure 2, second case):

- A dominant advective regime (K1)
- An intermediate regime (K2)
- A dominant diffusive regime (K3)

The plume is injected into the bottom of the fracture and spreads to the top of the fracture. We take into account advection/dispersion in the fracture and diffusion in matrix zones. The three regimes show matrix zone retention effects and illustrate PA modeling of slow regimes.

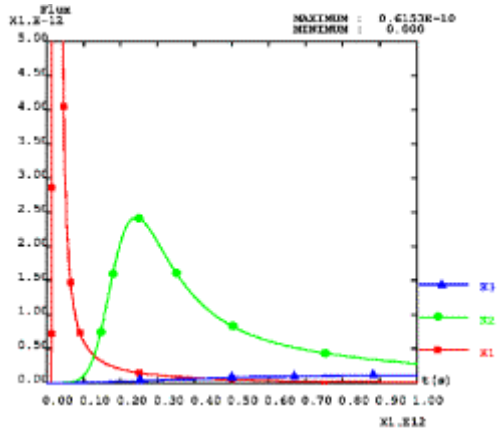

Figure 3. Breakthrough curves for three different transport regimes.

In Figure 3, we show the breakthrough curves for a Dirac injection into the system. The influence of the flow regimes shows up classically as delays in arrival times and a decrease from the peak level (Figure 3). We plot (in Figures 4 to 6) the total flux exiting the system for the three regimes considered and for different levels of discretization. The curve with the large circle corresponds to the reference calculation obtained by meshing explicitly the fracture and the block. Globally, the smeared fracture approach (1) works better for diffusive dominant regimes than for advective dominant, (a result that is not surprising since matrix blocks in the smeared fracture approach are potentially underdiscretized for dominant advective regimes); and (2) provides better results when refining the mesh. The same trends are observed for other quantities, like evolution of total mass in the fracture or matrix subsystems (not illustrated here).

More detailed comments follow:

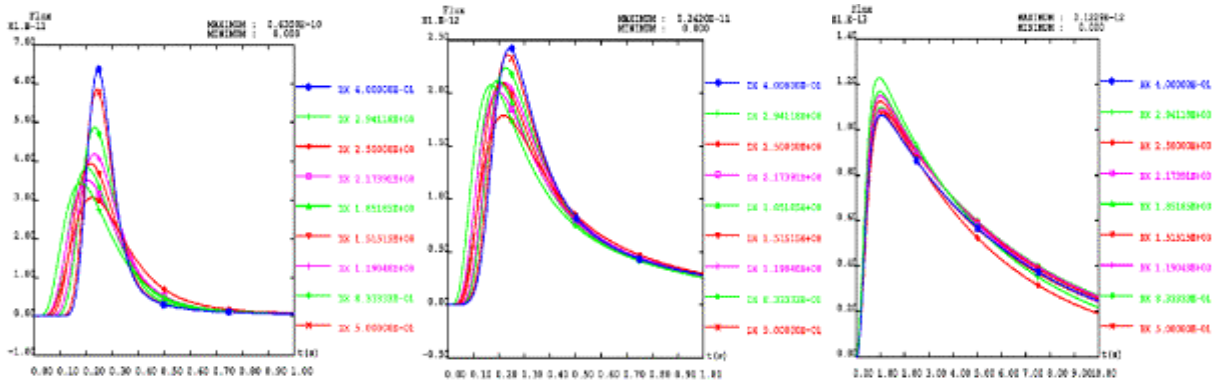

Figures 4, 5, and 6. Total fluxes at the outlets for regimes K1, K2, K3, respectively.

- Case K1: (dominant advective regime, Figure 4): Peak arrival time is well met, with errors on the order of 5%, but the peak level can be misguided by 50% for coarse discretizations.

- Case K2: (intermediate regime, Figure 5): The level of the peaks as well as their arrival times are better predicted.

- Case K3 (diffusive regime, Figure 6): Modeling shows overall good qualitative as well as

quantitative results. Whatever the discretization, we obtain a relatively accurate peak arrival time and peak maximum differs by less than 10%.

To conclude, precision is maximal when matrix diffusion plays a major role (this conclusion was confirmed by other simulations). It is acceptable for the intermediate regime to be within a precision range of 10%. For the dominant advective regime, we must use a refined discretization or other strategies to model transfers with equivalent precision.

2. *Influence of Mesh Size for the Äspö site (Sweden) Geometry and a Typical Postclosure Flow Regime*

We tested the smeared-fractures approach on a 2-D case resulting from a cut in the actual 3-D geometry (200 m block scale) (Figure 7), seeking to determine the influence of discretization on the results. For some coarse discretization the geometries of the fracture media is lost (Figure 7 Case 3). Matrix meshes between different fractures can count as fracture meshes. Consequently, for these cases, we obtain results corresponding to another fracture network (Figure 8, dotted curves). Nevertheless if we choose a sufficient discretization, we obtain reasonable results (Figure 8). The curve with large circles corresponds to the reference calculation obtained by meshing (explicitly) the fracture network and the block. The other curves are obtained with smeared-fracture simulations.

The continuous-curve correspondence at proper space discretization is good in terms of peak arrival time and peak maximum. Nevertheless, the smeared-fracture approach smoothes the breakthrough curves; we do not see the effect of each fracture as well as we do in the reference curve, (Figure 8, continuous curves).

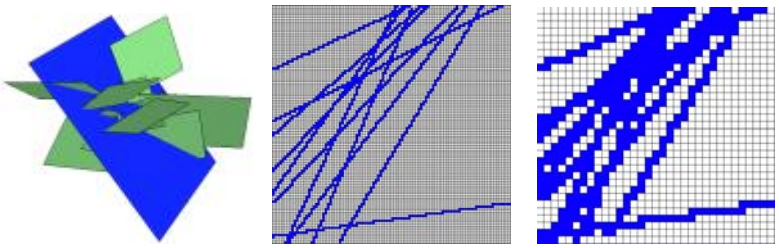

Figure 7. Three-dimensional view of the Äspö fractured site at 200 m scale and smeared fracture mesh (high and low levels of discretization).

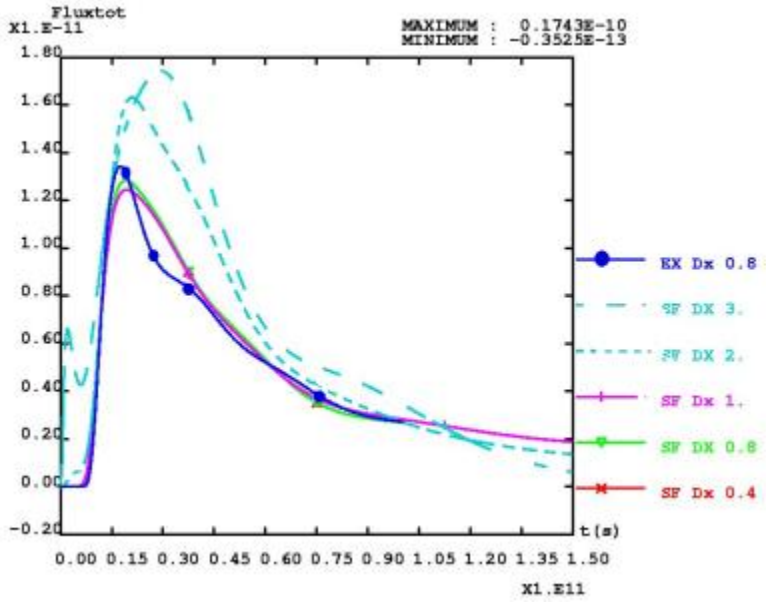

Figure 8. Total fluxes at the outlets for different discretizations.

Conclusions

The smeared-fracture approach provides accurate results in terms of precision, and low computer cost (10 times less than reference simulation). The quality of the results depends closely on matrix diffusion as well as mesh size. The smeared-fracture approach is especially useful for long transport times (as in postclosure conditions) where the actual geometry of the matrix blocks has to be taken into account. We are presently extending the approach to 3-D systems with similar purposes.

References

Dabbene F (1998) Mixed Hybrid Finite Elements for transport of pollutants by underground water. Proc. 10th conference on finite elements in fluids, Tucson, Arizona.

Svensson U (2001) A continuum representation of fracture networks. Part I : Method and basic test cases. Journal of Hydrology 250, pp. 170-186.

Tanaka Y, Minyakawa K, Igarashi T, Shigeno Y (1996) Application of 3D smeared fracture model to the hydraulic impact of the Äspö tunnel. SKB Report. ICR 96-07.

Navier-Stokes Simulations of Fluid Flow through a Rock Fracture

Azzan H. Al-Yaarubi, Chris C. Pain, Carlos A. Grattoni and Robert W. Zimmerman
Department of Earth Science and Engineering, Imperial College, London SW7 2BP, UK

Fluid flow through rock fractures is important in numerous geological processes and geotechnical applications (Lowell et al., 1993; Aydin, 2000; Menand and Tait, 2001). Nearly half of all hydrocarbon reserves are located in naturally fractured rocks, as are most geothermal reservoirs and most of the sites that have been tentatively chosen for the location of underground radioactive waste repositories. Traditionally, flow through rough-walled rock fractures has been modeled using the Reynolds lubrication equation (Brown, 1987), which is a two-dimensional simplification of the more fundamental Navier-Stokes equations, derived by ignoring out-of-plane components of the velocity. The applicability of the Reynolds equation to flow in real rock fractures has recently been questioned (Brown et al., 1995; Mourzenko et al., 1995; Yeo et al., 1998, Nicholl et al., 1999). In this work, we have made the first Navier-Stokes simulations of fluid flow through an actual three-dimensional fracture profile and compared the simulated fracture transmissivities with those measured in the laboratory. Our results confirm that the Reynolds equation may overestimate fracture transmissivity by 10–100%.

Fundamentally, fluid flow through a fracture is governed by the Navier-Stokes equations, with no-slip boundary conditions imposed at the fracture walls. In steady state, these equations take the form (Schlichting, 1968)

$$\rho(\mathbf{u}\cdot\nabla)\mathbf{u} = -\nabla P + \mu\nabla^2\mathbf{u}\,, \tag{1}$$

where ρ is the density, P is the pressure, and $\mathbf{u}$ is the velocity vector. This equation must be supplemented by the conservation of mass equation, which for an incompressible fluid is

$$\nabla\cdot\mathbf{u} = 0\,. \tag{2}$$

Equations (1) and (2) form a set of four coupled partial differential equations. The complexity of these equations, combined with the irregular geometry of rock fractures, renders them difficult to solve.

To circumvent the difficulties of working with the Navier-Stokes equations, most attempts to model fracture flow have tended to be based on the Reynolds lubrication equation, originally derived by Osborne Reynolds in 1888 to study lubrication flows in geometries in which one dimension is much smaller than the other two. In contrast to the Navier-Stokes equations, which are four coupled partial differential equations for the three velocity components and the pressure, the Reynolds lubrication equation is a single PDE for the pressure:

$$\nabla\cdot(h^3\nabla P) = 0\,, \tag{3}$$

where $h(x,y)$ is the local aperture. The Reynolds equation can be derived from the Navier-Stokes equations under the assumption that flow is sufficiently slow and the slope of the fracture walls is not too steep (Schlichting, 1968; Zimmerman and Bodvarsson, 1996). The derivation

requires that the "wavelength" of aperture variations is large compared to the mean aperture, and that the Reynolds number is sufficiently small, although these criteria are difficult to quantify *a priori*.

In the absence of high-resolution fracture-aperture data and accurate laboratory measurements, until recently it had not been possible to judge the accuracy of the Reynolds equation for fracture flow. In the last few years, however, evidence has been accumulating to indicate that the Reynolds equation may only be capable of yielding transmissivities to within a factor of two of the actual values. Mourzenko et al. (1995) and Brown et al. (1995) solved the Navier-Stokes equations in simulated fracture profiles and found transmissivities 20–50% less than those yielded by the Reynolds equation. Yeo et al. (1998) measured the aperture of a fracture in a red Permian sandstone, used the data as input to a Reynolds equation simulation, and then compared the predicted transmissivities to the experimentally measured values. They found that the experimental transmissivities were about 10–60% less than those predicted by the Reynolds equation, depending on factors such as the amount of shear deformation that the fracture had undergone. Nicholl et al. (1999) reached similar conclusions using artificial fractures bounded by rough glass surfaces. All of this evidence points to the necessity of using the Navier-Stokes equations to model flow through rock fractures. Yet, in none of these previous studies have the Navier-Stokes equations been solved in actual rock fractures geometries. As described below, we have conducted what appear to be the first Navier-Stokes simulations of fluid flow in an actual rock-fracture geometry.

Replicas of the surface of a natural fracture in a red Permian sandstone were made using Araldite; the process is described in detail by Yeo et al. (1998). The surface profiles of both opposing surfaces were measured using a Talysurf profilometer, a device commonly used in tribological studies of automotive parts. This device utilizes a diamond stylus of 2 μm radius at the end of a cantilevered arm, the vertical motion of which is measured with a laser, to within an accuracy of ±10 nm, as the stylus traverses the surface. Surface elevations of the fracture surface were thereby measured to within a vertical accuracy of much better than 1 μm, every 20 μm in both x and y directions. Previous fracture-profile measurements have either lacked the proper vertical resolution, or have not been sampled at sufficiently small spacings within the fracture plane, to be able to capture the small-scale roughness that may influence the flow field. In our work, measurements were made of several 2 cm × 2 cm regions of the surface, leading to data files containing on the order of 10^6 profile height values for each of the two surfaces (Figure 1).

The surface data were then used as input to the mesh generator GEM (Pain, 2000), which generates a computational mesh consisting of quadratic elements. The mesh was taken to have a spacing of 200 mm in the x and y-directions, which is somewhat coarser than the grid on which the surface data was measured. However, a comparison of the discretized boundary as used in the mesh, to the original data, showed a root-mean-squared discrepancy between the measured profiles and the computational grid that was less than 1% of the mean aperture. Hence, the small-wavelength roughness components lost in this smoothing process are clearly of small amplitude, consistent with the findings of Brown and Scholz (1985). As the transmissivity is, to first-order, proportional to the cube of the aperture, the error induced by this smoothing should be no greater than 3%. The grid contained ten (or fifteen) layers of elements in the transverse (z) direction, giving a total of 100,000 (or 150,000) elements.

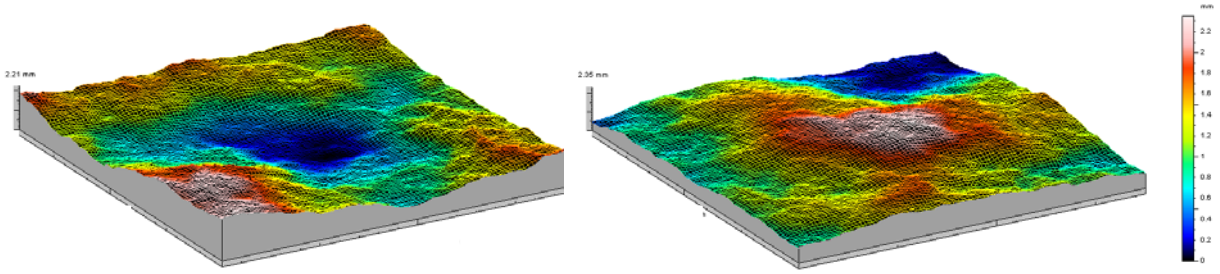

Figure 1. Upper and lower fracture surfaces, measured over a 2 cm × 2 cm region.

The finite element code FLUIDITY (de Oliveira, 1999) was used to solve the flow equations in the 2 cm × 2 cm region. The boundary conditions were taken to be uniform pressures P_1 and P_2 on two opposing faces (say, $x = 0$ and $x = 2$ cm), with zero normal velocities along the two lateral faces ($y = 0$ and $y = 2$ cm). These latter conditions are equivalent to imposing periodicity in the y-direction. All velocity components were taken to vanish along the upper and lower boundaries of the flow region, which corresponded to the two rock walls. The calculations were done for several Reynolds numbers in the range 10^{-5}-10^{-1}, in which range the transmissivity is independent of Reynolds number. The total flux Q [m^3/s] through the fracture was found by integrating the normal component of the velocity across the outlet face at $x = 2$ cm. Finally, the transmissivity T [m^3] was found from its defining equation, $Q = (Tw/\mu)(dP/dx)$, where μ [Pa s] is the viscosity of the fluid, dP/dx [Pa/m] is the overall pressure gradient, and w [m] is the depth of the fracture in its plane, in the direction normal to the flow (in this case, 2 cm). For comparison, the Reynolds lubrication equation was also solved in this same geometry, with the same boundary conditions, using a finite element code written by Yeo (1998).

The computed transmissivities are shown in Figure 2, expressed as the cube of the hydraulic aperture, normalized with respect to the cube of the mean aperture. The x-axis is the relative smoothness, defined as the ratio of the mean aperture to the standard deviation, i.e., $\langle h \rangle / s_h$. In this format, the "cubic law" would plot as unity. The calculations were made for various values of the mean aperture, which was changed by mathematically translating one of the two surfaces perpendicular to the nominal fracture plane (Brown, 1987). This process was continued until the two surfaces came into contact at (at least) one point, as indicated by the dotted vertical line in Figure 2. As is typically found, the hydraulic aperture is less than the mean aperture, according to both models. But the Navier-Stokes equations yield transmissivities that are less than those given by the Reynolds equation. The difference seems to be between 10–100% of the Navier-Stokes value, and varies as a function of relative roughness (smoothness). As the mean aperture increases, the effect of surface roughness diminishes; both models converge towards the cubic law, and the difference between the two predictions decreases.

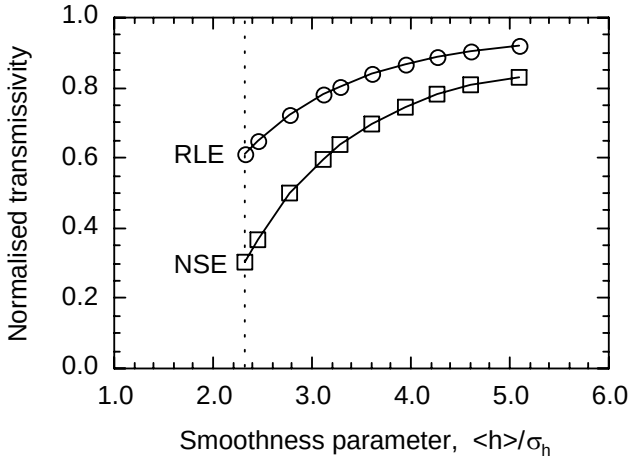

Figure 2. Normalized transmissivities, defined as $12T/\langle h\rangle^3$, calculated using the Reynolds lubrication equation (RLE) and the Navier-Stokes equations (NSE), for the 2 cm × 2 cm fracture region discussed in the text and shown in Figure 1.

The transmissivities of two 2 cm × 2 cm regions of fracture were also measured in the laboratory. The top and bottom halves of the fracture casts were first connected to extensions (V shape channels), which provided the inlet and the outlet sections for the flow. These extensions are designed so that the fluid will spread uniformly throughout the inlet and the outlet when the top and bottom halves are put together. Four pressure-monitoring ports of 0.75 mm diameter, two at each end of the fracture, were drilled through the upper half of the fracture, terminating at the fracture plane. The two fracture halves were then brought together until they contact each other at a few contact points, after which the sides of the device were sealed to prevent leakage of the fluid during the flow experiment. The mean aperture of the assembled fracture apparatus was then determined by a procedure described in detail by Al-Yaarubi (2003).

Two holes with 2 mm diameter were drilled at the two ends of the flow system, one for the inlet and the other for the outlet. The inlet was connected to two 50 ml syringes, which were connected to one another through a Y junction (connector), from which the fluid is pumped into the fracture. The outlet was connected to a graduated measuring cylinder (± 0.05 cm^3) to collect and measure the outflow fluid during a specific period of time. The four pressure ports on the top of the device were attached to liquid manometers (± 0.5 mm) to measure the liquid heads at the inlet and outlet of the fracture.

Distilled water was used as the pore fluid. Steady-state flow tests were run at several flow rates, with Reynolds numbers in the range of about 0.4–4. The flowrate versus pressure drop was found to be linear, thereby allowing the transmissivity to be calculated. For both of the fracture regions tested, the measured transmissivities were found to be closer to the values obtained from the solution of the Navier-Stokes equations than to the values obtained from the solution of the Reynolds lubrication equation (Table 1). We interpret these results as verifying that the Navier-Stokes equations, with the associated no-slip boundary conditions, do indeed provide the proper model for single-phase flow in a rock fracture. More details of the experiments and simulations, including results at higher Reynolds numbers, can be found in Al-Yaarubi (2003).

Table 1. Measured and calculated hydraulic apertures of two fracture regions.

Sample	h_m (μm)	σ (μm)	h_{EXP} (μm)	h_{NS} (μm)	h_{RLE} (μm)
1	130	72	71±1	69	75
2	149	56	117±1	121	132

Acknowledgments

Azzan Al-Yaarubi thanks Petroleum Development Oman (PDO) for financial support and encouragement. The fracture casts were made with help from a grant from the Natural Environment Research Council of the UK. The authors thank Ismail Jalisi of Imperial College for assistance in using the Talysurf system.

References

Al-Yaarubi, A. Numerical and Experimental Study of Fluid Flow in a Rough-Walled Rock Fracture, Ph.D. dissertation, Imperial College, London, 2003.

Aydin, A. Fractures, faults and hydrocarbon entrapment, migration and flow. Marine Petrol. Geol., **17**, 797-814, 2000.

Brown, S. R. Fluid flow through rock joints: the effect of surface roughness. J. Geophys. Res., **92**, 1337-47, 1987.

Brown, S. R. & Scholz, C. H. Broad bandwidth study of the topography of natural surfaces. J. Geophys. Res., **90**, 12575-82, 1985.

Brown, S. R., Stockman, H. W. & Reeves, S. J. Applicability of the Reynolds equation for modeling fluid flow between rough surfaces. Geophys. Res. Letts., **22**, 2537-40, 1995.

de Oliveira, C. GEM: A Finite Element Mesh Generator, Internal report, Imperial College, London, 1999.

Lowell, R. P., Van Cappellen, P. & Germanovich, L. N. Silica precipitation in fractures and the evolution of permeability in hydrothermal upflow zones. Science, **260**, 192-99, 1993.

Menand, T. & Tait, S. R. A phenomenological model for precursor volcanic eruptions. Nature, **411**, 678-80, 2001.

Mourzenko, V. V., Thovert, J. F. & Adler, P. M. Permeability of a single fracture - validity of the Reynolds equation. J. Phys. II, **5**, 465-82. 1995.

Nicholl, M. J., Rajaram, H., Glass, R. J. & Detwiler, R. Saturated flow in a single fracture: Evaluation of the Reynolds equation in measured aperture fields. Water Resour. Res., **35**, 3361-73, 1999.

Pain, C. C. A Brief Description and Capabilities of the General Purpose CFD Code FLUIDITY, Internal report, Imperial College, London, 2000.

Schlichting, H. Boundary-Layer Theory, McGraw-Hill, New York, 1968.

Yeo, I. W. Anisotropic Hydraulic Properties of a Rock Fracture under Normal and Shear Loading, Ph.D. dissertation, Imperial College, London, 1998.

Yeo, I. W., deFreitas, M. H. & Zimmerman, R. W. Effect of shear displacement on the aperture and permeability of a rock fracture. Int. J. Rock Mech., **35**, 1051-70, 1998.

Zimmerman, R. W. & Bodvarsson, G. S. Hydraulic conductivity of rock fractures. Transp. Porous Media, **23**, 1-30, 1996.

Lattice Boltzmann Simulation of Flow and Solute Transport in Fractured Porous Media

Dongxiao Zhang and Qinjun Kang
Los Alamos National Laboratory, Los Alamos, NM 87545

Flow and solute transport in naturally fractured porous media have attracted the attention of many investigators due to their importance in hydrology, pollution migration in aquifers, and radioactive waste reposition [1]. Owing to statistically complex distribution of geological heterogeneity and the multiple length and time scales in natural porous media, three approaches [2,3] are commonly used in describing fluid flow and solute transport in natural fractured porous formations: (1) discrete fracture models, (2) continuum models using effective properties for discrete grids, and (3) hybrid models that combine the above two. In this study, we develop a unified method applicable to various length scale systems as well as to systems where multiple length scales coexist. The length scales of this method can be as small as pore scales (on the order of microns), and as large as field scales (on the order of meters to kilometers), or both, depending on the porous formations under consideration.

This method is based on the lattice Boltzmann (LB) method, a powerful tool for numerical modeling. Unlike conventional numerical schemes based on discretizations of macroscopic continuum equations, the LB method is based on microscopic models and mesoscopic kinetic equations. This feature gives the LB method the advantage of studying non-equilibrium dynamics, especially in fluid flow applications involving interfacial dynamics and complex boundaries (geometries). Since its appearance, the LB method has proved to be competitive in studying a variety of flow and transport phenomena (see [4] for a review), including single- or multi-phase flow [5-8] and chemical dissolution [9] in porous media. The same feature, however, also makes it difficult for the original LB method to apply to systems with larger length scales. Previous efforts have been made to develop macroscopic porous media models for lattice gas and lattice Boltzmann methods, using the basic concept of introducing a resistance force by dynamically altering the local flow velocity [10-12]. This idea, when applied on non-uniform grids, enables the LB method to simulate flow and transport in multiscale porous media. Readers may refer to reference [13] for details of the numerical method.

Figure 1 shows a simplified fractured system, where l is the length along the flow direction, h is the width of the fracture, and h_p is the width of the porous matrix. In our simulations, l is 200 and h is 20, both in lattice units. Two values of h_p (200 and 400) are used.

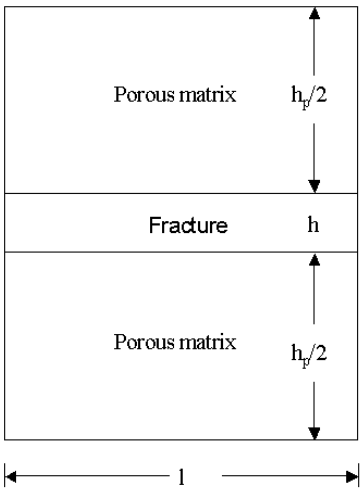

Figure 1. Geometry of a simplified fractured system.

Figure 2 shows the dependency of the normalized permeability of the fracture and the whole system on the normalized permeability of the porous matrix for both h_p/h=10 and h_p/h=20. The value k_c is the permeability calculated by the cubic law with the fracture width, and k_0 is the effective permeability of the whole system under the condition that the porous matrix is impermeable. The value k_p is the permeability of the porous matrix, k_f is the permeability of the fracture, and k_e is the permeability of the whole fractured system. The ratio of k_e to k_0 can be used as an indication of error caused by the cubic law used to calculate the permeability of the whole fractured system. It is clear that when k_p/k_c is less than 10^{-4}, k_e/k_0 and k_f/k_c are very close to 1 in both cases. At this small value of k_p/k_c, the permeability of the porous matrix is so small, compared to that of the fracture, that the matrix contributes little to flow in the whole system. Hence, the total effective permeability of the fractured system can be calculated as though the porous matrix is impermeable, and the permeability of the fracture can be calculated by the cubic law based on the width of the fracture. As k_p/k_c increases to about 10^{-4}, k_e/k_0 of case h_p/h =20 begins to increase. With the further increase of k_p/k_c, the k_e/k_0 of case h_p/h=10 also begins to increase. As k_p/k_c exceeds 10^{-3}, k_f/k_c in both cases begins to increase. The dependency curves of k_f/k_c on k_p/k_c in two geometries coincide with each other. This is reasonable: when h_p is big enough the flow in the porous matrix away from the fracture becomes uniform; the permeability of the fracture does not depend on h_p. The normalized permeability of the whole system, k_e/k_0, however, does depend on the width ratio of the porous matrix to the fracture. At a given value of k_p/k_c greater than 10^{-4}, the k_e/k_0 of h_p/h =20 is larger than that of h_p/h =10. That is, when the width ratio is big enough, although the flow in the porous matrix is still very small, the contribution of the porous matrix to the fractured system is not negligible due to its large size compared to the fracture. The cubic law used in this case to calculate the fracture permeability will incur significant error. This also means that the higher the ratio, the more significant the error caused by using the cubic law.

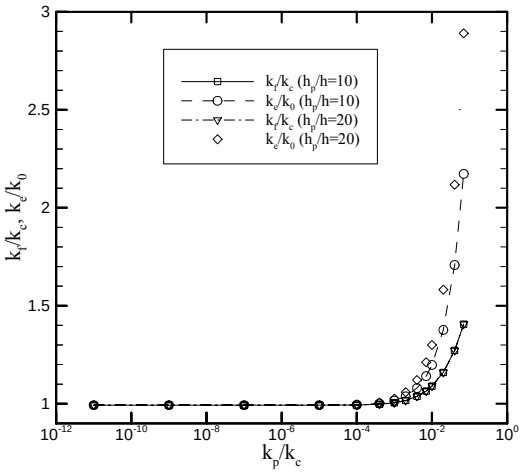

Figure 2. Dependency of the normalized permeability of the fracture and the whole system on the normalized permeability of the porous matrix.

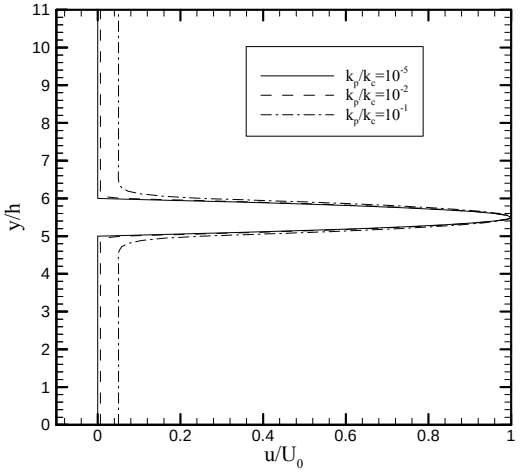

Figure 3. Horizontal velocity profiles (normalized by the center-line velocity of the fracture) of the flow through the fractured system.

Figure 3 illustrates the horizontal velocity profiles (normalized by the center-line velocity of the fracture) of the flow through the fractured system with h_p/h =10 at k_p/k_c =10^{-5}, 10^{-2}, and 10^{-1}.

At k_p/k_c =10^{-5}, the velocity profile in the fracture is parabolic, and the velocity is almost zero in porous matrix. The interface between the porous matrix and the fracture is very sharp. At k_p/k_c =10^{-2} and 10^{-1}, the flux in the porous matrix has a finite value, although small, makes a significant contribution to the system since the size of the porous matrix is much larger than that of the fracture. Now the interface between the porous matrix and the fracture is smoother, indicating an interaction between the porous matrix and the fracture. As a result, the flux in the porous matrix very close to the interface is larger than that far from it; the velocity profile in the fracture is no longer parabolic because the no-slip boundary condition is not satisfied at the interface. In this situation, a direct use of the cubic law will cause a significant error.

Figure 4 shows a simple fractured system used in our numerical simulation of solute transport. In the middle of a homogeneous porous medium with a porosity of 0.601 is a fracture of width 32 (in lattice unit). For flow of fluid B, periodic conditions are enforced on all four boundaries and a body force drives the flow from left to right. When flow reaches a steady state, a slug of solvent A (entirely miscible with B) is injected at time zero into the fracture. We investigate the effect of the porosity (and hence the permeability) of the porous matrix on the fracture. Apparently, when the matrix porosity is zero, this is simply a dispersion problem in a two-dimensional channel that has an analytical solution.

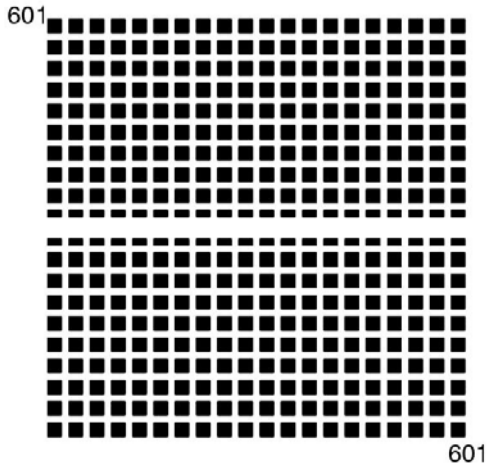

Figure 4. A simple fractured system.

In this study, the velocity field and the solute concentration are solved using the LB method. Figure 5 shows snapshots of the concentration field at two dimensionless times for three scenarios (with matrix porosity ε = 0, 0.301, and 0.601). It is seen that both the mass transfer into the matrix block and the plume tailing in the facture are enhanced as ε increases. As such, the overall dispersion of a plume increases as the matrix becomes more permeable.

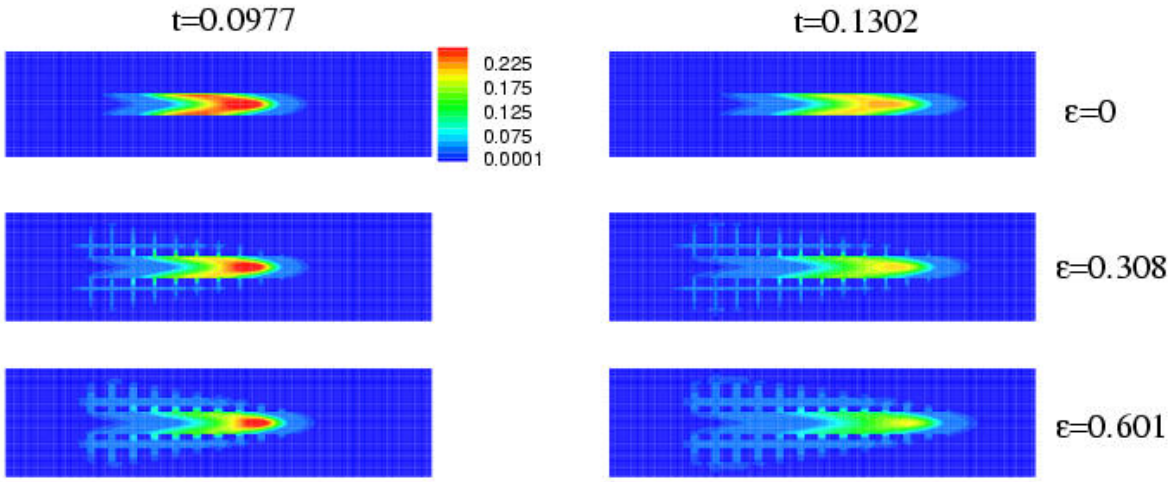

Figure 5. Snapshots of concentration fields for three scenarios of matrix porosity (ε) at two dimensionless times, which are defined as the plume residence time normalized by the characteristic time $t_c=h^2/D_m$, where h is the channel width and D_m is the molecular diffusivity.

The mean plume velocity and the dispersion tensor of the solute plume are calculated by the method of Brenner (1980) [14]. Figures 6-8 show the time evolution of the mean plume velocity (U), longitudinal dispersion coefficient (D_{xx}), and transverse dispersion coefficient (D_{yy}), respectively, at different porosity values of the porous matrix and under the same body force strength. For the channel, both U and D_{xx} have a steady-state value when time is long enough. Hence, the dispersion in the channel is Fickian. For the fractured porous medium, however, as time goes on, the solute samples more interstitial space, where the mean plume velocity is

smaller than that in the fracture, therefore, the averaged velocity over all the interstitial space decreases with time, while D_{xx} increases with time. Hence, dispersion in the fractured porous medium is non-Fickian, at least within the scale considered here. At a fixed time instance, both dispersion coefficients increase with the increase of the porosity of the porous matrix. However, contrary to intuition, the mean plume velocity decreases as the porosity of the porous matrix increases when the time is long enough. This is so because as the porosity increases, more interstitial space where the velocity is smaller than that in the channel is taken into account in calculating the mean velocity, hence the mean velocity decreases.

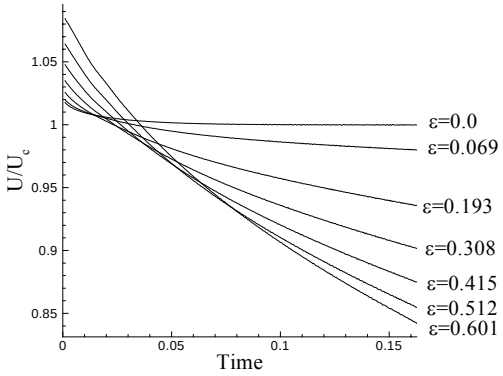

Figure 6. Time evolution of the mean plume velocity. Time is normalized by $t_c=h^2/D_m$. U_c is the steady-state mean velocity for $\varepsilon = 0$.

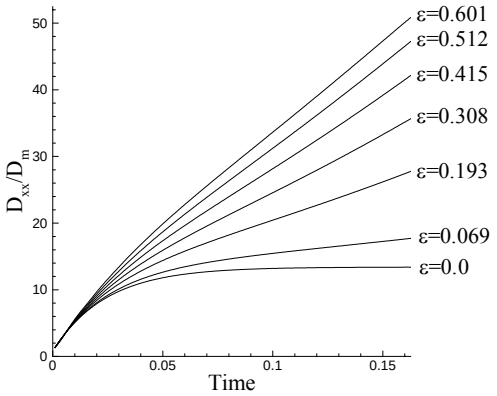

Figure 7. Time evolution of the longitudinal dispersion coefficient. Time is normalized by $t_c=h^2/D_m$.

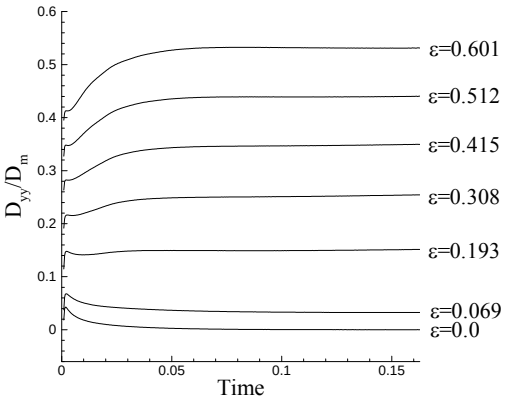

Figure 8. Time evolution of the transverse dispersion coefficient. Time is normalized by $t_c=h^2/D_m$.

Figures 9-10 show the dependence of longitudinal and transverse dispersion coefficients on the Peclet number, respectively. The Peclet number is defined as $Pe=Uh/D_m$, where h is the channel width and D_m is the molecular diffusivity. The porosity of the porous matrix is 0.601. The results of the numerical simulation are in good agreement with those of the analytical solution. At a fixed Peclet number, the fractured porous medium has a larger D_{xx} than the matrix without a fracture, and the channel has the smallest D_{xx}. For D_{yy}, however, the porous medium without a fracture has the largest value. D_{yy} for the channel is zero in the numerical simulation due to the way by which the solute is introduced.

For the porous medium with or without a fracture, the dependence of D_{xx} on the Peclet number is a general second-order polynomial. Therefore, the so called dispersivity, defined as D_{xx} /U, is not just a property of the medium but also a function of the flow characteristics.

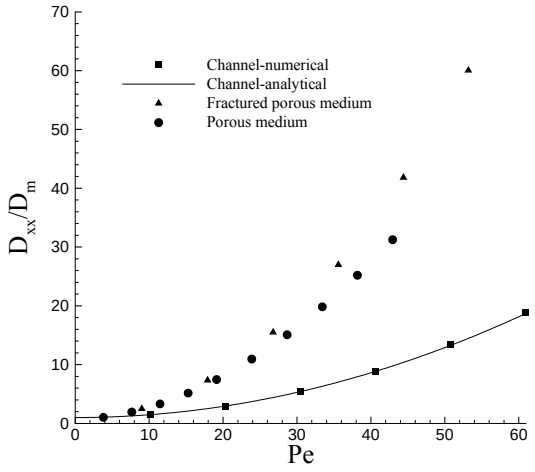

Figure 9. Dependency of the longitudinal dispersion coefficient on the Peclet number.

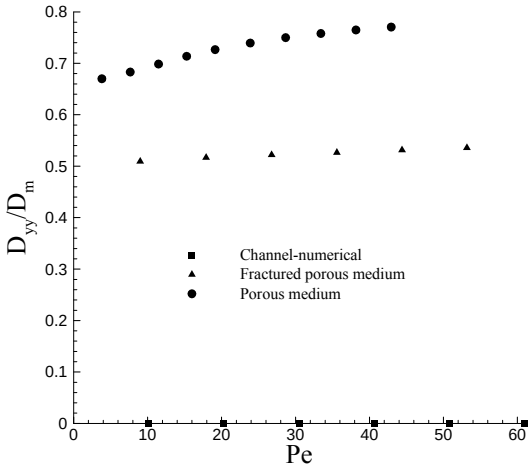

Figure 10. Dependency of the transverse dispersion coefficient on the Peclet number.

When the fractured porous media are conceptualized with dual-porosity and/or double-permeability models, the mass transfer between the facture and matrix systems is commonly described by $\frac{\partial c_f}{\partial t} = \omega(c_m - c_f)$, where c_f and c_m are the solute concentration in the facture and the matrix, respectively, and ω is the mass transfer coefficient. Assuming ω to be uniform spatially and integrating the relationship over space leads to $\omega = M'_f/(M_m - M_f)$ where M_f and M_m are the respective total solute mass in the facture and the matrix systems and $M'_f = dM_f/dt$ is the rate change of the mass in the facture. Figure 11 shows the time evolution of the dimensionless mass transfer coefficient ω for different matrix porosity values. It is seen that the coefficient goes to a constant for all matrix porosity values under consideration. Figure 12 shows the dependency of this coefficient on the Peclet number. It is seen that the dimensionless mass transfer coefficient is more or less constant for small to moderate porosity values and increases slowly as Pe for a high porosity value.

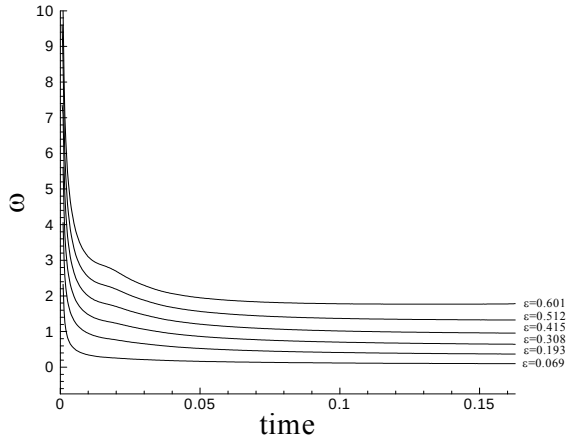

Figure 11. Time evolution of the mass transfer coefficient at *Pe*=51.35. The coefficient and time are normalized with respect to t_c.

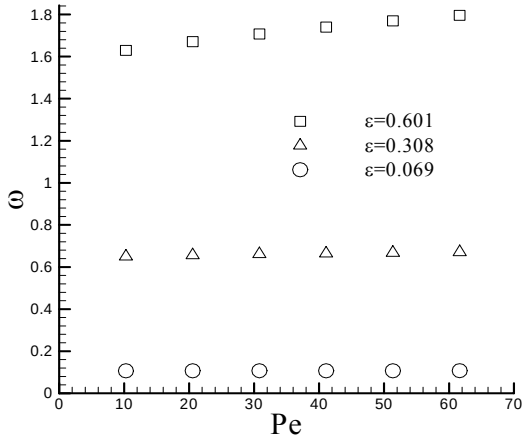

Figure 12. Dependency of dimensionless mass transfer coefficient on the Peclet number.

References

[1] J. Bear, C. F. Tsang, and G. de Marsily, *Flow and contaminant transport in fractured rock*, Academic, San Diego, Calif., 1993.

[2] L. Smith and F. W. Schwartz, Solute transport through fracture networks, in *Flow and contaminant transport in fractured rock,* edited by J. Bear, C. F. Tsang, and G. de Marsily, pp. 129-167, Academic, San Diego, Calif., 1993.

[3] S. H. Lee, M. F. Lough, and C. L. Jensen, Hierarchical modeling of flow in naturally fractured formations with multiple length scales, *Water Reso. Res.*, **37,** 443 (2001).

[4] S. Chen and D. Gary, Lattice Boltzmann Method for Fluid Flows, *Annu. Rev. Fluid Mech,* **30,** 329 (1998).

[5] S. Succi, E. Foti, and F. Higuera, Three-dimensional flows in complex geometries with the lattice Boltzmann method, *Europhys. Lett.* **10,** 433 (1989).

[6] A. W. J. Heijs and C. P. Lowe, Numerical evaluation of the permeability and the Kozeny constant for 2 types of porous-media, *Phys. Rev. E* **51,** 4346 (1995).

[7] A. K. Gunstensen and D. H. Rothman, Lattice-Boltzmann studies of immiscible two-phase flow through porous media, *J. Geophys. Res.* **98,** 7431 (1993).

[8] D. Zhang, R. Zhang, S. Chen, and W. E. Soll, Pore scale study of flow in porous media: Scale dependency, REV, and statistical REV, Geo phys. Res. Lett. **27,** 1195 (2000).

[9] Q. Kang, D. Zhang, S. Chen, and X. He, Lattice Boltzmann simulation of chemical dissolution in porous media, *Phys. Rev. E,* 036318, 2002.

[10] K. Balasubramanian, F. Hayot, and W. F. Saam, Darcy law from lattice gas hydrodynamics, *Phys. Rev. A*, **36,** 2248 (1987).

[11] M. A. A. Spaid and F. R. Phelan, Jr., Lattice Boltzmann methods for modeling microscale flow in fibrous porous media, *Phys. Fluids*, **9,** 2468 (1997).

[12] D. M. Freed, Lattice Boltzmann method for macroscopic porous media modeling, *Inter. J. Modern. Phys*, **9(8),** 1491 (1998).

[13] Q. Kang, D. Zhang, and S. Chen, Unified lattice Boltzmann method for flow in multiscale porous media, *Phys. Rev. E,* **66,** 056307 (2002).
[14] H. Brenner, Dispersion resulting from flow through spatially periodic porous media, *Philos. Trans. R. Soc. London* Ser. A, **297,** 81 (1980).

Quantification of Non-Fickian Transport in Fractured Formations

Brian Berkowitz and Harvey Scher
Department of Environmental Sciences and Energy Research
Weizmann Institute of Science
Rehovot 76100 Israel
972-8-9342098 (Fax: 972-8-9344124)
brian.berkowitz@weizmann.ac.il; harvey.scher@weizmann.ac.il

Fractured aquifers are highly complex systems. Within them, groundwater movement is influenced by several superposing factors, which lead to highly variable velocity fields. Controlling factors include, to varying degrees, fracture network geometry, physical and/or geochemical interaction with the host rock matrix, small- and large-scale roughness of the fracture walls, and the presence of fracture-filling material. A principal challenge is to describe the movement of chemicals in these velocity fields. Realistic quantification of this movement is complicated by the uncertainty in characterization of aquifer properties. As a consequence, modeling approaches are needed that describe the important features of the problem, within various levels of uncertainty. We focus here on the movement of conservative chemicals in saturated fractured aquifers.

A general approach to quantifying transport—one that does not rely on Fickian transport assumptions—is based on continuous time random walk (CTRW) theory (Scher and Lax, 1973a,b). In the context of geological materials, CTRW theory was developed and applied to numerical studies of transport in random fracture networks (Berkowitz and Scher, 1997; 1998), and to modeling tracer transport in laboratory flow cells containing heterogeneous porous media (Berkowitz et al., 2000; Levy and Berkowitz, 2003). We have recently demonstrated (Berkowitz and Scher, 2001) how a modeling approach based on the CTRW framework accounts for a very wide range of non-Fickian (anomalous) and Fickian transport behaviors, and how the advection-dispersion equation (ADE) can be derived from it under specific, well-defined conditions. We have also demonstrated application of the CTRW approach on previously published measurements from a natural gradient tracer test, performed in a large, isolated block of fractured till (Kosakowski et al., 2001).

The CTRW is based on a physical picture of contaminant motion consistent with the geometric and hydraulic characterization of fracture systems. In these systems, contaminants (particles) migrate through the labyrinth of interconnected fracture fragments (ff). The motion can be envisioned as particles executing a series of discrete transitions between ff intersections. The size distribution of the ff sets the spatial scale, but the transport is primarily controlled by the distribution of transit times in each ff, due to the flow velocities (v). Non-Fickian transport behavior occurs if the latter distribution is broad, i.e., there is a slow algebraic power tail for long transit times. A sufficient encounter between the migrating particle along a flow path and a wide velocity range can produce this tail.

The CTRW accounts naturally for the cumulative effects of a sequence of these transitions. The transitions are characterized by $\psi(\mathbf{s},t)$, the probability rate for a displacement $\mathbf{s}$ with a difference

of arrival times of t. In the CTRW approach, one can determine the evolution of the particle distribution (plume), $P(\mathbf{s},t)$, for a general $\psi(\mathbf{s},t)$, so there is no *a priori* need to consider the moments of $P(\mathbf{s},t)$. The challenge is to map the important aspects of the physical picture of the particle motion in the fracture network onto a $\psi(\mathbf{s},t)$.

A key consequence of disorder or strong heterogeneity is the appearance of a power law, i.e., $\psi(\mathbf{s},t) \rightarrow t^{-1-\beta}$, over a large range of the long time behavior of $\psi(\mathbf{s},t)$. In general, non-Fickian transport arises for $0 < \beta < 2$. In this range, distinctly different transport behaviors can be identified. The relative shapes of the transport curves, and the rate of peak advance , vary strongly as a function of β. For $0 < \beta < 1$, transport is highly non-Fickian, and the concentration peak moves much more slowly than the Fickian, with a longer forward advance of particles (Figure 1). For $1 < \beta < 2$, the mean particle plume moves with the average fluid velocity, but the tails remain broader ("heavier") than those of a Fickian distribution. For $\beta > 2$, the transport becomes Fickian. For $0 < \beta < 1$, both the mean and the standard deviation of the migrating plume scale as t^{β}; in contrast to Fickian transport, where the mean and standard deviation scale as t and $t^{0.5}$, respectively.

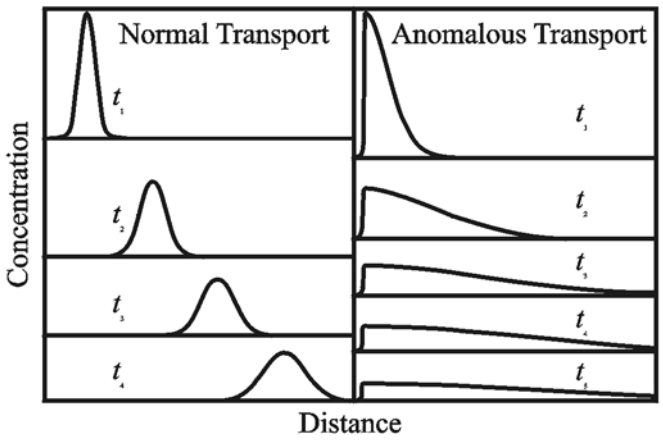

Figure 1. Schematic illustration of the contrast between non-Fickian (anomalous) and Fickian (normal) transport, in terms of spatial concentration profiles (adapted from Scher et al., 1991; after Berkowitz et al., 2000).

The value of β can be determined from the algebraic behavior of the large values for the ξ ($\equiv 1/v$) tail of the ξ distribution in the fracture network, or from breakthrough curve measurements. Through the parameter β, the range of random low velocities controls the character of the transport.

Tracer test measurements often consist of breakthrough curves of tracer concentrations as a function of time t, at selected distances from the tracer source. The breakthrough usually refers to the plane of exiting particles, and the curve corresponds therefore to a first-passage time distribution (FPTD). The FPTD evaluated with a range of β-values are shown in Figure 2. The

early and late arrival time behavior displayed in the breakthrough curves, and their asymmetry, are typical of non-Fickian transport. Although transport of particles in fast "channels" controls the early arrival times, the bulk of the transport behavior is influenced by particles that encounter low-velocity pathways (including relatively stagnant zones in fractures and in the host rock). The shape of the curves steepens as β increases, although the front becomes steeper than Fickian and the trailing tail is longer than Fickian.

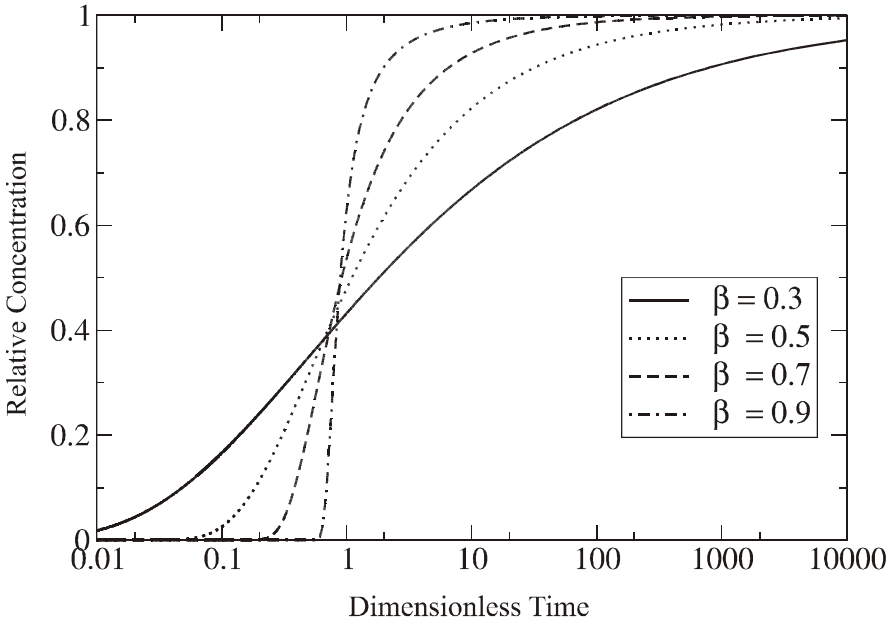

Figure 2. Semilog plots showing a range of cumulative FPTD curves versus a dimensionless time, for $\beta = 0.3, 0.5, 0.7, 0.9$ (after Kosakowski et al., 2001). The parameter β controls the shape of the curve. Thus, β can be considered as a "dispersion" parameter.

To illustrate application of the theory, we consider breakthrough data from a natural gradient tracer test conducted in a fractured till. A detailed description of the site and the tracer test can be found in Sidle et al. (1998). Breakthrough curves were obtained in sampling devices at two depths (2.5 m, 4 m) for different sampling locations. Figure 3 shows measurements and results of our analysis for one sampler (F5) at the larger depth. As seen in Figure 3, the FPTD curve convincingly captures the full evolution of the breakthrough measurements; it can be shown that the β exponent is correlated to the spatial and temporal scale of the experiment. In particular, the early and late time behaviors are captured remarkably well; these behaviors distinguish non-Fickian transport from Fickian transport. Significantly, Sidle et al. (1998) demonstrated that equivalent medium (identical to the ADE) and discrete parallel fracture network models were not able to capture the measured breakthrough curves.

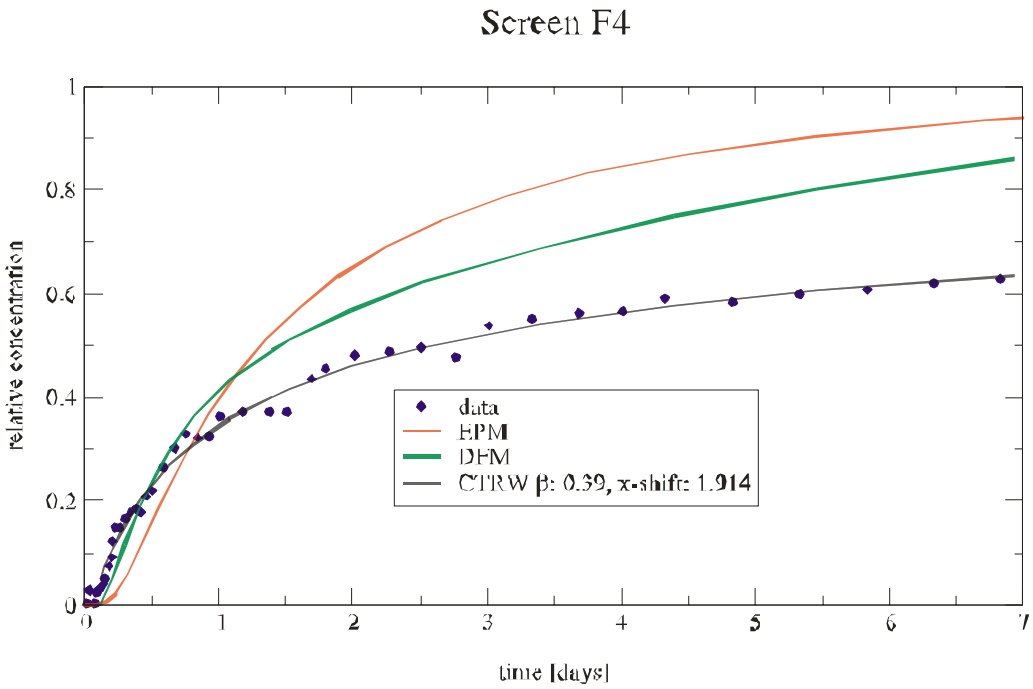

Figure 3. Best fit theoretical breakthrough curves based on the continuous time random walk (CTRW) theory and on the equivalent porous medium (EPM) and discrete fracture model (DFM) approaches. The relatively low value of β is indicative of an heterogeneous flow field. This is consistent with the geological mapping, which indicates that fracturing becomes sparser with depth (Kosakowski et al., 2001).

In summary, the CTRW framework quantitatively captures a broad range of non-Fickian and Fickian transport behaviors, and can be used in a predictive capacity. The solutions are robust and require a minimum number of fitting parameters. These parameters can be estimated on the basis of one or more measured breakthrough curves, and/or on the basis of information about the distribution of the velocity field and the relative scale of heterogeneity. The exponent β is advanced as a more useful characterization of the transport than the dispersion tensor, which is based on moments of the plume. The CTRW thus represents a valuable tool for the assessment of dispersive processes in fractured and heterogeneous porous media that are not amenable to analysis using classical advection-dispersion and stochastic theories.

There have recently been a number of advances The theory has been extended to deal with completely general $\psi(\mathbf{s},t)$ (e.g., a power law truncated at a large "cutoff" time t_c, so that the transport evolves to Fickian for $t > t_c$), and a unified framework has been developed to quantitatively account for transport in large-scale, nonstationary aquifer systems. In this framework the large spatial scales, with resolved structure, are treated deterministically while the small scales, with uncertain features, are treated probabilistically with the CTRW.

References

Berkowitz, B. and H. Scher, Anomalous transport in random fracture networks, Physical Review Letters, 79(20), 4038-4041, 1997.

Berkowitz, B. and H. Scher, Theory of anomalous chemical transport in fracture networks, Physical Review E, 57(5), 5858-5869, 1998.

Berkowitz, B. and H. Scher, The role of probabilistic approaches to transport theory in heterogeneous media, Transport in Porous Media, 42(1-2), 241-263, 2001.

Berkowitz, B., H. Scher and S.E. Silliman, Anomalous transport in laboratory- scale, heterogeneous porous media, Water Resources Research, 36(1), 149-158, 2000. (Minor correction: Water Resources Research, 36(5), 1371, 2000)

Kosakowski, G., B. Berkowitz and H. Scher, Analysis of field observations of tracer transport in a fractured till, Journal of Contaminant Hydrology, 47(1), 29-51, 2001.

Levy, M. and B. Berkowitz, Measurement and analysis of non-Fickian dispersion in heterogeneous porous media, Journal of Contaminant Hydrology, 64(3-4), 203-226, 2003.

Scher, H. and M. Lax, Stochastic transport in a disordered solid, I. Theory, Physical Review B, 7(10), 4491-4502, 1973a.

Scher, H. and M. Lax, Stochastic transport in a disordered solid, II. Theory, Physical Review B, 7(10), 4502-4519, 1973b.

Scher, H., M. F. Shlesinger and J. T. Bendler, Time-scale invariance in transport and relaxation, Physics Today, January, 26-34, 1991.

Sidle, C.R., B. Nilsson, M. Hansen and J. Fredericia, Spatially varying hydraulic and solute transport characteristics of a fractured till determined by field tracer tests, Funen, Denmark, Water Resources Research, 34(10), 2515-2527, 1998.

Modeling of Solute Transport Using the Channel Network Model: Limited Penetration into the Rock Matrix

Luis Moreno, James Crawford, and Ivars Neretnieks
Department of Chemical Engineering and Technology, Royal Institute of Technology
SE-100 44 Stockholm, Sweden

The Channel Network Model (CNM) implemented in the program CHAN3D was developed to calculate fluid flow and solute transport in fractured media specifically for cases in which flow occurs through channels within rock fractures (Moreno and Neretnieks, 1993). The model includes advection in the channels, sorption on the channel surfaces, diffusion into the rock matrix, and sorption within the matrix. The extent of the matrix is considered to be infinite.

To calculate the transport of radionuclides in the geosphere, the Channel Network Model (CNM) first determines the flow field. Once this is known, the transport is calculated by a particle-following technique. Each particle is followed from the source location to the outlet. The relation of Flow Wetted Surface (FWS) to flow rate, FWS/q, water residence time, and the interaction parameters between the radionuclides and the rock (the so-called Material Property Group, MPG), are determined for all the channels through which the particle has traveled. When the particle arrives at the exit point, the travel time for this particle is then determined from the sum of the product MPG*FWS/q in each channel:

$$\sum_{i}^{n_j} (\mathrm{MPG})_i \frac{(\mathrm{FWS})_i}{q_i}$$

where

$$\mathrm{MPG} = \varepsilon_p \sqrt{D_p (1 + \frac{(1-\varepsilon_p)K}{\varepsilon_p})}$$

where D_p, is the pore diffusivity, K the sorption coefficient, ε_p the matrix porosity, and q the water flow rate. The residence time distribution (RTD) is then determined by repeating the same procedure for many particles (several thousands).

The assumption of an infinite matrix depth is a good approximation for sorbing nuclides, since their penetration depth is rather small. However, nonsorbing nuclides can penetrate very deep into the rock matrix during the typical times used in performance assessment. In this paper, the Channel Network Model is improved to calculate the transport of solute through fractures when the penetration into the rock matrix is limited. This may occur, for example, in parallel fractures when the distance between the fractures is not large enough.

The analytical solution by Sudicky and Frind (1982) is used to generate type curves, which are used when particle tracking is applied. For a limited matrix depth, a new parameter has to be included to take into account the maximum penetration depth, B

$$\text{Sigma} = \left(\frac{K}{D_e} \right)^{0.5} \cdot B$$

The impact of limited diffusion into the rock matrix is schematically shown in Figure 1 below. The breakthrough curves may correspond to a situation in which the maximum penetration length is varied. For a small value of the parameter sigma, the breakthrough occurs very early. If the penetration depth is increased, keeping the other parameters constant, the breakthrough curve coincides with that for an infinite matrix (broken curve) at early times; only at longer times are differences observed.

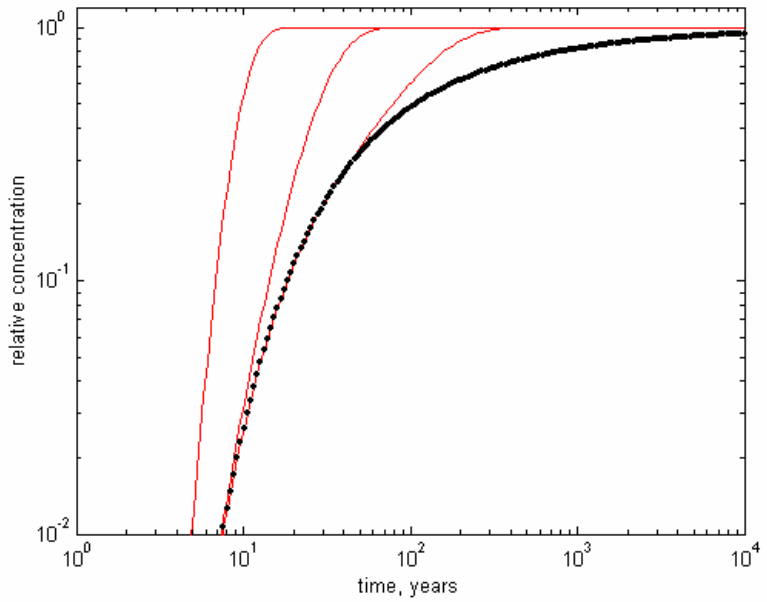

Figure 1. Breakthrough curves for different maximum penetration depths. The leftmost curve is for the smallest value of the Sigma parameter. The broken line is for an infinite matrix.

References

Moreno L. and I. Neretnieks, fluid flow and solute transport in a network of channels, Journal of Contam Hydrol 14 (3-4): 163-192, 1993.

Sudicky, E.A. and E.O. Frind, Contaminant transport in fractured porous media: Analytical solutions for a system of parallel fractures, Water Resour. Res., 18(6), 1634-1642, 1982.

Modeling Flow and Transport in a Sparsely Fractured Granite: A Discussion of Concepts and Assumptions

Urban Svensson
Computer-aided Fluid Engineering AB, Krokvägen 5, 602 10 Norrköping, Sweden

Modeling flow and transport in a sparsely fractured granite introduces a number of concepts and assumptions. When assessing the credibility of a computer code, it is essential that these concepts and assumptions are clearly defined and described. Here, we describe those of the code DarcyTools, which is currently being developed for the Swedish Nuclear Waste Management Company (SKB AB). The situation considered is outlined in Figure 1; essentially it is a fracture network contained in some domain with a length scale, L.

A key assumption of DarcyTools is that "*the number of fractures in a certain length interval follows a power law.*" This seems to be an undisputable assumption, since it basically states that there are more small fractures than big ones.

Numerical models normally discretize space in some way. DarcyTools is a finite-volume code and the domain created by it in Figure 1 is meshed to consist of a large number of cells. Typically a grid of 100 × 100 × 100 cells is used. The next assumption introduced is related to this grid and can be stated as follows: "*In a sparsely fractured granite, flow is assumed to be distributed on relatively few flow channels, that are due to large scale fractures and zones. It is assumed that all essential flow channels are due to fractures and zones that are larger than the grid size.*" The grid size, Δ 0.01L, indicates the lower limit for water-carrying fractures.

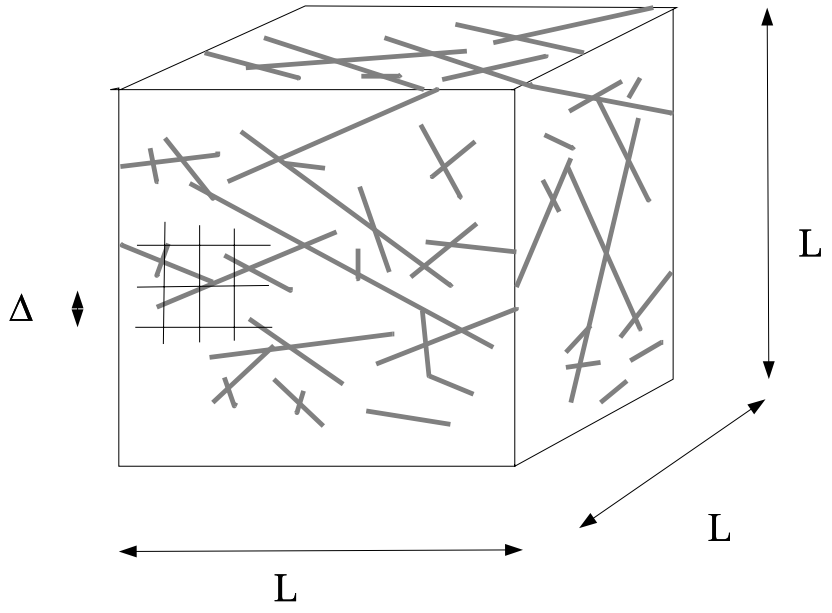

Figure 1.Situation considered. A fractured network in a domain of length scale L. A grid with a cell size equal to Δ is also indicated.

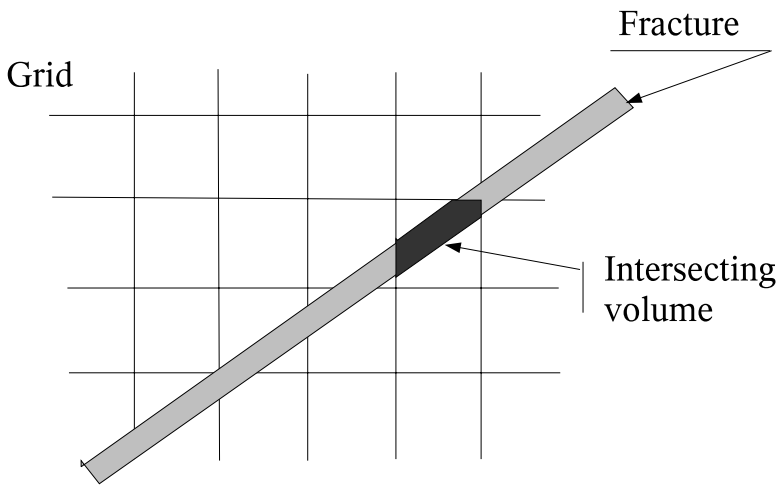

Figure 2. The intersecting volume concept.

Next, we will show how the resolved fractures (i.e. larger than Δ) are represented on the grid. Here, we will simply assume that a fracture, or a zone, can be described as a plane rectangular feature with a certain thickness and certain properties (conductivity, porosity, storativity, etc). The following concept is then used: "A fracture contributes to the grid value of a variable by an amount which is equal to the intersecting volume times the value of the variable in question. Contributions from all fractures that intersect the cell are added and the sum is divided by the volume of the cell" (as an example, see Figure 2). For porosity, the intersecting volume times the porosity yields the free space of the cell. It can be shown that this method gives accurate results for flow, transport (advection/diffusion equation) and particle tracking. (Some early examples can be found in Svensson [2001 a, b].)

As discussed above, fractures smaller than the grid size, Δ, are assumed to contribute negligible to the flow rate, but are assumed to be essential for dispersion and retention, when dealing with transport. A subgrid model, FRAME (FRActal scaling laws and Multirate Equations), has been developed to handle these processes. FRAME rests on a number of concepts and assumptions the most essential of which are:

- Fractures smaller than Δ are assumed to be filled with stagnant water (immobile volumes) and exchange matter with the flowing water (mobile volumes) by diffusion only.
- Subgrid fractures are assumed to follow a power-law (same as for resolved fractures).
- All immobile volumes can be represented by a set of boxes(or storage volumes), each with its own length scale, volume, and effective diffusion coefficient.

In Figure 3, some subgrid processes and concepts are illustrated. Let us consider a computational cell with a through flow, i.e. a cell with a flow channel. The flow "sees" a certain surface area, the flow wetted surface (FWS), as it passes the cell. The FWS may bring the flowing water in

contact with other fractures, gouge material, stagnant pools, etc. Most of these volumes can be expected to have stagnant water, and mass exchange is hence caused by molecular diffusion. For a stagnant pool, the relevant diffusion coefficient may be that for pure water, whereas diffusion into crossing fractures and the rock matrix may proceed at a diffusion rate that is several orders of magnitude smaller. As above, we will call the volume with flowing water the "mobile zone" and the volumes with no advection the "immobile zone." Fractures and volumes not in contact with the mobile zone are of course of no relevance and can be excluded from the discussion. The situation outlined in Figure 3 is quite complicated and does not lend itself to direct descriptions of individual processes.

The idealized problem is illustrated in Figure 4. The box with the smallest length-scale (dimension perpendicular to the mobile zone) will have the largest diffusion coefficient and normally also the largest contact area with the mobile zone. This volume will hence have a fast response. The multirate diffusion technique (Haggerty and Gorelick, 1995) provides an efficient way to handle this problem computationally.

In summary, the computer code DarcyTools is based on a number of concepts and assumptions that need to be scrutinized and tested. These have briefly been introduced here in a very descriptive way. However, the corresponding mathematical models have not been discussed. Another consideration is that concepts and assumptions should result in an effective code, if they are of practical value. This has actually been a guiding principle in the development of DarcyTools and one can state that "*DarcyTools can simulate flow and transport in a fracture network consisting of one million resolved fractures as represented in a grid of ten million cells,, all on a high end PC*." One may further claim that "*By the subgrid model FRAME, fractures with length scales from mm to km can be treated as a continuous field*."

References

Haggerty R. and Gorelick S.M., 1995. Multiple-rate mass transfer for modelling diffusion and surface reactions in media with pore-scale heterogeneity. *Water Resour. Res.*, 31 (10), pp 2383-2400.

Svensson U., 2001 a**.** A continuum representation of fracture networks. Part I: Method and basic test cases. *Journal of Hydrology*, 250, pp 170-186.

Svensson U., 2001 b. A continuum representation of fracture networks. Part II: Application to the Äspö Hard Rock Laboratory. *Journal of Hydrology*, 250, pp 187-205.

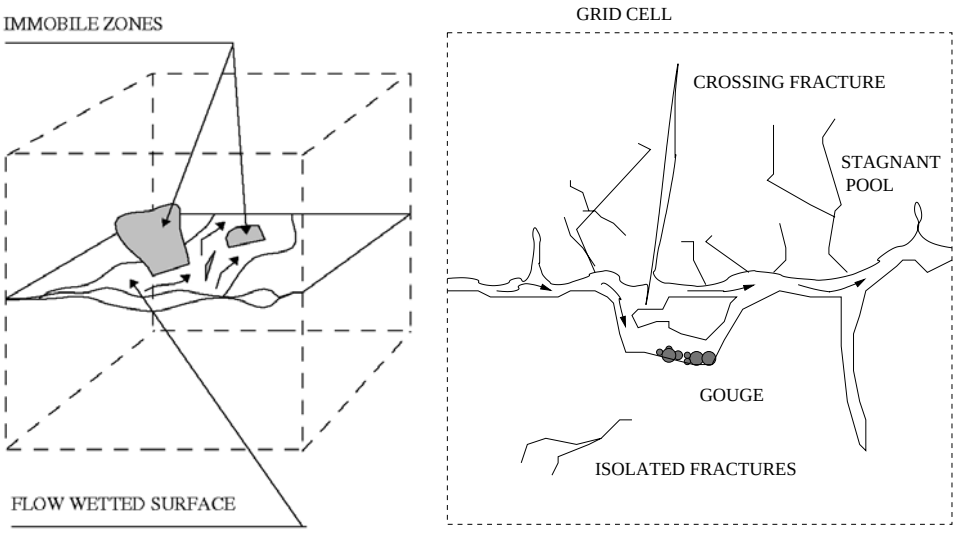

Figure 3. Illustration of subgrid processes and concepts.

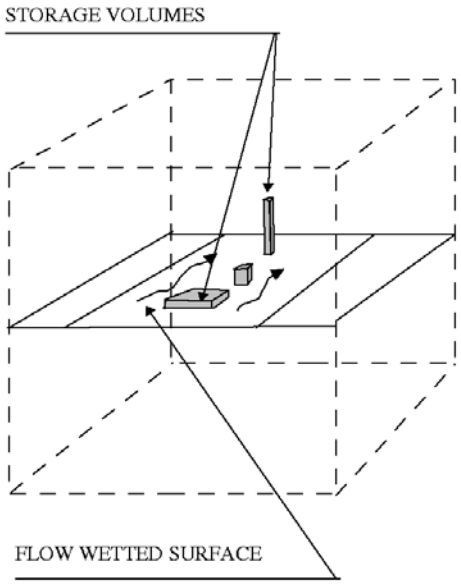

Figure 4. The assumed structure of subgrid volumes and areas.

Upscaling Discrete Fracture Network Simulations of Solute Transport

S. Painter[1], V. Cvetkovic[2], J.O. Selroos[3]
[1]Center for Nuclear Waste Regulatory Analyses, Southwest Research Institute, San Antonio Texas
[2]Royal Institute of Technology, Stockholm, Sweden
[3]Swedish Nuclear Fuel and Waste Management Company, Stockholm, Sweden

Introduction

Transport in fractured rock is sometimes modeled using discrete fracture network (DFN) simulations. These DFN models avoid the volume averaging required for traditional equivalent continuum models and generally represent a wider range of transport phenomena. DFN models play an important role in fundamental conceptual model evaluations, but site-specific applications are generally limited to near-field scales (50–100 m) owing to the large computational demands. Many applications, particularly those involving geological disposal of high-level nuclear waste, involve spatial scales of a few hundred meters to a few kilometers in three dimensions. Thus, the need exists for methods to bridge the gap between the spatial scale at which DFN simulations are tractable, and the repository geosphere scale.

One approach for bridging this gap in scales is to use near-field scale DFN simulations to inform or "train" a more computationally efficient method, which can then be used at the larger scale. The implicit assumption is that the fracture network model used in the DFN simulation is representative of the fracture network of the larger domain. This general approach has been referred to as the hybrid approach (National Research Council, 1996) and can also be thought of as an upscaling problem. In this paper, we describe a new method for upscaling the results of DFN particle-tracking simulations. Specifically, we extract relevant information from DFN particle-tracking simulations and use these in a Monte Carlo random walk at the geosphere scale. Retention in the rock matrix, including the effects of random spatial variations in retention parameters, is accounted for rigorously using a stochastic Lagrangian formalism.

Transport Model

Consider a hypothetical solute source located in a fractured rock volume. Steady-state groundwater flow driven by a regional hydraulic gradient carries solutes toward a monitoring boundary located downstream. Diffusive mass exchange with the host rock and sorption in the host rock delay the downstream movement. We are interested in the time-dependent mass flux at this monitoring boundary. In general, multiple meandering transport pathways (trajectories) connect the source location to the monitoring boundary, and the flow velocities, fracture apertures, and possibly retention properties fluctuate along each trajectory. Because of these unobserved fluctuations in the transport velocities and retention properties along the pathways, the flux at the monitoring boundary and related quantities are random variables. We wish to characterize the distributions for these random quantities.

Previous work (Cvetkovic et al., 1998, 1999) has shown that the fundamental solution—the impulse response function—for a Lagrangian (streamline) representation of transport with retention in fractured rock is given by

$$\gamma_l(t;\tau,B) = \frac{H(t-\tau)B}{2\sqrt{\pi}(t-\tau)^{3/2}} \exp\left[\frac{-B^2}{4(t-\tau)} - \lambda t\right] \tag{1}$$

where λ is the radionuclide decay constant, τ is the water residence time along the trajectory, H is the Heaviside function, and B involves retention properties integrated along the streamline. The function $\gamma_l(t;\tau,B)$ is the conditional impulse response function, the time-dependent flux at a monitoring boundary located at distance l from a Dirac-δ input for given values of τ and B. To characterize the distribution for this and related random quantities, $f(\tau,B)$, the joint probability density for τ and B, is needed.

The groundwater residence time can be written in integral form as $\tau = \int_0^l \frac{dx}{V_x}$ where x is the coordinate in the direction of mean flow and V_x is the velocity component in that direction. Similarly, $B = \int_0^l (\vartheta D R)^{1/2} \frac{dx}{bV_x}$ where ϑ, D, R, b are the matrix porosity, effective diffusion coefficient, retardation factor, and fracture half aperture, respectively.

Equation (1) is valid for the situation of unlimited diffusion in the rock matrix, which is the most widely applied retention model (e.g., Neretnieks, 1980). However, it is emphasized that this is only a special case of a more general approach and that it is straightforward to apply the upscaling method to be discussed in the following section using other retention models.

Random Walk Representation for τ and B

The two Lagrangian quantities τ and B characterize transport and retention along a given trajectory. Specifically, given a value for τ and B, we can calculate the conditional time-dependent discharge from Equation (1). Given a distribution for τ and B, we can calculate the unconditional discharge and measures of uncertainty in the predicted discharge. Thus, the challenge is to obtain a model or algorithm for the joint distribution of τ and B.

Consider a discretization of the trajectory into a number of jumps, with each jump corresponding to transit through an individual fracture. Let $\Delta_1, \Delta_2, \cdots$ denote independent and identically distributed random variables that model the change in the x coordinate for the jumps. Similarly, let $\Delta\tau_1, \Delta\tau_2, \cdots$ and $\Delta B_1, \Delta B_2, \cdots$ denote random variables modeling the change in τ and B, respectively. We allow correlation between $\Delta\tau_i$ and ΔB_i, but each pair in the sequence is independent of the other pairs in the sequence.

After n jumps, the x-position is $L(n)=\sum_{i=1}^{n}\Delta_i$ and the τ and B values are $\tau(n)=\sum_{i=1}^{n}\Delta\tau_i$ and $B(n)=\sum_{i=1}^{n}\Delta B_i$. The number of jumps required to hit the monitoring boundary is a random variable $N_l=\min\{n : L(n)\geq l\}$, and the corresponding τ and B are:

$$\tau(N_l)=\sum_{i=1}^{N_l}\Delta\tau_i \qquad B(N_l)=\sum_{i=1}^{N_l}\Delta B_i \tag{2}$$

The stochastic process $\{\tau(N_l),B(N_l)\}_{l>0}$, which defines the desired distribution of τ and B for a given l, is an example of a continuous-time random walk in a two-dimensional space, with the x-position taking the usual role of time and τ,B taking the role of position. Formal solutions in the one-variable case (i.e., ignoring B) exist (e.g., Berkowitz and Scher, 1997), and these formal solutions can be extended to the two-variable case. These formal solutions are, however, not useful for calculations.

Monte Carlo Simulation

For calculations, two steps remain: (1) determining the joint distribution of individual fracture values $\Delta,\Delta\tau,\Delta B$ appropriate for a given site, and (2) determining the global distribution of τ,B given the individual fracture distribution.

At present, DFN simulation is the only viable method for determining the joint distribution of individual fracture values. In this approach, realizations of the DFN at the near-field scale are generated using standard tools such as FracMan (Dershowitz et al., 1998), taking into account as much site-specific information as possible to constrain the network properties. Site-appropriate hydraulic boundary conditions are applied and the resulting flow is solved. Particles are then tracked through the DFN velocity field. For each fracture segment traversed by each particle, the $\Delta,\Delta\tau,\Delta B$ triplet is recorded. The set of these triplets represents Monte Carlo samples from the joint distribution.

The results of the DFN simulation can then be used to upscale the individual fracture values to obtain global τ,B distributions. The procedure is to form a particle trajectory by repeatedly selecting values at random from the library of $\Delta,\Delta\tau,\Delta B$ triplets and forming the running sums [Equation (2)]. A trajectory is terminated once the x value exceeds l, indicating that the monitoring surface of interest has been reached. The τ,B at that point becomes one Monte Carlo sample of the global distribution. Because this procedure is very fast, it can be executed for large l and is not limited by the same computational constraints as DFN simulations. Thus, it can be used to upscale the results of DFN simulations, provided that the fracture-network model used in the DFN simulations is representative of conditions throughout the larger region of interest.

The upscaling approach is similar to the "statistical continuum" approach of Schwartz and Smith (1988), who fit probability distributions to velocities derived from DFN particle tracking simulations and then sample these fitted velocities distributions to simulate transport of conservative tracers. We do not attempt to fit a distribution, but use the DFN simulated values

directly. Moreover, we include the effects of retention, as opposed to Schwartz and Smith, who only considered conservative tracers.

Accounting for Sequential Correlation on the Trajectory

An underlying assumption in the random walk representation is that each particle jump is independent from the other jumps. However, numerical experiments (Painter et al., 2002) using two- and three-dimensional DFN simulations reveal a small degree of correlation in velocity (and hence $\Delta\tau$ and ΔB) between successive jumps. The Monte Carlo upscaling procedure can be modified slightly to capture this weak sequential correlation.

To account for correlation, we give each particle an internal state and use the value of this state to bias the selection of the next $\Delta,\Delta\tau,\Delta B$ triplet in the sequence. Specifically, we record, in addition to the $\Delta,\Delta\tau,\Delta B$ triplets, the particle speed for each segment of each particle trajectory in the DFN simulation. These speeds are then binned into a small number (typically 10) of speed classes, which define the internal state of the particle. When executing the Monte Carlo simulation, the state of the current segment is used to constrain the selection of the next $\Delta,\Delta\tau,\Delta B$ triplet. Specifically, if the sampled segment has state (speed class) designated K, then only those segments that have K as their preceding state are eligible for selection. Using this algorithm, the sequence of internal states represents a discrete-state Markov process, which directs the random walk simulation of the particle trajectory in the x,τ,B space.

Numerical Tests of the Upscaling Method

Three-dimensional DFN simulations (Outters, 2003) designed to mimic the fracture network near the Äspö hard Rock Laboratory, Sweden were used to test the upscaling method. The DFN and particle tracking simulations were generated using the FracMan/MAFIC (Dershowtiz et al., 1998) software. The computational domain was a 100 m × 100 m × 100 m cube. Each of the 20 realizations contained about 20,000 disk shaped fractures tessellated into triangular finite elements. In each of the generated realizations, generic boundary conditions were prescribed so as to obtain a globally unidirectional flow. Once the flow field was solved, a large number of inert particles were released from a 50 m × 50 m square on the upstream boundary and traced though the network assuming perfect mixing at each intersection.

In the DFN simulations, the retention properties ϑ, D, and R were assumed to be spatially constant and known. In this case, variability in B arises from variability in aperture and velocity along the pathway, $B=(\vartheta D R)^{1/2}\beta$, and the new variable $\beta=\int_0^l \frac{dx}{bV_x}$ captures this variability. This assumption of constant retention properties is reasonable, given that little information on retention property variability is available. However, we emphasize that spatial variability in the retention properties can easily be accommodated in the upscaling procedure. The $\Delta,\Delta\tau,\Delta\beta$ values for each particle in each fracture segment were recorded and saved. The global τ and β values for each particle were also saved for comparison purposes.

The marginal distributions of τ and β from the DFN simulations and the two Monte Carlo upscaling methods are compared in Figure 1. The data points represent the results of the DFN simulation, the dashed lines are from the random walk (RW) upscaling procedure, and the solid lines are the result of the Markov-directed random walk (MDRW). The RW upscaling method generally reproduces the distributions of τ and β in the right tail and in the bulk of the distribution, but generally predicts slightly higher values of τ and β in the left tail. The MDRW produces a better fit to the left tail for both distributions.

Figure 1 suggests that the upscaling procedures provide reasonable approximations to the τ and β distributions. To assess the adequacy of the approximations in a more quantitative way, we consider two scalar measures of geosphere performance: the mass-fraction released μ, which is obtained by integrating Equation (1) over all times, and the maximum value for γ, denoted γ^*, which is also obtained from Equation (1). The latter index is of interest because it is closely related to the peak radiological dose. Both of these performance indices are random variables, and we consider the expected values. Table 1 provides expected values for μ and γ^* as calculated from the DFN, the RW, and the MDRW representations of the τ and β distributions using three radionuclides. In all cases, the MDRW representation is better than the RW representation. Both upscaling methods represent $<\mu>$ better than $<\gamma^*>$, but even for $<\gamma^*>$, the MDRW values are within a factor of 2 of the DFN simulation value, which is likely to be adequate for performance-assessment purposes.

The computational requirements for the MDRW algorithm are smaller than those of a full DFN simulation by many factors of ten, and once a small-scale DFN simulation has been completed, the MDRW can be used to extrapolate to larger scales. An example is shown in Figure 2. In constructing this figure, the MDRW algorithm was executed for l = 500 m. The resulting τ,β joint distribution was then used to construct the distributions for μ and γ^* for ^{126}Sn and ^{135}Cs. DFN simulations at this scale would not have been feasible because of computational limitations.

Conclusions

The two random-walk methods for upscaling DFN simulations provide alternatives to site-scale continuum transport models. The suggested procedure is to first perform small-scale DFN simulations utilizing site-specific information on the fracture network, and then use the results collected from these DFN simulations in a Monte Carlo calculation to obtain transport results at the field scale. This approach avoids volume averaging and other assumptions inherent in the continuum approach. It also considers retention processes, and the effects of random spatial variations in flow velocities and retention properties. Although not specifically addressed here, variations in fracture aperture within each fracture can also be accommodated.

The main limitation of the upscaling approach presented here is that it requires that the geometrical properties of the network not vary in space. For anisotropic networks, it also presumes that the direction of macroscopic head gradient does not vary over the region of interest. Variants of the upscaling approach that address these considerations are under development.

Acknowledgments

The authors thank the Swedish Nuclear Fuel and Waste Management Company (SKB) and the Southwest Research Institute Advisory Committee for Research for supporting this research.

References

B. Berkowitz and H. Scher, Anomalous transport in random fracture networks. 1997. Phys. Rev. Lett., 79, 4038-4041.

V. Cvetkovic, G. Dagan and H. Cheng, 1998. Contaminant transport in aquifers with spatially variable hydraulic and sorption properties, Proceedings of the Royal Society, London, 454:2173-2207.

V. Cvetkovic, J.O. Selroos and H. Cheng, 1999. Transport of reactive tracers in rock fractures. *Journal of Fluid Mechanics*, 378:335-356.

W.S. Dershowitz, G. Lee, J. Geier, T. Foxford, P. LaPointe, and A. Thomas. 1998. *FracMan Interactive Discrete Feature Analysis, Geometric Modeling and Exploratory Simulations User Documentation, V2.6*, Golder Associates Inc, Seattle, Washington.

National Research Council. 1996. *Rock Fractures and Fluid Flow: Contemporary Understanding and Applications*. National Academy Press, Washington, D.C.

I. Neretneiks, 1980. Diffusion in the rock matrix: An important factor in radionuclide retention. Journal of Geophysical Research, 85(B8), 1703-1713.

N. Outters, 2003. A generic study of discrete fracture network transport properties using FracMan/Mafic, SKB Report R-03-13. Swedish Nuclear Fuel and Waste Management Company, Stockholm, Sweden.

S. Painter, V. Cvetkovic, and J.O. Selroos, 2002. Power-law velocity distributions in fracture networks: Numerical evidence and consequences for tracer transport. Geophys. Res. Lett 29(14).

F.W. Schwartz and L. Smith, 1988. A continuum approach for modeling mass transport in fractured media. *Water Resources Research*, 23(8):1360-1372.

Table 1. Expected values for $< \gamma^* >$ and $<\mu>$ for three tracers, as generated with the RW and MDRW upscaling methods compared with those from DFN simulations.

Tracer	$t_{1/2}$ yr	D m^2/yr	K_d m^3/kg	$< \gamma^* >$ RW	MDRW	DFN	$<\mu>$ RW	MDRW	DFN
^{126}Sn	1.0e5	1.3e-6	1.0e-3	1.5e-8	6.4e-8	1.1e-7	0.086	0.12	0.14
^{129}I	1.6e7	3.9e-6	0	2.3e-4	8.5e-4	1.4e-3	0.97	0.97	0.97
^{135}Cs	2.3e6	1.3e-6	5.0e-2	5.0e-12	2.9e-11	5.1e-11	0.013	0.029	0.037

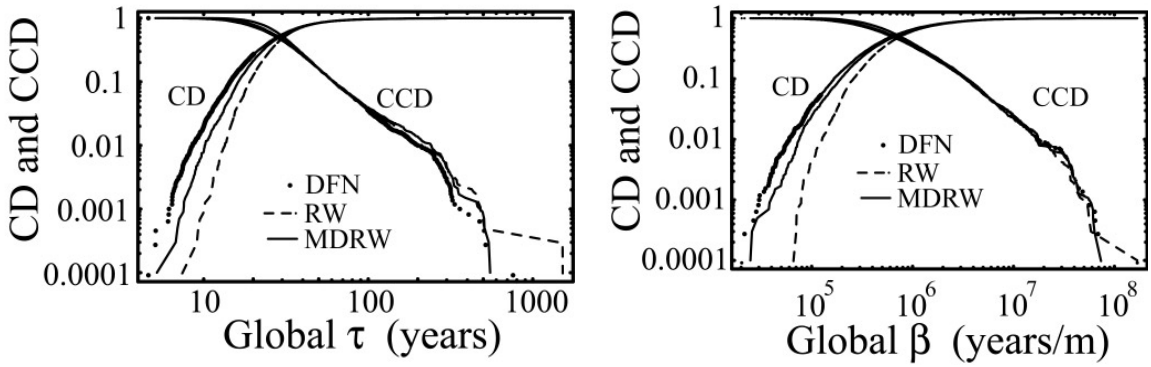

Figure 1. Cumulative distribution (CD) and complementary cumulative distribution (CCD) of global τ and β from discrete fracture network simulations compared with upscaling results, based on a random walk (RW) and Markov-directed random walk (MDRW) simulation.

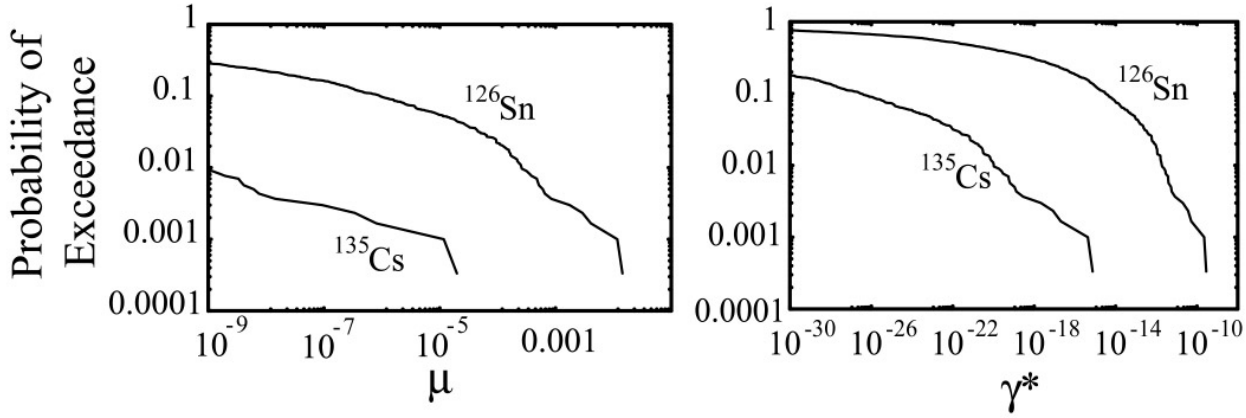

Figure 2. Distributions of μ and γ^* for two radionuclides after upscaling to the 500 meters scale. DFN simulations at this scale are impractical due to computational limitations.

Uncertainty Evaluation of Groundwater Flow by Multiple Modeling Approach at Mizunami Underground Research Laboratory Project, Japan

Atsushi Sawada[1], Hiromitsu Saegusa[2], and Yuji Ijiri[3]
[1] Japan Nuclear Cycle Development Institute, Tokai Works, Waste Management & Fuel Cycle Research Center, Waste Isolation Research Division, 4-33 Muramatsu Tokai Ibaraki, 319-1194, Japan
[2] Japan Nuclear Cycle Development Institute, Tono Geoscience Center, Mizunami Underground Research Laboratory, 1-64, Yamanouchi Akeyo Mizunami Gifu, 509-6132, Japan
[3] Taisei Corporation, Engineering Division, 1-25-1 Nishi Shinjuku Shinjukuku Tokyo, 163-0606, Japan

Introduction

The Japan Nuclear Cycle Development Institute (JNC) is conducting research to establish a technical basis for high-level radioactive waste (HLW) disposal in Japan. In the so called "H12 report" [1], the second progress report compiling Japanese R&D studies relevant to HLW disposal, analyses of radionuclide migration in a natural barrier were conducted based on simplified and conservative assumptions, in order to consider a broad range of geological environments and a flexible repository layout. One of the main issues consequent to the general study of the H12 report is the need to integrate multi-disciplinary applications of various knowledge bases and technologies to a specific site. Subsequently, JNC has been conducting the "Mizunami Underground Research Laboratory (MIU) project" [2] and the "Regional-scale Hydrological (RSH) study" [3] in the Tono area, Gifu prefecture, Japan, as part of the geo-scientific research program in J NC. The MIU project is being conducted step by step and is currently in the ground-surface based investigation phase, which will be followed by the underground construction phase and then by the investigation phase at the underground research facility.

In order to facilitate integration between site investigation and performance assessment (PA), an iterative approach using a geo-synthesis flow chart has been taken. The geo-synthesis flow chart, shows the data flow from acquisition to PA input via analysis and/or numerical model simulations, such as hydrogeological modeling and groundwater simulation. We have been evaluating uncertainties involved in hydrogeological modeling by employing multiple modeling experts and/or conceptual models [4,5]. Several performance measures (PMs) for the groundwater simulation are specified to identify the differences among multiple modeling experts and/or conceptual models. By defining PMs from the PA point of view, the current understanding of groundwater flow conditions at the site can be clarified for PA.

Table 1. Five multiple modeling experts and/or conceptual models.

Model	Effective continuum model				Channel network model
Code name	TOUGH2 [6]	POR-SALSA [7]	EQUIV_FLO [8]	Frac-Affinity [9]	Don-Chan [10]
Organization	LBNL	Sandia	Taisei corp.	JNC Tono	Saitama Univ.
Modeling method	Continuum parameters from hydraulic characteristics	Continuum parameters from hydraulic characteristics	Continuum parameters from fracture characteristics	Continuum parameters from hydraulic characteristics	Channel pipe parameters from fracture characteristics
Analysis method	Integrated finite difference method	Finite element method	Finite element method	Finite difference method	Finite difference method
Modeled structures	Tsukiyoshi F. 2 lineaments Sediments Unconformity	Tsukiyoshi F. lineaments Unconformity	Tsukiyoshi F. Fracture zone along F. Sediments Unconformity 3 sub-domains in granite	Tsukiyoshi F. Lineaments Fracture zone along F. Sediments Unconformity 3 sub-domains in granite	Tsukiyoshi F. Lineaments Fracture zone along F. 3 fracture sets

Table 2. List of data used in this study.

Type of data	Data	Objective and description
Literature survey	Topographic data	Interpretation of topography
	Geologic map	Interpretation of geological structure
Remote sensing	Aerial photograph	Identification of lineaments
	Landsat image	
	Spot Image	
Ground surface investigations	Seismic surveys	Identification of geological structures mainly conducted at MIU site
	Electromagnetic surveys (MT)	Identification of unconformity
	Measurement of groundwater level	Total 158 holes
	Measurement of water-balance	Tono mine (discharge from the mine), Garaishi area (evapotranspiration, amount of recharge, river flow)
Borehole investigations	Observation of drill core	Interpretation of geologic columnar section
	Water leakage during drilling	Measurement of highly conducting zone
	Borehole Television logging	Observation of fracture characteristics
	logging	Caliper, density, flow, natural g-ray, resistivity, neutron, temperature, acoustic velocity, etc.
	Hydraulic head measurement	Distribution of hydraulic head
	Hydraulic conductivity test	Interpretation of hydraulic conductivity

Modeling Region

The study area was defined as a 6 km × 4 km region centered on the MIU site, as shown in Figure 1. Topographic ridges bound the study area to the north, east and west sides and the Toki River forms the southern boundary. The site is almost pentagonal in shape and elongated in a NNW-SSE direction. The bottom boundary is set at -3,000 meters above see level (masl). Figure 1 also shows the geological map around the study area. In the study area, the Tertiary

sedimentary rocks unconformably overlie the Cretaceous Toki Granite and the upper parts of the Toki Granite have been weathered. The Tsukiyoshi fault extends into the study area with strike of E-W and a dip of 70^{o} to 80^{o} S. The Toki Granite and Mizunami Group are displaced by the fault, with approximately 30 m of vertical displacement.

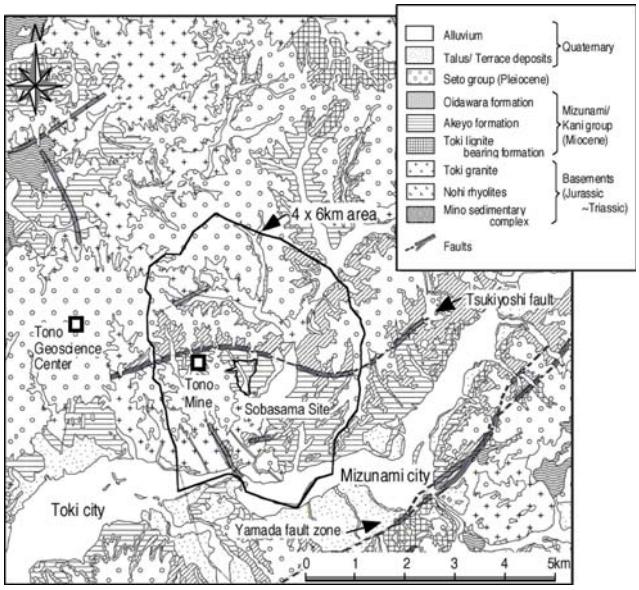

Figure 1. Study area (4 ×6 km area).

Multiple Modeling Experts and/or Conceptual Models

We chose five modeling experts and/or conceptual models as described in Table 1, which include effective continuum models and a channel network model. All modeling experts started by reviewing the existing data that were obtained from the surface-based investigation of the MIU project and the RSH study, (such as geological, geophysical and hydrological investigation on the ground surface and along the boreholes, as listed in Table 2). Making some assumptions, checking data availability for each model input and considering computational restrictions, we each built hydrogeological and numerical models according to their conceptual models.

Groundwater Flow Simulations and PMs

Each numerical model was then applied to calculate performance measures (PMs) under steady state, isothermal groundwater flow. In this study, the groundwater travel times and travel lengths from the specified points deep underground to the downstream boundary of the model were defined as the PMs relevant to the PA.

Results and Discussion

Figure 2 shows an example of PM results. There are two groups from the travel-time point of view: (1) several years and (2) several hundred to several thousand years. The main reason for the several orders of difference among the travel times might be the differences in the effective porosity used in each model. The former group estimated the effective porosity from the fracture data considered in each hydrogeological model, whereas the latter used 0.01~0.035 as a general

porosity value for granitic rocks. Two groups can also be identified from the particle trajectories: those flowing to the surface along the Tsukiyoshi fault and those flowing through the Tsukiyoshi fault at depth. This might be caused by the differences between hydraulic properties assigned to the Tsukiyoshi fault and the boundary conditions, which were differently defined for each model (since there were no reliable data).

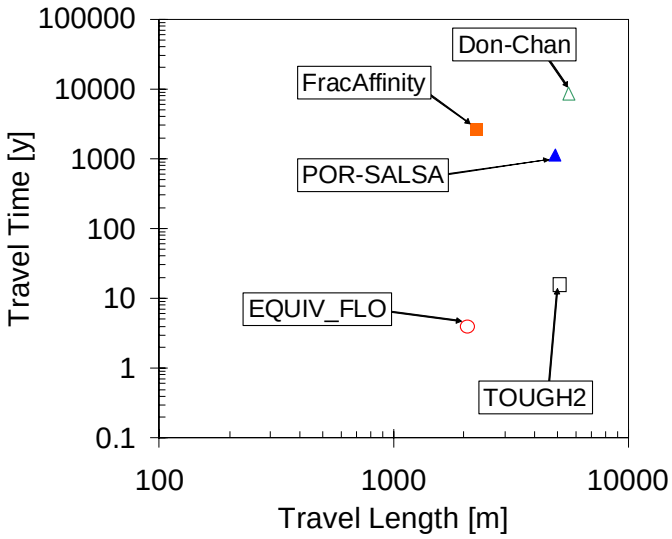

Figure 2. An example of PM results.

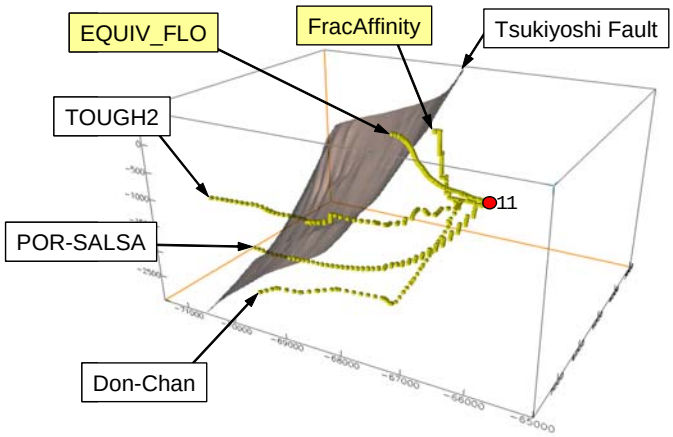

Figure 3. An example of travel paths from the specified point.

The two examples described above are the main uncertain factors on the PMs defined in this study. From the results of a more comprehensive analysis of the differences in PMs, we found the following shortcomings in the site characterization data set:

- No data for larger structure w/o lineaments
- No quantitative data for hydraulic properties of Tsukiyoshi fault
- No data for defining BCs
- No data for estimating effective porosity

This information was transferred to our site investigation team to aid in their investigation, making certain that it incorporates use of the geo-synthesis flow chart and the iterative approach.

Acknowledgments

Modeling and simulation was conducted by the following persons: TOUGH2—Drs. Doughty and Karasaki of Lawrence Berkeley National Laboratory; POR-SALSA—Drs. Mckenna and Eliassi of Sandia National Laboratories; EQUIV_FLO—Messrs. Shimo, Nishijima; and Fumimura of Taisei Corp.—Don-Chan: Dr. Watanabe of Saitama University and Mr. Morita of Saitama Package-D. The authors would like to thank all of them.

References

[1] JNC, H12: Project to Establish the Scientific and Technical Basis for HLW Disposal in Japan – Project Overview Report -, JNC TN1410 2000-001, 2000.
[2] JNC (2001) Mizunami Underground Research Laboratory Project. Results from 1996-1999 Period. JNC Technical Report, JNC TN7400 2001-001.
[3] JNC (2000) Regional Hydrogeological Study Project. Results from 1992-1999 Period. JNC Technical Report, JNC TN7400 2000-014, 2000.
[4] Sawada, A., H. Saegusa, K. Nakano, H. Oaswa, A study of uncertainties for evaluating groundwater flow by multiple modeling approaches, Proceedings of the 32nd Symposium of Rock Mechanics, Japan Society of Civil Engineer, pp.161-166, 2003.
[5] Sawada, A., H. Saegusa, S. Takeuchi, K. Nakano, and Y. Ijiri, Evaluation of Uncertainties due to Hydrogeological Modeling and Groundwater Flow Analysis, Proc. "Symposium on flow problems in fractured rocks," Japanese Geotechnical Society, pp. 249-258, 2001.
[6] Doughty C, and K. Karasaki, Evaluation of Uncertainties due to Hydrogeological Modeling and Groundwater Flow Analysis (2) -LBNL Effective Continuum Model Using TOUGH2-, Proceedings of "Symposium on flow problems in fractured rocks," Japanese Geotechnical Society, pp. 259-268, 2001.
[7] McKenna, A., M. Eliassi, K. Inaba, H. Saegusa, Evaluation of Uncertainties due to Hydrogeological Modeling and Groundwater Flow Analysis (Pt. 5) Groundwater Flow Modeling focused on complexity in the interpreted fault network using POR-SALSA, Proc. "Symposium on flow problems in fractured rocks," Japanese Geotechnical Soc., pp. 289-298, 2001.
[8] Shimo, M., N. Nishijima and K. Fumimura, Evaluation of Uncertainty due to Hydrogeological Modeling and Groundwater Flow Analysis (3) - Taisei Equivalent Heterogeneous Continuum Model using EQUIV_FLO -, Proceedings of "Symposium on flow problems in fractured rocks," Japanese Geotechnical Society, pp. 269-278, 2001.
[9] Saegusa, H., K. Maeda and K. Inaba, Evaluation of Uncertainties due to Hydrogeological Modeling and Groundwater Flow Analysis (Part 6) - Hydrogeological Modeling and Groundwater Flow Analysis focused on Hydraulic Characteristics of Discontinuous Structures and Hydraulic Boundary Condition , Proc. "Symposium on flow problems in fractured rocks," Japanese Geotechnical Society, pp. 299-308, 2001.
[10] Morita, Y. and K. Watanabe, Evaluation of Uncertainties due to Hydrogeological Modeling and Groundwater Flow Analysis (Part 4) -Modeling of Large Fault System and Groundwater Analysis by a Fracture Network Model (Don-Chan)-, Proceedings of "Symposium on flow problems in fractured rocks," Japanese Geotechnical Society, pp. 279-288, 2001.

Uncertainty and Sensitivity Analysis of Groundwater Flow and Radionuclide Transport in the Saturated Zone at Yucca Mountain, Nevada

Bill W. Arnold and Stephanie P. Kuzio
Sandia National Laboratories, P.O. Box 5800, MS 0778, Albuquerque, NM 87185
e-mail: bwarnol@sandia.gov.

Introduction

Transport in groundwater of the saturated zone (SZ) is a process by which radionuclides from the high-level radioactive waste repository at Yucca Mountain could be released to the accessible environment. Probabilistic analyses of risk using the Total System Performance Assessment (TSPA) approach (e.g., CRWMS M&O, 2000) require a quantitative evaluation of the uncertainty in models and parameters for all components of the disposal system, including the SZ. Numerical modeling of groundwater flow and radionuclide transport in the SZ incorporates parameter uncertainty in multiple realizations conducted in support of TSPA analyses for Yucca Mountain (BSC, 2003). This modeling and the incorporated uncertainty are satisfactory for their intended use supporting a license application for the repository at Yucca Mountain.

In addition to contributing to the probabilistic risk assessment, the uncertainty analyses of groundwater flow and radionuclide transport provide quantitative information on which aspects of the SZ system are most important to our uncertainty in the overall behavior of the system. Sensitivity analyses performed in conjunction with sampling-based uncertainty analysis (Helton and Davis, 1999) can provide valuable insights regarding which input uncertainties are most important to the range of uncertainty in model results. These insights then can be used to prioritize research aimed at reducing uncertainties in the migration of radionuclides in the SZ, in a manner that efficiently utilizes limited resources.

Modeling Approach

Simulations of flow and transport for uncertainty analysis are conducted using the calibrated 3-D SZ site-scale flow and transport model. Figure 1 shows the 30 km by 45 km model domain and the simulated SZ flow paths from beneath the proposed repository projected onto the water table surface. Radionuclide breakthrough curves are derived for nine classes of radioelements at the boundary of the accessible environment located about 18 km south of the repository, as defined by regulations. A particle-tracking method implemented by the FEHM code is used to simulate the processes of advection, dispersion, sorption, and matrix diffusion.

Analyses of uncertainties in key input parameters were conducted and multiple realizations of the SZ site-scale flow and transport model were evaluated to analyze the impacts on simulated transport in the SZ (BSC, 2003). An example of the results is shown in Figure 2, in which a histogram of the median simulated transport times for neptunium (i.e., mid-points of the breakthrough curves) is shown for 200 realizations of the model. Please note that radioactive

decay is not included in these simulations; the radioactive decay process for individual radionuclides is included in a later step in the TSPA model.

Sensitivity analyses were performed to evaluate the relative importance of the uncertain input parameters using the stepwise linear regression method (Hann, 1994). This method consists of constructing a multiple regression model one variable at a time, adding the variable that explains the largest amount of variability in the output at each step. The change in the coefficient of determination (ΔR^2) with the addition of each input variable represents the fraction of the total variability in the output accounted for by that input variable. The stepwise linear regression analysis was conducted on the rank transformed values of the relevant input parameters and the resulting values of median transport time for each of the nine classes of radioelements.

Results and Discussion

The bar chart in Figure 3 shows the ΔR^2 value in the stepwise linear regression model for each of 17 input parameters with a significant impact on the uncertainty in radioelement transport and for nine classes of radioelements. Descriptions of the uncertain input parameters are given in Table 1.

Groundwater specific discharge (GWSPD) is the most important input parameter with regard to uncertainty in SZ flow and transport for all of the radioelement classes, except for plutonium and americium irreversibly attached to colloids. GWSPD is a scaling factor for the groundwater flux in the site-scale model. About 18% to 67% of the uncertainty in median simulated SZ transport time is due to uncertainty in the groundwater specific discharge.

Two parameters related to diffusion into the matrix of the fractured volcanic units have a significant impact on the uncertainty in radioelement transport. The flowing interval spacing in volcanic units (FISVO) is indicative of the degree of flow channelization in the fractured volcanic units and accounts for about 7% to 30% of the uncertainty in median transport times among the radioelement classes. The uncertainty in effective diffusion coefficient in the volcanic rock matrix (DCVO) is related to approximately 1% to 5% of the uncertainty in median transport times. These results do not include transport of radioelements irreversibly attached to colloids, which do not experience matrix diffusion.

Uncertainty in the transport of plutonium and americium irreversibly attached to colloids is dominated by uncertainty in the retardation factor for colloids in alluvium (CORAL), which accounts for about 58% of the uncertainty in simulated median transport times in the SZ. For the transport of americium, thorium and protactinium that are reversibly attached to colloids, uncertainties in the concentration of colloids in groundwater (CONC_COL) and the sorption coefficient for these radioelements onto colloids (KD_AM_COL) account for about 12% and 5% of the uncertainty in transport times, respectively.

Other parameters related to flow and sorption account for small, but significant portions of uncertainty in the radioelement transport results. Uncertainty in horizontal anisotropy in permeability in the volcanic units (HAVO) accounts for about 1% to 3% of the uncertainty in simulated median transport times in the SZ. The sorption coefficient for neptunium in alluvium (KDNPAL) is related to about 6% of the uncertainty in neptunium transport times.

These results indicate that even though uncertainties in groundwater specific discharge have been reduced somewhat relative to previous analyses (Arnold et al., 2003), the uncertainty in this parameter still dominates the uncertainty analyses for radionuclide transport in the SZ. The degree of uncertainty in groundwater flow rates in the SZ is due to the limited testing; long-term multi-well pump testing has been conducted at only one location in the volcanic aquifer. This suggests that additional hydraulic testing in the SZ at Yucca Mountain would have a significant impact on our uncertainty in transport times in the SZ.

These results also show that uncertainty in matrix diffusion in the fractured volcanic units has a significant impact on the uncertainty in radionuclide transport times in the SZ. In particular, the flowing interval spacing in the volcanic units is a parameter that strongly influences overall uncertainty in SZ radionuclide transport times. Knowledge of this parameter is based on flowmeter surveys in a limited number of wells, some of which were surveyed with relatively low-resolution methods. Additional high-resolution testing of wells could reduce uncertainty in the flowing interval spacing parameter and significantly reduce uncertainty in radionuclide transport simulations.

There is large uncertainty in the retardation factor for colloids in alluvium primarily because planned cross-hole tracer testing in the alluvium using microspheres tracer has not yet been conducted. These results indicate that reduction of uncertainty in this parameter associated with this field testing would significantly reduce uncertainty in the transport times for plutonium and americium irreversibly attached to colloids in the SZ.

Acknowledgments

This work was supported by the Yucca Mountain Site Characterization Office as part of the Civilian Radioactive Waste Management Program, which is managed by the U.S. Department of Energy, Yucca Mountain Site Characterization Project. Sandia is a multiprogram laboratory operated by Sandia Corporation, a Lockheed Martin Company, for the United States Department of Energy under Contract DE-AC04-94AL85000.

References

Arnold, B.W., S.P. Kuzio and B.A. Robinson, Radionuclide transport simulation and uncertainty analyses with the saturated-zone site-scale model at Yucca Mountain, Nevada, *Journal of Contaminant Transport*, v. 62-63, p. 401-419.

BSC (Bechtel SAIC Company), 2003. *SZ Flow and Transport Model Abstraction.* MDL-NBS-HS-000021 REV 00. Las Vegas, Nevada: Bechtel SAIC Company.

CRWMS M&O, 2000, *Total System Performance Assessment for the Site Recommendation,* TDR-WIS-PA-000001 REV 00, Las Vegas, Nevada: CRWMS M&O.

Hann, C., 1994, *Statistical Methods in Hydrology*, Iowa State Univ. Press, Ames, Iowa, 6th printing.

Helton, J. and F.J. Davis, 1999, *Sampling-Based Methods for Uncertainty and Sensitivity Analysis*, SAND99-2240, Albuquerque, NM: Sandia National Laboratories.

Table 1. Parameters with significant impact on transport simulation results ($\Delta R^2 > 0.01$) and descriptions.

Parameter	Parameter Description
GWSPD	Groundwater specific discharge
FISVO	Flowing interval spacing in volcanic units (effective fracture spacing)
HAVO	Horizontal anisotropy in permeability in volcanic units
DCVO	Effective diffusion coefficient in volcanic matrix
CONC_COL	Concentration of colloids in groundwater
NVF19	Effective porosity in alluvium
KDNPAL	Sorption coefficient of neptunium in alluvium
KDUVO	Sorption coefficient of neptunium in volcanic units
SRCX1	X location of the point source below the repository (zone 1)
CORAL	Retardation factor for colloids in alluvium
CORVO	Retardation factor for colloids in volcanic units
FPVO	Flowing interval porosity in volcanic units (effective fracture porosity)
KD_AM_COL	Sorption coefficient of americium onto colloids
KDRAAL	Sorption coefficient of radium in alluvium
KDRAVO	Sorption coefficient of radium in volcanic units
KDSRAL	Sorption coefficient of strontium in alluvium
KDSRVO	Sorption coefficient of strontium in volcanic units

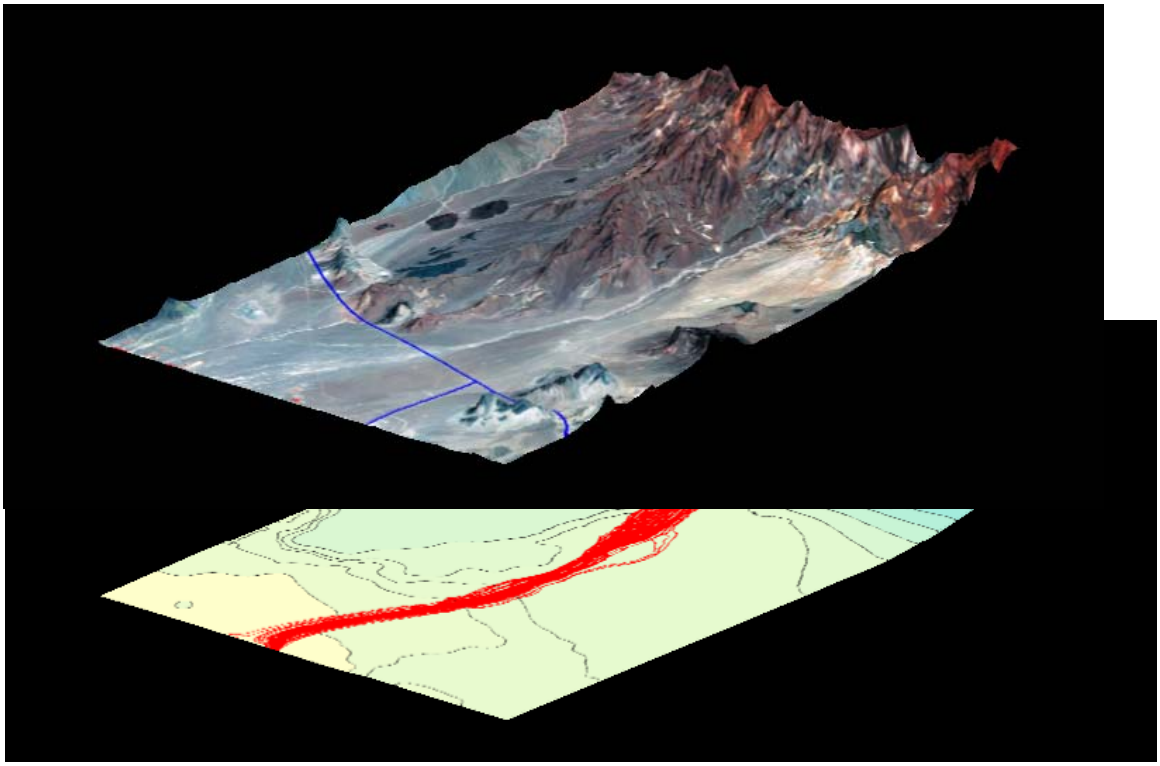

Figure 1. Topographic surface with satellite photo for the area of the SZ site-scale flow model (above) and the water table surface with simulated particle tracks shown in red (below).

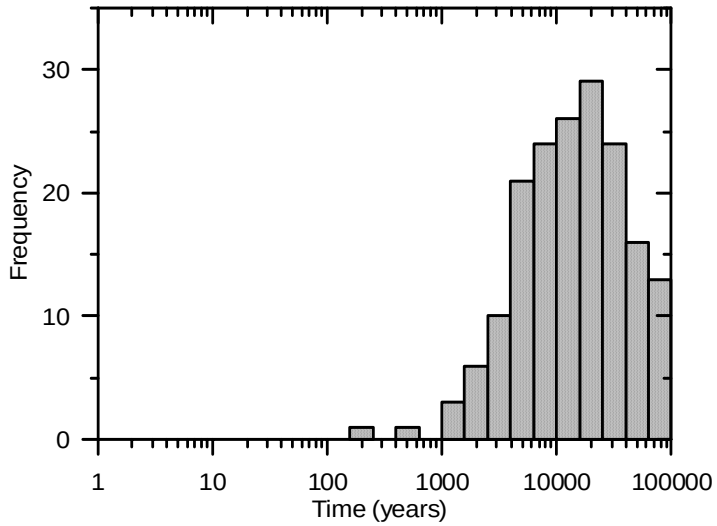

Figure 2. Histogram of median simulated transport times for neptunium in the SZ to the 18 km regulatory boundary of the accessible environment for 200 realizations.

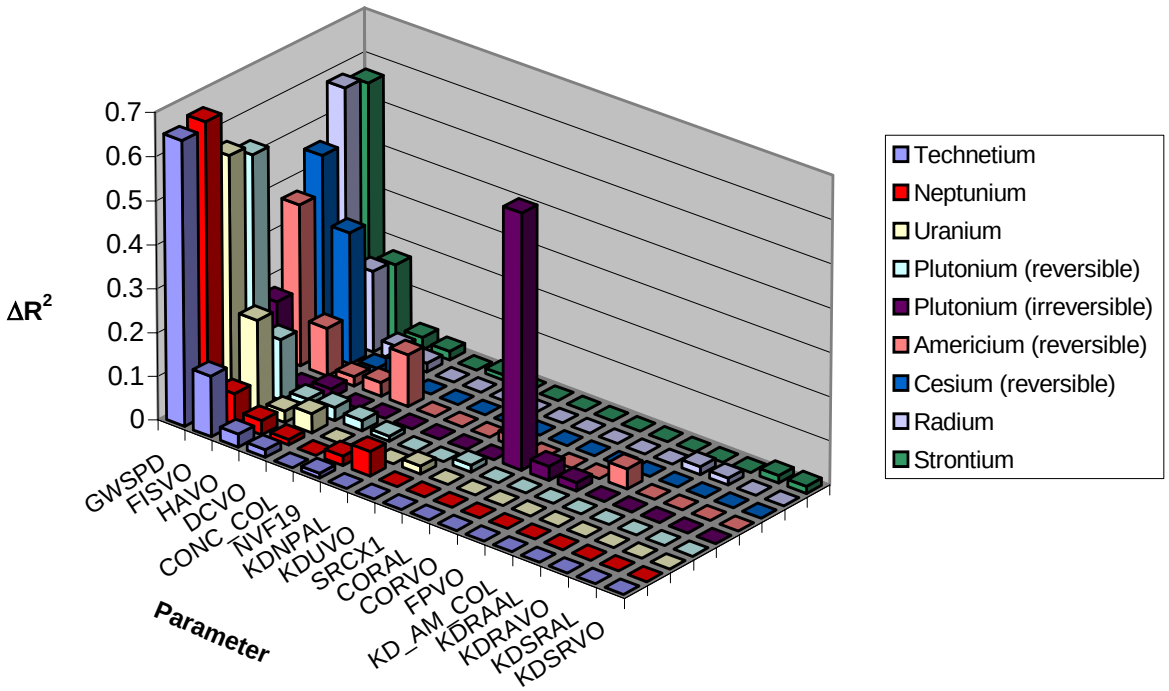

Figure 3. Perspective bar chart showing the results of the stepwise linear regression analysis for nine radioelement classes from 200 realizations of simulated transport in the SZ.

Assessment of Retention Processes for Transport in a Single Fracture at Äspö (Sweden) Site: From Short Time Experiments to Long-Time Predictive Models

Christophe Grenier[1], André Fourno[1,2], Emmanuel Mouche[1], Hakim Benabderrahmane[2]
[1] CEA (Commissariat à l'Energie Atomique). C.E. Saclay. 91191 Gif sur Yvette Cedex. France
[2] ANDRA (Agence nationale pour la gestion des déchets radioactifs). Parc de la Croix Blanche. 1-7 rue Jean Monnet. 92298 Châtenay-Malabry. FRANCE

Abstract

We report here the results obtained within the SKB Task Force international exercise, addressing issues related to nuclear waste disposal in fractured media. The present task (Task 6) aims at providing a bridge between models based on a detailed knowledge of the object studied, calibrated against experiments conducted at month scale and models pertinent for postclosure time scale (thousands of years). This question of change in time scale is an issue of major importance to the field of nuclear waste storage. The present case is limited to a single fracture case at the Äspö site (Sweden). We focus mainly on addressing the influence of matrix zones heterogeneity in the retention processes. We first describe the role played by the various types of immobile zones for the different regimes considered. Then, we build a model suited for performance assessment time scale, study the level of information provided by the tracer tests and other measurements, explain the need for additional data requirements, and characterize the most important features as identified from sensitivity analysis.

Introduction

Within the framework of nuclear spent fuel storage, special concern is put on experimentation and modelling work to improve the modelling capacities for the transfers of radionuclides within a natural fractured media. Several aspects make it a challenging task, among which the heterogeneity of the system, the scarcity of the available information, the strong contrasts in the parameter values between mobile and immobile zones. An additional difficulty is related to the fact that the experimental programs provides a view into the system for transfers over short distances and time scales although the predictions should be considered over much longer distances and time scales.

We provide below the results obtained within the SKB Task Force focusing on different issues associated with the Äspö site (Sweden). This site is one of the best characterized and documented area providing unique opportunities for realistic modeling exercises. The objective of present Task 6 is to build a bridge between site characterization (SC) models and performance assessment (PA) models (refer to Selroos and Elert 2002). The first type of models are typically complex, incorporating detailed physical and geochemical properties and calibrated against short term and small scale in situ experiments. Performance assessment models can be simpler, restrained to the main physical features, generally used to study a variety of possible configurations and apply to long time scales as well as larger spatial scales. The present part of the work deals with a single fracture case (Feature A, part of TRUE-1, Tracer Understanding

Experiment, extension roughly 10 m), and fully saturated flow conditions. Transfer for several tracers is considered (nonsorbing to moderately sorbing) within this unit in different flow conditions corresponding to experimental tracer test time scale (monthly) as well as post closure conditions (thousands of years, PA time scale). The flow conditions considered are detailed on Figure 1. The first case (referred as 6A): corresponds to experimental radial flow conditions (resulting from pumping at well KXTT3R2) for a quick flow regime. Associated tracer tests take well KXTT1R2 as injection point. Participants were asked to calibrate their models to match the breakthrough curves obtained for three tracers ranging from nonsorbing to weakly sorbing. Second case radial flow conditions (6B1) correspond to converging flow for a 1,000 times lower pumping rate. This situation is relative to the prediction time scale for which (of course) no experimentation was conducted. For this test case, tracer is injected at the same location as for 6A, following the same flow path as previously. The third configuration (6B2) is pertinent to postclosure conditions: uniform flow field (tracer injection along the represented line). The 6B1 ad 6B2 conditions are typical of PA time scales, but involve different travel paths.

Several approaches were conducted by the different teams participating in the SKB Task Force, with methods ranging from discrete to continuous. We limit the presentation here to our own results and conclusions. We focused on the issue of retention processes resulting from the presence of heterogeneous matrix zones along the flow path. In fact, we went into a learning process introducing several models, ranging from simple to more complex matrix zone geometries, all in agreement with the conceptual model of the fracture (Figure 2). These models (Figures 3, 4, 5) are calibrated against the experimental breakthrough curves for a series of non-sorbing to moderately sorbing tracers. We address herewith the issue of finding a suitable compromise between model complexity and the levels of information available (as well as required) to model PA time scale. The level of information provided by tracer tests is studied. We also study the transport regimes of these systems for quick and slow velocity cases (typical of experimental and PA time scale). From these regimes, we construct a suitable model of retention processes for the PA time scale (Figure 3) and stress the major features that have to be identified for this regime, based on sensitivity analysis studies.

Results

The role played by the different matrix zones for the different flow regimes was first studied for simple systems providing realistic matrix zone geometry (Model 1 in Figure 3 and Model 2 in Figure 4). These include the material properties measured *in situ*: gouge material, fracture coating, mylonite, altered and nonaltered diorite. Results show that for the quicker forced radial converging flow, only the higher diffusive zones in the vicinity of the fracture play a role (gouge material and fracture coating). For postclosure flow regimes, all units are involved. Fracture coating plays a minor role due to its reduced depth.

For low-velocity regimes, the behavior of the different matrix zones falls into two main categories: (1) zones acting as classical matrix diffusion zones transitorily storing mass (altered and nonaltered diorite) and (2) zones instantaneously invaded by the plume, following the kinetics of the fracture (gouge, fracture coating, mylonite). The latter ones can be equivalently treated within a single continuum model considering an equivalent sorption coefficient Ka. As a consequence, the PA model finally constructed for whole-system postclosure time scales is

rather simple. It is similar to Model 1 (see Figure 3) and consists of an equivalent conducting zone (fracture with gouge material, fracture coating and mylonite considered by means of an equivalent surface sorption coefficient) and a matrix diffusion zone corresponding to altered and unaltered rock properties explicitly modeled.

Nevertheless, the real heterogeneity in the fracture system is badly constrained. The information available consists of measurements conducted on samples obtained from the boreholes, borehole imaging, measurements conducted on samples from geologically analogous zones, and results from different hydraulic and tracer tests. One of the issues considered is related to the level of information contained in the tracer tests conducted (iodine and two moderately sorbing tracers, strontium and cobalt). Results show the following points:

- All three models considered (Model 1 to 3) allow for a good fit of the provided tracer test breakthrough curves (6A conditions). High complexity is not required to match the results.

- The plume explores (1) the zones in the vicinity of the fracture and (2) the larger diffusion coefficient values (gouge, fracture coating, partly mylonite).

- Considering the different flow regimes at stake (quick forced flow in pumping conditions vs. post closure slow flow conditions), the matrix zones explored by the tracer test behave as classical matrix zones for the quicker flow case, but as immediate buffer for slow flow conditions (as mentioned before).

- The information contained in a breakthrough curve is an averaged value of the diffusion zones "seen" by the plume. No local identification is possible; complex experimental procedures involving multiple/cross tracer tests could possibly reduce the uncertainties.

- The simplest model considered (Model 1 in Figure 3) involves four parameters. The parameter group controlling matrix diffusion importance involves porosity, diffusion coefficient, fracture aperture, Kd (see (Maloszewski and Zuber, 1985)). For PA time scale, the parameter group controlling the retention processes roughly corresponds to the total porosity offered by the most diffusive zones in the vicinity of the travel path (requires porosity, depth, Kd). So strictly speaking, no extrapolation from one time scale to the other is possible without independent measurements.

Further, steps were made along this same line of assessing the level of information provided by tracer tests by introducing further information inferred from available measurements. The problem of identification can indeed be posed in terms of diffusion coefficient alone, if one introduces a deterministic relationship between porosity, diffusion coefficient and Kd (and constant fracture aperture). Such a relationship is inferred based on available measurements; this relationship finally allows for identification of one single parameter (diffusion coefficient). We addressed the question of identification for the more complex case of a diffusion coefficient field along the fracture with Model 3 (Figure 5). Different matrix zones are found along the flow path contrary to the Model 2 case, for which the heterogeneity is transversal to the flow path. In addition, for Model 3, the properties decrease with depth into the matrix as one comes to nonaltered rock. We considered here a Monte Carlo simulation approach to address this inverse

problem issue, with a trial and error procedure to fit the iodine test (nonsorbing tracer).

Results again show that tracer tests only provide averaged information about the matrix diffusion zones encountered along the flow path. In addition to this (1) the level of information introduced can be quantitatively measured from the variance reduction of the fitting diffusion coefficient fields; and (2) the information weighting function is represented by the variance reduction function along the flow path. Results show that ultimately, the tracer test poorly constrained the system. A significant level of variance reduction is only observed locally, in the vicinity of the injection borehole, where the contact times are larger as a consequence of the radial structure of the flow (flow is slow far from the pumping well).

These results are in line with conclusions from former studies considering the transport regimes (Ostensen, 1998), parameter groups definition (Maloszewski and Zuber, 1985), and equivalent properties (Carrera et al., 1998). Globally, only limited levels of information can be expected from tracer tests when it comes to predictions at PA time scales. For this time scale, one should (as a consequence) rely upon direct measurements of the fractured system, involving (in first place) the most precise characterization possible for the flow path and (in second) a precise definition of the different matrix zones along the flow path (volumes, geometry, and so forth).

Prediction of the breakthrough curves exiting the system was produced for five tracers with increasing Kd. This phase was conducted on the Model 2 system (Figure 4) which is indeed the most complex and reliable system that could be inferred from available data. Results are provided in Figure 6, showing that the more sorbing the tracer is, the later its arrival time. Sensitivity analysis to the different units of the system was conducted for these postclosure flow regimes. We observed a high sensitivity to the most diffusive zone parameters (porosity, and depth for gouge, fracture coating, mylonite) but low sensitivity for altered and nonaltered Diorite (porosity, diffusion coefficient, depth). However, these latter zones could potentially provide the larger diffusion volumes if the contact time were sufficiently long.

Major Conclusions and Perspectives

Tracer tests provide a very limited amount of information. One should rely upon direct measurements (possibly from geologically analogous zones). The matrix zones show two distinct behaviors for PA time scale. The resulting PA model is very simple. Retention effects are most relevant for high diffusion and porosity zones close to the mobile zones. Refined characterization of the former is required, involving their statistical spatial structure.

In this study, we kept to simple flow paths (typically one channel). Future phases of the task force will involve a 200 m fractured block (Äspö-like), including different scales of fracturation as well as a refined local description of fractured zones.

References

Selroos JO, Elert M (2001) TASK 6A and B modeling task specifications. Äspö Task Force, April 2001. (refer as well to http://www.skb.se).

Ostensen R (1998) Tracer tests and contaminant transport rates in dual porosity formations with application to the WIPP. Journal of Hydrology, 204 (1998) 197-216.

Maloszewski P, Zuber A (1985) On the theory of tracer experiments in fissured rocks with a porous matrix. Journal of Hydrology, 79 (1985) 333-358.
Carrera J, Sanchez Vila X, Benet I, Medina A, Galarza G, Guimera J (1998) On matrix diffusion: formulations, solution methods and qualitative effects. Hydrogeology Journal 6:178-190.

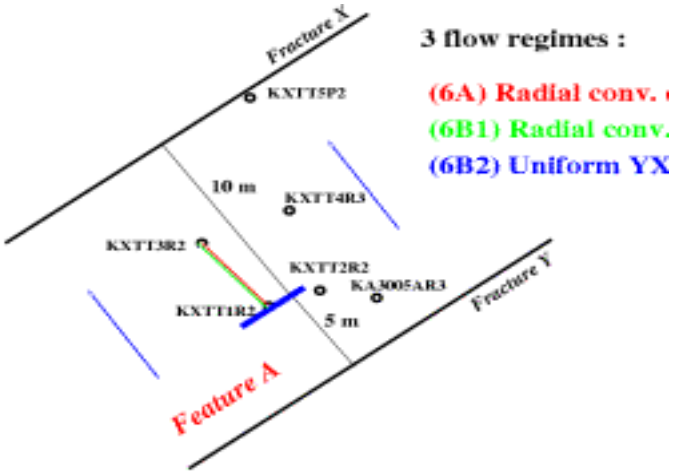

Figure 1. Flow regimes considered: quick (6A), slow (6B).

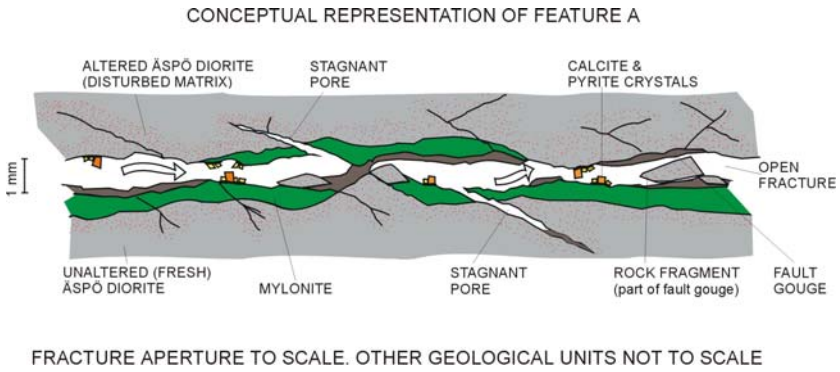

Figure 2. Conceptual model of the fractured zone.

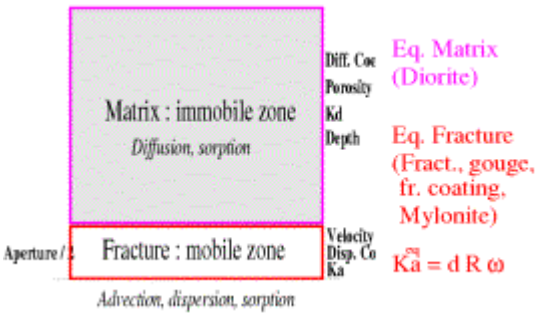

Figure 3. Model 1 and equivalent PA model.

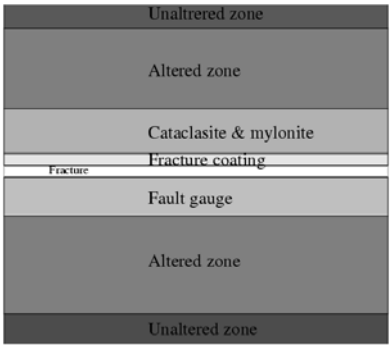

Figure 4. Model 2, deterministic heterogeneity.

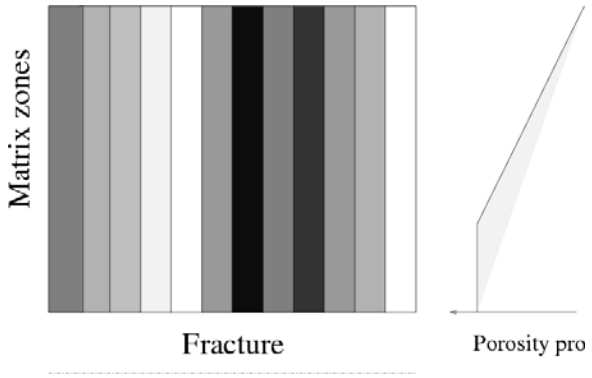

Figure 5. Model 3, stochastic heterogeneity.

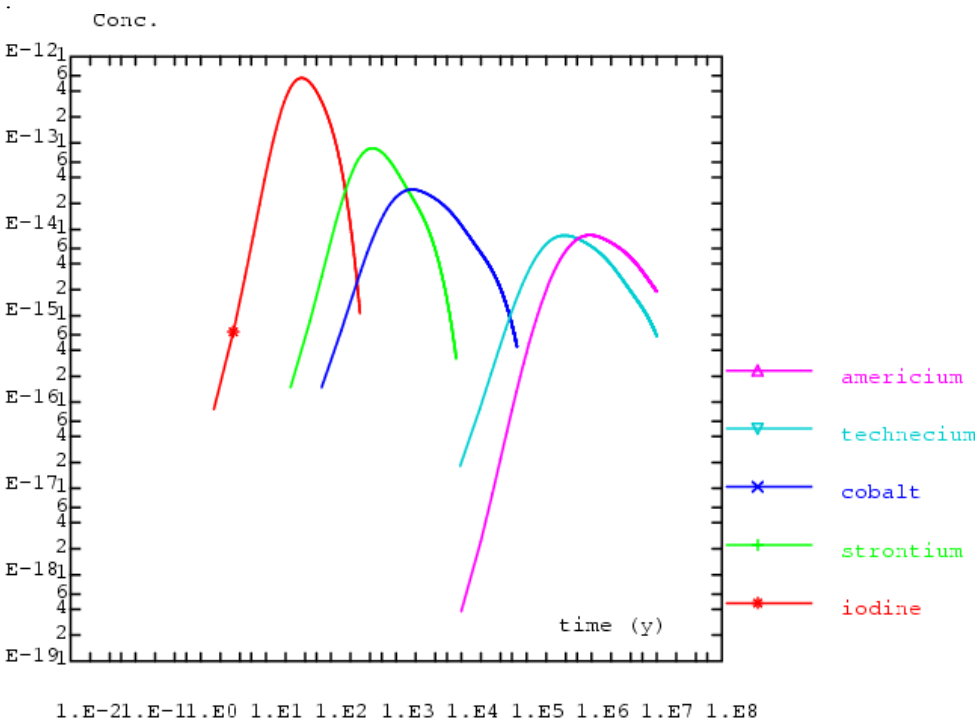

Figure 6. Breakthrough curves predictions for 5 tracers (iodine, strontium, cobalt, technetium, Americium). Based on Model 2 geometry.

A Probabilistic Analytical Method to Calculate Dispersion Coefficients in Fractured Rock

James R. Kunkel
Knight Piésold and Co., 1050 Seventeenth Street, Suite 450, Denver, CO 80265;
PH (303) 629-8788; FAX (303) 629-8789; email: jkunkel@kpco.com

Introduction

Measuring dispersion coefficients in fractured rock (in support of contaminant transport) is often difficult and expensive. A probabilistic method can be used, based on an analytical solution of calculating dispersion coefficients exclusions from fracture set data obtained from outcrops or oriented core. This probabilistic analytical solution was developed by de Josselin de Jong in the 1970s, but has been rarely used to facilitate calculation of dispersion coefficients in fractured rock. This paper presents the general analytical probabilistic equations to calculate the positions of particles in an infinite number of intersecting fracture families, and to calculate the two-dimensional (x,y) dispersion coefficients for the major and minor principal directions of dispersion. The equation to calculate the direction of the major principal axis with respect to an x,y coordinate system also is presented. A sample problem, using more than two fracture families, is presented to demonstrate the use of the probabilistic analytical solution in calculating dispersion coefficients in fractured rock.

Estimation of dispersion coefficients in fractured rock, based on fracture characteristics and aquifer hydraulic properties, was first proposed by de Josselin de Jong (1972) and de Josselin de Jong and Way (1972). The equations used by de Josselin de Jong and Way (1972) were developed using probability theory (Chandrasekhar, 1943) to relate the dispersion of particles to fracture characteristics, hydraulic gradient, directional hydraulic conductivity, and porosity. The application of de Josselin de Jong's theory was used by Way and McKee (1981) to assess groundwater restoration of *in situ* coal gasification sites. This application used four identifiable fracture sets (families).

Schwartz and Smith (1988) compared de Josselin de Jong's continuum approach to dispersivity results from a numerical, discrete fracture model, but only for two orthogonal fracture families. They concluded that de Josselin de Jong's theory could not be extended to complex networks of fractures. Field tracer tests in fractured basalts (McKee and Way, 1988; Kunkel, Way and McKee, 1988; Kunkel and Way, 1995; and Kunkel, 2002) showed that de Josselin de Jong's theory can predict longitudinal and transverse dispersion coefficients within about 30% of the tracer test values. The field tracer tests were performed in a fractured basalt that had 20 fracture families. They demonstrated that de Josselin de Jong's theory appears to work well in complex fracture networks.

The analytical solution of dispersion coefficients using de Josselin de Jong's theory is based on several assumptions. These assumptions allow a discrete fracture network to be characterized as a continuum. Any number of fracture families can be used; however, each fracture within a given family is assumed to be equally spaced and infinite in length. These assumptions, while

appearing to give an oversimplified view of fractured rock aquifers, provide an easy method to assess dispersion coefficients in fractured rock without the need for expensive and time-consuming tracer tests. The result of using the theory is a somewhat idealized Gaussian distribution (plume) of particles generated by a point source injection in fractured rock with multiple fracture families.

This paper describes in a detail the equations necessary to apply de Josselin de Jong's theory to two or more intersecting fracture families. Of particular importance is the extension of the equations for two fracture families to give relative fracture lengths for three or more intersecting fracture families. A spreadsheet example of three fracture families is presented to demonstrate application of the theory.

Dispersion Equations

The basic equation for solute transport in saturated porous media is given by Bear (1972):

$$\frac{\partial C}{\partial t} = - < V_i > \frac{\partial C}{\partial X_i} + D_{ij} \frac{\partial^2 C}{\partial X_i \partial X_j} - R_x , \qquad (1)$$

where C is concentration, t is time, $<V_i>$ is the mean value of the i^{th} component of fluid velocity, x_i and x_j are space coordinates, D_{ij} is the i,j component of the dispersion tensor, and R_x is the rate of conversion or adsorption of solute.

Using probability theory, de Josselin de Jong (1972) developed equations to describe dispersion coefficients in Equation (1) for fractured rock. The probabilistic approach enables relating the dispersion coefficient to the elementary properties of the fractured medium and the fluid flowing through it.

De Jong showed that the elements of the dispersion coefficient are given by the following

$$D_{ij} = \frac{1}{2 < t >} \left\{ < X_i X_j > - < X_i t > \frac{< X_j >}{< t >} - < X_j t > \frac{< X_i >}{< t >} + < tt > \frac{< X_i >< X_j >}{< t >^2} \right\} \qquad (2)$$

where X_i, X_j, and t are stochastic variables corresponding to the fracture system chosen. $< X_i >$ and $< X_j >$ are the mean values of the displacement coordinates X_i, X_j,, $<t>$ is the mean residence time, and $< X_i X_j >$, $< X_i t>$, $< X_j t>$, and $<tt>$ are the mean values of the products of the stochastic variables X_i, X_j, and t as combined between brackets <>.

For two intersecting fracture families as shown on Figure 1, a simplified derivation of the equations is possible. The theory is two-dimensional, with only the x and y coordinate directions considered. For the two-dimensional case, D_{ij} can be expressed by the following determinants as (de Josselin de Jong and Way, 1972):

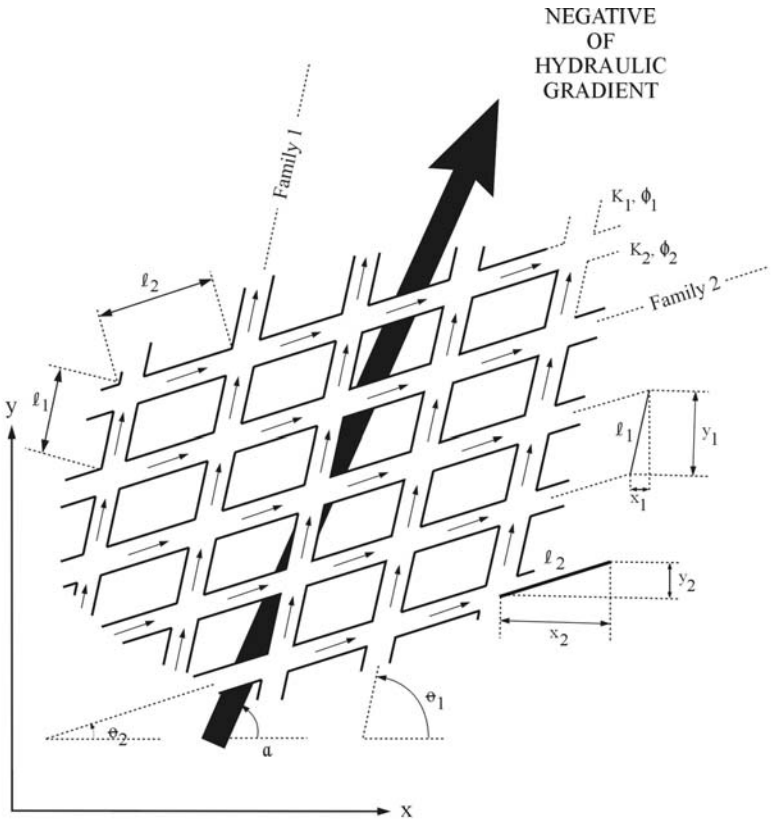

Figure 1. Two fracture families and model parameters.

$$D_{ij} = \begin{bmatrix} \frac{D_{xx}}{D_{yx}} & \frac{D_{xy}}{D_{yy}} \end{bmatrix} = \begin{bmatrix} \frac{D_{11}}{0} & \frac{0}{D_{22}} \end{bmatrix} \tag{3}$$

$$D_{xx} = \frac{1}{2 < t >} \left\{ < xx > -2 < xt > \frac{< x >}{< t >} + < tt > \frac{< x >^2}{< t >^2} \right\} \tag{4}$$

where:

$$D_{xy} = D_{yx} = \frac{1}{2 < t >} \left\{ < xy > - < xt > \frac{< y >}{< t >} - < yt > \frac{< x >}{< t >} + < tt > \frac{< x >< y >}{< t >^2} \right\} \tag{5}$$

$$D_{yy} = \frac{1}{2 < t >} \left\{ < yy > -2 < yt > \frac{< y >}{< t >} + < tt > \frac{< y >^2}{< t >^2} \right\} \tag{6}$$

The mean values in Equations (4) through (6) are computed by summing the products of the stochastic variables and the corresponding probability, g_m, of flow in each fracture family. Using the geometry for two intersecting fracture families shown in Figure 1, the probabilities of flow in

each fracture family as a result of a uniform negative hydraulic gradient J applied on the flow field, and the values of the stochastic variables, can be calculated.

The principal values of the dispersion tensor, D_{ij}, can be calculated as D_{11} and D_{22} from the equations (Way and McKee, 1981)

$$D_{11} = \frac{1}{2}\left(D_{xx} + D_{yy}\right) + \frac{1}{2}\sqrt{\left(D_{xx} - D_{yy}\right)^2 + 4D_{xy}^{\ 2}} \tag{7}$$

$$D_{22} = \frac{1}{2}\left(D_{xx} + D_{yy}\right) - \frac{1}{2}\sqrt{\left(D_{xx} - D_{yy}\right)^2 + 4D_{xy}^{\ 2}} \tag{8}$$

Note that for this analytical solution, if only two fracture families are used, one of the values of the principal dispersion coefficient, either D_{11} or D_{22}, is always zero. This is because the analytical solution does not allow for particles within a given fracture to lag behind each other. The angle ψ, between the major principal axis of dispersion D_{11} and the x-axis is given by the equation (Way and McKee, 1981)

$$\tan\psi = \frac{2D_{xy}}{\left(D_{xx} - D_{yy}\right) + \sqrt{\left(D_{xx} - D_{yy}\right)^2 + 4D_{xy}^{\ 2}}} \tag{9}$$

Conclusion

The probabilistic, analytical solution of particles moving in a multifamily fracture network can give a relatively quick and useful estimate of two-dimensional dispersion coefficients. These coefficients can be used in numerical models to assess transport without the expense of time-consuming and costly tracer tests in fractured rock. Inputs to the analytical solution include the frequency and direction of fractures and the hydraulic characteristics of the fractured rock.

References

Chandrasekhar, S. (1943). "Stochastic problems in physics and astronomy." *Reviews of modern physics*, v. 15, 1-87.

de Josselin de Jong, G. (1972). "Dispersion of a point injection in an anisotropic porous medium." *Unpublished report, Geoscience Department*, New Mexico Institute of Mining and Technology, Socorro, New Mexico, 68 p.

de Josselin de Jong, G. and S.C. Way (1972). "Dispersion fissured rock." *Unpublished report, Geoscience Department*, New Mexico Institute of Mining and Technology, Socorro, New Mexico, 36 p.

Kunkel, J.R. (2002). "Model-calculated dispersivity using fracture characteristics from core data and other field information." *Proceedings of the symposium on fractured rock aquifers 2002*, Denver, Colorado, Mar. 13-15, 137-141.

Kunkel, J.R. and S.C. Way (1995). "A field-tracer test for estimating dispersion coefficients in saturated, fractured media." Mayer, L.R., N.G.W. Cook, R.E. Goodman and C.-F. Tsang

[Editors], *Fractured and jointed rock masses*, Proceedings of the conference on fractured and jointed rock masses, Lake Tahoe, California, June 3-5,1992, Rotterdam: A.A. Balkema, 619-623, ISBN 90 5410 591 7.

Kunkel, J.R., S.C. Way, and C.R. McKee (1988). "Comparative evaluation of selected continuum and discrete-fracture models." U.S. Nuclear Regulatory Commission, Washington, D.C. NUREG/CR-5240, 61 p., 1 Appendix.

McKee, C.R. and S.C. Way (1988) "The tensorial nature of effective porosity and large-scale dispersion coefficients," U.S. Nuclear Regulatory Commission, Washington, D.C. NUREG/CR-5277, 55 p.

Schwartz, F.W. and L. Smith (1988). "A continuum approach for modeling mass transport in fractured media." *Water Resources Research*, v. 24, no. 8, 1360-1372.

Way, S.C. and C.R. McKee (1981). "Restoration of in-situ coal gasification sites from naturally occurring groundwater flow and dispersion." *In Situ*, v. 16, no. 6, 1016-1024.

Comparing Unsaturated Hydraulics of Fractured Rocks and Gravels

Tetsu K. Tokunaga (tktokunaga@lbl.gov); Keith R. Olson (kolson@lbl.gov)
Jiamin Wan (jmwan@lbl.gov)
Lawrence Berkeley National Laboratory, 1 Cyclotron Rd., Berkeley, CA 94720

The unsaturated hydraulics of soils, sediments and rocks encompass a wide range of scales, properties, and processes, making it difficult to reliably predict the behavior of one type of medium based on relations developed for another. Although the unsaturated hydraulics of fine to medium textured granular media have been rather thoroughly developed, especially in terms of bulk properties, application of some basic soil physics concepts to unsaturated fractured rocks have often not yielded reliable predictions without introducing additional adjustable parameters. This failure indicates that some key phenomena and processes cannot be arbitrarily transferred from one scale to another. We have been examining the unsaturated hydraulics of sands, gravels, and rocks in an attempt to better understand scaling relations and limitations. This presentation summarizes recent finding in three areas: (1) general limits to classical capillary scaling, (2) surface roughness constraints on capillary film flow, and (3) scaling of fast flow paths in low storage capacity rocks.

Hysteresis in the relation between water saturation (S) and matric potential (ψ) is generally regarded as a basic aspect of unsaturated porous media. However, since hysteresis depends on whether or not capillary rise occurs at the grain-scale, this criterion can be used to predict combinations of grain size (λ), surface tension (σ), fluid-fluid density differences ($\Delta\rho$), and acceleration (a) that prevent hysteresis. Vanishing of $S(\psi)$ hysteresis was predicted to occur for $\lambda > 11$ mm, for water-air systems under the acceleration of ordinary gravity, based on Miller-Miller scaling and Haines' original model for hysteresis. The Haines number, Ha, is proposed as a dimensionless number useful for separating hysteretic ($Ha < 15$) versus nonhysteretic ($Ha > 15$) behavior. Disappearance of hysteresis was tested through measurements of drainage and wetting curves of sands and gravels. For λ up to 7 mm, hysteresis loops remain well defined. At $\lambda = 9$ mm, hysteresis is barely detectable. At $\lambda \approx 11$ mm, hysteresis loops are difficult to reproduce, having energy offsets comparable to measurement uncertainties. For $\lambda > 13$ mm, hysteresis is not observed. The influence of σ was tested through measurements of moisture retention in 7 mm gravel, without and with a surfactant (sodium dodecylbenzenesulfonate, SDBS). At $\lambda = 7$ mm, the ordinary water system ($\sigma = 71$ mN m^{-1} and $Ha = 7$) exhibited hysteresis, while the SDBS system ($\sigma = 27$ mN m^{-1} and $Ha = 18$) did not. These experiments prove that hysteresis is not a fundamental feature of unsaturated porous media. This finding is important to be aware of in studies of unsaturated flow in fractures for example, when using a centrifuge to conduct experiments at higher accelerations than that of gravity at the earth surface.

Preferential flow paths for unsaturated flow in fractured rocks remain an outstanding challenge to understand and predict. The balance between gravity and capillarity is critical to this problem, over a wide range of length scales. How well dispersed or localized will flow paths be? The approach we take on this problem starts at the scale of fracture surface roughness, along individual fractures. At this scale, a number of flowpath configurations can accommodate any

specific boundary condition that preserves near-zero matric potentials. We show that surface topography, as described by root mean square roughness or similar parameters, can often constrain film transmissivity relations, but is inadequate for predicting film flow, even when supplemented with information on surface wettability. This limitation is analogous to the more familiar inability to predict fracture transmissivity, saturated or unsaturated, solely from information on average aperture.

At the larger scale of an unsaturated fracture network, models for flow paths can largely ignore capillarity. The physical basis for this gravity-only approximation in low storage capacity rocks is presented, along with supporting experimental evidence. We conclude with some models that fail and some that succeed in predicting (at present) unsaturated flow path distributions.

Improved Description of the Hydraulic Properties of Unsaturated Structured Media near Saturation

M. Th. van Genuchten and M. G. Schaap
George E. Brown, Jr. Salinity Laboratory, USDA, ARS
450 West Big Springs Road, Riverside, CA 92507
rvang@ussl.ars.usda.gov, mschaap@ussl.ars.usda.gov

Summary

Dual-porosity and dual-permeability models for preferential flow in unsaturated structured media (macroporous soils, fractured rock) generally assume that the medium consists of two interacting pore regions, one associated with the macropore or fracture network, and one with micropores inside soil aggregates or rock matrix blocks. A simple but effective approximation of preferential flow results when a single Richards equation is still used in an equivalent continuum approach, but with composite (bimodal type) hydraulic conductivity curves, rather than the single unimodal curve used in most traditional analyses. Field data indicate that the macropore conductivity is generally about one order of magnitude larger than the matrix conductivity at saturation. Neural-network analysis of the UNSODA unsaturated soil hydraulic database revealed a similar difference between the macropore and matrix saturated hydraulic conductivities. Further analysis of the database shows that a piece-wise log-linear function can be used for the macropore hydraulic conductivity between pressure heads of 0 and -40 cm. Results significantly improve the description of the hydraulic properties of structured field soils.

Introduction

This paper focuses on the problem of preferential flow, a major challenge when dealing with flow and contaminant transport in the vadose zone. Preferential flow is caused by a broad range of processes. In structured or macroporous soils, water may move through interaggregate pores, decayed root channels, earthworm burrows, and drying cracks. Similar processes occur in unsaturated fractured rock, where water may move preferentially through fractures, thus bypassing much of the rock matrix.

Process-based descriptions of preferential flow generally are based on dual-porosity or dual-permeability models which assume that the soil consists of two interacting pore regions, one associated with the macropore or fracture network and one with micropores inside soil aggregates or rock matrix blocks. Different formulations arise depending upon how water and/or solute movement in the micropore region is modeled, and how water and solutes in the micropore (matrix) and macropore (fracture) regions are allowed to interact.

Application of dual-porosity or dual-permeability models requires estimates of the hydraulic properties of the fracture pore network, the matrix region, or some composite of these. Dual-permeability models typically contain two water-retention functions, one for the matrix and one for the fracture pore system, and two or three conductivity functions in terms of their local pressure heads, h, (i.e., $K_f(h_f)$for the fracture network, $K_m(h_m)$ for the matrix, and possibly a

separate conductivity function $K_a(h_a)$ for the fracture/matrix interface [e.g., Gerke and van Genuchten, 1993]). Of these functions, K_f is determined primarily by the structure of the fracture pore system (i.e., the size, geometry, and continuity of the fractures, and possibly the presence of fracture fillings). Similarly, K_m is determined by the hydraulic properties of single matrix blocks and the degree of hydraulic contact between adjoining matrix blocks during unsaturated flow.

A simple but still effective approximation of flow in structured media results when a single Richards' equation is used in an equivalent continuum approach, but with composite (bimodal type) hydraulic conductivity curves rather than the single unimodal curve used in most traditional analyses of variably-saturated flow. Measurements of the composite (fracture plus matrix) hydraulic properties are greatly facilitated by the use of tension infiltrometers. An advantage of tension infiltrometer methods is that negative soil water pressures at the soil-infiltrometer interface can be maintained very close to zero, and that they can be decreased in small increments to yield well-defined conductivity functions near saturation (e.g., Mohanty et al., 1997). In several studies, the composite hydraulic properties of structured soils and rocks have been modeled using sums of two or more van Genuchten-Mualem type functions or similar formulations (e.g., Peters and Klavetter, 1988; Durner, 1994; Mohanty et al., 1997).

Hydraulic Property Description Near Saturation

Evidence from field measurements suggests that the macropore conductivity of soils generally is about one order of magnitude larger than the matrix conductivity at saturation. We revisited this finding, as well as the general shape of the unsaturated conductivity function near saturation, using a detailed neural network analysis of the UNSODA unsaturated soil hydraulic database (Leij et al., 1996; Nemes et al., 2001; www.ussl.ars.usda.gov/models/unsoda.htm). Our analysis also addressed the issue of second-order continuity of the soil water retention curve $\theta(h)$ at h=0. Second-order continuity is not satisfied when the exponent n in the soil hydraulic model of van Genuchten (1980) becomes less than 2. The discontinuity in the second derivative of $\theta(h)$ may lead to extremely nonlinear $K(h)$ functions for fine-textured (clay) soils, especially when n becomes less than about 1.1 (thus approaching its lower limit of n=1 when the van Genuchten-Mualem formulation is used). Following Vogel et al. (2000), we used a slightly modified hydraulic model that incorporates a small air-entry pressure (h_s) into the water retention curve (referred to by Vogel et al. as the minimum capillary height). This modification only minimally affects the water-retention curve, but avoids numerical instabilities in simulations when n becomes less than about 1.1 or 1.2. A recent analysis (Schaap and van Genuchten, 2004) of the UNSODA database showed that the air-entry value of the fracture hydraulic conductivity should be about - 4 cm.

The model of Vogel et al. (2000) was further modified to account for the effects of soil structure. For this purpose, we first determined the matrix saturated hydraulic conductivity K_{ms}, which should be much smaller than the measured saturated (matrix plus fracture) soil hydraulic conductivity, K_s. The matrix saturated conductivity may be viewed as a parameter that is extrapolated from unsaturated conductivity data associated with mostly soil textural (matrix) properties. The soil structural part of the conductivity function (associated with the fractures and macropores) in the near-saturation range was analyzed in terms of scaled conductivity residuals, as follows:

$$R(h) = \frac{\log K(h) - \log K_m(h)}{\log K_s - \log K_m(h)} \tag{1}$$

where $K_m(h)$ is the matrix conductivity function modified according to Vogel et al. (2000) using an air-entry value of -4 cm. Equation (1) shows that $R(h)$ varies between 0, in the dry range when the effects of macroporosity are no longer present, to 1.0 when the medium is saturated (h=0).

Hydraulic Conductivity Optimization Results

The residuals $R(h)$ of Equation (1) were analyzed using 235 UNSODA data sets that had at least six θ-h pairs and at least five K-h pairs. Results indicate that $R(h)$ decreases from 1.0 at h=0 cm to 0 at approximately h=-40 cm. The data revealed a relatively sharp decrease in R near saturation and a slower decrease afterwards. A two-element piecewise linear function was used to describe this pattern, with R=0 at h=-40, a change in slope at -4 cm and R=1 at h=0 cm. The change in slope was purposely located at -4 cm to be consistent with the second-order continuity modification of the van Genuchten-Mualem model, as found earlier. A least-squares analysis of the residuals produced the following approximation for $R(h)$:

$$R(h) = \begin{cases} 0 & h < \text{-40 cm} \\ 0.2778 + 0.00694h & -40 \le h < \text{-4 cm} \\ 1 + 0.1875h & -4 \le h \le 0 \text{ cm} \end{cases} \tag{2}$$

Given Equation (2), the conductivity function now applicable to all pressure heads (matrix and fracture regions) is given by Equation (1), which can be rearranged to give

$$K(h) = \left(\frac{K_s}{K_m(h)} \right)^{R(h)} K_m(h) \tag{3}$$

We refer to Schaap and van Genuchten (2004) for a detailed analysis and discussion of Equations (2) and (3).

Equation (3) was next fitted to all available hydraulic conductivity data in the UNSODA database for the purpose of comparing the fitted matrix saturated conductivities, K_{ms}, with independently measured (fracture plus matrix) saturated conductivities, K_s. This analysis also allowed adjustment of the tortuosity factor L in the soil hydraulic equations of van Genuchten (1980) and Vogel et al. (2000). The ratio of measured (K_s) and extrapolated (K_{ms}) values was found to be larger than those obtained earlier by Schaap and Leij (2000), mostly because the micropore (matrix) and macropore (fracture) contributions to the overall conductivity function were now analyzed independently in terms of Equations (2) and (3). The average Root-Mean-Square Error ($RMSE_K$) of the fitted log hydraulic conductivity data using Equation (3) with fitted K_{ms} and L values was found to be 0.261, which is substantially lower than the average $RMSE_K$ value (1.301) of the original van Genuchten model with fitted K_{ms} (but with L fixed at 0.5), and also lower when L was allowed to vary ($RMSE_K$=0.410). The very low $RMSE_K$ for Equations (2) and (3) reflects the substantially better description of unsaturated conductivity data we obtained

with this model in the near-saturated region. Also, as opposed to previous van Genuchten-Mualem type formulations with and without fitted K_{ms} and L values, Equations (2) and (3) were found to produce very small systematic errors across the entire pressure range between 0 and -150 m.

We further found that the average fitted $RMSE_W$ values associated with water- retention data differed only marginally between the original and modified approaches. This shows that it is possible to immediately use the original van Genuchten retention parameters instead of needing to fit the more complicated retention model of Vogel et al. (2000) to the data. However, it is still necessary to use the modified retention model in calculations of variably saturated flow in structured media.

Concluding Remarks

Our analysis of the UNSODA unsaturated soil hydraulic database shows that a piece-wise log-linear function can be used to represent the soil macropore contribution to the overall hydraulic conductivity function, $K(h)$. While the macropore contribution is most significant between pressure heads 0 and -4 cm, its influence on the conductivity function was found to extend to pressure heads as low as -40 cm. The analysis leads to Equation (3) for $K(h)$, with $R(h)$ as defined by Equation (2). We emphasize that these equations define a composite hydraulic conductivity model that lumps the contributions of the matrix and the fractures into one equation. When used in conjunction with the traditional Richards equation, the resulting formulation is unable to distinguish between flow in the matrix and in fractures. Hence the model still generates a uniform moisture front, and as such cannot reproduce non-uniform moisture distributions typical of preferential flow. Dual-porosity or dual-permeability models are required to generate such non-uniform flow. Still, deconvolution of the bimodal conductivity functions discussed in this paper may well provide useful guidance to estimating separate matrix and fracture conductivities for use in such dual-permeability flow models.

Acknowledgment

This study was partially supported by the SAHRA Science Technology Center as part of NSF grant EAR-9876800.

References

Durner, W. 1994. Hydraulic conductivity estimation for soils with heterogeneous pore structure. *Water Resour. Res*. 30:211-223.

Gerke, H. H., and M. Th. van Genuchten. 1993. A dual-porosity model for simulating the preferential movement of water and solutes in structured porous media. *Water Resour. Res*. 29(2): 305-319.

Leij, F. J., W. J. Alves, M. Th. van Genuchten, and J. R. Williams. 1996. The UNSODA Unsaturated Soil Hydraulic Database; User's Manual, Version 1.0. *EPA/600/R-96/095*, National Risk Management Laboratory, Office of Research and Development, U.S. Environmental Protection Agency, Cincinnati, OH. 103 p.

Mohanty, B. P., R. S. Bowman, J. M. H. Hendrickx, and M. Th. van Genuchten. 1997. New piecewise- continuous hydraulic functions for modeling preferential flow in an intermittent flood-irrigated field. *Water Resour. Res*. 33(9):2049-2063.

Nemes, A., M.G. Schaap, F.J. Leij and J.H.M. Wösten. 2001. Description of the unsaturated soil hydraulic database UNSODA version 2.0. *J. Hydrol.* 251:151-162.

Peters, R. R., and E. A. Klavetter. 1988. A continuum model for water movement in an unsaturated fractured rock mass. *Water Resour. Res*. 24: 416-430.

Schaap, M.G., and F.J. Leij. 2000. Improved prediction of unsaturated hydraulic conductivity with the Mualem-van Genuchten Model, *Soil Sci. Soc. Am. J.* 64: 843-851.

Schaap, M. G., and M. Th. van Genuchten. 2004. A modified van Genuchten-Mualem formulation for improved prediction of the soil hydraulic conductivity function near saturation. *Vadose Zone J.* (submitted).

van Genuchten, M. Th. 1980. A closed-form equation for predicting the hydraulic conductivity of unsaturated soils. *Soil Sci. Soc. Am. J*. 44:892-898.

Vogel, T. M. Th. van Genuchten, and M. Cislerova. 2000. Effect of the shape of the soil hydraulic functions near saturation on variably-saturated flow predictions. *Adv. Water Resour.* 24(2):133-144.

Theoretical, Numerical, and Experimental Study of Flow at the Interface of Porous Media

Ravid Rosenzweig and Uri Shavit
Civil and Environment Engineering, Technion, Haifa 32000, Israel
rravid@tx.technion.ac.il, aguri@tx.technion.ac.il

Introduction

Water flow over surfaces of porous media is a fundamental phenomenon in both surface and subsurface hydrology. Such flows include runoff during a rainfall event, submerged vegetation flows, and flow in fractured media. The velocity field at the porous media interface affects processes such as resuspension, dissolution, erosion, heat, and mass transfer. A comparison between the flow inside the porous media and the flow in the nonporous region reveals some differences. The flow inside the porous media is typically treated using Darcy's law, but the Navier-Stokes equations, which are used to solve the flow above the interface, involve both inertial and viscous terms—high order terms that are missing in Darcy's law. Modeling the flow field around the interface must include the effect of both Darcy flow inside the porous media and the free flow above it. Another significant difference between the two regions is the spatial scales needed for the analysis of the flow conditions. Whereas Darcy law is macroscopic and, therefore, describes the local average velocity, the Navier-Stokes equations are microscopic and do not consider resistance other than viscous. Modeling the flow conditions in the vicinity of the interface therefore requires a technique that bridges the differences between these two distinct regions.

The formulations that were used in the past to solve the problem of flow over porous surfaces are the Brinkman equation (Brinkman, 1947) and the Beavers and Joseph (1967) interface condition. Both require empirical coefficients. The empirical coefficients of the Brinkman equation are the apparent viscosity, μ^*, and a variable permeability, k. The Beavers and Joseph interface condition relates the interface velocity gradient and the relative slip velocity through the permeability and an empirical slip coefficient, α_{BJ}. Many studies have shown that neither the Brinkman equation nor the Beavers and Joseph interface condition is general enough. It has been shown that both require experimental fitting and adjustments (Taylor, 1971; Sahraoui and Kaviany, 1992; James and Davis, 2001).

Recently, we presented a modification to the Brinkman equation, named the Modified Brinkman Equation (MBE), which predicts the vertical macroscopic laminar velocity profile (Shavit et al. 2002; Shavit et al. 2004). Here we investigate the flow in and above an artificial porous geometry and test the applicability of the MBE further. The microscopic velocity within the porous media was computed numerically and measured in a laboratory physical model. The macroscopic vertical velocity profile was obtained by averaging the computed and measured microscale velocity and compared with the solution of the MBE.

Theory

The Modified Brinkman Equation (MBE) is a spatially averaged form of the unidirectional Navier-Stokes equation for a steady-state, fully developed laminar flow, assuming a Newtonian fluid, a stagnant solid phase, and constant liquid properties. The averaging procedure presented by Shavit et al. (2002) divides the flow domain into three regions within which the average porosity varies linearly from $\theta = 1$ outside the porous media to $\theta = n$ inside the porous media:

$$\theta = \begin{cases} 1 & z \geq \dfrac{Hrev}{2} \\ \left(\dfrac{1-n}{Hrev}\right)\cdot z + \left(\dfrac{1+n}{2}\right) & \dfrac{-Hrev}{2} \leq z \leq \dfrac{Hrev}{2} \\ n & z \leq \dfrac{-Hrev}{2} \end{cases} \tag{1}$$

Here, H_{rev} is the height of the representative averaging volume, n is the porosity of the porous media and z is the vertical coordinate with $z = 0$ at the interface. The averaging procedure across the three regions results in the following:

$$\begin{cases} -\dfrac{\partial\langle P\rangle}{\partial x} + \mu\left(\dfrac{\partial^2\langle u\rangle^f}{\partial z^2}\right) = 0 & z \geq \dfrac{Hrev}{2} \\ -\dfrac{\partial\langle P\rangle}{\partial x} + \mu\left(\left(\left(\dfrac{1-n}{Hrev}\right)\cdot z + \dfrac{1+n}{2}\right)\dfrac{\partial^2\langle u\rangle^f}{\partial z^2} + \dfrac{2(1-n)}{Hrev}\dfrac{\partial\langle u\rangle^f}{\partial z} - \alpha\langle u\rangle^f\right) = 0 & \dfrac{-Hrev}{2} \leq z \leq \dfrac{Hrev}{2} \\ \dfrac{\partial\langle P\rangle}{\partial x} + \mu\left(n\dfrac{\partial^2\langle u\rangle^f}{\partial z^2} - \alpha\langle u\rangle^f\right) = 0 & z \leq \dfrac{-Hrev}{2} \end{cases} \tag{2}$$

With $\langle u\rangle^f$ the average velocity in the fluid phase. Equation (2) is a simple differential equation, which assumes a linear change in porosity across the interface and contains three parameters: the porosity n a resistance coefficient α, and H_{rev}. The MBE converges to the Brinkman equation in the porous region and to the Stokes equation in the nonporous region. The intermediate region reflects the transition between the Stokes flow and the porous media flow. As the velocity spatial variations in the porous region decay, the Brinkman equation and the Darcy equation become identical.

Realizing that n and α are known for a given porous media, but H_{rev} is to be specified, we have developed a relationship between H_{rev}, permeability, and porosity (Shavit et al., 2004). Note that the resistance coefficient is the ratio between the porosity and the permeability, $\alpha = n/k$. Shavit et al. (2004) investigated the applicability of Equation 2 by using 37 geometrical sets representing a wide variety of brush configurations. Each set contained grooves and walls

arranged symmetrically to create a wide range of porosity and permeability values. It was found that the height of the representative averaging volume, H_{rev}, is accurately computed by:

$$H_{rev}(n,k) = ae^{-bn}\sqrt{k} \tag{3}$$

with $a \cong 8.49$ and $b \cong 2.29$. We were able to show that the combination of Equation 2 and Equation 3 provides an accurate tool for calculating the vertical macroscopic velocity profile given the fundamental properties of the porous media, *n* and *k*, the fluid viscosity, the flow height, and the flow driving force dP/dx. A good agreement was found between the micro-scale Stokes solution and the MBE prediction when both slip (free flow) and nonslip (bounded flow) conditions were applied at the top boundary. The MBE is a general solution that may be applied to any laminar flow problem that involves an interface between porous media that consist of a series of deep grooves and a relatively fast moving flow region.

Geometrical Configuration

Most porous-media configurations and most interface flow scenarios do not produce a microscale flow field that is unidirectional and fully developed. In this paper, we have modified the groove geometry. A Sierpinski carpet was chosen to represent a more complex case in which all velocity components coexist and a fully developed velocity field cannot develop locally. The Sierpinski Carpet is a fractal set, which is created by dividing a square into nine identical squares, removing the middle one and repeating the procedure on each of the remaining squares. The porous media is simulated by an array composed of five parallel rows of 29 Sierpinski sets (a subsection is shown in Figure 1a). This geometry maintains both a complex microstructure and a periodic macroscale pattern. A side view of the Sierpinski set covered by 4 mm of water is shown in Figure 1b. Its height and total width are 36 mm.

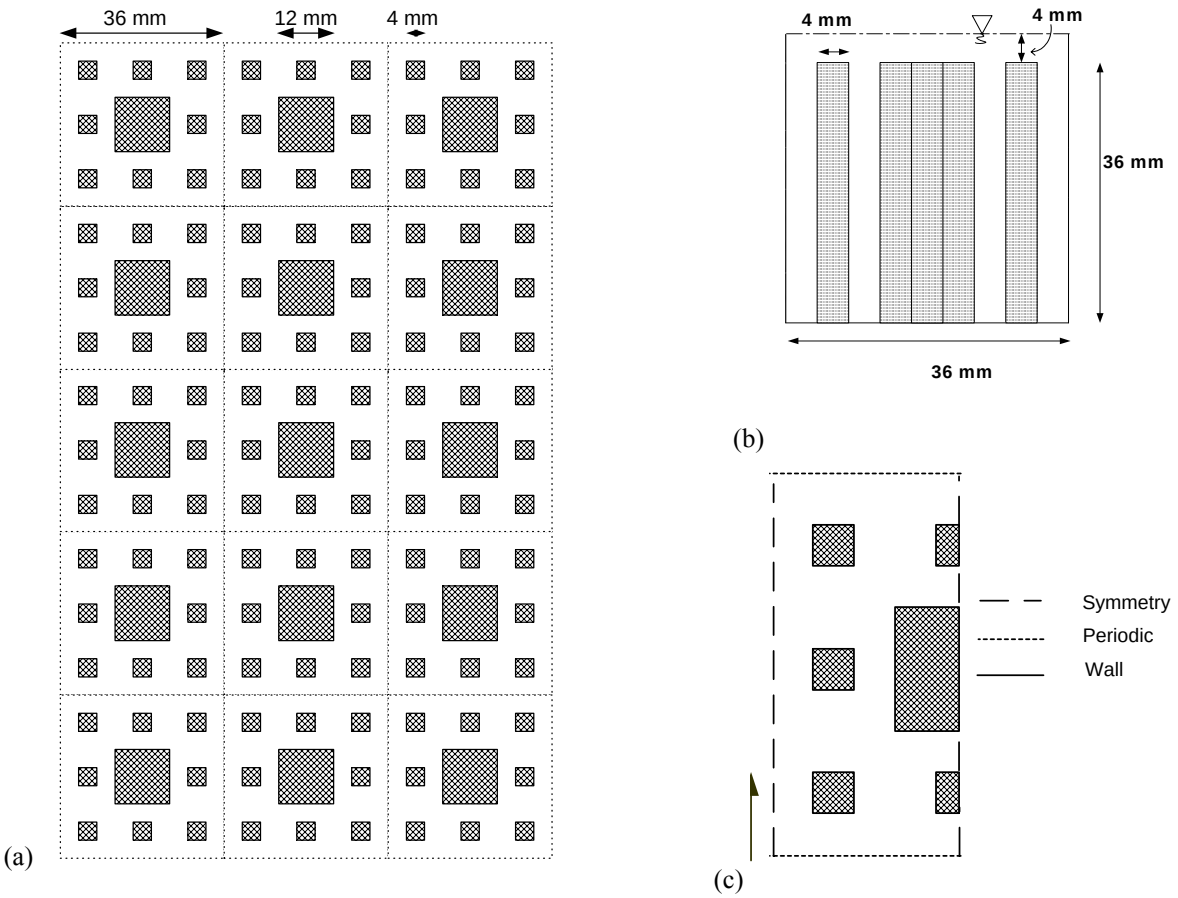

Figure 1: (a) A top view of the Sierpinski sets. (b) A side view of one Sierpinski set. (c) A top view of the domain used for the PIV and for the numerical solution. Boundary conditions are specified.

Results and Discussion

Five parallel rows of 29 Sierpinski sets were installed in the middle of a 220 cm long glass flume positioned on top of a tunable optical table. Water was forced to circulate through the flume, keeping a constant level by using an array of cylinders (3 cm in diameter) positioned at the far end of the flume. Flow rate was measured and controlled by a Coriolis acceleration flow meter. A particle image velocimeter (PIV), composed of a Nd:YAG double laser system and a cross correlation eight-bit 1Kx1K CCD camera, was applied to measure the velocity field in multiple horizontal planes. Twenty-five such planes were obtained starting from the Darcy flow region and moving upwards by 0.5 mm steps until the top free boundary was reached. Assuming that the average velocity field is symmetric, the PIV measurements were obtained at only one half of a Sierpinski set located in the middle of the flume. Fifty realizations were obtained separately at two quarters of the set covering two domains of 18 mm × 18 mm each. A uniform interrogation area of 32 × 32 pixels with 50% overlay was used with time between pulses of 2 ms. The rejection rate was between 5% and 15% when applying a signal-to-noise filter followed by a local median filter.

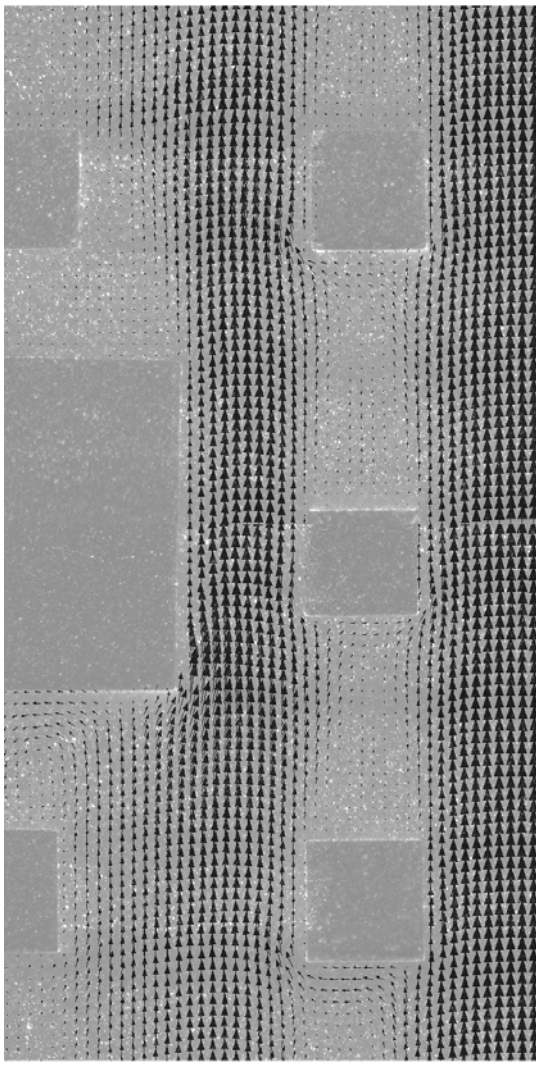

Figure 2. PIV results 3 mm below the interface.

Figure 2 shows the average velocity field at a horizontal cross section 3 mm below the interface when the water level was 4 mm above the interface. The figure shows some features of this flow field. Low-velocity regions with complex vortical motion appear behind the solid square columns. Separation occurs at their corners, mostly when facing upstream. Back-and-forth mass exchange is observed in between the channels separated by the 4 mm × 4 mm columns. By and large, Figure 2 shows that under the specific flow conditions most of the flow is directed through the main grooves formed by the Sierpinski arrangement. We therefore expect a good prediction by the MBE, as was obtained by Shavit et al. (2004).

A steady-state three-dimensional numerical solution of the microscale flow field was obtained. Because of the periodic nature of the Sierpinski structure, the numerical solution was generated for only half the basic unit. We applied symmetric boundary conditions on the sides, a periodic boundary condition at the inlet and outlet, a zero shear (free water surface) at the top (4 mm

above the Sierpinski structure), and a no- slip condition on the walls. A mesh built out of 102,510 hexahedral elements was used to cover the three-dimensional flow domain. The geometry and the mesh were created using GAMBIT 2. The mesh was refined near the walls and at the interface region. The 3-D steady-state Navier-Stokes equations were solved using the finite volume commercial CFD package FLUENT 6. The numerical solution was obtained using a laminar viscous model, a second-order upwind discretization scheme for the momentum, and a standard scheme for the pressure. The SIMPLE pressure-velocity coupling algorithm was used. A solution convergence was achieved after a maximum number of 5,000 iterations, keeping all relative residuals below 5×10^{-6}. The computed velocity field was averaged, and the vertical velocity profiles generated by the MBE, the numerical solution, and the PIV were compared. Figure 3 shows the excellent agreement between the velocity profiles generated by the MBE and by the numerical simulation.

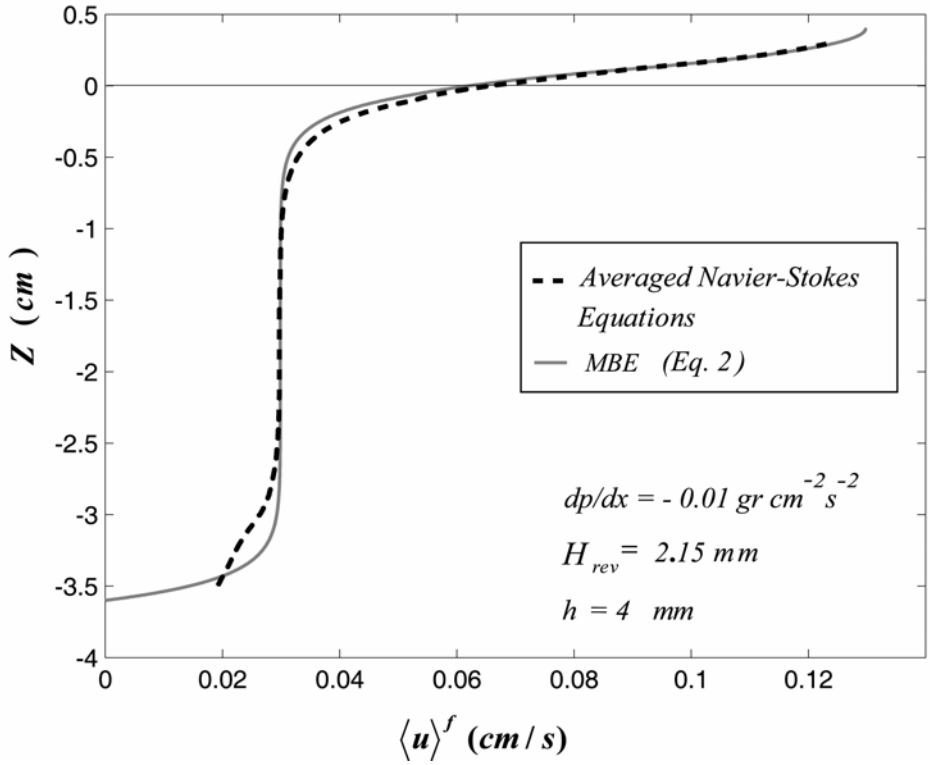

Figure 3. A comparison between the MBE and the result of the numerical simulation.

References

Beavers, G.S. and Joseph, D.D. 1967, Boundary conditions at a naturally permeable wall, *J Fluid Mech* 30, 197-207.

Brinkman, H.C. 1947, A calculation of the viscous force exerted by a flowing fluid on a dense swarm of particles, *Appl Sci Res*. 1, 27-34.

James, D.F. and Davis, A.M.J. 2001, Flow at the interface of a model fibrous porous medium, *J. Fluid Mech.* 426, 47-72.

Sahraoui, M. and Kaviany, M. 1992, Slip and no-slip velocity boundary conditions at interface of porous, plain media, *Inter. Journal of Heat and Mass Transfer* **35**, 927-943.

Shavit, U., Bar-Yosef, G., Rosenzweig, R., and Assouline, S. 2002, Modified Brinkman Equation for a Free Flow Problem at the Interface of Porous Surfaces: The Cantor- Taylor Brush Configuration Case. Water Resources Research, 38(12), 1320-1334,.

Shavit, U., Rosenzweig, R., and Assouline, S., 2003, Free Flow at the Interface of Porous Surfaces: Generalization of the Taylor Brush Configuration. Transport in Porous Media.

Taylor, G.I., 1971, A model for the boundary condition of a porous material. Part 1*., J. Fluid Mech*., 49, 319-326.

Evaluating Hydraulic Head Data as an Estimator for Spatially Variable Equivalent Continuum Scales in Fractured Architecture, Using Discrete Feature Analysis

Tristan Paul Wellman, Eileen Poeter
Department of Geology and Geological Engineering, Colorado School of Mines
tpwellma@mines.edu, epoeter@mines.edu Golden, CO, USA

Accurate representation of large-scale fracture-controlled fluid movement presents a significant challenge for both continuum and discrete-feature network simulators. Discrete feature network (DFN) simulation is a robust numerical approach in which transmissivity, storage, geometry, and orientation are explicitly defined for each fracture within a three-dimensional region. While conceptually robust, computational expense can be prohibitive for large-scale models. By using an equivalent continuum model (ECM), numerical expense may be substantially reduced. An intrinsic assumption of the ECM approach is that the geologic media is represented accurately as a continuum, requiring that grid-scale discretization correspond to the representative elementary scale (RES) at each location within a fractured aquifer. Fracture heterogeneity and compartmentalization may cause spatial variability of effective permeability and connectivity, resulting in spatially variable RES. Consequently, while regional flow may be honored using essentially any grid pattern, failure to properly represent spatially variable RES can lead to erroneous predictions of local flow and transport, especially in highly heterogeneous zones. We hypothesize that hydraulic head data can delineate spatially variable RES in fractured aquifers, and thus provides a method for estimating appropriate grid-cell discretization for a continuum representation of the fractured aquifer. We demonstrate that the head can be expressed as an extensive property in terms of energy per unit volume, so it is an appropriate parameter for use in identifying RES. We compare RES estimates using porosity to those estimated by averaging sparse, randomly distributed head observations at multiple scales. Using our algorithm and fracture-flow predictions by the discrete feature simulator package FracMan-MAFIC (Dershowitz et al., 1998; Miller et al., 1999), we find hydraulic head observations are useful in estimating spatially variable RES. We present our averaging methodology and results for a range of fracture architectures and differing spatial distributions of observations.

References

Dershowitz, B., G. Lee, G., Geier, J., Foxford, T., P. LaPointe, P, and A. Thomas, 1998, FracMan - interactive discrete feature data analysis, geometric modeling, and exploration simulation, version 2.6, Golder Associates Inc. 1-184

Miller, I., G. Lee, and W. Dershowitz, 1999, MAFIC - matrix/fracture interaction code with heat and solute transport-user documentation, version 1.6, Golder Associates Inc., Redmond, WA, 1-87

The Mathematical Model of the Flow of Gas-Condensate Mixtures in Fissurized Porous Rocks with an Application to the Development of Tight Sand Gas Deposits

G.I. Barenblatt
Department of Mathematics, UC Berkeley, and
Lawrence Berkeley National Laboratory

A plausible explanation and quantitative investigation of fast pressure decrease during intense exploitation of tight sand gas deposits will be presented and discussed.

Two basic assumptions are made:

(1) The rock of the stratum is fissurized, and
(2) A weak precipitation takes place of the gas condensate formed due to the retrograde gas condensation.

The qualitative scheme of the phenomenon is as follows. During an intensive exploitation of the deposit the pressure in fissures is sharply decreasing due to the large permeability and small relative volume of cracks. Therefore, a large pressure drop is arising between the fissures and the porous blocks, which contain the basic mass of gas, and where the permeability is low. The precipitation rate of the gas condensate in a porous medium grows fast with the pressure gradient; it can be assumed to be proportional to the pressure gradient squared. However, the pressure gradient is concentrated basically near the boundaries of the porous blocks. Therefore in the basic internal part of the porous blocks the pure gas filtration regime takes place: due to small pressure gradient inside the porous blocks the rate of condensate precipitation is small and can be neglected. Also, the condensate which is precipitated inside the block is at rest, because its amount and condensate-saturation is small. Contrary to that near the boundaries of blocks the pressure gradient is large, and so is the condensate precipitation rate. Therefore— and this is the basic distinction from gas motion in a purely porous media—at the boundaries of the porous blocks thin skin shells are formed where an intensive condensate precipitation takes place. In these shells a two-phase flow of gas-condensate mixture is developed, and the relative permeability of gas is substantially reduced. The thin skin shells at the boundaries of the porous blocks create a substantial resistance to the gas flow. It can therefore substantially decrease the gas recovery in spite of the fact that the amount of condensate can be tiny and even unnoticed in the process of the development of the deposit.

In the present lecture a quantitative model of gas-condensate mixture flow in a fissurized porous medium, taking into account the formation of thin skin shells of two phase gas-condensate flow will be presented and discussed. Some qualitative conclusions concerning the development of tight sand gas deposits will be discussed also.

Acknowledgments

Prof. K.S. Basniev and Prof. I.N. Kochina participated in the work, reported in the lecture.

Reservoir Characterization and Management Using Soft Computing

Masoud Nikravesh
BISC Program, EECS Department, CS Division
University of California, Berkeley and
NERSC, National Energy Research Scientific Computing Center
Lawrence Berkeley National Laboratory

Introduction

With oil and gas companies presently recovering, on the average, less than a third of the oil in proven reservoirs, any means of improving yield effectively increases the world's energy reserves. Accurate reservoir characterization through data integration (such as seismic and well logs) is a key step in reservoir modeling & management and production optimization.

There are many techniques for increasing and optimizing production from oil and gas reservoirs, which are based on precisely characterizing the petroleum reservoir, finding the bypassed oil and gas, processing the huge databases such as seismic and wireline logging data, extracting knowledge from corporate databases, finding relationships between many data sources with different degrees of uncertainty, optimizing a large number of parameters, deriving physical models from the data, and optimizing oil/gas production.

This presentation address the key challenges associated with development of oil and gas reservoirs. Given the large amount of by-passed oil and gas and the low recovery factor in many reservoirs, it is clear that current techniques based on conventional methodologies are not adequate and/or efficient. We are proposing to develop the next generation of Intelligent Reservoir Characterization (IRESC) tool, based on Soft computing which is an ensemble of intelligent computing methodologies using neuro computing, fuzzy reasoning, and evolutionary computing. Two main areas to be addressed are first, data processing/fusion/mining and second, interpretation, pattern recognition, and intelligent data analysis.

Results

An integrated methodology has been developed to identify nonlinear relationships and mapping between 3-D seismic and well logs data. This methodology has been applied to a producing field. The method uses conventional techniques such as geostatistical and classical pattern recognition in conjunction with modern techniques such as soft computing (neuro computing, fuzzy logic, genetic computing, and probabilistic reasoning). An important goal of our research is to use clustering and nonlinear mapping techniques to recognize the optimal location of a new well based on 3-D seismic and available well logs data. The classification, clustering, and nonlinear mapping tasks were accomplished in three ways: (1) classical statistical techniques; (2) fuzzy reasoning; and (3) neuro computing to recognize similarity cubes. The relationships between each cluster and well logs were recognized around the wellbore and the results used to reconstruct and extrapolate well logs data away from the wellbore. This advanced 3-D seismic and log analysis and interpretation can be used to predict: (1) mapping between production data

and seismic data; (2) reservoir connectivity based on multi-attribute analysis; (3) pay zone estimation; and (4) optimum well placement.

Future Trends

Hybrid systems: So far we have seen the primary roles of neurocomputing, fuzzy logic and evolutionary computing. Their roles are in fact unique and complementary. Many hybrid systems can be built. For example, fuzzy logic can be used to combine results from several neural networks; GAs can be used to optimize the number of fuzzy rules; linguistic variables can be used to improve the performance of GAs; and extracting fuzzy rules from trained neural networks. Although some hybrid systems have been built, this topic has not yet reached maturity and certainly requires more field studies.

In order to make full use of soft computing for intelligent reservoir characterization, it is important to note that the design and implementation of the hybrid systems should aim to improve prediction and its reliability. At the same time, the improved systems should contain small number of sensitive user-definable model parameters and use less CPU time. The future development of hybrid systems should incorporate various disciplinary knowledge of reservoir geoscience and maximize the amount of useful information extracted between data types so that reliable extrapolation away from the wellbores could be obtained.

Computing with words: One of the major difficulties in reservoir characterization is to devise a methodology to integrate qualitative geological description. One simple example is the core descriptions in standard core analysis. These descriptions provide useful and meaningful observations about the geological properties of core samples. They may serve to explain many geological phenomena in well logs, mud logs and petrophysical properties (porosity, permeability and fluid saturations). Yet, these details are not utilized due to the lack of a suitable computational tool.

Computing with words (CW) aims to perform computing with objects which are propositions drawn from a natural language or having the form of mental perceptions. In essence, it is inspired by remarkable human capability to manipulate words and perceptions and perform a wide variety of physical and mental tasks without any measurement and any computations. It is fundamentally different from the traditional expert systems which are simply tools to “realize” an intelligent system, but are not able to process natural language which is imprecise, uncertain and partially true. CW has gained much popularity in many engineering disciplines (Zadeh 1999a,b). In fact, CW plays a pivotal role in fuzzy logic and vice-versa. Another aspect of CW is that it also involves a fusion of natural languages and computation with fuzzy variables.

In reservoir geology, natural language has been playing a very crucial role for a long time. We are faced with many intelligent statements and questions on a daily basis. For example: If the porosity is high then permeability is likely to be high? As most seals are beneficial for hydrocarbon trapping, if a seal is present in reservoir A, what is the probability that the seal in reservoir A is beneficial? High-resolution log data is good, the new sonic log is of high resolution, so what can be said about the quality of the new sonic log?

CW has much to offer in reservoir characterization because most available reservoir data and information are too imprecise. There is a strong need to exploit the tolerance for such imprecision, which is the prime motivation for CW. Future research in this direction will surely provide a significant contribution in bridging reservoir geology and reservoir engineering.

Given the level of interest and the number of useful networks developed for the earth science applications and specially oil industry, it is expected soft computing techniques will play a key role in this field. Many commercial packages based on soft computing are emerging. The challenge is how to explain or "sell" the concepts and foundations of soft computing to the practicing explorationist and convince them of the value of the validity, relevance and reliability of results based on the intelligent systems using soft computing methods.

References

Masoud Nikravesh, Fred Aminzadeh, and Lotfi A. Zadeh, "Intelligent Data Analysis for Oil Exploration," Developments in Petroleum Science, 51; ISBN: 0-444-50685-3, Elsevier (March 2003)

Patrick Wong, Fred Aminzadeh, and Masoud Nikravesh, "Soft Computing for Reservoir Characterization and Modeling, Series Studies in Fuzziness and Soft Computing, Vol 80, Physica-Verlag, Springer, 2002.

M. Nikravesh, F. Aminzadeh and L.A. Zadeh, Soft Computing and Earth Sciences (Part 2), Journal of Petroleum Science and Engineering, Volume 31, Issue 2-4, January 2001; Special Issue.

M. Nikravesh, F. Aminzadeh and L.A. Zadeh, Journal of Petroleum Science and Engineering, Soft Computing and Earth Sciences, Volume 29, Issue 3-4, May 2001; Special Issue.

P.M. Wong and M. Nikravesh (2001), A thematic issue on "Field Applications of Intelligent Computing Techniques," Journal of Petroleum Geology, 24(4), 379-476; Special Issue.

Zadeh, L. and Kacprzyk, J. (eds.): *Computing With Words in Information/Intelligent Systems 1: Foundations*, Physica-Verlag, Germany (1999a).

Zadeh, L. and Kacprzyk, J. (eds.): *Computing With Words in Information/Intelligent Systems 2: Applications*, Physica-Verlag, Germany (1999b).

Lotfi A. Zadeh and Masoud Nikravesh, Perception-Based Intelligent Decision Systems, AINS; ONR Summer 2002 Program Review, 30 July-1 August, UCLA

Numerical Simulation of Air Injection in Light Oil Fractured Reservoirs

Sébastien Lacroix, Philippe Delaplace, and Bernard Bourbiaux
Institut Français du Pétrole, 1-4 avenue de Bois-Préau, 92852 Rueil-Malmaison, France

Introduction

Air injection can be an economical alternative for pressure maintenance of fractured reservoirs as it avoids re-injecting a valuable associated gas and/or generating or importing a make-up gas. In addition, the oil recovery can be enhanced thanks to the thermal effects associated with oil oxidation. However, such an improved recovery method requires a careful assessment of the involved reservoir displacement mechanisms, in particular the magnitude and kinetics of matrix-fracture transfers. Actually, the latter will largely control the displacement efficiency as well as the composition of well effluents from which residual oxygen has to be absent for obvious safety reasons. Considering the situation of a light-oil fractured reservoir, compositional thermal simulations of matrix-fracture transfers are carried out on a fine-grid single-porosity model of a matrix block surrounded by air-invaded fractures to first identify the main physical mechanisms controlling matrix-fracture transfers during air injection. Then a new matrix-transfer formulation is introduced in the equivalent (up-scaled) dual-porosity model in order to dispose of a reliable simulation tool usable for field-scale prediction as, in conclusion, it will be demonstrated on a cross-section case.

Physical Background and Driving Mechanisms for Matrix-Fracture Exchanges

Simulation Data

The petrophysical and thermodynamic properties used in our simulations are largely inspired from the Ekofisk field. The matrix medium has a permeability K of 1mD, a porosity Φ equal to 30% for a total calorific capacity of 2.35 $Jg^{-1}°C^{-1}$ and a thermal conductivity of 1.8 $Wm^{-1}°C^{-1}$. These are actually mean values for an homogeneous chalk. The initial pressure is 5600 Psi and temperature is 266°F. Capillary pressures and permeability curves are described as shown below:

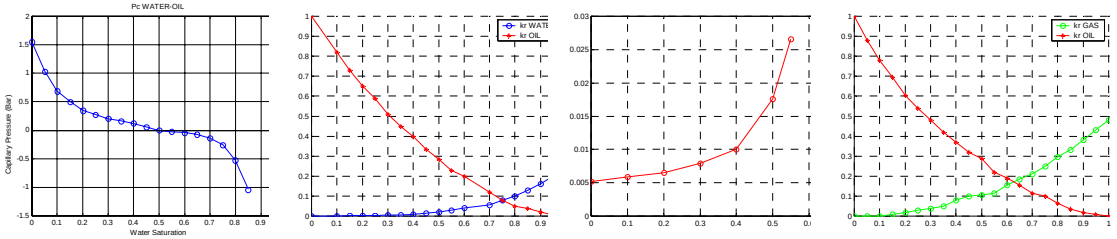

Figure 1. Capillary and permeability curves for the water-oil and oil-gas systems.

The irreducible water saturation S_{wi} is 0.15, the critical gas saturation S_{gc} is 0.01 and residual oil saturations are respectively S_{orw} = 0.25 and S_{org} = 0.25.

In order to accurately take into account the vaporisation of the light fractions and the oxidation of the heavy fractions of oil while avoiding excessive calculations, an optimal set of pseudo-constituents is considered. This set is divided into pure light components (nitrogen, oxygen, carbon dioxide and methane), intermediate pseudo-components (C2C3,C4C9) and heavy pseudo-components (C10-C17,C18-C30). Finally the reaction scheme and molecular diffusion flux in the "*p"* phase for the component "*k*" are described by the respective formulations:

$$[CH_2]n + \frac{3n}{2}O_2 \rightarrow n[CO_2] + nH_2O \tag{1}$$

$$(F_k^{(p)}) = \left[T_k \frac{\phi}{\tau} \Delta(C_k) \right]^{(p)} \tag{2}$$

where T_k is the diffusion transmissivity involving the pressure and temperature dependent diffusion coefficient D_k, τ the matrix tortuosity and $\Delta(C_k)$ the component concentration gradient.

Simulation Results and Physical Issues

The following results show the evolution against time of the oil in place in the matrix medium as well as the evolution of each component both in the matrix (mass in place) and the surrounding media (produced mass).

Table 1. Comparison of the effects of drainage (---), drainage-diffusion (---), and drainage-diffusion-reaction (---) processes on the mass in place of light and intermediate components.

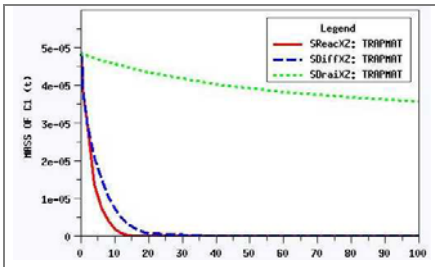

Figure 1. Mass in place for the C1 component.

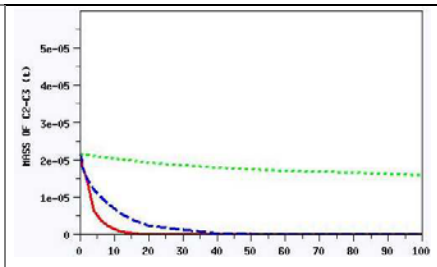

Figure 2. Mass in place for the C2C3 component.

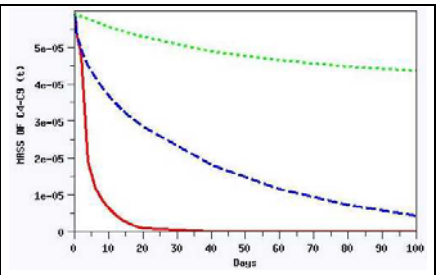

Figure 3. Mass in place for the C4C9 component.

Table 2. Comparison of the effects of drainage (---), drainage-diffusion (---), and drainage-diffusion-reaction (---) processes on the mass in place of heavy components and the oil phase.

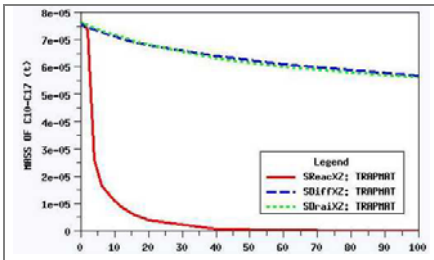

Figure 4. Mass in place for the C10C17 component.

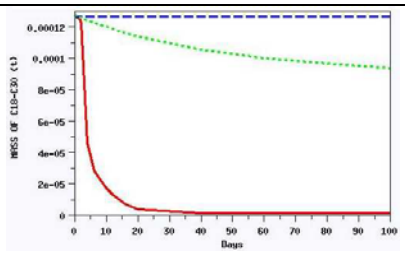

Figure 5. Mass in place for the C18C30 component.

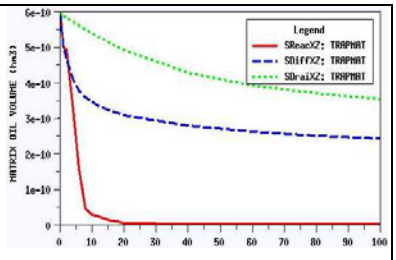

Figure 6. Mass in place for the Oil phase.

Table 3. Comparison of the effects of drainage (---), drainage-diffusion (---), and drainage-diffusion-reaction (---) processes on the recovery of light, intermediate and heavy components.

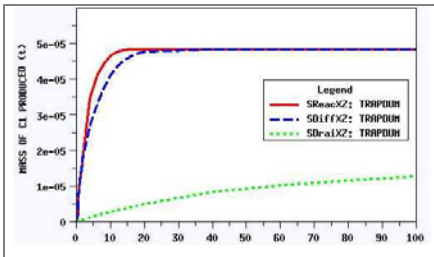

Figure 7. Produced mass for the C1 component.

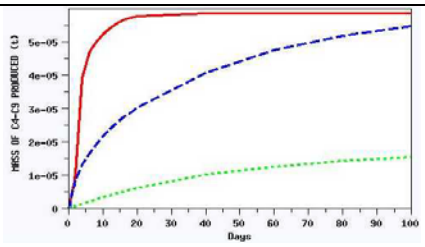

Figure 8. Produced Mass for the C4C9 component.

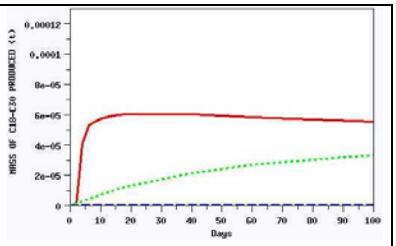

Figure 9. Produced mass for the C18C30 component.

First, the reference fine-grid simulations show that gas diffusion and thermodynamic transfers are the major physical mechanisms controlling the kinetics of matrix-fracture transfers and the resulting oxidation of oil. The chronology of extraction of oil components from the matrix blocks is clearly interpreted in relation with phase transfers. As indicated by Figure 6 diffusion and reaction have an additional effect on oil recovery. What is the impact of the different mechanisms on each component? It is first of all noticeable that the mere process of air-oil drainage results in the same recovery for each component, whereas diffusion and reaction have a compositional effect. Figures 1 and 2 show that vaporization and mass transfer by diffusion control the recovery of the light components. Comparing mass in place (Figures 1 and 3) to production curves (Figures 7 and 8) puts the emphasis on the fact that diffusion accounts for most of the light and intermediate components production. On the other hand, only half of the heavy component is produced and this only if a reaction process is taking place in addition to diffusion (Figure 9). As a matter of fact, because vaporization is faster than drainage and concerns the light components, the remaining oil becomes highly concentrated in heavy components and less and less mobile, thus explaining the trapping and capillary retention of the tail fraction (Figure 5).

Field Scale Simulation of the Exchanges in a Dual Porosity Model

The conceptual dual-porosity model was introduced in the early sixties (Warren et al., 1963). It represents the fractured reservoir as an array of parallelepipedic matrix blocks limited by a set of uniform orthogonal fractures (Figure 16). Fracture flows are computed within the fracture grid, and matrix-fracture transfers are computed at each gridblock position. However, the extension of the expression proposed by Warren and Root to matrix-fracture mass transfers involving molecular diffusion and multiphase flows results in difficulties linked to the representation of the actual local-scale physics. Moreover, transient phenomena are hardly reproducible without a discretization of the matrix block. Therefore a discretization of the matrix blocks has been proposed (Saïdi, 1983) and introduced in some simulators (Pruess et al., 1985; Gilman, 1986; Chen et al., 1987). This approach is satisfactory, but has computation requirements which cannot be met for large or complex reservoir models. The difficulties are even greater if we deal with multiphase transfers of fluids in thermodynamic nonequilibrium because mass transfer of components occurs at the interface between phases in addition to convective and diffusive transfers occurring within each phase. The influencing transfer mechanisms that have to be up-scaled are mainly gravity drainage, molecular diffusion, and thermal conduction. Even though we dispose of an adapted formulation for the thermal conduction phenomena, we won't discuss it in the following since, due to the small block size, the reaction heat is instantaneously spread through the media. On the other hand, the diffusion mechanism has to be carefully reproduced as it is a key point to initiate the reaction. Our formulation combined with other improvements (Sabathier et al., 1998) takes into account the diffusion in the gas phase (the diffusion in the liquid phase being neglected) and a thermodynamic equilibrium within the matrix block independently of the saturations; in other words it replaces the common pseudo-permanent formulations expressed with the mean values of matrix variables by a dynamic process reflecting the gradual penetration of the diffusing elements.

Table 4. Comparison of the single (---) and dual approach (---) for the different processes.

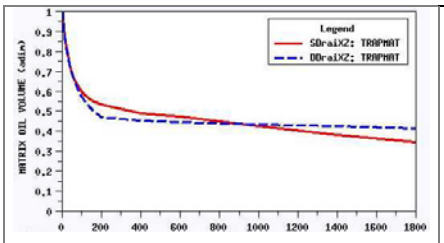

Figure 10. Mass in place: drainage.

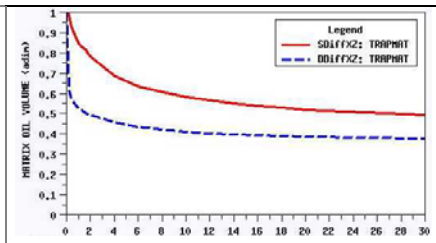

Figure 11. Mass in place: drainage-diffusion.

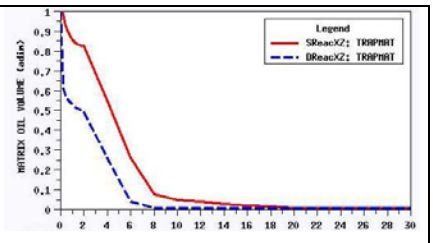

Figure 12. Mass in place: drainage-diffusion-reaction.

Due to our numerical formulation ensuring a proper up-scaling of diffusion and inter-phase transfers at the overall scale of matrix blocks, the predictions of the dual-porosity model are shown to be in very good agreement with those of the reference model for all three kinetics (Figures 10, 11, and 12).

Conclusion and Application to a Cross-Section Case

We showed in the previous section that our dual porosity model satisfactorily predicted the matrix-fracture transfers at the scale of one matrix block subjected to fixed boundary conditions. To further upscale the matrix-fracture transfers in view of reservoir simulation, we simulated air injection across a vertical reservoir cross section made up of 10 matrix blocks represented by a unique dual medium gridblock. Due to air injection and matrix-fracture transfers, the boundary conditions are changing with time and are different from one block to another. Table 5 compares the results to whose obtained on a model with 10 gridblocks of one matrix block each, considered as a reference, for three representative components and a drainage-diffusion-reaction process (up-scaling scheme in Figure 17).

Table 5. Subgridded (---) and monoblock (---) cross section with drainage-diffusion-reaction.

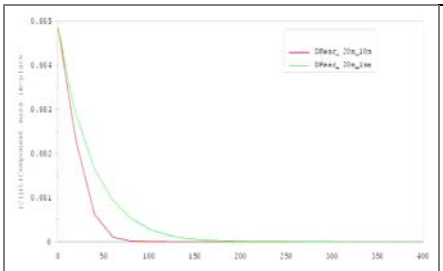

Figure 13. C1Mass in place.

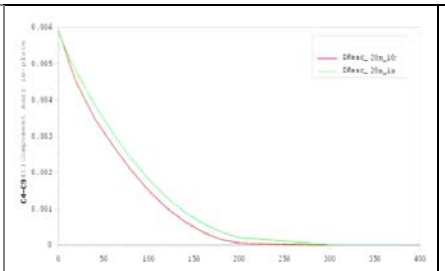

Figure 14. C4-C9 Mass in place.

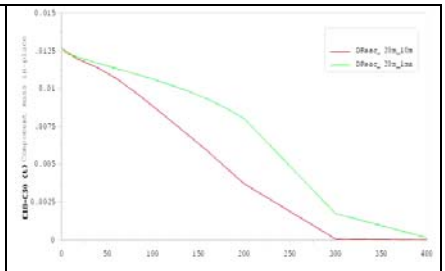

Figure 15. C18-C30 Mass in place.

As expected, the single gridblock dual porosity model is quite representative of the reference model. To conclude, we now dispose of a reliable field simulation with all the required capabilities to predict air or other gas injection scenarios in fractured reservoirs involving multiphase compositional matrix-fracture transfers. Once the reservoir fluid system PVT behavior and its reactivity in the presence of air have been characterized, the field implementation scheme of the process, in terms of well location, injection rate can be designed in a reliable and numerically efficient way using such a dual-porosity simulator.

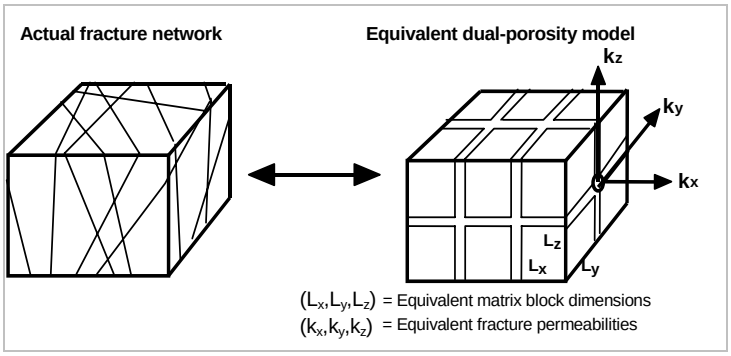

Figure 16. Conventional Warren and Root representation of a fractured reservoir (gridblock scale).

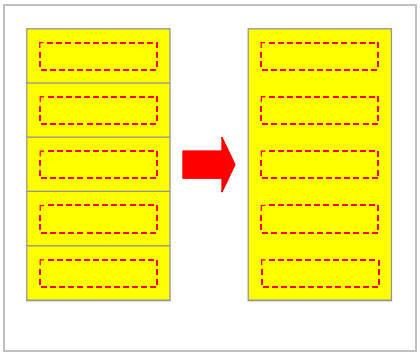

Figure 17. Gridblocks representation for the cross-section case.

Acknowledgments

This work was supported by Total, and the authors would like to thank D. Foulon and Y. Lagalaye for the fruitful discussions and ideas.

References

Chen, W.H., M.L. Wasserman and R.E. Fitzmorris 1987. *A Thermal Simulator for Naturally Fractured Reservoirs*. Paper SPE 16008 presented at the 9th SPE Symposium on Reservoir Simulation held in San Antonio, Tx, Feb. 1-4, 1987.

Pruess, K. and T.N. Narasimhan 1985. *A Practical Method for Modelling Fluid and Heat Flow in Fractured Porous Media*. SPE Journal, Feb. 1985. Pages 14-26.

Sabathier, J.C., B.J. Bourbiaux, M.C. Cacas and S. Sarda 1998. *A New Approach of Fractured Reservoirs*. Paper SPE 39825 presented at the SPE International Petroleum Conference and Exhibition of Mexico held in Villahermosa, Mexico, 3-5 March 1998.

Saïdi, A.M. 1983. *Simulation of Naturally Fractured Reservoirs*. Paper SPE 12270, 7th SPE Symposium on Reservoir Simulation held in San Francisco, CA, Nov. 15-18, 1983.

Warren, J.E. and P.J. Root 1963. *The Behaviour of Naturally Fractured Reservoirs*. Society of Petroleum Engineers Journal, Sept. 1963. Pages 245-255.

Two-Phase Flow through Fractured Porous Media

P.M. Adler [1], I.I.Bogdanov [1,2], V.V.Mourzenko [2], and J.-F.Thovert [2]
[1] IPGP, tour 24, 4 Place Jussieu, 75252 Paris Cedex 05 (adler@ipgp.jussieu.fr)
[2] LCD-PTM , SP2MI, BP 179, 86960 Futuroscope Cedex, France

Introduction

Consider a set of fractures embodied in a porous solid matrix as displayed in Figure 1; both the matrix and the fractures are permeable, with permeabilities which may vary with space.

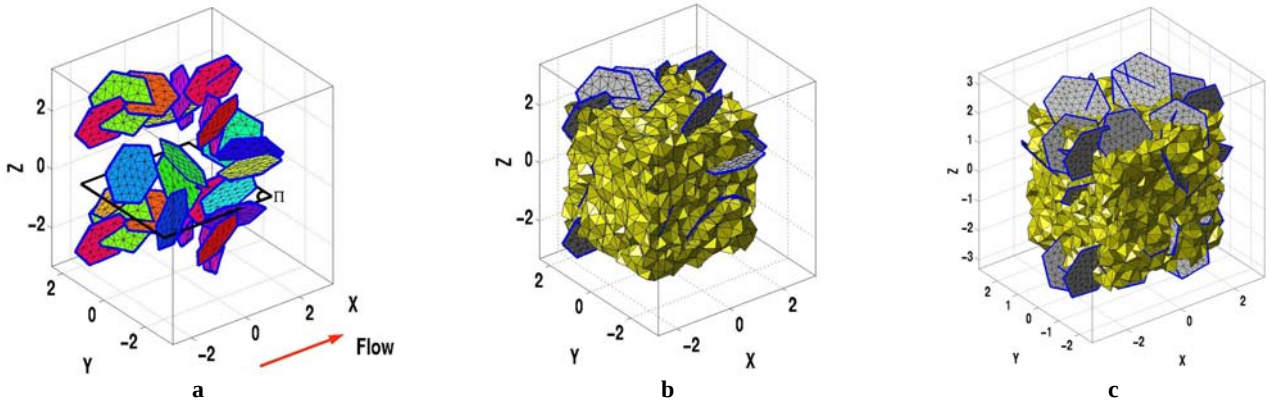

Figure 1. The network of N_{fr}=16 fractures in the sample used for the simulations in Figures 2 and 3 (a). The saturation maps in Figure 2 correspond to the horizontal marked plane *Π*. The three-dimensional meshes of the same fractured medium (b) and of another sample with N_{fr} =32 (c). Distances are normalized by the fracture circumscribed radius R. Both samples are spatially periodic, with cell size L=4R. For the sake of clarity, the edges and the intersection lines of the fractures have been thickened.

Historically, flow in this complex situation was first addressed by [1,2] which motivated many further works such as [3-5] (see also more recent papers in [6-8]).

The present work is based on a three-dimensional discrete description of the fracture network. Hence, arbitrary fracture network geometry, various types of boundary conditions, and distribution of the fracture and matrix properties can be addressed, without simplistic approximations. The purpose of this paper is to briefly present the methodology and the first results obtained in the determination of the two-phase flow properties of fractured porous media.

Equations for Two-Phase Flow

Transport Equations

Let the porous rock matrix have a porosity ε_m and a bulk permeability K_m [L^2] that can vary with space. The flow in the matrix is described by a generalized Darcy law for each phase, with

relative permeabilities $K_{r,i}$ (i=w,n). Subscripts *w* and *n* refer to wetting and nonwetting fluids, respectively. The local seepage velocities $\bar{v}_i$ are given by

$$\bar{\mathbf{v}}_i = -\frac{K_m K_{r,i}}{\mu_i}\nabla(P_i - \rho_i g z) \qquad \text{(i=1,2)} \tag{1}$$

where μ_i is the viscosity, ρ_i is the density, and P_i is the pressure for fluid *i*. For concision, denote Φ_i the potential P_i-$\rho_i gz$ and Λ_i=$K_{r,i}/\mu$ the phase mobilities. Two continuity equations and a global condition on the saturations S_i can be written

$$S_1 + S_2 = 1 \quad , \quad \varepsilon\frac{\partial \rho_i S_i}{\partial t} + \nabla.(\rho_i \bar{\mathbf{v}}_i) = 0 \qquad \text{(i=1,2)} \tag{2}$$

Equations similar to (1,2) are applied for the flow in the fractures whose hydraulic properties can be described by an effective conductivity σ [L^3]. The in-plane flow rates $\mathbf{j}_{s,i}$ per unit width are related to the surface pressure gradients $\nabla_s P_i$ by two-dimensional generalized Darcy laws

$$\mathbf{j}_{s,i} = -\frac{\sigma\sigma_{r,i}}{\mu_i}\nabla_s\Phi_i \qquad \text{(i=w,n)} \tag{3}$$

where $\sigma_{r,i}$ are the relative permeabilities of the fractures. The conductivity σ can be position dependent, and it can differ for different fractures. For a fracture that can be viewed locally as a plane channel of aperture *b*, filled with a porous material with permeability K_f, σ is given by

$$\sigma = b\ K_f \tag{4}$$

It is assumed that the fractures oppose no resistance to flow normal to their plane. Hence, the pressures P_i, P_c, and the potentials Φ_i are continuous across the fractures.

Constitutive equations

A particular choice for the constitutive equations has been made for the closure of the transport equations. Due to interfacial tension, a pressure jump P_c takes place across the interface, which is called the capillary pressure

$$P_c = P_n - P_w = \Phi_n - \Phi_w + \Delta\,\rho\,g\,z \tag{5}$$

The most widely used models for P_c and $K_{r,i}$ are the ones proposed by [9]

$$S_w = \left[1 + \left(\frac{P_c}{P_0}\right)^n\right]^{\frac{1}{n}-1} \quad , \qquad K_{r,i} = S_i^{1/2}\left[1 - \left(1 - S_i^{\frac{n}{n-1}}\right)^{\frac{n-1}{n}}\right]^2 \tag{6}$$

On physical grounds, one expects that

$$\frac{P_{o,f}}{P_{o,m}} \approx \sqrt{\frac{K_m}{K_f}} = \kappa \tag{7}$$

Two-phase flows in fractures have given rise to comparatively less experimental studies than three-dimensional porous media, but a few references can be found in the literature. They are reviewed, for instance, by [10]. In the present simulations, we used a simple model for $\sigma_{r,n}$

$$\sigma_{r,n} = S_n^{\,q} \tag{8}$$

with the exponent q equal to 2. This model was also applied for $K_{r,n}$ in the rock matrix. Moreover, $\sigma_{r,n}$ was described by an equation of the type of (6).

Numerical Model

The fracture network is triangulated first as described by [11]; then, the space between the fractures is paved by an unstructured boundary-constrained tetrahedral mesh, according to an advancing front technique; three-dimensional views of two triangulated fractured media are shown in Figure 1. The nonwetting phase potential Φ_n and the capillary pressure P_c are evaluated at the mesh points located at the vertices of the tetrahedra and triangles; a finite volume formulation of the problem is obtained by applying the balance equations to control volumes Ω surrounding each of the mesh points. The strong nonlinearity of the coefficients in the equations requires an implicit time formulation such as [12]. The routine was thoroughly tested by two regular structures which will be discussed during the presentation.

Randomly Fractured Porous Media

Illustrative Example

A detailed set of results is presented in this section, relative to a homogeneous matrix rock containing the fracture networks shown in Figures 1a and 1c. The fractures are plane regular hexagons, with a constant permeability $\sigma'=1$ with $\kappa = 10^{-3/2}$. The network does not percolate. Constitutive parameters are set as $n_m=n_f=q=2$. The fluid densities are equal and $\mu_n/\mu_w = 10$.

All the frames in Figure 2 are wetting-phase saturation maps S_w within the matrix in the horizontal section Π in Figure 1a. Starting from very different configurations, an identical steady regime is reached, where saturation is not uniform.

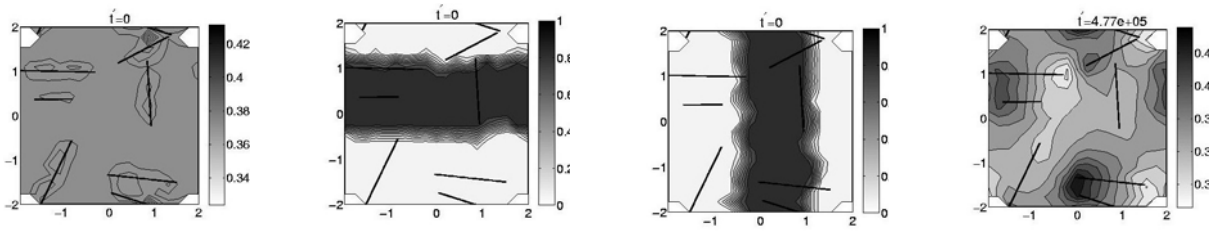

Figure 2. Wetting phase saturation at in the plane Π marked in Figure 1a. The mean flow is oriented from the left to the right of the figure. The mean saturation is always $\overline{S_w}$ =0.371. The first three columns correspond to the initial saturation; the fourth to the common final saturation.

Steady State Relative Permeabilities as Functions of Mean Saturation

The previous example shows that it is possible to define steady-state macroscopic phase-relative permeabilities for this medium at a given mean saturation $\overline{S_w}$. These relative permeabilities $\overline{K}_{r,i}$ are intrinsic in the sense that they do not depend on initial conditions; it was shown in a few examples that they do not depend neither on the magnitude of the applied macroscopic pressure gradient, nor on the viscosity ratio, at least within a reasonable range.

The results are shown in Figure 3 for the 16- and 32-fracture samples. The symbols correspond to the statistical averages over 27 calculations, and the error bars to the full range of variation of the individual data. The solid lines are the relative permeabilities for the fractures and the rock matrix, which in the present case are identical functions of the saturation.

In spite of the difference in percolation probability between the two cases, the general aspects of the results are similar. The presence of fractures increases the relative permeability for the nonwetting phase and decreases the relative permeability for the wetting phase, with respect to the intact matrix material. However, the amplitude of these variations is larger for the denser fracture networks.

The strongest effects are observed for the largest saturations, and for the nonwetting fluid permeability $\overline{K}_{r,n}$. This is a consequence of the different capillary functions of the fractures and rock matrix (see Equation 7). For the same value of P_c, the nonwetting phase saturation is much larger in the fractures than in the surrounding matrix, and the relative permeability $\sigma_{r,n}$ is larger than $K_{r,n}$. Thus, the fractures are preferential paths for the nonwetting phase.

Conversely, $\overline{K}_{r,w}$ is smaller than $K_{r,w}$ in the rock matrix, but this is mostly a consequence of increasing the absolute permeability induced by the presence of the fractures, $\overline{K} > K_m$. The products $\overline{K}\ \overline{K}_{r,w}$ and $K_m K_{r,w}$ are identical, which means that the fractures do not significantly affect the wetting-phase flow rate, with respect to the intact rock.

Influence of the Other Parameters

The influence of the fracture permeability σ', the magnitude G of the driving pressure gradient, the viscosity ratio, and the exponents n_m and n_f, was briefly tested by varying a single parameter at a time with respect to the base case considered previously. Calculations were run for a few values of the mean saturation $\overline{S}_w$, on fractured media containing N_{fr}=16 or 32 fractures.

Concluding Remarks

We presented in this paper a numerical tool for the simulation of two-phase flows in fractured porous media, together with a set of applications that demonstrated its ability to handle steady or transient flows in complex random media.

Moreover, a simplified model was built that corresponds to a small value of the capillary number. It was shown to be in good agreement with the full numerical results.

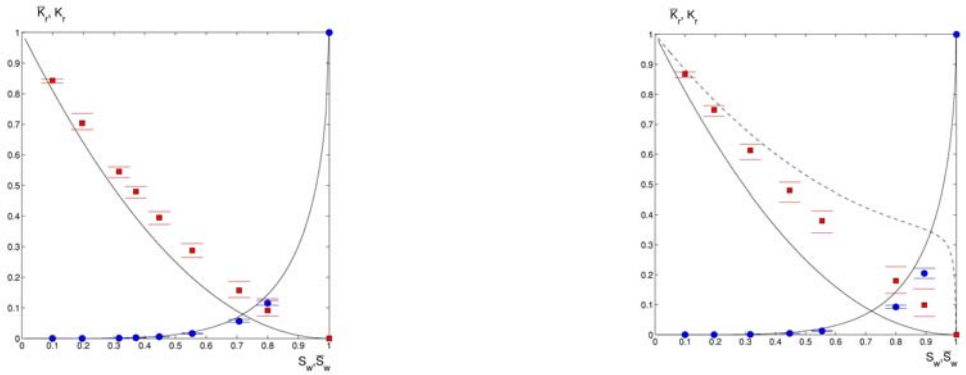

Figure 3. Macroscopic relative permeabilities $\overline{K}_{r,i}$ as functions of the mean saturation $\overline{S}_w$. Data are for samples containing 16 (a) or 32 (b) hexagonal fractures. The cell size is L=4R. The fractures have a permeability σ'=1, and $\kappa=10^{-3/2}$. The fluids have equal densities. The horizontal lines show the full variation range of the individual data. The solid lines are the relative permeabilities for the fractures and for the rock matrix, with $n_m=n_f=q=2$. The broken line in (b) is a prediction for infinite plane fractures with the same characteristics and the same global intrinsic permeability.

References

[1] Barenblatt G.I. and Zheltov Yu.P., 1960, Soviet Dokl. Akad. Nauk, 13, 545-548.
[2] Barenblatt G.I., Zheltov Yu.P. and Kochina I.N., 1960, Soviet Appl. Math. Mech. (P.M.M.), 24, 852-864.
[3] Warren J.R. and Root P.J., 1963, Soc. Pet. Eng. J., 228, 245-255.
[4] Odeh A.S., 1965, Pet. Eng. J., 5, 60-66.
[5] van Golf-Racht T.D., 1982, Fundamentals of fractured reservoir engineering, Developments in Petroleum Science, 12, Elsevier, Amsterdam.
[6] Chen J., Hopmans J.W. and Grismer M.E., 1999, Advances in Water Resources, 22, 479-493.
[7] Adler P.M. and Thovert J.-F., 1999, Fractures and fracture networks, Kluwer Academic Publishers, Dordrecht.

[8] Bogdanov I.I., Mourzenko V.V., Thovert J.-F. and Adler P.M., 2002, Effective permeability of fractured porous media in steady-state flow, Water Resour.Res., 39, 10.1029/2001WR000756, 2003.
[9] van Genuchten M.T., 1980, Soil.Sci.Soc.Am.J., 44, 892-898.
[10] Fourar M., 1998, SPE paper 49006, presented at 1998 SPE Annual Technical Conference and Exhibition, New Orleans, Louisiana, 27-30 September, 1998.
[11] Koudina N., Gonzalez Garcia R., Thovert J.-F. and Adler P.M., 1998, Phys. Rev., E57, 4466-4479.
[12] Celia M.A., Bouloutas E.T. and Zarba R.L., 1990, Water Resour.Res., 26, 1483-1496.

Session 7:
RECENT ADVANCES IN MODELING AND OPTIMIZATION OF FRACTURED ROCK INVESTIGATIONS

Deformation and Permeability of Fractured Rocks

I. Bogdanov[(1)], V.V. Mourzenko[(2)] , J.-F. Thovert[(2)], P.M. Adler[(1)]
[(1)] IPGP, 4, place Jussieu, 75252-Paris, France (adler@ipgp.jussieu.fr)
[(2)] LCD, SP2MI, BP 30179, 86962-Futuroscope, France

Introduction

We provide here an account of our calculations related to the deformation and resulting permeability of fractured rocks. Some general elements about the analysis of the mechanical deformations are given first, and results relative to the deformation of a single fracture are recalled; then, the deformation of a fractured porous medium is addressed. The second part is devoted to the coupling of mechanical deformations with flow. Again, some general elements are recalled, and flow in a deformed fractured porous medium is studied numerically.

Mechanical Deformations

General

The deformations of an elastic porous medium are governed by the Navier elastostatic equation; for an elastic solid, the stress tensor $\boldsymbol{\sigma}$ is related to the deformation tensor $\boldsymbol{e}$ by the Hooke law,

$$\nabla.\boldsymbol{\sigma} = 0 \ , \qquad \boldsymbol{\sigma} = \frac{E}{1+\upsilon}\left(\mathbf{e} + \frac{\upsilon}{1-2\upsilon} tr\,\mathbf{e}\cdot\mathbf{I}\right) \tag{1}$$

where E is the Young modulus, and ν the Poisson ratio. These equations are solved in a general way for porous media [1,2]. Macroscopic properties such as the effective Lamé coefficients or the Young modulus and Poisson ratio are systematically derived.

The very same approach was used to derive the deformation of a single fracture contained in a solid block [3]. The closure V is defined as the difference between the initial mean mechanical aperture b_{m0} and the mechanical aperture b_m under a normal load σ_n . The normal joint stiffness is $k_n = d\sigma_n / dV$. Systematic calculations were performed for various types of fractures, and a self-consistent analysis was developed to rationalize the numerical results. The fracture properties essentially depend on their closure. From Hertz theory, one can derive k_n as

$$k_n = \frac{d\sigma_n}{dV} = \frac{E}{4(1-\upsilon^2)L_c} \frac{S_c^2}{\Psi_\tau(S_c)(1-S_c)} \tag{2}$$

where L_c is the correlation length and ν the Poisson ratio. The contact area S_c and Ψ_τ can be related to the aperture and to the statistical distribution of the fracture surface roughness.

The previous ingredients can be combined to address the deformation of fractured porous media. The matrix is considered as an elastic solid and its deformations are governed by the elastostatic equation [Equation (1)]. The boundary conditions at a fracture are given by two conditions: The nonlinear relationship between the normal stress and the aperture is given by:

$$\sigma_n = \int_{b_{mo}}^{b_m} k_n(b)\, db \tag{3}$$

where $k_n(b)$ results from (Equation 2). The tangential stress σ_t is proportional to the tangential displacement, and we assume that the tangential stiffness is $k_t = 0.6\, k_n$.

Two major steps are needed in the numerical solution of this problem, which are detailed in [4]. First, the fractures and the porous matrix located in between should be meshed; second, the equations should be discretized. An example is shown in Figure 1. The equations are discretized for the flow equations by a finite volume technique.

Results

An example of uniaxial compression is given in Figure 2. When the normal stress is increased, the fracture apertures decrease; note that the fractures perpendicular to the external stress are more compressed than the one almost parallel to it.

Macroscopic quantities denoted by an overbar could be derived by integrating the local fields over the unit cells; they were calculated in three limiting situations:

- "Initial effective moduli," where the medium is in rest state with totally opened fractures.
- "Nonlinear effective moduli," where the external stresses are increased and the fractures are progressively closed.
- "Terminal effective moduli," where the external stresses are very large and the fractures are totally closed . The normal joint stiffness k_n is now infinite. The two surfaces of each fracture are allowed to slip tangentially, one with respect to the other, when a Coulomb-type failure criterion is fulfilled.

The calculations were performed for a cubic unit cell with periodic boundary conditions containing up to 65 fractures. The sample size L is equal to 3 or $4R$ where R is the radius of the circle in which the fractures are inscribed. The fracture surface roughness is denoted by σ_h. The initial fracture aperture b_{m0} is equal to $4.5\sigma_h$, and ν_m is equal to 1/4. The deformation tensor is increased by successive increments $\delta\mathbf{e}$ measured in the unit equal to σ_h /R.

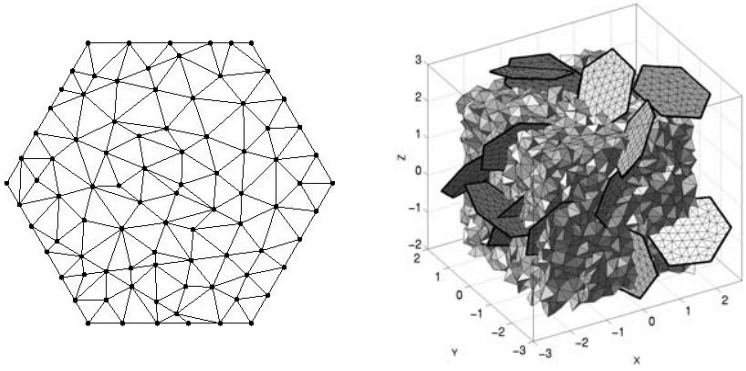

Figure 1. Meshing of a single fracture and of a matrix block straddled with hexagonal fractures.

Initial effective moduli, averaged over the three directions of space and over ten realizations, are shown in Figure 3. First, the moduli follow exponential laws. Moreover, two regimes can be distinguished depending on the fracture density relative to the percolation density $\rho'_c \approx 2.26$. The reason for the existence of these two regimes is not yet well understood.

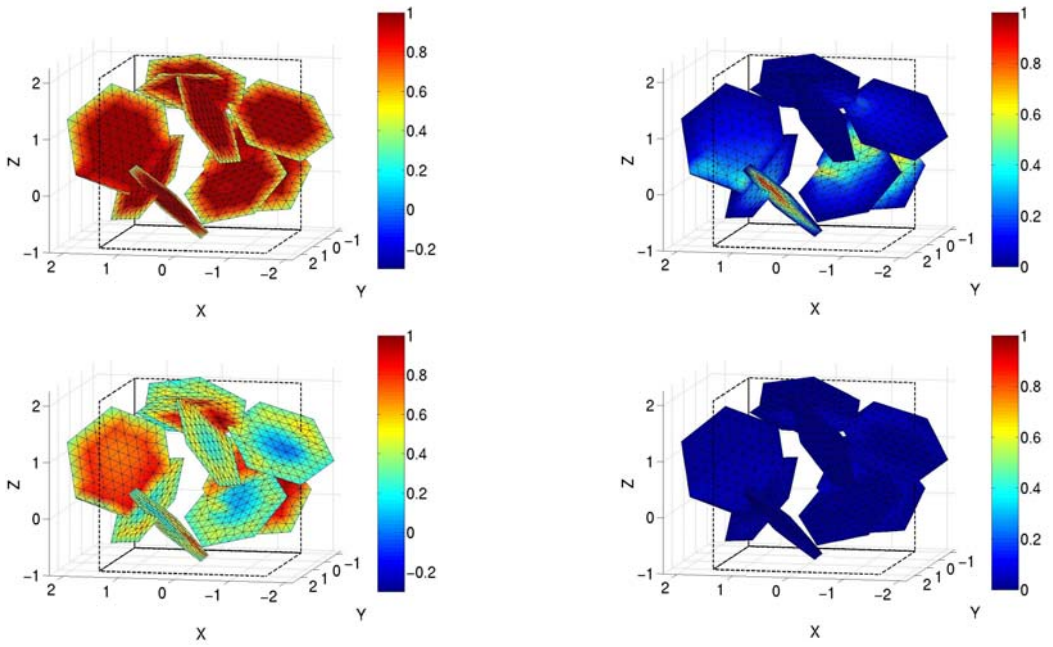

Figure 2. Uniaxial compression along the *z*-axis. The normal stress is increased from top to bottom. The fracture aperture is shown in the left column, with the colour code given by the vertical bars. The initial aperture is equal to 1 in dimensionless units. Flow rate in the fractures is shown in the right column, where an interstitial pressure gradient is applied along the *x*-axis. The color code for the velocity modulus, normalized by the largest value in the initial rest state, is indicated by the color bars.

Because of the nonlinear character of the problem, the results in the general nonlinear case depend on the type of solicitation. Results for a tri-axial test are plotted in Figure 4a as functions of the compression rate $1/3\,\nabla.\boldsymbol{d}$, for various network densities ρ'=2 to 8. The mean stress $1/3\,tr(<\boldsymbol{\sigma}>)$ is shown as a continuous line, and it decreases as ρ' increases. At any load level, an instantaneous bulk modulus K can be defined from the slope of the curves. K also decreases with the fracture density, and it increases from its initial value when the fractures are totally open (Figure 2) to the bulk modulus K_m of the matrix rock when the fractures are totally closed.

Finally, the terminal effective moduli are displayed in Figure 4b; in this situation, the fractures have infinite normal stiffness, but their two surfaces may freely slide. Note that the macroscopic behavior is then elastic, at least as long as the mechanical continuity of the matrix rock is maintained. It is interesting to note that $\overline{E}$ is a decreasing function of ρ' while $\overline{\nu}$ is increasing. The same opposite trends are observed on the effective Lamé moduli λ and μ.

Hydromechanical Coupling

Let us now analyze the influence of fracture deformation on the overall flow properties of the fractured porous medium. The rock matrix is assumed to have a permeability K_m, unaffected by

the rock deformation. The flow is governed by the Darcy law. Fractures are assumed to have a surface permeability σ, and possibly a resistance ω to cross flow. (A complete analysis of the permeability of fractured rocks at rest can be found in [4].) The fracture permeability can be obtained by solving the Stokes equation, as done in [5] and [3], for undeformed and deformed fractures, respectively. However, it was decided in this first approach to approximate the fracture permeability by means of a lubrication formula, i.e., a cubic law of the aperture.

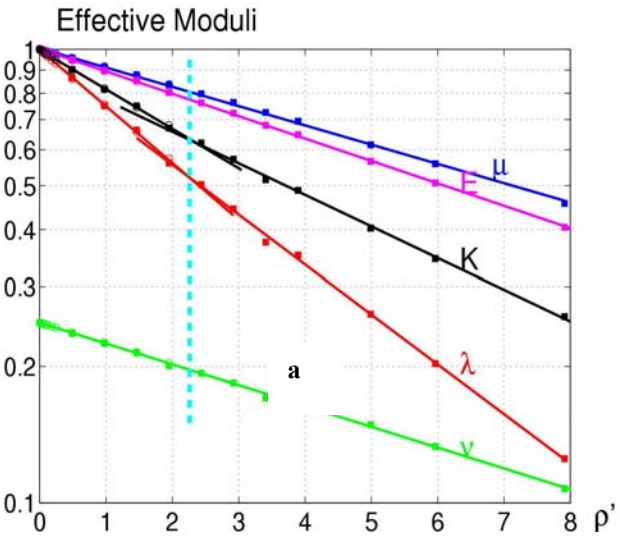

μ / μ_m	$1.006\ e^{-\rho'/10.20}$	
E / E_m	$1.002\ e^{-\rho'/8.76}$	
K / K_m	$0.998\ e^{-\rho'/4.99}$	$0.907\ e^{-\rho'/6.24}$
λ / λ_m	$1.000\ e^{-\rho'/3.43}$	$0.922\ e^{-\rho'/3.95}$
ν	$0.250\ e^{-\rho'/9.43}$	

Figure 3. The initial effective moduli as functions of the dimensionless density ρ', averaged over ten realizations. The least-square fits are given in the table on the right. The vertical line corresponds to the fracture network percolation density. E, K, λ and μ are normalized by the corresponding matrix moduli.

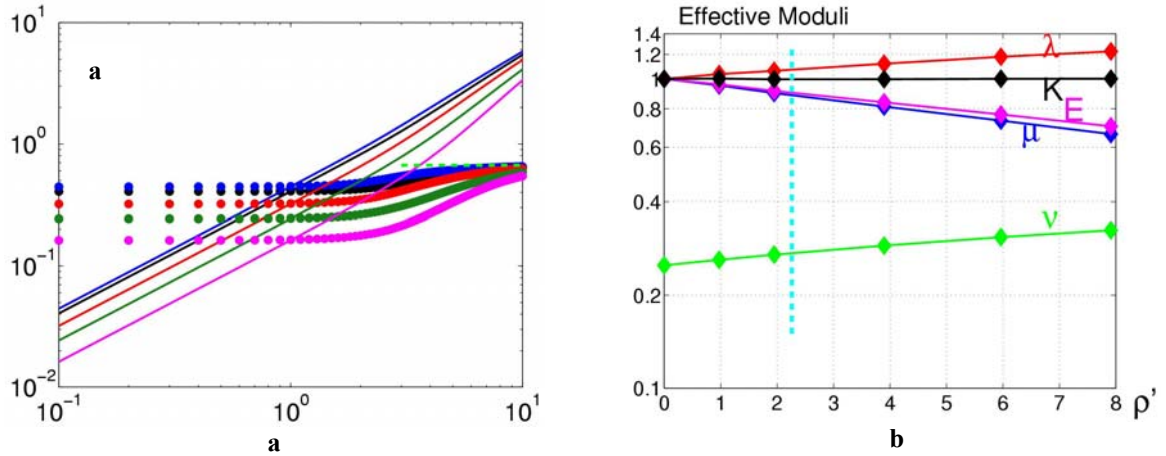

Figure 4. (a): Nonlinear effective moduli for a tri-axial test; the abcissa is $\nabla.\boldsymbol{d}\ /3$; the lines correspond to *1/3 trace(⟨**σ**⟩)*, while the dots correspond to the bulk modulus K; the colors correspond to ρ' = 2 (blue), 3 (black), 4 (red), 6 (green), 8 (purple); (b) Terminal effective moduli as functions of the fracture density.

The calculations were run as follows: The deformation of the fractured porous medium was determined first as explained in the previous section. Then, the macroscopic permeability was calculated for each stress increment. The influence of the stresses on the flow through the fractures is illustrated in the right column of Figure 2. This example corresponds to a flow along the *x*-direction (left to right), when the medium is submitted to an increasing uni-axial compression along the *z*-axis, as shown in the left column of Figure 2. The flow is seen to progressively decrease in the fractures.

The corresponding effect on the macroscopic permeability tensor is shown in Figure 5. In Figure 5a, it is seen that the initial permeability tensor is quite anisotropic; this character hides the influence of the stress on the flow. The permeability components are divided by their initial value in Figure 5b; it is quite interesting to see that the components in the horizontal plane *xy* are more diminished than the component parallel to the external stress. This corresponds to the fact that the apertures in the fractures parallel to the *z*-axis are less diminished than the ones which are perpendicular to it (see Figure 2).

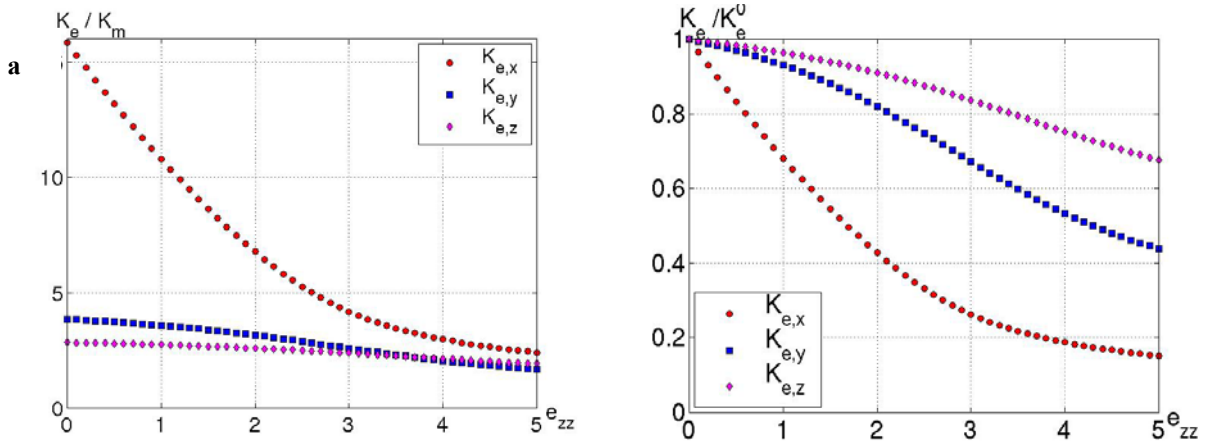

Figure 5. The components of the macroscopic permeability tensor for the fractured porous media in Figure 2. Absolute permeability (a) and permeability relative to the initial state.(b).

Concluding Remarks

A methodology for the determination of the deformations of fractured porous media, of their effective mechanical moduli, and of the influence of these deformations on the permeability tensor has clearly been put on a firm basis. An extensive set of results relative to the mechanical aspects, and preliminary results on the permeability tensor have been obtained. Further investigation of the permeability is to be conducted, and the modeling of creep and fracturation will be addressed in a near future.

References

[1] J. Poutet, D. Manzoni, F. Hage-Chehade, C.G. Jacquin, M.J. Bouteca, J.-F. Thovert, P.M. Adler, *The effective mechanical properties of reconstructed porous media*, Int. J. Rock Mech. Min. Sci., **33**, 409, 1996a.

[2] J. Poutet, D. Manzoni, F. Hage-Chehade, C.G. Jacquin, M.J. Bouteca, J.-F. Thovert, P.M. Adler, *The effective mechanical properties of random porous media,* J. Mech. Phys. Solids, **44**, 1587, 1996b.
[3] V.V. Mourzenko, O. Galamay, J.-F. Thovert, P.M. Adler, *Fracture deformation and influence on permeability,* Phys. Rev. E, **56**, 3167, 1997.
[4] I.I. Bogdanov, V.V. Mourzenko, J.-F. Thovert, P.M. Adler, *Effective permeability of fractured porous media in steady-state flow,* Water Resour. Res., **39**, 10.1029, 2001WR000756, 2003.
[5] V.V. Mourzenko, J.-F. Thovert, P.M. Adler, *Permeability of a single fracture: validity of the Reynolds equation,* J. Physique II, **5**, 465, 1995.

Modeling Poroelastic Earth Materials that Exhibit Seismic Anisotropy

Patricia A. Berge
Lawrence Livermore National Laboratory
7000 East Ave., L-221, Livermore, CA 94550 USA
Phone: 925-423-4829, Internet: berge1@llnl.gov

Seismic anisotropy caused by layering, foliation, or aligned fractures is pervasive in sediments and rocks such as silty sands, clay-bearing sandstones, shales, and fractured igneous rocks (e.g., Berge et al., 1991; Hornby, 1995). Earth materials with interconnected pores or fractures can behave mechanically as poroelastic media (e.g., Murphy, 1984; Green and Wang, 1986). Recent advances in laboratory (e.g., Hornby, 1995; Hart and Wang, 1995) and field (e.g., Alkhalifah and Tsvankin, 1995) techniques allow measurement of all the constants needed to characterize mechanical behavior of some earth materials that are either anisotropic or poroelastic. Current research efforts in the oil industry and university collaborations may provide ways to measure the many anisotropy parameters and poroelastic constants needed to characterize poroelastic, anisotropic sediments and rocks. These earth materials are important in many environmental cleanup, energy resource, and civil engineering applications.

The availability of reliable lab and field data gives incentive for developing better theoretical methods for analyzing poroelastic, anisotropic earth materials. Some models do exist, but they have significant limitations. Rock physics theories and models for layer-induced or fracture-induced anisotropy generally do not explicitly include poroelastic parameters or fluid effects (e.g., Backus, 1962; Schoenberg et al., 1996), and most are limited to the case of transverse isotropy (i.e., only one set of aligned fractures or layers). Some models that do include fluid effects (e.g., Schoenberg and Sayers, 1995; Bakulin et al., 2000) are awkward in their treatment of partial saturation. One poroelastic thin-layer model (Berryman, 1998) can be used to study materials that exhibit transverse isotropy, but no lower-symmetry systems.

Incorporating fluid effects into some of the common anisotropy models yields insight into the implicit assumptions in the models as well as into material behavior. These results and preliminary work on new theoretical models for anisotropic, poroelastic earth materials will be presented.

Acknowledgments

This work was performed under the auspices of the U.S. Department of Energy by the University of California Lawrence Livermore National Laboratory under contract W-7405-ENG-48 and supported specifically by the DOE Office of Science's Basic Energy Sciences Program, UCRL-JC-145697-ABS.

References

Alkhalifah, T., and Tsvankin, I., 1995, Velocity analysis for transversely isotropic media: Geophysics, 60, 1550-1566.

Backus, G. E., 1962, Long-wave elastic anisotropy produced by horizontal layering: Journal of Geophysical Research, 67, 4427-4440.

Bakulin, A., Grechka, V., and Tsvankin, I., 2000, Estimation of fracture parameters from reflection seismic data -- Part I: HTI model due to a single fracture set: Geophysics, 65, 1788-1802.

Berge, P. A., Mallick, S., Fryer, G. J., Barstow, N., Carter, J. A., Sutton, G. H., and Ewing, J. I., 1991, In situ measurement of transverse isotropy in shallow-water marine sediments: Geophysical Journal International, 104, 241-254.

Berryman, J. G., 1998, Transversely isotropic poroelasticity arising from thin isotropic layers: in Golden, K. M., Grimmett, G. R., James, R. D., Milton, G. W., and Sen, P. N., eds., Mathematics of Multiscale Materials, Springer-Verlag, New York, 37-50.

Green, D. H., and Wang, H. F., 1986, Fluid pressure response to undrained compression in saturated sedimentary rock: Geophysics, 51, 948-956.

Hart, D. J., and Wang, H. F., 1995, Laboratory measurements of a complete set of poroelastic moduli for Berea sandstone and Indiana limestone, J. Geophys. Res., 100, 17741-17751.

Hornby, B. E., 1995, The Elastic Properties of Shales: Ph.D. thesis, University of Cambridge, Cambridge, U. K.

Murphy, W. F., III, 1984, Acoustic measures of partial gas saturation in tight sandstones: J. Geophys. Res., 89, 11549-11559.

Schoenberg, M., Muir, F., and Sayers, C., 1996, Introducing ANNIE: A simple three-parameter anisotropic velocity model for shales: Journal of Seismic Exploration, 5, 35-49.

Schoenberg, M., and Sayers, C., 1995, Seismic anisotropy of fractured rock: Geophysics, 60, 204-211.

Homogenization Analysis for Fluid Flow in a Rough Fracture

B.-G. Chae[a], Y. Ichikawa[b], Y. Kim[c]
[a] Geological and Environmental Hazards Div., Korea Institute of Geoscience and Mineral Research, Daejon, 305-350, Korea; bgchae@rock25t.kigam.re.kr
[b] Division of Environmental Engineering and Architecture, Nagoya University, Nagoya 464-8603, Japan; YIchikawa@nucc.cc.nagoya-u.ac.jp
[a] Groundwater and Geothermal Resources Div., Korea Institute of Geoscience and Mineral Research, Daejon, 305-350, Korea; yjkim@rock25t.kigam.re.kr

Abstract

This study is conducted to calculate the permeability within a single fracture while taking the true fracture geometry into consideration. The fracture geometry is measured using the confocal laser scanning microscope (CLSM). The CLSM geometry data are used to reconstruct a fracture model for numerical analysis using a homogenization analysis (HA) method. The HA is a new type of perturbation theory developed to characterize the behavior of a micro-inhomogeneous material that involves periodic microstructures (Sanchez-Palencia, 1980; Ichikawa et al., 1999). The HA permeability is calculated based on the local geometry and local material properties (water viscosity in this case). The results show that the permeability coefficients do not follow the theoretical relationship of the cubic law.

Theory of Homogenization Analysis Method

The HA is here applied to the flow problem with periodic micro-structures (Fig. 5.1: Sanches-Palencia, 1980; Ichikawa et al., 1999). For this problem, the Navier-Stokes equation is assumed for the local flow field.

Let us introduce the local coordinate system $\boldsymbol{y}$, which is related to the global system, $\boldsymbol{x}$, by $\boldsymbol{y} = \boldsymbol{x}/\varepsilon$. The following incompressible Navier-Stokes flow field is introduced:

$$-\frac{\partial P^{\varepsilon}}{\partial x_i}+\eta\frac{\partial^2 V_i^{\varepsilon}}{\partial x_k \partial x_k}+F_i=0 \quad \text{in } \Omega_{\varepsilon f}, \tag{1}$$

$$\frac{\partial V_i^{\varepsilon}}{\partial x_i}=0 \quad \text{in } \Omega_{\varepsilon f} \tag{2}$$

where V^{ε}_i is the velocity vector with the shearing viscosity η, P is the pressure, F_i is the body force vector, and $\Omega_{\varepsilon f}$ the water flow region in the global coordinate system.

By several mathematic procedures, we can get a microscopic equation

$$-\frac{\partial p^k}{\partial y_i}+\eta\frac{\partial^2 v_i^k}{\partial y_j \partial y_j}+\delta_{ik}=0 \qquad \text{in} \quad Y_f \tag{3}$$

In a similar manner, the mass conservation law (2) is written as

$$\frac{\partial v_i^k}{\partial y_i}=0 \qquad \text{in} \quad Y_f \tag{4}$$

Equations (3) and (4) are called the 'micro scale equations' (MiSE) for the water flow problem.

By an averaging operation for Equation (3), the following "macroscale equation" (MaSE), called the HA-flow equation, is specified:

$$\frac{\partial \tilde{V}_i^0}{\partial x_i}=0 \quad \text{or} \quad \frac{\partial}{\partial x_i}\left[K_{ji}\left(F_j-\frac{\partial P^0}{\partial x_j}\right)\right]=0 \ \text{ in } \Omega. \tag{5}$$

Finally, the following relationship between the HA-permeability K_{ij} and the C-permeability K'_{ij} is specified:

$$K'_{ij}=\varepsilon^2 \rho g \, K_{ij}. \tag{6}$$

Note that this C-permeability K'_{ij} can be compared with the conventional experimental and theoretical values. The validity of the HA-permeability concept has been proved by the several works (Ichikawa et al., 1999).

Input Parameters for the Homogenization Analysis

Fracture roughness

The specimens used for the HA are granites that have a single natural fracture. The fracture roughness is measured using a confocal laser scanning microscope. Sample spacing is 2.5 μm in both x-and y-directions. The highest resolution in the z-direction is 0.05 μm, which is more sensitive than the previous methods (Chae et al., 2003a).

The 3-D configuration of roughness as well as the 1-D roughness profile are measured for each specimen. The resolutions in the x- and y-directions are fixed as 1,024 × 768 pixels (2.56 × 1.92 mm in area) and the resolution of z-direction is 10 μm.

The Fourier spectral analysis is conducted to quantitatively identify roughness characteristics (Chae et al., 2003a). After the spectral analysis and noise filtering is completed for all of the data for each specimen, a reconstruction of the roughness geometry is performed using only the influential frequencies among the components (Figure 1). The reconstructed roughness profiles are used for the fracture models in the HA numerical simulation.

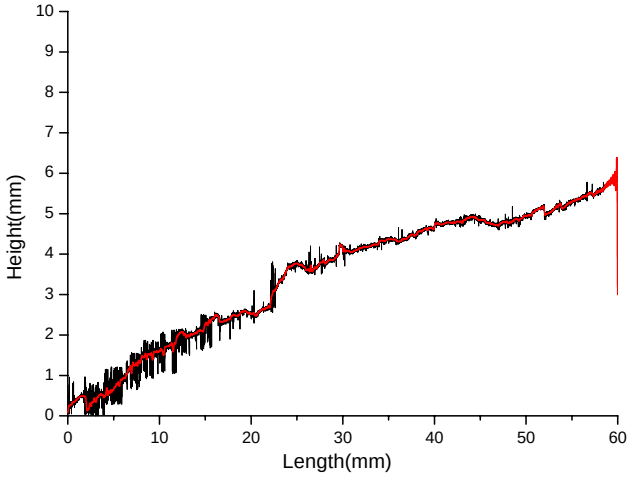

Figure 1. An example of roughness patterns that show both noises (black) and the smoothed roughness data (red).

Aperture Variation Dependent upon Uniaxial Compression

The fracture apertures are also used as input parameters for the HA simulation. They are measured by the CLSM while applying normal stress. Among all of the aperture data, three stress levels (10, 15, and 20 MPa) of stresses are applied. The mechanical apertures are equal to the mean value of the measured apertures for each specimen using the CLSM. The hydraulic apertures are calculated using an equation satisfying the cubic law (Zimmerman and Bodvarsson, 1996). The hydraulic conductivities both calculated with the mechanical aperture, the measured aperture by the CLSM, and the hydraulic aperture are also calculated from an equation based on the cubic law [Equation (7)].

$$K_f = k_f \frac{\gamma}{\mu} = \frac{e_h^2}{12} \frac{\gamma}{\mu} \tag{7}$$

where k is intrinsic permeability coefficient, γ is unit weight of water, μ is viscosity of water, e_h is hydraulic aperture, and L is length of specimen.

Computation of Permeability using HA under Various Fracture Conditions

The 2-D fracture models are now constructed for the HA simulation. The computation is performed assuming a temperature condition of 300 K. The water viscosity, η, is equal to 0.8×10^{-3} Pa $\cdot$ sec and the mass density, ρ is equal to 0.99651 g cm^{-3}. The HA permeability characteristics are shown under various roughness and aperture conditions. That is, under various types of observed roughness features the upper fracture wall is displaced at intervals of every 1 mm in the shearing direction. This shear displacement is introduced for five stages, which results in various aperture values along the fracture. Permeability is calculated at every stage of the displacement.

An example of the fracture models are shown in Figure 2. These models represent various roughness features and aperture due to the displacement. Every model shows different geometrical features at each stage of the displacement.

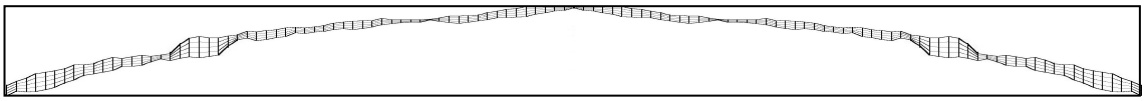

Figure 2. An example of fracture models showing various roughness and apertures at each stage. Exaggerated 50 times in vertical direction.

The calculation results and the relationships between the square of the mean aperture, b^2, and the calculated permeability are drawn in Figure 3. We find that the permeability coefficients are irregularly ranged from 10^{-4} to 10^{-1} cm/sec, while the coefficients of the previous parallel-plate models are uniformly distributed in some range. This is due to the complicated change in the aperture increasing the shear displacement in the current models. In this figure it is not possible to find any relationship, so the cubic law is not suitable for the rough fracture case (Chae et al., 2003b).

Conclusion

Considering the change of aperture and roughness pattern simultaneously along a fracture, the permeability is calculated by using the rough fracture models. The upper wall is assumed to be displaced by shearing in the five stages. The calculation results show various changes of permeability, which depend on the roughness patterns and aperture values. It is understood that the cubic law is not appropriate for fractures with rough walls. The irregular distribution of aperture along a fracture may introduce a negative proportional relationship between the aperture and the permeability, even though the mean aperture becomes larger. This proves clearly that permeability is very sensitive to the geometry of the roughness and aperture. The approach will be effectively applied to the analysis of permeability characteristics, as well as the fracture geometry in discontinuous fractured rock masses.

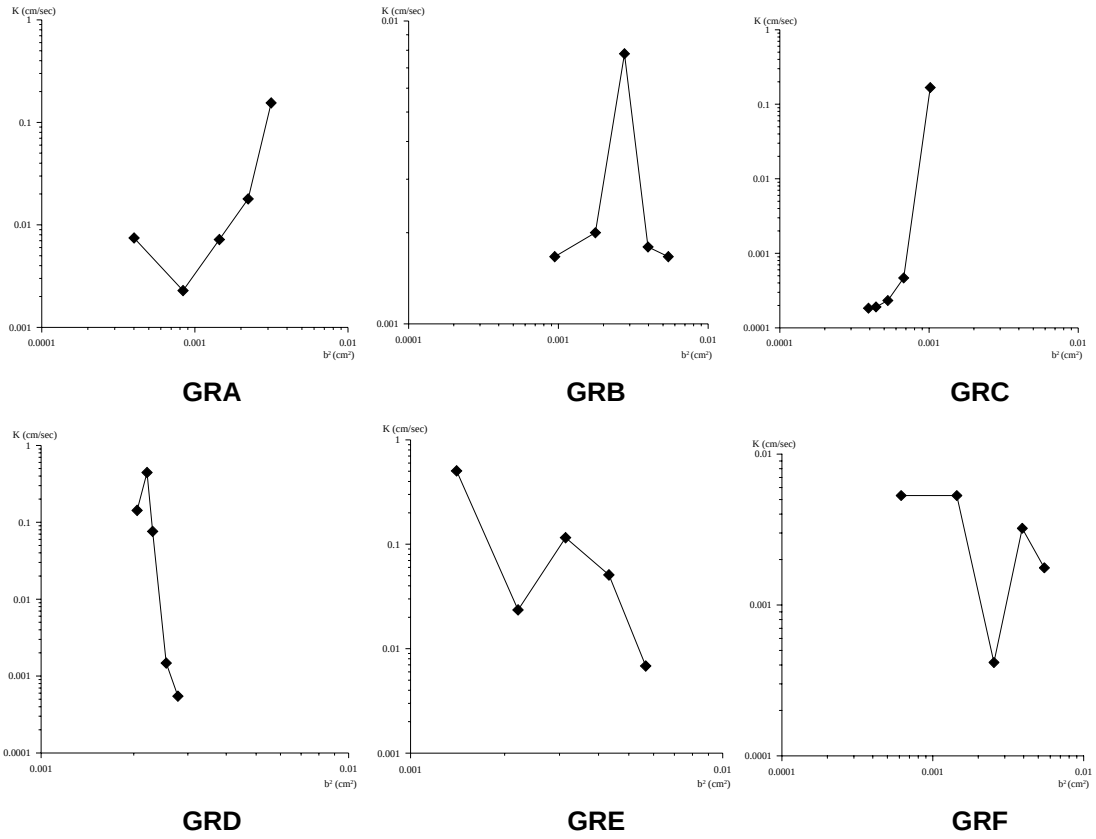

Figure 3. Relationship between permeability coefficients and aperture square.

Acknowledgments

This research was supported by a grant (3-2-1) from Sustainable Water Resources Research Center of 21st Century Frontier Research Program.

References

Chae, B. G., Y. Ichikawa, G. C. Jeong, Y. S. Seo and B. C. Kim, Roughness measurement of rock discontinuities using a confocal laser scanning microscope and the Fourier spectral analysis, Engineering Geol., Accepted and in printing, 2003a.

Chae, B. G., Y. Ichikawa, G. C. Jeong, Y. S. Seo and B. C. Kim, Computation of hydraulic conductivity along a rock fracture using a homogenization analysis Method, Engineering Geol. Submitted, 2003b.

Ichikawa, Y., K. Kawamura, M. Nakano, K. Kitayama and H. Kawamura, Unified molecular dynamics and homogenization analysis for bentonite behavior: current results and future possibilities, Engineering Geol., 54, 21-31, 1999.

Sanchez-Palencia, E., Non-homogeneous media and vibration theory, Springer-Verlag, 190, 1980.

Microscale Modeling of Fluid Transport in Fractured Granite Using a Lattice Boltzmann Method with X-Ray Computed Tomography Data

Frieder Enzmann[1], Michael Kersten[1] & Bernhard Kienzler[2]
[1]Geoscience Institute,University of Mainz, Becherweg 21, D-55099 Mainz, Germany
[2]Institute for Nuclear Waste Management, Forschungszentrum Karlsruhe, D-76021 Karlsruhe, Germany

Introduction

The Hard Rock Laboratory (HRL) was established in Sweden in a Precambrian granite rock formation for *in situ* experiments to increase scientific understanding of a spent nuclear fuel repository's margins (Stanfors et al., 1997). Within the scope of a bilateral cooperation between Svensk Kärnbränslehantering (SKB) and the Institute for Nuclear Waste Management, Forschungszentrum Karlsruhe, Germany, an actinide migration experiment is currently being performed at the HRL (Kienzler et al., 2003). This extended abstract describes a nondestructive analysis method to characterize the complex flow paths in such core samples. X-ray computer microtomography (XCT) was used to visualize the fracture structure, and a quantitative methodology was developed for modeling fluid flow and tracer transport in the CT-reconstructed fractures. The modeling data show that tracer particles do not move through the fractures in a uniform front.

Materials and Methods

To minimize core damage, the borehole drilling axis was chosen parallel to the fault strike, with the master fault open fracture centered parallel to the cylindrical core axis. The rock cores thus extracted were 5 cm in diameter. To run the migration experiments, core subsamples were cut to 170 mm length and kept in their stainless steel liners. The periphery between core and liner was filled with epoxy resin so as to minimize artifacts caused by coring damage. The top and bottom ends were closed with acrylic glass covers sealed relative to the steel liner with an O-ring, which contained the bores for feeding and extracting tracer solutions. The tightness of the columns was tested at 60 bar fluid pressure. XCT scans of the rock cores were made using the Linear Computed Axial Tomography (LCAT) setup of the Bundesanstalt für Materialforschung (BAM) in Berlin. This industrial LCAT is based on a rotate-only fan-beam system equipped with an 420 kV/4 mA tube as an x-ray polychromatic point source collimated to 0.8 × 1.5 mm, and a 15-element solid-state linear diode array x-ray detector. Beam hardening effects, such as ring artifacts typical for geologic materials, and star artifacts caused by secondary radiation were reduced by prehardening the polychromatic beam, using attenuation filters (3 mm Al foil an 8 mm Cu foil) between the x-ray tube and the samples in addition to the 5 mm stainless steel liner encasing the cores. For CT imaging, the core was scanned by 180 projections of 60 mm imaging diameter for each 1.5 mm slice to establish a three-dimensional image at a resulting voxel resolution of 0.25 × 0.25 × 1.5 mm³. During reconstruction of the CT images, the raw intensity data were converted to CT numbers in an 8-bit scale (255 mass absorption values are possible).

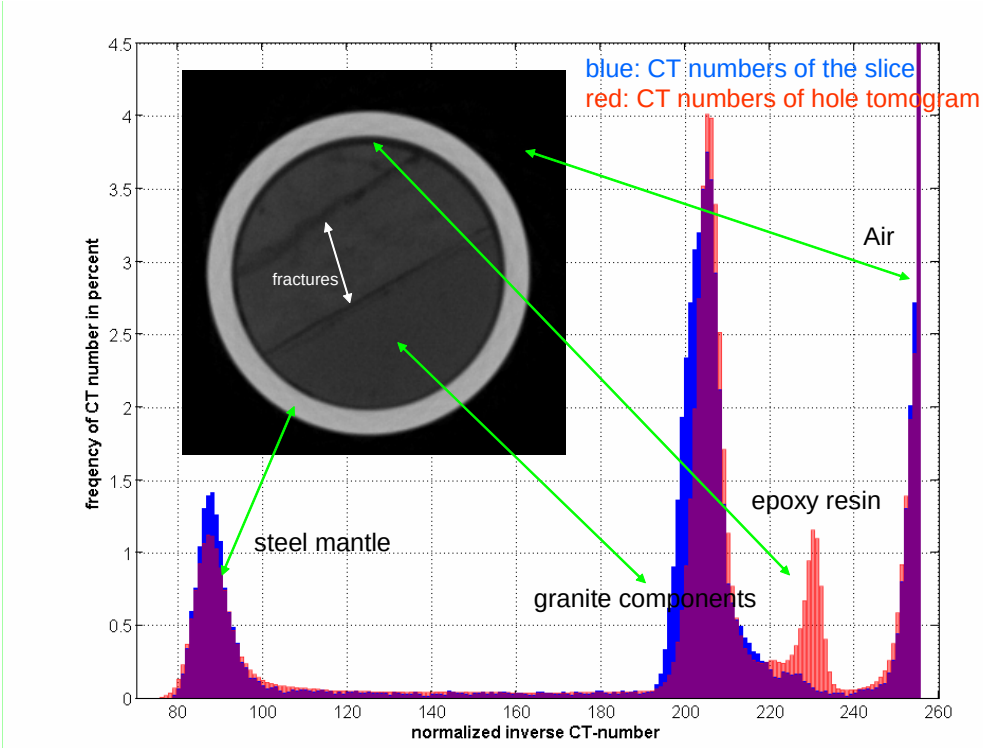

Figure 1. CT number representation of a granite core slice example.

The CT number is a function of the average density and composition of any material voxel, increasing gradually in the order of air, water, impregnating resin, quartz and feldspar, biotite, hornblende, heavy minerals, and the steel liner.

For *ab initio* simulations of a migration experiment, only the connected (open) fracture structure is of interest. Given a digital image or tomogram of a porous material, one can easily access the connectivity of any phase using the so-called "burning algorithm" (Stauffer, 1975). This algorithm enables identification of all cluster members of connected voxels with equal or quasi-equal CT numbers in a tomogram.

Results of Tomographic Fracture Reconstruction and Fluid Migration Simulations

Figure 2 shows the derived open pore network connecting inflow and outflow of the core samples. Core #1 contains a single fracture parallel to the cylindrical axis traversing the entire length of the core, while the fracture system of core #2 comprises three fracture planes. The aperture fields generated from the XCT images were generally consistent with a lognormal scale distribution, and aperture in a single fracture spanned more than one order of magnitude. Although the fine structure of the aperture field (such as gauges) could not be resolved at the measurement resolution used (0.25 mm), the results suggest that at least the major features in the aperture field, such as regions of predominantly small and large apertures (i.e., higher-conductivity regions), can be reconstructed using XCT.

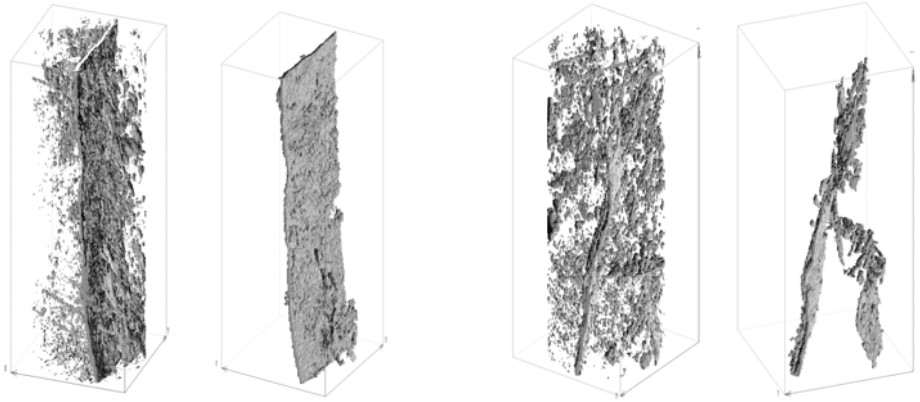

Core #1 a b Core #2 a b

Figure 2. Total (a) and open (b) pore-structure tomograms from Cores #1 and #2

The lattice Boltzmann equation (LBE) method has been used for fluid migration simulations, because it relies on the real pore space structure as an input for the boundary conditions (Ferreol and Rothman, 1995). Our code "PoreFlow" uses a D3Q19 geometry (3-D cell spanned by 19 lattice vectors; Qian et al., 1992). The given formalism and special conditions (e.g., low numerical mach numbers and Knudson numbers) lead to a velocity field as a solution of the Navier-Stokes equation at a given kinematic viscosity (Marthys and Chen, 1996; Nourgaliev et al., 2003). The simulation was performed with two different stationary inflow boundary conditions (Case #1.1 at 0.001 mL/min, and Case #1.2 at 0.05 mL/min). The result is an inhomogeneous flow field in the open fracture (Figure 3), with variations of velocity values and directions leading to a disperse transport of conservative tracer particles. Figure 4 shows the correlation between fluid velocity and slice porosity of core slices as derived from this forward simulation.

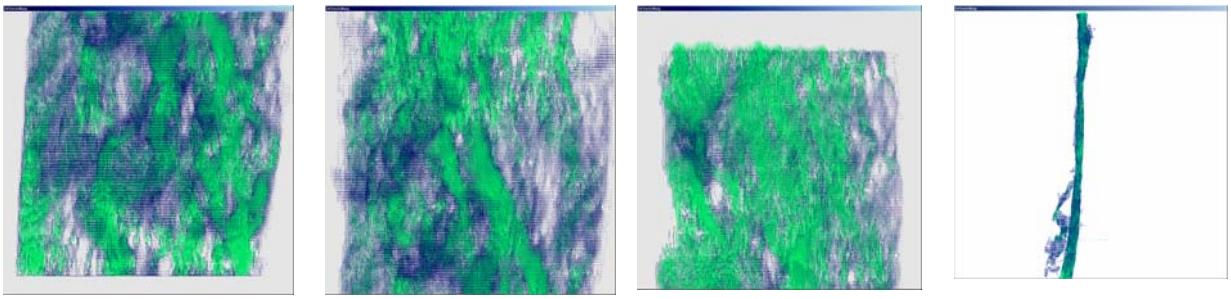

Fracture plane Bottom Middle Top Site view

Figure 3. Fluid velocity vectors in the fracture plane (green represents high fluid velocities)

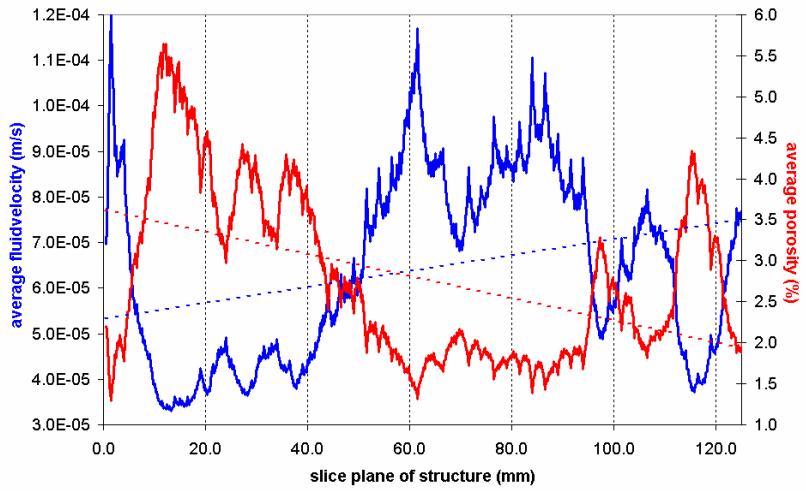

Figure 4. Correlation between porosity and average fluid velocity according to the Core #1.1 model.

Diffusion and advection of a conservative species dissolved in a fluid is given by the hydrodynamic transport equation, $\partial c/\partial t = -u \cdot \nabla C + D \cdot \nabla^2 C$, where C is the species concentration, D is the molecular diffusion coefficient, and u is the fluid velocity vector. Given the known velocity field, a numerical particle-tracking scheme can be used to move particles from one position to another in order to approximate the advection of any contamination front. For our model, we used a fourth-order Runge-Kutta algorithm. For the diffusive transport step, we used stochastic algorithm. The flux of tracer particles across the fracture surfaces can be determined by particle counting and averaging over ensembles of tracer trajectories. Grid based schemes suffer significantly from numerical diffusion, leading to errors in the concentration distribution at Peclet numbers typical of flow in fractures (see Verberg and Ladd, 2002). The forward simulation results with the tomograms have been verified subsequently by a laboratory migration experiment at the same inflow velocities and with a HTO tracer pulse injection (Kienzler et al., 2003). Figure 5 shows the simulated particle breakthrough for Case #1.1, while Figure 6 gives the respective breakthrough curve for the HTO tracer experiment.

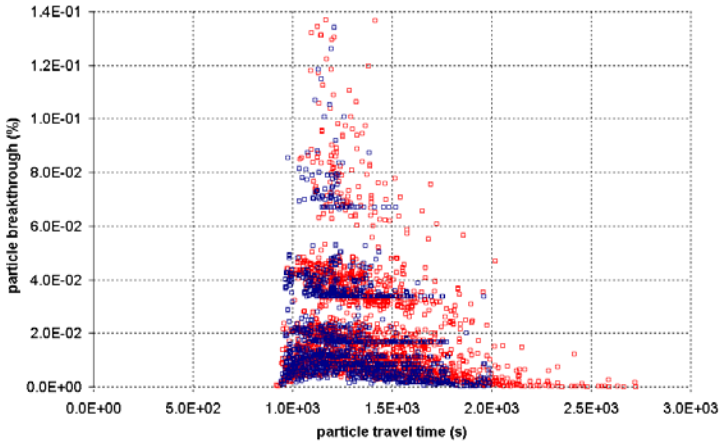

Figure 5. Simulated particle breakthrough for Case #1.1 with two different diffusion coefficients (blue and red).

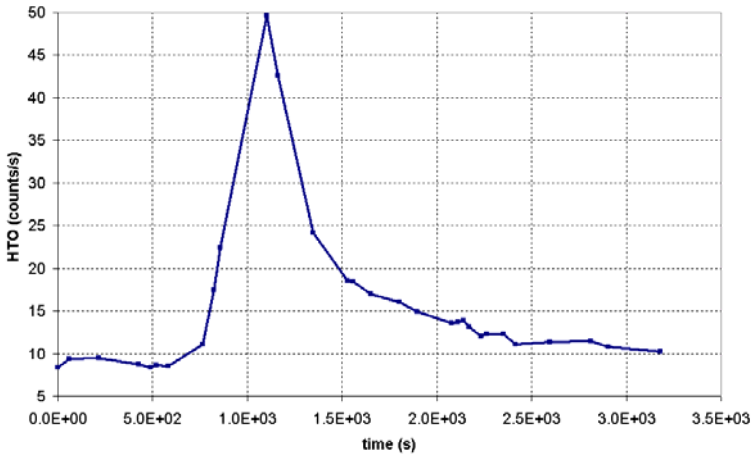

Figure 6. Breakthrough curve for the HTO tracer experiment.

The latter experimental breakthrough curve provides a fairly good envelope for the former particle breakthrough model. Note that the model contains no macroscopic fit parameters such as porosity and dispersivity. Breakthrough of the model tracer particles depends only on the complex flow paths in the open fracture network of Core #1 (Figures 2 and 3). The tailing of the experimental curve reproduced by the model results from the variation in effective fluid velocity.

Acknowledgments

XCT scans were performed by Dietmar Meinel and Jürgen Goebbels at Bundesanstalt für Materialforschung (BAM, Berlin). Dietmar Schenk and Thilo Hofmann are thanked for support and encouragement during initial state of this study.

References

Ferreol B. and Rothman D.H. (1995): Lattice-Boltzmann simulations of flow through Fontainebleau sandstone. Trans. Porous Media 20, 3-20.

Kienzler B., Vejmelka P., Römer J., Fanghänel E., Jansson M., Eriksen T.E., Wikberg P. (2003): Swedish-German Actinide Migration Experiment at Äspö Hard Rock Laboratory. J. Cont. Hydrol. 61, 219– 233.

Martys N.S. and Chen H. (1996): Simulation of multicomponent fluids in complex three-dimensional geometries by the lattice Boltzmann method, Phys. Rev. E, 53,743-750.

Nourgaliev R.R., Dinh T.N., Theofanous T.G. and Joseph D. (2003): The lattice Boltzmann equation method: theoretical interpretation, numerics and implications. Int. J. Multiphase Flow 29, 117-169.

Qian Y.H., D'Humières D. and Lallemand P. (1992): Lattice BGK models for Navier-Stokes equation. Europhys. Lett. 17, 479-484.

Stanfors R.M., Erlström M. and Markström I. (1997): Äspö HRL – Geoscientific evaluation 1997. 1. Overview of site characterisation 1986 - 1995. SKB-ICR Technical Report TR 97-02, SKB, Stockholm, Sweden.

Stauffer D. and Aharony A. (1992): Introduction to Percolation Theory, Taylor & Francis, London.Verberg R. and Ladd A.J.C. (2002): Simulations of erosion in rough fractures. Phys. Rev. E, 65:056311.

Modeling Flow and Transport in Fractured Media Using Deterministic and Stochastic Approaches

Souheil M Ezzedine
WA, ERD, Lawrence Livermore National Laboratory
Mail Stop L-530; 7000 East Avenue, Livermore CA-94550
Ezzedine1@llnl.gov

A geological formation consisting of a fractured layer underlaying a weathered-rock layer is considered important as both a water and thermal resource. Two approaches are considered to model the flow in this formation. In the first approach, an analytical solution is proposed assuming that the fractured layer is a homogeneous double porosity medium, and the weathered-rocks layer is a homogeneous porous medium. In the second approach the layers are assumed to be heterogeneous and, consequently, a stochastic discrete fracture network is adopted. An analytical model of flow through the two-layered formation, where a fractured medium is assumed to be a double porosity medium, is derived using Laplace and Hankel transformations. Asymptotic solutions are derived to validate the model for long and short pumping periods. By introducing further geometrical simplification into our model, the resulting solutions are compared with existing analytical solutions. The proposed analytical model is applied to three sites, located in France, Upper Volta, and Uganda. Results of these applications demonstrate that our model is capable of representing the governing physical phenomena quite accurately.

In many applications, however, the assumption of homogeneity is restrictive. Therefore, we propose to treat the media as a heterogeneous ensemble of many stochastically generated fractures. The flow at the fracture scale is derived analytically using the Laplace transform. Flow at the formation level is then achieved by combining the solution of the generated individual fractures. To validate the proposed model, one-, two- and three-dimensional problems are investigated. A comparison between the homogeneous and the heterogeneous, approaches is performed. A flow injection test, performed at the Hot Dry Rock (HDR) site Soultz-sous-Forêts in Alsace/France, is simulated. Results show that the mechanical properties of the media influenced by the flow injection must be incorporated into the proposed model. In particular, changes in the hydraulic conductivity and the storage coefficient function of the effective stress appear to be quite significant. Consequently, the model is adjusted accordingly and applied again to the flow injection problem. As expected, model results showed significant improvements over the previous one.

Heat extraction from HDR is not limited to the hydrological phenomena discussed thus far, but rather necessitates that thermal and geochemical processes must be considered. A geochemical model is developed which takes into account the equilibrium and/or non-equilibrium transport of the chemical species and the water/rock interaction. Thermal processes are modeled using a double porosity approach. The hydrothermal and chemical transport at the formation level is obtained by simultaneously combining the solution of the stochastically generated individual fractures. Finally to demonstrate the applicability of the proposed coupled model, a calcite precipitation example is simulated.

Modeling of Hydrogeologic Systems Using Fuzzy Differential Equations

Boris A. Faybishenko
Earth Sciences Division, Lawrence Berkeley National Laboratory, Berkeley, CA 94720
bafaybishenko@lbl.gov

1. Introduction

The main motivation for using fuzzy logic in soil sciences and hydrology arises is that imprecise and incomplete data are usually gathered in field conditions. Data sets collected under field conditions are often uncertain because of the inconsistency between the real physical processes and the physics of the measurements, using discretely measured, random variables, so that data are incomplete or vague, or measurements are inaccurate. Approximate estimations (volume-averaging and scaling) are used instead of direct measurements, providing qualitative information. One of the modern approaches to deal with uncertain data is the use of the fuzzy systems modeling Several papers have recently been written on the application of fuzzy logic to soil physics and water resources, such as the application of fuzzy regression in hydrology (Bardossy and Duckstein, 1990), soil mapping (De Gruijter et al., 1997; Franssen et al., 1997), and prediction of infiltration (Bardossy and Disse, 1993; Bardossy and Duckstein, 1995). Significant progress has been made in using fuzzy models in reservoir simulations for oil exploration (Nikravesh and Aminzadeh, 2001).

The goal of this paper is to introduce an approach to fuzzy-systems modeling of flow in unsaturated-saturated fractured-porous media. To accomplish this goal, I will:

- Develop a rationale for representing a fractured rock system as a fuzzy system.
- Present fuzzy-forms of Darcy's and cubic law equations for flow in unsaturated-saturated subsurface media.
- Present an example of fuzzy-systems modeling of flow in fractured rock and compare the results of modeling with those from field infiltration test in fractured basalt.

2. Basic Concepts of Fuzzy-Systems Modeling

Fuzzy logic is based on fuzzy set theory, which is an extension of classical set theory. Scientific motivations for fuzzy logic are based on the fact that conventional Boolean models (based on the consideration of only two values: 0, indicating a complete non-truth; and 1, indicating an absolute truth) are inadequate for describing real practical problems with fuzzy boundaries between the system elements. A fuzzy variable is defined by its minimum and maximum values, and a fuzzy membership function (FMF) that varies from 0 to 1. A FMF indicates the degree of a membership of an element in a fuzzy set.

The fuzzy-systems approach assumes the continuity of the medium with imprecise boundaries between different classes of the media (Franssen et al., 1997). Fuzzy systems modeling is

capable of handling both linear and nonlinear problems, using mathematical equations written in terms of fuzzy numbers (Kauffmann and Gupta, 1985).

Operations on fuzzy numbers. Algebraic operations on fuzzy numbers are performed based on the Zadeh's extension principle (Kauffmann and Gupta, 1985). The extension principle implies that fuzzy subsets and logic are generalizations of classical set theory and (Boolean) logic. The main concept of fuzzy algebraic operations is as follows:

$$\mu_{I^f * J^f}(z) = \underset{x*y=z}{\vee} \left(\mu_{I^f}(x) \wedge \mu_{J^f}(y)\right) \tag{1}$$

where I^f and J^f are fuzzy numbers defined on real lines X and Y, respectively; the symbol * denotes a fuzzy arithmetic operation (+), (-), (·), or (:). An arithmetic operation (mapping) of two fuzzy numbers denoted as $I^f * J^f$ will be defined on universe Z, and μ denotes a fuzzy membership function. Equation (1) can also be written in the following form:

$$\mu_{I^f * J^f}(z) = \max\left(\min\left(\mu_{I^f}, \mu_{J^f}\right)\right) \tag{2}$$

Fuzzy-systems modeling involves several steps: (1) *Fuzzification*, which implies replacing a set of crisp (i.e., precise) numbers with a set of fuzzy numbers, using fuzzy membership functions based on the results of measurements and perception-based information. Several types of membership functions are used for fuzzy systems modeling, such as: triangular, trapezoid, sigmoid, gaussian, bell-curve, Pi-, *S*-, and *Z*-shaped curves. (2) *Granulation*, which implies a decomposition (partitioning) of a whole object into parts or number of granules. A granule (crisp or fuzzy) is a clump of objects, pulled together by their indistinguishability, similarity, proximity, or functionality (Zadeh, 1997). For example, granules of fractured rock could be matrix and fractures. Each fuzzy granule is characterized by a set of fuzzy attributes (e.g., in the case of the fuzzy granule *soil*, the fuzzy attributes are color, structure, texture, particle size distribution, hydraulic conductivity, etc). Each of the fuzzy attributes is characterized by a set of fuzzy values (e.g., in the case of fuzzy attribute hydraulic conductivity of soils, the fuzzy values could be very high, high, average, small, very small, etc.). (3) *Defuzzification* means the calculation of the crisp output from the results of fuzzy modeling, using such methods as center of gravity, largest of maximum, middle of maximum, or bisector of the area.

3. Hydrogeologic System as a Fuzzy System

Despite the continuous variability of hydraulic properties, our understanding about soil or rock processes is obtained from discrete measurements. Assuming that we have a stationary random flow field and that the relevant statistics can be derived from experimental data, we usually treat hydraulic conductivity as a log-normally distributed parameter and porosity as a normally distributed parameter. The probability distribution functions (PDFs) characterizing the spatial distribution of soil properties can be used to construct fuzzy membership functions for these properties. For example, to construct a FMF, we can normalize the PDF function to the maximum value of the PDF. By representing a hydrogeologic system as a fuzzy system, hydrogeological parameters such as hydraulic head, water flux, hydraulic conductivity, hydraulic gradient, porosity, etc., could be presented as fuzzy variables. This approach provides

background for the development of fuzzy partial differential equations as the basis for modeling hydrogeologic systems.

4. Fuzzy Darcy's Equation

Using fuzzy variables, a fuzzy form of Darcy's law can be presented as a fuzzy product:

$$q^f = k^f (\cdot) (\text{grad}H^f)^f \quad (3)$$

where q^f is the fuzzy water flux, k^f is the fuzzy hydraulic conductivity, and D^f is the fuzzy hydraulic diffusivity, H^f is the fuzzy hydraulic head, and Θ^f is the fuzzy saturation. Equation (3) takes into account the fuzzy gradient of the fuzzy hydraulic head. The fuzzy membership function for q^f is expressed by

$$\mu_{q^f}(X,Y) = \min[\mu_{k^f}(X), \mu_{(gradH^f)^f}(Y)] \quad (4)$$

where $\mu_k^f(X)$ is the fuzzy membership function for k^f, and $\mu_{(\text{grad}H^f)^f}$ is the fuzzy membership function for the fuzzy hydraulic gradient. The types of membership functions for each fuzzy set can be determined using the probability distribution function for k and grad$H$. Equations (5) and (6) are a general form of fuzzy Darcy's law, from which follow that deterministic Equations (3) and (4) are particular cases (for FMF=1) of the fuzzy Darcy's law.

5. Calculation of the Water Travel Time Based on Fuzzy Darcy's Law

Based on the fuzzy Darcy's equation [Equation (3)], and assuming the actual water velocity is given by

$$q^f = n^f (\cdot) [(dz)^f (:) (dt)^f) \quad (5)$$

where dz^f is the fuzzy depth to the water table, n^f is the fuzzy porosity, and dt^f is the fuzzy water travel time. Equation (5) can be given by

$$n^f (\cdot) [(dz)^f (:) (dt)^f)] = k^f (\cdot) (\text{grad}H^f)^f \quad (6)$$

from which the water travel time can be determined using fuzzy operations.

As an example, we compare the results of the solution to Equation (6) with the data from the Box Canyon infiltration tests.

6. Conclusions

The amount of data collected from field experiments, which are often imprecise, ambiguous, or vague (and therefore uncertain), is usually inadequate to characterize flow processes in sufficient detail and to construct detailed deterministic or stochastic models. Such parameters as hydraulic head, water flux, hydraulic conductivity, hydraulic gradient, porosity, saturation, and temperature

can be represented as fuzzy variables. The spatial distribution of these parameters can be used to generate fuzzy membership functions for these parameters. Fuzzy membership functions can, in turn, be used to characterize the degree of heterogeneity of a subsurface system. The relationships between fuzzy variables, such as hydraulic pressure and water content vs. hydraulic pressure, are given by fuzzy functions. Using the basic concepts of fuzzy logic, fuzzification, and fuzzy granulation, we develop a fuzzy form of Darcy's equation and the second-order fuzzy partial differential equations. Using a fuzzy Darcy's equation, we present an example of calculations of the water travel time through fractured basalt and compare these results with those from field observations.

Acknowledgments

Investigations presented in this paper were partially supported by the mini-grant program of the Earth Sciences Division of Lawrence Berkeley National Laboratory. This work was supported by the Director, Office of Science, Office of Basic Energy Sciences, Division of Materials Sciences and Engineering, of the U.S. Department of Energy under Contract No. DE-AC03-76SF00098.

References

Bardossy, A., and L.Duckstein, Fuzzy regression in hydrology, *Water Resour. Res*., 26(7), 1497-1508, 1990.

Bardossy, A., and L.Duckstein, *Fuzzy Rule-Based Modeling with Applications to Geophysical, Biological abd Engineering Systems*, CRC Press, New York, 113 p., 1995.

Bardossy, A., and M.Disse, Fuzzy rule-based models for infiltration, *Water Resour. Res*., 29, 373-382, 1993.

De Gruijter, J.J., D.J.J.Walvoort, and P.F.M.Gaans, Continuous soil maps - a fuzzy set approach to bridge the gap between aggregation levels of process and distribution models, *Geoderma*, 77, 169-195, 1997.

Faybishenko, B., Introduction to modeling of hydrogeologic systems using fuzzy differential equations, In: "*Fuzzy Partial Differential Equations and Relational Equations,*" (edited by M. Nickravesh, L.A. Zadeh, and V. Korotkikh (Eds.), Physica-Verlag, Springer, the Series Studies in Fuzziness and Soft Computing, 2003.

Franssen, Hendricks, H.J.W.M., A. C. van Eijnsbergen, and A. Stein, Use of spatial prediction techniques and fuzzy classification of mapping soil pollutants. *Geoderma* 77(2-4), 243-262, 1997.

Kaufmann, A. and M.M. Gupta. *Introduction to Fuzzy Arithmetic: Theory and Applications*, New York, N.Y.: Van Nostrand Reinhold Co., 1985.

Nikravesh M. and F. Aminzadeh, Past, present and future intelligent reservoir characterization trends. *Journal of Petroleum Science & Engineering*. 31(2-4):67-79, 2001

Zadeh, L.A. Towards a theory of fuzzy information granulation and its centrality in human reasoning and fuzzy logic, *Fuzzy Sets and Systems*, 19, 111-127, 1997.

Possible Scale Dependency of the Effective Matrix Diffusion Coefficient

H. H. Liu and G. S. Bodvarsson
Earth Sciences Division, Lawrence Berkeley National Laboratory, Berkeley, CA 94702, USA

Because of the orders-of-magnitude slower flow velocity in rock matrix compared to fractures, matrix diffusion can significantly retard solute transport in fractured rock. Therefore, matrix diffusion is an important process for a variety of problems, including remediation of subsurface contamination and geological disposal of nuclear waste. Matrix-diffusion-coefficient values measured from small rock samples in the laboratory are generally used for modeling field-scale solute transport in fractured rock (Boving and Grathwohl, 2001; Moridis et al., 2003). Recently, several research groups have independently found that effective matrix diffusion coefficients much larger than laboratory measurements are needed to match field-scale tracer-test data (Shapiro, 2001; Neretnieks, 2002; Liu et al., 2003a,b). By compiling results from a number of field tracer tests, Liu et al. (2003c) suggested that the effective matrix diffusion coefficient might be scale-dependent. The objective of this study is to further explore this possible scale-dependent behavior.

Effective matrix-diffusion-coefficient values have been estimated from a number of field test sites characterized by different rock types. To compile these values (corresponding to different tracers) as a function of test scale, we define a matrix-diffusion-coefficient ratio, RD**,** as an effective coefficient value (estimated from field data) divided by a local value. It is an indicator of scale dependency that is expected to exist when RD is always larger than one at field scale and is a function of the test scale.

The local matrix-diffusion-coefficient values, D_e, refer to values from laboratory measurements for small rock samples, or values estimated using the following relationship (when laboratory measurements are not available):

$$D_e = \tau D_0 \tag{1}$$

where D_0 is the molecular diffusion coefficient in free water, and τ is the tortuosity factor determined here with Archie's law (Boving and Grathwohl, 2001):

$$\tau = \phi^{m-1} \tag{2}$$

Here, ϕ is the matrix porosity, and m is an empirical parameter. Boving and Grathwohl (2001) compiled m values for different types of rock and found that m is generally larger than 2 in materials of low porosity (≤ 0.2). To avoid potential exaggeration of scale effects (or an artificial increase in estimated RD values), we use m = 2 in this study.

Figure 1 shows the relationship between effective matrix diffusion coefficients, determined from a number of sites by different research groups (Maloszewski and Zuber, 1993; Jardine et al. 1999; Becker and Shapiro, 2000; Callahan, 2000; Shapiro, 2001; Neretnieks, 2002; Liu et al.,

2003a,b), and the corresponding test scales. Although some uncertainties exist, the data shown in Figure 1 seem to suggest that the effective matrix diffusion coefficient, like permeability and dispersivity, increases with test scale (Liu et al., 2003c).

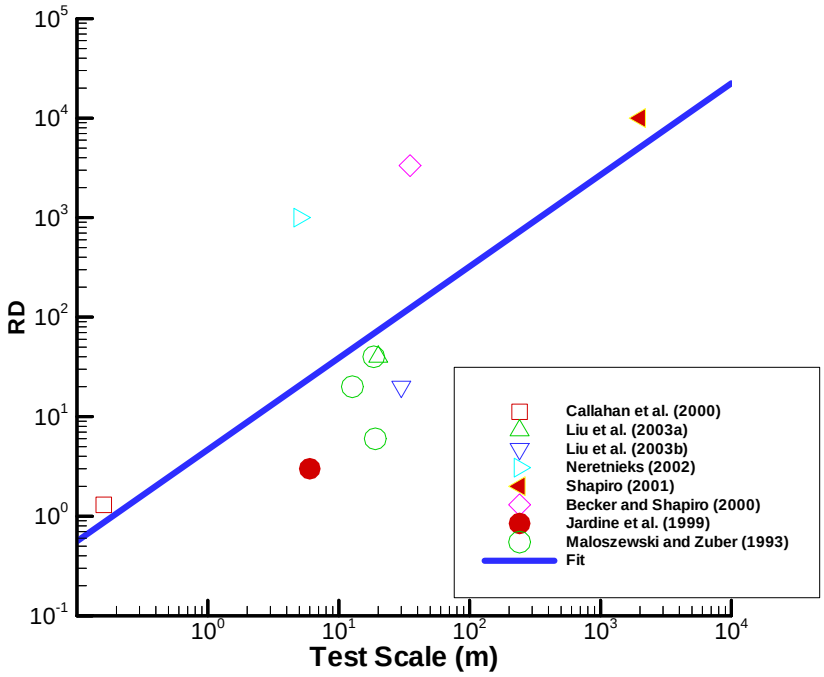

Figure 1. Effective matrix diffusion coefficient as a function of test scale. *RD* refers to the effective coefficient value (estimated from field data) divided by the corresponding local value.

In this study, we also propose a fractal-based explanation for the scale-dependent behavior of the effective diffusion coefficient. The fractal concept has been found to be useful for describing both subsurface heterogeneity and many flow and transport processes. In commonly used numerical and analytical models of solute transport, including matrix diffusion (e.g., Sudicky and Frind, 1982; Wu et al., 2003), an actual fracture network is generally conceptualized using parallel vertical or horizontal fractures. A fracture wall is approximated as a flat wall. In this case, solute particle travel paths within fractures are generally straight lines. However, the actual solute particle travel path is much more intricate and tortuous for the following reasons. First, fracture walls are not flat but rough. The rough surface generates a much larger fracture-matrix interface area than a flat fracture wall, and the fracture roughness is characterized by fractals (National Research Council, 1996). Second, fractures exist at different scales, with small-scale fractures generally excluded from modeling studies (Wu et al., 2003). However, these small-scale fractures can make flow and transport paths much more tortuous than straight lines, as demonstrated by Liu et al. (2002). Considering that both fracture roughness and fracture-network geometry can be characterized by fractals (e.g., Barton and Larsen, 1985), it is reasonable to hypothesize that a solute travel path within a fracture network is fractal, rather than a straight line (as assumed in many numerical or analytic models).

The length of the fractal solute travel path (L) between tracer release and monitoring points depends on the spatial scale (or length of a ruler, δ) used to measure it. We denote the straight-line distance between the release and monitoring points as L*. We can also approximate $(RD)^{1/2}$ as a ratio of actual fracture-matrix interface area to the area used in numerical or analytical models (e.g., Neretnieks, 2002):

$$RD^{1/2} = \frac{L(\delta)}{L^*} \tag{3}$$

Following the procedure of Feder (1988) to determine the length of the coast of Norway, L can be determined by

$$L(\delta) = N(\delta) * \delta = (\frac{L^*}{\delta})^D \delta \tag{4}$$

where N is the number of rulers with length δ (needed to measure the length of fractal solute travel path between tracer release and monitoring points), and D >1 is the fractal dimension of a solute travel path. Assuming that a solute travel path within a small interval δ can be approximated as a straight line, we obtain the following relationship based on Equations (3) and (4)

$$RD = (\delta^{1-D}(L^*)^{D-1})^2 \propto (L^*)^{2(D-1)} \tag{5}$$

The above equation indicates that RD is a power function of test scale L*. Because D >1, RD increases with L*, consistent with results showed in Figure 1. Fitting Equation (5) to data points (Figure 1) results in D = 1.46.

In summary, we have demonstrated that the effective matrix diffusion coefficient may be scale-dependent and increases with test scale. This finding has many important implications for problems involving matrix diffusion. We also presented a fractal-based explanation for this possible scale-dependent behavior. However, uncertainties exist in the estimated effective diffusion coefficients given in Figure 1, because these coefficients have been obtained from inverse modeling, which cannot give unique parameter values. Also note that the data presented in Figure 1 are relatively limited. More studies are needed to confirm this scale-dependent behavior and to develop more rigorous theoretical explanations.

References

Barton, C.C., and E. Larsen. 1985. Fractal geometry of two-dimensional fracture networks at Yucca Mountain, southwestern Nevada. in Proceedings of Int. Symposium on Fundamentals of Rock Joints, Bjorkliden, pp. 77-84.

Becker, M.W., and A. M. Shapiro. 2000. Tracer transport in fractured rock: Evidence of nondiffusive breakthrough tailing. Water Resour. Res. 36(7): 1677-1686.

Boving, T. B., and P. Grathwohl, 2001. Tracer diffusion coefficients in sedimentary rocks: Correlation to porosity and hydraulic conductivity. J. Contam. Hydrol. 53:85-100.

Callahan, T.J., P.W. Reimus, R.S. Bowman, and M.J. Haga. 2000. Using multiple experimental methods to determine fracture/matrix interactions and dispersion of nonreactive solutes in saturated vocanic tuff. Water Resour. Res. 36(12): 3547-3558.

Feder J. 1988. Fractals. Plenum Press, New York.

Jardine, P.M., W. E. Sanford, J. P. Gwo, O.C. Reedy, D.S. Hicks, J.S. Riggs, and W.B. Bailey. 1999. Quantifying diffusive mass transfer in fractured shale bedrock. Water Resour. Res. 35(7): 2015-2030.

Liu, H.H., G.S. Bodvarsson, and S. Finsterle. 2002. A note on unsaturated flow in two-dimensional fracture networks. Water Resour. Res. 38 (9): 1176, doi:10.1029/2001WR000977.

Liu, H.H., R. Salve, J. S. Y. Wang, G. S. Bodvarsson, and D. Hudson. 2003a. Field investigation into unsaturated flow and transport in a fault: Model analysis. J. Contam. Hydrol. (in review).

Liu, H.H., C. B. Haukwa, F. Ahlers, G. S. Bodvarsson, A. L. Flint, and W. B. Guertal. 2003b. Modeling flow and transport in unsaturated fractured rocks: An evaluation of the continuum approach. J. Contam. Hydrol. 62-63: 173-188.

Liu, H.H., G.S. Bodvarsson, and G. Zhang. 2003 c. The scale-dependency of the effective matrix diffusion coefficient, Vadose Zone Journal (accepted).

Maloszewski, P., and A. Zuber. 1993. Tracer experiments in fractured rocks: Matrix diffusion and the validity of models. Water Resour. Res. 29(8): 2723-2735.

National Research Council. 1996. Rock Fractures and Fluid Flow: Contemporary Understanding and Applications. National Academy Press, Washington, D.C..

Neretnieks, I. 2002. A stochastic multi-channel model for solute transport – Analysis of tracer tests in fractured rock. Water Resour. Res., 55: 175-211.

Shapiro, A.M. 2001. Effective matrix diffusion in kilometer-scale transport in fractured crystalline rock. Water Resour. Res. 37(3): 507-522.

Sudicky, E.A., and E.O. Frind. 1982. Contaminant transport in fractured porous media: Analytical solutions for a system of parallel fractures. Water Resour. Res. 18(6): 1634-1642.

Wu, Y.S., H.H. Liu, and G.S. Bodvarsson. 2003. Effects of small fractures on flow and transport processes at Yucca Mountain, Nevada. in Proceedings of 10th International High-Level Radioactive Waste Management Conference**,** Las Vegas, Nevada.

Simulation of Hydraulic Disturbances Caused by the Underground Rock Characterisation Facility in Olkiluoto, Finland

Jari Löfman[1], Mészáros Ferenc[2]
[1]VTT Processes, P.O. Box 1608, FIN-02044 VTT, Espoo, Finland, Tel. +358 9 4561, Fax. +358 9 4566390, E-mail: jari.lofman@vtt.fi
[2]The Relief Laboratory, P.O. Box 1, 8442 Hárskút, Hungary, Tel., Fax. +36 88 272644, E-mail: ferenc@relief.hu

Background

Spent fuel from the Finnish nuclear power plants will be disposed of in a repository to be excavated in crystalline bedrock at a depth of 400-700 m. Based on the extensive site investigations carried out since the early 1980s Olkiluoto in Eurajoki, Finland (Figures 1 and 2) has been chosen to be the site for the final disposal facility and subject of the further detailed characterization. This further effort will focus on the construction of *an underground rock characterization facility (ONKALO)* in 2004-2010. The facility will consist of a system of exploratory tunnels extending to a depth of about 500 m and accessed by a downward spiralling tunnel and a vertical shaft (Figure 4). The total underground volume of the facility will be approximately 330000 m^3 and the combined length of tunnels and shaft approximately 8,500 m.

Inflow of groundwater into the open tunnel system will constitute a major hydraulic disturbance for the site's groundwater conditions (e.g. drawdown of groundwater table and intrusion of surface water containing oxygen and carbon dioxide deep into the bedrock) for hundreds of years. Especially, upconing of deep saline groundwater (saline water has been observed not only deep in the bedrock but also relatively close to the surface in Olkiluoto) is a major concern from a point of view of the performance of the tunnel backfill after the closure of the tunnels.

Modeling Hydraulic Disturbances

Our study aimed to assess inflow of groundwater into the open ONKALO tunnel system, a resulting drawdown of groundwater table, and effects of inflow on the salinity distribution (upconing of deep saline groundwater) by means of a finite element simulation.

The size of the modelled bedrock volume was about 6.3 km x 4.3 km horizontally and 1.5 km in depth and covered the entire Olkiluoto island. The modeled volume was conceptually divided into hydraulic units, planar fracture zones and sparsely fractured rock between the zones, for which the equivalent-continuum model was applied separately. The geometry of the fracture zones (Figures 3 and 4) was based on the latest geological bedrock model and it contained 41 fracture zones, all of which were modeled explicitly (Figures 5 and 6).

The three phenomena were analyzed separately by using somewhat different modeling approaches and assumptions. Since the open tunnels constitute a very strong sink in the host rock, the effect of groundwater salinity on flow was considered negligible in the vicinity of the tunnels, and inflow of water was computed assuming fresh water and steady-state conditions.

The drawdown of groundwater table was simulated employing a free surface approach, in which only the saturated part is included in the modeled volume and the transiently sinking water table constitutes the free surface, an irregular and time-dependent top of the modeled volume. The modeling approach is based on determining the shape of the evolution of the saturated zone in time with the implicit scheme by Huyakorn and Pinder (1983), which involves two phases at each time step: *a meshing phase* and *a finite element analysis phase*. The finite element program package FEFTRA (2003) has recently been complemented with an adaptive and automatic mesh generator *octree*, which enables an efficient creation of a new mesh according to the free surface for each time step. The salinity does not affect significantly the drawdown of groundwater table and was thus neglected in the simulation of drawdown as well.

The evolution of salinity distribution was simulated employing a coupled (flow and salt transport) and transient model. As it is computationally a very demanding task to combine the drawdown of groundwater table and the coupled flow and transport into the same truly transient simulation, the drawdown was ignored when simulating the evolution of salinity. The whole tunnel system was made hydraulically active at the beginning of the simulation and was assumed to be open for hundred years. Both inflow and upconing phenomena were modelled within a rectangular and static volume.

Results

Simulations show that without engineering measures (e.g., grouting) taken to limit inflow of groundwater into the open tunnels, the hydraulic disturbances could be drastic. The tunnels draw groundwater from all directions in the bedrock (Figure 7). A major part of inflow, which could be as high as 1,100 L/min, comes from the well-conductive subhorizontal fracture zones intersected by the access tunnel and the shaft. The simulations show that the resulting drawdown of groundwater table might sink to a depth of about 300 m and the depressed area extend over about 2.5 km^2 (Figures 8-10). The results also indicate that the salinity of groundwater is gradually rising around and below the tunnel system, and locally concentration (TDS) may rise up to 50-55 g/L in the vicinity of the tunnels (Figures 12-14). Transport of salt was enhanced by the relatively low flow porosity (10^{-4} in the sparsely fractured rock and 10^{-3} in the fracture zones) and by the negligence of the effects of matrix diffusion in the simulations.

The disturbances can significantly be reduced by the grouting of rock. In the case of very tightly grouted tunnels, where the total inflow rate was only 19 l/min, the simulations showed clearly lesser disturbances. Drawdown of groundwater table was at most about 30 m and the depression area remained in the immediate vicinity of the accesses of the tunnels (Figure 11). The upconing of saline water decreases as well, although the maximum calculated salinity of groundwater in the vicinity of the tunnels at 500 m was still 40-45 g/L.

References

FEFTRA, 2003. The finite element program package for modelling of groundwater flow, solute transport and heat transfer. VTT Processes. Espoo, Finland. http://www.vtt.fi/pro/pro1/feftra

Huyakorn, P. S. & Pinder, G. F. 1983. Computational Methods in Subsurface Flow. Academic Press Inc, Orlando. pp. 121-125.

Vieno, T., Lehikoinen, J., Löfman, J., Nordman, H. and Mészáros, F. 2003. Assessment of disturbances caused by construction and operation of ONKALO. POSIVA 2003-06.

Figure 1. Eurajoki, Finland.

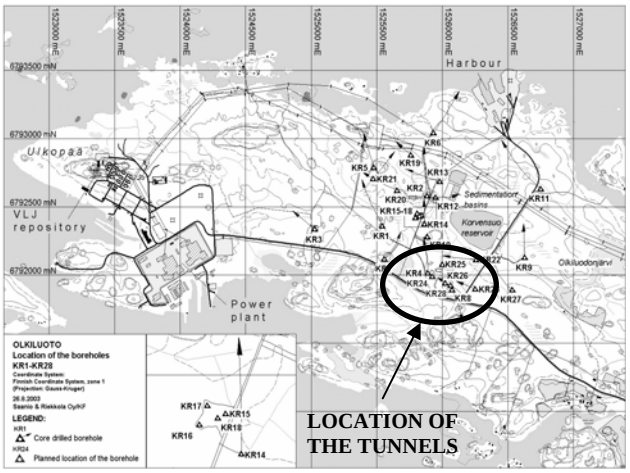

Figure 2. The Olkiluoto site in Eurajoki, Finland.

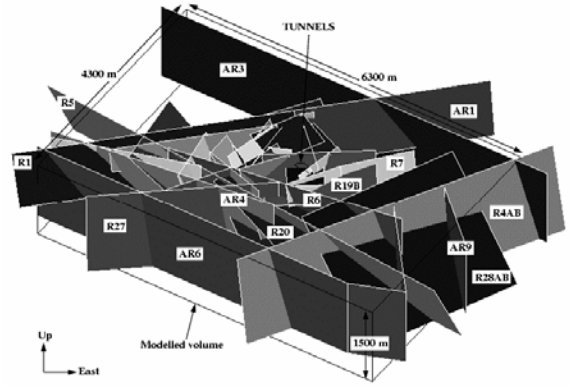

Figure 3. A conceptual fracture zone geometry for the bedrock of the Olkiluoto site (41 planar zones).

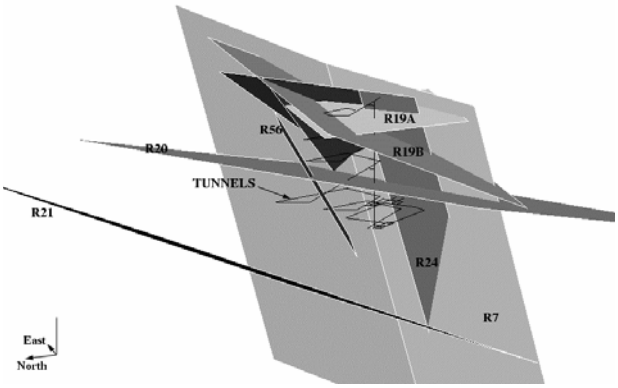

Figure 4. A close-up of the tunnel layout and some of the nearby fracture zones.

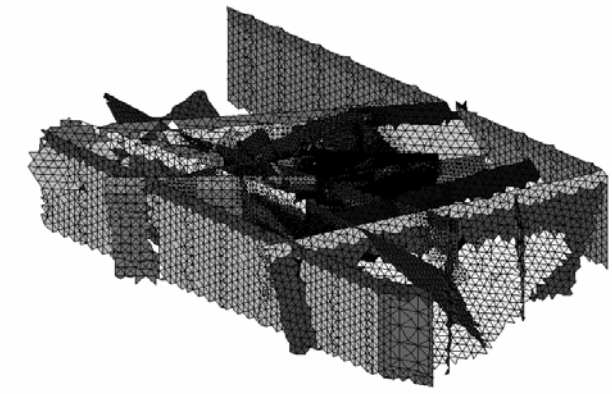

Figure 5. Finite element mesh. Triangular elements added on the faces of the tetrahedra for the fracture zones (tetrahedra for the sparsely fractured rock between the zones not shown in the figure).

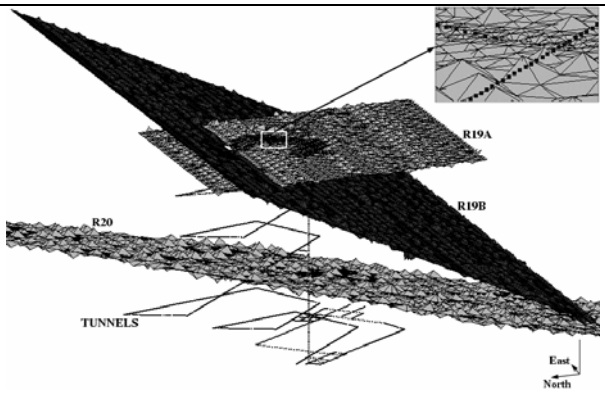

Figure 6. Finite element mesh. A close-up of the tunnels (a set of blue nodes) and some of the nearby fracture zones.

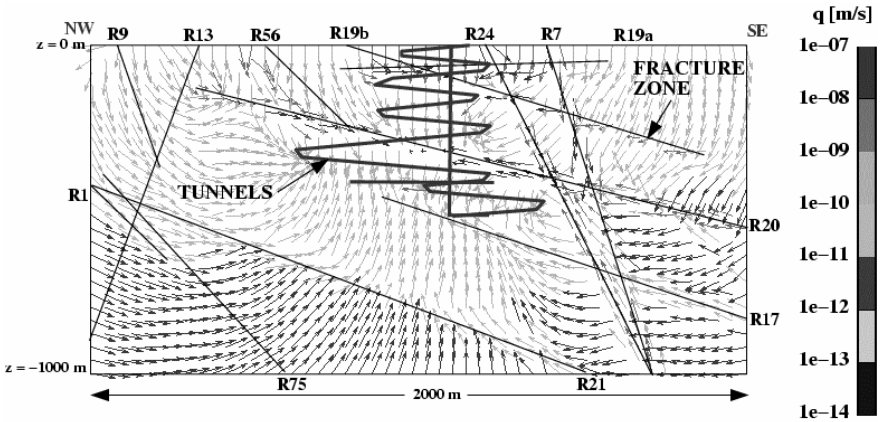

Figure 7. Darcy velocity at the vertical northwest-southeast cross section at 50 years after the opening of the tunnels (ungrouted tunnels).

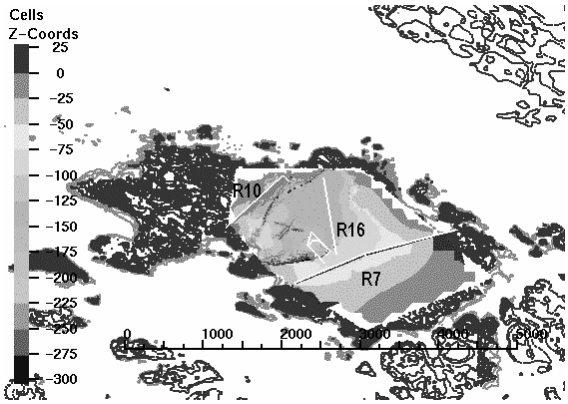

Figure 8. The drawdown of groundwater table (ungrouted tunnels) and its extension over the Olkiluoto island.

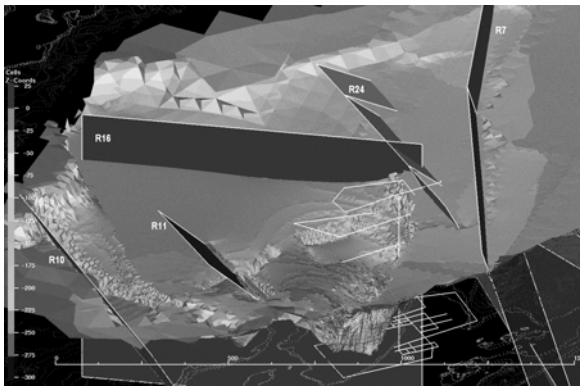

Figure 9. The drawdown of groundwater table (ungrouted tunnels). A close-up of the tunnels and some of the nearby fracture zones.

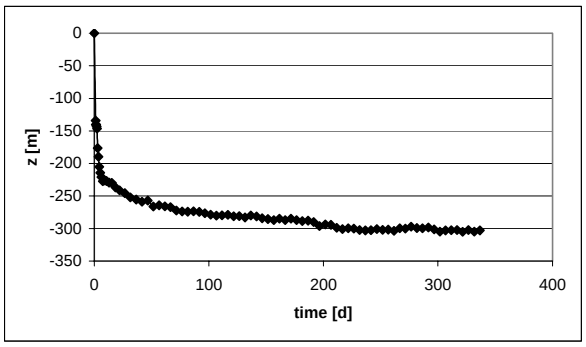

Figure 10. Drawdown at the lowermost point as a function of time (ungrouted tunnels).

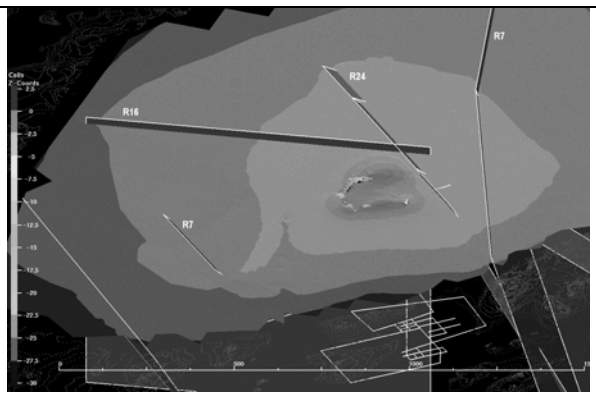

Figure 11. The drawdown of groundwater table (grouted tunnels). A close-up of the tunnels and some of the nearby fracture zones.

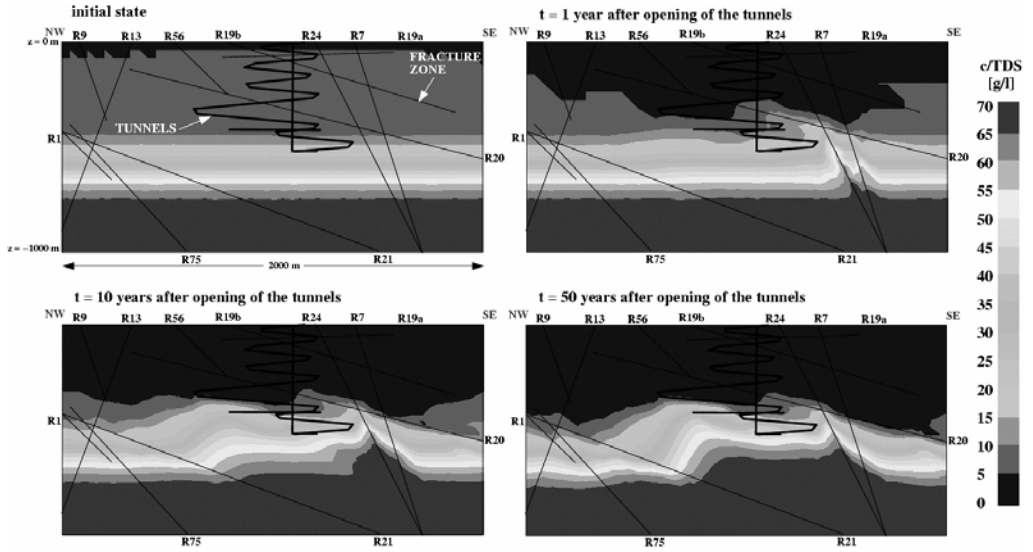

Figure 12. Salinity of groundwater at the vertical northwest-southeast cross section after the opening of the tunnels (ungrouted tunnels).

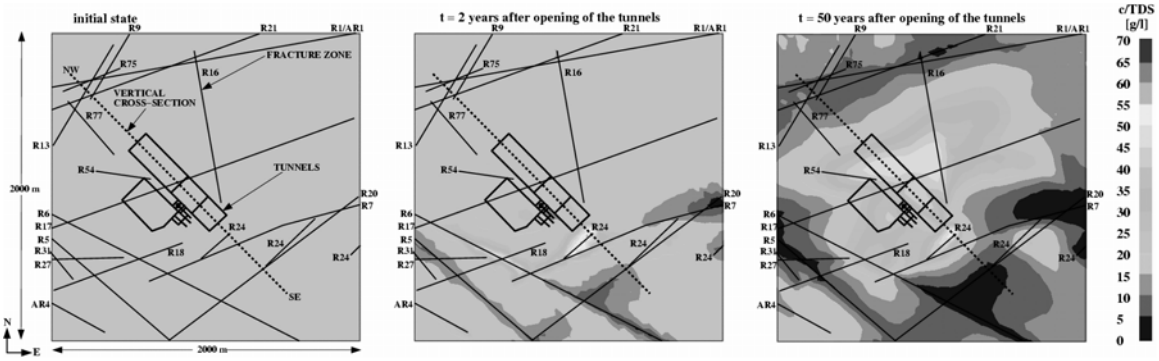

Figure 13. Salinity of groundwater at the horizontal cross section at a depth of 500 meters after the opening of the tunnels (ungrouted tunnels).

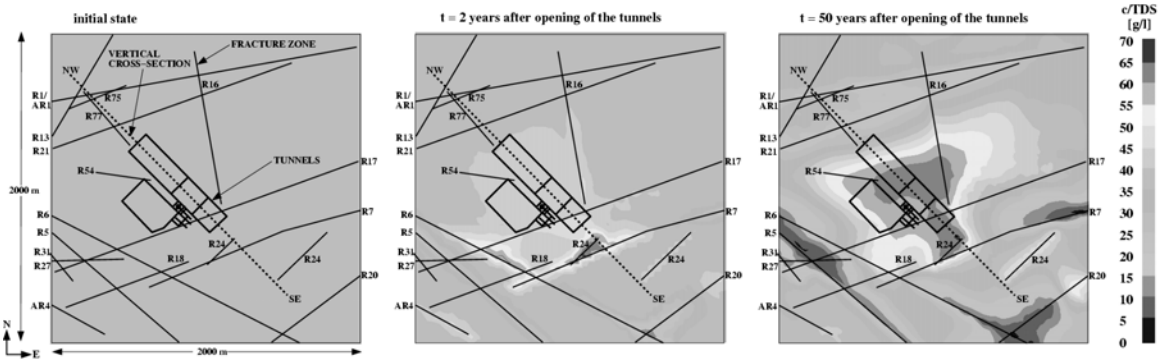

Figure 14. Salinity of groundwater at the horizontal cross section at a depth of 600 meters after the opening of the tunnels (ungrouted tunnels).

Constraining a Fractured-Rock Groundwater Flow Model with Pressure-Transient Data from an Inadvertent Well Test

Christine Doughty and Kenzi Karasaki
Earth Sciences Division
E.O. Lawrence Berkeley National Laboratory

Introduction

Starting with regional geographic, geologic, surface and subsurface hydrologic, and geophysical data for the Tono area in Gifu, Japan, we have developed an effective continuum model to simulate subsurface flow and transport in a 4 km by 6 km by 3 km thick fractured granite rock mass overlain by about 100 m of sedimentary rock (Doughty and Karasaki, 2001, 2002). Individual fractures are not modeled explicitly. Rather, continuum permeability and porosity distributions are inferred from well-test data and fracture density measurements. Lithologic layering and one major fault, the sub-vertical, E-W striking, Tsukiyoshi Fault, are assigned deterministically. Figure 1 shows a perspective view of the model, identifying the different material types. Within each material type, grid-block permeability and porosity are assigned stochastically.

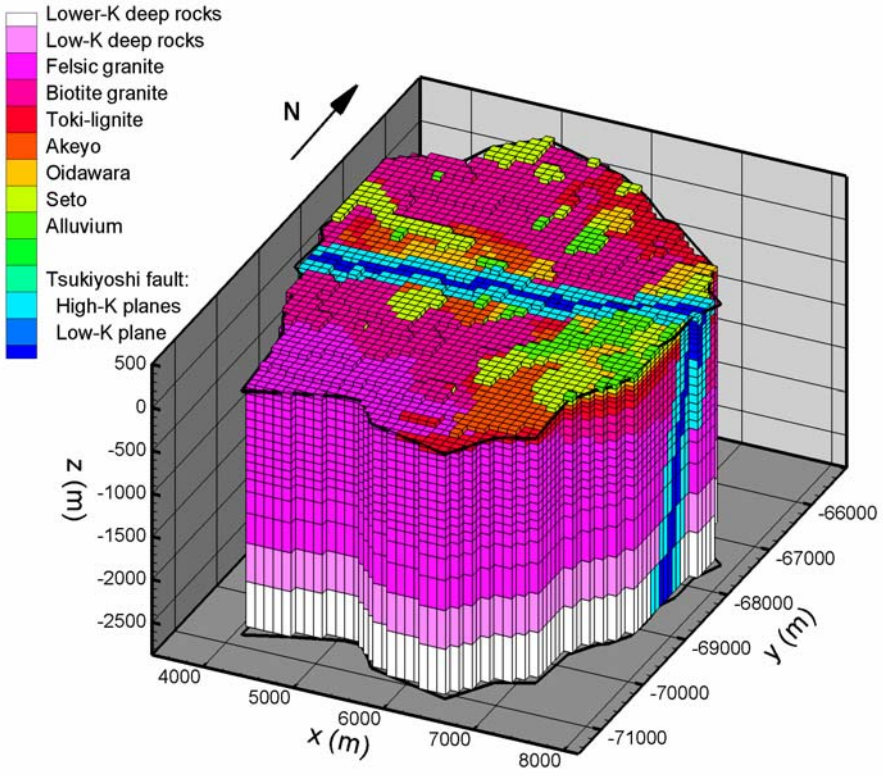

Figure 1. Perspective view of the 4 by 6 by 3 km model of the Tono area. Lateral boundaries are open (hydrostatic pressure) except for the southern model boundary, which coincides with the Toki River and is closed at depth and constant pressure at the surface; the top of the model is the ground surface (presumed to coincide with the water table); the bottom of the model is closed.

The natural-state hydraulic head distribution shows head values 30-40 m higher on the north side of the Tsukiyoshi fault, suggesting that it acts as a low-permeability impediment to regional groundwater flow from highlands in the north to a river valley in the south. Analysis of interference well-tests have suggested that the low-permeability core of the fault is bounded on either side by higher permeability zones (Takeuchi et al., 2001), creating what we call a "sandwich" structure. Many wells in the Tono area are instrumented with a multi-packer (MP) system consisting of strings of pressure probes separated by packers to hydraulically isolate various depth ranges in the wells. Several wells in the central area of the model, known as the MIU area, intersect the Tsukiyoshi fault at a depth of about 1,000 m, with the pressure probes below the fault showing higher hydraulic head. The MP systems prevent the wells from acting as high-permeability conduits through the low-permeability Tsukiyoshi fault core.

Inadvertent Well Test

In November 2001, when the packers in well MIU-2 were removed in preparation for a long-term pumping test, strong pressure transients were observed in the surrounding wells. In fact, observed pressure changes in response to the MIU-2 packer removal were far larger and more widespread than those subsequently observed during the long-term pumping test, which we had planned to use for model calibration. Therefore, we decided to analyze the packer removal itself as an "inadvertent" well test, by modeling the event with different spatial distributions of permeability and porosity and comparing simulated pressure-transients with observed responses. In order to accurately simulate the response to packer removal, a local area grid refinement is done for the vicinity of well MIU-2. Following packer removal, we anticipate upward flow through well MIU-2, but we have no basis for assuming that it occurs under either constant-flow or constant-pressure conditions, precluding well-test analysis by matching pressure-transients to type curves based on analytical solutions. Unfortunately, well flow rate was not monitored. We model packer removal as a sudden increase in vertical permeability in the model column representing well MIU-2, and by allowing the well permeability to be one of our adjustable parameters, the model determines the variable flow rate that produces pressure-transients that best match the observed ones. Other adjustable parameters are the permeability and porosity values for various material types and for individual grid blocks for a few critical locations.

Figure 2 shows the wells used for model calibration to the inadvertent well test. Wells MIU-2, MIU-3, and MIU-4 all have MP systems with probes on both sides of the Tsukiyoshi fault, well MIU-1 and the two AN wells have MP systems with probes only on the south side of the fault, and the two SN wells are shallow wells without packers on the north side of the fault.

Figure 3 shows the observed pressure response to packer removal, along with the simulated response using our original (uncalibrated) model, which was constructed to reproduce the natural-state hydraulic head difference observed across the Tsukiyoshi fault. Packer removal allows fluid to flow up the well from the deeper, high head region (the footwall north of the fault) to the shallower, low head region (the hanging wall south of the fault). Consequently, pressures in the footwall decrease while pressures in the hanging wall increase. The model reproduces these responses qualitatively, but not quantitatively. The main problems with the model response are that well MIU-1, well MIU-3, and the SN wells show responses that are too small, whereas well MIU-4 and the AN wells show responses that are too big. All modeled responses tend to occur too quickly, reaching a steady-state not observed in the field data.

The calibration process consists of modifying the permeability and porosity of selected material types or individual grid blocks. Given a new property distribution, first a new steady state for packer-in-place conditions is generated, and we confirm that it reproduces the natural-state head difference observed across the Tsukiyoshi fault. Then the permeability is increased in the MIU-2 grid blocks to represent packer removal, and the 26-day pressure transients are simulated and compared to the observed values. After many repetitions of this process, the pressure-transient match shown in Figure 4 is obtained.

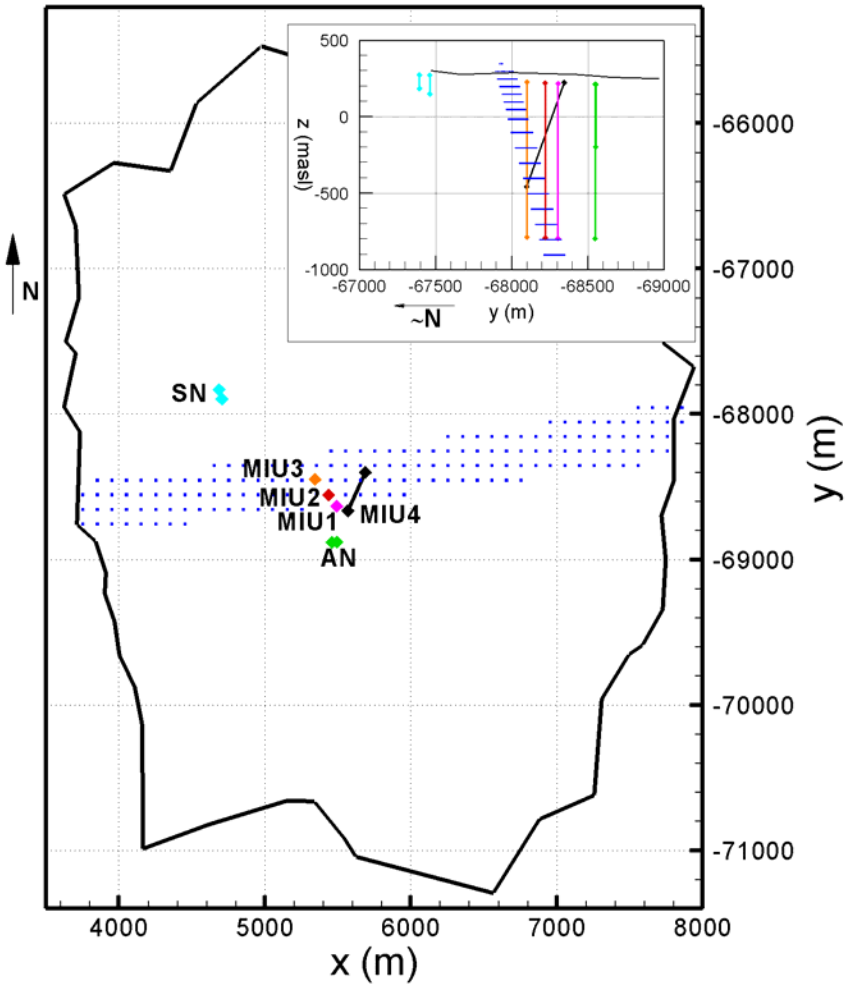

Figure 2. Plan view of the model showing the locations of the MIU-area wells. The blue shaded region is a horizontal projection of the Tsukiyoshi fault plane from the surface to a depth of 1000 m. The inset shows a vertical cross-section perpendicular to the strike of the Tsukiyoshi fault (roughly north-south).

Calibration Results

In general, it is not possible to get good matches to the large rapid pressure responses in wells MIU-1 and MIU-3 unless there is a relatively large flow rate up the wellbore (at least 400 L/min). This large flow rate requires that the footwall sandwich layer permeability be increased. Fault core permeability must be decreased to lessen certain responses in wells MIU-3 and MIU-4. Bulk granite permeability is correspondingly decreased to maintain the ratio between bulk

and fault core permeability that produces the observed steady-state head difference across the fault. Lower bulk granite permeability also serves to lessen the response in the AN wells. However, in the vicinity of the SN wells, granite permeability must be increased to enhance the response there. Porosity is increased in all materials to slow the pressure responses.

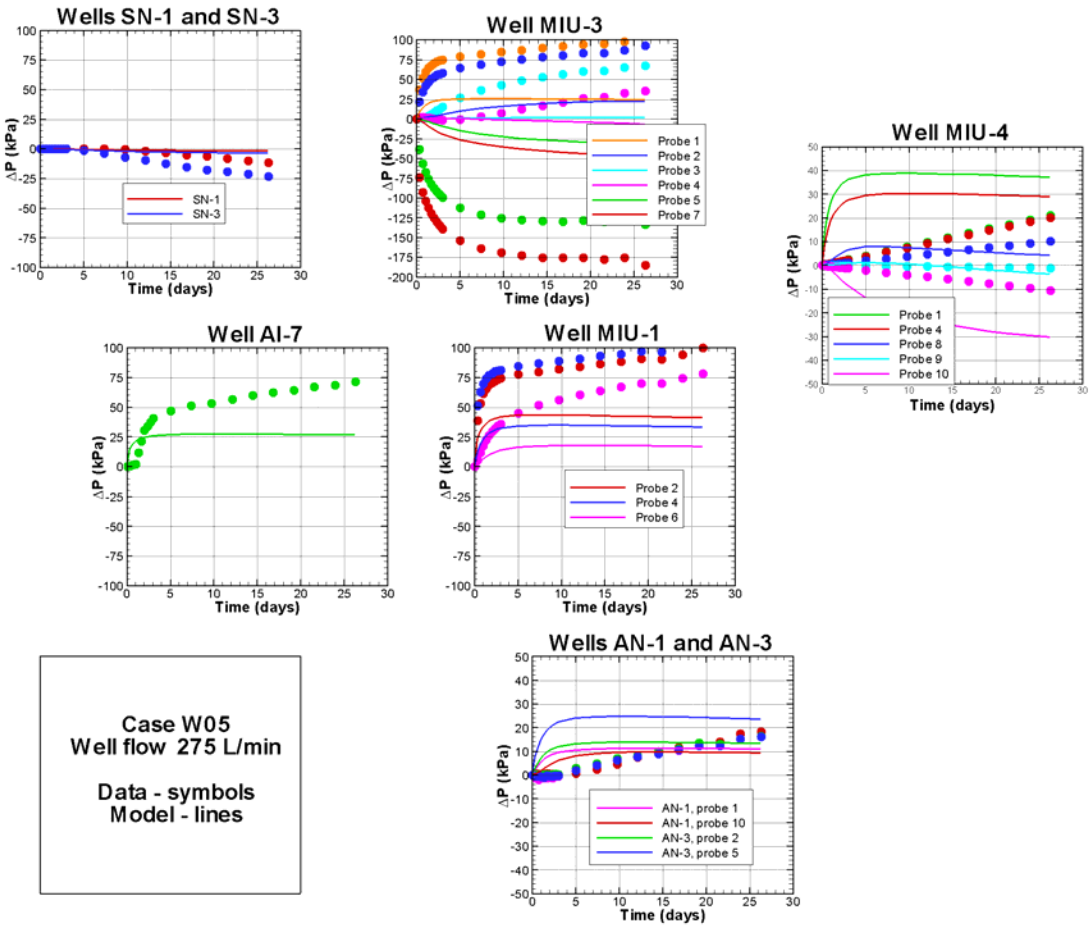

Figure 3. Observed and modeled pressure responses to packer removal in well MIU-2: uncalibrated model. The arrangement of plots on the page roughly corresponds to well location in plan view. For MP wells, probe depth increases with probe number. Well AI-7 is a shallow well near well MIU-2.

After the calibration process is complete, the calibrated model is used to predict travel times from specified monitoring points to the model boundaries. The model changes arising from the calibration process (primarily decreases in permeability and increases in porosity) serve to lengthen the travel times through the model by a factor of about 100, a significant change.

Conclusions

Analyzing the pressure-transient data resulting from the removal of the Well MIU-2 packer has proved to be a useful means of improving estimates of fracture porosity, which has always been considered one of the least well constrained model parameters. A key benefit is the large flow rates that are attainable, due to the large steady-state pressure difference across the Tsukiyoshi fault. This enables large pressure signals to be generated, which in turn enables large spatial

regions to be analyzed. One difficulty of using well-test data to try to infer porosity is that field-scale rock compressibility is still an unknown. It is difficult to determine rock compressibility independently from porosity since pressure-transient responses just depend on their product through specific storage. One possibility might be to do a tracer test in a local area to infer porosity, then do a well test focusing on the same area to enable rock compressibility to be better inferred from specific storage.

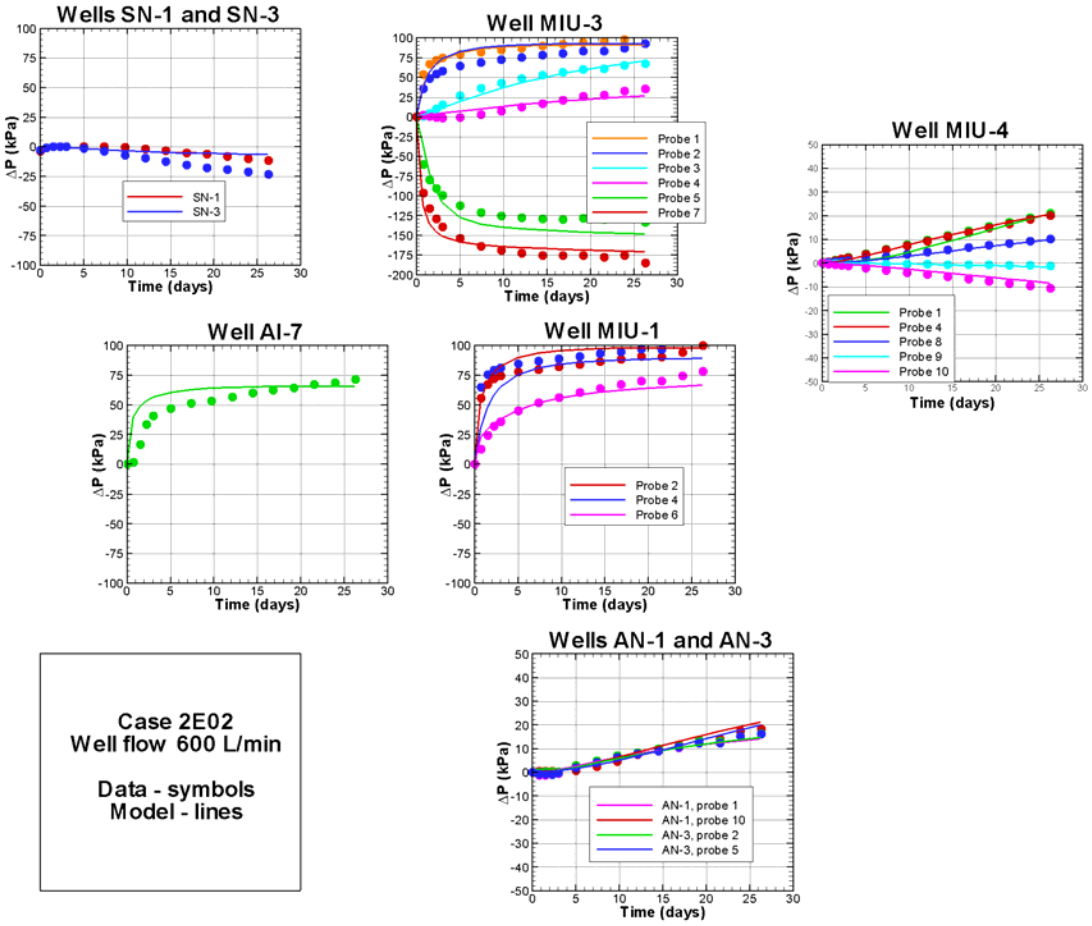

Figure 4. Observed and modeled pressure responses to packer removal in well MIU-2: calibrated model.

Acknowledgments

We thank S. Finsterle and K. Ito for reviewing this paper. This work was supported by Japan Nuclear Cycle Development Institute (JNC) and Taisei Corporation of Japan through the U.S. Department of Energy Contract No. DE-AC03-76SF00098. We are particularly indebted to A. Sawada of JNC and Y. Ijiri of Taisei Corp. for useful discussions. We would also like to thank S. Takeuci and H. Saegusa for making the field data available, and K. Ito for providing the grid refinement program.

References

Doughty, C. and K. Karasaki, Evaluation of uncertainties due to hydrogeological modeling and groundwater flow analysis: Effective continuum model using TOUGH2, Rep. LBNL-48151, Lawrence Berkeley National Lab., Berkeley, Calif., 2001.

Doughty, C. and K. Karasaki, Evaluation of uncertainties due to hydrogeological modeling and groundwater flow analysis: Steady flow, transient flow, and thermal studies, Rep. LBNL-51894, Lawrence Berkeley National Lab., Berkeley, Calif., 2002.

Takeuchi, S., M. Shimo, N. Nishijima, and K. Goto, Investigation of hydraulic properties near the fault by pressure interference test using 1000 m depth boreholes, The 31st Japanese Rock Mechanics Symposium, pp. 296-300, 2001.

Fluid Displacement between Two Parallel Plates: a Model Example for Hyperbolic Equations Displaying Change-ff-Type

M. Shariati[1], L. Talon[2], J. Martin[2], N. Rakotomalala[2], D. Salin[2] and Y.C. Yortsos
Department of Chemical Engineering
University of Southern California
Los Angeles, CA 90089-1211, USA
[1]Now with CFD Research
[2]Laboratoire Fluides Automatique et Systemes Thermiques
Universites P. et M. Curie and Paris Sud, C.N.R.S. (UMR 7608)
Batiment 502, Campus Universitaire, 91405 Orsay Cedex, France

A number of physical problems are modeled in terms of systems of quasilinear hyperbolic equations. In certain cases, an elliptic region develops and the system shows change-of-type from hyperbolic to elliptic. The solution of Riemann problems that span the elliptic region has been attempted using shocks and by adding a small amount of diffusion. Using an exact example, we show that this approach is incorrect. We consider miscible displacement between parallel plates in the absence of diffusion, with a concentration-dependent viscosity. By selecting a piece-wise viscosity function, this can also be considered as "three-phase" flow in the same geometry. Assuming symmetry across the gap and based on the lubrication approximation, which is necessary for consistency at steady-state, a description in terms of two quasilinear hyperbolic equations is obtained. The system is genuinely hyperbolic and can be solved analytically, when the mobility profile is monotonic, or when the mobility of the middle phase is smaller than its neighbors. In the opposite case, a change of type is displayed, an elliptic region developing in the parameter space. Numerical solutions of Riemann problems spanning the elliptic region, with small diffusion added, show good agreement with the analytical, outside, but an unstable behavior, inside the elliptic region. In these problems, this region arises precisely at the displacement front, where the, underlying to the hyperbolic formalism, lubrication approximation fails. Solving the problem correctly near the front requires use of the full, higher-dimensional model, obtained here using Lattice Gas simulations. We conjecture that the hyperbolic-to-elliptic change-of-type reflects the failing of the quasilinear hyperbolic model to describe the problem uniformly, and suggest that in such cases the full higher-dimensionality problem must be considered.

Equivalent Heterogeneous Continuum Model Approach for Flow in Fractured Rock—Application to Regional Groundwater Flow Simulation at Tono, Japan

Michito Shimo[1], Hajime Yamamoto[2], and Kenichi Fumimura[1]
[1]Taisei Corporation, Technology Research Center, 344-1, Totsuka, Yokohama, 245-0051, JAPAN
[2]Lawrence Berkeley Laboratory, Earth Science Division, One Cyclotron RD, Berkeley, CA 94740

Introduction

Discontinuities, such as joints and fractures, are considered important for flow and transport in fractured rocks. The discrete Fracture Network model (DFN) is one of the promising approaches that can incorporate geometrical and hydraulic properties of individual fractures in the model. In dealing with regional flow, however, it is sometimes unrealistic to model all fractures. The authors have proposed an equivalent heterogeneous continuum model (EHCM) that represents fractured rock as a heterogeneous continuum with locally distributed hydraulic tensors. Since there is no limitation in number of fractures to be modeled, EHCM is suitable for regional flow and transport simulation, taking discontinuity of various scales into account.

The Mizunami Underground Research Laboratory site (MIU site) at Tono, Gifu prefecture in Japan was selected as a site to study the application of EHCM to regional groundwater flow simulation.

This paper describes the hydrogeological model for the MIU site by using an EHCM approach. The uncertainty associated with flow paths in the study area is discussed, based on the simulation results for different fracture generations. The importance of transient pressure observation for improving the reliability of the model is also discussed

Equivalent Heterogeneous Continuum Model

The proposed equivalent heterogeneous continuum model (EHCM) is an extension of the conventional equivalent continuum model[1), 2)] In the EHCM approach, heterogeneity of the fractured rock mass is modeled by a group of regions with different hydraulic conductivity tensors. A unique feature of the EHCM approach is the link between the DFN and continuum models. In the conventional equivalent continuum model, heterogeneity is usually defined either deterministically or stochastically, independent of fracture distribution. In the EHCM approach, however, the discrete fractures are first generated within the rock mass, and the whole volume is then divided into small regions, similar to finite element meshes. Equivalent rock properties, such as hydraulic conductivity tensor and porosity, are evaluated element by element through volume-averaging the contributions from individual fractures.

Figure 1 shows an image of the fractured rock mass representation by the EHC model. We have developed a three dimensional saturated unsaturated flow simulator using EHCM, EQUIV_FLO, and used it in this study.

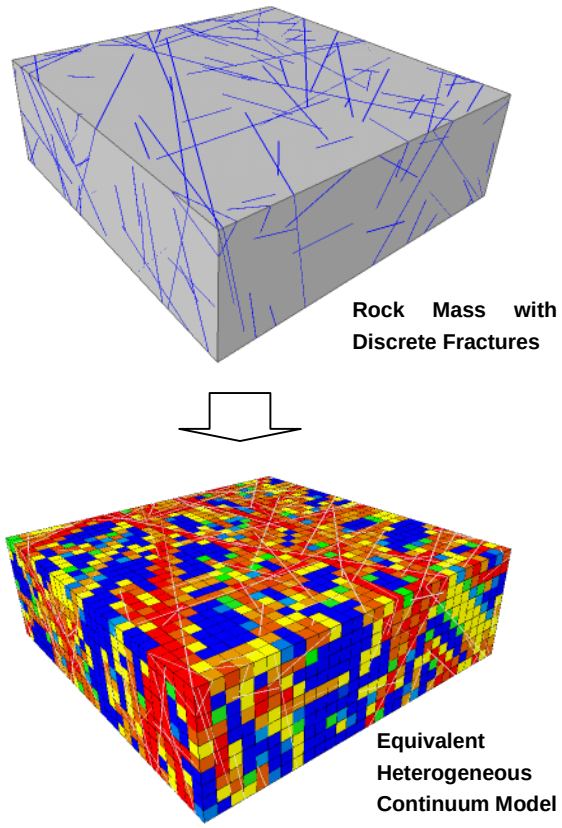

Figure 1. Equivalent Heterogeneous Continuum Model.

Hydrogeological Modeling of Study Site

EHCM approach has been applied to regional groundwater simulation around the Mizunami Underground Research Laboratory site (MIU site) in Gifu prefecture at central Japan. A 4 km by 6 km area has been selected as a study site (Figure 2). Geology of this site consists of a crystalline rock, Toki Granite, overlain by a Miocene sedimentary rock. The Tsukiyoshi fault has been found to intersect the two 1,000 m boreholes in two MIU sites, MIU-2 and MIU-3, at 890 to 915 m and 699 to 721 m below the ground surface, respectively. From core observations and borehole TV studies, the approximately 100 m thick fractured zones were found to exist along the faults. A hydrogeological model was constructed by considering the above geological structure, and a finite element mesh was created for simulation (Figure 3).

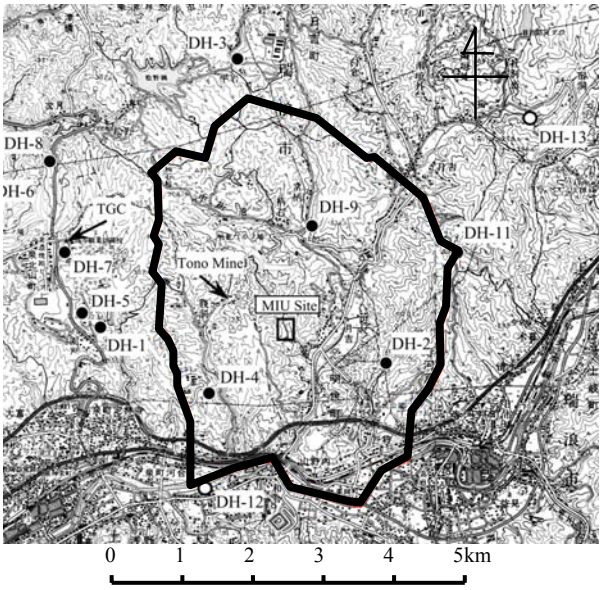

Figure 2. Study site (within a closed line).

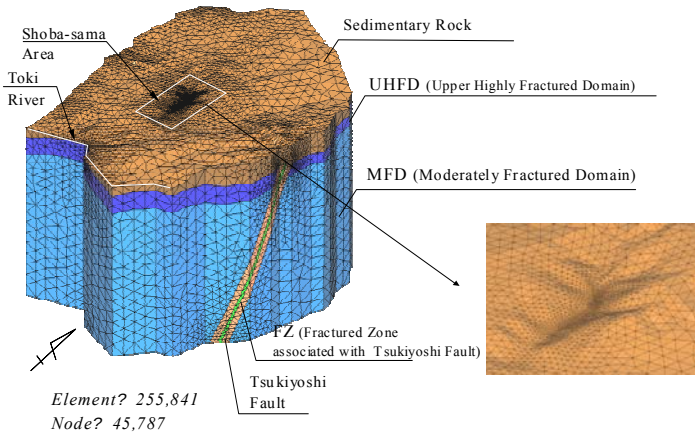

Figure 3. Finite element mesh.

Fracture Statistics for EHCM

Figure 4 shows a flow diagram defining the key parameters required for the EHCM approach. Three geometric parameters, fracture orientation distribution, fracture intensity and geometric aperture distribution, are determined based on borehole TV and core observations. Figure 5 shows the fracture orientation distribution obtained at the three 1000 m boreholes, MIU-1 to MIU-3. Fractures were divided into four groups by orientation, and each group was fitted by the Bingham distribution function. To determine the fracture size and the hydraulic aperture distribution, we developed a new approach, the virtual water injection test, VWIT. In VWIT, water injection tests are conducted numerically, and a fracture size distribution and mean hydraulic aperture are found that can reproduce the hydraulic conductivity distribution from well test[2)]. An example of comparison between observed and simulated hydraulic conductivity distribution is shown in Figure 6. The hydraulic aperture obtained from VWIT was equal to one tenth of the geometric aperture.

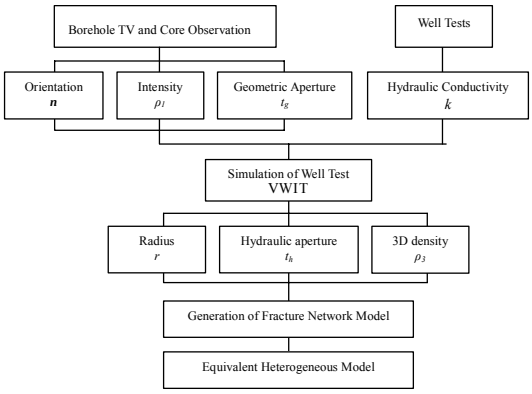

Figure 4. Flow diagram for determination of fracture statistics for EHC modeling.

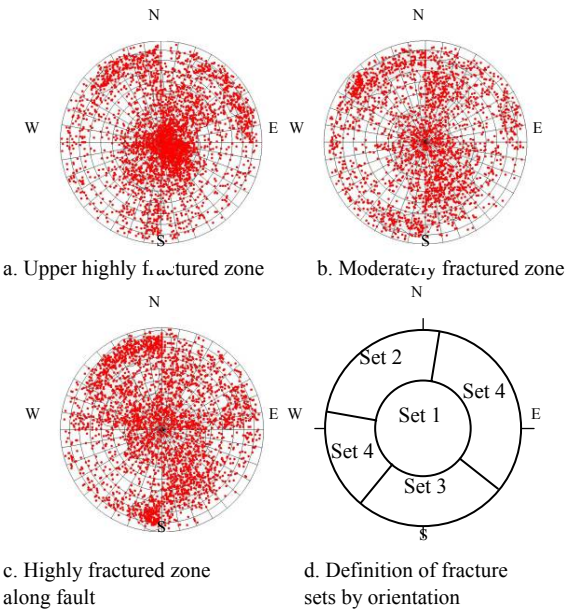

Figure 5. Lower hemisphere stereonet projection for three fracture zones.

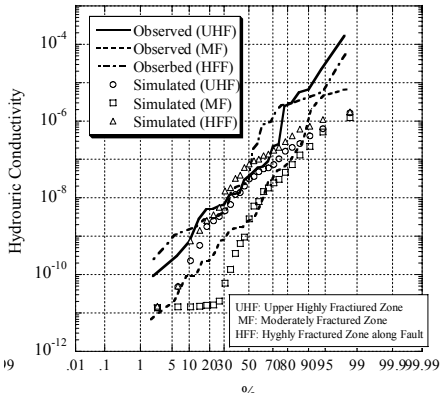

Figure 6. Cumulative plot of hydraulic conductivity and results of VWIT.

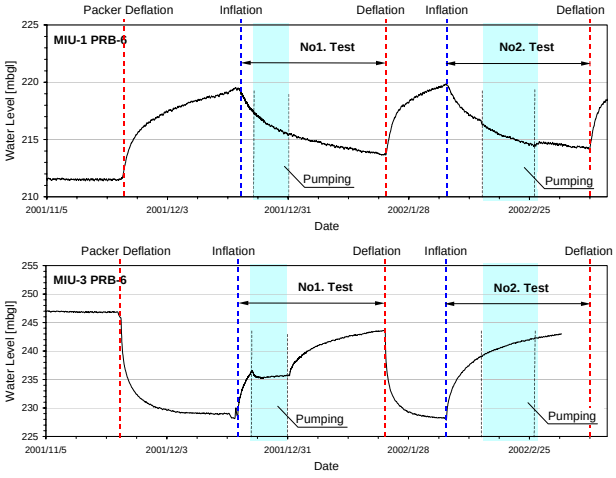

Figure 7. Examples of pressure responses used for model calibration.

Boundary Conditions

Various type of boundary conditions have been tried to reproduce the observed pore pressure. Typical boundary conditions are as follows;

1. Ground surface: a prescribed head boundary
2. Bottom: no-flow boundary
3. Sides: no-flow boundary, except for the river, where a constant-head condition is applied

Regional Groundwater Simulation

Regional scale groundwater simulation was conducted in two stages. A series of steady-state flow calculations were conducted using an EHC for number of different fracture realizations. The purpose of the simulation is to evaluate how much the result in flow calculation, such as flow rate, Darcy velocity, and travel length in the study site will be affected by fracture network realization. The model was then calibrated against the observed hydraulic responses generated by inflating and deflating the packer located at the core zone of Tsukiyoshi fault[3)]. Figure 7 shows the example of the responses. Since the Tsukiyoshi fault is considered to be acting as a barrier separating two hydraulic units, the pressure responses were clearly detected even at boreholes 300m away from the source well, MIU-2. Through the calibration process, the original model was reevaluated and a “best estimate” of the hydraulic properties was determined.

Simulation Results

Figure 8 shows an example of the hydraulic head distribution obtained for a fracture network realization. Figure 9 shows the histogram of the calculated Darcy velocity in Toki granite. Despite rather smooth profile in head distribution, Darcy velocity ranges over several orders of magnitude, reflecting a significant heterogeneity in flow though fractured granite. Figure 10 shows the trajectories of a particle, released from a point at 500m below the ground surface, for ten realization of fracture network. It is recognized that, even though the same probability functions is used for fracture generation, a particle can reach different point suggesting an uncertainty associated with the predicted flow paths.

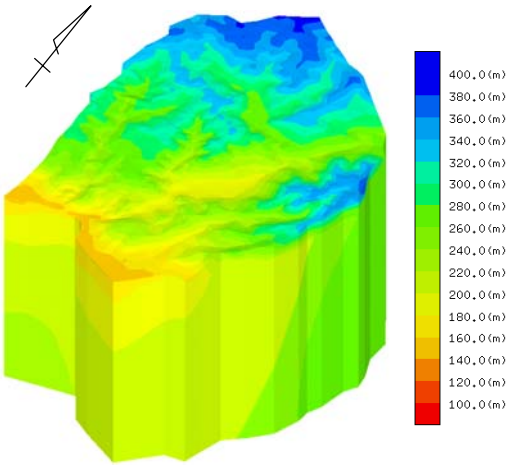

Figure 8. Hydraulic head distribution.

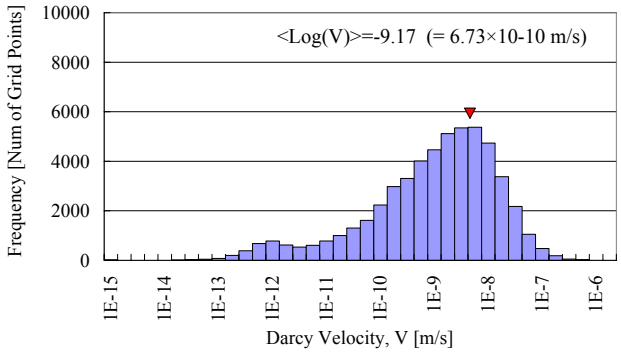

Figure 9. Distribution of calculated Darcy velocity within Toki Granite.

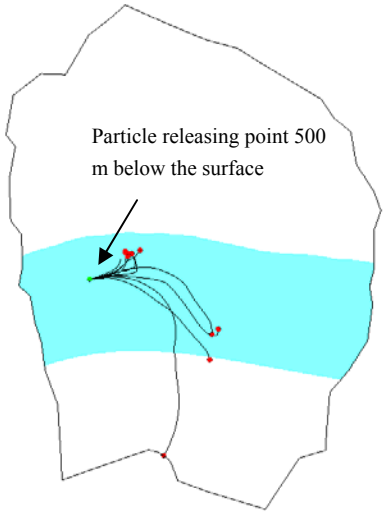

Figure 10 Particle trajectories from a releasing point for ten different fracture generations.

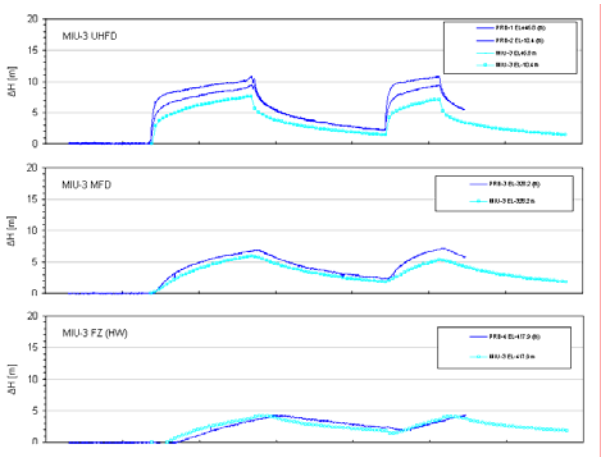

Figure 11 Example of comparison of pressure responses between model and observation.

Figure 11 shows an example of responses obtained by calibrated EHC model for the MIU site. Highly conductive horizontal fracture in the upper fractured zone was added to the original model. Without adding this feature, it was impossible to explain quick responses observed at several monitoring sections at neighboring borehole. Geologists suggested the possibility of the existing sheeting joints at the upper fractured zone. Open fractures were observed by borehole TV, however, its extension was not clear before this study.

Average hydraulic conductivity at several fractured zones was “tuned” so that the peaks and the magnitudes of the hydraulic responses at the monitoring holes can be reproduced reasonably well

by the model. The biggest change in hydraulic conductivity was that of Footwall of Tsukiyoshi fault, where the hydraulic conductivity of the fractured zone was increased by an order of magnitude.

As shown in Figure 12, the predicted flow paths within the study area were drastically changed by updating the hydraulic conductivity. Because of higher contrast between moderately fractured Toki Granite and the fractured zone beneath the Tsukiyoshi fault, the particles released from northern part of the site directly reach the nearest point in the fractured zone and move upward to the surface.

Figure 13 shows the comparison between the calculated and observed pore pressure. It is recognized that calibrated model can reproduce the observation much better than pre-calibration model.

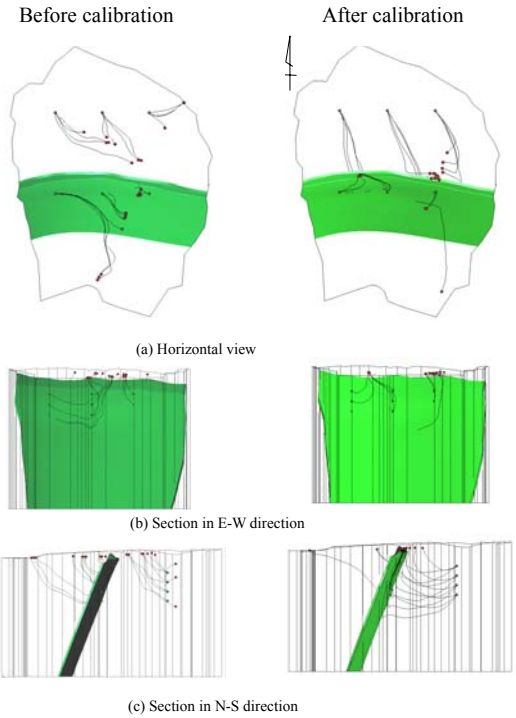

Figure 12. Comparison of particle movement before and after calibrating the model.

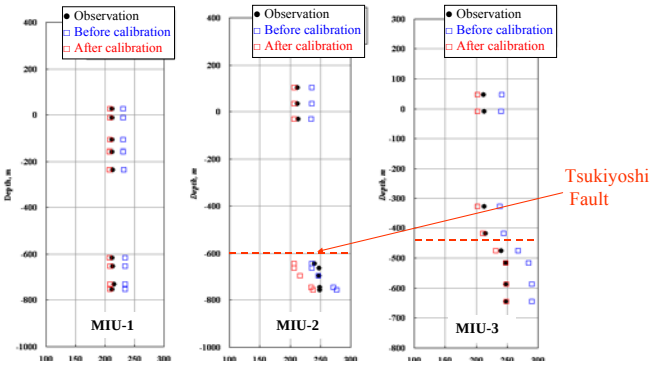

Figure 13. Comparison of pore pressure profile before and after calibrating the model.

Conclusions

EHCM approach was applied to modeling of regional ground water flow in fractured granitic rock.

It was shown that the EHCM approach can create a heterogeneous model reflecting geometrical and hydraulic properties of the fractures.

It was also learned that the transient data such as pressure responses is highly useful to increase the reliability of the prediction results.

References

[1] Shimo, M., and H. Yamamoto, Groundwater Flow Simulation for Fractured Rocks using an Equivalent Heterogeneous Continuum Model, Taisei Corporation Annual Report, pp.257-262, 1996.

[2] Shimo, M., H. Yamamoto, H. Matsui, and T. Senba, Groundwater Flow Simulation around Kamaishi Underground Test Site using an Equivalent Heterogeneous Continuum Model, The 28-th Japanese Rock Mechanics Symposium, pp.278-282, 1997.

[3] Takeuchi, S., M. Shimo, N. Nishijima, and K. Goto, Investigation of the Hydraulic Properties near the Fault by Pressure Interference Test using the 1000 m Depth Boreholes, The 31-th Japanese Rock Mechanics Symposium, pp.296-300, 2001.

On Damage Propagation in a Soft Low-Permeability Formation

D.B. Silin[1], T.W. Patzek2, and G.I. Barenblatt3
1Earth Sciences Division Lawrence Berkeley National Laboratory;
2Civil and Environmental Engineering University of California Berkeley, and Earth Sciences Division; Lawrence Berkeley National Laboratory
3Department of Mathematics, University of California Berkeley, and Computing Sciences, Mathematics Department Lawrence Berkeley National Laboratory

Introduction

We have developed a mathematical model of fluid flow with changing formation properties. Modification of the formation permeability is caused by the development of a connected system of fractures. As fluids are injected or withdrawn from the reservoir, the balance between the pore pressure and the geostatic formation stresses ceases to hold. If the rock strength is insufficient to accommodate such an imbalance, the cement bonds between the rock grains break. This process is called *rock damage propagation*. The micromechanics and the basic mathematical model of damage propagation have been studied in [7]. The rock damage theory was further developed in [3], where a new nonlocal damage propagation model was studied. In [2] this theory was enhanced by incorporation of the coupling between damage propagation and fluid flow. As described above, the forced fluid flow causes changes in the rock properties, including the absolute permeability. At the same time, changing permeability facilitates fluid flow and, therefore, enhances damage propagation.

One of the principal concepts introduced in [2,3] is the characterization of damage by a dimensionless ratio of the number of broken bonds to the number of bonds in pristine rock. It turns out that the resulting mathematical model consists of a system of two nonlinear parabolic equations.

As shown in [6], by modeling the micromechanical properties of sedimentary rocks, at increasing stress the broken bonds coalesce into a system of cracks surrounding practically intact matrix blocks. These blocks have a characteristic size and regular geometry. The initial microcracks expand, interact with each other, coalesce and form bigger fractures, and so forth. Therefore, as rock damage accumulates, a growing system of connected fractures determines the permeability of the reservoir rock.

Significant oil deposits are stored in low-permeability soft rock reservoirs such as shales, chalks, and diatomites [9,10]. The permeability of the pristine formation matrix in these reservoirs is so low that oil production was impossible until hydraulic fracturing was applied. For the development of correct production policy, one should adequately understand and predict how fast and to what extent the initial damage induced by drilling and hydrofracturing will propagate into the reservoir.

The importance of fractures for rock flow properties is a well-established and recognized fact [4,9,5]. Different conceptual models have been developed [8]. In this study, we propose a damage propagation model based on a combination of the model of double-porosity and double-permeability medium [4] and a modification of the model of damage propagation developed in [2].

The Model

One of the basic assumptions of the dual porosity model proposed in [4] (see also [1]), states that the pore space in many natural rocks can be split into two categories. The first category consists of the "classical" pore matrix, where the pores are the openings between the grains. Bigger openings, "pore bodies," are connected by narrow channels, "pore throats." The geometry, connectivity, and the pore sizes determine the porosity and the permeability of the rock. The rock consists of matrix blocks surrounded by fractures. Fractures are the regions where the bonds between the grains are broken and the broken links coalesce into two-dimensional structures. The length scales of fractures can vary widely. However, due to small apertures, the total volume of the fractures is small compared with the volume of the matrix pores. At the same time, the geometry of fractures is simpler than that of matrix pore channels; therefore, if a pressure gradient is applied, the fractures transport the fluids much more easily than the matrix. Consequently, the fluid in the matrix blocks first flows into the bounding fractures, after which it can be transported away through the connected system of fractures. Thus, the matrix blocks support the fluid storage capability of the rock, whereas the system of fractures determines the permeability.

Often, the fracture permeability is an anisotropic parameter, i.e., the Darcy velocity is not necessarily aligned with the pressure gradient [9,10]. For simplicity, in this study we assume that the difference between the eigenvalues of the permeability tensor can be neglected, and the fracture permeability coefficient k_f is a scalar quantity.

Further, we assume that both the matrix blocks and the connected fractures are intertwined in a representative elementary volume. Therefore, at each point of the rock both conductive fractures and matrix are present simultaneously. The fluid pressure in the matrix blocks, p_m, can be different from fluid pressure in the fractures, p_f. At every point of this dual medium, the difference between these two pressures defines the rate of the cross-flow between the matrix and fractures, q. Using dimensional considerations, it has been obtained in [4] that

$$q = \alpha \frac{p_m - p_f}{\mu} \tag{1}$$

where μ is the fluid viscosity. The dimensionless coefficient α depends on the characteristic length L associated with the matrix blocks, on the permeability of the matrix k_m, and on the geometric structure of matrix-fracture configuration. In a homogeneous reservoir, the elastic-drive equation for fluid pressure in the fractures, p_f, has the following form [4]

$$\frac{\partial p_f}{\partial t} - A\frac{\partial}{\partial t}\left(\frac{1}{\alpha}\nabla\cdot\left(k_f(\alpha)\nabla p_f\right)\right) = B\nabla\cdot\left(k_f(\alpha)\nabla p_f\right) \tag{2}$$

where

$$A = \frac{\beta_{mm} + \beta}{\beta_{mm} + \beta - \beta_{fm}} \tag{3}$$

and

$$B = \frac{1}{\phi_m \mu (\beta_{mm} + \beta - \beta_{fm})} \tag{4}$$

Here the coefficient β_{fm} characterizes the decrease of matrix porosity when the pressure in the surrounding fractures increases and coefficient β_{mm} characterizes the pore space expansion at increasing pore pressure in the matrix. Finally, β is the fluid compressibility. A similar equation can be obtained for the matrix pressure p_m. One can show that these two pressures are related by the following equation:

$$\begin{aligned} p_m \quad = \quad & e^{-\frac{B}{A}\int_0^t \alpha d\tau} \left[p_m\big|_{t=0} - \left(1 - \frac{1}{A}\right) p_f\big|_{t=0} \right] \\ & + \left(1 - \frac{1}{A}\right) p_f + \frac{B}{A^2} \int_0^t e^{-\frac{B}{A}\int_\tau^t \alpha d\xi} \alpha p_f d\tau \end{aligned} \tag{5}$$

In particular, if initially both fluid pressures were equal to the reservoir pressure p_r, then

$$p_m = \frac{1}{A} e^{-\frac{B}{A}\int_0^t \alpha d\tau} p_r + \left(1 - \frac{1}{A}\right) p_f + \frac{B}{A^2} \int_0^t e^{-\frac{B}{A}\int_\tau^t \alpha d\xi} \alpha p_f d\tau \tag{6}$$

Damage accumulation is the increase in the number of broken bonds between rock grains. To quantify the rock damage, it was proposed in [3] to use the ratio of the number of broken bonds and the number of bonds in pristine rock, ω. Since the rock flow properties are determined by a connected system of fractures, it is natural to replace the parameter ω with coefficient α introduced in Equation (1). In fact, the coefficient α is a function of ω. By virtue of Equation (1), an increase of α results in a faster equilibration between the fracture and matrix pressures.

Further weakening of the skeleton due to damage accumulation may result in a significant rearrangement and collapse of the matrix blocks that may lead to even more significant permeability changes. In this study, we consider the stage where such a collapse does not occur and both coefficients of fracture permeability k_f and matrix-fracture cross-flow α remain monotonically increasing functions of the damage parameter ω. Therefore, we assume a one-to-one correspondence between the two and parameter ω can be eliminated. In other words, the coefficients k_f and α are the damage parameters. We select α as the basic damage parameter and express the fracture permeability as the dependent variable:

$$k_f = k_f(\alpha) \tag{7}$$

We remark that the parameter ω is not available from direct measurement, whereas both coefficients α and k_f can be determined, for instance, from a well test. Using the one-to-one correspondence between ω and α, the damage accumulation model [3] can be reformulated in terms of parameter α. Therefore, we obtain:

$$\frac{\partial \alpha}{\partial t} = G(\alpha)\nabla \cdot (D_\alpha(\omega, p_m)\nabla \alpha) + F_\alpha(\alpha, p_m) \tag{8}$$

Here

$$G(\alpha) = \frac{1}{\omega'(\alpha)} \tag{9}$$

Function G characterizes how the increasing number of broken bonds affect the cross-flow coefficient α. Function D characterizes the spacial correlation between local damage accumulation at different locations. Finally, function F determines the rate of damage accumulation at changing pore pressure. All three functions have to be determined from experiment.

To make the model complete, the differential equations must be complemented by initial and boundary conditions. To formulate these conditions, we need to analyze the dependence of the fracture permeability on the cross-flow factor α.

Let us start with initial conditions by assuming that the permeability of pristine rock is practically zero. If the rock is intact, the matrix blocks are large and the coefficient α is close to zero. At the same time, both the density and connectedness of the fracture system are scarce and therefore we can assume that

$$k_f(0) \approx 0 \tag{10}$$

Moreover, at steady-state conditions, the pressures do not change; therefore, the pressures p_m and p_f are equal. Hence, we obtain the following initial condition

$$p_f\big|_{t=0} = p_m\big|_{t=0} = p_r \tag{11}$$

where p_r is the initial reservoir pressure.

Inasmuch as the pristine formation has a sparse system of fractures, the initial condition for the damage parameter can be formulated in the following way

$$\alpha\big|_{t=0} = \alpha_* \tag{12}$$

Now, let us proceed with the boundary conditions. At infinity, the reservoir is intact:

$$\lim_{x^2+y^2\to\infty} p_f = \lim_{x^2+y^2\to\infty} p_m = p_r \tag{13}$$

$$\lim_{x^2+y^2\to\infty} \alpha = \alpha_* \tag{14}$$

It is known [1], that if the damage is initially localized in a finite zone, say, near a wellbore or a hydrofracture, then in many cases the solutions to quasi-linear parabolic equations like Equations (2) and (8) have a finite speed of propagation. The model can be formulated as a *free-boundary* problem.

Equations (2) and (8) are coupled. The structure of the solution needs to be determined from further analysis and numerical simulations.

References

[1] G. I. Barenblatt, V. M. Entov, and V. M. Ryzhik, *Theory of fluid flows through natural rocks*, Kluwer Academic Publishers, Dordrecht, 1990.

[2] G. I. Barenblatt, T. W. Patzek, V. M. Prostokishin, and D. B. Silin, *SPE75230 oil deposits in diatomites: a new challenge for subterranean mechanics*, Thirteenth SPE/DOE Symposium on Improved Oil Recovery (Tulsa, OK), SPE, 2002.

[3] G. I. Barenblatt and V. M. Prostokishin, *A mathematical model of damage accumulation taking into account microstructural effects*, European Journal of Applied Mathematics **4** (1993), 225–240.

[4] G. I. Barenblatt, I. P. Zheltov, and I. N. Kochina, *Basic concepts in the theory of seepage of homogeneous liquids in fissured rocks*, Applied Mathematics and Mechanics **24** (1960), no. 5, 1286–1303.

[5] A. C. Gringarten and P. A. Witherspoon, *A method of analyzing pump test data from fractured aquifers*, Int. Soc. Rock Mechanics and Int. Assoc. Eng. Geol., Proc. Symp. Rock Mechanics (Stuttgart, Germany), vol. 3-B, 1972, pp. 1–9.

[6] G. Jin, T. W. Patzek, and D. B. Silin, *SPE83587 physics-based reconstruction of sedimentary rocks*, SPE Western Regional Meeting (Long Beach, CA), SPE, 2003.

[7] L. M. Kachanov, *On the life-time under creep conditions*, Izvestia of USSR Academy of Sciences. Technical Sciences (1958), no. 8, 26–31.

[8] K. Pruess, B. Faybishenko, and G. S. Bodvarsson, *Alternative concepts and approaches for modeling flow and transport in thick unsaturated zones of fractured rocks*, Journal of Contaminant Hydrology **38** (1999), no. 1-3, 281–322.

[9] E. S. Romm, *Filtration properties of fractured rocks*, Nedra, Moscow, 1966.

[10] T. D. van Golf-Racht, *Fundamentals of fractured reservoir engineering*, Elsevier Scientific Publishing Company, Amsterdam, 1982.

Improved Estimation of the Activity Range of Particles: The Influence of Water Flow through Fracture-Matrix Interface

Lehua Pan, Yongkoo Seol and Gudmundur S. Bodvarsson
Earth Sciences Division, Lawrence Berkeley National Laboratory, Berkeley, CA 94720, USA

In a previous paper (Pan and Bodvarsson, 2002), the concept of particle activity range was introduced within the framework of the dual-continuum random-walk particle tracking approach. This enhanced particle tracking method was shown, through comparison to analytical solutions, to accurately simulate transport within the fracture-matrix system. This method is attractive because it can achieve high accuracy in simulating mass transfer through the fracture-matrix interface, without using additional matrix gridcells (thus maintaining optimum efficiency) and without requiring a passive matrix (thus being applicable to cases where global water flow exists in both continua). Although included in the scheme, the effect on activity range of water flow through the fracture-matrix interface (f-m water flow) had not yet been tested, because the test cases, for which analytical solutions exist, do not have both f-m water flow and global flow within the matrix. However, for transport in the variably saturated fractured porous media, both f-m water flow and global matrix flow could be significant. The objectives of this study are (1) to investigate the influence of the fracture-matrix water flow on the activity range and (2) to develop improved schemes for calculating the activity range. The improved particle-tracking model will be verified against analytical solutions and a multiple-continuum numerical model (MINC).

The approach proposed by Pan and Bodvarsson (2002) was based on the fact that particle penetration is confined within a certain range in the matrix, depending on the time elapsed since the pulse of particles was injected. Such a range is its activity range, which is a function of the particle's "age", t_p. Therefore, two key parameters, the characteristic distance S_{fm} and the matrix volume V_m, should be replaced (in calculating the particle transfer probability in the dual-continuum particle tracking method) with the effective characteristic distance $S_{fm}(t_p)$ and the effective matrix volume $V_m(t_p)$, respectively. These parameters are related to the activity range in the following manner:

$$S_{fm}(t_p) = S_{fm}\frac{B^*(t_p)}{B} \tag{1a}$$

$$V_m(t_p) = V_m\frac{B^*(t_p)}{B} \tag{1b}$$

where $B^*(t_p)$ is the activity range, the value of which varies from 0 to B, the maximum activity range (e.g., one-half the fracture spacing for a system of parallel-plate fractures separated by porous rock). Based on the analytical solutions of the one-dimensional diffusion process, Pan and Bodvarsson (2002) found that the activity range is proportional to the square root of t_p if no water flow through the fracture-matrix interface occurs:

$$B^*(t_p) = \min\left(\alpha\sqrt{4D_m t_p/R_m}\, W(t_p), B\right) \tag{2}$$

where the weighting function $W(t_p)$ in (2) was used to account for the secondary effects of the neighboring fractures on the expansion of the activity range. The parameters α, D_m, and R_m are the empirical coefficient, the effective matrix diffusion coefficient, and the retardation factor in the matrix, respectively. The effect that water flow through the fracture-matrix interface has on the activity range was simply accounted for by assuming a constant velocity from the fracture-matrix interface into the rock matrix (Pan and Bodvarsson, 2002). As a result, the final formula for calculating the activity range was defined as follows:

$$B^*(t_p) = \min\left(\alpha \sqrt{4 D_m t_p / R_m}\, W(t_p) + \text{sign}(q_{fm}) \min\left(\frac{|q_{fm}|\, t_p}{\theta_m}, 2b \right), B \right) \quad (3)$$

where 2b is the effective fracture aperture, θ_m is the volumetric water content in the matrix, and q_{fm} is the water flux at the interface. Equation (3) implies that the activity range B^* as a function of t_p is a simple sum of two components, the diffusion term and the advection term. However, this may not be correct, because: (1) the water velocity is not constant away from the fracture-matrix interface (e.g., it becomes zero at the middle point between two parallel fracture planes); and (2) the f-m water flow will interact with the global matrix water flow. As a result, the expansion of the activity range could be very complex if significant f-m water flow exists. Rigorously deriving such a relationship is actually beyond the capabilities of the dual-continuum approach for modeling transport in fractured porous media. This is why Equation (3) limits the influence of the f-m water flow within the confined range of 2b.

Fortunately, the purpose of calculating the activity range is not to describe the details of particle distribution within the matrix block. Instead, it is used to improve the accuracy of calculating the particle transfer probability of particles between the fractures and the matrix. Furthermore, in the dual-continuum model, the fracture-matrix connection actually constitutes the fourth dimension of a 4-D space. Therefore, we can focus on the first problem mentioned above (varying water velocity away from the f-m interface). Because there is no closed-form analytical solution available for the cases with variable water flux, we start with the previously used analytical solution with constant water flux (Pan and Bodvarsson, 2002) and take it as a good approximation. A new cross-interaction term is introduced to account for the effects of the varying f-m water flow on the activity range. As a result, we propose the following schemes to calculate the activity range:

$$B^*(t_p) = \min\left(\sqrt{(\alpha^2 + \frac{q_{fm} t_p}{\theta_m B}) 4 D_m t_p / R_m}\, W(t_p) + \frac{q_{fm} t_p}{\theta_m}, B \right) \quad (4)$$

This new scheme (4) includes a term that represents the influence of the f-m water flow on the f-m diffusion process. Quantitatively, the term $(-q_{fm}/\theta_m B)$ is the gradient of the f-m water velocity (assuming the velocity is linearly distributed and zero in the middle of the matrix).

Both Schemes (3) and (4) were tested against the analytical solution for solute transport in fractured porous media with parallel fractures (derived by Sudicky and Friend [1982]. Because

no water flow occurs through the fracture-matrix interface in this case, as expected, both methods [i.e., dual-continuum particle tracker [DCPT] with Equation (3) and DCPT with Equation (4) in Figure 1] predict breakthrough curves that are almost identical to the analytical solution.

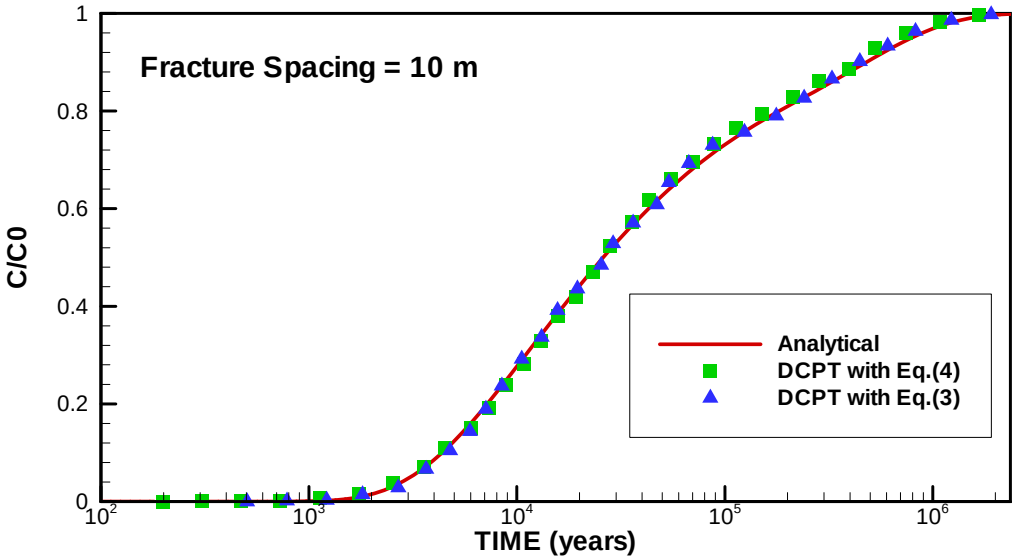

Figure 1. Comparison of particle-tracking methods against the analytical solution (no water flow through the fracture-matrix interface.

The second test case considered a vertical column consisting of multiple layers of tuffs. A conservative tracer was released in the middle elevation of the column, and the cumulative mass breakthrough at the bottom was simulated. The water flow was steady state, and significant water flow through the fracture-matrix interface occurred. Because no analytical solution is available for this case, the multiple interactive continuum (MINC) (Pruess and Narasimhan, 1985) numerical model was considered to be accurate, since it uses multiple matrix grid cells to capture the detailed processes within the matrix. The numerical code T2R3D (Wu and Pruess, 2000), was used to perform the simulations. Ten matrix cells per each fracture cell were used in the MINC model. A dual-permeability (2k) model (one matrix cell per each fracture cell) was also included as a reference. In this comparison, the same steady state flow field was used in all simulations.

As shown in Figure 2, although the particle tracker with the previous scheme [Equation (3)] effectively solved the early breakthrough problem associated with the conventional dual-continuum model (e.g., T2R3D-2k), it does not compare well with the MINC model (e.g., T2R3D-MINC). Especially at late time, it may be even more inaccurate than the conventional dual-continuum model when significant water flow occurs through the fracture-matrix interface. On the other hand, the particle tracker with the new proposed scheme [Equation (4)] predicts breakthrough curves that are almost identical to the MINC model (Figure 2). In other words, the particle tracker with the new scheme can attain accuracy similar to the MINC model in

predicting the breakthrough curves, but without using MINC's additional matrix gridcells (9 in this case), provided that the flow fields are the same.

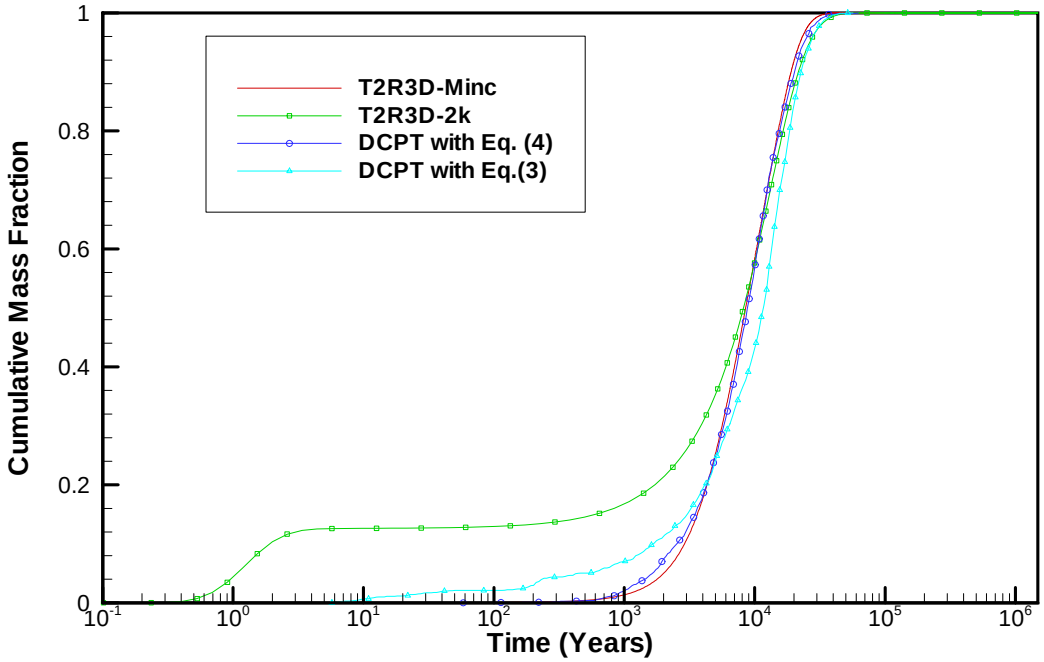

Figure 2. Comparison of particle tracking methods against the MINC numerical models (with significant water flow through the fracture-matrix interface).

References

Pan, L., and G. S. Bodvarsson, Modeling transport in fractured porous media with the random-walk particle method: The transient activity range and the particle transfer probability. Water Resources Research, 38(6):1029-1037, 2002.

Pruess, K., and T. N. Narasimhan, A practical method for modeling fluid and heat flow in fractured porous media. Soc. Pet. Eng. J. 25:14-26, 1985.

Sudicky, E. A., and E. O. Frind, Contaminant transport in fractured porous media: Analytical solutions for a system of parallel fractures, Water Resources Research, 18:1634-1642, 1982.

Wu, Y. S., and K. Pruess, Numerical simulation of non-isothermal multiphase tracer transport in heterogeneous fractured porous media. Advances in Water Resources. 23:669-723, 2000.

Comparison between Dual and Multiple Continua Representations of Nonisothermal Processes in the Repository Proposed for Yucca Mountain, Nevada

Scott Painter
Center for Nuclear Waste Regulatory Analyses
Southwest Research Institute
San Antonio Texas

Introduction

Numerical simulation of nonisothermal, multiphase flow and associated reactive transport in fractured rock is an important tool for understanding geothermal systems, certain petroleum extraction processes, and, more recently, the behavior of potential geological repositories for high-level nuclear waste. A variety of approaches is available, depending on how interactions between the fractures and matrix are modeled, and whether the fracture system is treated as an effective continuum or as a collection of discrete fractures. In studies of a potential high-level waste repository at Yucca Mountain, Nevada, a dual-continuum representation has emerged as the standard approach for modeling processes in the unsaturated zone near emplacement tunnels (e.g., Wu and Pruess, 2000). In the dual-continuum representation, the fracture network is modeled as an effective continuum that interacts with a second continuum representing the matrix system. Contemporary incarnations of the dual-continuum approach have roots in the classical double-porosity models, but are more general in that coupled multiphase flow, heat transport, and solute transport are included. The primary motivation for the approach is to represent both the rapid response of the small-volume fractures and the slower response of the matrix system.

The chief limitation of the dual-continuum representation is that it neglects any gradients within a matrix block. The more general (and arguably more rigorous) multiple interacting continua (MINC) representation (Pruess and Narasimhan, 1985) allows for gradients in pressures, temperature, and concentrations in the vicinity of fractures. The essence of the MINC approach is that changes in fluid conditions will propagate more slowly in tight matrix blocks compared with the smaller volume fractures, an effect that causes local conditions in the matrix to be controlled by the proximity to a fracture. This phenomenology is captured in the MINC model by using several interacting continua to represent the matrix; all matrix material within a certain distance range from the fracture is lumped into one of the matrix continua. The dual-continuum model (DCM) is the special MINC case with only one matrix continuum. The dual-continuum is understood to be an adequate approximate for steady state or weakly transient systems, but the appropriateness of the approximation is more questionable for strongly transient systems that may have large gradients in the vicinity of fractures. However, few studies comparing the MINC and DCM representations at the field scale are available. In particular, studies specifically addressing the differences between MINC and dual continua representations of processes in a potential high-level waste repository at Yucca Mountain are lacking. Such a comparison is given here. Specifically, MINC and DCM representations of multiphase flow and reactive transport in the strongly heated repository near field are compared.

Model Description

The MULTIFLO code Version 1.5.2 (Lichtner, 1996; Lichtner and Seth, 1996; Painter et al., 2001) is used in this study. MULTIFLO simulates nonisothermal, multiphase flow and multicomponent reactive transport in fractured porous media. It is based on the integrated finite difference method, which allows for fully unstructured grids with arbitrary intercell connectivity. The DCM representation is implemented explicitly. MINC models can be implemented through grid construction. Time stepping is fully implicit with newton iterations to resolve the nonlinearities. The general formulation and underlying mathematical models for the flow code are similar to that of Wu and Pruess (2000).

The two-dimensional computational domain (Figure 1) is a "chimney" type (tall and narrow). The base of the 450-meter high domain is at the water table, about 600 m below the land surface. The emplacement tunnels for the proposed repository are about 300 m above the water table. Horizontally, the domain spans one-half of the tunnel spacing (40.5 m) with no-flow (symmetry) conditions on either side. Flow and heat transport processes within the tunnel are not modeled; instead, the heat emanating from the waste packages is applied as a time-dependent heat flux directly to the tunnel walls.

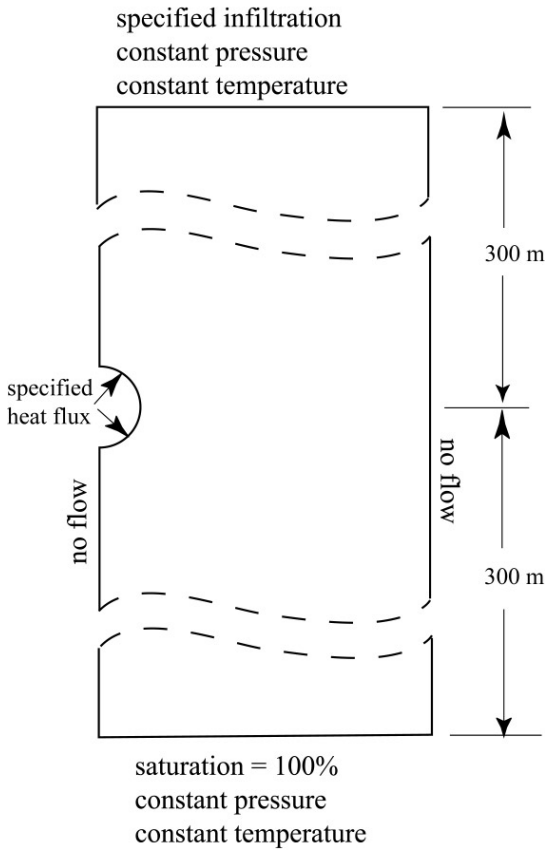

Figure 1. Two-dimensional computational domain (not to scale).

Thermal and hydrological property values for the major stratigraphic units considered in this work were taken from U.S. Department of Energy reports (2000). The model of van Genuchten (1978) is used to relate capillary pressures and liquid saturations. Capillary pressures and relative

permeabilities for the fracture continuum and relative permeability for fracture-to-matrix flow are modified according to the active fracture model (Liu et al., 1998).

In the MINC and DCM approaches, the *primary grid* partitions the physical space into computational cells. Each cell in the primary grid is partitioned in turn by the secondary grid into fracture and matrix continua. The entire collection forms the aggregate or composite grid, which is used in the numerical simulation. The MINC model used here has three matrix continua, resulting in an aggregate grid of size 3N+N=4N. A detail from the primary grid is shown in Figure 2. The unstructured grid is relatively fine in the vicinity of the emplacement tunnels and becomes much coarser away from the strongly heated region. The primary grid contains 690 computational cells.

Initial conditions for the thermal hydrology simulation were established by running an ambient non-heated simulation without the emplacement tunnel. Once this ambient run reached steady state, the computational cells in the tunnel region were removed and the heat turned on. The time-dependent power applied to the tunnel walls is shown in Figure 3. Two scenarios were considered. In the first, the power output of the waste package was reduced by 75% to simulate the effects of forced ventilation during the first 50 years. This scenario is roughly consistent with time- and space-averaged values for ventilation efficiency as calculated from three-dimensional simulations incorporating self-consistent representation of ventilation processes (Painter et al, 2001). However, the ventilation effectiveness is dependent on time and position along the length of the emplacement tunnel. For this reason, a second scenario was considered, in which the power was reduced by 50% during the first 50 years.

Fully coupled reactive transport simulations were also performed. These highly idealized simulations were designed to test the sensitivity to choice of fractured rock conceptual model, and were not intended to provide an accurate representation of the complex geochemical processes. Thus, one generic mineral was used as a proxy for the set of silica minerals present or expected to form at high temperatures near the emplacement tunnels. Other minerals were ignored. The principal phenomenon of interest is possible deposition of silica at the position of a boiling front in the fractured tuff rock.

Results

Liquid saturations in the matrix and fracture continua at the first node above the drift crown are plotted versus time in Figure 4. The heating scenario is the 75% reduction case. For both the MINC and DCM approaches, the liquid saturation decreases strongly at 50 years, corresponding to the end of the ventilation period. At late times (> 1,000 years), the thermal pulse has passed, and the liquid saturation returns to the initial conditions. In the intermediate period (50-1000 years), there are significant differences, with the MINC representation generally predicting dryer conditions. For the matrix system, the liquid saturation never drops below 20% in the DCM simulation, whereas total dryout occurs in the matrix system over the period of 70-150 years in the MINC simulation. Rewetting also occurs earlier in the DCM system. Results for the fracture system are generally similar to the matrix, with rewetting occurring at about 200 years in the dual continua simulation compared with 800 years in the MINC simulation.

Results for the alternative heating scenario of 50% heat reduction are shown in Figure 5. As with the 75% reduction case, significant differences between the MINC and DCM approaches can be seen for limited times. In the case of the 50% reduction, large differences in saturation occur during the first 50 years and also in the rewetting time, again with the MINC approach predicting drier conditions. This difference in saturation is partly due to differences in matrix pressure (right plot in Figure 5). During the strong heating period, the pressure in the matrix blocks increases in both the MINC and DCM approaches. However, matrix pressures decay more slowly in the DCM approach, and this pressure buildup raises the boiling temperature and allows significant liquid to remain in the matrix.

The amount of silica deposited in the fractures is also significantly different between MINC and DCM. In simulation using the 50% heat reduction assumption, small amounts of silica are deposited in the fractures in a limited area about 2-3 meters above the emplacement tunnels. In the DCM simulations, the silica occupies about 6% of the original fracture void space. In the MINC simulation, the fracture void space is reduced by only 2%. In either case, the reduction in porosity is too small to have significant effect on fracture permeability. The results are very insensitive to the actual mineral reaction rate, because the mineral forming reaction is limited by the rate at which aqueous silica is brought to the boiling zone where deposition occurs. It is noted that fracture porosity in the Yucca Mountain region is uncertain, and that smaller values of fracture porosity would result in a larger relative change in fracture porosity and permeability. Nevertheless, the conclusions about the MINC and DCM would remain unchanged.

Conclusions

1. The DCM and MINC representations yield different results for fracture and matrix saturation under strongly heated conditions. However, the differences are significant only when temperatures are close to the nominal boiling temperature for water.

2. The MINC representation produces lower values for matrix and fracture saturation, as well as significantly longer periods of totally dry conditions at the tunnel crown.

3. The DCM predicts about three times as much silica deposition in fractures compared with the MINC representation. In either case, however, the amount of silica deposited is insignificant for the reference conditions considered here.

4. Because the DCM representation results in wetter conditions as compared with the MINC model, the dual continua appears to be a conservative assumption from the perspective of repository performance assessment. However, studies aimed at comparing simulation models with the results of thermal hydrology experiments may benefit from MINC type models.

Acknowledgments

This paper was prepared to document work performed by the Center for Nuclear Waste Regulatory Analyses (CNWRA) for the Nuclear Regulatory Commission (NRC) under Contract No. NRC-02-02-012. The activities reported here were performed on behalf of the NRC Office of Nuclear Material Safety and Safeguards, Division of Waste Management. This paper is an

independent product of the CNWRA and does not necessarily reflect the view or regulatory position of the NRC.

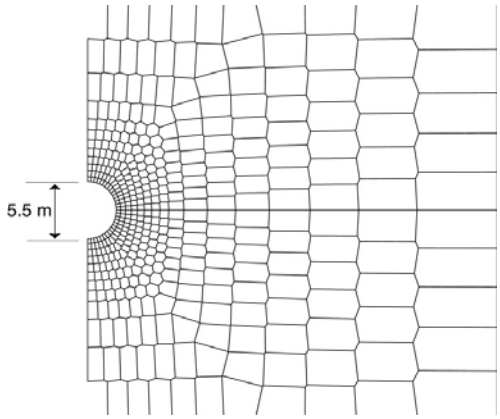

Figure 2. Detail from the primary grid.

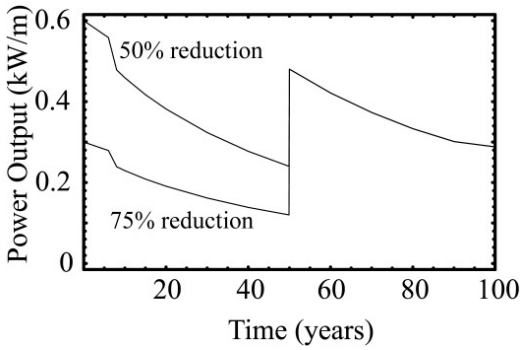

Figure 3. Heat load at the tunnel wall versus time after emplacement for different assumptions about ventilation effectiveness during the 50 year ventilation period.

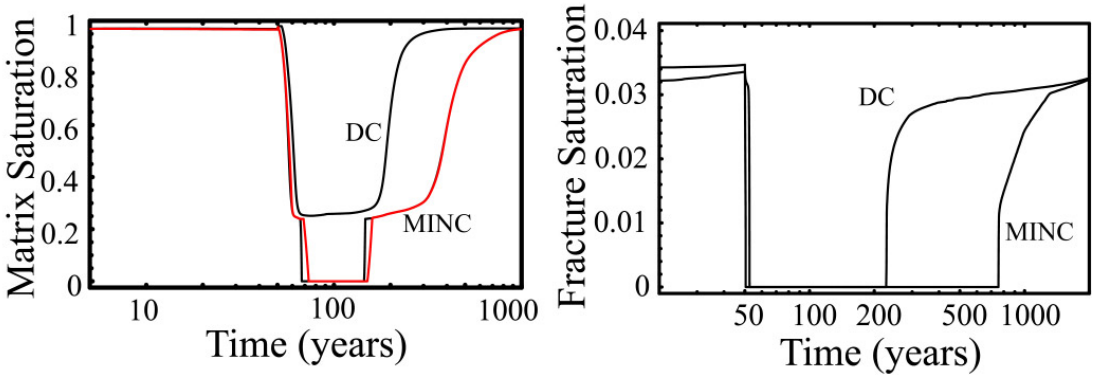

Figure 4. Matrix and fracture saturations at the tunnel crown versus time for dual continua (DC) and MINC representations. The heat flux into the rock is reduced by 75% during the first 50 years.

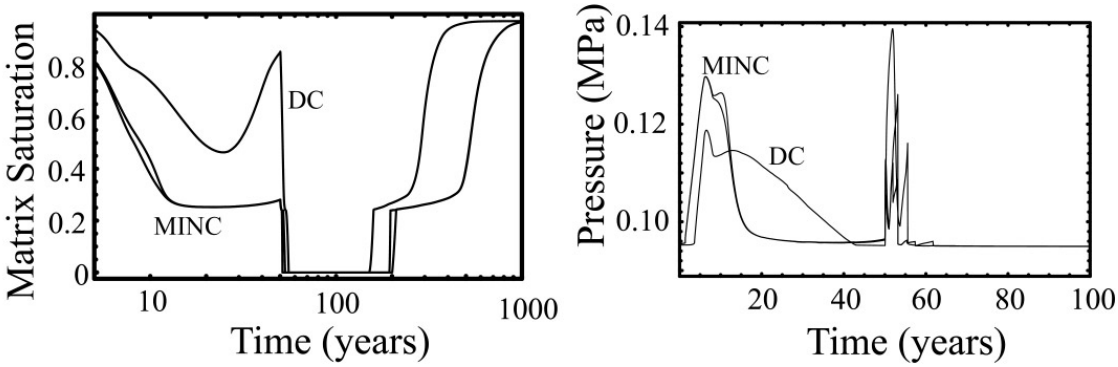

Figure 5. Matrix saturation and pressure at the tunnel crown versus time for dual continua (DC) and MINC representations. The heat flux into the rock is reduced by 50% during the first 50 years.

References

Lichtner, P.C., 1996. Continuum formulation of multicomponent-multiphase reactive transport. In: *Reviews in Mineralogy 34: Reactive Transport in Porous Media*, P.C. Lichtner, C.I. Steefel, and E.H. Oelkers, eds., Mineralogical Society of America, Washington, D.C.

Lichtner, P.C and M Seth, 1996. Multiphase-multicomponent nonisothermal reactive transportin partially saturated porous meda. In: *Proceedings of the International Conference on Deep Geological Disposal of Radioactive Waste*, Canadian Nuclear Society, p 3-133–42.

Liu, H.H., C. Doughty, and G.S. Bodvarsson. 1998. An active fracture model for unsaturated flow and transport in fractured rocks. *Water Resources Research* 34(10), 2633–2646.

Painter, S., Lichtner, P.C. and M. Seth, 2001, *MULTIFLO Version 1.5 User's Manual: Two-Phase Nonisothermal Coupled Thermal-hydrological-chemical Flow Simulator*, Center for Nuclear Waste Regulatory Analyses, San Antonio, Texas.

Painter, S., C. Manepally, and D.L. Hughson, 2001. Evaulation of U.S. Department of Energy Thermohydrological Data and Modeling Status Report, Center for Nuclear Waste Regulatory Analyses, San Antonio, Texas.

Pruess, K and T.N. Narasimhan. 1985 A practical method for modeling fluid and heat flow in fractured porous media. *Soc Pet Eng J* 25, 14–26.

U.S. Department of Energy, Office of Civilian Radioactive Waste Management, 2000, Multiscale thermohydologic model, revision 00. Las Vegas, Nevada.

Van Genuchten, 1978. A closed-form equation for predicting the hydraulic conductivity of unsaturated soils, *Soil Sci. Soc. Am. J*. 44, 892.

Wu, Y-S. and K. Pruess, 2000. Numerical simulation of non-isothermal multiphase tracer transport in heterogeneous fractured porous media, Advances in Water Resources 23, 699–723.

Identification of the Water-Conducting Features and Evaluation of Hydraulic Parameters using Fluid Electric Conductivity Logging

Shinji Takeuchi[1], Michito Shimo[2], Christine Doughty[3], and Chin-Fu Tsang[3]
[1]Mizunami Underground Research Laboratory, Tono Geoscience Center,
Japan Nuclear Cycle Development Institute
[2]Civil engineering Research Institute, Technology Center, Taisei Corporation
[3]Earth Sciences Division, E.O. Lawrence Berkeley National Laboratory, University of California

Summary

Multi-rate fluid electric conductivity logging was performed in a 500 m borehole, (DH-2) located at adjacent to the Mizunami Underground Research Laboratory (MIU) site in Gifu Prefecture, central Japan. The purpose of this activity was to identify water-conducting features (WCFs) of fractured rock in the deep borehole and to evaluate their hydraulic propertiesm such as transmissivity, hydraulic head and electric conductivity (salinity). Nineteen WCFs were identified by logging, and three different pumping rates and hydraulic properties were evaluated with numerical simulation based on the one dimensional advection-diffusion equation. The transmissivity, hydraulic head and electric conductivity (salinity) resulting from the analysis were consistent with observed values.

We propose that FEC logging, combined with analysis, would be an effective, useful method for evaluating hydraulic properties of underground fractured rock.

Introduction

In the groundwater flow model/simulation, in fractured rock, knowledge of the locations of water-conducting features (WCFs) and their hydraulic properties is essential. Such knowledge is obtained using deep boreholes penetrating the fractured rock. Fluid electric conductivity (FEC) logging is effective for determining WCF properties (Tsang, et al., 1990; Doughty and Tsang, 2002) provides a means to determine the hydrological properties of fractures, fracture zones, or other permeable layers intersecting a borehole in saturated rock.

In this method, the borehole water is first replaced by de-ionized water or, alternatively, by water of a constant salinity distinctly different from that of the formation water. This is done by passing the de-ionized water down a tube to the bottom of the borehole at a given rate, while simultaneously pumping from the top of the well at the same rate, for a time period. Next, the well is shut in or pumped from the top at a constant low flow rate (e.g., several liters or tens of liters per minutes), while an electric conductivity probe is lowered into the borehole to scan the fluid electric conductivity (FEC) as a function of depth (Figure 1). With constant pumping conditions, a series of five or six FEC logs are typically obtained over a one- or two-day period. At depth locations where water enters the borehole (the feed points), the FEC logs display peaks. These peaks grow with time and are skewed in the direction of water flow. By analyzing these logs, it is possible to obtain the flow rates and salinities of groundwater inflow from the individual fractures. The method is more accurate than spinner flow meters. Recent development

provides the possibility to determine the initial pressure head levels and relative transmissivity of these fractures, if two or more sets of these logs at different pumping rates are available (Doughty and Tsang, 2002).

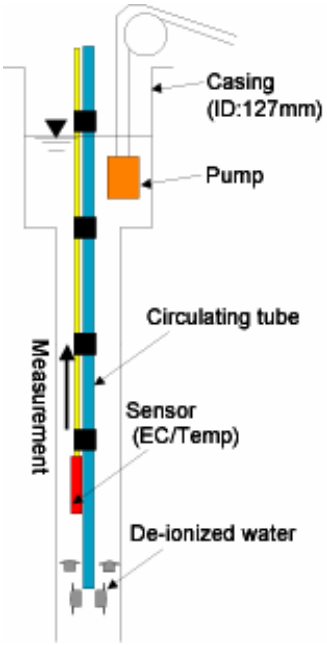

Figure 1. Field logging setup.

The numerical model BORE-II (Doughty and Tsang, 2000) calculate the time evolution of ion concentration (salinity) through the wellbore, given a set of feed-point locations, strengths, and concentrations. Some analytical solutions are available for FEC profiles obtained from simple feed-point configurations (e.g., Drost et al., 1968; Tsang et al. 1990), but BORE-II broadens the range of applicability of such analytical solutions by considering multiple inflow and outflow feed points, isolated and overlapping FEC peaks, early-time and late-time behavior, time-varying feed-point strengths and concentrations, and the interplay of advection and diffusion in the borehole.

FEC logging was conducted at a 500 m depth vertical borehole in the Tono area, central Japan. From the result of the time-evolution of fluid electric conductivity, numerical analysis was carried out for estimating WCFs and their properties, such as transmissivity, hydraulic head, and electric conductivity.

Location and Geological Setting

The 500 m deep borehole (DH-2) is located at outer boundary of the Mizunami Underground Research Laboratory (MIU) site (Figure 2). Cretaceous granite (Toki granite) is overlain mainly by the tertiary sedimentary formation (Mizunami group) around the borehole. five-inch casings are installed at the part of sedimentary formation (depth about 170 m from the top of the borehole). The 98.6 mm borehole is drilled in the granite deeper than the top of the casing. As a

result of the geological investigations, two low angle fracture zone at the section of 200-250 m, three fracture zones at 300-350 m and two fracture zone at 430-46 m were identified (Figure 3).

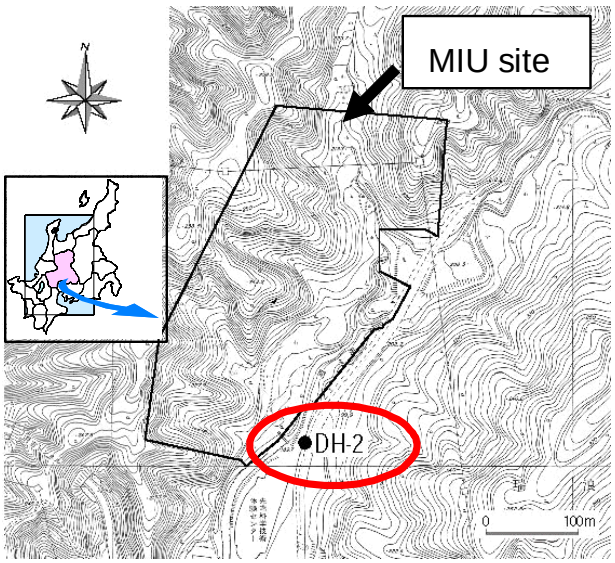

Figure 2. Location of test site.

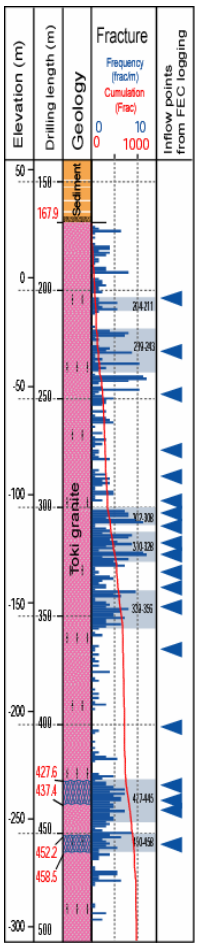

Figure 3. Geological column.

Test and Analysis Results

FEC logging performed at this time replaced borehole water with de-ionized water. Three sets of FEC logs were obtained for three pumping rates Q: Test 1 Q = 10 L/min, Test 2 Q = 20 L/min, Test 3 Q = 5L/min.

For each test, seven FEC logs were measured at one-hour intervals, which pumping maintained at the constant flow rate. An example of the result of the measurement (Test 2) is shown in Figure 4. The numerical analysis for matching with the measurement data was performed using BORE-II. The best match from the observed FEC profiles is shown also in Figure 4.

Nineteen WCFs, over the interval 200-460 m, were identified. These WCFs are located mainly at the fractured zone at 200-250m, 300-350m and 430-460m. Also inflow rates from these WCFs, when the total pumping rates Q are 5, 10 and 20 L/min were calculated. All 19 inflow rates

calculated are different because of their different transmissivity and different initial or far-field pressure heads.

Combined analysis were carried out using the results of Test 2 and Test 3 Q = 20 L/min and 5 L/min, respectively to obtain consistent result during the two tests. The reasoning for using Test 2 and 3 is as follows. First, Test 1 is the first test made and the field operators were still trying to familiarize themselves with the procedure and thus the data may not be as good as the later two tests. Second, Test 2 and Test 3 are the tests with the largest and lowest pumping rates and may thus cover the range of fracture inflow rates more efficiently. For example, the large Q will define better smaller inflows from less conductive fractures, while the smaller Q will define the larger-conductive fractures better.

Figure 5a presents the transmissivity T_i of the each 19 conductive fractures relative to the average transmissivity (T_{avg}) over the entire borehole. The latter can be obtained by a standard well test analysis given the borehole pumping rate and water level decreases. The values of T_i/T_{avg} vary more than one order of magnitude among the 19 fractures. Figure 5a shows WCFs which have higher transmissivity exist at the 200-250m and 300-350m respectively.

Figure 5b presents the initial pressure heads of the 19 conductive fractures obtained by our analysis. It is seen that fractures at depths 300, 320, 340, 360, 400, 430 and 440 m have pressure heads above the mean borehole pressure. This means that at Q = 0, with no pumping of borehole, there will be internal flow in the borehole, with inflows coming in from these fractures.

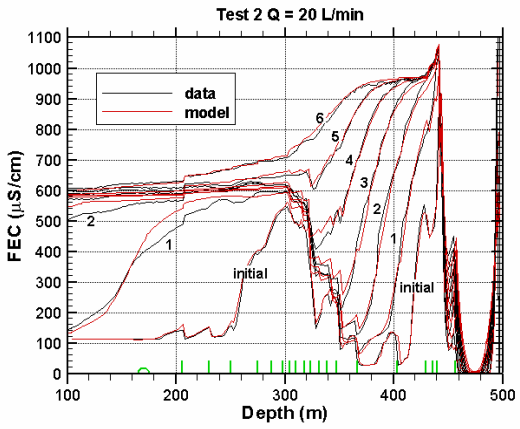

Figure 4. FEC profiles. (The green ticks indicate the feed point locations. The green semi-circle shows where the wellbore diameter changes.)

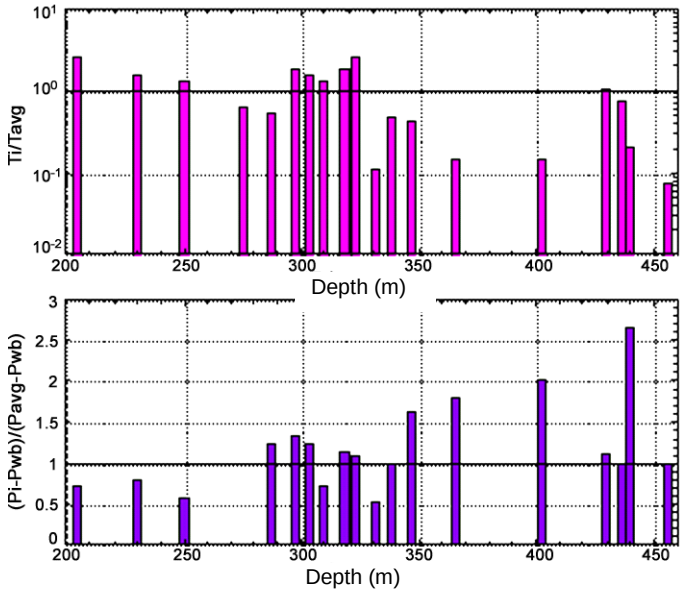

Figure 5. (a) Calculated Ti/Tavg and (b) (Pi-Pwb)/(Pavg-Pwb).

Figure 6 shows the FEC of the water from each of the 19 conductive fractures. There is a general trend of the deeper water being more saline. Independent verifying data were found and plotted as red bars in this figure. These are the FEC values of water samples obtained from different depths. Two horizontal red lines are shown in the figure corresponding to FEC values of the

water samples corrected, or not corrected, for temperature values at the depths they were sampled from. The agreement is quite good, especially for deeper fractures. Generally, since the FEC values from our analyses are those of fracture water, one may expect them to be higher than FEC values of water samples, which may include fracture water mixed with neighboring waters, dependent on sampling methods and conditions.

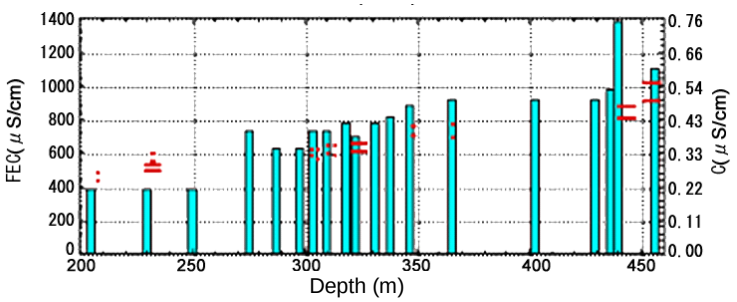

Figure 6. Calculated FEC or salinity. (Red bar indicates measured value.)

Figure 7 present measured transmissivity (Ti) relative to the total transmissivity (Ttot) mainly focused on the WCFs by packer tests and estimated value based on the result of the numerical analysis. Measured transmissivity includes both long and short interval tests. The total transmissivity from measured integral of the longer interval test is aiming to obtain along the whole borehole sections. On the other hand, estimated total transmissivity are calculated based on the relationship between the total drawdown and pumping rate. So both measured and estimated Ttot are almost the same. In conclusion, the estimated transmissivity in each WCF are appropriate.

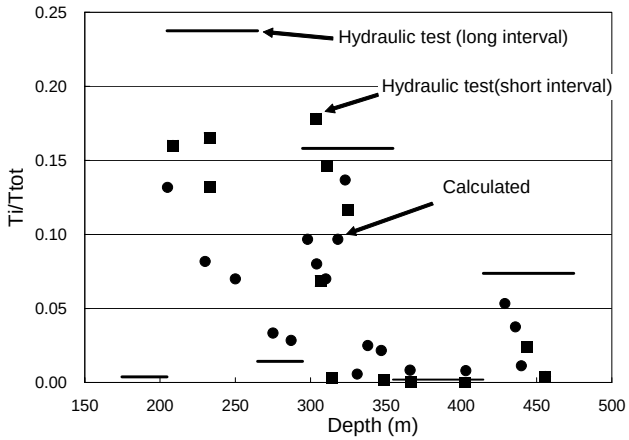

Figure 7. Comparison of transmissivity between observed and calculated.

Conclusion

FEC logging was conducted at 500 m borehole penetrating the granite. Numerical simulation was carried out to be matched with the FEC logs. Based on these techniques, following results were concluded:

1. 19 WCFs were effectively identified,

2. WCF properties such as transmissivity, hydraulic head and electric conductivity calculated with the numerical simulation were consistent with the measured ones.

The FEC logging combined with numerical simulation is the effective method identifying the location and properties of WCFs effectively.

References

1) Christine Doughty and Chin-Fu Tsang: Inflow and outflow signatures in flowing wellbore electrical-conductivity logs, rep. LBNL-51468, Lawrence Berkeley National Laboratory, Berkeley, CA, 2002
2) Chin-Fu Tsang, Peter Hufschmied and Frank V. Hale: Determination of Fracture Inflow parameters with a Borehole Fluid Conductivity Logging Method, Water Resources Research, vol.26, No.4, pp.561-578, 1990
3) Drost, W., Klotz, A. Koch, H. Moser, F. Neumaier, and W. Rauert: Point dilution methods of investigating ground water to flow by means of radioisotopes, Water Resources Research, 4, 125-146, 1968

Observation and Modeling of Unstable Flow during Soil Water Redistribution

Zhi Wang[1], William A. Jury[2], and Atac Tuli
[1] Department of Earth and Environmental Sciences, California State University, Fresno, CA 93740. (zwang@csufresno.edu)
[2] Department of Environmental Science, University of California, Riverside, CA 92521 (wajury@mail.ucr.edu)

Introduction

Our laboratory and field experiments confirmed that unstable (finger) flow forms during redistribution following the cessation of ponded infiltration in porous sand and concrete surfaces under both dry and wet initial conditions. Fingers form and propagate rapidly when the porous media are initially dry, but form more slowly and are larger when the media are wet. The porous medium retained a memory of the fingers formed in the first experiment. A conceptual model is presented to simulate the development of unstable flow during redistribution. The flow instability is caused by a reversal of matric potential gradient behind the leading edge of the wetting front where a high water-entry potential is maintained. This pressure profile inevitably results in the propagation of fingers that drain water from the wetted matrix until equilibrium is reached. The model uses soil retention and hydraulic functions, plus relationships describing finger size and spatial frequency. The model predicts that all soils are unstable during redistribution, but shows that only coarse-textured soils and sediments will form fingers capable of moving appreciable distances. Once it forms, the finger moves downward at a rate governed by the rate of loss of water from the soil matrix, which can be predicted from the hydraulic conductivity function.

Experimental Evidence of Unstable Flow during Redistribution

We continued our investigation on unstable flow in unsaturated soils. The main purpose was to study the effects of soil water redistribution on the occurrence of finger flow after the ponded infiltration. Our lab and field experiments (Wang et al., 2003a,b) confirmed that unstable flow forms during redistribution following the cessation of ponded infiltration in homogeneous sands under both dry and wet initial conditions. Fingers form and propagate rapidly when the sand is dry, but form more slowly and are larger when the sand is wet. A 5 cm water application in a coarse sand resulted in fingers extended more than 100 cm below the surface. The porous medium retained a memory of the fingers formed in the first experiment, so that fingers formed in subsequent redistribution cycles followed the old finger paths, even after 28 days had elapsed. This experimental study has confirmed that unstable flow unavoidably happens during redistribution if it did not happen during the infiltration process. Unstable flow was more often observed during infiltration in layered, water-repellent, or uniform soils due to a variety of *soil reasons* such as fine-over-coarse structure, water-repellency and air-entrapment. Redistribution is a *hydraulic cause* that happens commonly in all soils and fractured rocks.

(a)

(b)

(c)

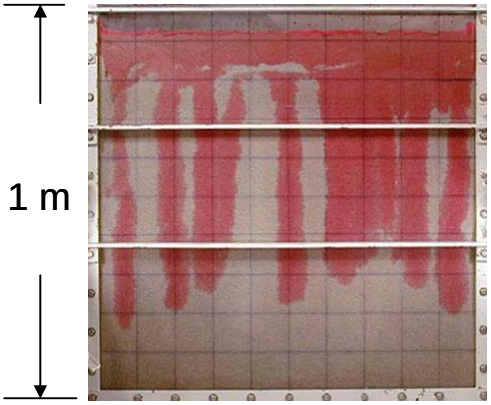

(d)

Figure 1. (a) Fingers formed on a concrete surface during rainfall. (b) 3-D illustration of a finger formed during redistribution in a 10 cm diameter column with transparent walls. The column was frozen after the experiment ended to preserve the shape of the finger. The picture was taken after the column was removed from the freezer and the loose soil that had no water in it fell out. The brown object is, therefore, an ice sculpture with soil sticking to it. (c) Unstable flow patterns formed in field soil during redistribution of irrigation water. (d) Fingers formed during redistribution after a 5 cm water application in a slab chamber.

Prediction of Unstable Flow

A conceptual model (Jury et al., 2003) was developed for predicting the development of unstable flow during redistribution. The flow instability is caused by a reversal of matric potential

gradient behind the leading edge of the wetting front during the transition from ponded infiltration to redistribution. The wetting front is considered to maintain a matric potential at the water-entry value. This pressure profile inevitably results in the propagation of fingers that drain water from the wetted upper matrix until equilibrium is reached. The model uses soil retention and hydraulic functions, plus relationships describing finger size and spatial frequency. The model predicts that all soils are unstable during redistribution, but shows that only coarse-textured soils and sediments will form fingers capable of moving appreciable distances. Once it forms, the finger moves downward at a rate governed by the rate of loss of water from the soil matrix, which can be predicted from the hydraulic conductivity function.

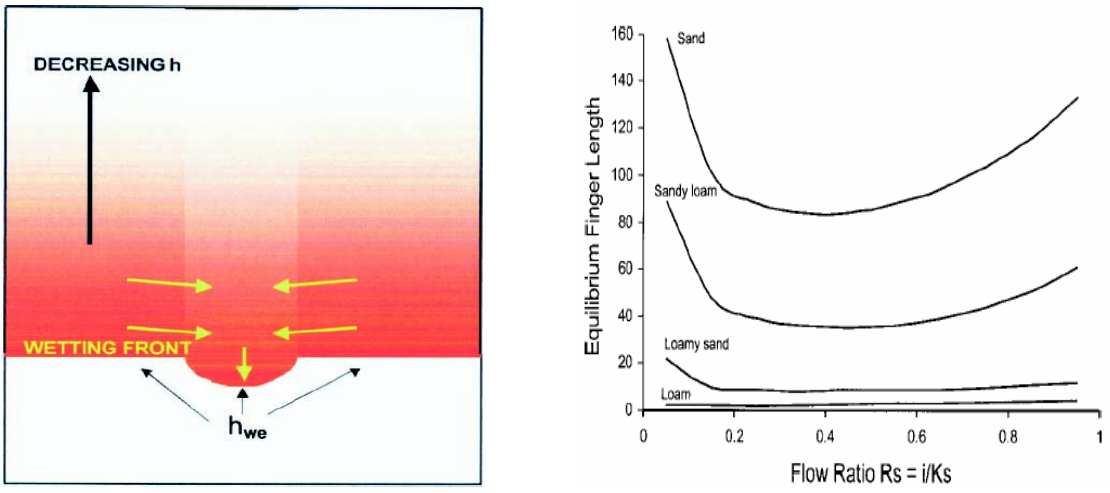

(a) (b)

Figure 2. (a) Development of a fluid instability during redistribution, when the pressure distribution decreases toward the surface. When the front advances ahead at one location, the pressure distribution above it shifts downward, creating a lateral flow gradient from adjacent regions. Darker red color indicates wetter soil at higher matric potential. (b) Equilibrium finger depth reached during redistribution as a function of infiltration rate. Curves were calculated with Equations (6)–(9) in Jury et al. (2003) assuming that 10 cm of soil is initially saturated during ponded infiltration.

The Critical Amount of Infiltration for Unstable Flow during Redistribution

The effect of hysteresis and initial amount of water application on the development of unstable flow was also considered for assessing the initiation of unstable flow (Wang et al., 2004). In this study, we predict that if the initial depth (L) of soil saturated during the ponded infiltration exceeds a critical length of capillarity (S = water-entry potential – air-entry potential), the redistribution flow should become unstable. Otherwise, the flow should remain stable. We further demonstrate that if the matric potential gradient (dh/dz) becomes positive during redistribution, a perturbation at the wetting front will cause finger flow. However, if dh/dz remains negative, the perturbation will be dissipated. A series of point-source and line-source infiltration experiments were conducted using a slab-box filled with uniform sands. The results

confirmed that as soon as the *S* value was exceeded a finger was formed at the bottom of the wetting front, channeling the flow and stopping water movement between the fingers. The implications of this phenomenon for practical irrigation and leaching designs are discussed.

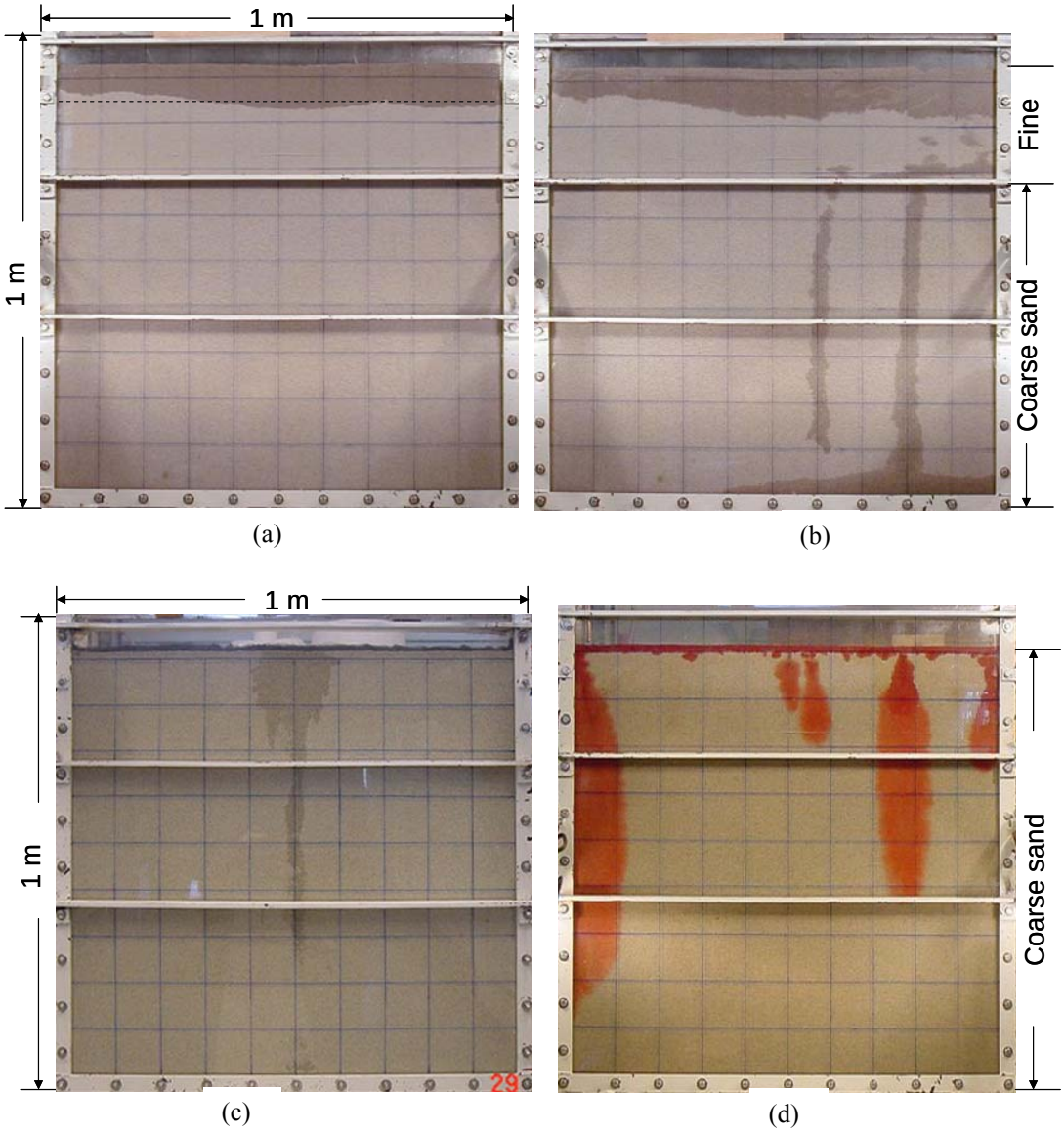

Figure 3. (a) Wetting pattern at the end of infiltration (dashed line shows the critical depth of infiltration). (b) Unstable flow developed during redistribution in a fine sand and extended to a coarse sand. (c) When a point-source application in the coarse sand exceeded the critical depth of wetting, a finger started at the bottom. (d) Finger diameters are relatively small in the drier layer near the soil surface and are larger in the wetter layers in the subsurface.

Conclusions

- Our laboratory experiments have shown that the redistribution process following the cessation of infiltration is unstable in homogeneous soil, producing a series of fingers that move far ahead of the original front. We demonstrated that ponded infiltration is stable and uniform in our system, so that the fingering observed is not due to soil heterogeneity.
- The most critical features of a porous medium that create and maintain fingering are hysteresis, which allow fingers to stay narrow as they advance, and the water entry pressure, which quickly blocks the water in the soil between the fingers from moving downward once fingering begins.
- Redistribution flow in all soils can be unstable, depending on the amount of infiltration (wetted depth L) and the capillary length ($S = h_{we} - h_{ae}$) of the soil.

References

Jury, W.A., Z. Wang, and A. Tuli. A conceptual model of unstable flow in unsaturated soil during redistribution, Vadose Zone Journal, 2: 61-67. 2003.

Wang, Z, A. Tuli, and W.A. Jury. Unstable flow during redistribution in homogeneous soil, Vadose Zone Journal, 2: 52-60. 2003a.

Wang, Z., L. Wu, T. Harter, J. Lu and W.A. Jury. A field study of unstable preferential flow during soil water redistribution. Water Resources Research. Vol. 39 (4): 1075, doi:10.1029/2001WR000903. 2003b.

Wang, Z., W.A. Jury, A. Tuli, and D.J. Kim. Unstable flow during redistribution: Controlling factors and practical implications. Vadose Zone Journal, in press. 2004.

Analytical Solutions for Transient Flow through Unsaturated Fractured Porous Media

Yu-Shu Wu and Lehua Pan
Earth Sciences Division
Lawrence Berkeley National Laboratory
Berkeley CA 94720 USA

Introduction

This paper presents several analytical solutions for one-dimensional radial transient flow through horizontal, unsaturated fractured rock. In these solutions, unsaturated flow through fractured media is described by a linearized Richards' equation, while fracture-matrix interaction is handled using the dual-continuum concept. This work shows that although linearizing Richards' equation requires a specially correlated relationship of relative permeability and capillary pressure functions for both fractures and matrix, these specially formed relative permeability and capillary pressure functions are still physically meaningful. These analytical solutions can thus be used to reveal the entire transient behavior of unsaturated flow in fractured media under the described model conditions. They can also be useful in verifying numerical simulation results, which are otherwise difficult to validate.

Background

Fluid flow through variably saturated porous and fractured media occurs in many subsurface systems related to vadose zone hydrology and soil sciences. Quantitative analysis of such flow in unsaturated soil or rock is fundamentally based on Richards' equation. However, because of its nonlinear nature, Richards' equation solutions for general unsaturated flow may be obtained mainly with a numerical approach. In response to this limitation, significant progress in research has been made in mathematical modeling of unsaturated flow and infiltration since the late 1950s. In particular, a number of analytical solutions have been developed. In general, these analytical solutions derived for Richards' equation are dependent upon the level of the applied linearizations or approximations: (1) steady-state solutions using the exponential hydraulic conductivity model and quasi-linear approximations; (2) transient infiltration solutions using special forms of soil retention curves or using linearization and the Kirchhoff transformation; and (3) approximate and asymptotic solutions.

Linearization

Recently, we presented a class of new analytical solutions for unsaturated flow within a matrix block for examining numerical solutions for fracture-matrix interactions (Wu and Pan, 2003). These analytical solutions require a specially correlated relationship between relative permeability and capillary pressure functions. We need two sets of capillary pressure and relative permeability functions, respectively, for fracture and matrix:

Relative permeability

$$k_{r\xi}(S_\xi) = C_{k\xi}\left(S_\xi^*\right)^{\alpha_\xi} \tag{1}$$

and capillary pressure in the form:

$$P_{c\xi}(S_\xi) \equiv P_{g\xi} - P_{w\xi} = C_{p\xi}\left(S_\xi^*\right)^{-\beta_\xi} \tag{2}$$

where subscript ξ is an index for fracture (ξ = F) or matrix (ξ = M); $P_{g\xi}$ is constant air (or gas) pressure in fractures and the matrix; $P_{w\xi}$ is water pressure in fractures and the matrix, respectively; $C_{k\xi}$ and $C_{p\xi}$ are coefficients (Pa); α_ξ and β_ξ are exponential constants of relative permeability and capillary pressure functions, respectively, of fracture and matrix; and S_ξ^* is the effective fracture or matrix water saturation

$$S_\xi^* = \frac{S_\xi - S_{\xi r}}{1 - S_{\xi r}} \tag{3}$$

with $S_{\xi r}$ as the residual water saturation of fracture or matrix.

If the following conditions

$$\beta_\xi = 1 \tag{4}$$

and

$$\alpha_\xi = \beta_\xi + 1 = 2 \tag{5}$$

are satisfied, the Richards' equation can be readily linearized.

Governing Equations

The governing equation of unsaturated radial flow through fractures can be derived using a mass balance on a control volume and the dual-continuum concept (Lai et al., 1983), as follows:

$$\frac{\partial^2 S_F}{\partial r^2} + \frac{1}{r}\frac{\partial S_F}{\partial r} - \frac{6 D_M \phi_M}{D_F B}\frac{\partial S_M}{\partial x}\bigg|_{z=B/2} = \frac{1}{D_F}\frac{\partial S_M}{\partial t} \tag{6}$$

where r is radial distance along fractures, x is explained below, and D_ξ is called soil-water or moisture diffusivity, defined by

$$D_\xi = \frac{k\, k_{rw}}{\phi\, \mu_w}\frac{\partial P_w}{\partial S_w} = \frac{k_\xi C_{k\xi} C_{p\xi}}{\phi_\xi\, \mu_w (1 - S_{\xi r})} \tag{7}$$

with a dimension of m^2/s. B is the dimension of the uniform matrix cubic block.

With the 1-D spherical-flow MINC approximation, the unsaturated flow inside a cubic matrix block can be generally derived, following the procedure in Lai et al. (1983), as

$$\frac{\partial^2 S_M}{\partial x^2} + \frac{2}{x}\frac{\partial S_M}{\partial x} = \frac{1}{D_M}\frac{\partial S_M}{\partial t} \tag{8}$$

where x is the distance from a nested cross-sectional surface within the matrix block (having an equal distance to the matrix surface) to the center of the cube.

Analytical Solutions

To derive analytical solutions, the linearized governing Equations (6) and (8) are used with the initial and boundary conditions for both imbibition (adsorption) and drainage (desorption) processes. Uniform initial conditions within fractures and matrix are:

$$S_\xi\big|_{t=0} = S_{\xi r} \tag{9}$$

The boundary conditions at the well are at a constant saturation,

$$S_F(r = r_w, t) = S_0 \tag{10}$$

or a constant rate,

$$-\frac{2\pi r_w h k_F C_{kF} C_{pF}}{\mu_w}\frac{\partial S_F}{\partial r}\bigg|_{r=r_w} = q \tag{11}$$

Far away from the well,

$$S_F(r = \infty, t) = S_{Fr} \tag{12}$$

At the matrix surface, the continuity in pressure is enforced:

$$P_{cF}(r, t) = P_{cM}(x = B/2, t; r) \tag{13}$$

At the matrix block center, we propose

$$S_M(x = 0, t; r) = \text{Finite} \tag{14}$$

Let us first introduce the following dimensionless variables. The dimensionless distances are defined as

$$r_D = \frac{r}{r_w}, \quad x_D = \frac{2x}{B} \tag{15}$$

and the dimensionless time is

$$t_D = \frac{D_F t}{(B/2)^2} \tag{16}$$

The normalized(or scaled) water saturation is

$$S_{\xi D} = \frac{S_\xi - S_{\xi r}}{1 - S_{\xi r}} \tag{17}$$

In terms of these dimensionless variables, we have:

$$\frac{\partial^2 S_{FD}}{\partial r_D^2} + \frac{1}{r_D}\frac{\partial S_{FD}}{\partial r_D} - A_1 \left.\frac{\partial S_{MD}}{\partial x_D}\right|_{z=B/2} = A_2 \frac{\partial S_{FD}}{\partial t_D} \tag{18}$$

and

$$\frac{\partial^2 S_{MD}}{\partial x_D^2} + \frac{2}{x_D}\frac{\partial S_{MD}}{\partial x_D} = A_3 \frac{\partial S_{MD}}{\partial t_D} \tag{19}$$

where

$$A_1 = \frac{12 D_M \phi_M r_w^2}{D_f B}\frac{1 - S_{Mr}}{1 - S_{Fr}} \tag{20}$$

$$A_2 = \frac{4 r_w^2}{B^2} \tag{21}$$

and

$$A_3 = \frac{D_F}{D_M} \tag{22}$$

The initial and boundary conditions become:

$$S_{\xi D}\Big|_{t_D=0} = 0 \tag{23}$$

The boundary conditions of constant saturation at the well become

$$S_{FD}(r_D = 1, t_D) = \frac{S_0 - S_{Fr}}{1 - S_{Fr}} = S_{0D} \tag{24}$$

The constant rate turns into

$$\left.\frac{\partial S_{FD}}{\partial r_D}\right|_{r_D=1} = -\frac{q\mu_w}{2\pi h k_F C_{kF} C_{pF}} \frac{1}{1-S_{Fr}} = q_D \tag{25}$$

Far away from the well,

$$S_{FD}\left(r_D = \infty, t_D\right) = 0 \tag{26}$$

At the matrix surface, the continuity in pressure is enforced:

$$P_{cF}\left(r, t\right) = P_{cM}\left(x = B/2, t; r\right)$$

or

$$C_{pF} S_{FD}^{-1}\left(r_D, t_D\right) = C_{pM} S_{MD}^{-1}\left(x_D = 1, t_D; r_D\right)$$

or

$$S_{MD}\left(x_D = 1, t_D; r_D\right) = \frac{C_{pM}}{C_{pF}} S_{FD}\left(r_D, t_D\right) \tag{27}$$

At the matrix block center,

$$S_{MD}\left(x_D = 0, t_D; r_D\right) = \text{Finite} \tag{28}$$

Applying Laplace transformation to Equations (18) and (19), incorporating the initial condition (23) yields:

$$\frac{\partial^2 \overline{S}_{FD}}{\partial r_D^2} + \frac{1}{r_D}\frac{\partial \overline{S}_{FD}}{\partial r_D} - A_1 \left.\frac{\partial \overline{S}_{MD}}{\partial x_D}\right|_{z=B/2} - pA_2 \overline{S}_{FD} = 0 \tag{29}$$

and

$$\frac{\partial^2 \overline{S}_{MD}}{\partial x_D^2} + \frac{2}{x_D}\frac{\partial \overline{S}_{MD}}{\partial x_D} - pA_3 \overline{S}_{MD} = 0 \tag{30}$$

The transformed boundary conditions are:

$$\left.\overline{S}_{FD}\right|_{r_D=1} = S_{0D}/p \tag{31}$$

$$\left.-\frac{\partial \overline{S}_{FD}}{\partial r_D}\right|_{r_D=l_w} = q_D/p \tag{32}$$

$$\overline{S}_{FD}\Big|_{r_D=\infty} = 0 \tag{33}$$

At the matrix surface,

$$\overline{S}_{MD}\Big|_{x_D=1} = \frac{C_{pM}}{C_{pF}}\overline{S}_{FD} = A_4\overline{S}_{FD} \tag{34}$$

and at the matrix block center,

$$\overline{S}_{MD}\left(x_D = 0, t_D; r_D\right) = \text{Finite} \tag{35}$$

The solution for the dimensionless matrix saturation of Equations (30), (34), and (35), in the Laplace space, is;

$$\overline{S}_{MD} = A_4\frac{\overline{S}_{FD}}{\sqrt{x_D}}\frac{I_{1/2}\left(\sigma x_D\right)}{I_{1/2}\left(\sigma\right)} \tag{36}$$

where $\sigma = \sqrt{A_3 p}$ and $I_{1/2}$ is the modified Bessel function of the first kind.

Using Equation (36) in Equation (29), the solution with constant water saturation at the well of (29), (31), and (33) is given by:

$$\overline{S}_{FD} = \frac{S_{0D}}{p}\frac{K_0\left(\sqrt{x_2}\,r_D\right)}{K_0\left(\sqrt{x_2}\right)} \tag{37}$$

where $x_2 = A_1A_4\left[\sigma\coth\sigma - 1\right] + A_2 p$.

For the case of constant flow rate, the solution for Equations (29), (32), and (33) is

$$\overline{S}_{FD} = \frac{q_D}{p}\frac{K_0\left(\sqrt{x_2}\,r_D\right)}{\sqrt{x_2}K_1\left(\sqrt{x_2}\right)} \tag{38}$$

where K_0 and K_1 is the modified Bessel function of the second kind for zero and first order, respectively.

Discussion and Conclusion

This paper shows that it is possible to obtain analytical solutions for transient unsaturated flow in fractured-matrix systems. With the analytical solutions in the Laplace space, exact or asymptotic solutions can be obtained in real space or using numerical inversion techniques. The analytical solutions are based on the special forms of capillary pressure and relative permeability functions. The analytical-solution approach of this work can be easily extended to other boundary

conditions and different flow geometries, such as linear, and multidimensional unsaturated flow through fractured formation.

The analytical solutions, though limited by the assumptions for their applications, can be used to obtain some insight into the physics of transient imbibition and drainage processes related to fracture-matrix interactions. They can also be useful in verifying numerical models and their results for flow through unsaturated fractured rock, using a dual-continuum approach.

Acknowledgments

The authors would like to thank Yingqi Zhang and Dan Hawkes for their review of this abstract. This work was supported in part by the Assistant Secretary for Energy Efficiency and Renewable Energy, Office of Geothermal Technologies, of the U.S. Department of Energy under Contract No. DE-AC03-76SF00098.

References

Lai, C. H., G. S. Bodvarsson, C. F. Tsang, and P. A. Witherspoon, A new model for well test data analysis for naturally fractured reservoirs. SPE-11688, Presented at the 1983 California Regional Meeting, Ventura, California, March 23–25, 1983.

Wu, Y. S. and L. Pan, Special relative permeability functions with analytical solutions for transient flow into unsaturated rock matrix. LBNL-50443; *Water Resources Research*, 39 (4), 3-1–3-9, 2003.

Propellant Fracturing Demystified for Well Stimulation

Alexander Zazovsky
Schlumberger Product Center, 125 Industrial Blvd, MD 125-1, Sugar Land, TX 77478, USA,
Tel: 281-285-7364, Email: zazovsky@slb.com

A simple mechanical model of propellant fracturing for well stimulation is presented. It involves the pressure buildup caused by propellant burning, accompanied by the propellant gas generation, the wellbore pressurization caused by gas bubble expansion and the fracturing of rock, followed by the propagation of created fractures. The main difficulty in simulating fracturing phenomena is related to the absence of initial conditions for fracture initiation and propagation models. For conventional hydraulic fracturing, this is not crucial because the final size of fracture is usually much larger than that used in artificially imposed initial conditions, and multi-wing fractures do not form. For propellant fracturing however, this is not the case; the fracture pattern is more complicated, and fractures created during propellant fracturing are much shorter. Breakdown pressure is also hard to predict. This makes any quantitative predictions of fracture size and geometry by propellant-fracturing simulation unreliable [1]. For this reason, the main focus in this study is on qualitative analysis of propellant fracturing, using simplifications of rock properties, fracture propagation patterns, and wellbore hydraulics.

In contrast to conventional hydraulic fracturing simulations [2], the initial size of fractures is assumed to be equal to zero and the breakdown pressure is known as is the geometry of propagating fractures (in particular, the KGD model has been used). It has been found that, for the typical kinetics of propellant burning, the pressure buildup to breakdown pressure is followed by a fracture "jump" to the distance of about a few meters from the wellbore (see Figure 1 below). This fracture jump corresponds to the dynamic phase of fracture propagation [3], which cannot be modeled within the conventional approach developed for hydraulic fracturing. This fracture jump occurs because the pressure drop inside the wellbore, required for quasi-steady fracture propagation, cannot be achieved by propagation of small fractures during continuous propellant burning. The total volume of fractures is much smaller than the pressurized wellbore volume; consequently, unless these fractures jump, the pressure buildup would continue. Since the next phase of fracturing depends strongly on an unknown fracture pattern and the final fracture size is not as important as in hydraulic fracturing, the predictable phase of the propellant fracturing, which should be subject to design, is probably restricted to the pressure buildup prior to the breakdown of the wellbore. The breakdown pressure, however, cannot be obtained from modeling. It has to be determined experimentally, for example by recording the downhole pressure during propellant-fracturing activity executed under similar conditions.

Possible applications of propellant fracturing include (1) pre-fracturing before conventional hydraulic fracturing, to reduce the pressure of fracture initiation and the risk of undesirable fracture propagation (halo effect, fracture tortuosity effect, small stress barriers) and (2) the injectivity enhancement, which also may be useful for re-injection during testing (Zero Emission Testing or ZET technology). The application of propellant fracturing to productivity stimulation seems to be limited to tight gas formations under *in situ* stress contrast unless an efficient technique for fracture closure prevention is found and implemented.

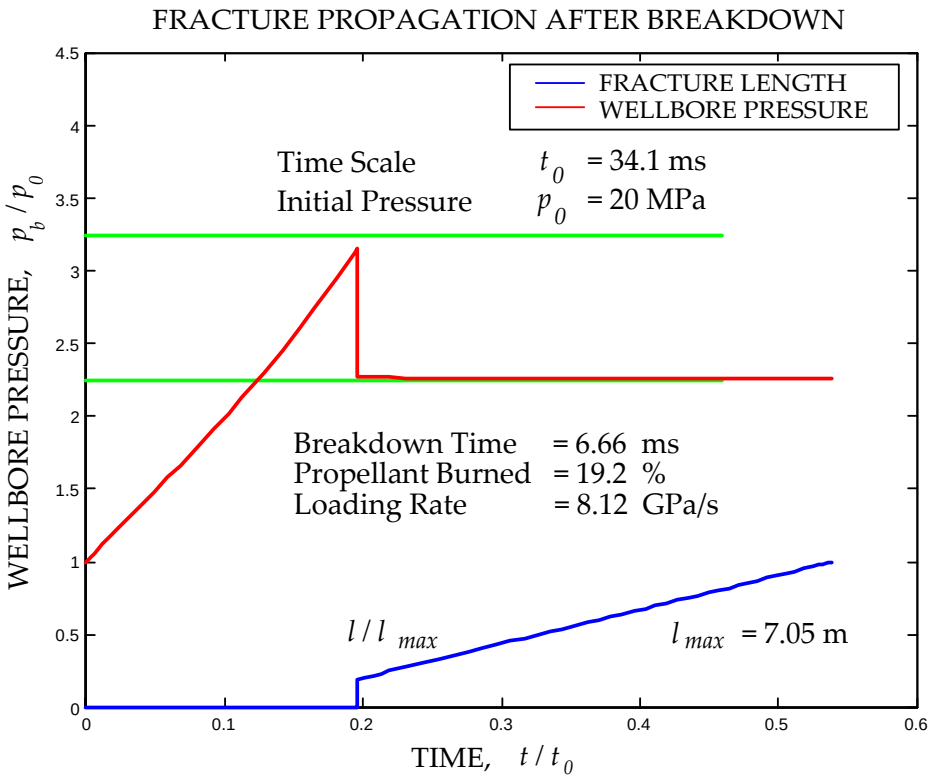

Figure 1. The fracture length (blue) and the bubble pressure (red) versus time during pressure buildup and fracture propagation after wellbore breakdown.

References

1. *Dynamic Gas Pulse Loading® / STRESSFRAC® - A Superior Well Stimulation Process*, Servo Dynamics Inc., http://www.west.net/~servodyn/brochure.doc.
2. *Reservoir Stimulation*, 3rd Edition, Eds. M. J. Economides and K. G. Nolte, John Wiley & Sons (2000).
3. Freund, L. B. *Dynamic Fracture Mechanics*, Cambridge University Press, Cambridge (1990).

Constraints on Flow Regimes in Unsaturated Fractures

Teamrat A. Ghezzehei
Earth Sciences Division, Lawrence Berkeley National Laboratory
1 Cyclotron Rd., MS 90R1116, Berkeley, CA 94720

In recent years, significant advances have been made in our understanding of the complex flow processes in individual fractures, aided by flow visualization experiments and conceptual modeling efforts (Fourar et al., 1993; Kneafsey and Pruess, 1998; Nicholl et al., 1994; Su et al., 1999; Tokunaga and Wan, 1997). These advances have led to recognition of several flow regimes in individual fractures subjected to different initial and boundary conditions. Of these, the most important regimes are film flow, rivulet flow, and sliding of droplets. The existence of such significantly dissimilar flow regimes has been a major hindrance in the development of self-consistent conceptual model of flow for single fractures that encompasses all the flow regimes. The objective of this study is to delineate the existence of the different flow regimes in individual fractures. For steady state flow conditions, we developed physical constraints of the different flow regimes that satisfy minimum energy configurations, which enabled us to segregate the wide range of fracture transmissivity (volumetric flow rate per fracture width) into several flow regimes. These are, in increasing order of flow rate, flow of adsorbed films, flow of sliding drops and bridges, rivulet flow, stable film flow, and unstable (turbulent) film flow.

References

Fourar, M., S. Bories, R. Lenormand, and P. Persoff, 2-phase flow in smooth and rough fractures—measurement and correlation by porous-medium and pipe flow models, *Water Resources Research*, *29* (11), 3699-3708, 1993.

Kneafsey, T.J., and K. Pruess, Laboratory experiments on heat-driven two-phase flows in natural and artificial rock fractures, *Water Resources Research*, *34* (12), 3349-3367, 1998.

Nicholl, M.J., R.J. Glass, and S.W. Wheatcraft, Gravity-driven infiltration instability in initially dry nonhorizontal fractures, *Water Resources Research*, *30* (9), 2533-2546, 1994.

Su, G.W., J.T. Geller, K. Pruess, and F. Wen, Experimental studies of water seepage and intermittent flow in unsaturated, rough-walled fractures, *Water Resources Research*, *35* (4), 1019-1037, 1999.

Tokunaga, T.K., and J.M. Wan, Water Film Flow Along Fracture Surfaces of Porous Rock, *Water Resources Research*, *33* (6), 1287-1295, 1997.

On the Brinkman Correction in Uni-Directional Hele-Shaw Flows

Jie Zeng and Yannis C. Yortsos
Department of Chemical Engineering
University of Southern California, Los Angeles, CA 90089-1211 and

Dominique Salin
Laboratoire Fluides Automatique et Systemes Thermiques,
Universites P. et M. Curie and Paris Sud, C.N.R.S. (UMR 7608)
Batiment 502, Campus Universitaire, 91405 Orsay Cedex, France

We study the Brinkman correction to Darcy's equation for unidirectional flows in a Hele-Shaw cell (between two parallel plates). Three examples, describing gravity-driven flow with variable density, pressure-driven flow with variable viscosity, and pressure-driven flow in a cell with a specific variation in aperture are discussed. The latter allows for a direct conformal mapping of the problem. In general, the Brinkman correction involves non-local terms, and it is not simply equal to an effective viscous shear stress involving the gap-averaged velocity. The latter is applicable at long-wavelengths, however, provided that the viscosity is augmented by a prefactor equal to $12/\pi^2$.

Education and Outreach in Environmental Justice

H. F. Wang, M. A. Boyd, and J. M. Schaffer
University of Wisconsin-Madison

Introduction

The environmental justice (EJ) project originated as the initiative of a group of freshmen in a first-year interest group seminar on Environmental Justice. One group of students organized an EJ teach-in. Their keynote speaker was Cheryl Johnson, executive director of People for Community Recovery (PCR). PCR is a grassroots, community-based EJ organization in the Chicago Housing Authority's public housing community Altgeld Gardens, in southeast Chicago. Another group of students developed a proposal to the Ira and Ineva Reilly Baldwin bequest, which the University of Wisconsin uses to fund grants furthering the "Wisconsin Idea" (outreach activities). The core of that proposal was to develop a summer field course in EJ, to bring in outside speakers in environmental justice, and to develop service learning opportunities in partnership with community organizations.

Summer Field Course (www.geology.wisc.edu/~wang/SummerEJ/)

The purpose of the three-week Summer Field Course was to introduce college students and high school teachers to EJ issues in a multidisciplinary and experiential way. Five full days were devoted to field trips to visit locally unwanted land uses (landfills, power plants, recycling plants, sewage treatment plants), and EJ communities (Altgeld Gardens, Sixteenth Street Community Health Center in Milwaukee, and the Menominee Reservation in northeastern Wisconsin). Classroom days were devoted to readings, videos, and discussions, which covered the history of the EJ movement and its connections to the civil rights and anti-toxics movements; case histories covering political, legal, economic, scientific, and health aspects; critical evaluation of demographic and socioeconomic evidence for inequitable location of hazardous waste sites; global environmental justice; and the future of the EJ movement.

Enrollment consisted of seven students and three high school teachers. The teachers were from Marin Academy in San Rafael, California, West High School in Madison, Wisconsin, and South Milwaukee High School in Milwaukee, Wisconsin. Service learning activities in the Summer Field Course included additions to the web site for People for Community Recovery in Chicago and a mercury pollution web page for the Clean Water Action Council (CWAC), an environmental group in Green Bay, Wisconsin, who provided the tour of PCB contamination of the Fox River. The outreach goals of the course were met by teachers producing curriculum for their term projects. One teacher created "Environmental Justice Monopoly" in which players do not all start with the same amount of money and on "Chance" they uncover cards of environmental pollution or "get out of the hospital." A typical student reaction to the Altgeld Gardens trip follows: "Visiting Altgeld Gardens was an intense experience. I had previously read about the situation as a whole in *Garbage Wars* by David Naguib Pellow, but seeing the area in person explained a great deal that could not be expressed by a book. The story that Cheryl told us that affected me the most was when she explained how children from the community liked to

play in the tunnels that use to dump sludge into the Little Calumet River until it was boarded up. It seemed like something we all would have done in our childhood, and while mine might have been a little dangerous, theirs was toxic and causing them to get life-threatening diseases. Just being there for a few hours and seeing the never-ending barrage of industrial sites, landfills, and any other polluting facility made me understand their situation on a more personal level."

Altgeld Gardens

Built in 1942, Altgeld Gardens is a Chicago Housing Authority project of approximately 5,000 African-American residents in southeast Chicago. The Altgeld Gardens-Murray Homes are among the oldest public housing communities in the United States. A third to half of its housing units stand dilapidated and vacant, and there are concerns about lead and asbestos in the buildings (Figure 1). Many people are worried about air quality and its impact on rising asthma rates, especially among children. Seventy percent of residents in Altgeld Gardens-Murray Homes experience some form of respiratory infection. Claiming a variety of illnesses that may be related to environmental contaminants, a group of Altgeld's residents who suffer health problems are currently litigating a "mass action" lawsuit against the CHA. Several times over the past twenty years, PCR has challenged land-use decisions like the siting of landfills and their operations, in particular the CID Landfill immediately southeast of the community, and more than twice its size.

The environment of and around Altgeld Gardens holds soil contamination from prior land uses and ongoing illegal dumping, air contaminants from area industry and highways, and water contamination from decades of industry outflow and landfill operations. Since the late 1800s, heavy industry such as coke ovens and steel plants, manufacturing facilities, paint and pesticide factories, refineries, landfills, incinerators, and sewage treatment have impacted the environment and communities of the area around Lake Calumet. More than 100 industrial plants and 50 active or closed waste disposal sites surround the Altgeld community. The former railroad company town of Pullman, now a Chicago neighborhood to the northwest, once pumped its residential and industrial sewage to spread on the land beneath and adjoining Altgeld Gardens and the adjacent Golden Gate Park neighborhood of small single-family houses.[1]

Currently, Chicago Metropolitan Water Reclamation District sludge beds lie just north of Altgeld. Both closed and active landfills surround Altgeld Gardens, including the Paxton Landfill, Land & Lakes, Cottage Grove Landfill, and the CID Landfill, several of these bordering the waterways that drain into shallow Lake Calumet. Over the Expressway to the east are former and existing steel plants and the Ford Motors Chicago Assembly plant, which in 2001 accounted for a third of total air emissions reported to the Toxics Release Inventory for manufacturers in the Calumet Area. Ford reported 526,858 pounds of air emissions. Other local manufacturers released over 1.1 million pounds of 70 reported substances, including over 2,000 pounds of lead and lead compounds, 260 pounds of mercury, and other heavy metals, assorted polycyclic aromatic hydrocarbons, pesticides, and hydrochloric and sulfuric acids.[2]

---

[1] Colten, C. 1985. *Industrial Wastes in the Calumet Area 1869-1970: An Historical Geography*, Illinois State Museum and Department of Energy and Natural Resources.

[2] *Toxics Release Inventory*, 2001, USEPA.

To date, thorough characterization of potential environmental contaminants in the soil or housing units has not been undertaken. In 1998, the ATSDR asked the Illinois Department of Public Health to review ten surface soil samples taken from Altgeld's 200 acres in 1996, on which basis the IDPH determined that the contaminants were not a widespread or worrisome problem. In 1997, Kimberly Gray, Ph.D., of Northwestern University's Department of Civil and Environmental Engineering developed a plan for assessing hazards and subsequent phyto-remediation; however, the CHA has not pursued her recommendations. Concern remains that the environmental health hazards in and around the homes and wider community have not been sufficiently characterized or determined "safe" for habitation, let alone expansion of the population.

Figure 1. Sludge sewage outlet from the Pullman factory where it enters the Little Calumet River. The outlet was bricked shut to keep children from walking through the pipe. Photo by Josh Grice.

The challenges facing PCR and the Altgeld community span environmental health conditions, housing, employment availability and preparation, transportation, regional industry and land-use. Altogether, they present clear demands for collaborative problem-solving and leveraging partners' skills and resources. Over time, developing healthier relationships between the community and both the Chicago Housing Authority and dominant regional industries is a further goal. In the meantime, we propose to engage in the development of skills, knowledge, data resources, practical grassroots problem-solving, and environmental health protection and remediation that will provide us with alternatives to offer to the process.

Partnership with People for Community Recovery

Eleven students in Professor Gregg Mitman's course, Environment and Health in Global Perspective (History of Medicine 513), developed a web site for PCR, under the leadership of J.M. Schaffer. An independent study student, E.L. Eggebrecht, spent spring semester doing a service learning project in which she helped PCR with the paper work associated with purchasing a computer. M.A. Boyd organized a 20-person meeting on April 2003 at Loyola

University's Center for Urban Research and Learning (CURL), where a discussion was held on creating an Environmental Justice Research and Training Center in Altgeld Gardens, a long-standing vision of PCR's. This vision was presented in PCR's submission of a community problem-solving grant proposal to the EPA in September 2003. UW-Madison is one of four partners. PCR was notified in December 2003 that it received one of fifteen awards. Also in December, a group of students in an Honors Seminar held an EJ Awareness Day for high school students, the college community, and the public. The half-day of events included workshops and a keynote presentation by Cheryl Johnson. Other student groups added to the PCR website and identified additional grant opportunities for PCR.

Conclusions

Connecting to community organizations can be both an educational experience for students and a benefit to the community. Communities will teach students about the issues of environmental justice from first-hand experience, and universities can provide student, staff, and faculty assistance where their needs overlap with academia's traditional missions of teaching, research, and service. Connecting service learning opportunities to a broad scholarship area provides a motivating entry point for interested students. EJ is local, regional, national, and global in scope. It is a lens through which the Wisconsin Idea can be projected.

Session 8:
OPTIMIZATION OF FRACTURED ROCK INVESTIGATIONS AND DATA ANALYSIS

Advective Porosity Tensor for Flux-Weighted

S.P. Neuman, University of Arizona, USA

Advective (effective, hydraulic, kinematic) porosity relates the macroscopic velocity of an inert solute to the Darcy flux. It is generally taken to be a scalar, implying that flux and advective velocity are collinear. Yet, in some tracer experiments, solute transport velocity appears to vary with direction. The phenomenon was documented and analyzed most thoroughly in connection with convergent flow tracer tests using conservative tracers conducted between 1981 and 1988 by Sandia National Laboratories in the fractured Culebra Dolomite Member of the Rustler Formation, at the Waste Isolation Pilot Plant (WIPP) site in New Mexico (Jones et al., 1992). These and more recent tests conducted in 1995–1996 exhibited strong directional dependence (Meigs and Beauheim, 2001). Some of the earlier tests were explained by Jones et al. using a combination of anisotropic transmissivity and matrix diffusion. At one tracer test site (Hydropad H-6), directional variations in transmissivity were previously determined on the basis of separate hydraulic tests by Gonzalez (1983) and Neuman et al. (1984). Whereas the hydraulic and tracer tests yielded similar principal directions of anisotropy, the anisotropy ratio of 7:1 inferred by Jones et al. (1992) from tracer tests exceeded the ratio of approximately 2:1 inferred by Gonzalez (1983) and Neuman et al. (1984) from hydraulic tests. At Hydropad H-4, the direction of rapid tracer breakthrough (not analyzed quantitatively) was significantly different than that of maximum principal transmissivity as determined by Gonzalez (1983; see Figure 5-5 of Jones et al., 1992). According to Meigs and Beauheim (2001), the more recent tests provide added support for the influence of matrix diffusion on transport in the Culebra.

Directional advective porosity effects have been studied computationally by Endo et al. (1984) and Endo and Witherspoon (1985; see also Long et al., 1995). The authors simulated flow and advective transport through networks of continuous and finite-length fractures in two dimensions. Flow through a fracture was taken to be proportional to the cube of its aperture and unaffected by cross-flow at fracture intersections. Purely advective transport was taken to take place through stream-tubes filling all or part of each fracture space and splitting or coalescing at fracture intersections in accord with local hydrodynamics. Whereas flow was thus free to follow paths of relatively high permeability, solute advection was forced to zigzag between high- and low-permeability fractures, being thus artificially retarded in comparison to flow. This inconsistency in treatment resulted in nonphysical advective porosities which (a) exceeded the porosity of the conducting pore space and (b) exhibited sharply localized discontinuities with direction in hydraulically isotropic systems of continuous fracture sets. In systems whose (inverse square root) directional permeabilities delineated an ellipse, the computed advective porosities varied with direction in a continuous but irregular manner (the irregularities resulting at least in part from averaging over a small number of random network replicates). Based on the common belief that the advective porosity of a porous continuum must be a scalar, the authors took its directional dependence to imply that fracture networks behaving as equivalent continua with respect to flow may not do so vis-à-vis advective transport.

We show mathematically that when an inert solute is introduced into and advected through a fractured medium at a rate proportional to the local distribution of fluxes, advective porosity may become a tensor. If medium permeability is a symmetric positive-definite tensor, so is advective

porosity. However, the principal directions and values of the two tensors are generally not the same. If the medium is isotropic with respect to advective porosity, the latter is generally smaller than the interconnected porosity. Full mixing of the solute across all local transport channels renders the advective porosity a scalar equal to the interconnected medium porosity. The same can be shown to hold for porous continua. The anisotropic nature of advective porosity may help explain observed variations of solute travel velocities with direction.

Flux-Weighted Transport

Following Romm and Pozinenko (1963), consider an impermeable medium intersected by R sets of fractures saturated with fluid. Each set r conducts fluid in a plane normal to a unit vector $\mathbf{n}_r$ but does not conduct fluid parallel to $\mathbf{n}_r$. The set has an interconnected porosity ϕ_r and (for simplicity) a scalar equivalent permeability k_r (in a plane normal to $\mathbf{n}_r$). Imposing a uniform hydraulic gradient ∇h on the system would generate a uniform flux

$$\mathbf{q}_r = -\frac{\gamma}{\mu} k_r \nabla h_r \tag{1}$$

in the plane of the r^{th} set (ignoring interference due to intersecting fracture sets for reasons discussed by Snow (1969)) where γ is the unit weight of fluid, μ its dynamic viscosity, and ∇h_r the projection of ∇h onto the plane of the set. Let $\mathbf{m}$ be a unit vector parallel to ∇h_r. Then $\nabla h_r = \mathbf{m}_r \left(\mathbf{m}_r \cdot \nabla h \right) = \mathbf{m}_r \mathbf{m}_r^T \nabla h = \left(\mathbf{I} - \mathbf{n}_r \mathbf{n}_r^T \right) \nabla h$ where T denotes transpose and $\mathbf{I}$ is the identity tensor. Hence $\mathbf{q}_r = -\left(\gamma / \mu \right) \mathbf{k}_r \nabla h$ where $\mathbf{k}_r = k_r \left(\mathbf{I} - \mathbf{n}_r \mathbf{n}_r^T \right)$ is a symmetric tensor. It follows that

$$\mathbf{q} = \sum_{r=1}^{R} \mathbf{q}_r = -\frac{\gamma}{\mu} \mathbf{k} \nabla h \tag{2}$$

where

$$\mathbf{k} = \sum_{r=1}^{R} \mathbf{k}_r = \sum_{r=1}^{R} k_r \left(\mathbf{I} - \mathbf{n}_r \mathbf{n}_r^T \right). \tag{3}$$

In addition to being symmetric, the permeability tensor $\mathbf{k}$ of the system is positive-definite provided the latter consists of at least two intersecting fracture sets, $R \geq 2$. This means that $\mathbf{k}$ has real positive eigenvalues (principal values) and orthogonal eigenvectors (principal directions). It further means that $\mathbf{k}$ delineates ellipsoids $\mathbf{x}\mathbf{k}\mathbf{x} = 1$ and $\mathbf{x}\mathbf{k}^{-1}\mathbf{x} = 1$ having radius vectors $k_{\nabla h}^{-1/2}$ and $k_{\mathbf{q}}^{1/2}$, respectively, where $\mathbf{x}$ is a position vector, $k_{\nabla h}$ is directional permeability parallel to the hydraulic gradient, and $k_{\mathbf{q}}$ is directional permeability parallel to the flux (e.g., Bear, 1972). The equivalent permeability $\mathbf{k}$ being a tensor implies that hydraulic gradient and flux are generally not collinear.

Consider now a mass M of solute introduced into the above flow system in proportion to the flux such that $M_r\mathbf{q} = M\mathbf{q}_r$ and $\sum_{r=1}^{R} M_r\mathbf{q} = \sum_{r=1}^{R} M\mathbf{q}_r = M\mathbf{q}$. Then $M_r\mathbf{k}\nabla h = M\mathbf{k}_r\nabla h$ and

$$\frac{M_r}{M}\nabla h = \mathbf{k}^{-1}\mathbf{k}_r\nabla h\,. \tag{4}$$

In the absence of mixing, the solute center of mass is advected at a rate

$$\mathbf{u}_M = \frac{1}{M}\sum_{r=1}^{R} M_r\mathbf{u}_r = -\frac{1}{M}\frac{\gamma}{\mu}\sum_{r=1}^{R} M_r\phi_r^{-1}\mathbf{k}_r\nabla h = -\frac{\gamma}{\mu}\sum_{r=1}^{R}\phi_r^{-1}\mathbf{k}_r\mathbf{k}^{-1}\mathbf{k}_r\nabla h = \sum_{r=1}^{R}\phi_r^{-1}\mathbf{k}_r\mathbf{k}^{-1}\mathbf{k}_r\mathbf{k}^{-1}\mathbf{q} \tag{5}$$

where $\mathbf{u}_r = \phi_r^{-1}\mathbf{q}_r$ is advective (seepage) velocity in the plane of the r^{th} fracture set and we took account of (1) – (2) and (4). It follows that the flux is related to the advective solute mass velocity through

$$\mathbf{q} = \mathbf{\Phi}\mathbf{u}_M \tag{6}$$

where $\mathbf{\Phi}$ is an advective porosity tensor given by

$$\mathbf{\Phi} = \mathbf{k}\left(\sum_{r=1}^{R}\phi_r^{-1}\mathbf{k}_r\mathbf{k}^{-1}\mathbf{k}_r\right)^{-1}. \tag{7}$$

It is clear that if $\mathbf{k}$ is symmetric positive-definite, so is $\mathbf{\Phi}$. This means that $\mathbf{\Phi}$ has real positive eigenvalues (principal values) and orthogonal eigenvectors (principal directions) which, however, are generally different from those of $\mathbf{k}$. It further means that $\mathbf{\Phi}$ delineates ellipsoids $\mathbf{x}\mathbf{\Phi}\mathbf{x} = 1$ and $\mathbf{x}\mathbf{\Phi}^{-1}\mathbf{x} = 1$ having radius vectors $\Phi_{\mathbf{u}_M}^{-1/2}$ and $\Phi_{\mathbf{q}}^{1/2}$, respectively, where $\Phi_{\mathbf{u}_M}$ is directional advective porosity parallel to the advective velocity and $\Phi_{\mathbf{q}}$ is directional advective porosity parallel to the flux. That the advective porosity $\mathbf{\Phi}$ is a tensor implies that advective velocity and flux are generally not collinear.

Suppose that all fracture sets have identical porosity $\phi_r = \phi/R$ where ϕ is the total interconnected porosity of the system and identical permeability k_f. Suppose further that the system is isotropic with respect to permeability, such that $\mathbf{k} = k_f\sum_{r=1}^{R}\left(\mathbf{I} - \mathbf{n}_r\mathbf{n}_r^T\right) = k\mathbf{I}$. Then $k_f\sum_{r=1}^{R}\left(\mathbf{I} - \mathbf{n}_r\mathbf{n}_r^T\right)^2 = k_f\sum_{r=1}^{R}\left(\mathbf{I} - \mathbf{n}_r\mathbf{n}_r^T\right) = k\mathbf{I}$, (7) reduces to

$$\mathbf{\Phi}^{-1} = \frac{R}{\phi}\left(\frac{k_f}{k}\right)^2\sum_{r=1}^{R}\left(\mathbf{I} - \mathbf{n}_r\mathbf{n}_r^T\right)^2 = \frac{R}{\phi}\frac{k_f}{k}\mathbf{I} \tag{8}$$

and

$$\mathbf{\Phi} = \Phi\mathbf{I} \tag{9}$$

where $\Phi = (\phi / R) k / k_f$ is a scalar advective porosity. In general not all R fracture sets contribute fully to k so that $k / k_f \le R$ (as us illustrated below). It follows that

$$\Phi \le \phi , \tag{10}$$

i.e., advective porosity can never exceed the total interconnected porosity (and will generally be smaller, as is illustrated below).

For illustration consider the simple case of three mutually orthogonal fracture sets. Define a system of Cartesian coordinates parallel to the fracture intersections such that $\mathbf{n}_1 = (1,0,0)^T$, $\mathbf{n}_2 = (0,1,0)^T$ and $\mathbf{n}_3 = (0,0,1)^T$. Then (3) yields

$$\mathbf{k} = \begin{bmatrix} k_2 + k_3 & 0 & 0 \\ 0 & k_1 + k_3 & 0 \\ 0 & 0 & k_1 + k_2 \end{bmatrix} \tag{11}$$

which, upon substitution into (7), gives

$$\mathbf{\Phi} = \begin{bmatrix} \dfrac{(k_2 + k_3)^2}{\left(\dfrac{k_2^2}{\phi_2} + \dfrac{k_3^2}{\phi_3} \right)} & 0 & 0 \\ 0 & \dfrac{(k_1 + k_3)^2}{\left(\dfrac{k_1^2}{\phi_1} + \dfrac{k_3^2}{\phi_3} \right)} & 0 \\ 0 & 0 & \dfrac{(k_1 + k_2)^2}{\left(\dfrac{k_1^2}{\phi_1} + \dfrac{k_2^2}{\phi_2} \right)} \end{bmatrix} \tag{12}$$

In this special case, the principal directions of $\mathbf{k}$ and $\mathbf{\Phi}$ coincide, but their principal (diagonal) values differ. If flow takes place through two intersecting sets (r = 1, 2) in two dimensions, (11) and (12) simplify to

$$\mathbf{k} = \begin{bmatrix} k_2 & 0 \\ 0 & k_1 \end{bmatrix} \tag{13}$$

$$\mathbf{\Phi} = \begin{bmatrix} \phi_2 & 0 \\ 0 & \phi_1 \end{bmatrix} \tag{14}$$

In both of these special cases, the components of $\mathbf{k}$ and $\mathbf{\Phi}$ in any principal direction depend only on permeabilities and porosities of fracture sets that are parallel to the same direction. If each orthogonal fracture set has the same permeability k_f, (11)–(13) simplify to

$$\mathbf{k} = 2k_f\mathbf{I} \tag{15}$$

$$\mathbf{\Phi} = 4\begin{bmatrix} \left(\frac{1}{\phi_2}+\frac{1}{\phi_3}\right)^{-1} & 0 & 0 \\ 0 & \left(\frac{1}{\phi_1}+\frac{1}{\phi_3}\right)^{-1} & 0 \\ 0 & 0 & \left(\frac{1}{\phi_1}+\frac{1}{\phi_2}\right)^{-1} \end{bmatrix} \tag{16}$$

$$\mathbf{k} = k_f\mathbf{I} \tag{17}$$

while (14) remains unchanged. The system is then isotropic with respect to permeability but anisotropic with respect to advective porosity. If additionally each fracture set has the same porosity, (16) and (14) simplify to

$$\mathbf{\Phi} = \frac{2}{3}\phi\mathbf{I} \tag{18}$$

$$\mathbf{\Phi} = \frac{1}{2}\phi\mathbf{I}\,. \tag{19}$$

In both cases, the system is isotropic with respect to advective porosity, which is strictly smaller than the interconnected system porosity, $\Phi < \phi$.

Complete Mixing

Suppose that a mass M of solute is introduced into a rock volume V in a way which renders it evenly distributed, at a resident concentration $c = M/V$, across all fracture sets intersecting the volume. Then the solute center of mass is advected at a rate

$$\mathbf{u}_M = \frac{1}{M}\sum_{r=1}^{R} M_r\mathbf{u}_r = \frac{1}{c\phi V}\sum_{r=1}^{R} c\phi_r V\mathbf{u}_r = \frac{1}{\phi}\sum_{r=1}^{R}\mathbf{q}_r = \frac{1}{\phi}\mathbf{q} \tag{26}$$

from which it is evident that, in this fully mixed situation, the advective porosity is a scalar equal to the total interconnected porosity of the system.

Conclusions

1. Flux-weighted transport taking place without mixing may be characterized by an anisotropic advective porosity such that advective solute velocity and flux are generally not collinear.

2. If permeability is a symmetric positive-definite tensor, so is advective porosity. However, the principal directions and values of the two tensors are generally not the same.

3. A scalar advective porosity cannot exceed the interconnected porosity of the medium and is generally smaller.

4. If a solute mixes fully across all local transport channels that it encounters on its path, the advective porosity becomes a scalar equal to the interconnected medium porosity.

References

Endo, H.K. and P.A. Witherspoon, Mechanical transport and porous media equivalence in anisotropic fracture networks, 527-537, in *The Hydrogeology of rocks of Low Permeability*, Proceedings 17th IAH International Congress, Tucson, Arizona, January 1985.

Endo, H.K., J.C.S. Long, C.R. Wilson, and P.A. Witherspoon, A model for investigating mechanical transport in fracture networks, Water Resour. Res., 20(10), 1390-1400, 1984.

Gonzalez, D.D., Groundwater flow in the Rustler Formation, Waste Isolation Pilot Plant (WIPP), Southeast New Mexico (SENM), *Interim Rep. SAND82-1012*, Sandia Natl. Lab., Albuquerque, N.M., 1983.

Jones, T.L., V.A. Kelley, J.F. Pickens, D.T. Upton, R.L. Beauheim, and P.B. Davies, Integration of interpretation results of tracer tests performed in the Culebra dolomite at the Waste Isolation Pilot Plant site, *Rep. SAND92-1579*, Sandia Natl. Lab., Albuquerque, N.M., 1992.

Long, J.C.S., H.K. Endo, K. Karasaki, L. Pyrak, P. MacLean, and P.A. Witherspoon, Hydraulic behavior of fracture networks, 449-462, in *The Hydrogeology of rocks of Low Permeability*, Proceedings 17th IAH International Congress, Tucson, Arizona, January 1985.

Meigs, L.C. and R.L. Beauheim, Tracer tests in fractured dolomite, 1. Experimental design and observed tracer recoveries, *Water Resour. Res.*, 37(5), 1113-1128, 2001.

Neuman, S.P., G.R. Walter, H.W. Bentley, J.J. Ward. and D.D. Gonzalez, Determination of Horizontal Aquifer Anisotropy with Three Wells, *Ground Water*, 22(1), 66-72, 1984.

Romm, E.S. and B.V. Pozinenko, Permeability of anisotropic fractured rocks (in Russian), *Eng. J.*, 3(2), 381-386, 1963.

Snow, D.T., Anisotropic permeability of fractured media, *Water Resour. Res.*, 5(6), 1273-1289, 1969.

Hydrologic Characterization of Fractured Rock Using Flowing Fluid Electric Conductivity Logs

Christine Doughty and Chin-Fu Tsang
Earth Sciences Division
E.O. Lawrence Berkeley National Laboratory

Introduction

Flowing fluid electric conductivity logging provides a means to determine hydrologic properties of fractures, fracture zones, or other permeable layers intersecting a borehole in saturated rock. The method involves replacing the wellbore fluid by deionized water, then conducting a series of fluid electric conductivity (FEC) logs while the well is being pumped at a constant low flow rate Q (typically a few L/min). At depth locations where formation water enters the borehole (denoted as "feed points"), the FEC logs display peaks, which grow with time and are skewed in the direction of water flow. The time-series of FEC logs are analyzed by modeling fluid flow and solute transport within the wellbore, treating feed points as mass sources or sinks, and optimizing the match to the observed FEC logs by varying the feed point properties. Results provide the location, hydraulic transmissivity, salinity, and ambient pressure head of each permeable zone.

The flowing FEC logging method is found to be more accurate than spinner flow meters and much more efficient than packer tests in evaluating hydraulic transmissivity values along the wellbore (Tsang et al., 1990; Paillet and Pedler, 1996; Karasaki et al., 2000). Spinner flow meters are very sensitive to variations in wellbore radius, because they measure a local fluid velocity that is inversely proportional to wellbore radius. In contrast, fluid FEC logging provides a more integrated measure of fluid velocity in the well, as reflected by the movement of FEC peaks, making it less sensitive to minor variations in wellbore radius. However, large washout zones may create fluid velocity changes that introduce spurious effects into the FEC logs. Engineered changes in wellbore radius also affect the fluid velocity in the wellbore, but these may be accounted for explicitly in the analysis if their depth and magnitude are known.

Analysis Methods

The original analysis method (Tsang et al., 1990) employed a numerical model called BORE (Hale and Tsang, 1988) and was restricted to the case in which flows from the fractures were directed into the borehole (inflow). Recently, the method was adapted to permit treatment of both inflow and outflow, which enables analysis of natural regional flow through the permeable zone and internal wellbore flow, by development of a modified model BORE II (Doughty and Tsang, 2000). Generally, inflow points produce distinctive signatures in the FEC logs (Figure 1), enabling the determination of location z_i, inflow rate q_i, and salinity C_i for the *ith* feed point.

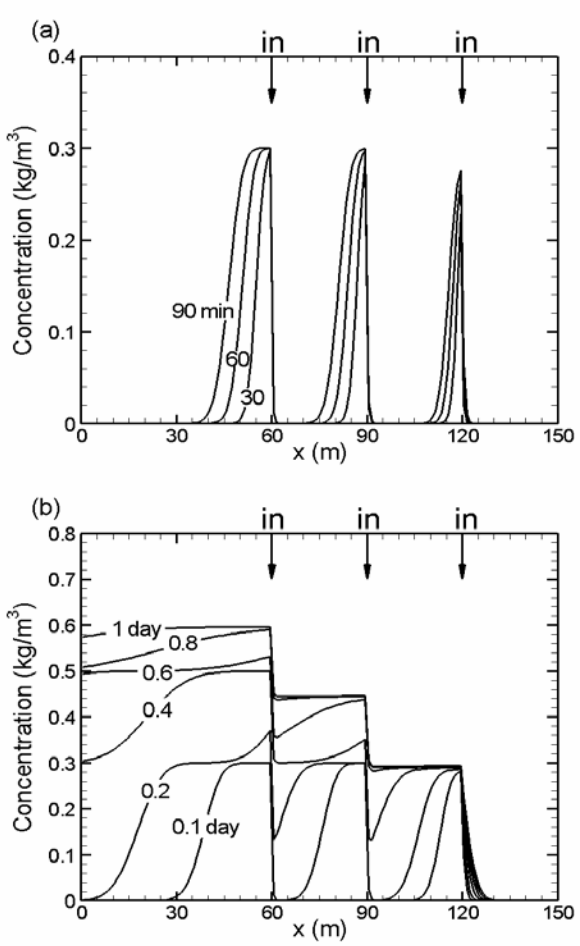

Figure 1. Synthetic flowing FEC data showing a typical time series of logs produced by inflow feed points for (a) early times, before peaks from individual feed points interfere with one another; and (b) late times, when peaks begin to interfere. The one-day log shows nearly steady-state conditions.

Outflow feed points

Identifying outflow locations and flow rates is more difficult, because outflow feed points generally do not produce a distinct signal of their own in the FEC logs, but do influence the evolution of peaks from deeper (or upstream) inflow points (Figure 2a). Therefore, we utilize the depth-integral of the FEC log, denoted M, and examine its time variation $M(t)$ to infer outflow point location and flow rate (Figure 2b). As long as an inflow peak has not encountered an outflow point as it moves up the wellbore, $M(t)$ increases linearly, with constant slope dM/dt denoted S_{early}. When the peak reaches one or more outflow points, some fluid leaves the wellbore, and the rate of $M(t)$ increase slows. When the peak has passed the uppermost outflow point, $M(t)$ again becomes linear, with a smaller constant slope S_{late}. By comparing the time-series of FEC logs with the $M(t)$ plot, outflow point location can be bracketed. The decrease in slope of the $M(t)$ plot determines outflow point flow rate q_i according to

$$q_i = \frac{S_{\text{early}} - S_{\text{late}}}{C_{\max}}. \tag{1}$$

where C_{max} is the maximum salinity of the peak passing the outflow point.

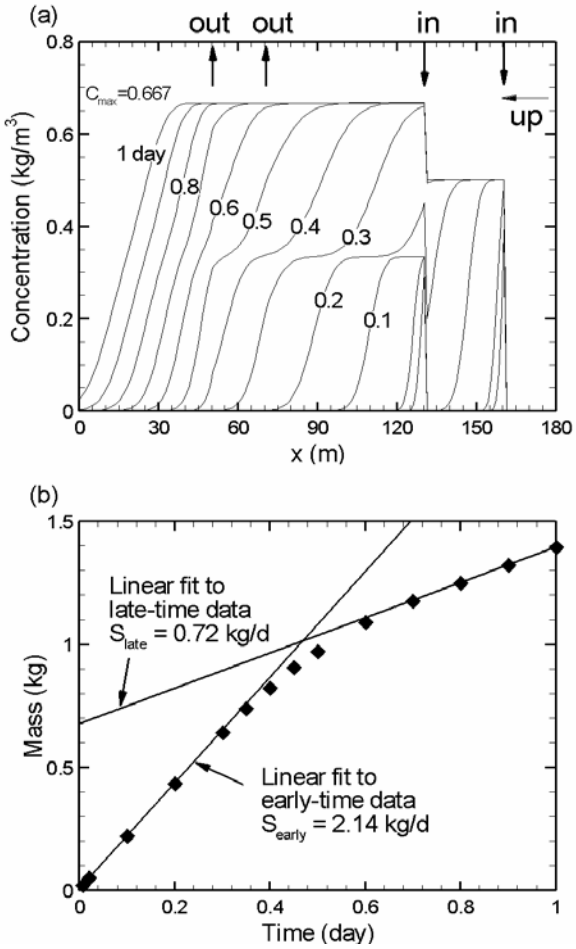

Figure 2. (a) Synthetic flowing FEC data showing a time series of logs produced by inflow and outflow feed points; (b) the corresponding mass integral M as a function of time (symbols) and linear fits for early and late times (lines).

Multi-rate analysis

If the pressure drawdown in the wellbore during pumping is measured, and if the ambient pressure heads h_i of all the feed zones are assumed to be equal, then feed-point flow rate q_i can be converted to the hydraulic transmissivity T_i of the corresponding fracture or permeable zone using Darcy's law. Conducting flowing FEC logging using two different pumping rates can provide information on T_i and h_i in the general case when all the h_i are not the same. For each pumping rate Q, FEC logs are analyzed to produce a set of feed-point strengths q_i and salinities C_i. We generally assume that the C_i values do not change with Q, so feed-point properties are adjusted until a single set of C_i values produces a good match for all pumping rates. We then examine the changes in q_i for a given change in Q. Specifically, suppose that two sets of flowing FEC logs are collected, using $Q^{(1)}$ and $Q^{(2)}$, with $Q^{(2)} - Q^{(1)} = \Delta Q$, and that the resulting BORE II analyses yield $q_i^{(1)}$ and $q_i^{(2)}$, with $q_i^{(2)} - q_i^{(1)} = \Delta q_i$. Then a simple derivation (Tsang and Doughty, 2003) gives

$$\frac{T_i}{T_{tot}} = \frac{\Delta q_i}{\Delta Q} \tag{2}$$

$$\frac{(h_i - h_{avg})}{(h_{avg} - h_{wb}^{(1)})} = \frac{q_i^{(1)}/Q_1}{\Delta q_i/\Delta Q} - 1 \tag{3}$$

where $T_{tot} = \Sigma T_i$ can be obtained by a normal well test over the whole length of the borehole, $h_{avg} = \Sigma(T_i h_i)/T_{tot}$ is the steady-state pressure head in the borehole when it is shut in for an extended time, and $h_{wb}^{(1)}$ is the pressure head in the wellbore during the logging conducted while $Q = Q_1$. Figure 3 illustrates this procedure, using field data.

Signature catalog

We have found that the inverse problem of determining feed-point properties by matching modeled and observed FEC logs can be expedited by developing a catalog of typical FEC signatures produced by specific feed-point features (Doughty and Tsang, 2002). With such a catalog, complex FEC logs can be interpreted in terms of the individual features, not only yielding parameter values for hydraulic properties of the fractures or permeable layers corresponding to feed points, but also providing insight into flow processes occurring at the site.

Acknowledgments

We thank Kenzi Karasaki and Curt Oldenburg for their reviews of this paper. This work was jointly supported by the Office of Science, Office of Basic Energy Sciences, Geosciences Division, of the U.S. Department of Energy (DOE), and by the Japan Nuclear Cycle Research Institute (JNC) under a binational agreement between JNC and DOE, Office of Environmental Management, Office of Science and Technology, under DOE contract DE-AC03-76SF00098.

References

Doughty, C. and C.-F. Tsang, Inflow and outflow signatures in flowing wellbore electrical-conductivity logs, *Rep. LBNL-51468*, Lawrence Berkeley National Lab., Berkeley, CA, 2002.

Doughty, C. and C.-F. Tsang, BORE II – A code to compute dynamic wellbore electrical-conductivity logs with multiple inflow/outflow points including the effects of horizontal flow across the well, *Rep. LBL-46833,* Lawrence Berkeley National Lab., Berkeley, CA, 2000.

Hale, F.V. and C.-F. Tsang, A code to compute borehole conductivity profiles from multiple feed points, *Rep. LBL-24928*, Lawrence Berkeley National Lab., Berkeley, CA, 1988.

Karasaki, K., B. Freifeld, A. Cohen, K. Grossenbacher, P. Cook, and D. Vasco, A multidisciplinary fractured rock characterization study at Raymond field site, Raymond, CA, *J. of Hydrology*, 236, 17-34, 2000.

Paillet, F.L. and W.H. Pedler, Integrated borehole logging methods for wellhead protection applications, *Engineering Geology*, 42(2-3), 155-165, 1996.

Tsang, C.-F. and C. Doughty, Multirate flowing fluid electric conductivity logging method, *Water Resources Res*., in press, 2003.

Tsang, C.-F., P. Hufschmeid, and F.V. Hale, Determination of fracture inflow parameters with a borehole fluid conductivity logging method, *Water Resources Res.*, 26(4), 561-578, 1990.

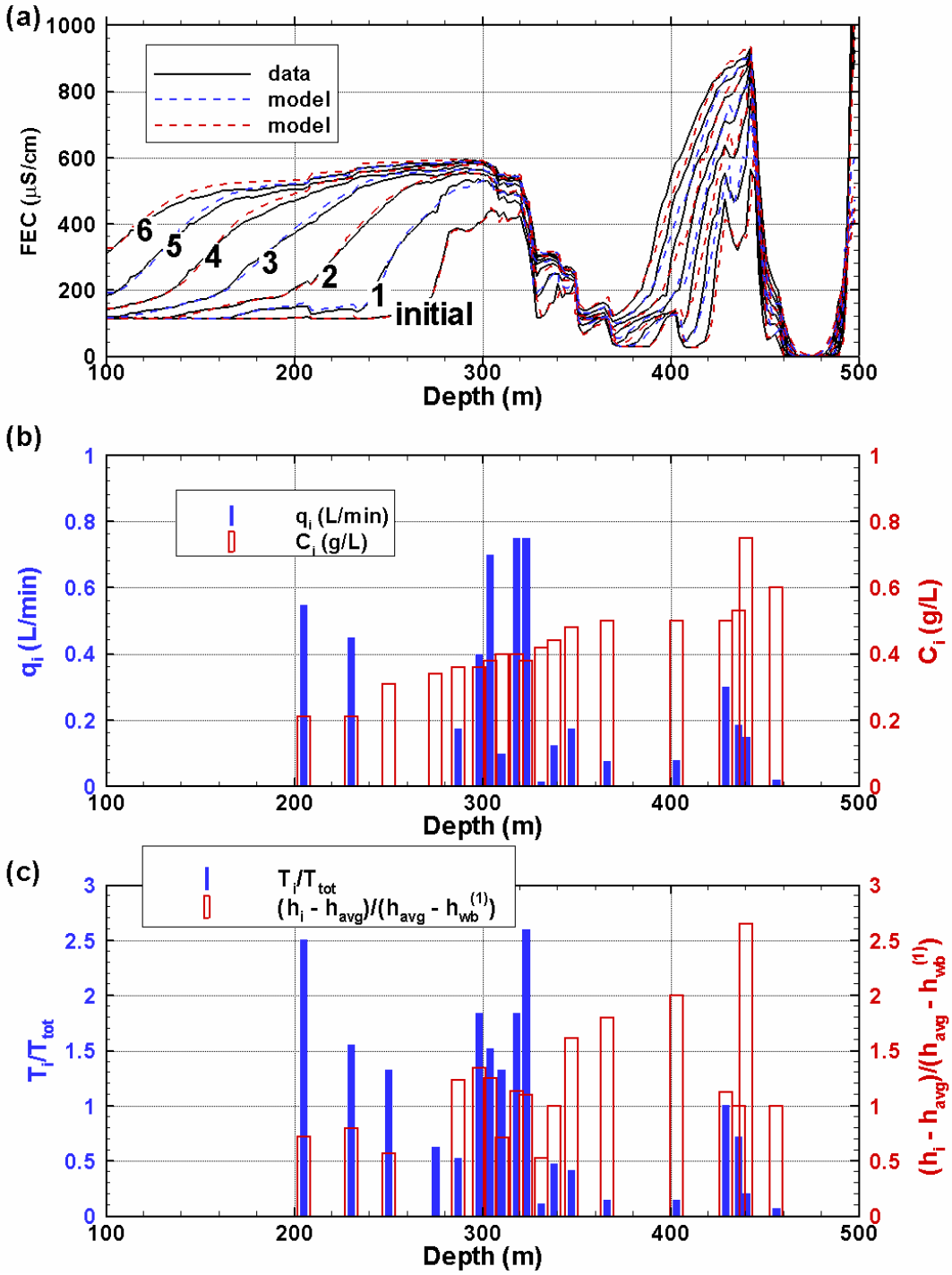

Figure 3. (a) Flowing FEC data showing a time series of logs for field data (black lines) and a calibrated model (red and blue lines). This is the result of analyzing one set of logs at one constant *Q*. (b) Feed-point inflow rates and salinities inferred from the match shown in (a); and (c) Feed-point transmissivities and ambient pressure heads inferred from flowing FEC logging conducted at two pumping rates by combining two sets of result like (a) and (b) and using Equations (2) and (3).

Groundwater Inflow into Tunnels—Case Histories and Summary of Developments of Simplified Methods to Estimate Inflow Quantities

Jon Y. Kaneshiro
Technology Leader for Tunnels
Parsons Corporation, 110 West A Street, Suite 1050, San Diego, CA 92101
jon.y.kaneshiro@parsons.com, 619-515-5122, fax: 619-687-0401

The Underground Technology Research Council co-sponsored by the Society of Mining Engineers and the American Society of Civil Engineers formed a Ground-water Inflow into Tunnels Committee, which is also sponsored by the Association of Engineering Geologists. The Committee consists of 12 members from the tunneling industry, which was formed over 10 years ago in the interest of documenting case histories and lessons learned as well as to summarize and/or develop reliable methods to predict and control ground-water inflow into underground excavations.

Ground water is probably the cause of more rock (and soil) tunneling difficulties and cost overruns than any other single factor. Really practical and reliable methods to predict inflow into tunnels from fractured rock masses have not been developed, and there appears to be little research oriented in this direction. There is a need to define simple parameters defining this problem, to find ways to predict the inflow and the effects of water, including how inflows diminish with time. Just as N. Barton's Q (Quotient) and Z. Bieniawski's RMR (Rock Mass Rating) rock mass classification methods brought some semblance of order in the art of ground support selection, one could hope for similar order in the art of ground-water inflow prediction.

The Committee summarizes the developments and tunnel industry contributions of ground-water inflow prediction into fractured rock tunnels since R. Goodman et al.'s equations in 1965. The Committee summarizes contributions and modifications by R. Heuer in 1995, the Army Corps of Engineers in 1997, C. Laughton in 1998, J. Raymer in 2001, and the Norwegian Tunnelling Society in 2002.

Heuer proposes modifying Goodman et al.'s equations and provides means for estimating long term steady state flows and peak flush flows based on case histories. Emphasis is placed on getting a statistically meaningful amount of packer tests and developing permeability histograms and using the high end tail of the distribution. The Army COE provides simplified closed-form solutions for various tunnel and shaft and body of water configurations. Laughton divides groundwater inflow into categories from small, to moderate, to high inflow and criteria where ground-water inflow presents problems in tunneling excavation and support. Raymer evaluates permeability values from packer tests based on a log-normal distribution to predict the lower and upper bound steady state ground-water inflows. The Norwegian Tunnelling Society has also gathered fractured rock tunnel case histories and introduces proposed prediction methods and associated legislation based on a percentage of the hydrologic basin area that the tunnel impacts.

The Committee's database includes more than 150 case histories, dating back to over a century. This paper and presentation will summarize some of the more illuminating case histories, summarizing the impact to tunnel construction as well as the unpredictable nature of ground-

water inflow into tunnels and the important geologic parameters to identify and bracket for more accurate prediction.

References

Army Corps of Engineers, 1997, Engineering and Design Manual, Tunnels and Shafts in Rock.

Goodman, R. E., D.G. Moye, A. Van Schalkwyk, and I. Javandel, 1964, Groundwater inflows during tunnel driving, Annual Meeting of the Association of Engineering Geologists.

Heuer, R. E., 1995, Estimating rock tunnel water inflow, in G.E. Williamson and I.M. Gowring, Proceedings: Rapid Excavation and Tunneling Conference, p. 41 -60.

Laughton, C., 1998, Evaluation and prediction of tunnel boring machine performance in variable rock masses, Ph.D. thesis University of Texas at Austin, 327 p.

Norwegian Tunnelling Society, 2001, Water Control in Norwegian Tunnelling, Publication No. 12.

Raymer, J. H., 2001, Predicting groundwater inflow into hard-rock tunnels: estimating the high-end of the permeability distribution, in W.H. Hansmire and I.M. Gowring, Proceedings: Rapid Excavation and Tunneling Conference, p.1027 to 1038.

The Porous Fractured Chalk of the Northern Negev Desert: Lessons Learned from Ten Years of Study

R. Nativ[1] and E. Adar[2,3]

[1] Seagram Centre for Soil and Water Sciences, The Hebrew University of Jerusalem, P.O. Box 12, Rehovot 76100, Israel

[2] Department of Geological and Environmental Sciences, Ben-Gurion University of the Negev, P.O. Box 653, Beer-Sheva 84105, Israel.

[3] IWST—Institute for Water Sciences and Technologies, J. Blaustein Institutes for Desert Research Ben-Gurion University of the Negev, Sede Boqer Campus 84990, Israel.

For the past 28 years, the northern Negev desert in Israel has become a prime target for siting a variety of chemical industries rejected by, or transferred from, more populated areas. In addition, the National Site for the Treatment and Isolation of Hazardous Waste has been operating there since 1975. The aridity of the area (180 mm/y rainfall) and the low permeability of the underlying Eocene chalk (~2 mD; Dagan, 1977a,b) were considered major assets in preventing potential groundwater contamination resulting from these activities. This concept of a natural barrier to contaminant migration was challenged, however, when monitoring wells for the National Site for Hazardous Waste were first placed in 1985. Groundwater in these wells (at ~18 m below land surface) displayed high concentrations of heavy metals and organic compounds. The low-permeability, fractured chalk contains brackish water and is not considered a major ground-water resource. However, potential natural leakage of contaminated ground water from these formations into the adjacent Coastal Plain aquifer is of major concern.

Consequently, in 1995, the Israeli Ministry of the Environment asked us to assess: (1) the extent of groundwater contamination within and outside the industrial complex; (2) the off-site migration rates and directions of the various contaminants; (3) the risk for potable water resources; and (4) to provide guidelines and protocols for the proper monitoring of this complex. Following this first assessment, we carried out further studies onsite, funded by the Israeli Science Foundation, the European Union, the Israel Water Authority, the Ministry of Science, International Atomic Energy Association and the council of the industrial complex. Twenty-two researchers and 17 graduate students from Israel, Denmark, Germany, the UK and the US joined us in the study of various geological, hydrological, geochemical and microbiological aspects of flow and transport in fractured rocks. These processes were explored on a variety of scales, including the northern and central Negev area (hundreds of square kilometers, Nativ and Nissim, 1992; Nativ et al., 1997), the site scale (~ 50 km^2; Nativ et al., 1999; Adar and Nativ, 2003), a few meters (Berkowitz et al., 2001; Dahan et al., 2001; Nativ et al., 2003; Weisbrod et al., 2000a) and down to the single-fracture scale, in the laboratory (Polak et al., 2002, 2003a, 2003b; Wefer-Roehl et al., 2000; Weisbrod et al., 1998, 1999, 2000b) and in the field, in both the vadose (Nativ et al., 1995; Dahan et al., 1998, 1999, 2000) and saturated zones (Nativ et al., 2003).

The following are the most important conclusions from these studies (which are not site-specific), regarding the chalk matrix and the fractures intersecting it.

The Chalk Matrix

Chalk mineralogy

- Aside from the biomicritic calcite, the Eocene chalk of the Negev contains a higher percentage of impurities (up to 20%, including siliceous cements, zeolites, and clays) than the more homogeneous Cretaceous chalk of NW Europe.

- Whereas white chalk is found near land surface and contains traces of organic carbon, gray chalk dominates at depths exceeding 20 m and contains ~1% of organic carbon that has been defined as immature kerogen of marine origin (Bloomfield and Nygaard, 2003). The white chalk contains a higher percentage of impurities than the gray chalk.

- Pore-throat size and hydraulic conductivity

- The dominant pore-throat sizes range from 0.3 to 0.009 microns with an average size of 0.15 microns. These pore-throat sizes are smaller and more variable than those found in typical Cretaceous chalks of NW Europe (Bloomfield and Nygaard, 2003).

- Since pores with throat diameters of <10 microns are thought not to drain under gravity, water held in the matrix is unable to contribute to specific yield. The low matrix permeability of the chalk (ranging from 0.008 to 1.5 mD, with a geometric mean of 0.2 mD) reflects this property and implies that there is essentially no water flow or advective contaminant transport through the matrix. Where fractures are present, all effective transport takes place through the fracture network.

- Porosity and diffusion

- The chalk differs from other fractured hard rocks in the sense that it is highly porous (15-47%, averaging 35%) and friable.

- These high porosity values imply that a larger contaminant mass is likely to migrate into and be stored within the pores of the chalk matrix when contaminated ground water flows along the intersecting fractures. Polak et al. (2003a) calculated that chalk matrix that had been subjected to 20 years of contaminant diffusion would require more than 200 years before it would stop releasing contaminants into the intersecting fractures. According to these calculations, remediation efforts based on clean-water injection into the fractures (e.g., pump-and-treat practice) are not a feasible option.

- The diffusion coefficient was found to be more dependent on the porosity of the chalk matrix than on its mineralogy or permeability.

- The effective diffusion coefficient values for the Eocene chalk in the northern Negev are related to the porosity by a linear curve ($D_e / D_0 = 0.315\varepsilon + 0.015$) (Polak et al., 2002). This relationship can be used in the study area for less costly prediction of the diffusion coefficient.

- The lateral concentration variation observed within the chalk matrix following a tracer diffusion suggests two distinct concentration-variation patterns. A sharp decrease within a thin layer near the matrix/fracture interface ("transition layer") and a diffusion-type concentration decrease along the rest of the matrix width (Polak et al., 2003a). These spatial concentration patterns are related to the presence of mini-fissures and small fractures that developed along the fracture/matrix interface when the fracture was formed.

Mineralogy and Sorption

Whereas the sorption capacity of the white chalk is very limited, the gray chalk has a very high sorption capacity (Wefer-Roehl et al., 2000).

The Fractures Intersecting the Chalk Formations

A Monitoring Network for the Site (Nativ et al., 1999):

- The monitoring of the site was designed to capture large-extension, through-going multilayer fractures and joints, considered as the major contaminant conduits; these were identified in the study site using aerial photographs, lineament tracing techniques and field measurements.

- The presence of these prevailing fracture systems at each drilling site was confirmed by trenching, and slanted boreholes were drilled to intersect the fractures below the water table.

- This protocol of siting monitoring boreholes was used to construct tens of new boreholes in the study site. Water level in the new holes recovered within hours to days following purging, and responded immediately to large precipitation events. Most of the new boreholes contained contaminants in their ground water. These observations contrasted with those made in a large fraction of the older, vertical holes (also located near contaminant sources) which did not contain pollutants in their ground water and recovered slowly following pumping. Such contradictory observations suggest that the new boreholes intersecting the fracture systems (as evidenced from the cores and logs) are better connected to the main conduits along which ground water flows and contaminants migrate.

Fracture Characterization on a Scale of Meters (Nativ et al., 2003):

- Fault and fracture mapping in outcrops, commonly carried out in study areas in fractured terrain, cannot determine the proportion of hydraulically active fractures out of the total number of potentially meaningful (i.e., multi-layer, extensional) fractures. The information from coreholes and trenches provided a three-dimensional visualization of the fracture network and enabled identification of the hydraulically active fractures from the other, similar fractures mapped along the outcrops. Consequently, fracture spacing—important data for modeling—could be more realistically determined.

- The information about the location of the most pronounced fractures and the general shapes of their apertures gleaned from the cores and video logs had to be complemented by testing and heat-pulse logging to assess their current hydraulic meaning.

- Slug tests of unpacked coreholes provided a first approximation of the highest equivalent hydraulic conductivity of the fractures intersected by the corehole, at a much lower cost than slug tests carried out in packed-off intervals. Considering the similar values obtained from the slug and pumping tests, slug tests may be the preferred method where pumping contaminated ground water could pose an environmental problem.

- The distribution of the equivalent hydraulic conductivity values of the fractures in our study area appeared log normal. The highest hydraulic conductivity values were observed where two fracture systems intersected each other.

- The high values in the coreholes were limited to the upper 25 m, perhaps because of larger near-surface apertures, resulting from unloading. Considering the observations on fractures to a depth of 100 m, this information is essential for placing future monitoring boreholes and assessing the depth of remediation activities for contaminated ground water on-site.

Fracture Characteristics Estimated from Tracer Tests

- Estimated fracture apertures were 397 to 405 microns and 317 to 385 microns in tests performed on a scale of tens of meters (Reichert et al., 2003), and 29 to 38 microns in tests performed on a single-fracture scale (Bernstein et al., 2003).

- Estimated fracture porosity was 0.02 to 0.035% (Reichert et al., 2003).

- Estimated linear velocity was 2 to 3 m/h (Reichert et al., 2003).

- Estimated dispersivity was 0.11 m (Reichert et al., 2003).

Flow in a Single Fracture

- Flow in the fractures is restricted to small fracture segments along the fracture plane. These segments are generally associated with dissolution channels formed at the intersection of two fractures (Dahan et al., 2000; Bloomfield and Nygaard, 2003). *As little as 20% of the fracture void was found to account for over 80% of the fracture flow (Dahan et al., 1999).

- Experiments of up to 5 days' duration did not result in steady-state flow, suggesting temporal variations in the effective fracture void controlling fluid percolation through fractures (Dahan et al., 1999).

- The likely reason for this instability is particle shearing from the relatively soft fracture surfaces and the disintegration of fracture-filling materials (Dahan et al., 2000).

- Under conditions of variable water content, the aperture, roughness and flow channels of fractures in chalk are transient properties (Weisbrod et al., 1999, 2000b).

Site Remediation

Pumping contaminated ground water from the fracture network through wells is limited by the low volume of ground water contained there and the low-permeability matrix.

Alternatively, passive drainage of the shallow ground water into trenches dug normal to the prevailing fracture systems ensures the intersection of many hydraulically active fractures. Pumping of the accumulated ground water in the trenches for further treatment appears to be a satisfactory solution for our site.

References

Adar, E. and Nativ, R., 2003. Isotopes as tracers in a contaminated fractured chalk aquitard. J. Contaminant Hydrol. 60:on-line.

Berkowitz, B., Nativ, R., and Adar, E., 2001. Evaluation of conceptual and quantitative models of fluid flow and chemical transport in fractured media, in: Conceptual Models of Flow and Transport in the Fractured Vadose Zone. National Research Council, National Academy Press, 115-147.

Bernstein, A., 2003: Spatial distribution of solute transport along fractures in saturated chalk formations. M.Sc. Thesis, Ben Gurion University of the Negev, 93 pp. and app.

Bloomfield, J. and Nygaard, E., 2003. Geological summary for the northern Negev site, in: Contaminant Transport, Monitoring and Remediation Strategies in Fractured Chalk in the Northern Negev.(Eds. Adar,E. and Nativ, R.). Annual Report for the Year 2002.

Dagan, G., 1977a. Hydrological analysis of BS-3, BS-4 and TH-5 exploratory well data. Petroleum Services, Ltd., Israel, 12 pp.

Dagan, G., 1977b. Hydrological analysis of BS-5, BS-10 exploratory well data and summary of hydrological results from Ramat Hovav area. Petroleum Services, Ltd., Israel, 14 pp.

Dahan, O., Nativ, R., Adar, E., and Berkowitz, B., 1998. A measurement system to determine water flux and solute transport through fractures in the unsaturated zone. Ground Water 36:444-449.

Dahan, O., Nativ, R., Adar, E., Berkowitz, B., and Ronen, Z., 1999. Field observation of flow in a fracture intersecting unsaturated chalk. Water Resour. Res. 35:3315-3326.

Dahan, O., Nativ, R., Adar, E., and Berkowitz, B., 2000. On fracture structure and preferential flow in unsaturated chalk. Ground Water 38:444-451.

Dahan, O., Nativ, R., Adar, E. and Berkowitz, B., 2001. Water flow and solute transport in unsaturated fractured chalk, in: Flow and Transport Through Unsaturated Fractured Rock (Eds. Evans, D. D., Nicholson, T. J., and Rasmussen, T. C.). Geophys. Mon. Ser. Vol. 42, 2nd Edition.

Nativ, R. and Nissim, I., 1992. Characterization of an aquitard—the Avdat Chalk, Negev desert, Israel. Ground Water 30:598-606.

Nativ, R., Adar, E., Dahan, O., and Geyh, M., 1995. Water percolation and solute transport through the vadose zone of fractured chalk under desert conditions. Water Resour. Res. 31:253-261.

Nativ, R., Adar, E., Dahan, O., and Nissim, I., 1997. Water salinization in arid regions—observations from the Negev Desert, Israel. J. Hydrol. 196:271-296.
Nativ, R., Adar. E., and Becker, A., 1999. A monitoring network for groundwater in fractured media. Ground Water 37:38-47.
Nativ, R., Adar, E., Asaf, L., and Nygaard, E., 2003. Characterization of the hydraulic properties of fractures in chalk. Ground Water 41:532-543.
Polak, A., Nativ, R., and Wallach, R., 2002. Matrix diffusion in northern Negev chalk formations and its correlation to porosity. J. Hydrol. 268:203-213.
Polak, A., Grader, A. S., Wallach, R., and Nativ, R., 2003a. Chemical diffusion between a fracture and the surrounding matrix: measurement by computed tomography and modeling. Water Resour. Res. 93 (4):106. doi:10.1029/2001WR000813,2003 (on-line).
Polak, A., Grader, S. A., Wallach, R., and Nativ, R., 2003b. Tracer diffusion from a horizontal fracture into the surrounding matrix: measurement by computed tomography. J. Contaminant Hydrol. 60:on-line.
Reichert, B., Witthuser, K., and Hotzl H., 2003. Diffusion and sorption in the northern Negev chalk and its implication on monitoring and remediation, in: Contaminant Transport, Monitoring and Remediation Strategies in Fractured Chalk in the Northern Negev (Eds. Adar, E. and Nativ, R.). Annual Report for the Year 2002.
Wefer-Roehl, A., Graber, A. R., Borisover, M. D., Adar, E., Nativ, R., and Ronen, Z., 2000. Sorption of organic contaminants in a fractured chalk formation. Chemosphere 44:1121-1130.
Weisbrod, N., Nativ, R., Adar, E., and Ronen, D., 1998. On the variability of fracture surfaces in unsaturated chalk. Water Resour. Res. 34:1881-1887.
Weisbrod, N., Nativ, R., Adar, E. and Ronen, D., 1999. The impact of intermittent rainwater and wastewater flow on coated and uncoated fractures in chalk. Water Resources Res. 35:3211-3222.
Weisbrod, N., Nativ, R., Adar, E., and Ronen, D., 2000a. Salt accumulation and flushing in unsaturated fractures in an arid environment. Ground Water 38:452-461.
Weisbrod, N., Nativ, R., Adar, E., Ronen, D., and Ben-Nun, A., 2000b. Impact of coating and weathering on the properties of chalk fracture surfaces. J. Geophys. Res. 105:27,853.

Fracture and Bedding Plane Control of Groundwater Flow in a Chalk Aquitard: A Geostatistical Model from the Negev Desert, Israel

Menachem Weiss, Hebrew University of Jerusalem, Department of Soil and Water Sciences, Rehovot, Israel 76100, Telephone: 972-8-9489150, Cellular Phone: 052608387. E-mail: weissm@agri.huji.ac.il

Yoram Rubin, Department of Civil and Environmental Engineering, University of California at Berkeley, Berkeley, California, U.S.A

Ronit Nativ, Seagram Center for Soil and Water Sciences, Faculty of Agriculture, Hebrew University of Jerusalem, Rehovot, Israel

Eilon Adar, Jacob Blaustein Institute for Desert Research and Department of Geological and Environmental Sciences, Ben Gurion University of the Negev, Sde Boker, Israel

The mechanisms of groundwater flow in fractured rock environments have received much attention since the 1980s because of the interest in using low permeability (commonly fractured) settings as final repositories for hazardous and nuclear waste. Fractures create a unique flow problem, in that hydraulic conductivity variations are extreme and localized, and the discontinuities are typically large in comparison to boreholes and measurement devices (Long et. al. 1998). Flow in fractured rock is highly dependent on the variable aperture of the discontinuity plane and indeed much effort has been expended in understanding aperture geometries (Weisbrod et al. 1998; Dijk and Berkowitz, 1999). Because of the complex nature of these systems, and our inadequate investigative techniques (which often rely on extrapolating exposed features and indirect measurements), statistical network models have been adapted to characterize the discontinuous rock system and quantify the flow processes within (Odling, 1997; Berkowitz et al., 1999; Rubin, 2002).

Groundwater in the northern Negev desert of Israel flows preferentially through a complex system of vertical and horizontal discontinuities within a low conductivity, high porosity Eocene chalk. Fractures and bedding planes were observed along approximately 1,200 m of scanline, 600 m of core and 30 two-dimensional trace planes. Data regarding discontinuity orientation, size, intensity and hydraulic conductivity provided the statistics for the development of a discrete fracture network (DFN) groundwater flow model. The discontinuity size distribution for the stochastic model was defined using both circular window sampling methods and a simulated annealing optimization technique. A bi-modal distribution of size was established for the vertical-type discontinuities that corresponds to their mode of development—burial, syntectonic, or uplift.

Based upon the statistical information obtained from the field surveys, two sets of vertical fractures as well as horizontal bedding planes were simulated in alternative models, using the FracMan® modeling software. The models lack the minor elements of site-wide non-stationarity found regarding fracture orientation and intensity. Furthermore, the model only considers subsets of the actual discontinuity population. These subsets were defined by evaluating the percentage of the overall fracture intensity that shows evidence of past flow (staining, mineralization, etc.) or actual seepage.

Hydraulic conductivity values were obtained in the field through slug tests conducted within eight different boreholes (Assaf, 2000; Nativ et al., 2003; Kurtzman, unpublished). The slug tests were conducted using inflatable double packers to isolate mostly 2 m long sections within each of the boreholes. Each interval was chosen to include fractures previously observed in core logs and video logs of the borehole walls. Because the chalk matrix at the site has extremely low hydraulic conductivity (Nativ et al., 2003), the high values of calculated hydraulic conductivity are expected to represent the effective hydraulic conductivity of the discontinuities isolated within each packed-off interval. The Bouwer and Rice method (1976;1989) was used to analyze the field results and calculate the hydraulic conductivity values. There are a number of issues regarding the applicability of using the Bouwer and Rice method to analyze packed-intervals in a fractured rock environment which are somewhat elaborated upon here.

A histogram analysis of the log-transmissivity values obtained from the packer slug tests shows that the data follows a bi-modal trend of log-normality that is proposed here to be an artifact of the variation in transmissivity being provided by the horizontal discontinuities (bedding planes) and the vertical fractures. A comparison of the slug-test results with the core logs, video logs, and subsequent detailed mapping of the cores revealed that in general the highest hydraulic conductivity values are obtained where horizontal discontinuities are prevalent. Sections tested where only vertical fractures are present show lower values of hydraulic conductivity. Although these results may lead one to believe that the bedding planes are the primary flow conduits, the results are biased due to the orientation of tested borings (drilled near-vertically into the fractured rock) in relation to vertical fractures, causing many (potentially) high-conductivity vertical fractures to be overlooked during the slug-tests.

In fact, visual observations of flow within trenches dug into the saturated zone showed that vertical fractures provided the majority of flow, especially where conjugate sets bisected each other (Figure 1). Horizontal bedding planes appeared to contribute much less seepage into the trenches. Simulations of packer slug-tests were conducted in many alternative three-dimensional DFN models in an attempt to test the above hypothesis, and indeed, some of the models developed were able to capture the bi-modal transmissivity phenomena.

In the DFN models developed for the site, transmissivity was assigned to the vertical-type fractures according to a positive correlation with fracture size. A number of researchers have shown that fracture size and aperture can be statistically correlated. There are geologically based, qualitative and quantitative arguments for possibly high degrees of correlation between the length distribution and the aperture distribution (Stone, 1984; Odling, 1993; Hatton et al., 1994; Vermilye and Scholz, 1995; Johnston and McCaffrey, 1996; Renshaw and Park, 1997). However in nature, the secondary effects of dissolution, chemical action, fault gouge development and/or normal pressures caused by overburden can obliterate any underlying size/aperture relationships (Bonnet et al., in press). Parameters C_1 and C_2 in Equation 1 (below), which shows this relationship, were initially chosen within the range shown in the literature and were subsequently modified iteratively in an attempt to match the field data (Figure 2). Horizontal-type discontinuities in the model were assigned transmissivity values deterministically, according to a lognormal distribution with a mean and standard deviation chosen (iteratively) in an attempt to match the field data. The two correlation parameters were established and utilized as the basis for final calibration of the simulated model to the field observations. An analysis of the residuals created from this inverse problem of trial and error

(Figure 3) shows that while a window of non-unique parameters can be defined, there is still a need to develop a more sophisticated statistical technique to maximize the probabilities.

The following equation accounts for either a linear or non-linear correlation between discontinuity length (L) and transmissivity (T_e):

$$T_e = \left(C_1^2 L^{2C_2}\right) \times \frac{\rho g}{12\mu} \times L \tag{1}$$

where C_1 and C_2 are the correlation coefficients (assuming perfect positive correlation), and ρ, g and μ are the fluid density, the acceleration of gravity, and dynamic viscosity, respectively.

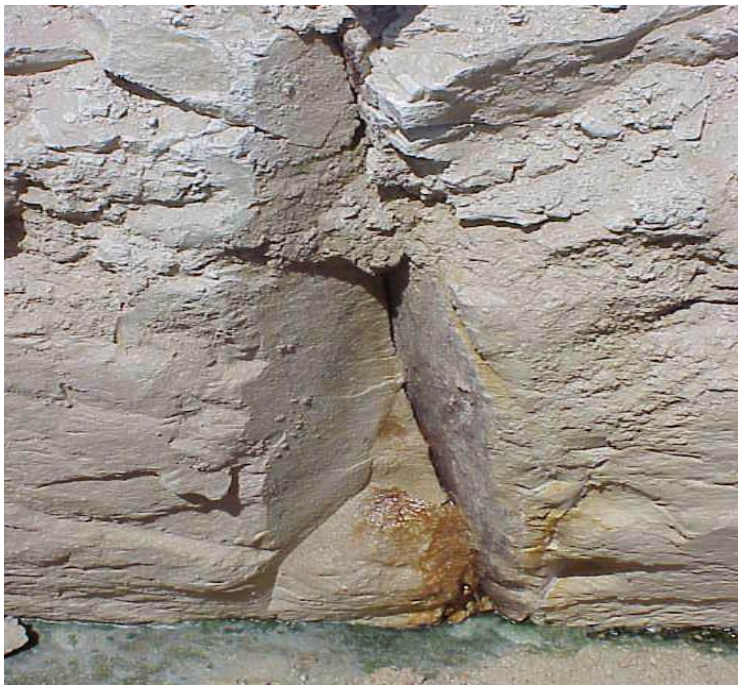

Figure 1. Photograph of two bisecting vertical fractures with seepage of groundwater. Outcrop is approximately 2 m below surface. Scale from top to bottom of photograph is approximately 1 m.

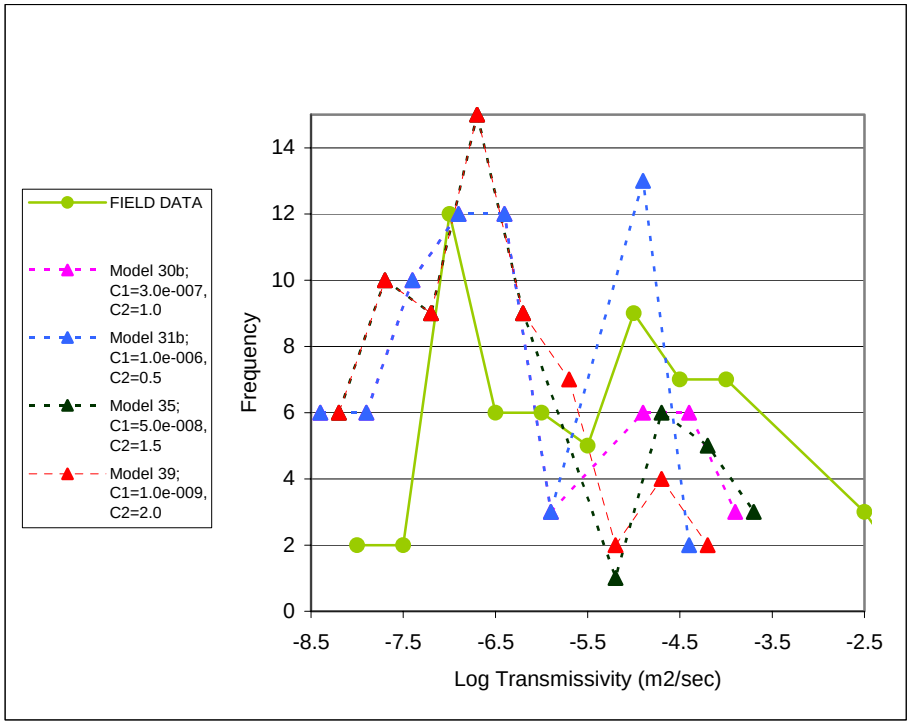

Figure 2. Trial and error calibration of transmissivity in four simulated DFN models based on varying the correlation coefficients relating fracture size and aperture.

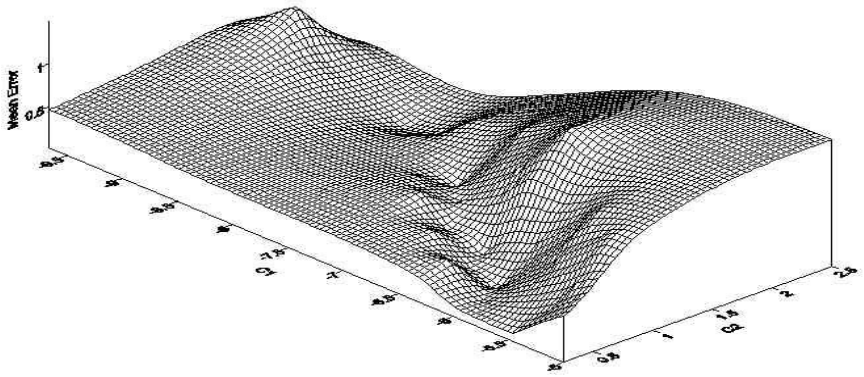

Figure 3. 3-D wireframe plot of mean transmissivity error as a function of C_1 and C_2 parameters (Model 1).

Predicting Fractured Zones in the Culebra Dolomite

Richard L. Beauheim[1], Dennis W. Powers[2], and Robert M. Holt[3]
[1]Sandia National Laboratories, 4100 National Parks Highway, Carlsbad, NM 88220
[2]Consulting Geologist, 140 Hemley Road, Anthony, TX 79821
[3]Department of Geology and Geological Engineering, University of Mississippi, University, MS 38677

Introduction

Fracturing in the Culebra Dolomite Member of the Permian Rustler Formation exhibits a high degree of spatial variability in the vicinity of the Waste Isolation Pilot Plant (WIPP) in southeastern New Mexico. The WIPP is the U.S. Department of Energy's deep geological repository for transuranic (TRU) and mixed wastes resulting from the nation's defense programs. The WIPP repository is located 655 m below ground surface in bedded halite of the Salado Formation. Culebra transmissivities (T's) in the vicinity of the WIPP vary over six orders of magnitude, with higher T's (log T (m^2/s) > -5.4) reflecting fracturing. In some areas, high T is clearly related to dissolution of halite from the upper Salado Formation and subsidence and collapse of the overlying Rustler Formation, forming surface depressions. In other areas, however, occurrences of high Culebra T appear more random, with no obvious cause. Understanding the distribution of fractures in the Culebra is important because the Culebra provides the most transmissive groundwater pathway for radionuclides that might be released from the WIPP repository by inadvertent human intrusion. Therefore, a study is under way to identify the causes of fracturing where possible and develop tools to predict fracturing in areas where its existence is uncertain.

Fracturing and Dissolution

To the west of the WIPP site, dissolution of the upper Salado and subsidence of the overlying strata have formed a trough known as Nash Draw (Figure 1). The surface expression of Nash Draw covers approximately 400 km^2 with as much as 100 m of relief from the edge of the draw to its center. Culebra log T (m^2/s) values are –3.6 or greater at all tested wells in Nash Draw and cores, where recovered, show extensive fracturing.

Dissolution of the upper Salado can be inferred from abrupt changes in contours of the thickness of the upper Salado and lower Rustler derived from geological and geophysical log analysis (Powers et al., 2003). (Over 1,000 oil, gas, and/or potash exploration holes have been drilled in the Delaware Basin in the vicinity of the WIPP site.) Along the edge of Nash Draw, the section from the top of the Culebra to the base of the Vaca Triste Sandstone Member within the Salado Formation thins from approximately 190 m to less than 150 m over lateral distances of 200-400 m (Figure 2).

Dissolution of the upper Salado may also have occurred in smaller areas where either no surface expression was formed or the subsidence has been masked by deposition of overlying sediments. Three areas have been identified where lesser degrees of thinning of the Culebra-Vaca Triste interval occur with no obvious surface expression. Two of these areas appear to be connected to

Nash Draw and are inferred to be dissolution re-entrants (Figure 3). The third area (at SNL-12 on Figure 1) appears to be isolated.

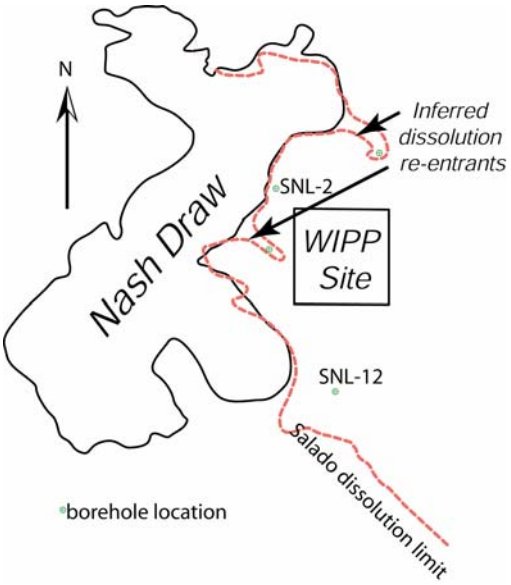

Figure 1. Outline of surface expression of Nash Draw and areas of inferred dissolution.

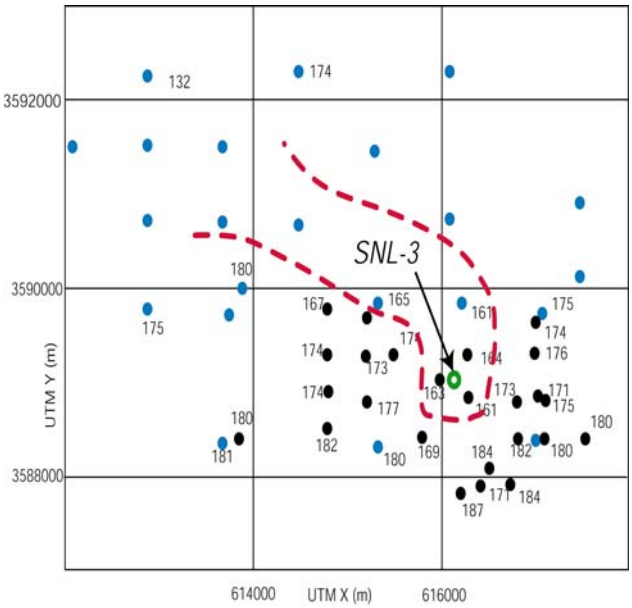

Figure 2. Cross section across the edge of Nash Draw showing thinning of the Culebra-Vaca Triste interval.

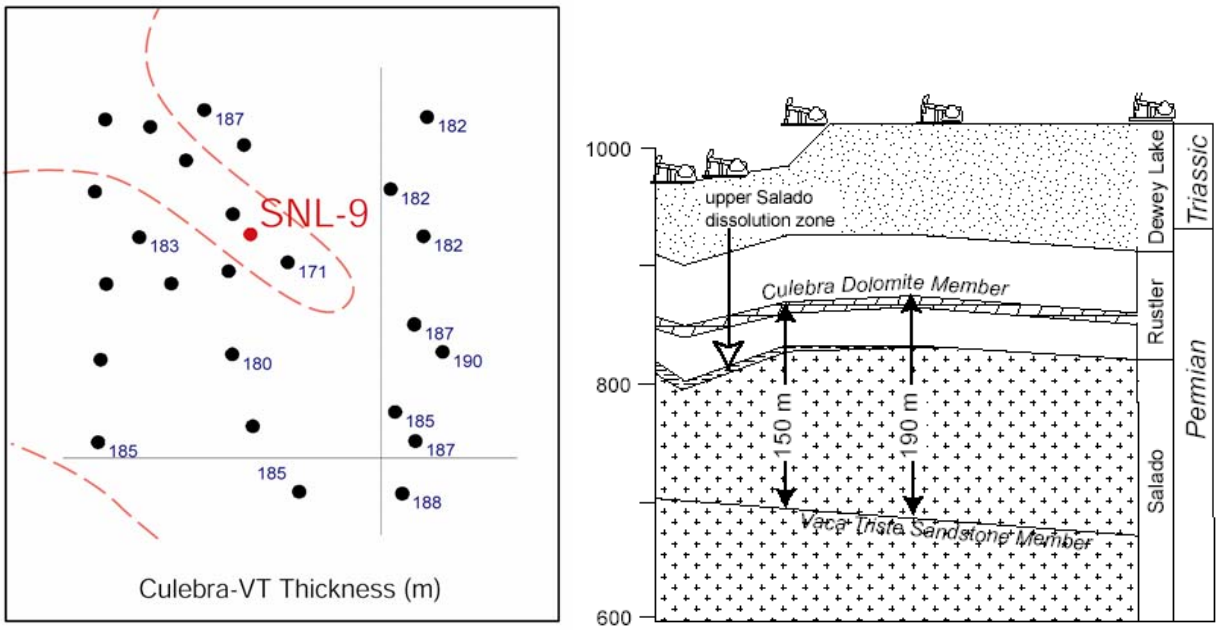

Figure 3. Dissolution re-entrants inferred from thinning of Culebra-Vaca Triste interval.

In addition to dissolution of the upper Salado, dissolution of halite may also have occurred in the Rustler Formation in certain areas. Halite was deposited within portions of the mudstone facies tracts in the three non-dolomite members of the Rustler (Figure 4). The Culebra is directly underlain by claystone of the Los Medaños Member. East of the WIPP site, halite is found in this claystone unit (designated M2/H2). Although extensive post-depositional dissolution of this halite is not believed to have occurred, some dissolution may have occurred along the present-day halite margin, resulting in Culebra subsidence and fracturing. Thus, fracturing of the Culebra might be expected along this halite margin.

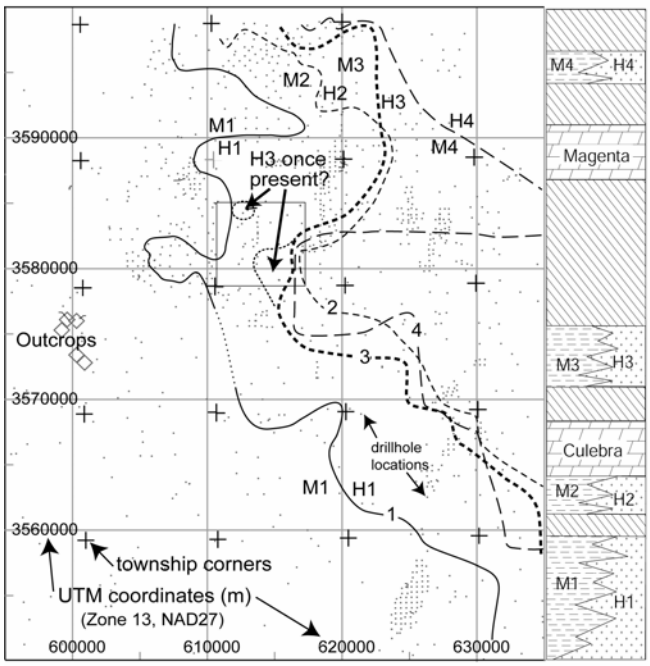

Figure 4. Margins of present-day halite in non-dolomite members of the Rustler Formation. Halite is present east of the margins

Halite margins are also important because the presence of halite in mudstones above and below the Culebra can be construed as evidence for the absence of fracturing. We conceptualize fracturing as being associated with increased groundwater flow through the Culebra. Culebra groundwater salinity varies widely, with densities ranging from 1,000 to 1,150 kg/m^3, but the salinity is below saturation with respect to halite everywhere it has been tested. Higher fluid densities (>1,100 kg/m^3) are found in areas of low Culebra T (no fracturing), generally close to or within the areas where halite is present in the Rustler above and/or below the Culebra. The high fluid densities are probably caused by slow advection of pore waters from the mudstones and/or diffusion of halite into the Culebra, accompanied by very slow Culebra groundwater movement (Kröhn and Schelkes, 1996). If the Culebra were fractured, allowing rapid flow, the diffusion gradient would be much higher, and any nearby halite would be expected to have been dissolved. The halite margins in the Rustler (Figure 4) can be mapped reasonably well from the abundant well logs available, allowing predictions of where the Culebra is *not* likely to be fractured.

Other Controls on Fracturing

Holt (1997) has estimated that as much as 600 m of overburden was eroded from above the Culebra during the Cenozoic. The stress relief that would have accompanied this erosion probably induced fracturing in the Culebra, particularly at bedding planes of weakness. The probability and hydraulic significance of stress-relief fractures should increase with decreasing thickness of overburden above the Culebra. Because the Culebra dips to the east, hydraulically significant fractures should be more prevalent to the west. This hypothesis is supported by a correlation derived by Holt and Yarbrough (2002) between log T and depth to the Culebra.

However, stress relief alone does not fully explain why the Culebra is observed to be fractured in some areas but not in others.

In some locations, the Culebra is fractured but the fractures are filled, primarily with anhydrite or gypsum. Consequently, the distribution of high and low Culebra T may, in some areas, be related more to flow patterns that have dissolved (or precipitated) fracture fillings and altered the degree to which existing fractures are interconnected than to the occurrence of fracturing *per se*. Structural deformation below the Rustler may be another local factor that influences Culebra fracturing.

While dissolution explains some fracturing and stress relief helps explain its intensity, some fractured areas have been found by chance for which no obvious explanation can be adduced. Between the limit of Salado dissolution shown on Figure 1 and the M2/H2 and M3/H3 margins shown on Figure 4, 12 wells have encountered fractured, high-T conditions while 24 wells have encountered unfractured, low-T conditions. While the high T's at a few of the wells appear to be related to dissolution in the Rustler, the fracturing at the majority of the wells is currently unexplained.

Evidence for Fracturing from Hydraulic Tests

Whether the reasons for fracturing are known or not, large-scale hydraulic tests can help us to differentiate fractured from unfractured regions. Numerous pumping tests have been conducted in fractured areas of the Culebra that produced observable drawdown responses in observation wells as much as 6 km from the pumping wells. The patterns of responses observed provide evidence of fracturing in areas where it is not known to be present from direct observation. When wells that had fractured cores and show high T in pumping tests show rapid, high-magnitude responses to pumping in fractured areas several kilometers away (e.g., H-3b2 in Figure 5), we infer that the pumping and observation wells are connected by fractures. When wells that had unfractured core and show low T in slug tests nevertheless show rapid, high-magnitude responses (e.g., H-15 in Figure 5), we infer that fractures must pass near to these observation wells, although outside the radii of influence of the slug tests. Conversely, when delayed, low-magnitude responses are all that are observed (e.g., H-14 in Figure 5), we infer that fractures do not pass near the observation wells. These qualitative inferences have been substantiated by model simulations that cannot reproduce observed rapid, high-magnitude responses without extending high-T zones close to wells known to have low T. Similarly, high T cannot be present in other locations where low-magnitude, delayed responses were observed.

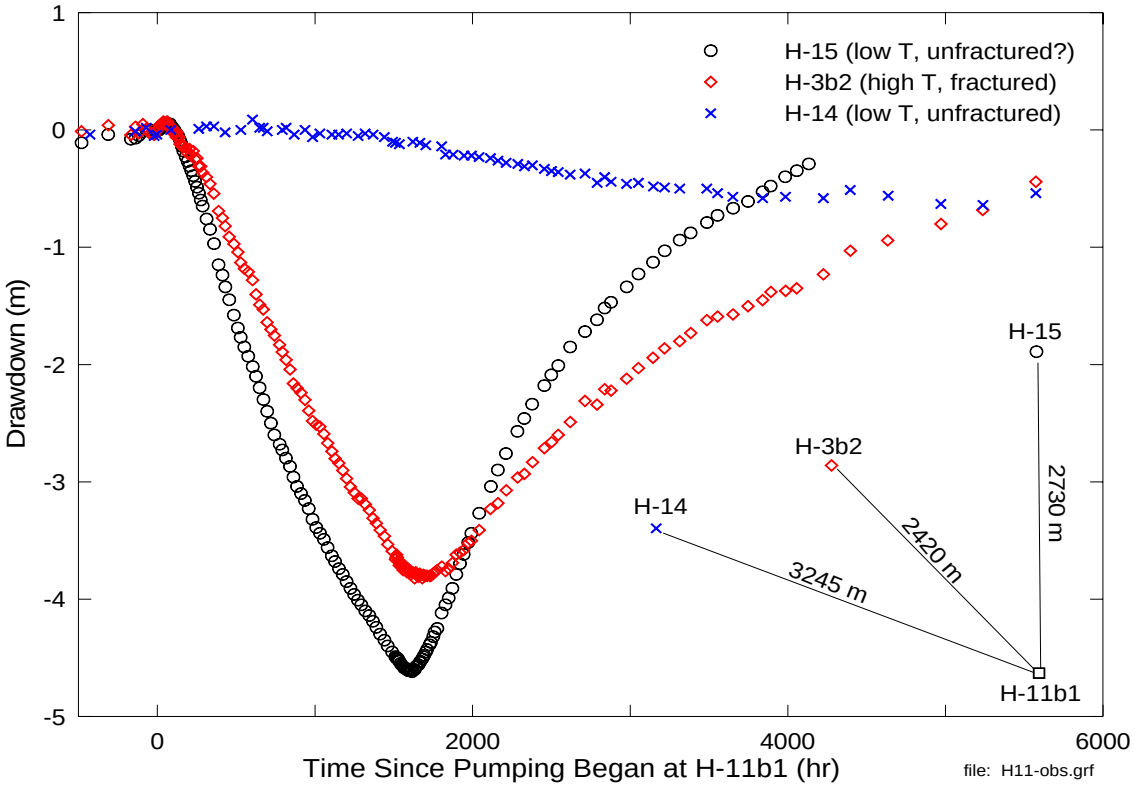

Figure 5. Drawdown responses in fractured and unfractured zones to pumping in a fractured zone.

Field Verification

A field program was initiated in 2003 to test our hypotheses about Culebra fracturing and provide additional information about the causes of fracturing. This program involves installing and testing wells in areas where fracturing is expected and where it is not expected. Two wells have been located in areas where geological/geophysical log interpretation indicates dissolution of the upper Salado has likely occurred despite the lack of surface expression of that dissolution (SNL-3 and SNL-9, Figure 3). These wells were cored into the upper Salado to provide direct evidence of dissolution. Both wells encountered fractured Culebra and high T. A third well (SNL-12 in Figure 1) was located behind the indicated Salado dissolution margin and adjacent to an oil well where the Culebra-Vaca Triste interval is thin relative to surrounding wells. SNL-12 encountered high T; a zone of the Culebra is fractured. A fourth well was installed near the margin of Salado dissolution, but where no dissolution was expected (SNL-2 in Figure 1). This well encountered unfractured Culebra and low T.

Other wells are proposed near the margins of present-day halite in the Rustler and where simulation of hydraulic tests indicates high T must be present. Still other wells are proposed in areas where halite is present below the Culebra and low T is expected, to verify our conceptual model. Core is being taken in all new wells to identify features in overlying and underlying strata that might be related to Culebra fracturing.

Once all of the proposed wells have been installed, large-scale tests will be performed by pumping at some of the new high-T wells to see if the responses observed at surrounding wells suggest the existence of additional high-T areas.

Conclusions

Fracturing in the Culebra can be related, in some areas, to dissolution of the upper Salado and/or dissolution within the Rustler. In other areas, the causes of fracturing are unknown, but large-scale hydraulic tests allow us to infer what regions are and are not fractured. New wells are being drilled and tested in areas expected and not expected to be fractured. Through these new investigations, we hope to improve the existing conceptual model for Culebra fracturing and develop a predictive tool for fracturing and high T in non-dissolution areas.

Acknowledgment

This research is funded by WIPP programs administered by the U.S. Department of Energy.

References

Holt, R.M. 1997. Conceptual Model for Transport Processes in the Culebra Dolomite Member, Rustler Formation. SAND97-0194. Albuquerque, NM: Sandia National Laboratories.

Holt, R.M., and L. Yarbrough. 2002. Analysis Report, Task 2 of AP-088, Estimating Base Transmissivity Fields. ERMS# 523889. Carlsbad, NM: Sandia National Laboratories, WIPP Records Center.

Kröhn, K.P., and K. Schelkes. 1996. "Modelling of regional variable density groundwater flow in an area in New Mexico: importance of influencing parameters and processes," *Calibration and Reliability in Groundwater Modelling* (Proceedings of the ModelCARE 96 Conference, Golden, Colorado, September 1996), IAHS Publication no. 237, pp 353-361.

Powers, D.W., R.M. Holt, R.L. Beauheim, and S.A. McKenna. 2003 (in press). "Geological factors related to the transmissivity of the Culebra Dolomite Member, Permian Rustler Formation, Delaware Basin, Southeastern New Mexico," in Johnson, K.S., and J.T. Neal, eds., *Evaporite Karst and Engineering/Environmental Problems in the United States*. Oklahoma Geological Survey Circular 10.

Hydraulic Test Interpretation with Pressure Dependent Permeability—Results from the Continental Deep Crystalline Drilling in Germany

W. Kessel[1], R. Kaiser[2], and W. Gräsle[1]
[1] Leibniz Institute for Applied Geosciences, Stilleweg 2, D-30655 Hannover, Germany
[2] Institute of Fluid Mechanics and Computer Applications in Civil Engineering, University of Hannover, Appelstraße 9A, 30167 Hannover, Germany

Summary

A new concept for fracture hydraulic test interpretation is presented. The aim of this concept is the derivation of a fracture porosity from the results of hydraulic testing. With this porosity, a realistic first-step transport modeling, especially for deep low porous fractured rock, is possible. This concept is based on the microscopic model of parallel fractures with limited variations in the elastic behavior. The elastic behavior of the fractures in the tested interval can be derived from the pressure dependent transmissivity. Two examples of testing fault zones at great depth are shown. First, interpretations from the German continental deep drilling project (KTB) from a fault zone in 4000 m depth are discussed. Second, a tracer-test interpretation from the Soultz-sous-Fôrets geothermal project is presented.

Introduction

In the classical interpretations of hydraulic tests, the two reservoir parameters, transmissivity and storativity, are derived (Earlougher, 1977) assuming a plane aquifer of constant thickness. The microscopic structure of the reservoir fractures and pores and the reservoir thickness does not influence the result. To assess the parameters aquifer thickness and porosity necessary for transport modeling we need additional observations from cores or logging. Especially in deep crystalline formations stress relaxations and temperature variations in core and borehole wall will lead to micro cracking and a related change of the porosity about an order of magnitude. Berckhemer (1997) gave porosity values for the KTB cores in a range of 0.1% to 1.0%. Kessels (1987) showed by calculations that thermo-mechanically induced microscopic stress on the minerals can easily produce all this porosity by microcracking. To overcome this problem, Kessels and Kück (1995) presented the concept of hydraulic fracture interpretation with an example of test interpretation for the hydraulic communication between the two KTB boreholes in a depth of 4,000 m. They introduce the two parameters apparent frac density n and mean fracture widths W. The relation of both parameters to the classic parameters of transmissivity and storativity is derived by the model of parallel fractures and the cubic law. In Figure 1 this mean fracture compressibility in dependency of the effective stress is given. This corresponds well to the assumption that the distortion of a fracture in a linear elastic rock depends only on the fracture shape and the elastic behavior of the main minerals, and is independent of the mean fracture width. The conclusion of Figure 1 is that natural fractures have similar shapes.

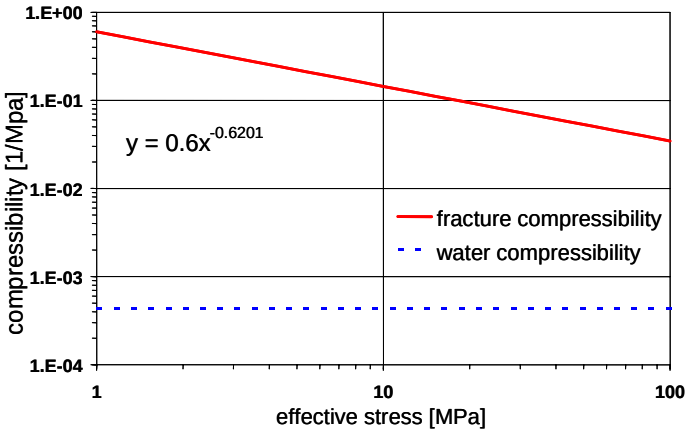

Figure 1. Average fracture compressibility in dependency of the effective stress (σ_n – P) regarding Kessels & Kück (1995).

Concept of Fracture Test Interpretation

In the following, we discuss a hydraulic fault model of n parallel fractures of constant width (see Figure 2). In this model, without vertical hydraulic pressure gradients in the case of test interpretation, the fractures may be connected or not.

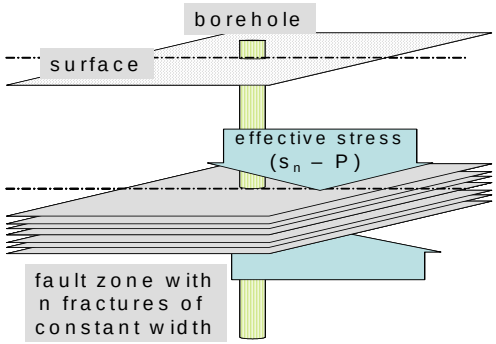

Figure 2. Fracture model.

Mass conservation in a single fracture is given by Equation (1).

$$\frac{T_f}{\eta}\frac{1}{r}\cdot\frac{\partial}{\partial r}r\frac{\partial P}{\partial r}-S_f\frac{\partial P}{\partial t}=0 \qquad (1)$$

$$T_f=\frac{W^3}{12}=\textit{fracture transmissivity}\quad W=\textit{fracture width}\quad S_f=\textit{fracture storativity}$$

$$P=\textit{pressure}\quad r=\textit{radius}\quad t=\textit{time}\quad \eta=\textit{vis cos ity}$$

For a fault zone consisting of n parallel fractures, the contribution of the fractures add up to Equation (2).

$$\frac{T}{\eta}\cdot\frac{1}{r}\cdot\frac{\partial}{\partial r}r\frac{\partial P}{\partial r}-S\frac{\partial P}{\partial t}=0 \qquad (2)$$

$$T=n\cdot\frac{W^3}{12}=\textit{fault transmissivity} \quad S=n\cdot S_f=\textit{fault storativity}$$

The fracture storativity S_f of a single fracture can be described by compressibilities as written in Equation 3. Here, we take the fracture compressibility C_f instead of the pore compressibility c_p in the classic interpretation. C_w denotes the water compressibility and ρ the water density.

$$S_f=W\cdot\left(C_f+C_w\right)=W\cdot\left(\frac{\partial W}{W\cdot\partial P}+\frac{\partial\rho}{\rho\cdot\partial P}\right) \qquad (3)$$

The fracture compressibility C_f can be derived by a hydraulic test regarding Kessels and Kück (1995) from the pressure dependency of the fault transmissivity. Basis for the relation in Equation (4) is the cubic law (Witherspoon et al.,1980) for fracture transmissivity:

$$C_f=\frac{\partial W}{W\cdot\partial P}=\frac{1}{3}\frac{\partial T}{T\cdot\partial P} \qquad (4)$$

If no determination of the pressure dependency of the transmissivity is possible, we get a first C_f value from Figure 1. The hydraulic diffusivity can also described by the fracture parameters according to Equation (5):

$$D=\frac{T}{\eta\cdot S}=\frac{T_f}{\eta\cdot S_f}=\frac{W^3/12}{W\cdot\eta\cdot\left(C_f+C_w\right)}=\frac{W^2}{12\cdot\eta\cdot\left(C_f+C_w\right)} \qquad (5)$$

Once the hydraulic diffusivity and the fracture compressibility are derived from the hydraulic test data, the mean fracture width can be calculated using Equation 6:

$$W=\sqrt{12\cdot\eta\cdot\left(C_f+C_w\right)\cdot D} \qquad (6)$$

With the transmissivity T determined from the classic hydraulic test interpretation, we can derive an apparent fracture number n (Kessels, 1993):

$$n=\frac{12\cdot T}{W^3} \qquad (7)$$

We can now derive the fracture porosity Φ_f of the aquifer according to Equation (8). For this, the aquifer (reservoir) thickness M must be measured on cores or by logging.

$$\Phi_f=\frac{n\cdot W}{M} \qquad (8)$$

With this fracture porosity, a new connection between hydraulic parameter and transport parameter is established.

Continental German Deep Drilling Project (KTB)

In the hilly Bavarian area of Oberpfalz, there are two boreholes drilled up to 4,000 m (pilot hole) resp. 9,100 m depth (main hole) in the crystalline rock. It was the objective of this project to improve the understanding of processes in the deeper crystalline crust. Hydraulic and transport processes coupled with the stress field are one of the main targets of the project (Kessels, 1991; Kessels et al., 1992, Möller et al., 1997; Zoback et al., 1993; Huenges et al., 1997). Two major fault zones are penetrated in a depth range of 4,000 m (500 m thick) and 7,200 m as shown in Figure 3. The best transmissivity and storativity for the upper fault zone were derived from a hydraulic communication between pilot and main hole (Kessels & Kück, 1995). Presuming a viscosity $\eta = 2.7 \cdot 10^{-4}$ Pa (corresponding to the formation temperature of 120°C) and a thickness of 300 m, they found the following hydraulic parameters:

$$D = 0.12 \text{ m}^2/\text{s}$$
$$T = 1.62 \cdot 10^{-13} \text{ m}^3$$
$$S = 5.0 \cdot 10^{-9} \text{ m/Pa}$$

In the KTB main hole, the fracture compressibility is derived from a hydraulic fracture test on a depth of 6,000 m. The pressure history of this test is shown in Figure 4; technical details are given by Engeser et al. (1993). From the pressure steps running here, Huenges and Kessels (1993) derived the pressure-dependent permeability. From these, the fracture compressibility also shown in Figure 4 was calculated. The values are in a good agreement with the mean values given in Figure 1. The hydraulic fracture parameters resulting from this are

$$log\left(\frac{c}{MPa^{-1}}\right) = -0.2218 - 0.62 \cdot log\left(\frac{S_{eff.}}{MPa}\right)$$

fracture width $W = 4.41\ 10^{-6}$ m
mean fracture number n = 20000 [-]
fracture porosity $\Phi_f = 0.0002$ [-]

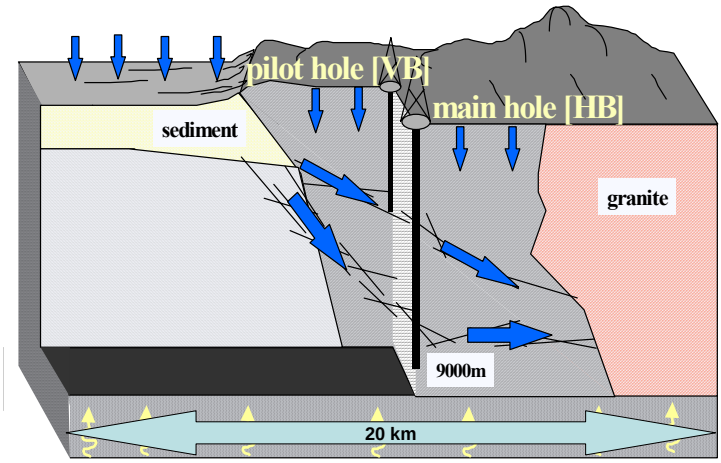

Figure 3. Sketch of the KTB holes and the geological structure with the two fault zones (arrows = flow).

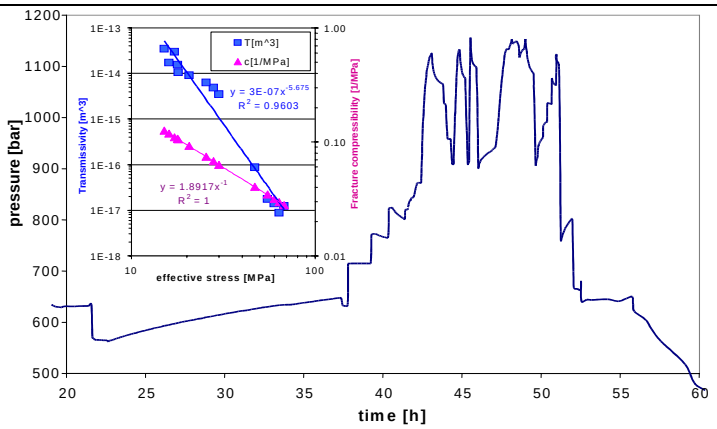

Figure 4. Pressure history during the 6,000 m fracturing test in the KTB main hole.

Test Interpretation of a Tracer Test in the Soultz Boreholes

The Soultz project is a geothermal Hot-Dry-Rock (HDR) project near the French-German border in the Rhine Graben area. Between and within the two nearly 3,500 m deep boreholes GPK1 and GPK2 some hydraulic tests were carried out (Jung et al., 1995; Hettkamp et al., 2002; Grecksch et al., 2003). Both holes were hydraulically connected by fault zones and stimulated by hydraulic injection. The transport along this fault zone is observed by a tracer test. With the help of flow logs, geophysical logging, and cores, a fracture network shown in Fig. 5 was built using the FE program RockFlow (Kaiser, 2000). The hydraulic parameters of these fractures (determined by inverse modeling) are given in Table 1.

Table 1. Hydraulic fracture parameters determined by pressure history matching (Pribnow and Kaiser, 2001).

fault zone	GPK1 depth [m]	GPK2 depth [m]	storativity [m/Pa]	transmissivity [m^3]
1	2870		$1 \cdot 10^{-08}$	$1.8 \cdot 10^{-13}$
2	2960		$6 \cdot 10^{-09}$	$1.28 \cdot 10^{-13}$
3	3500		$2 \cdot 10^{-09}$	$1.1 \cdot 10^{-13}$
4		3250	$2 \cdot 10^{-09}$	$1.1 \cdot 10^{-13}$
5		3350	$1 \cdot 10^{-08}$	$1.1 \cdot 10^{-13}$
6		3470	$2 \cdot 10^{-09}$	$1.3 \cdot 10^{-13}$

No good matching for the break through curves was found when modeling the tracer test characterizing every fault zone by a single fracture according to the cubic law. The peak occurred much too early (break through after a few hours). The first try of the fracture model discussed here gave a break through curve in the right time scale. The measured and calculated break through curves are given in Figure 6. Note that these curves are based on hydraulic parameters only derived from hydraulic data and not yet optimized for transport.

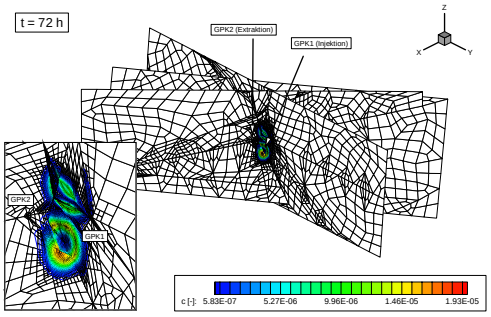

Figure 5. Fracture model for the fault zones between the Soultz boreholes GPK1 and GPK2.

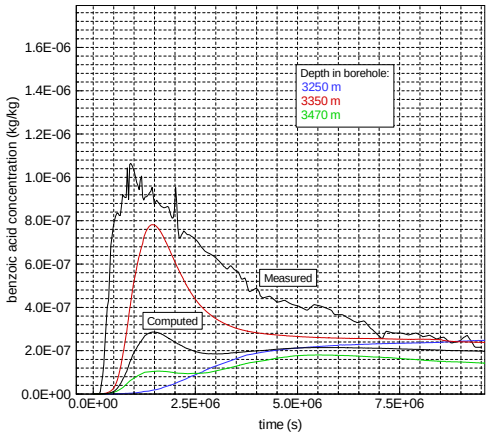

Figure 6. Measured and calculated break through curves in the GPK2 borehole.

Conclusion

Despite the simplification of the fracture interpretation discussed here, the model provided a good boundary of the possible parameterization also if only hydraulic tests for transport parameterization exist.

References

Berckhemer H, Rauen A, Winter H, Kern H, Kontny A, Lienert M, Nover G, Pohl J, Popp T, Schult A, Zinke J, Soffel HC (1997) Petrophysical Properties of the 9 km Deep Crustal Section at KTB. J Geophys Res, 102,B8:18337-18361.

Engeser B, Huenges E, Kessels W, Kück J, Wohlgemuth L (1993) The 6000 m hydrofrac test in the KTB main borehole—design, implementation and preliminary results. KTB-Report 93-1:301-336, Niedersächsisches Landesamt für Bodenforschung, Hannover, Germany

Earlougher RC Jr (1977) Advances in well test analysis. Henry-L.-Doherty Memorial Fund of AIME, Society of Petroleum Engineers, 264 pp, New York.

Grecksch G, Jung R, Tischner T, Weidler R (2003) Hydraulic fracturing at the European HDR/HFR test site Soultz-sous-Forêts (France)—a conceptual model. Proc European Geothermal Conf, Szeged, May 25-30, 8 pp.

Hettkamp T, Teza D, Baumgärtner J, Gérard A, Baria R (2002) Stand des europäischen Hot Dry Rock Forschungsprojektes Soultz-sous-Forêts. In: 20 Jahre Tiefe Geothermie in Deutschland, Geothermische Vereinigung e.V., Geeste, ISBN 3-932570-46-4, 48-55.

Huenges E, Kessels W (1993) Effective stress dependency of permeability and transmissibility of rocks during the 6 km hydrofrac-experiment in the KTB main hole. Annales Geophysicae Suppl I,12.

Huenges E, Engeser B, Erzinger J, Kessels W, Kück J (1997) The Permeable Crust: Geohydraulic Properties Down to 9000 m Depth—Results from the German Continental Deep Drilling Project (KTB). J Geophys Res 102,B8:18255–18265.

Jung R, Willis-Richards J, Nicholls J, Bertozzi A, Heinemann B (1995) Evaluation of hydraulic tests at Soultz-sous-Forêts, European Hot-Dry-Rock site. World Geothermal Congress, Florence, May 18–31, 2671–2676.

Kaiser R, Rother T, Kolditz O, Zielke W (2000) Automatic grid adaptation for modeling coupled flow and transport processes in fractured aquifers. Proc XIII Int Conf Computational Methods in Water Resources, Calgary, Alberta, Canada, June 25-29, Balkema, Rotterdam/Brookfield, ISBN 90 5809 1236, 279–283.

Kessels W (1987) Das Spannungsfeld der Erdkruste und seine Wirkung auf eine übertiefe Bohrung. KTB-Report 87-2:183-208, Niedersächsisches Landesamt für Bodenforschung, Hannover, Germany.

Kessels W (1991) Objectives and execution of hydraulic experiments in the KTB-Oberpfalz borehole within the long-term measurement and test programme. Sci Drill 2:287–298.

Kessels W (1993) The fracture compressibility and the effective stress dependency of the transmissibility. Annales Geophysicae Suppl I,12.

Kessels W, Kück J (1995) Hydraulic Communication in the Crystalline Rock Between the two Boreholes of the Continental Deep Drilling Programme in Germany. Int J Rock Mech Min Sci & Geomech Abstr 32:37-47.

Kessels W, Kück J, Zoth G (1992) Hydraulische Untersuchungen in der Bohrung KTB-Oberpfalz HB bis 5000m. KTB Report 92-1:169–198, Niedersächsisches Landesamt für Bodenforschung, Hannover, Germany.

Möller P, Weise S, Althaus E, Bach W, Behr HJ, Borchardt R, Bräuer K, Drescher J, Erzinger J, Faber E, Horn E, Huenges E, Kämpf W, Kessels W, Kirsten T, Landwehr D, Lodemann M, Machon L, Pekdeger A, Pielow HU, Reutel C, Simon K, Walter J, Weinlich FH, Zimmer M (1997) Paleo- and Recent Fluids in the Upper Continental Crust – Results from the German Continental Deep Drilling Projekt (KTB). J Geophys Res 102,B8:18223–18254.

Pribnow D, Kaiser R (2001) Gemeinsame Interpretation hydraulischer und geothermischer Daten ein lokales 3D-Modell des natürlichen und des künstlich erzeugten Kluftsystems. BMBF Project 032 66 90 A / 032 72 18, GGA Institut, report 0 121 418, Hannover.

Witherspoon PA,Wang JSY, Iwai K, Gale JE (1980) Validity of cubic law for fluid flow in a deformable rock fracture. Wat Resour Res 16:1016–1024.

Zoback M, Apel R, Baumgärtner J, Brudy M, Emmermann R, Engeser B, Fuchs K, Kessels W, Rischmüller H, Rummel F, Vernik L (1993) Upper-crustal strength inferred from stress measurements to 6 km depth in the KTB borehole. Nature 365:633–635.

Quantification of Contact Area and Aperture Distribution of a Single Fracture by Combined X-Ray CT and Laser Profilometer

A. Polak[1,2], H. Yasuhara[2], D. Elsworth[2], Y. Mitani[3], A. S. Grader[2] , and P. M. Halleck[2]*
[1]Department of Civil and Environmental Engineering, Technion, Israel Institute of Technology, Haifa 32000, Israel. amirp@tx.technion.ac.il
[2]Energy Institute and Department of Energy and Geo-Environmental Engineering Pennsylvania State University, University Park, PA 16802, USA
[3]Institute of Environmental Systems, Dept. of Civil Engineering, Faculty of Engineering, Kyushu University, 6-10-1, Hakozaki, Higashi-ku, Fukuoka, 812-8581 JAPAN

Introduction

Fractures are well known to affect the mechanical and hydraulic properties of rock-masses, such as stress-strain behavior and fluid permeabilities. Mechanical behavior of a single fracture, such as deformability and strength, are strongly dependent upon its surface properties, and cannot be fully understood without quantifying the contact area and the roughness of two mating surfaces. Similarly, fluid flow, which typically dominates in fractured rock masses, is controlled by the connectivity of fractures and the topography of the fracture surfaces. Thus, a quantitative understanding of contact area and fracture aperture distribution is critical to predict fluid-flow and mechanical properties of a rock mass.

Several experimental techniques have been applied to determine fracture morphology and the connectivity of porosity, and are categorized into two groups-non-destructive methods and injection methods. The former involve non-destructive measurements by X-ray computed tomography (Johns et al., 1993; Keller, 1997; Pyrak-Nolte, et al., 1997; Scavia, 1999) and by roughness profilometers (e.g. Durham and Bonner, 1993; Xia et al., 2003). The impregnation methods use wood's metal (Pyrak-Nolte, et al., 1987) and various resins (Baraka-Lokmane, 2002; Gentier, et al., 1989). X-ray imaging of fractures has the distinct advantage of providing quantitative aperture data even under confining pressure or other applied environmental conditions. However, conventional medical CT is limited in spatial resolution (typical resolutions are the range 0.1 mm to 1 mm) and the definition of the characteristic CT-number-threshold that defines the fracture is complicated. Impregnation methods can also present quantitative characterization of the aperture distributions, but injection of foreign materials such as wood's metal and resins may disturb the fracture surfaces. Imperfect casts of some void spaces due to high viscosities and/or wetting characteristics may also present a problem.

In contrast, surface profilometers has a potential spatial accuracy, in the axis perpendicular to the fracture surface, of the order of 1 micron. It provides a high-resolution image of the topography of the faces of the fracture. However, the rock sample must be opened in book format to provide the laser or stylus access to the surfaces of the fracture, preventing application under applied environmental conditions. It is also difficult to accurately mate the digital surfaces of the fracture and construct a single fracture with aperture distributions under stressed conditions. We compare the resolution of profilometry and micro-CT, and note an example where each method may be used to its full potential—profilometry to define extremely fine-scale texture, and X-ray micro-CT to project this texture to the interior of a stresses fracture.

Materials and Methods

The measurements were conducted on a cylindrical core of Arkansas Novaculite (55 mm diameter × 90 mm length) containing a single diametral natural fracture. After coring, the fracture was pried-open using narrow-taper wedges and the two halves of the core were reassembled using 1-mm foam plastic spacers to keep the fracture open. The sample was first scanned using a custom-made industrial scanner (HD-600, Universal Systems Inc.). The scanner was tuned to produce slices perpendicular to the core axis each with a thickness of 58 μm and an in-plane pixel resolution of 54 μm. The X-ray energy level used in the experiment was 160 kV at 500 μA. A total of 1456 adjacent slices were produced covering the entire length of the sample. A detailed description on the use and limitations of X-ray CT in core analysis may be found in Stock (1999), and Wildenschild et al. (2002).

Subsequently, the sample was removed from the scanner, opened in book format, cast face-up in gypsum, and profiled in 3-D using a laser scanner (Figure 1). The surface profiling system is comprises of an X-Y positioning table (±15 μm) and a 3-D laser scanner (maximum resolution of 0.5 μm), both controlled by a data acquisition computer (Figure 2). Fracture elevations are recorded on a rectangular grid with 50 μm spacing between adjacent data points. Considering errors due to temperature changes, the effective vertical resolution of the profiling system in this specific case was 10 μm.

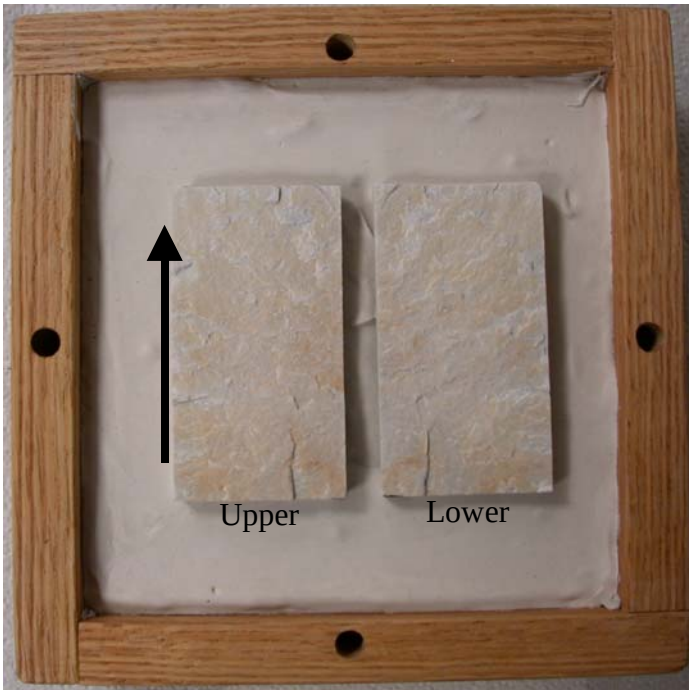

Figure 1. A picture of the rock sample in an open book view, cased in a gypsum mold inside a wooden box.

Results and Discussion

The two data sets can both be reduced to separate top and bottom surfaces. Figure 3 is a direct comparison of profilometer and X-ray CT data for one of the surfaces. The two images illustrate extremely good correspondence, although the CT data are somewhat lower resolution than the profilometer data. Figure 4 shows detail of a step in the surface (circled in the image of Figure 3). The side dimension of these square panels is approximately 10 mm. Virtually every feature visible in the profilometer data is present in the CT data, although again, the difference in resolution is evident. The comparison shows that the high-resolution CT data are nearly as effective as the profilometer data in defining the fine-scale texture of the fracture surface, with additional advantage that the measurements may be made under realistic environmental conditions of applied stress, temperature, and with saturating fluids.

In order to determine a relationship between the aperture and the contact area of the fracture, it is necessary to digitally manipulate the two surfaces into contact. The basic method is to move the two surfaces together until one point from each of the surfaces comes into contact. The surfaces are then rotated and translated incrementally, observing the volume of the fracture until a minimum value is obtained. Finally, the separation between the two surfaces is varied, noting the areas of interpenetration (loosely defined as contact area) and correlating it with corresponding fracture volume. Figure 5 depicts the relation between the mean aperture and the contact-area ratio, R_c, defined as the ratio of the number of profile points representing interpenetrated surfaces, to the total number of measurement points. These data can also be displayed graphically. Figure 6 shows the spatial distribution of these contact areas with different mean aperture conditions.

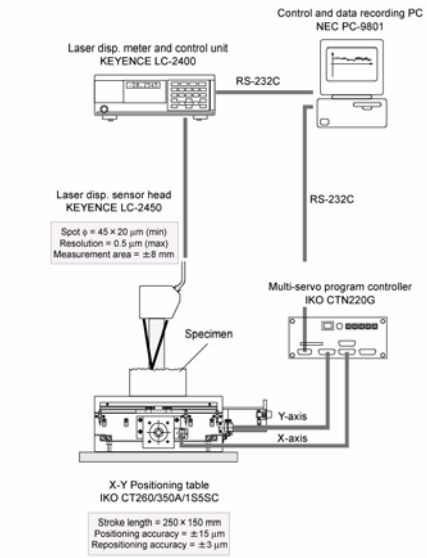

Figure 2. Schematic view of three-dimensional laser scanning system for measurement of fracture surface topography.

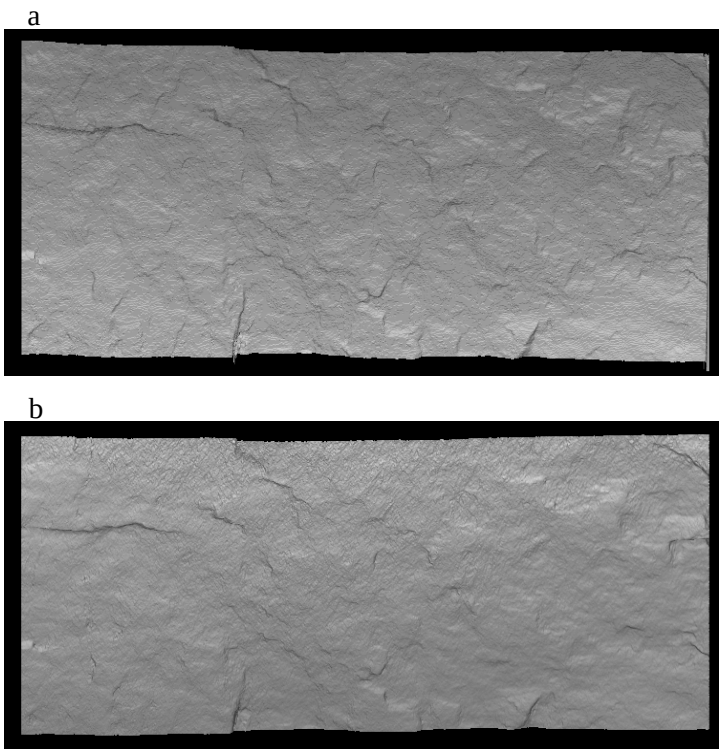

Figure 3. Surface maps of one side of the fracture surface. (a) Micro-CT data. (b) Profilometer data.

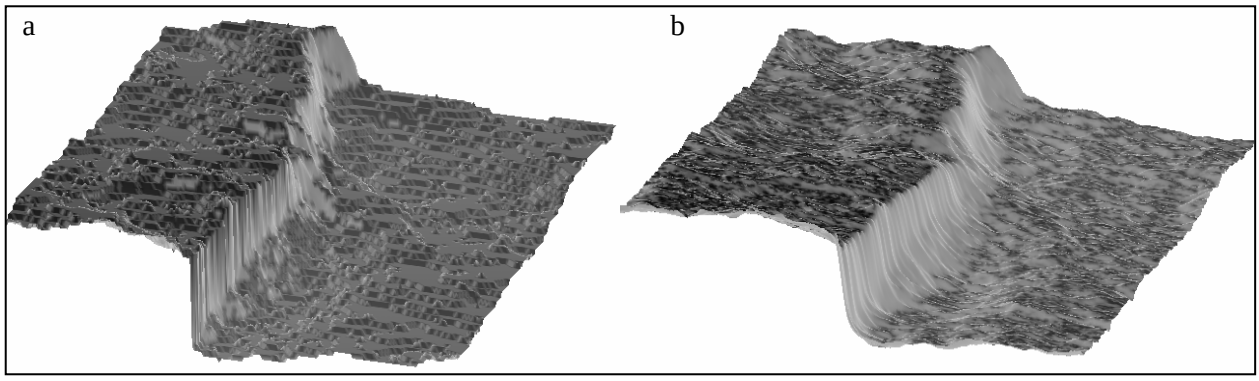

Figure 4. Details of surface maps of one side of the fracture surface. The area of the detail is about 10x10 mm. a: Micro-CT data. b. Profilometer data.

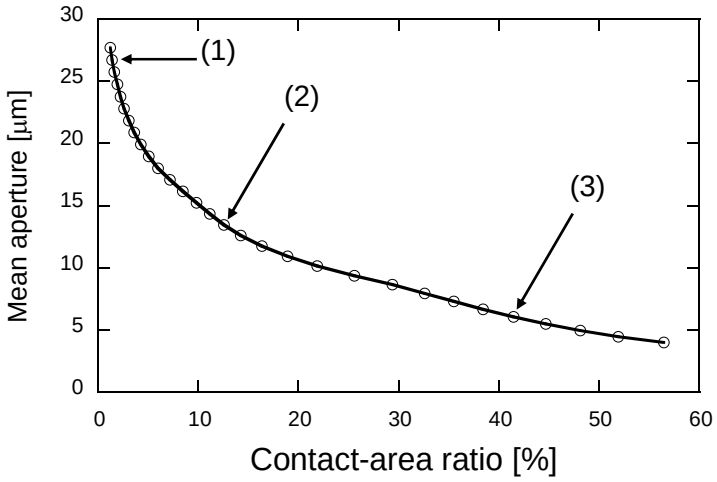

Figure 5. Mean aperture vs. contact area ratio. Profilometer data with 50 μm and 10 μm resolution for x-y and z directions, respectively. The numbers in the graph mark the points that were used in Figure 6.

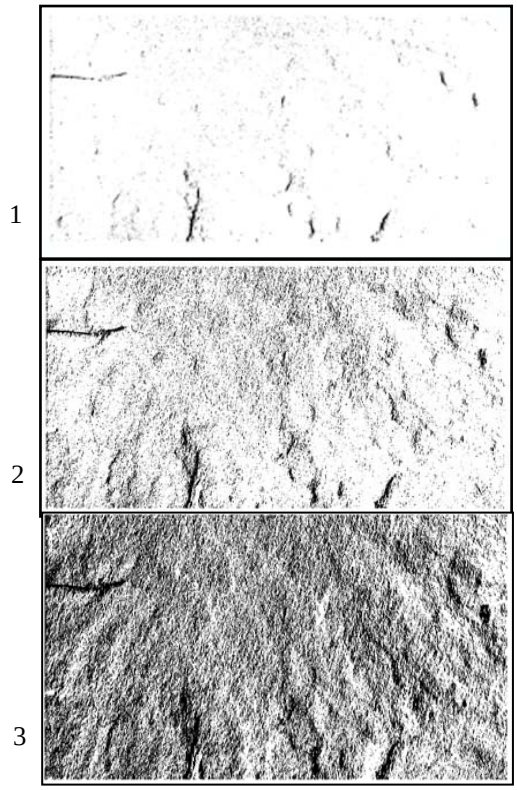

Figure 6. Contact area distribution that was calculated by subtracting the two measured by the profilometer. Black colors represent the contact points for (1) mean aperture of 27.7 μm for contact area of 1.25 %, (2) mean aperture of 13.5 μm for contact area of 12.6 % and (3) mean aperture of 6.05 μm for contact area of 41.5 %.

The two methods for quantifying the topography of the fracture are complimentary. Profilometry provides the highest resolution measurement of the fracture surface in all dimensions, but requires that the sample is destructively opened and that apertures are recovered from assumptions on the mated condition. Micro-CT measures the distribution of fracture apertures directly, albeit at slightly lower resolution, but may be used under applied environmental conditions of stress, temperature and fluid pressure and saturation. Both methods permit the use of the digital data to create various fracture aperture distributions that can be used for fluid transport and solid mechanics modeling.

References

Baraka-Lokmane, S., A new resin impregnation technique for characterizing fracture geometry in sandstone cores, *Int. J. Rock. Mech. Min. Sci., 39*, 815-823, 2002.

Durham, W. B. and B. P. Bonner, PEAK: A new kind of surface microscope, *Int. J. Rock. Mech. Min. Sci. Geomech. Abstr., 30*, 699-702, 1993.

Gentier, S., D. Billaux, and L. van Vliet, Laboratory testing of the voids of a fracture, *Rock Mech. Rock Eng., 22*, 149-157, 1989.

Johns, R. A., J. S. Steude, L. M. Castanier, and P. V. Roberts, Nondestructive measurements of fracture aperture in crystalline rock cores using X ray computed tomography, *J. Geophys. Res., 98*, 1889-1900, 1993.

Keller, A. A., High resolution CAT imaging of fractures in consolidated materials, *Int. J. Rock. Mech. Min. Sci., 34*, 155, 1997.

Pyrak-Nolte, L. J., L. R. Myer, N. G. W. Cook, and P. A. Witherspoon, Hydraulic and mechanical properties of natural fractures in low permeability rock, *Proc. 6th. Int. Cong. Rock. Mech.*, eds. G. Herget and S. Vongpaisal, Montreal, Pubs. A. A. Balkema, 225-231, 1987.

Pyrak-Nolte, L. J., C. D. Montemagno, and D. D. Nolte, Volumetric imaging of aperture distributions in connected fracture networks, *Geophys. Res. Lett., 24*, 2343-2346, 1997.

Scavia, F. Re, C., Determination of contact areas in rock joints by X-ray computer tomography, *Int. J. Rock. Mech. Min. Sci., 36*, 883-890, 1999.

Stock, S.R., X-ray microtomography of materials. Int. Mater. Rev. 44(4):141-164, 1999.

Wildenschild, D., J.W. Hopmans, C.M.P. Vaz, M.L. Rivers, D. Rikard, and B.S.B. Christensen, Using X-ray computed tomography in hydrology: systems, resolutions, and limitations. J. Hydrol. 267:285-297, 2002.

Xia, C. C., Z. Q. Yue, L. G. Tham, C. F. Lee, and Z. Q. Sun, Quantifying topography and closure deformation of rock joints, *Int. J. Rock. Mech. Min. Sci., 40*, 197-220, 2003.

A Comparison between Hydrogeophysical Characterization Approaches Applied to Granular Porous and Fractured Media

Jinsong Chen, Susan Hubbard, and John Peterson
Earth Sciences Division, Lawrence Berkeley National Laboratory

This paper compares the use of geophysical data for subsurface characterization based on data collected at two different DOE field sites: the NABIR South Oyster site in Virginia and the Oak Ridge Field Research Center in Tennessee. The granular porous aquifer at the first site is relatively homogenous. At this site, petrophysical relationships between hydrogeological properties measured at wellbore locations and geophysical attributes could be developed using co-located wellbore and tomographic data. However, the aquifer at the second site is fractured and very heterogeneous, and reliable petrophysical relationships could not be developed using such co-located data sets. Different Bayesian models have been developed based on specific field conditions of the two sites to incorporate geophysical data into hydrogeological parameter estimation. Results show that despite the difference in aquifer heterogeneity, geophysical data provide useful information for hydrogeological characterization.

Introduction

Geophysical methods have found many applications in subsurface characterization (Hyndman et al., 1994; Hubbard and Rubin, 2000; Chen et al., 2001). The main reason for the success is that geophysical methods are less invasive and provide more information than traditional characterization methods. However, several obstacles still hinder the routine use of geophysics for hydrogeological characterization (Hubbard and Rubin, 2002).

One key obstacle is the lack of understanding of petrophysical relationships between geophysical attributes and hydrogeological parameters, especially in complex media such as fractured rock. In addition, the discrepancy in scale and resolution between geophysical and hydrogeological measurements, and uncertainty associated with geophysical data acquisition and interpretation make it difficult to develop petrophysical relations for linking geophysical attributes to hydrogeological properties. Consequently, applications of geophysical data for site characterization are often site-specific, and the petrophysical relationships are simple linear regression models obtained using co-located geophysical and hydrogeological data.

This study demonstrates the use of geophysical data for hydrogeological characterization at two DOE field sites that have dramatically different aquifer heterogeneity. We estimate the spatial distributions of hydraulic conductivity at the first site and hydrogeological zonation at the second site, using geophysical data and different Bayesian models. We discuss a comparison between the two Bayesian models developed according to site-specific petrophysical models.

Case Study at Granular Porous Media Site

Site information

The South Oyster Site is located near the town of Oyster on Virginia's Eastern Shore Peninsula between Chesapeake Bay and the Atlantic Ocean. The sediments at the South Oyster Site consist of unconsolidated to weakly indurated, well-sorted, medium- to fine- grained Late Pleistocene sands and pebbly sands. The water table at the site is located approximately 3 m below ground surface. Within the South Oyster Site, two study areas exist: the South Oyster Focus Area and the Narrow Channel Focus Area. This case study focuses on the Aerobic Flow Cell in the Narrow Channel Focus Area. Forced gradient chemical and bacterial tracer test experiments were performed within the flow cell in 1999 (Hubbard et al., 2001).

Extensive geophysical and hydrological data have been collected within the saturated portion of the Aerobic Flow Cell, approximately between depths of 0–6 m below the mean sea level (MSL), to characterize the subsurface before the tracer test experiments. These included ground-penetrating radar (GPR) and seismic tomographic data along each transect, and flowmeter and slug test data at 10 wellbores. Our goal was to provide detailed hydraulic conductivity estimates, by integrating crosswell geophysical data and borehole flowmeter data, that could be used to constrain numerical modeling of flow and contaminant transport at the site.

Data Analysis

Hydraulic conductivity values obtained from wellbore flowmeter data displayed only a small variation at this site; the natural logarithmic conductivity had a variance of 0.30. The log-conductivity had a good spatial structure, which could be fit using an exponential model with a vertical range of 0.6 m and a horizontal range of 5 m. The geophysical tomographic data (including GPR and seismic velocity, and GPR attenuation), inverted from their corresponding travel time data, also varied over small ranges. The ranges of GPR velocity, GPR attenuation, and seismic velocity were 5.9–6.3 cm/ns, 0.18–0.38 1/m, and 1.61–1.73 km/s, respectively.

We developed petrophysical models between hydraulic conductivity and geophysical attributes using co-located hydraulic conductivity and geophysical data at the wellbore locations. Although both log-conductivity and geophysical data displayed small variations, good correlations exist between those parameters. Correlation coefficients of log-conductivity versus GPR velocity and log-conductivity versus seismic velocity were 0.68 and 0.67, respectively.

Estimation Method

Since petrophysical models between the geophysical attributes and hydrogeological parameters could be developed, and log-conductivity had a good spatial structure, we developed a Bayesian model to integrate the geophysical data and borehole measurements. To illustrate this approach, we only use GPR velocity (for more types of geophysical data and details of the method, see Chen et al., 2001). Let v_i be the known GPR velocity at pixel-i (referred to as data). Let K_i be the unknown hydraulic conductivity at pixel-i (referred to as a random variable), which is spatially correlated to the hydraulic conductivity at its surrounding pixels. Thus, the Bayesian model is given as follows:

$$f(K_i \mid v_i) = C \bullet f(v_i \mid K_i) \bullet f(K_i) \,, \quad (1)$$

where C is a normalizing constant that insures integration of the left side is equal to one. The $f(K_i \mid v_i)$ term is referred to as the posterior probability density function (PDF), the $f(K_i)$ term is referred to as the prior PDF, and the $f(v_i \mid K_i)$ term is referred to as the likelihood function.

The posterior PDF in Equation 1 is obtained numerically. We first derive the prior PDF using geostatistical kriging of borehole hydraulic conductivity measurements. We then derive the likelihood function from the co-located log-conductivity and GPR velocity data at or near wellbores. For the given prior PDF and likelihood function, we divide the entire domain of prior distribution into many small intervals. For each data point on the domain, we evaluate the values of the prior PDF and likelihood function. Consequently, we obtain the posterior distribution of hydraulic conductivity at each point (0.25 m × 0.25 m pixel) in space along the 2D tomograms (Figure 1). Cross-validation suggests that this approach provides accurate estimates of hydraulic conductivity. The subsequent research also suggests that these data are very useful for constraining numerical models for flow and contaminant transport simulation (Scheibe and Chien, 2003) and for helping to understand bacterial transport in natural porous media (Malloux et al., 2003).

Case Study at the Fractured Media Site

Site Information

The NABIR Field Research Center (FRC) is located on the Oak Ridge Reservation in Tennessee. The geology at this site is complicated. The Nolichucky shale bedrock under the site dips approximately 45 degrees to the southeast and has a strike of N55E. Overlying the bedrock is unconsolidated material that consists of weathered bedrock (referred to as residuum or saprolite), man-made fill, alluvium, and colluviums. The thickness of residuum is typically between 5 m and 10 m thick. Between the unconsolidated residuum and competent bedrock is a transition zone of weathered fractured bedrock. Remnant fracturing in the residuum and transition zone increases the permeability relative to the silt and clay matrix (Watson et al., 2003).

Several types of geophysical data have been collected at this site to characterize hydrogeological properties in the saturated, fractured media. Those data included surface seismic and electrical data, crosswell seismic and GPR data, various types of borehole geophysical logs, and flowmeter data. Our goal is to integrate crosswell geophysical tomographic data and borehole hydrogeological measurements to provide the spatial distribution of hydrogeological properties for understanding field-scale bioremediation experiments carried on this area.

Data Analysis

Hydraulic conductivity at this site obtained from wellbore flowmeter data varied over a large range (3–4 orders of magnitude). Crosswell seismic tomographic data, gamma-ray logs, flowmeter data, and lithology logs collected at this site showed that two zones exist: the upper layer and the lower layer, with the interface at depths 8–10 m. The upper layer had low hydraulic conductivity, high clay content, and low seismic velocity. The lower layer was fractured media

with low clay content. Although crosswell GPR tomographic data were also collected along cross sections, the quality of GPR data was much lower than seismic data. We expect seismic data to be sensitive to the rock stiffness and thus the presence of fractures. Consequently, we choose to use crosswell seismic data only in the following analysis.

We developed petrophysical models for linking seismic tomographic data to hydraulic conductivity following a procedure similar to what was described in the preceding case study. The cross correlation between log-conductivity and seismic velocity, based on co-located data available at or near boreholes, was poor and thus could not be directly used to improve hydrogeological characterization. The weak correlation have been caused by the difference in sampling volumes between crosshole seismic surveys and borehole flowmeter tests. Seismic methods sense seismic properties along a two-dimensional cross section, whereas flowmeter test senses hydraulic properties within a localized 3D volume around boreholes.

However, several other studies, including laboratory and field experiments, have shown that low seismic velocity in a fractured rock or media primarily is caused by the presence of fracture networks and thus can be used for hydraulic conductivity estimation (Pyrak-Nolte et al., 1987; Majer et al., 1997; Ellefsen et al., 2002; Daley et al., 2003). Accordingly, although we could not develop a good petrophysical relationship between hydraulic conductivity and seismic velocity based on co-located data at the wellbore, we believe that seismic velocity data could be useful for characterizing the fractured subsurface.

Estimation Method

To incorporate seismic information into hydrogeological characterization, we improve the Bayesian model used in the first case study. It is necessary that the new model permit consideration of crosswell seismic velocity as unknown variables, which could be estimated by conditioning to both crosswell travel-time and borehole flowmeter data. This model should also allow for consideration of petrophysical models to be known up to unknown parameters, which are estimated during the joint inversion process.

Several assumptions are made and justified based on information available at this site. We estimate hydrogeological zonation (high or low conductivity zone) instead of continuous values of hydraulic conductivity. We assume that in the fractured media, the low seismic velocity is primarily caused by fracture networks. Therefore, high seismic velocity in this zone likely corresponds to low hydraulic conductivity, whereas low seismic velocity likely corresponds to a high conductivity zone. However, since some fracture networks may not be connected and some clayey sandstone may also exist in the deeper part of the aquifer, the qualitative relationship described above is subject to uncertainty. To handle this uncertainty, we consider that the inverse of seismic velocity (slowness) at a specific location has a Gaussian distribution with mean and variance related to fracture density and thus hydraulic conductivity at each pixel.

The Bayesian model is developed based on seismic travel time and flowmeter data collected at two adjacent wells, with the goal of estimating hydrogeological zonation along the 2D cross section passing through the two wells. The model can be directly applied to other wells for estimating hydrogeological zonation along other cross sections. Let t_j be the seismic travel time of the j-th raypath. Let K_i be the indicator of high conductivity zones (1—yes and 0—no) at pixel-i. Let S_i be the inverse of seismic velocity at pixel-i. Let vector θ be unknown parameters associated with petrophysical models. Variables σ_1 and σ_2 represent the standard deviations of

travel time measurement errors and petrophysical model errors, respectively. The Bayesian model is given by:

$$f(\{K_i\},\{S_i\},\theta,\sigma_1,\sigma_2 \mid \{t_j\}) \propto \prod_j f(t_j \mid \{S_i\},\sigma_1) \bullet \prod_i f(S_i \mid K_i,\theta,\sigma_2) \bullet f(\{K_i\}) \bullet f(\theta) \bullet f(\sigma_1) \bullet f(\sigma_2), \quad (2)$$

where "$\propto$" represents "proportional to." Therefore, Equation 2 is correct up to a normalizing constant, which is not needed for the method that we use to solve this problem.

Equation 2 is a coupled, complex statistical model, which considers both geophysical and hydrogeological parameters as random variables. Our goal is to estimate each individual unknown variable using the joint distribution function defined in Equation 2. The Bayesian model used in the first case study is a special case of this model. In that case, geophysical data at each pixel are considered as hard data, petrophysical relationships are known, and measurement errors of travel time are not considered. Consequently, we decouple the estimation problem and solve it pixel by pixel. However, in this case, because many unknown variables are correlated and the number of variables involved is very large, conventional methods (such as analytical and optimization based methods) are limited. We use Markov chain Monte Carlo (Gilks et al., 1996) methods to solve all unknown variables. We generate many samples for each individual variable by running a constructed Markov chain from given starting values. From those samples, we obtain estimates of each unknown variable, including its mean, variance, and even probability density function. Estimation results (Figure 2) suggest that over the study area, a localized high permeability zone has laterally varying thickness and geological dip, which is consistent with observations from field tracer experiments.

Conclusions

The two case studies demonstrated that geophysical data are useful for providing information for hydrogeological characterization under varying degree of heterogeneity. However, for complex hydrogeological systems (such as fractured media), where regression based petrophysical models cannot be developed with confidence, sophisticated Bayesian models can be used. This model is more general because it allows physical based petrophysical relationships and forward models to be incorporated into the estimation process.

Acknowledgments

The authors wish to thank D. Watson, T. Mehlhorn, and P. Jardine at the Oak Ridge National Laboratory, and M. Fienen at Stanford University for providing flowmeter and geological data for the second case study.

References

Chen, J., S. Hubbard, and Y. Rubin, Estimating the hydraulic conductivity at the South Oyster site from geophysical tomographic data using Bayesian techniques based on the normal linear regression model, Water Resources Research, 37(6), 2001.

Daley, T., E. Majer, and J. Peterson, Crosswell seismic imaging in a contaminated basalt aquifer, Geophysics, in press.

Ellefsen, K., P. Hsieh, and A. Shapiro, Crosswell seismic investigation of hydraulically conductive, fractured bedrock near Mirror Lake, New Hampshire, Journal of Applied Geophysics, 50, 2002.

Gilks, W., S. Richardson, and D. Spiegelhalter, Markov Chain Monte Carlo in Practice, Chapman & Hall/CRC, New York, 1996.

Hubbard, S. and Y. Rubin, Hydrogeological parameter estimation using geological data: a review of selected techniques, Journal of Contaminant Hydrology, 45, 2000.

Hubbard, S. and Y. Rubin, Study institute assesses the state of hydrogeophysics, Eos Trans., 51, 2002.

Hubbard, S., J. Chen, J. Peterson, E. Majer, K. Williams, J. Swift, B. Mailloux, and Y. Rubin, Hydrogeological characterization of the South Oyster bacterial transport site using geophysical data, Water Resources Research, 37(10), 2001.

Hyndman, D., J. Harris, and S. Gorelick, Coupled seismic and tracer test inversion for aquifer property Characterization, Water Resources Research, 30(7), 1994.

Mailloux, B., M. Fuller, T. Onstott, J. Hall, H. Dong, M. DeFlaun, S. Streger, R. Rothmel, M. Green, D. Swift, and J. Radke, The role of physical, chemical, and microbial heterogeneity on the field-scale transport and attachment of bacteria, Water Resources Research, 39(6), 2003.

Majer, E., J. Peterson, T. Daley, B. Kaelin, J. Queen, P. D'Onfro, and W. Rizer, Fracture detection using crosswell and single well surveys, Geophysics, 62(2), 1997.

Peterson, J., Pre-inversion corrections and analysis of radar tomographic data, Journal of Environmental and Engineering Geophysics, 6, 1—18, 2001.

Pyrak-Nolte, L., L. Myer, N. Cook, and P. Witherspoon, Hydraulic and mechanical properties of a natural fractures in low permeability rock, Proceeding of the 6th International Congress on Rock Mechanics, edited by G. Herget and S. Vongpaisal, Balkema, Rotterdam, The Netherlands, 1987.

Scheibe, T., and J. Chien, An evaluation of conditioning data for solute transport prediction, Ground Water, 41(2), 128—141, 2003.

Watson, D., W. Doll, T. Gamey, J. Sheehan, and P. Jardine, Demonstration and interpretation of improved geophysical profiling methods at the DOE NABIR Field Research Center, Ground Water, in press.

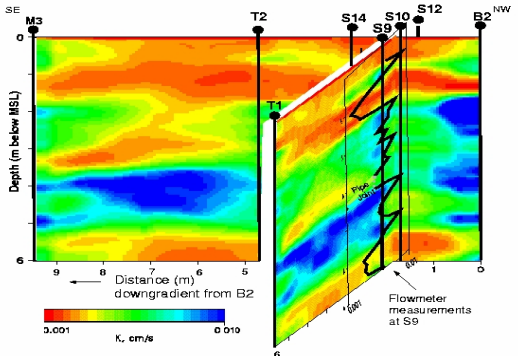

Figure 1. Estimated mean log-conductivity along geological dip and strike directions at the granular porous media site.

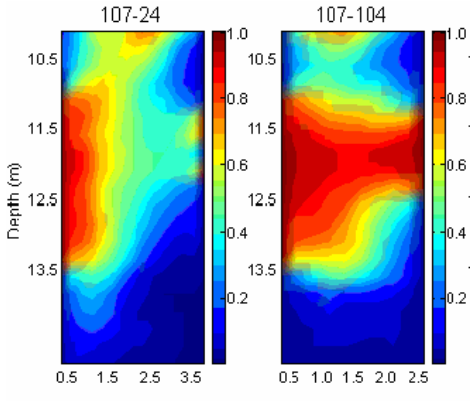

Figure 2. Estimated probability of high permeability zonation along two transects at the fractured media site.